Alignment of the ATLAS Silicon Tracker and measurement of the top quark mass.

Carlos Escobar Ibáñez
Tesis Doctoral
May 2010

Universitat de València
Facultat de Física
Departament de Física Atòmica, Molecular i Nuclear

Abstract

The Large Hadron Collider (LHC) era started with its first proton-proton collisions produced in November 2009 at the CERN laboratory. In the coming decade, the high energy physics program will be dominated by the LHC and its experiments. Discoveries such as the Higgs or supersymmetric particles are some of the dreams that hopefully the LHC will bring us. This thesis is framed within the ATLAS experiment, which is one of the four large detectors located at the LHC.

The work presented in this thesis is divided in two parts. The first part is dedicated to the alignment of the ATLAS silicon tracking detector using the Globalχ^2 algorithm, which is the actual baseline algorithm. It covers performance studies with Monte Carlo samples with a realistic detector description, with real cosmic rays as well as with LHC collisions at 900 GeV. The main achievement was the production of a set of alignment constants for the real ATLAS detector. Those constants were obtained from the alignment of real cosmic ray data, and they were used to successfully reconstruct the first ever LHC collisions. The second part is devoted to perform preliminary studies of the top quark mass measurement based on Monte Carlo samples at 14 TeV, and considering 1 fb^{-1} of integrated luminosity. In particular, the semileptonic decay channel of the $t\bar{t}$ pair is used to perform a kinematic fit based on the Globalχ^2 formalism. Actually, the main goal of this part is the introduction this method, though the achieved performance is evaluated, discussing its advantages, limitations and, of course, results.

La **Dra. Carmen García García** y el **Dr. Salvador Martí i García**, Profesora de Investigación e Investigador Científico, respectivamente, del CSIC

CERTIFICAN:

Que la presente memoria, "***Alignment of the ATLAS Silicon Tracker and measurement of the top quark mass***", ha sido realizada bajo nuestra dirección en el *Departament de Física Atòmica, Molecular i Nuclear* de la *Universitat de València* por Carlos Escobar Ibáñez y constituye su tesis para optar al grado de doctor en Física por la *Universitat de València*.

Y para que conste, en cumplimiento de la legislación vigente, firmamos el presente Certificado en Burjassot a 14 de Mayo de 2010.

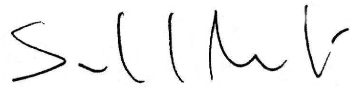

Dra. Carmen García García

Dr. Salvador Martí i García

Declaration

This dissertation is the results of my own work, except where explicit reference is made to the work of others, and has not been submitted for another qualification to this or any other university.

Carlos Escobar Ibáñez

Contents

Introduction

The end of 2009 has brought the first hadron collisions at the CERN laboratory, announcing the new Large Hadron Collider (LHC) era. The extraordinary energy densities of the LHC collisions will allow to study the instants just after the Big Bang, when the Universe was created. Hence, this has opened great expectations towards new and amazing physics knowledge.

This thesis summarizes a work framed in the commissioning phase of one of its experiments, ATLAS, though the first LHC collisions have been used.

A brief overview of the Standard Model, which is the actual theory that describes elementary particles and their interactions, is given in chapter 1. Also, the expected measurements that the LHC should provide within this theory are presented, being the Higgs boson the most wanted piece. Though the Standard Model has proven to be very successful up to the electroweak energy scale (i.e. $O(100)$ GeV), many questions and problems still remain. Trying to answer these open issues, physicists have developed some theories that go beyond the Standard Model. A review of the most promising models is given in this chapter.

In chapter 2, a general description of the experimental facilities at CERN laboratory and related with the LHC is given. In particular, the LHC and its experiments are presented. After that, an overview of the ATLAS experiment is discussed since this work has been developed with this detector.

The next three chapters are devoted to introduce and discuss all the relevant issues about the alignment of the ATLAS tracker. Since the first part of this thesis is related to the Silicon Tracker alignment, an overview of this subdetector is given in chapter 3. Also, the event data model is presented, where the tracking and trigger systems play a relevant role. Chapter 4 introduces the Globalχ^2 formalism, which is the actual baseline algorithm for the alignment of the ATLAS Silicon Tracker. A detailed mathematical description of the method is presented. Finally, many important issues that one should know about Globalχ^2 algorithm, such as how to solve a huge system of linear equations, are discussed in chapter 5.

Chapters 6 and 7 are devoted to present the results and the alignment performance achieved using simulated data and real data, respectively. Exercises based on realistic simulations provided the perfect testbed to develop and prove the Globalχ^2 algorithm within the full ATLAS software system. These tests evaluated the ATLAS physics performance and the capability to produce alignment constants for the reconstruction of physics events within 24h after data taking. At the same time, once cosmic ray data taking started as part of the commissioning phase, an alignment using the Globalχ^2 algorithm of the Silicon Tracker was performed using this data. The achieved alignment performance was good enough to estimate the expected ATLAS performance for early data. At the end, the first LHC collision events has provided enough data to perform an alignment based on this early LHC data, collected during 2009.

The second part of the thesis is dedicated to the top physics and it is contained in two chapters. Chapter 8 presents a brief introduction to the top quark physics with comments on the first measurements which are expected to be achieved with the early data as well as the possible earlier discoveries. This chapter also discusses the $t\bar{t}$ production and decay channels and the performance of the top quark reconstruction using Monte Carlo data. Chapter 9 assumes 1 fb^{-1} of accumulated data at low luminosity (10^{33} cm^{-2} s^{-1}) and at the nominal LHC energy ($\sqrt{s}$ = 14 TeV) to measure the mass of top quark using the semileptonic decay channel. The novelty of the mass reconstruction is the use of a kinematic fit based on the Globalχ^2 formalism. The application of this method within this context is presented and its advantages, limitations and results are discussed.

The final chapter, number 10, contains all the conclusions reached in this thesis.

1
Theoretical motivations

Since the dawn of mankind, human beings have been looking for the origin of their own existence. In that sense, physicists have been contributing to explain and understand some simple and fundamental questions: What is matter made of? What are the most fundamental particles of Nature? Which are the most fundamental interactions? What are the laws that describe the known Universe? What is the origin of the Universe? What makes life possible? etc...

Physicists have worked hard to find and identify the most basic building blocks of matter. Meanwhile they also treat to identify and understand the forces that govern their interactions. The first documented discussion goes back to the ancient greek times with Leucippus and Democritus (5th century BC), when the humans asked themselves what were they made of. They guessed that the world around us was built of little basic blocks, called atoms[1], because they maintained the impossibility of dividing things *ad infinitum*. So, the atoms were considered the most fundamental particles for many years but in the past century, it was experimentally discovered that atoms consist of even smaller particles, namely protons, neutrons and electrons. Afterwards, it was found that even those protons and neutrons consist of smaller particles, called quarks. Up to now, no evidence has been found that these blocks consist of yet smaller particles, therefore they are called "elementary" nowadays. In that sense, the interplay between theory and experiment has been crucial for the development of knowledge, and this interplay has bring to us the actual theory.

1.1 The Standard Model

During 1960's and 1970's, particle physicists developed a successful universal theory which describes in a coherent way the properties and interactions of the fundamental particles at the smallest known scales (up to 10^{-18} m) and up to energies of $\mathcal{O}(200\text{ GeV})$ [1], this theory is

[1] Atoms (Greek: $\alpha\tau o\mu o\varsigma$) means something that cannot be divided, i.e., "the smallest indivisible particle of matter".

called Standard Model (SM). It is a gauge quantum field theory which describes the interaction of point-like particles with half-integer spin, called fermions (particles described by the Fermi-Dirac statistics), whose interactions are mediated by integer spin gauge bosons (particles which obey the Bose-Einstein statistics). These bosons arise from the requirement of local gauge invariance[2] of the fermion fields and are manifestations of the symmetry group which for the SM is $SU(3)_C \otimes SU(2)_L \otimes U(1)_Y$ [1].

There are three generations or families of leptons and three of quarks, all of them being fermions. On the one hand, leptons interact by the electroweak force only and there are three leptons with charge -1, the electron (e), the muon (μ) and the tau (τ), and three electrically neutral, the neutrinos (ν_e , ν_μ and ν_τ). On the other hand, quarks carry also an additional charge-like, known as *color*, which is the charge of the strong interaction. There are three quarks with electric charge +2/3 (up (u), charm (c) and top (t)), and three with electric charge -1/3 (down (d), strange (s) and bottom (b)). Only the first generation, i.e. (u,d) and (e, ν_e) are found in ordinary matter. The quark model was first postulated independently by physicists Murray Gell-Mann and George Zweig in 1964 though the first evidence for up quarks was found in deep inelastic scattering experiments at Stanford Linear Accelerator Center (SLAC) [2] in 1968 and the latest discovered quark was the top which was found in 1995 by the Collider Detector at Fermilab (CDF) experiment at Fermilab (FNAL) [3].

In addition, there are five fundamental bosons, the photon (γ) which mediates electromagnetism, the W and Z bosons (directly observed at the CERN Super Proton Synchrotron (SPS) collider [4]) which mediate the weak force, the gluon which mediates the strong force and the Higgs boson which would explain the difference between the massless photon and the relatively massive W and Z bosons through the Spontaneous Symmetry Breaking (SSB) mechanism. Figure 1.1 shows a sketch of the fundamental SM particles and table 1.1 shows a summary of their experimentally measured properties [5].

Hadron is the name of a non-elementary particle which is built of quarks held together by the strong force. Moreover, the hadrons are sub-classified in *baryons* and *mesons* depending if they are formed by three or two quarks, respectively. Mathematically, quarks are triplets of the $SU(3)_C$ gauge group and it has been mentioned they carry color charges which are responsible for their participation in the strong interaction (Quantum ChromoDynamics theory (QCD)). The corresponding gauge bosons and force carriers of the strong force are called *gluons*. Eight-vector gluons mediate this interaction and these gluons carry color charges themselves (thus self-interacting) and they are supposed to be massless within the SM. On the one hand, quarks are never observed freely, they are always confined in bound states (i.e. in hadrons since they are color singlets). This property is known as *color confinement*. It is due to the fact that gluons, that are color charged, interact with each other, leading to an increase of the strong coupling constant (i.e. QCD coupling denoted by α_S) at large distances. On the other hand, at small distances (i.e. at high energy) the strong coupling constant decreases and therefore quarks and gluons can be understood as free particles (property known as *asymptotic freedom*). In that freedom state, quarks can exchange gluons which can produce addition $q\bar{q}$ pairs. Finally, the interaction between all these quarks and gluons can produce collimated groups of hadrons in the direction of the parent quark (so-called jets).

[2]The "gauge invariance" concept is a simple idea based in classical physics where the equations must remain invariant under a translation of the coordinate system. This is just a fancy way of saying that there are no absolute positions. Therefore, gauge theories are theories based on the idea that symmetric transformations can be performed locally as well as globally.

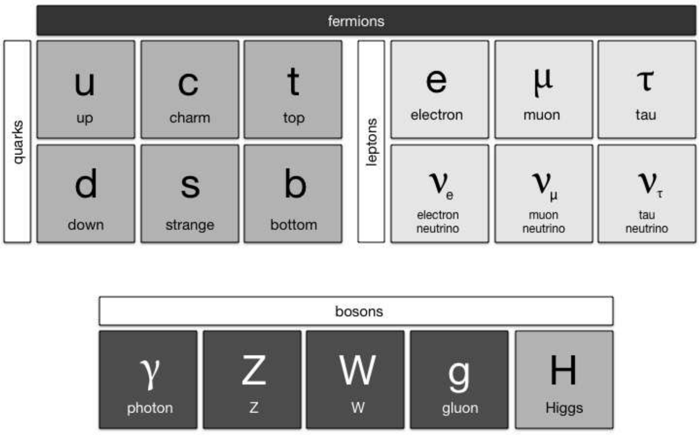

Figure 1.1: *Fundamental particles of the Standard Model.*

Family	Subfamily	Name	Symbol	Mass	Electric Charge	Spin
Fermions	Leptons	electron	e	0.511 MeV	-1	1/2
		muon	μ	105.7 MeV	-1	1/2
		tau	τ	1.777 GeV	-1	1/2
		electron neutrino	ν_e	< 2 eV	0	1/2
		muon neutrino	ν_μ	< 0.17 MeV	0	1/2
		tau neutrino	ν_τ	< 15.5 MeV	0	1/2
	Quarks	up	u	1.5 to 3.3 MeV	2/3	1/2
		charm	c	1.27 GeV	2/3	1/2
		top	t	171.2 GeV	2/3	1/2
		down	d	3.5 to 6.0 MeV	-1/3	1/2
		strange	s	104 MeV	-1/3	1/2
		bottom	b	4.20 GeV	-1/3	1/2
Bosons		photon	γ	$< 1 \cdot 10^{-18}$ eV	$< 5 \cdot 10^{-30}$	1
		W	W	80.398 GeV	± 1	1
		Z	Z	91.188 MeV	0	1
		gluon	g	0 (< MeV)	$SU(3)_C$	1
		Higgs	H	> 114.4 GeV	0	0

Table 1.1: *Properties of the fundamental Standard Model particles [5].*

Moreover, the particles interact with each other through four fundamental interactions or forces (see table 1.2): the electromagnetism, the weak interaction, the strong interaction and the gravitation. Every observed physical phenomenon is explained by these interactions and their magnitude and behavior vary greatly. These interactions are:

- **Strong**. In the SM, QCD is its quantum representation and it holds quarks together in hadrons and affects particles that have color charge, i.e. quarks and gluons. Gluons carry color charges themselves which makes that they are self-interacting. This limits the range of this interaction to 10^{-15} m (which is the diameter of a medium sized nucleus).

- **Electromagnetic**. This interaction occurs between particles that have an electrical charge. Fundamentally, both magnetic and electric forces are manifestations of an exchange force involving the exchange of photons (γ). The quantum approach to the electromagnetic force is called Quantum ElectroDynamics theory (QED). Since the photon is a massless boson, it and therefore also the interaction have infinite range which obeys the inverse square law.

- **Weak**. This interaction is described by the EW and it is responsible for radioactive decays, and for nuclear fusion in the sun. It is mediated by the $W^\pm$ and Z bosons. These particles have very large masses (~ 80 GeV/c^2 and ~ 91 GeV/c^2, respectively) which severely limits the strength and range of the interaction to 10^{-18} m which is about 0.1% of the diameter of a proton (this is the reason of its name "weak").

- **Gravity**. This interaction affects all particles and it is described by the General Relativity (GR). It has infinite range (obeying an inverse square law) as the hypothetical graviton (G), which is supposed to be its massless mediator.

Although the electromagnetic and the weak interactions appear very different at low energies, they are indeed two different aspects of the same force. The ElectroWeak (EW) interaction gives a unified description of both forces.

Interaction	**Theory**	**Mediators**	**Coupling Constant (Strength)**	**Range (m)**
Strong	QCD	g	$\alpha_S = 1$	10^{-15}
Electromagnetic	QED	γ	$\alpha = 1/137$	∞
Weak	EW	$W^\pm$, Z	$\alpha_W = 10^{-6}$	10^{18}
Gravitation	GR	G	$\alpha_g = 6 \cdot 10^{-39}$	∞

Table 1.2: *Fundamental Interactions.*

Formally, the SM theory is described by a Lagrangian ($\mathcal{L}$) that is invariant under transformations that correspond to gauge symmetries. These symmetries translate, in fact, into the three fundamental interactions. Moreover, $\mathcal{L}$ has terms for each individual particle type which describe its kinematics and interactions, but no mass terms. But, as has been pointed out, this can be solved through the Higgs mechanism (SSB) which breaks the EW part of the theory, giving masses to the particles. Thus is how the Higgs mechanism appears into the mathematical description of the SM, where its Lagrangian is:

$$\mathcal{L} = \partial_\mu \phi^\dagger \partial^\mu \phi + \frac{1}{2}\mu^2|\phi|^2 - \frac{1}{4}\lambda^2|\phi|^4$$

being ϕ a complex scalar field which generates the masses of the gauge bosons and the fermions.

Although the SM is a beautiful theory and arguably the most precisely tested, everything cannot be explained through the SM. The Large Electron Positron[3] (LEP), the Stanford Linear Collider[4] (SLC) and Tevatron[5] have established that the physics is really understood up to energies of $O(200)$ GeV. Now, one should see beyond and the physics should be understood at the LHC energies (TeV scale) where the Higgs boson could be found and the SM problems (see section 1.1.2) could be solved. Moreover, ATLAS and CMS physicists will investigate the behavior of known particles, including the W and Z bosons and top and bottom quarks and any discrepancy from the predicted measurements will point to a weakness in the SM.

1.1.1 Standard Model measurements in the LHC experiments

The LHC physics program is quite precisely defined, mainly based on proton-proton collisions (up to $\sqrt{s}$ =14 TeV) though also with short running periods with heavy-ion collisions (Pb-Pb collisions at $\sqrt{s}$ =1150 TeV). Although many LHC physics studies emphasize discoveries and the validation of new theories, there are an enormous number of measurements to be made in the SM realm. The following subsections describe the SM program at LHC.

1.1.1.1 Minimum bias studies

In general, inelastic processes will dominate as the LHC is a high energy hadron collider. These processes are characterized by multiple production of secondary mesons and baryon-antibaryon pairs and they are overpowered by small momentum transfers, i.e. soft collisions, with suppression of particle scattering at large angles. The final states arising from these soft collisions which are called minimum bias, represent by far the majority of the p-p interactions. The average number of such interactions per beam crossing is ~ 2 at low luminosity[6] (10^{33} cm^{-2} s^{-1}) and ~ 23 at high luminosity (10^{34} cm^{-2} s^{-1}). Minimum bias interactions have previously been studied at the CERN Intersecting Storage Rings (ISR), SPS and Tevatron colliders and based on these results, Monte Carlo (MC) models have been tuned to generate predictions for the LHC conditions (using generators like PYTHIA [6], etc).

Figure 1.2 shows the total cross section (σ_{tot}) and cross sections of individual SM processes (left axis) and expected event rates at a luminosity of 10^{33} cm^{-2} s^{-1} (right axis) for hard scattering processes as a function of the invariant mass. The σ_{tot} can then be written as $\sigma_{tot} = \sigma_{elas} + \sigma_{sd} + \sigma_{dd} + \sigma_{nd}$ where these cross-sections are elastic (σ_{elas}), single diffractive (σ_{sd}), double diffractive (σ_{dd}) and non-diffractive (σ_{nd}), respectively. The minimum bias events are the non-single diffractive (NSD) inelastic events, i.e. $\sigma_{nsd} = \sigma_{dd} + \sigma_{nd}$. At $\sqrt{s}$ =14 TeV, these cross sections are $\sigma_{elas} \approx 7.9 \cdot 10^7$ nb, $\sigma_{sd} \approx 1.1 \cdot 10^7$ nb, $\sigma_{dd} \approx 1.0 \cdot 10^7$ nb and $\sigma_{nd} \approx 5.5 \cdot 10^7$ nb [7] (estimated using PYTHIA).

[3] LEP was an electron and positron circular collider (up to $\sqrt{s}$ =210 GeV during 1996-2000) built in the tunnel where the LHC is nowadays. Up to now, it is the most powerful lepton accelerator ever built.

[4] The SLC was a linear electron and positron collider ($\sqrt{s}$ =90 GeV) at SLAC. It was designed to study the Z boson.

[5] The Tevatron is a proton and antiproton ($p\bar{p}$) collider which explores the TeV scale ($\sqrt{s}$ =1.96 TeV). Placed in Fermilab (Chicago, Illinois), it is a 6.28 km ring and therefore the highest energy particle collider in the world until collisions begin at the LHC.

[6] The luminosity gives the number of collisions in a cm^2 and in a second. It will be formally defined in the next chapter as it is an accelerator parameter.

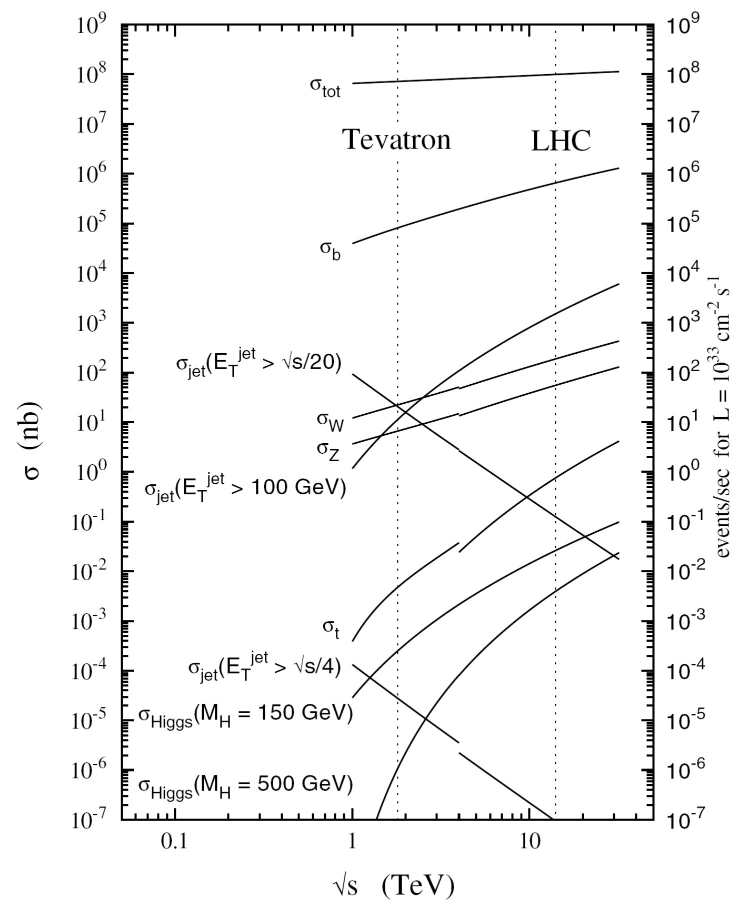

Figure 1.2: *Predictions of total cross section (σ_{tot}) and cross sections of individual SM processes (left axis) and expected event rates at a luminosity of 10^{33} cm^{-2} s^{-1} (right axis) for hard scattering processes as a function of the invariant mass, pointing out the LHC and Tevatron energy range [8].*

1.1.1.2 Electroweak measurements

Interesting physics events are extremely rare compared to soft interactions. Taken another look to figure 1.2 one see that the production of W bosons at LHC has a $\sigma_W \sim 1.5 \cdot 10^2$ nb while the minimum bias cross-section (σ_{mb}) is $\sim 6.5 \cdot 10^7$ nb, i.e. σ_W is 10^5 times smaller than σ_{mb}. Despite this difference, gauge bosons and gauge boson pairs will be abundantly produced at the LHC. The large statistics and the high center-of-mass energy will allow many precision measurements to be performed which will include high order perturbative corrections, which should improve significantly the precision achieved by LEP, SLC and Tevatron. Thus, precise measurements on the W boson and Z boson masses and on the top quark mass will constrain the mass of the SM Higgs boson as they are fundamental parameters of the SM and they are also related to other parameters of the theory. Figure 1.3 shows a consistency SM test where the relationship between the W boson mass and the top quark mass is used to constrain the SM Higgs mass. Moreover, the actual excluded regions, by LEP and Tevatron, for the Higgs mass are shown at 68% confidence level (CL). These precision EW measurements will allow to extensively test the consistency of the SM and therefore its validity.

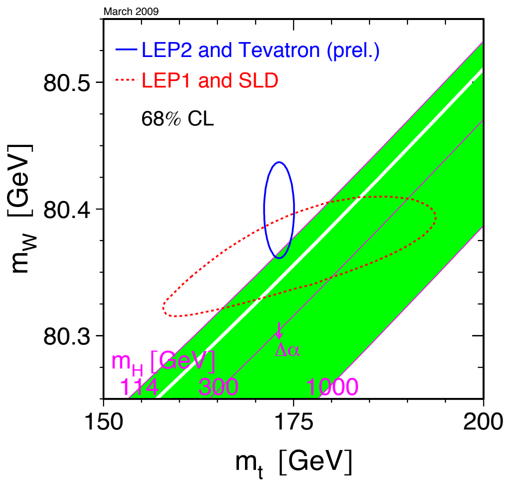

Figure 1.3: *Consistency SM test where the relationship between the W boson mass and the top quark mass is used to constrain the SM Higgs mass. Furthermore, the actual excluded regions, by LEP and Tevatron, for the Higgs mass are shown at 68% confidence level (CL) [9] [10].*

1.1.1.3 B-physics

The rate of B-hadron production at the LHC will be also very large due to the high cross-section for b quark production (from figure 1.2, $\sigma_b \approx 5 \cdot 10^6$ nb). It is expected that about one collision in every hundred will produce a b quark pair, being the B-event rate higher than in any other accelerator. The goal of the B-physics program is to test the SM with precision measurements of B-hadron decays: studies on $\mathcal{CP}$ violation in B-meson decays, measurements of B_s^0 oscillations and rare B-decays. If there are observations of measurable effects they would be clear signs of new physics beyond SM.

1.1.1.4 Top physics

The LHC will be a top quark factory since $\sim 8 \cdot 10^6$ $t\bar{t}$ pairs will be produced after 1 fb^{-1} of integrated luminosity. The total cross section of the $t\bar{t}$ production ($\sigma_{t\bar{t}}$), at next-to-leading order, is predicted to be ~ 800 pb at $\sqrt{s} = 14$ TeV. The $t\bar{t}$ pairs will be generated by hard processes, $gg \to t\bar{t}$ and $q\bar{q} \to t\bar{t}$. At the LHC the first process will dominate (90% for the gluon fusion and

10% for the $q\bar{q}$ annihilation). Thus, a very large variety of top physics studies will be possible. The top quark mass is an essential parameter of the SM as it is the only known fundamental fermion with a mass close to the EW scale and therefore new physics may be discovered in either its production or decay.

The most recent combined measurement of the top quark mass from the Tevatron experiments, CDF and DØ, using data from Run I and Run II is M_t = 173.1 ± 0.6 (stat) ± 1.1 (syst) GeV/c^2 [9]. With the expected large number of top quark pairs events at the LHC, the uncertainty in the measurement of top quark mass will be completely dominated by systematic errors. The top quark mass reconstruction will be possible with early LHC data. This was one of the main motivations of this work and it will be extensively discussed in the second part of this thesis (see chapters 8 and 9).

The large mass of the top quark implies that this quark would tend to couple strongly to other massive particles. Therefore, determining whether the top quark has the couplings and decays predicted by the SM provides a sensitive probe of physics beyond the SM. In addition, top quark events are the dominant background in many searches for new physics at the TeV scale. Then, high precision measurements and a very high understanding of its production rate and properties will be required.

1.1.1.5 Standard Model Higgs searches

As the Higgs boson has not been discovered yet the SM is nowadays incomplete. This is why Higgs hunting is one of the main goals of the LHC which will search in a wide variety of decay channels. The technical problem is that one does not know the mass of the Higgs boson itself. In figure 1.4 one can see how the branching ratios (BR) of the decay channels depend on the Higgs mass [11]. Although b quark pair production is the dominating decay channel at small Higgs boson masses, it will be hard to disentangle the Higgs signal in this channel from the large background from QCD processes. A cleaner signature and better signal to background ratios are achieved in the decay of the Higgs boson to two photons, two Z or W$^\pm$ pair, respectively. As a result, the discovery potential for a light Higgs boson (i.e. a Higgs with a mass window of 115-130 GeV/c^2) is the highest in the di-photon decay channel, while at higher masses the decay into the two Z or W$^\pm$ pair are the discovery channels. The important di-photon channel leads to high demands on the design of the electromagnetic calorimeter, where the photon energy is measured. The searches for the Higgs decaying to heavy gauge bosons, which then decay leptonically, set demands on the transverse momentum resolution of the tracking devices and on muon identification.

However, most of these decay channels suffer from their very small production rate and from very large QCD backgrounds. Excellent detector performance in terms of energy and momentum resolution and unprecedented particle identification capabilities are required.

1.1.2 Problems of the Standard Model

So far, the SM has been very successful explaining the data from different experiments. However, there are good reasons for expecting new physics beyond the SM. The most important problems within the SM are:

- The SM does not unify the strong and EW forces. Although the strong interaction is described by the SM is not as good described as the EW force. Is the Grand Unifying

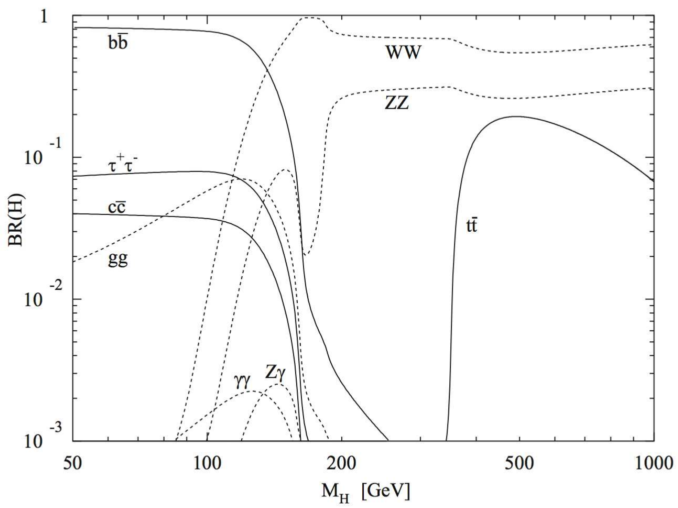

Figure 1.4: *Branching ratios for Higgs boson decay as a function of the Higgs boson mass [11].*

Theory (GUT) that really unifies these forces. The Georgi-Glashow model[7] [12] was the first model assuming a broken SU(5) symmetry which incorporates $SU(3)_C \otimes SU(2)_L \otimes U(1)_Y$. But this theory had also experimental problems because GUTs allow proton decays and its lifetime depends on the GUT scale. Very precise experiments have put lower limits on the proton lifetime and up to now no proton decays has been observed, implying that at least the proton lifetime is longer than the one predicted by GUT. Furthermore, gravity is not included. Therefore, new theories should be proposed.

- A key feature of the SM is the SSB mechanism of the EW symmetry group $SU(2)_L \otimes U(1)_Y$ which explains the generation of W, Z, quark and lepton masses. An attempt to describe this is the Higgs mechanism which leads to the predicted existence of a massive neutral scalar boson, the Higgs boson (H). The problem is that the Higgs boson is the only fundamental particle predicted by the SM which has not yet been experimentally discovered. The Higgs boson was directly searched for at the LEP experiments and a Higgs mass below 114 GeV/c^2 was excluded at the 95% CL. Nowadays, the production of a SM Higgs boson with mass between 160 and 170 GeV/c^2 has also been excluded at the 95% CL by the Tevatron experiments (CDF and DØ) at $\sqrt{s}$=1.96 TeV [13]. Figure 1.5 shows the 95% CL exclusion limit as a function of the SM Higgs mass.

- Another problem of the SM is the hierarchy problem which is the huge gap between two fundamental scales of physics: the EW scale ($\Lambda_{EW} \sim 10^2$ GeV) and the Planck scale ($M_P \sim 10^{19}$ GeV) where the gravitational interaction becomes important.

  One of the consequences is that, if no new physics exists between these two scales, and therefore the SM is valid up to the Planck mass, then the Higgs mass diverges, unless it is

[7]The Georgi-Glashow model was proposed by H. Georgi and S. Glashow in 1974.

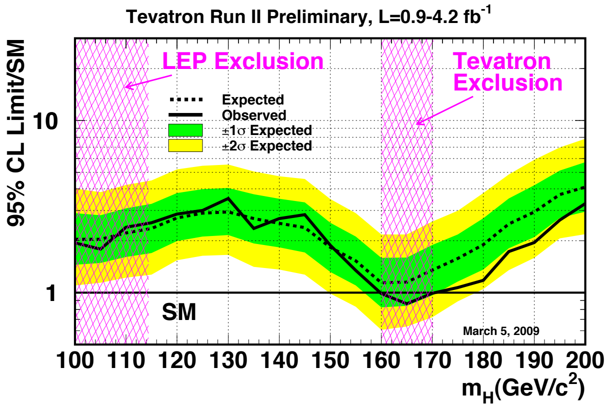

Figure 1.5: *Combined CDF and DØ upper limits (at 95% CL) on SM Higgs boson production with up to 4.2 fb^{-1} of data of Tevatron Run II [13].*

unnaturally fine tuned. The observable Higgs mass is composed of a bare mass (M_{H0}) and radiative corrections (δM_H). The leading term of the radiative corrections is quadratically dependent on the coupling constant of the corresponding interaction [14] and on the cut off energy (Λ), which can be associated to the Grand Unification Theory (GUT) scale ($\Lambda_{GUT} \sim 10^{16}$ GeV). Then, the radiative correction term has to be subtracted from the bare mass squared but only if the bare mass squared is know to 24 digits precision (to compensate almost the divergent corrections) a Higgs with M < 1 TeV/c^2 results at the EW scale i.e. $\mathcal{O}(100)$ GeV. The "solution" of this problem, which is know as the *fine tuning problem* of the SM, is extremely unnatural. Anyway, the necessity of this fine tuning does not mean that the SM is incorrect in the sense of falsifying observations but nevertheless indicate that a piece is missing.

Anyhow, if this large difference between the only fundamental energy scale in nature and the energy scale of the Higgs mass (and of the rest of the elementary particles in general) exists, the SM can be considered as a low-energy effective theory of a more general unified theory, where the lower energy scale would follow from symmetry breaking processes implied and described in the theory.

Some possible solutions come from several theories which use different techniques to explain this hierarchy. The most relevants are SUSY and extra dimensions which will be discussed in the next section. Anyhow, the hierarchy problem indicates that the SM is incomplete already at the TeV scale where LHC will be able to explore, and therefore new physics should either stabilize the Higgs mass, or, if the Higgs does not exist, provide mass to the weak gauge bosons by some other yet unknown mechanism. Both possibilities will of course be known at the same time once this energy range is explored.

- The reason why fermions are grouped in three generations [5], as well as the fact that we have different masses of each generation is not described by the SM and therefore it is still unknown.

- The down-quark mass eigenstates, i.e. d', s', b', which couple to the gauge bosons are not the same as the eigenstates for the weak interaction. In other words, the quark mass eigenstates are not the same as the physical masses, with mixing between the three generations of quarks, which in the SM is parametrized by the Cabibbo-Kobayashi-Maskawa (CKM) matrix (V_{CKM}).

$$\begin{pmatrix} d' \\ s' \\ b' \end{pmatrix} = V_{CKM} \begin{pmatrix} d \\ s \\ b \end{pmatrix} \quad \longrightarrow \quad V_{CKM} = \begin{pmatrix} V_{ud} & V_{us} & V_{ub} \\ V_{cd} & V_{cs} & V_{cb} \\ V_{td} & V_{ts} & V_{tb} \end{pmatrix}$$

  where V_{ij} is the matrix element coupling the i^{th} up-type quark to the j^{th} down-type quark. The problem is that although this is already parametrized in the SM it is not explained.

- Dark matter and dark energy observed in cosmology cannot be explained within the SM and possible candidates are proposed by new models beyond the SM.

- The neutrinos are massless particles in the SM, however from different experiments it is known that these particles have masses. The new models have to explain this fact.

All these problems need new theories which should solve them. Actually, these theories will be subject of extensive searches and studies at the LHC experiments and they are included in the LHC physics program.

1.2 Beyond the Standard Model

The most promising theories beyond the SM are Supersymmetry (SUSY) and Extra Dimensions theories although there are even more ambitious models. Some of them will be briefly described in this section.

1.2.1 Supersymmetry

Generally nature can be understood and explained using symmetries and this is the base of Supersymmetry model (SUSY). SUSY is a gauge theory which generalizes the space-time symmetries of quantum field theory that transforms fermions into bosons and viceversa. In other words, all SM particles have supersymmetric partners with the same quantum numbers but with the spin differing by $\pm 1/2$. This is done through a supersymmetric operation on the representation of a particle belonging to one group which transforms it to a member of the other group and thus changing the spin but not the mass and where couplings to other particles remain the same. For example, the electron with spin 1/2 would have a bosonic partner with spin 0 and the same mass in a supersymmetric world. Then, SUSY partners of quarks and leptons are called squarks and sleptons and they have spin=0 and the SUSY partners of force mediators (γ, W, Z, g, G) are known as photinos, winos, zinos, gluinos which have spin=1/2 and gravitinos which has spin=3/2. Therefore, an exact unbroken SUSY predicts that a particle and its superpartner have the same mass. But as these superpartners have not been observed, if SUSY exists, it must be broken allowing the sparticles to be heavy. ATLAS and CMS physicists will search for the range of particles predicted by the varied theories of SUSY: squarks, gluinos, supersymmetric Higgs, etc... which may have existed in the very early and high-energy Universe.

SUSY is one of the best candidates which will solve many of the SM problems, if it exists:

- SUSY also modifies the running of the SM gauge couplings "just enough" to provide the *Grand Unification* (SUSY unifies all the four forces: strong, weak, electromagnetic and gravitational interactions) which is governed by the Planck energy scale, $M_{Planck} \sim 10^{19}$ GeV (where the gravitational interactions become comparable in magnitude to the gauge interactions). Moreover, it is possible that SUSY will ultimately explain the origin of the large hierarchy of energy scales from the W and Z masses to the Planck scale, the so-called gauge hierarchy. The stability of the gauge hierarchy in the presence of radiative quantum corrections is not possible to maintain in the SM as was explained in the previous section, but can be maintained in supersymmetric theories. Figure 1.6 (a) and (b) show the inverse of running coupling constants being α_1^{-1}, α_2^{-1} and α_3^{-1} referred to the electromagnetic, the weak and the strong interaction, respectively. In particular, figure 1.6 (a) shows the case for the SM where the unification of the gauge couplings is not achieve and figure 1.6 (b) shows the same case but for the Minimal Supersymmetric SM (MSSM)[8] where unification of the coupling contants occurs at $\Lambda_{GUT} \sim 10^{16}$ GeV.

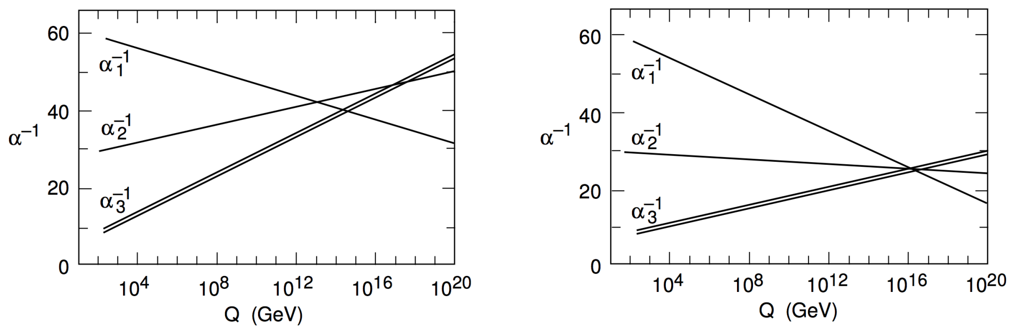

(a) *Running of coupling constants in the SM*

(b) *Running of coupling constants in the MSSM*

Figure 1.6: *Inverse of running coupling constants where α_1^{-1}, α_2^{-1} and α_3^{-1} are the inverse of the electromagnetic, the weak and the strong interaction, respectively. The thickness of the lines represent the errors in the couplings constants. As can be seen in figure (a) in the SM the unification of the gauge couplings is not possible. Within the Minimal Supersymmetric SM (MSSM), unification of the coupling contants occurs at $\Lambda_{GUT} \sim 10^{16}$ GeV at a Supersymmetry (SUSY) scale of O(1) TeV.*

- Adding the supersymmetric partner particles leads to radiative corrections which cancel

[8] The MSSM is the simplest possible supersymmetric extension of the SM with a minimal particle content.

the quadratically divergent terms of the Higgs mass, hereby solving the fine tuning problem of the SM.

- Another argument which supports the existence of SUSY is the fact that nowadays there are experimental evidences that about 90% of the matter of the universe is undetectable by its emitted radiation. This matter is called dark matter[9] and it cannot be explained within the SM. It is tempting to attribute the dark matter to the existence of a neutral stable thermal relic (i.e., a particle that was in thermal equilibrium with all other fundamental particles in the early universe at temperatures above the particle mass). Remarkably, the existence of such a particle could yield the observed density of dark matter if its mass and interaction rate were governed by new physics associated with the TeV-scale. Then, if the lightest SUSY particle is stable, it would be a dark matter candidate although not it will not be the unique.

1.2.2 Extra dimensions theories

One of the proposals to solve these problems, such as the hierarchy problem, comes from Extra Dimensions models which add more space dimensions on top of the usual three spatial dimensions. In these theories, the SM fields are confined to a 4-dimensional manifold, while gravity can propagate through all the dimensions, so-called "bulk". Considering a D-dimensional space-time with D = 4 + d, where d is the number of extra spatial dimensions, the SM fields would be localized on a 4-dimensional subspace. Then, the observed weakness of the gravitational interaction (compared with the other interactions) is then not fundamental, it is merely a consequence of the existence of the extra dimensions. Moreover, these extra dimensions are assumed to be curled up, such that their small size explains why they would be invisible to us in everyday life.

These extra dimensions may become detectable at very high energies. If extra dimensions exist they could manifest themselves in the ATLAS and CMS detectors through the appearance of new particles or an energy leak from our four dimensions into the others. Another possible consequence of extra dimensions may be the creation of microscopic black holes at the LHC [15]. The extra dimensions cause the Schwarzschild radius of the black hole to be much larger than expected from 4-dimensional gravity. Then, the black hole could be formed if the relative impact parameter of two colliding partons is smaller than the Schwarzschild radius. The increased strength of gravity in the bulk space-time means that quantum gravity effects would be observable in the TeV energy range reachable by the LHC. The generated black holes would decay semi classically via Hawking radiation emitting high energy SM particles. These events could be detected and they would be characterized by a high multiplicity of high energy objects in the final state. ATLAS and CMS will look for Extra Dimensions signatures and they also will exploit the potencial to discover such black holes.

There is a special theory which predicts seven undiscovered dimensions of space, the String theory. In this theory the basic idea is that fundamental particles would be tiny vibrating strings instead point-like objects. Then, each of their vibrational modes will carry a set of quantum numbers that corresponds to a distinct type of fundamental particle. The theory has many detractors however, the fact that string theory can include all "older" theories of physics, have led

[9] Dark matter is hypothetical matter that is undetectable by its emitted radiation, but whose presence can be inferred from gravitational effects on visible matter.

many physicists to believe that such a connection is possible.

1.2.3 M-theory

Now, mixing SUSY and Extra Dimensions one obtain a superstring theory which is in fact the first candidate for the theory of everything. This theory is known as M-theory[10] where a way to describe all the known natural forces (gravitational, electromagnetic, weak and strong) and matter (quarks and leptons) in a mathematically complete system could be achieved. To do that, string theories have to include more general objects than strings, called branes and also fermions and supersymmetry. Einstein was one of the first to propose that such a unified field theory must exist, and in fact he struggled for most of his later life to find this theory without success. From the experimental point of view, since superstring theories are supersymmetric, one can expect to see supersymmetry appearing in the low-energy approximation. Because of that, string theorists are waiting for the LHC collisions. Thus, tiny black holes, energy disappearing into higher dimensions in ATLAS or CMS could be interpreted as evidences of these theories.

1.2.4 The Unknown

In addition to the previous described theories, physicists will use ATLAS and CMS to search for unpredicted signals and phenomena since the LHC will reach up to unexplored energies. This is why many scientists expect some surprises from the discovery machine.

[10]The "M" is not specifically defined, but is generally understood in the academic field to stand for "membrane" although is also related with "mother", "master", "mathematical" or even "mystery".

2
The discovery machine

The largest international scientific project in the world nowadays is the LHC which includes a hadron accelerator, four huge detectors at its four collision points and a Computing Grid project which maintains the data storage and analysis infrastructure. The LHC, which is placed in Geneva (Switzerland), is the first accelerator that will explore extensively the TeV scale. It will provide answers to questions like the origin of the particle masses through the Higgs boson. Moreover it will also look for experimental proofs of new and exciting theories like Supersymmetry or Extra Dimensions. Therefore, it is understandable that physicists refer the LHC since the "the discovery machine" as it has been designed to reveal new frontiers of knowledge. Thus, physicists of the XXI century stand in front the LHC like the middle age explores in front of the *Terra Incognita*.

2.1 CERN

In 1952 a council was created by 11 european countries, being one of the first common european projects after the World War II. It was named *Conseil Européen pour la Reserche Nucléaire* (CERN) [16]. Two years later, this council became a laboratory which was placed in Switzerland. Today it is the world's largest particle physics laboratory with 20 european member states and many other countries which are involved in different ways such as Japan, United States, Russia, India, etc.

The first accelerator built at CERN was a 600 MeV SynchroCyclotron (SC) in 1957. Since then, a large list of accelerators and facilities have been built there. Then, in 1971 the Intersecting Storage Rings was built which was an early version of the actual colliders. Later on, the SPS, which was built in 1981, produced the massive W and Z bosons confirming the unification of electromagnetic and weak theories. At the end of 1989 the Large Electron-Positron Collider (LEP) came on the air which was the largest machine of its kind, housed in a 27 km long circular tunnel which nowadays houses the LHC. It performed very precise measurements of the Standard Model. One of its most important achievement was the measurement of the number of fermionic families. Meanwhile the technology was highly improved with state-of-the-art Research and Design (R&D) programs. For example, the invention of the multi-wire proportional chamber in the 60s or the World Wide Web (WWW) in the 80s were developed at CERN.

Nowadays, the CERN accelerator complex, shown schematically in figure 2.1, consists in several machines interconnected with higher and higher capabilities, i.e. particle beams are injected from one to the next, bringing them to higher energies successively.

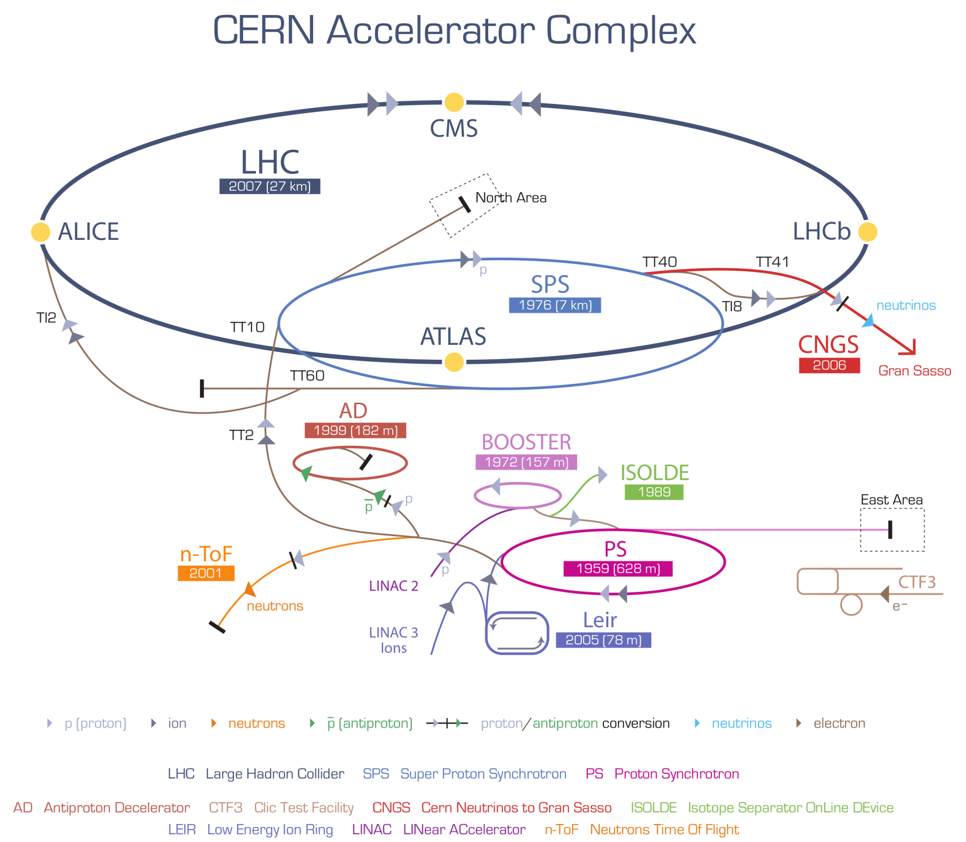

Figure 2.1: *CERN accelerator complex at LHC times (not to scale).*

2.2 Large Hadron Collider

The LHC [17] is the world's most powerful particle accelerator at this moment which produces two proton beams in opposite directions with an energy up to 7 TeV each (i.e. center of mass collision energies of up to 14 TeV) and with a design luminosity [1] ($\mathcal{L}$) up to 10^{34} cm^{-1} s^{-1}.

2.2.1 The accelerator

In order to accelerate the proton beams, the existing CERN accelerator complex is used. The path that the beams follow is shown in figure 2.1 and it starts at the LINACs (LINear ACceletators). There are two kinds of LINACs, LINAC2 which accelerates protons and LINAC3 which accelerates ions. Then, circular accelerators are used to increase the particle energy since they can speed up particles with much less physical space than linear accelerators and they can accelerate two different beams with opposite charge at the same time with a single magnetic field. The maximum energy which can be transferred to the beams is directly related with the accelerator radius ($p_T = 0.3qBr$ being p_T the transverse momentum of the particles, B the strength of the magnetic field and r the radius of curvature of the circular accelerator). This is why from LINACs, the beams are injected into the Proton Synchrotron Booster (PSB), later on through the Proton Synchrotron (PS) and after that into the SPS. The SPS is a 7 km length collider which is operated only as accelerator (only one beam at a time), leading proton beams up to 450 GeV. Finally, the last injection is in the LHC ring which is, nowadays, the longest hadronic accelerator ever built by the human beings with its 27 km long. In addition, the LHC is 100 m below ground as can be seen in the simulation of figure 2.2. Furthermore, the LHC will also collide Pb ions.

Each beam has an internal structure as they are arranged in bunches separated in space which condense up to $1.1 \cdot 10^{11}$ protons. Collisions will have a rate of 40 MHz (i.e. one collision every 25 ns). In table 2.1 one can find a summary of the main LHC parameters.

The LHC has 1232 superconducting dipole magnets which curve the beams through the LHC ring. This kind of magnets uses twin bore magnets which consist of two sets of coils and beam channels within the same mechanical structure and cryostat. This design comes to the fact that the LHC magnets have to accelerate two beams of equally charged particles but in opposite directions and there are obvious room constraints (there were not enough room for two separate magnets in the LHC tunnel). These magnets can generate bipolar magnetic field up to 8.33 T thanks to their superconductivity capabilities and they fill more than 66% of the LHC ring. The coils are made of niobium-titanium (NbTi) which is a material that allows to reach the superconducting regime when it is at 1.9 K. A detailed cross section of a dipole magnet is shown in figure 2.3 where all its parts are depicted.

In addition, there are also 392 quadrupolar magnets for beam focusing and beam corrections and also sextupole, octupole and decapole magnets mainly for compensating the systematic non-linearities.

Finally, in the LHC ring there are four detectors placed just at the LHC collision points. A brief description is given in the next section.

[1] The luminosity $\mathcal{L}$ is an accelerator parameter which depends on the number of particles per bunch in the two colliding beams, N_1 and N_2, on the bunch crossing frequency f and on the bunch area. Thus, assuming a gaussian transverse particle bunch profile, the $\mathcal{L}$ is defined as:

$$\mathcal{L} = \frac{1}{4\pi}\frac{N_1 N_2}{\sigma_x \sigma_y} f N_b$$

where N_b is the number of bunches and σ_x and σ_y are the gaussian widths in the horizontal and vertical plane of the bunch respectively.

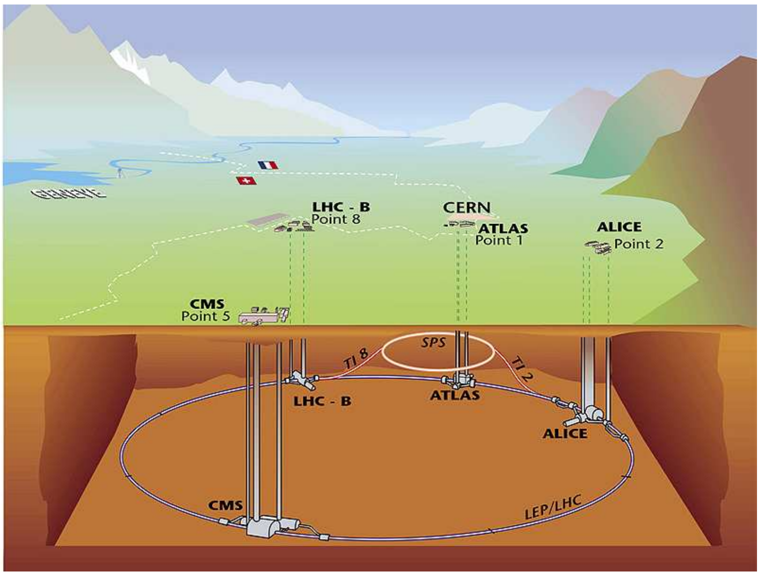

Figure 2.2: *Representation of the LHC ring with its detectors and all its services.*

LHC Parameter	p-p Collisions	Pb-Pb Collisions
Beam energy	7 TeV	570 TeV (2.76 TeV/u)
Injection energy	450 GeV	1.774 TeV/u
Center of mass energy ($\sqrt{s}$)	14 TeV	1250 TeV
Luminosity ($\mathcal{L}$)	10^{34} cm^{-2} s^{-1}	10^{27} cm^{-2} s^{-1}
Frequency (f)	40 MHz	10 MHz
Bunch separation	25 ns	100 ns
Number of particles per bunch (N_b)	$1.1 \cdot 10^{11}$	$7 \cdot 10^{7}$
Average size of a bunch	7.5 cm	
Average radius of a beam	16 μm	
Beam current	0.56 A	
Collision regions	3 (2 for high $\mathcal{L}$)	1
Circumference length	26.66 km	
Radius	4.24 km	
Number of dipole magnets	1232	
Length of the dipole magnets	14.3 m	
Nominal magnetic field (B)	8.33 T	
Number of quadrupole magnets	392	
Total mass	27.5 tons	

Table 2.1: *Main parameters of the LHC collider [17].*

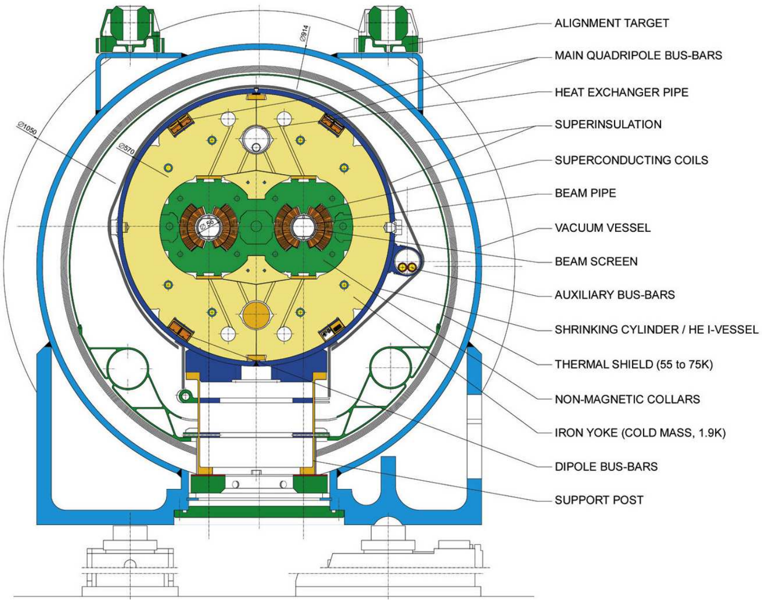

Figure 2.3: *Cross section of a LHC dipole magnet design showing its components [17].*

2.2.2 LHC Experiments

The LHC has four huge detectors (2.4) which are located in their corresponding caverns although six experiments take placed. These experiments are:

- **A Toroidal LHC ApparatuS (ATLAS)** [18]: It is a general purpose experiment for high luminosity (up to 10^{34} cm^{-2} s^{-1}) which will perform high precision measurements on SM parameters and the Higgs boson search. It is the largest LHC detector with 44 $\times$ 25 m^2 and 7000 tons. It has two magnets, one 2 T solenoid for the inner detector and a toroid which generates up to 6 T/m for the muon spectrometer.

- **Compact Muon Solenoid (CMS)** [19]: It is the other general purpose experiment for high luminosity (up to 10^{34} cm^{-2} s^{-1}) and it has the same discovery potential as ATLAS although its hardware and software design is different. It is smaller than ATLAS (21 $\times$ 15 m^2) although heavier with 12500 tons and it can generate an unique non-linear magnetic field up to 4 T.

- **Large Hadron Collider beauty (LHCb)** [20]: This experiment is a low luminosity experiment (up to 10^{32} cm^{-2} s^{-1}) for measuring the parameters of $\mathcal{CP}$ violation in the interactions of b-hadrons. The LHCb detector is a single arm spectrometer stretching for 20 metres along the beam pipe, with its subdetectors stacked behind each other like books on a shelf.

- **A Large Ion Collider Experiment (ALICE)** [21]: This experiment is focused on heavy

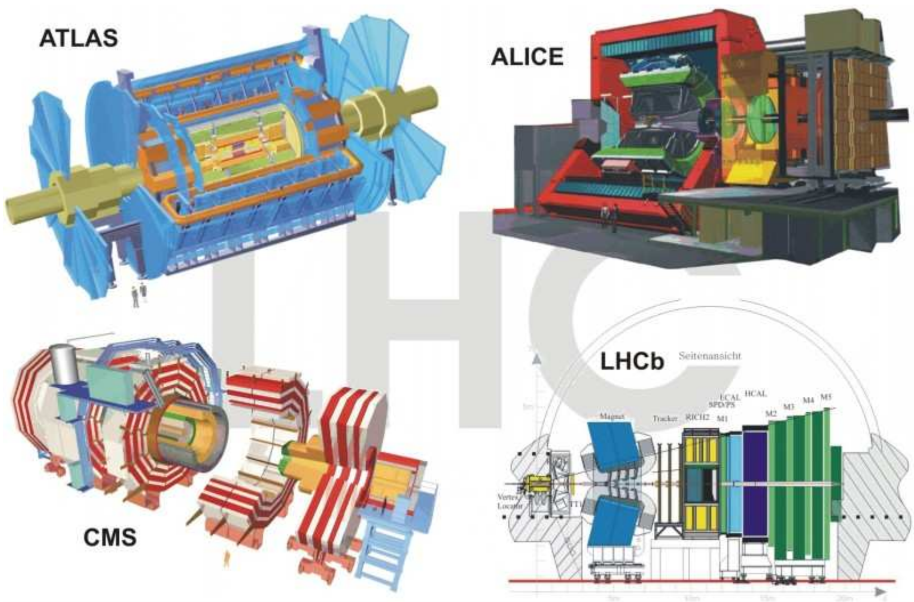

Figure 2.4: *Graphical simulation of the some LHC experiments (not to scale).*

ions and quark-gluon plasma studies. It will work at a peak luminosity of 10^{27} cm^{-2} s^{-1} for nominal Pb-Pb ion operation.

- **Total Cross Section, Elastic Scattering and Diffraction Dissociation (TOTEM)** [22]: The aim of this experiment is to measure total cross sections, elastic scatterings at small angles and diffractive processes at the LHC at low luminosities (up to $2 \cdot 10^{29}$ cm^{-2} s^{-1}). It shares intersection point with CMS.

- **Large Hadron Collider forward (LHCf)** [23]: It is a special purpose experiment for low luminosity (up to $2 \cdot 10^{28}$ cm^{-2} s^{-1}) which will study neutral pions produced in the forward region of collisions. It shares cavern but now with ATLAS and it consists of two detectors, 140 m on either side of the intersection point.

2.2.3 LHC Computing Grid

The last piece of the LHC project is its computing model which has the aim of building and maintaining a distributed data storage and analysis infrastructure for the entire community that will use the huge amount of data that the LHC will produce based on Grid technologies. This presents several challenges. One is related with the storage since the LHC will produce roughly 15 PB of raw data annually[2]. Another challenge is the fact that around 6000 scientists

[2] ATLAS will produce ~ 3.2 PB/year of raw data at high luminosity considering that it will see $2 \cdot 10^9$ events/year where each event is ~ 1.6 MB. Moreover, one has to add the processed data (i.e. high-level data) and the Monte Carlo production.

spread over the World will want to access to this huge amount of data to do their analysis almost simultaneously. Moreover this access must be efficient and stable. This project is split in three Grid flavours: LHC Computing Grid (LCG) [24] in Europe, NorduGrid/ARC [25] also in Europe (Nordic countries only) and Open Science Grid (OSG) in the US.

In the LHC distributed computing model there is a hierarchy based on sites called Tiers. Thinking in the LHC data, a primary backup is recorded on tape at CERN which is the unique Tier 0 centre. After the initial processing, this data is distributed to a series of Tier 1 centres (11 sites worldwide) which are large computer centres with sufficient storage and access capacity. The Tier 1 centres make data available to their Tier 2 centres (140 LCG sites worldwide) within their clouds (each Tier 1 defines a cloud), each consisting of one or several collaborating computing facilities, which can store sufficient data and provide adequate computing power for specific analysis tasks. Figure 2.5 shows the geographical distribution of all the LCG sites. Physics groups will access these facilities through their closest Tier 3 computing resources, which can consist from huge local clusters in their universities to even individual laptops. The main goal of this model is that the jobs should run where the requested data is, avoiding long data transmission.

Figure 2.5: *Geographical distribution of all the LCG sites for the LHC project.*

The spanish cloud, which belongs to the LGC flavour, has a multi-experiment Tier 1 placed at PIC (Barcelona) and its distributed Tiers 2: CIEMAT (Madrid) and IFCA (Santander) for CMS, IFIC (Valencia), IFAE (Barcelona) and UAM (Madrid) for ATLAS and UB (Barcelona) and USC (Santiago de Compostela) for LHCb.

2.3 The ATLAS detector

ATLAS is a general purpose experiment designed to realize the main physics goals of the LHC, namely searches for the Higgs boson and for supersymmetric particles. The formal proposal for ATLAS was introduced in 1994 [26] and 10 years later the detector installation in the cavern began [18]. The ATLAS collaboration is quite large with about 2500 physicists scattered around the world.

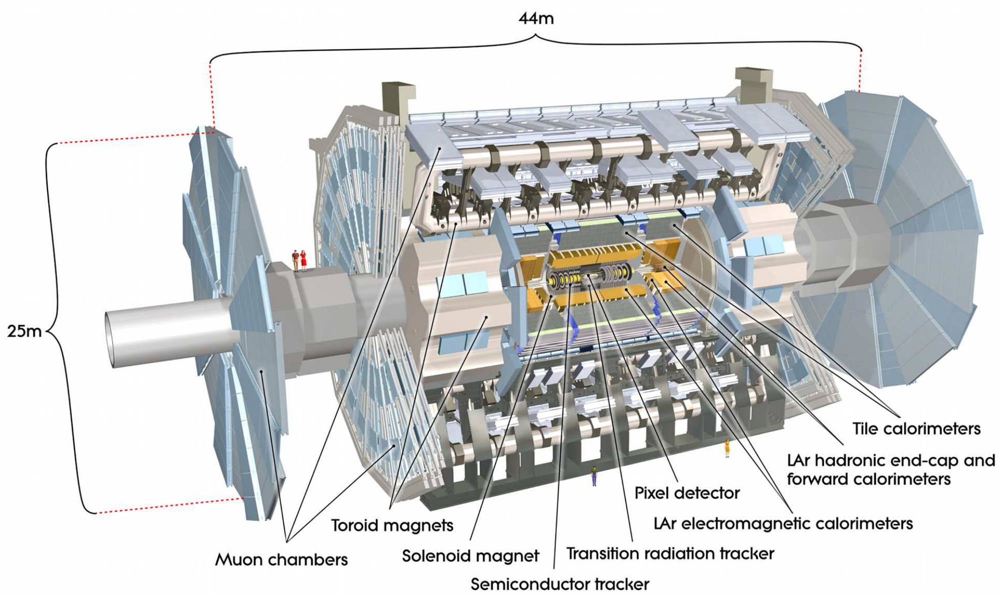

Figure 2.6: *The ATLAS detector with all its subdetectors labelled. Moreover, several human figures, barely visible, are included for a scale reference.*

The ATLAS general layout is fairly typical of a general purpose high energy physics collider detector with cylindrical shape (4π coverage) and layers of subdetectors, being 44 m long and 25 m high. The closest system to the beam pipe is the tracker. It operates embedded in a 2 T magnetic field and consists of silicon-based subdetectors and on drift tubes which is a continuos gaseous detector. This ensures a robust pattern recognition, momentum and charge determination, precise primary and secondary vertex reconstruction as well as particle identification capability with pion separation. Outside the solenoid are the calorimeters. First, the electromagnetic calorimeter uses liquid argon as an ionization medium, with the absorbers arranged in an accordion geometry. It allows the identification and measurement of electrons and photons. Surrounding the latter is the hadronic calorimeter that uses a scintillating tile technology allowing to measure hadronic jets[3] and helps to determine the missing energy. Outside the calorimeters, ATLAS has a large muon spectrometer which performs the measurements of muon momenta. It also includes fast response trigger chambers. Finally, the muon spectrometer rests inside an air

[3] A jet is a narrow cone of particles produced by the hadronization of a quark or gluon.

core toroidal magnetic field, being the outermost part of ATLAS.

2.3.1 Inner Detector

The ATLAS tracker, also known as the Inner Detector (ID) [27], performs the pattern recognition, momentum and vertex measurements together with electron identification, providing a pseudorapidity[4] coverage up to $|\eta| < 2.5$. These capabilities are achieved with a combination of discrete high-resolution semiconductor pixel and strip detectors in the inner part of the tracking volume, respectively the Pixel and the SemiConductor Tracker (SCT), and a straw-tube tracking detector, the Transition Radiation Tracker (TRT), with the capability to generate and detect transition radiation, in its outer part. The ID operates embedded in a 2 T axial magnetic field generated by a solenoid [28]. This magnetic field is used for bending the charged particles and measure their charge and momentum. A three dimensional view of the ID is shown in figure 2.7 where all its subdetectors are labelled together with its size: 6.2 m long and 2.1 m width.

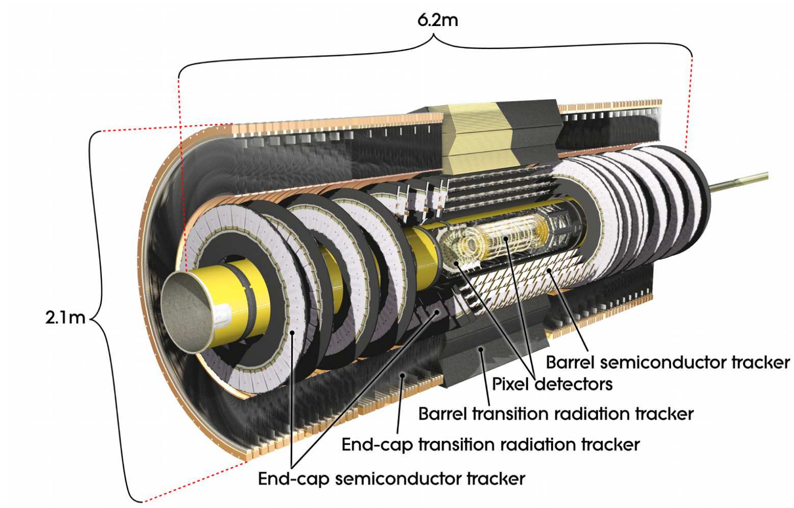

Figure 2.7: *A sketch of the ATLAS inner detector. The pixel detector has three barrel layers and three end-cap discs on each side. The SCT has four barrel layers and nine end-cap discs each. The TRT has three barrel layers and two end-cap wheels on each side.*

Due to the experimental conditions at the LHC, around 1500 charged particles will cross the ATLAS ID every 25 ns at high luminosity (10^{34} cm^{-2} s^{-1}). The ID electronics and all the sensor elements must be fast enough and of course radiation hard. In addition, a very fine granularity is needed to handle the particle fluxes and to reduce the influence of overlapping events. For this purpose the ID has 5832 individual silicon modules (with about 86 million of readout channels).

[4]In experimental particle physics, pseudorapidity (η) is related with the azimuthal angle θ (i.e. it is related with the angle of a particle relative to the beam axis) as follows:

$$\eta = -ln\left[tan\left(\frac{\theta}{2}\right)\right]$$

The Pixel subdetector is based on silicon pixel technology and it is arranged in three cylindrical barrels and three discs on each side of the central barrel. The pixel elements are 50×400 μm^2 resulting in an intrinsic resolution of 10 μm in the transversal direction with a direct 2D readout. This system is design to provide a very high granularity (with 80.4 million channels) as well as high precision set of measurements as close as possible to the interaction point. It consists in three barrels at average radii of 5.05 cm, 8.85 cm and 12.25 cm, and three discs on each side at 49.5 cm, 58.0 cm and 65.0 cm from center of the ATLAS coordinates system, i.e. Z=0 (this is described in chapter 3, section 3.3).

The SCT is a silicon microstrip based detector which is located just after the Pixel detector. The SCT modules are arranged on four barrel layers and nine end-cap discs on each side. It has been designed to provide eight precision measurements via 4 layers of back-to-back silicon microstrip detector modules with a relative 40 mrad stereo angle. There are five sensor topologies, one for the barrel which has parallel strips with 80 μm pitch and 4 for the end-caps with fan-out structure (54.53-90.34 μm pitch). With 80 μm strip pitch on average a SCT module ensures a 17 μm precision in $r\phi$ and its stereo angle of 40 mrad allows 580 μm in z. The SCT has 4088 modules (2112 barrel and 1976 end-cap modules) which means 61 m^2 of silicon sensors with 6.3 million channels.

Finally, the TRT consists of about 300.000 gaseous straw tubes arranged in a barrel and to end-caps on each side of this barrel. It has 176 modules, 73 layers in 3 rings in the barrel region and 2×160 straw planes in 40 four-plane assembly units in the end-cap regions. The TRT gas mixture $Xe/CF_4/CO_2$ (70%/20%/10%) provides an efficient X-ray absorption, a fast charge collection and a stable operation over a sufficient high-voltage range even at high particle rates. Its technology allows to have an intrinsic resolution of 130 μm per straw (i.e. in the direction perpendicular to the wire) where each straw tube has a diameter of 4 mm. From the practical design point of view it has been built to provide, in the barrel region and on average, 36 TRT hits for tracks coming from the interaction point.

2.3.2 Calorimetry

Outside the ID solenoid are the calorimeters which perform energy measurements and particle identification. The Electromagnetic Calorimeter (ECAL) uses liquid argon (LAr) as an ionization medium (it is also known as LAr calorimeter), with the lead absorbers arranged in an accordion geometry [29]. This kind of geometry provides complete ϕ symmetry without azimutal cracks and the lead thickness in the absorber plates is optimized as a function of η in terms of performance in energy resolution. It allows an excellent performance in terms of energy and position resolution as well as in the identification of electrons and photons providing coverage up to $|\eta| < 3.2$. It is surrounded by cryostat as it needs very low temperatures to operate.

Surrounding the latter is the Hadronic Calorimeter (HCAL) with a coverage up $|\eta| < 4.9$ which measures hadronic jets. A sampling technique with plastic scintillator plates (called tiles) embedded in an iron absorber is used for the hadronic barrel tile calorimeter (aslo known as TileCal) [30]. HCAL is separated into a large barrel and two smaller extended barrel cylinders, one on either side of the central barrel. In the end-caps ($|\eta| < 1.6$), LAr technology is also used for the hadronic calorimeters, matching the outer $|\eta|$ limits of end-cap electromagnetic calorimeters. The LAr forward calorimeters provide both electromagnetic and hadronic energy measurements, and extend the pseudorapidity coverage to $|\eta| < 4.9$.

Test beam results reveal that the ECAL will achieve an excellent energy resolution:

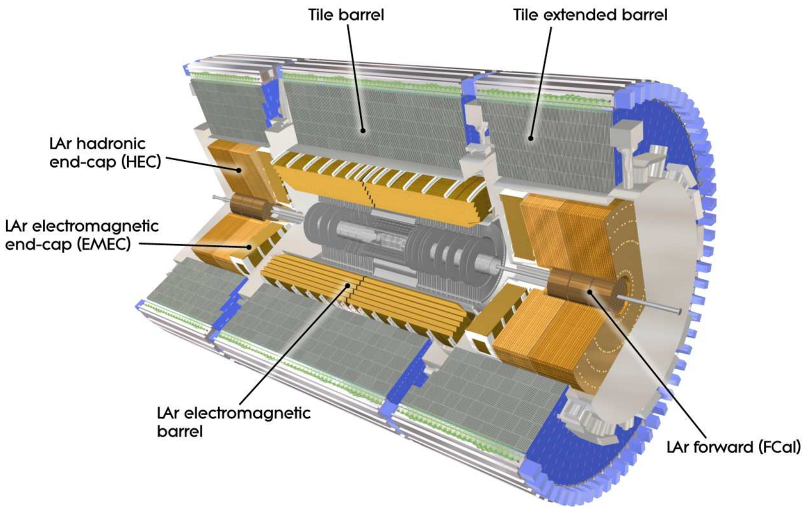

Figure 2.8: *Cut-away view of the ATLAS calorimeter system with its subdetectors labelled.*

$$\frac{\sigma_E}{E} = \frac{11.5\%}{\sqrt{E}} \oplus 0.5\% \quad (E \text{ in GeV})$$

and HCAL will reconstructed jets with an energy resolution:

$$\frac{\sigma_E}{E} = \frac{50\%}{\sqrt{E}} \oplus 3\% \quad (E \text{ in GeV})$$

Finally, a representation of the ATLAS calorimeters can be seen in figure 2.8 where they have a total diameter of 8.46 m and a length of 13.4 m.

2.3.3 Muon System

The outermost detector is the muon spectrometer which defines the overall dimensions of the ATLAS detector [31]. Its layout can be seen in figure 2.9. It consists in four technologies which are the Monitored Drift Tubes (MDT), the Cathode Strip Chambers (CSC), the Resistive Plate Chambers (RPC) and the Thin Gap Chambers (TGC). The former two detectors provide high precision momentum measurements for muons, needed to perform the tracking. The latter two detectors are used for triggering with timing resolution of the order of 1.5-4 ns and bunch crossing identification. The muon spectrometer is designed to achieve a transverse momentum[5] resolution of $\Delta p_T/p_T < 10^{-4}$ for p_T >300 GeV/c. At smaller momenta, the resolution is limited to a few per cent by Multiple Coulomb Scattering (MCS) effects in the magnet and detector structures, and by energy loss fluctuations in the calorimeters.

[5]The transverse momentum is defined as $p_T = psin\theta$, where p represents the momentum and θ is the polar angle in the spherical coordinate system.

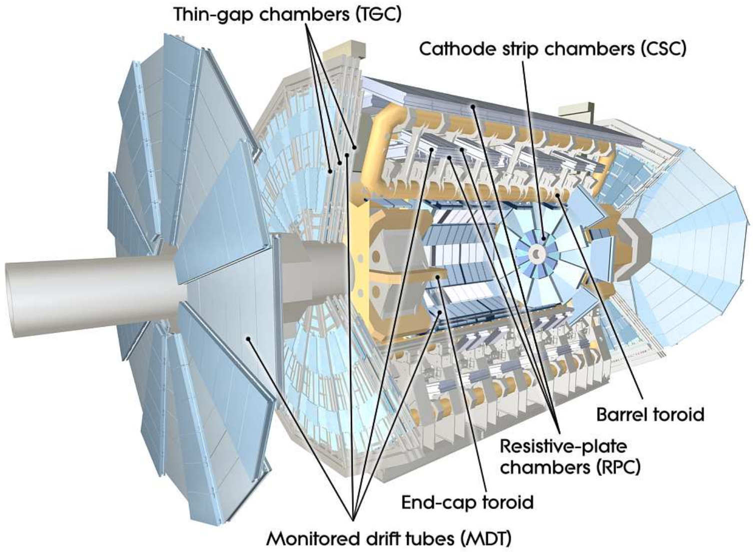

Figure 2.9: *Cut-away view of the ATLAS muon system.*

An air-core toroid system generates strong bending power in a large volume within a light and open structure. MCS effects are thereby minimised, and excellent muon momentum resolution is achieved with three layers of MDT chambers achieving a precision of $\sim$ 50 μm in muon position measurements. This magnetic system as can be seen in figure 2.10 has a barrel (25 m long, with an inner bore of 9.4 m and an outer diameter of 20.1 m) and two inserted end-cap magnets (with a length of 5.0 m, an inner bore of 1.65 m and an outer diameter of 10.7 m).

The barrel toroid consists of eight flat coils assembled radially and symmetrically around the beam axis and the magnetic field provides for typical bending powers of 3 Tm in the barrel and 6 Tm in the end-caps [28]. The end-cap toroid coils are rotated in azimuth by an angle of 22.5^0 with respect to the barrel toroid coils to provide radial overlap, and to optimize the bending power in the transition region.

2.3.4 Trigger System

The LHC proton bunches will collide at a frequency of 40 MHz, i.e. every 25 ns and at the design luminosity of 10^{34} cm^{-2} s^{-1} on average about 23 inelastic proton-proton collisions will be produced at each bunch crossing. Therefore, the trigger system needs to efficiently reject a large rate of background events and still select potentially interesting ones with high efficiency. To deal with this amount of data that these collisions will generate the ATLAS trigger is based on three levels of online event selection as it is shown in figure 2.11.

Each trigger level refines the event selection done by the previous level, applying new criteria. The level-1 trigger (LVL1) [32], which is hardware-based (i.e. it is implemented in custom electronics), is responsible for the first level of event selection, reducing the initial event rate to

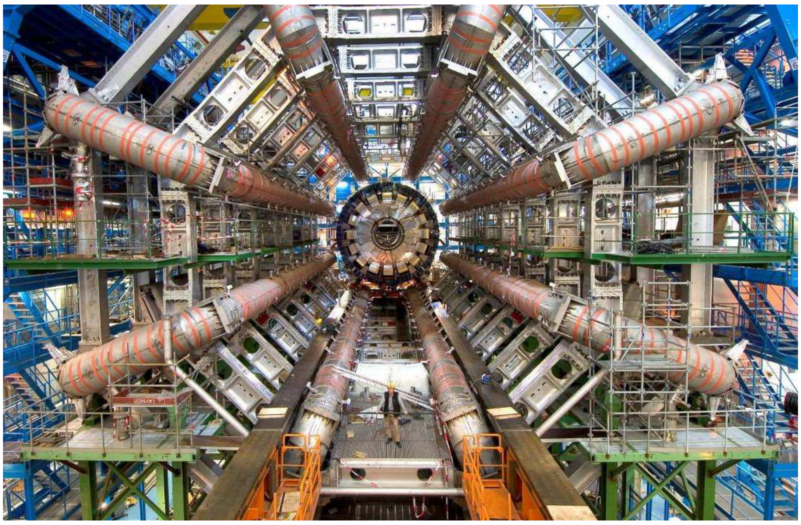

Figure 2.10: *Barrel toroid as installed in the underground cavern.*

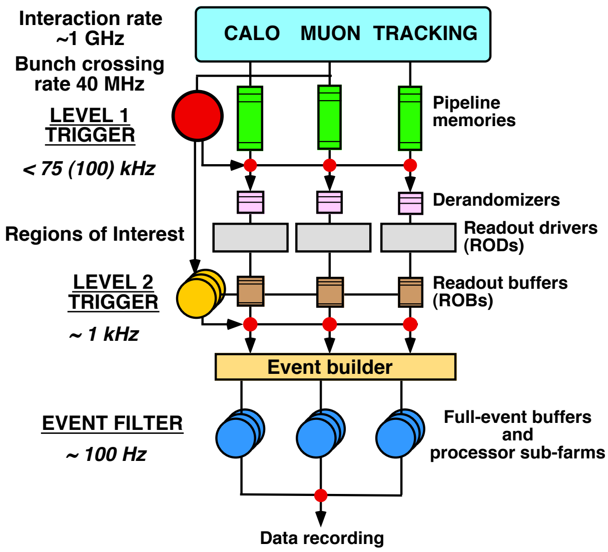

Figure 2.11: *Diagram of the ATLAS trigger/DAQ system showing the 3 trigger levels.*

less than 75 kHz (limited by the bandwidth of the readout system, which is upgradeable to 100 kHz). It uses information from the calorimeters and muon trigger chambers to make a decision on whether or not to continue processing an event in about 2.5 μs. The subsequent two levels are software-based and are collectively known as the High Level Trigger (HLT) [33]. On the one hand, the level-2 trigger (LVL2) decides in $O(10)$ ms if the event should be rejected making use of the Regions of Interest (RoI) provided by the LVL1 data with full granularity from all detectors. On the other hand, the Event Filter (EF) uses offline algorithms to perform its refine selection in $O(1)$ s. The HLT provides the reduction to a final data-taking rate of approximately 200 Hz where each selected event is estimated to have a total size of ~ 1.6 MB. This reduction is possible because the HLT uses seeded, step-wise and fast selection algorithms based on the reconstruction of potentially interesting physical objects like electrons, muons, jets, etc and which can provide the earliest possible rejection of background events.

In the next chapter, the relationship between the trigger system and the alignment procedure will be discussed.

3

The Silicon Tracker and the bases for track alignment

This chapter will treat all the required issues that one has to know before trying to align the ATLAS Silicon Tracker with success. Firstly, a good knowledge of the detector itself is completely necessary. Secondly, one has to know how the ATLAS software works and how the different services are integrated. Finally, the alignment procedure presented in the first part of this thesis has become a software package.

3.1 Motivations: Why the alignment is needed?

The ATLAS detector has been built with high resolution tracking devices such as the ID, the muon chambers and the highly segmented calorimeters which determine particle properties with very good precision. But although one can have the world's best measuring devices, they must be well-calibrated and well-aligned in order to exploit their capabilities.

Talking about the Silicon Tracker, any misalignment of its different detector elements will degrade the track measurements, the pattern recognition and therefore the reconstructed track parameters. Thus, the goal of the alignment is set such that the limited knowledge of the sensors location should not deteriorate the resolution of the track parameters by more than 20% with respect to the intrinsic tracker resolution [26]. This requirement translates into an alignment precision of about 7 μm for Pixels modules, and about 12 μm for SCT modules [34]. The detector degradation translates into a poor physics performance and limited discovery potential of the whole experiment. Then, in order to assure an excellent physics and detector performance, it will be necessary to understand few items [35]:

- Reach an ID alignment accuracy of $\mathcal{O}(10)$ μm in the transverse plane with respect beam direction (also referred as $r\phi$ plane) in order to achieve the maximum hit resolution.

- Understand the solenoid magnetic field to better than 0.02%, to compute correctly the momentum.
- Understand the ID detector material to $\sim 1\%$ of its value, to account for MCS effects.
- Understand the transverse momentum (p_T) resolution to 1%.

Moreover, algorithms which rely on tracks, such as vertex finders and b-tagging algorithms are also affected by misalignments, specially because these misalignments degrade the transverse impact parameter of the tracks (see section 3.4.3 for the track parameters definition), diminishing their efficiency and performance. From MC studies, it was estimated that random misalignments of about 10 μm in the transverse plane of the detector devices will result in a 10% reduction of the b-tagging efficiency at the same fake rate [36]. Furthermore, as these algorithms are used elsewhere in physics analysis, the alignment becomes crucial specially for SM precision measurements and new discoveries [37] [38] [39].

3.2 ATLAS Silicon Detector

As one can imagine one of the most important topics one should know with high detail before align a detector is how it has been built and what are all its characteristics. Thus, this section will discussed the ATLAS Silicon Tracker.

3.2.1 Generalities

The ID is the closest detector to the interaction point in ATLAS and its task is to reconstruct the trajectories of charged particles that are produced in the proton-proton collisions. Its design provides hermetic and robust pattern recognition, excellent momentum resolution and both primary and secondary vertex measurements for charged tracks (the later being needed to identify e.g. B-mesons and converted photons) above a given p_T threshold (nominally 0.5 GeV) and within the pseudorapidity range $|\eta| < 2.5$. It also provides electron identification over $|\eta| < 2.0$ and for a wide range of energies (between 0.5 GeV and 150 GeV). Anyhow, the expected performance which is required at the highest luminosities (10^{34} cm^{-2} s^{-1}) is at the limit of existing technology.

The ATLAS ID layout, which was shown in figure 2.7, was chosen with three different subdetectors based on different technologies:

- A silicon pixel detector, referred simply as the Pixel detector, provides generally three 3-dimensional spacepoints per track (this detector gives two measuring coordinates per hit), allowing spacepoints formation.
- A silicon strip detector, also known as SCT, surrounds the pixel detector and provides at least four 3-dimensional spacepoints (this detector gives one measuring coordinate per hit, but each module has two sides which can be combined in order to build a spacepoint).
- A straw tracker, called TRT, surrounds the other two subsystems and provides a large number of measurements (about 36) in the bending plane (i.e. the transverse plane to the beam pipe).

The pixel and strip detectors are based on silicon as a detection medium. A detailed and careful explanation on how a silicon detector works can be found in reference [40]. These detectors provide a very good granularity and very precise position measurements but they require a lot of material in the form of support structures and cooling pipes. This material has a negative effect on the performance of the tracker [18]. This was one of the main reasons to minimize the material used to build the outermost layer of the ID, being the TRT made of straws filled with a gas mixture.

Moreover, these subdetectors are installed in a solenoid magnet, which provides a magnetic field of 2 T, making possible to measure the momentum of the charged particles, by measuring the curvature of the tracks in the ID. Figure 3.1 shows a plan view of a quarter-section of the ATLAS ID where the exact position and dimensions of each barrel layer and discs of each subdetector are labeled. Also the solenoid and the ID services and patch-panels are shown in that figure. Moreover, ID is contained within a cylindrical envelope of length ± 3512 mm and of radius 1150 mm, within the solenoid [18] which can also be seen in that figure.

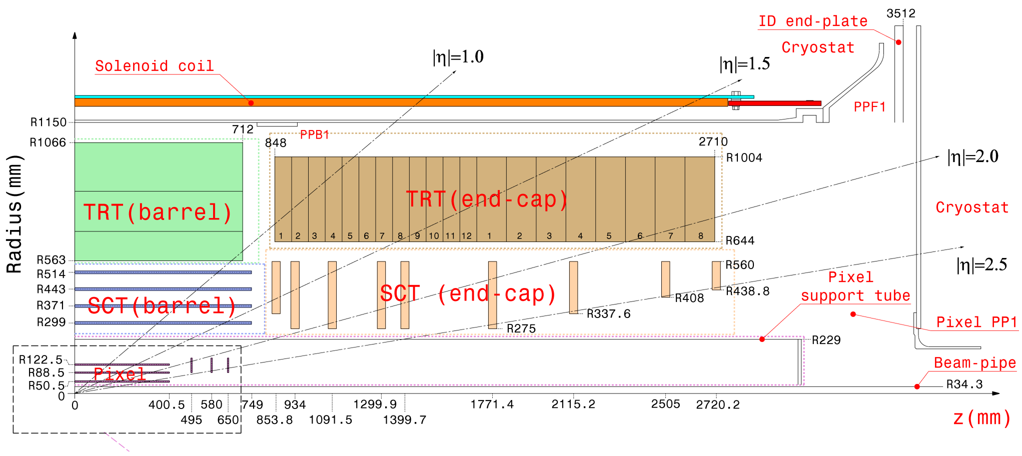

Figure 3.1: *Plan view of a quarter-section of the ATLAS ID showing the exact position of each part of each subdetector as well as their envelopes, patch-panels, services and the solenoid [18].*

Finally, figures 3.2 and 3.3 show nominal positions of each barrel layer and end-cap disc in the radial and transverse plane, respectively. The knowledge of these nominal positions is very important as these are the starting positions for the track-based alignment algorithms.

Since the alignment algorithm proposed in this thesis has been implemented to work so far only with the Silicon Tracker (Pixel and SCT), the following subsections will be focused on these subdetectors.

3.2.2 The silicon Pixel detector

The Pixel detector is designed very close to the collision point to provide a high tracking precision and to find relatively long lived particles such as b-quarks and τ-leptons. Hence, it will receive the higher radiation dose (158 kGy/year or 0.2×10^{15} n_{eq} cm^{-2} per year at high luminosity (10^{34} cm^{-2} s^{-1}) [18] compared with 8 kGy/year for the SCT subdetector).

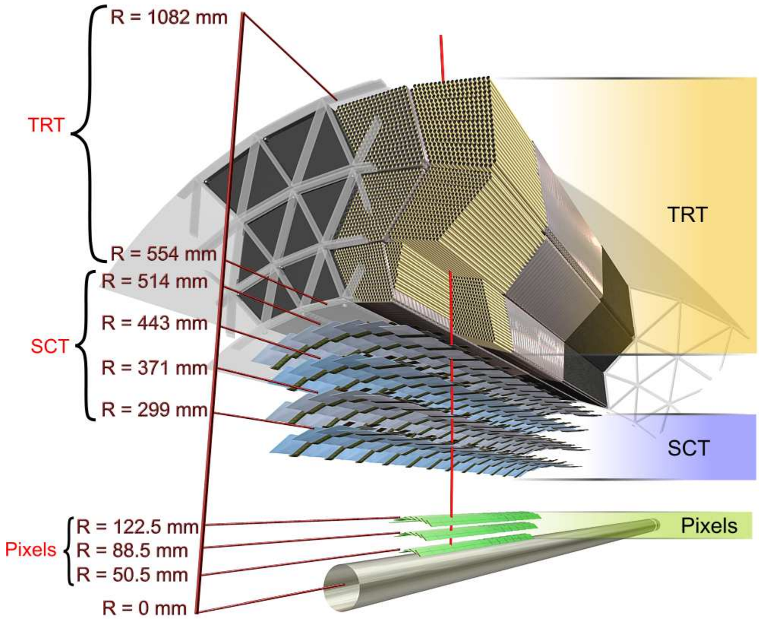

Figure 3.2: *Drawing showing the position of the barrel detectors and structural elements [18].*

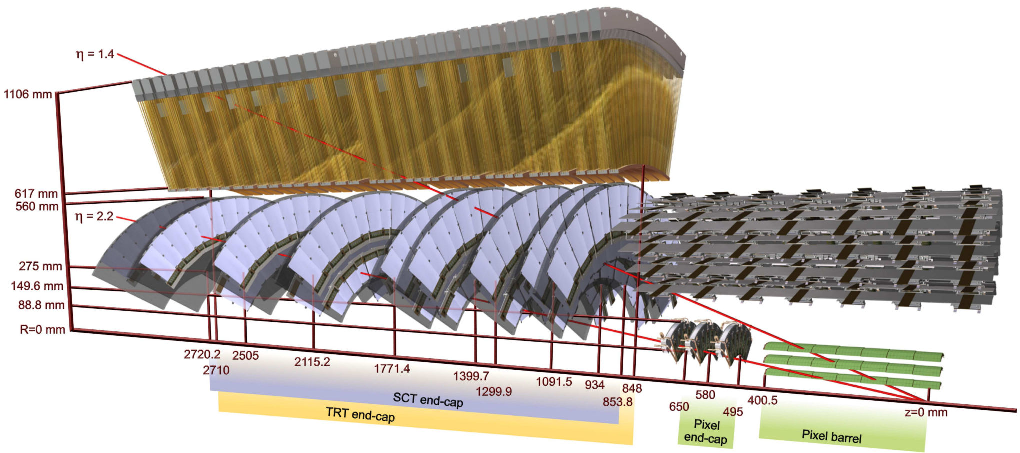

Figure 3.3: *Drawing showing the position of the barrel and end-cap detectors and end-cap structural elements. Tracks will traverse different detector layers depending on their eta [18].*

The detector is made up of three cylindrical layers in the barrel, and three discs each of the forward regions with a coverage of $|\eta|$ <2.5 as figures 3.2 and 3.3 show. Each of these structures consist on 1744 identical pixel modules as the one in figure 3.5, being 1456 in the barrel and 288 in the end-cap discs. Moreover, barrel modules are arranged along *staves* which are carbon-fibre structures (112 staves in total with 13 modules per stave). Figure 3.6 shows a bi-stave structure. These staves are lying parallel to the beam axis but they are inclined by an azimuthal angle of 20^o around the long axis which means that the superposition of two modules in each layer is about 200 μm as can be seen in figure 3.4. Moreover, staves are grouped in half-shells as the one in figure 3.7 and then these structures form the barrel layers. Finally, each end-cap disc contains 24 modules (divided in 8 sectors) per side as shown on figure 3.8. The table 3.1 gives the barrel layers and discs positions, together with the number of modules per structure.

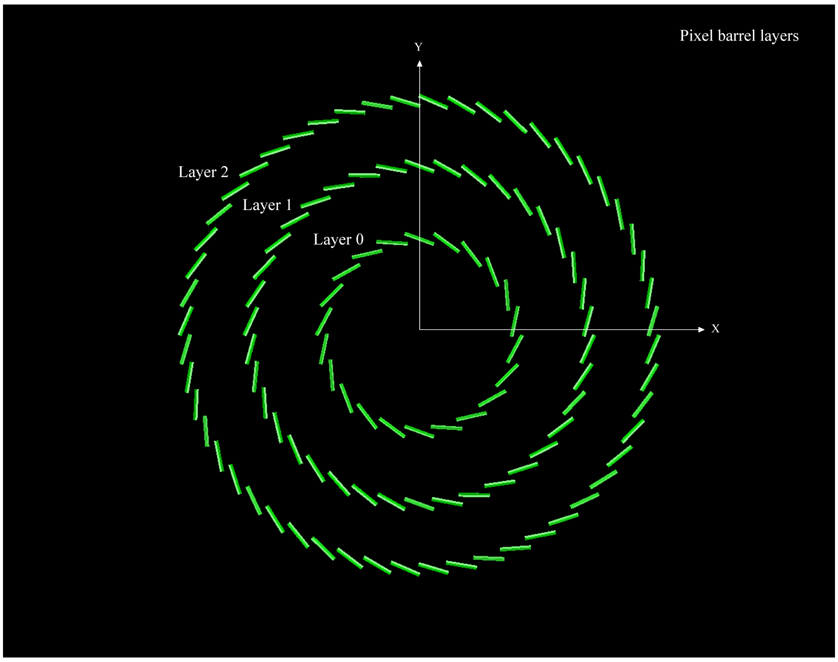

Figure 3.4: *Schematic transverse view of the Pixel detector where its layers can be observed as well as the module tilts.*

Each pixel module consists on a single silicon sensor which has highly doped n^+ implants on a $n - type$ substrate. The pn junction is located on the back-side, with a multi-guard structure controlling the potencial drop towards the cutting-edges. These sensors have a sensitive area of 16.4×60.8 mm^2 and 250 μm of thickness. One important issue is the fact that its components ensures that a single pixel module does not exceed 1.2% X_0[1] (neither including services nor support structures in this number). This low X_0 value is required in order to minimize the degradation of the particle trajectory due to material effects. The sensors are divided in *pixels*. Each silicon wafer contains 47268 pixels which are connected to 16 front-end readout chips. There are two sizes, 50×400 μm^2 (41984 pixels in total) and 50×600 μm^2 (5284 pixels in total) which are along $r\phi$ and z directions respectively . The later size is necessary to cover

[1]The radiation length, referred as X_0, is the length over which the energy of an electron is, on average, reduced by a factor e (where e is base of the natural logarithm, i.e. ≈2.71828).

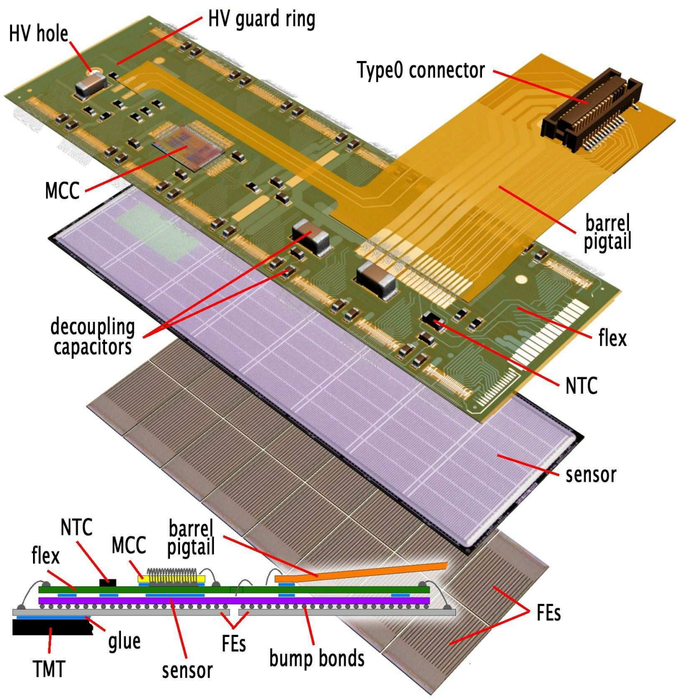

Figure 3.5: *Schematic view of a pixel module illustrating the major pixel hybrid and sensor elements, including the module-control chip (MCC), the front-end (FE) chips, the thermistors (NTC), the high-voltage (HV) elements and the Type0 signal connector. At the bottom there is a plan view showing the bump-bonding of the silicon pixel sensors to the polyimide electronics substrate.*

the gap between the readout chips. These front-end chips are 180 μm thick and they have 2880 electronics channels, arranged in two rows and bump bounded (In or PbSn) to the sensor (46080 channels in total). Anyhow, each module has only 46080 readout channels as there is a 200 μm gap in between readout chips on opposite sides of the module. In order to get full coverage, the last eight pixels at the gap are connected to only four channels (so called "ganged" pixels). Thus, in 5% of the cases there is a two-fold ambiguity that will be resolved offline. The intrinsic resolution of the pixel modules is 10 μm in the $r\phi$ (transversal) direction and 115 μm in the z (longitudinal) direction with a direct 2D readout. Much more information about the pixel module components like the sensor and the electronics can be found in reference [41].

Finally, the ATLAS Pixel layout has 2.2 m^2 of sensitive area with ~ 80 million readout channels as it is written down in table 3.1.

3.2.3 The silicon microstrip detector

The silicon microstrip detector, also referred as SemiConductor Tracker (SCT), surrounds the pixel detector and it uses also silicon planar sensors. The aim of the SCT is to provide precision track measurements in the intermediate radial region, contributing to the measurements of

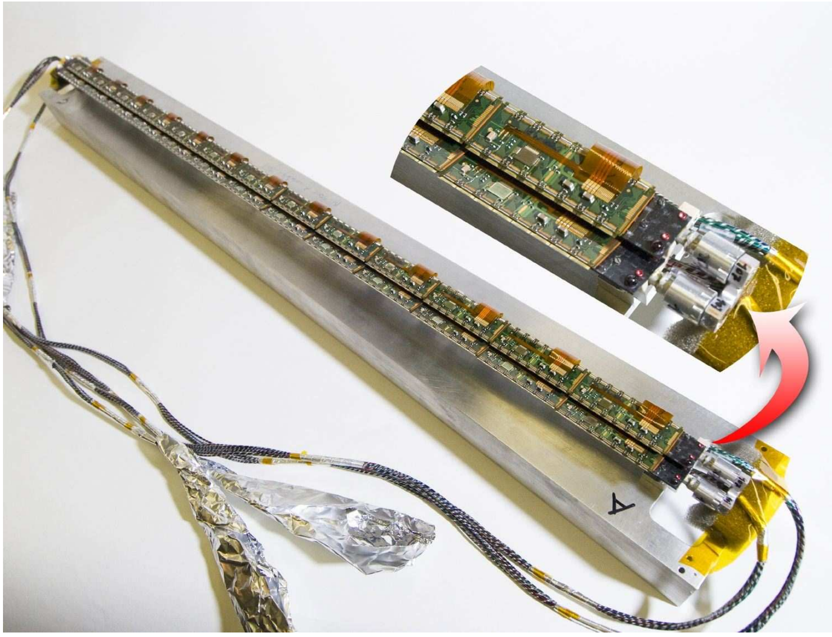

Figure 3.6: *Detail of a bi-stave loaded with pixel modules*.

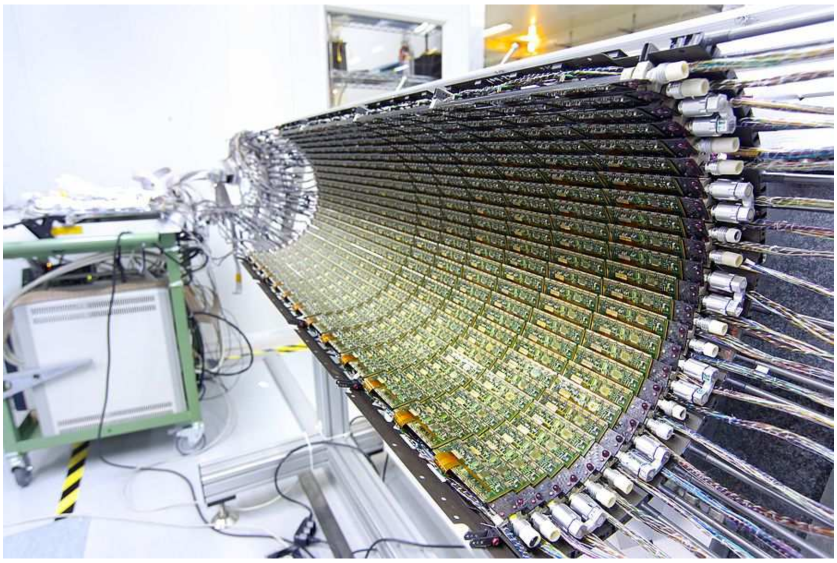

Figure 3.7: *Photograph of a pixel barrel half-shell*.

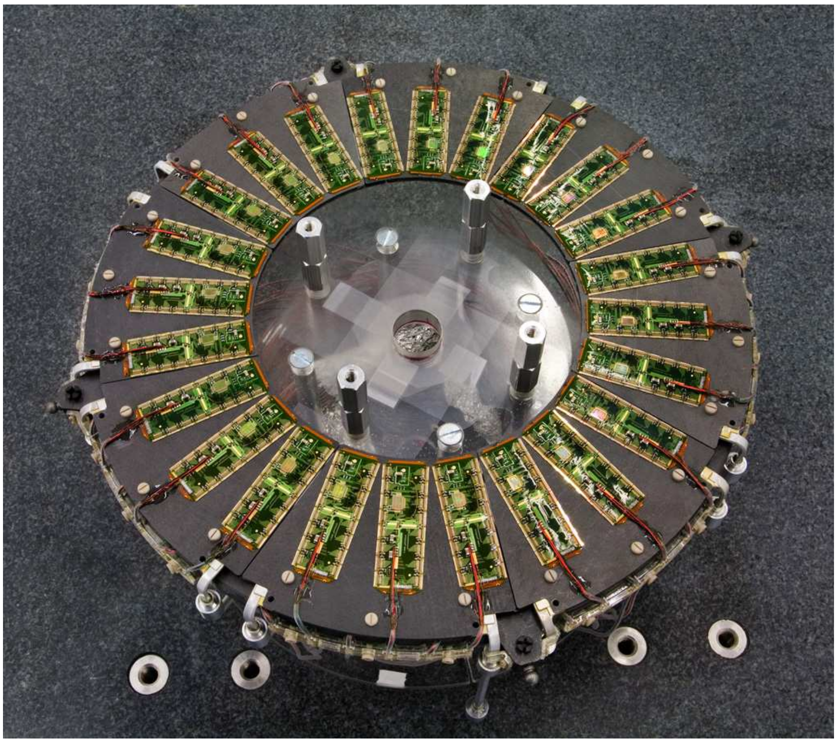

Figure 3.8: *Photograph of a pixel end-cap disc.*

Structure	Layer/Disc	Radius/Z (mm)	Staves/Sectors	Modules	Pixels
Barrel	0	50.5	22	286	$13.2 \cdot 10^6$
	1	88.5	38	494	$22.8 \cdot 10^6$
	2	122.5	52	676	$31.2 \cdot 10^6$
End-Cap	0	± 495	8	48	$2.2 \cdot 10^6$
	1	± 580	8	48	$2.2 \cdot 10^6$
	2	± 650	8	48	$2.2 \cdot 10^6$
All				1744	$80.4 \cdot 10^6$

Table 3.1: *Summary table of the Pixel detector for each of the barrel layers and end-cap discs [18].*

momentum, impact parameter and vertex position covering a pseudorapidity range $|\eta| < 2.5$.

The detector consists on four cylindrical layers in the barrel region and nine end-cap discs on each side. The barrel layer and discs distances are shown in figures 3.2 and 3.3 whilst tables 3.2 and 3.3 collect these numbers. The barrel layers and discs are mounted on carbon-fibre structures. The SCT has 4088 modules in total where 2112 are barrel modules and 1976 are end-cap modules. Figure 3.10 shows the picture of the SCT barrel once assembled. The barrel modules are mounted in staves and then these structures are mounted with a tilt angle of 11^o in the barrel layers, which translates in an overlap of 4 mm between modules. These tilts on the transverse plane can be observed on figure 3.9 as well as the barrel layer structure. Figure 3.11 shows a SCT end-cap disc. The geometry configuration of the end-caps is quite complex as each disc has a different number and type of SCT end-cap modules as can be read in table 3.3. Furthermore, some discs have the modules mounted on their front side (i.e. the side nearest to the barrel) and some of them (as discs number 9) have their modules on the opposite side [42].

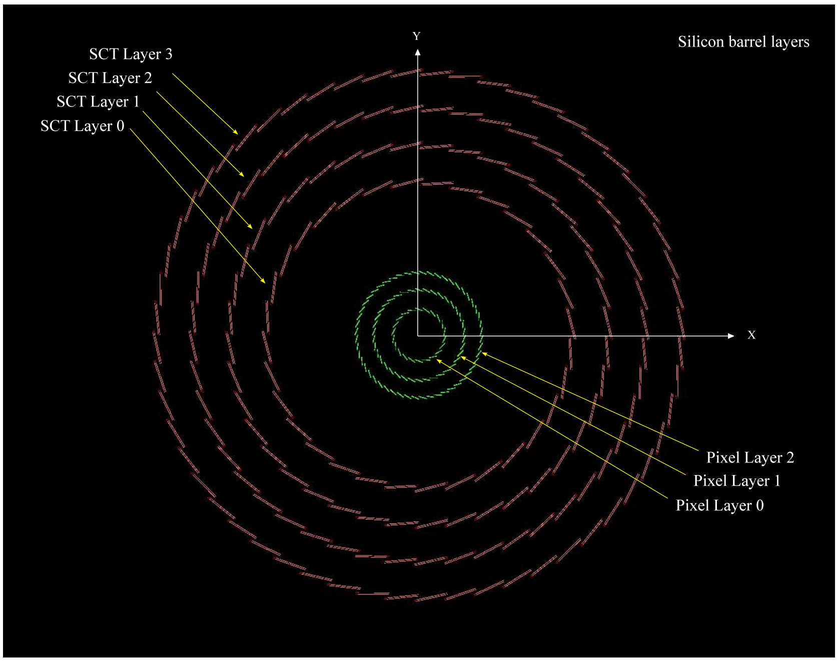

Figure 3.9: *Schematic transverse view of the barrel Silicon Tracker where the different layers can be observed as well as the module tilts for the Pixels and for the SCT.*

A SCT module consists on two silicon sensitive sensors which are based on *strips* that give 1-dimensional position measurements. Each side is built from two wire bonded 6×6 cm^2 silicon wafers forming the final 12×6 cm^2 side. These wafers consists on highly doped $p+$ readout implants on a $n-type$ silicon bulk (285 μm of thickness) and they have 768 parallel microstrips. Moreover, both SCT module sides are glued together back-to-back at a 40 mrad stereo angle. This implies that each SCT module has thickness of ~ 1 mm (285 μm of each silicon sensor + 500 μm spine + glue which sticks the three components. See figure 3.12) with 1536 strips in total. In the barrel, the module side parallel to beam pipe is called $r\phi$ side and the other side is known as the stereo side. The readout is performed by means of 12 binary ABCD front-end chips [43] (there are 6 chips per side and each chip reads 128 channels).

The SCT has a single module topology design for the barrel region (with a rectangular module type) and three topologies for the end-caps (having trapezoidal shapes), namely *outer*, *middle* and *inner* according to their position in the end-cap wheels [44]. In fact, there are two kinds of

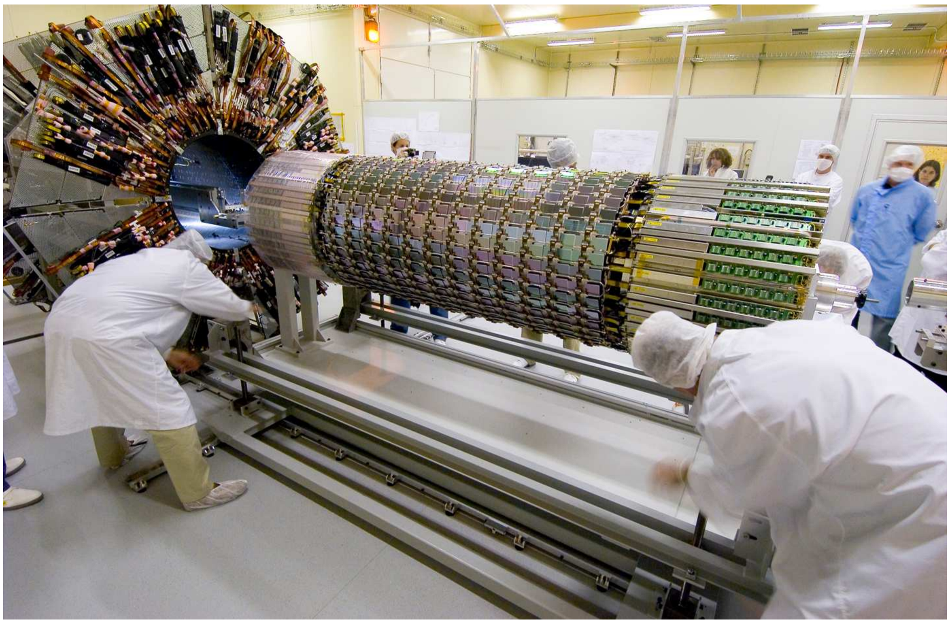

Figure 3.10: *Photograph of the SCT barrel finally assembled.*

middle modules, one with a long wafer (i.e. two bounded short silicon wafers) and one with a short wafer (the other wafer is a crystal dummy sensor). The five types of SCT modules can be seen in figures 3.13 (a), (b), (c), (d) and (e). Obviously, the strip pitch is only constant in the barrel module, which is 80 μm. For the end-cap modules, as the have a fan-out structure, the strip pitch is variable: from 54.53 μm to 90.34 μm, depending the wafer position. Thus, the barrel modules ensure a 23 μm precision in $r\phi$ (i.e. in the measuring coordinate), due to the fact that the intrinsic resolution of the binary readout for a single-strip hit is directly related with the strip pitch ($\mathcal{P}$): $\sigma = \mathcal{P}/\sqrt{12}$. Then, the combination of two back-to-back side measurements allows to determine the position of the hits along the strips giving to the SCT modules the capability for a 3-dimensional spacepoint reconstruction. Therefore, once a spacepoint is built, the intrinsic resolution of a whole SCT module is 17 μm in $r\phi$ and z is 580 μm.

Finally, considering the total number of SCT modules and their features, it is easy to conclude that the SCT covers a surface of 61.1 m^2 of silicon with $\sim$6.3 million of readout channels as can be extract from tables 3.2 and 3.3.

3.2.4 The solenoid magnet

As it has been commented the ID is housed in a superconducting NbTi/Cu solenoid that generates an axial magnetic field of around 2 T (1.998 T at the magnet's centre at the nominal 7.730 kA operational current), with a peak value of 2.6 T near the superconducting material. The solenoid has a diameter of 2.5 m and is 5.3 m long. It is shorter than the ID itself, which makes the field quite inhomogeneous in the forward region. Figure 3.14 shows the z and R

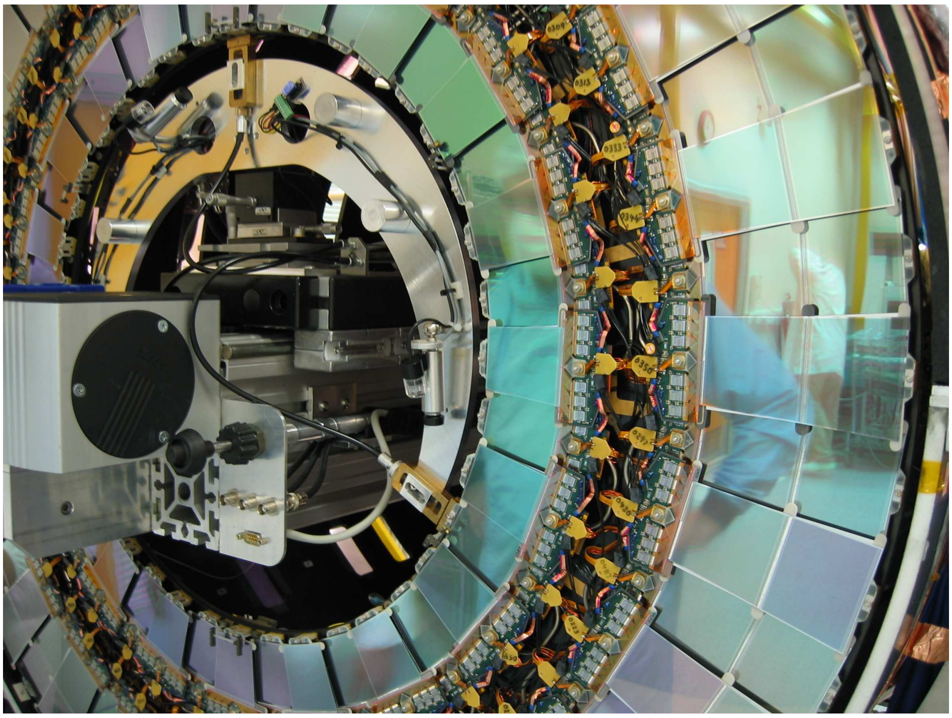

Figure 3.11: *Photograph of a SCT end-cap disc where its end-cap modules can be seen.*

Layer	Radius (mm)	Modules	Area (m^2)		
0	300.0	12 × 32	6.26	Barrel length:	1.4934 m
1	373.0	12 × 40	7.82	Strip pitch:	80.0 μm
2	447.0	12 × 48	9.4	Total number of modules:	2112
3	520.0	12 × 56	10.96	Total area:	34.4 m^2
				Number of channels:	3244032

Table 3.2: *Summary of the SCT Barrel specifications [18].*

components of the magnetic field (referred as B_z and B_R) as a function of z and radius (R). One can see that the z component of the field drops from 2 T to 1 T at the end of the tracker, while the R component reaches up to 0.6 T in the forward region. The inhomogenity of the magnetic field at the end-caps enforces the use of a field map in simulation and reconstruction.

From the Lorentz force, it can be derived that the charged particles follow a circular path in the transverse plane of their motion. The relationship between the transverse momentum (p_T) (in GeV), the charge (q), the magnetic field (B) (in Tesla) and the bending radius (r) (in m) is:

$$p_T = 0.3qBr \tag{3.1}$$

The resolution of the transverse momentum relates with the resolution in the *sagitta* measure-

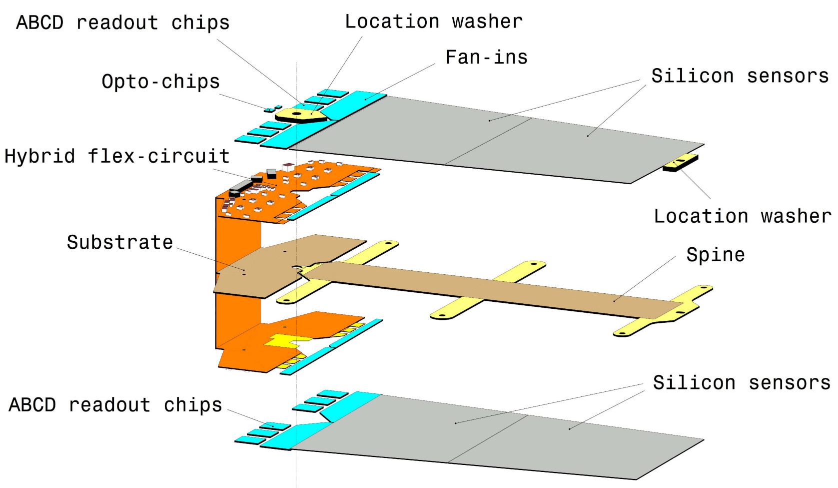

Figure 3.12: *Schematic view of a SCT end-cap module illustrating its components: silicon wafers, high thermal conductivity spine, polyimide hybrid, ABCD readout chips, etc.*

Disc	**Z (mm)**	**Radius (mm)** *[Inner/Outer]*	**Modules** [I / M / O]	
0	± 835.0	259 / 560	40 / 40 / 52	Strip pitch [min/max] (μm)
1	± 925.0	336 / 560	- / 40 / 52	- *Inner:* 54.53 / 69.43
2	± 1072.0	259 / 560	40 / 40 / 52	- *Middle:* 70.48 / 94.74
3	± 1260.0	259 / 560	40 / 40 / 52	- *Outer:* 70.92 / 90.34
4	± 1460.0	259 / 560	40 / 40 / 52	Types: 4
5	± 1695.0	259 / 560	40 / 40 / 52	Total number of mods: 1976
6	± 2135.0	336 / 560	- / 40 / 52	Total area: 26.7 m^2
7	± 2528.0	401 / 560	- / 40 / 52	Number of channels: 3035136
8	± 2788.0	440 / 560	- / - / 52	

Table 3.3: *Summary of the SCT End-Caps specifications [18].*

ment as:

$$\frac{\sigma(p_T)}{p_T} = \frac{\sigma_s}{s} \propto \frac{\sigma_s}{BL^2} p_T \tag{3.2}$$

where L is the half length of the chord (i.e. span) connecting the two ends of the arc as can be seen in figure 3.15 which shows a scheme with the sagitta definition in the XY plane (global plane). Moreover, expression 3.2 tells that the resolution on the transverse momentum is directly

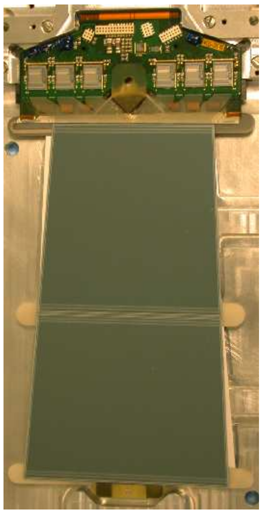

(a) *Outer*

(b) *Middle*

(c) *Short-middle*

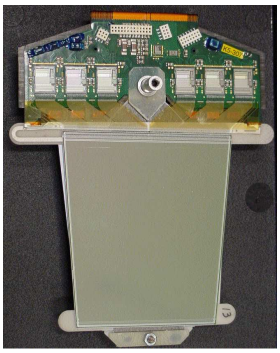

(d) *Inner*

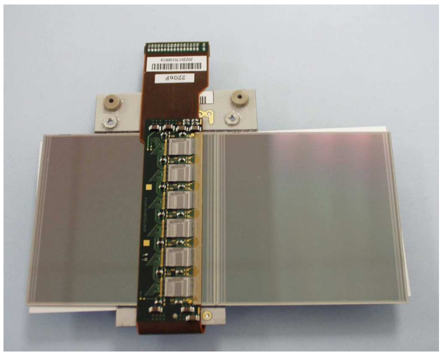

(e) *Barrel*

Figure 3.13: *Photographs of the five SCT modules topologies.*

proportional to the transverse momentum ($\sigma(p_T)/p_T \propto p_T$). This implies that the resolution will be worse for high momentum particles. From MC simulations the expected resolution is [7]:

$$\frac{\sigma(p_T)}{p_T} \sim 3.4 \cdot 10^{-4} p_T(\mathrm{GeV}) \oplus 0.015 \tag{3.3}$$

In the ATLAS solenoid, the integral $\int BdZ$ drops from about 2 Tm at $|\eta| = 0$ to about 0.5 Tm at $|\eta| = 2.5$ as can be seen in figure 3.14 (b), which means that the field strength in the end-caps

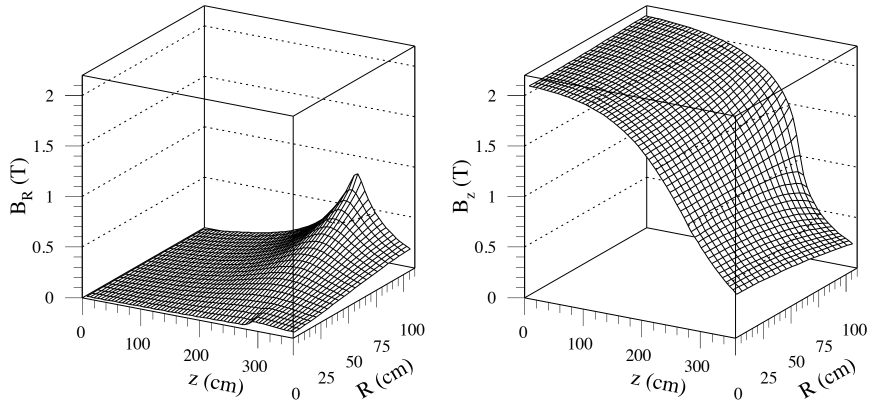

(a) B_R *component* (b) B_z *component*

Figure 3.14: *B_R and B_z as a function of R and z respectively [45].*

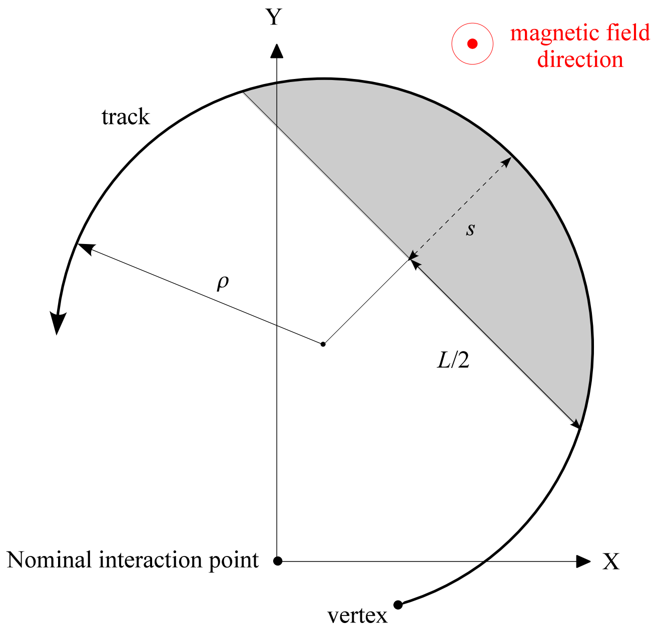

Figure 3.15: *Sagitta definition of a track in the XY plane (global frame).*

is lower than in the barrel. This reduces the length of the measured trajectory in the $r\phi$ plane (due to their "lever arm"), increasing the relative extrapolation distance to the beam line. Thus, the resolution on the impact parameter is also worse in the forward region. The resolutions in the forward region are further worsened because there is more material than in the barrel as will be shown in the next subsection.

3.2.5 Material budget

All the charged particles that traverse the ID will interact with the material (sensors, cables, support structures etc). The most important effects are:

- Charged particles suffer MCS, causing them to deviate from their ideal trajectory.
- Hadronic interactions between hadrons and the detector material can cause the hadrons to produce a stream of secondary particles.
- Electrons suffer from highly fluctuating energy losses due to Bremsstrahlung.
- Photons can convert into an electron-positron pair ($\gamma \rightarrow e^{+}e^{-}$).

With an overall weight of $\sim$4.5 tonnes, the ATLAS ID has much more material budget (in terms of radiation length X_0) than any previous tracking detector. Anyhow, the performance requirements of the ATLAS ID are more stringent than any tracking detector built so far for operation at a hadron collider. Hence, the ID is the result of a good compromise between material effects and physics performance.

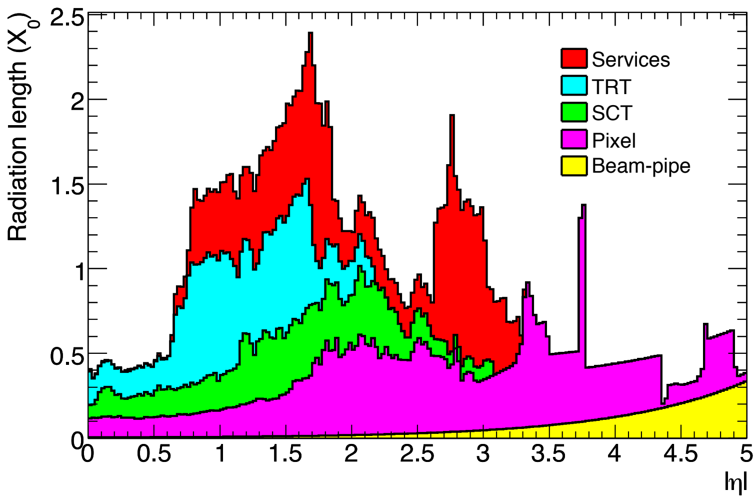

Figure 3.16: *Material distribution as a function of $|\eta|$ and averaged over ϕ, in terms of X_0 at the exit of the ID envelope. It includes the services and thermal enclosures. The breakdown indicates the contributions of external services and of individual subdetectors, including services and their thermal enclosures in their active volume [18].*

Material effects can be corrected up to a certain level at the reconstruction but the interactions always reduce the performance of the tracking and therefore they have an impact on the alignment. Thus the amount of material should be kept at an absolute minimum. Light-weight, low-Z materials like carbon fiber are used for the support structures. Figure 3.16 shows the amount of material that a particle traverses as a function of the pseudorapidity. The material is expressed in terms of radiation lengths (X_0).

3.3 ATLAS coordinates system

There are several coordinate frames being used in ATLAS although there are three right-handed frames with particular importance for alignment [46] [47], namely the global frame, the local module frame and the measurement frame. A general discussion of ATLAS frames can be found in [48].

- The **ATLAS *global frame* (X, Y, Z)** is the cartesian frame in which its origin is the nominal Interaction Point (IP) of the proton-proton collisions. X is the horizontal axis pointing towards the center of the LHC ring, Y is perpendicular to X and Z (i.e. it is $\sim 1.23^0$ from the vertical and Z is along the beam line [49].

  In this frame $+Z$ direction (also known as side-A) points to the Geneva's airport (and the nominal ID B-field also points to this direction) and the $-Z$ direction (also known as C-side) points the Jura mountains. The polar angle θ is measured from the positive Z-axis covering the range $\theta \in [0, \pi)$, the azimuthal angle ϕ is measured in the XY-plane, so that the positive X-axis has an azimuthal angle of $\phi = 0$ and the positive Y-axis an azimuthal angle of $\phi = \pi/2$, when ϕ covers the range $\phi \in [0, 2\pi)$. The azimuthal and polar angles can be expressed through the momentum components using the following relations:

$$tan\phi = \frac{p_y}{p_x} \quad \text{and} \quad cot\theta = \frac{p_z}{p_T}$$

  where p_x , p_y and p_z denote the components of the momentum corresponding to the axis system and p_T is the transverse momentum with respect to the beam axis:

$$p_T = \sqrt{p_x^2 + p_y^2} = psin\theta$$

  Finally, the pseudorapidity η depends on θ as was said in the previous chapter (in fact η is a way of parametrise θ at colliders) as:

$$\eta = -ln\left[tan\left(\frac{\theta}{2}\right)\right]$$

- The ***local module frame* ($\tilde{x}$, $\tilde{y}$ and $\tilde{z}$)** is different for each Pixel, SCT and TRT detector element but its origin is always placed in the midpoint of each detector module (for the SCT in most cases this is the point of stereo rotation) [47].

  For Pixel modules, $\tilde{x}$ is parallel to the short side of the Pixel wafers and $\tilde{y}$ parallel to its long side. In this case, the ϕ index (row number) goes in direction of $\tilde{x}$ and the η index (column number) goes in the direction of $\tilde{y}$. For SCT modules, $\tilde{x}$ is the direction crossing the strips and $\tilde{y}$ is parallel to the strip direction on the non-stereo side in the SCT as can be seen in figure 3.17 (a). Numbering of strips goes in the same direction as $\tilde{x}$. Finally, for TRT modules, $\tilde{x}$ is the direction crossing the straws and $\tilde{y}$ is parallel to the straw direction. In all cases, $\tilde{z}$ is perpendicular to the module plane and it is orientated to give a right-handed system.

Generally, in the barrel part the $\tilde{y}$ is always parallel to the Z-axis of the global reference frame and in the end-cap regions $\tilde{y}$ is radial. The $\tilde{z}$-axis goes outward radially in the barrel and in the negative global Z-axis direction in the end-cap.

- The ***measurement frame*** (x, y, z) is the coordinate frame in which the hit measurements are calculated (also known as *reconstruction frame*) [50].

  For Pixel modules, the measurement frame is equal to the module frame as its modules have just one side (which can measure two coordinates). In the SCT, the measurement frame is defined to have the same frame as the $r\phi$ side, being xy planes rotated by the stereo angle as can be seen in figure 3.17 (b). Finally, for the TRT measurement frame x is perpendicular to both track and straw, y is parallel to the straw and the z-axis is perpendicular to the xy plane. In this case, the origin is the middle of the straw wire. The motivation for defining the TRT frame like this is that the drift time of the TRT hit is a measurement of the distance between track and wire, i.e. $|x|$ in the measurement frame.

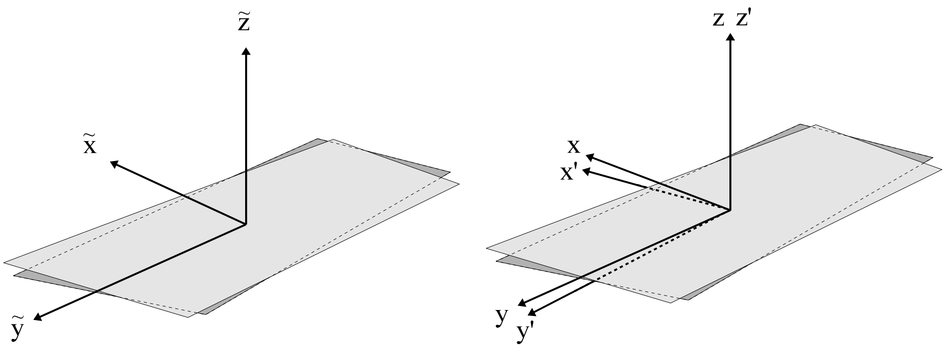

(a) *Local frame*

(b) *Measurement frame*

Figure 3.17: *Scheme of the local frame (a) and measurement frame (b) for a SCT module which has its two sides rotated by 40 mrad.*

3.4 Tracking

Another supporting column of the Silicon Tracker alignment is the track reconstruction software as all the existing software-based alignment algorithms are based on tracks. Thus, this section will discuss the raw data preparation of the silicon detectors just before give a brief description of the ATLAS Event Data Model where the tracking is framed as well as define the track parameters. Finally, the residual concept will be introduced and discussed.

3.4.1 Data preparation

Silicon hits (i.e. pixels or fired strips) have to be pre-processed in order to achieve a high precision track reconstruction. Therefore, a clusterization and a spacepoint formation have to be performed.

3.4.1.1 Clusterization

Neighbour pixels or strips with hits produced by the same crossing particle within a wafer plane are grouped into *clusters*. This clusterization is performed at hardware level for the SCT and at software level for Pixels. Thus, in the offline reconstruction the clusterization algorithm performs the grouping of the pixels that share at least one edge. Then, the cluster position could be corrected by taking the center of gravity of all the pixels or strips in that cluster or by charge interpolation from the Time-over-Threshold (ToT) measurement. This software also checks if there are ganged pixels or bad/dead strips (using a map from the conditions database) in the cluster candidate and remove them. At the end, the final position of the cluster is corrected by the Lorentz angle effects, and an error matrix is assigned. The SCT procedure is similar to the Pixels one but using the strips information. The precision achieved using the clusterization technique is higher than the resolution of a single pixel or strip.

3.4.1.2 Spacepoint formation in the SCT modules

The spacepoints (SP) are 3-dimensional points created from the pixels, strips or clusters positions, and they are given in the global frame. For the Pixels, a simple transformation from the local to global frame is applied. For the SCT, SP can be formed using both side measurements (fired strips or clusters) of a SCT module by calculating where the two strips or two clusters overlap. Note that the two sensors in an SCT module are about 1 mm apart, therefore the constructed SPs depend on the incidence angle of the track with respect to the module. Furthermore, a SP can also be created from two single measurements of two different overlapping modules.

For collision data, the SP formation assumes that the track comes from the ATLAS origin. For cosmic events, it assumes that the tracks originate from a point high in the sky. The SP is a very convenient quantity for the offline pattern recognition algorithms in ATLAS, but its dependence on the incident angle makes it less precise than the individual clusters that form the SP. Hence, the track fitters use the SCT clusters instead of the SPs in the final fit.

3.4.2 ATLAS Tracking Model

The strategy adopted for the ATLAS track reconstruction software is based on the Event Data Model (EDM) [51] [52] which uses a common track object which is suited to describe tracks in the innermost tracking subdetectors and in the muon detectors in offline as well as online reconstruction. Thus, the aim of this framework is to make the reconstruction software more flexible and maintainable, by delegating each reconstruction step to a dedicated software module. This provides a powerful and customizable tracking software as for each reconstruction step, the user can select and switch between different software modules at runtime since they all have to implement the same abstract interface that is associated with that step. In addition there is the possibility to store the event information on disc at different stage of the reconstruction, i.e. at the level of raw data, calibrated hits, particle trajectories and finally light-weight but concise physics objects. EDM comprises different consecutive stages like data preparation, track finding and post-processing. Following the particular ID tracking model one has:

- **Data preparation**. Once the hits have been collected the clusterization and spacepoint formation is performed as already commented in section 3.2,. Thus, silicon clusters and drift circles (in the TRT case), which are raw data objects (RDOs), are created either from the simulated digits or from the detector raw data and they are combined under a common base class called PrepRawData (PRD). These PRD objects form the input objects to the reconstruction, i.e. the input for finding and fitting tracks. In the case of real data, a byte-stream converter, specific for each subdetector, first creates the RDOs.

- **Pattern recognition and track fitting**. When a particle traverses a ID, it will generate, after the data preparation, silicon spacepoints (PRD) which are used to create track-seeds during the pattern recognition using a combinatorial Kalman Filter technique. Thus, the task of the pattern recognition is to determine which SPs belong to which tracks solving the possible ambiguities, and to give, for each track, an estimate of the track parameters. After extrapolation to the TRT, track fitting algorithm uses all compatible measurements (in the track fit silicon clusters are used instead of SPs due to their lower uncertainty) and tries to produce a track trajectory that is as close as possible to the true trajectory.

- **Post-processing**. The primary vertex is fitted and other reconstruction tools (bremsstrahlung recovery, etc.) are applied. The output is a common base class (same for ID and Muon Spectrometer) for the representation of a track in ATLAS (Trk class). Finally, a fit quality is associated to the track class.

3.4.3 Track parameters

The trajectory of a charged particle, i.e. a track, in an uniform magnetic field (B) is a helix, which can be parametrised by a set of five parameters: $\boldsymbol{\pi} = \{\ell_1, \ell_2, \phi, \theta, q/p\}$ where ℓ_1 and ℓ_2 denote the two coordinates in the intrinsic frame of a selected surface, ϕ, θ represent the azimuthal and polar angles and q/p is the momentum in the global frame. Evidently the meaning of ℓ_1 , ℓ_2 varies by the different surface types which can be surfaces associated to the detector or readout elements or even virtual tracking surfaces or trigger surfaces [51]. From the physics and alignment point of view, the most interesting representation is when it is given at the perigee, i.e. at the point of closest approach to a reference point, which is the origin of the global frame, (**P**), being the track parameters: $\boldsymbol{\pi} = \{d_0, z_0, \phi_0, cot\theta, q/p\}$.

As it is shown in figure 3.18, d_0 is the transverse impact parameter which is the signed distance to the XY plane, and that sign is defined to be positive when the direction of the track is clockwise with respect to the origin and therefore flipping the direction will flip the sign of the impact parameter. Then, z_0 is the longitudinal impact parameter which is the Z-coordinate of the perigee, ϕ_0 is the azimuthal angle in the XY plane at this point, and θ is the polar angle, i.e. the angle with the Z-axis. The fifth parameter is q/p which is the charge of the particle

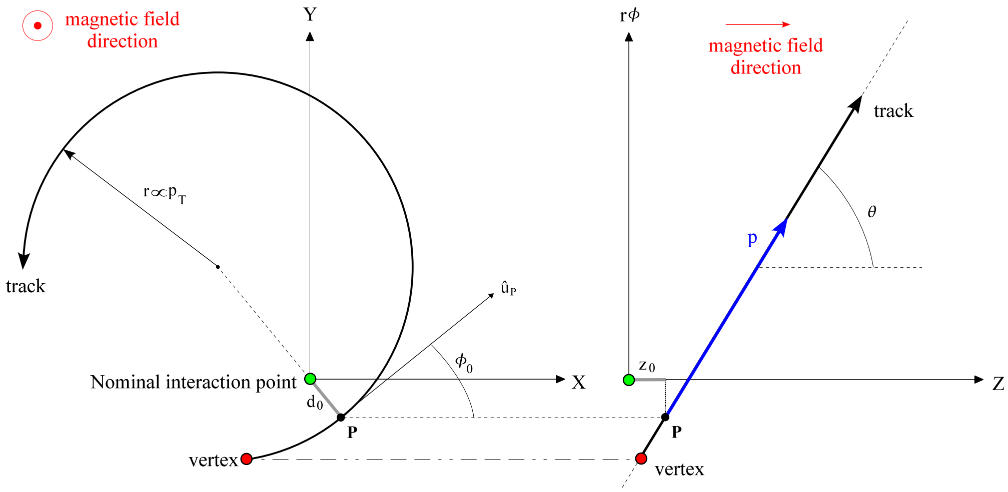

Figure 3.18: *Track parameters defined at the perigee computed with respect the origin of the global frame.*

divided by its momentum. Obviously, the later parameter only plays a role for curved tracks ($p_T = psin\theta = 0.3qBr$). Finally, $\mathbf{\hat{u}_P}$ is the unit vector which gives the direction transverse to the radius r at perigee: $\mathbf{\hat{u}_P} = (sin\phi_0, -cos\phi_0, 0)$.

In alignment, the representation is ϕ_0, $cot\theta$, q/p_T [45], where $cot\theta$ is the inverse slope of the track in the YZ-plane, instead of the one used in the tracking model (ϕ_0, θ, q/p). This is due to the fact that this was the representation frequently used for helix parametrisations in earlier versions of the ATLAS tracking model. Anyhow, the later representation has some advantages from the EDM point of view:

- The design of the local parametrisation should not be restricted to a specific detector part and should represent track states at any point in the detector. Since in a non-homogeneous magnetic field the transverse momentum in general is not a constant of motion, the choice of q/p is to be more appropriate to fulfill this requirement.

- Using (ϕ_0, θ, q/p) results in a better computing performance for material corrections in the tracking algorithms. Energy loss corrections have to be applied to the current value of the momentum. Introducing multiple scattering by correcting the angular direction and its uncertainty favours the angle-based parametrisation (ϕ_0, θ) for the momentum direction and also requires the knowledge of the momentum magnitude. Frequent transformations to and from the helical representation should therefore be avoided.

Anyhow, the EDM has set of different Jacobian matrices are available in the existing tracking tools (TrkEventPrimitives package) which can be used to transform covariances or errors from one representation to another.

The track parameters resolutions of the ID can be parametrised as a function of the transverse momentum (p_T) and the polar angle θ. These resolutions were estimated in the ATLAS

Physics TDR [45] using the layout as it was foreseen in 1999 and using the "old" momentum representation for the track parameters (ϕ_0, $cot\theta$, q/p_T) and they can be found in table 3.4.

Track parameter	**Resolution dependence**	**Units**
Transverse impact parameter	$\sigma(d_0) \simeq 11 \oplus \frac{73}{p_T\sqrt{sin\theta}}$	μm
Longitudinal impact parameter	$\sigma(z_0) \simeq 87 \oplus \frac{115}{p_T\sqrt{sin^3\theta}}$	μm
Azimuthal angle	$\sigma(\phi_0) \simeq 0.075 \oplus \frac{1.8}{p_T\sqrt{sin\theta}}$	mrad
Cotangent polar angle	$\sigma(cot\theta) \simeq 0.70 \oplus \frac{2.0}{p_T\sqrt{sin^3\theta}}$	$O(10^{-3})$
Inverse transverse momentum	$\sigma(\frac{1}{p_T}) \simeq 0.36 \cdot p_T \oplus \frac{13}{\sqrt{sin\theta}}$	TeV^{-1}

Table 3.4: *Expected track parameters resolutions of the ID [45]. d_0 and z_0 are the transverse and longitudinal impact parameters respectively. Then, ϕ_0 is the azimuthal angle, $cot\theta$ is the cotangent of polar angle and q/p is the inverse transverse momentum which is related with the track curvature.*

In the equations which appear in table 3.4, the first term on the right hand side represents the intrinsic resolution of the ID tracker on these parameters, which depends on the resolution of the position measurements and the strength of the magnetic field. The second term represents the resolution degradation due to multiple scattering effects. The factor $\sqrt{sin\theta}$ or $\sqrt{sin^3\theta}$ arises because particles have to traverse more material as the angle with the beam direction gets smaller, due to the angle of incidence with the material layers. The material in the end-caps is dominated by the support cylinders and services, therefore the same relation holds there as well.

3.4.4 Residuals

For tracking, a residual[2] is the distance between a hit and the intersection point of the extrapolated track in the sensor. From the point of view of the EDM, a hit is either a pixel/strip cluster (for the silicon tracker or the muon detector) or a drift circle (for the TRT).

Within the ATLAS alignment, two different residual concepts are used: within plane residuals (2-dimensional) and distance-of-closest-approach (DOCA [54]) residuals (3-dimensional). The first concept is defined as the perpendicular distance within the measurement plane of the strip or cluster middle with the extrapolated point of the reconstructed track. Thus, if one considers that $\mathbf{m}$ is the vector to the center of the pixel/strip/cluster, $\mathbf{e}(\boldsymbol{\pi}, \mathbf{a})$ is the vector to the intersection of the track with the surface (i.e. measurement sensor plane) that depends on a list of the track parameters ($\boldsymbol{\pi}$) and on a list of alignment parameters ($\mathbf{a}$), then, the residual vector ($\mathbf{r}$)[3] is defined as:

$$\mathbf{r} = (\mathbf{m} - \mathbf{e}(\boldsymbol{\pi}, \mathbf{a})) \tag{3.4}$$

At the end, each residual vector $\mathbf{r}$ is projected to the sensitive direction of the sensor under test to obtain a distance which will be the sensitive measurement. Thus, Pixel modules have

[2] In statistics, a residual of a sample is the difference between the sample and either the (observed) sample mean or the regressed (fitted) function value.

[3] From now onward, bold letters will represent vectors in this thesis.

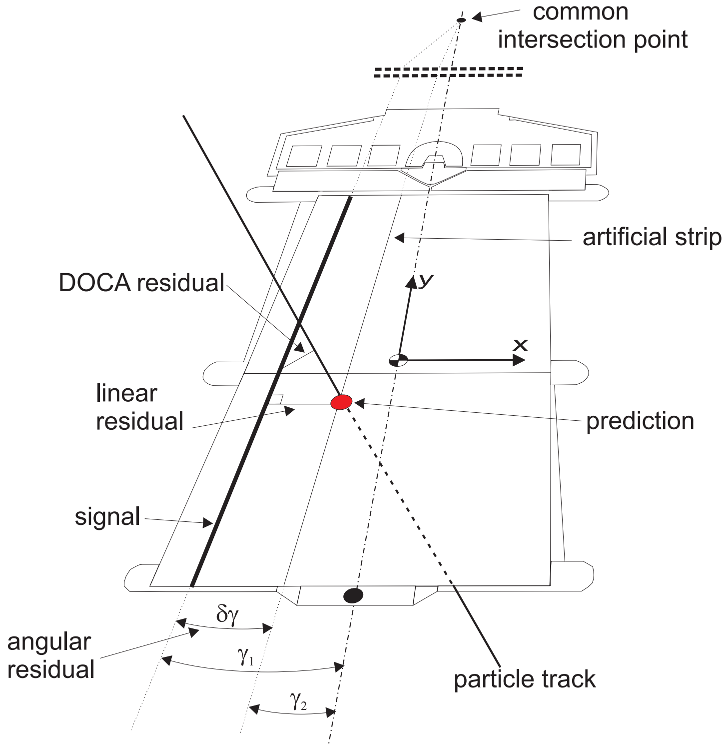

Figure 3.19: *Schematic representation of the residuals calculation (linear and distance-of-closest-approach (DOCA)) in a SCT end-cap module. Within plane residuals (also called, linear residuals) are always computed in the perpendicular direction to the cluster and the DOCA are computed as the distance of closest approach to the cluster (picture taken from [53]).*

two sensitive directions, then two residual components will be measured, called r_ϕ and r_η. SCT modules provides one sensitive direction which is perpendicular to the strips, then just one residual component is used.

On the other hand, the second concept is, as reads its name, the distance of closest approach (3-dimensional measurement) from the extrapolated track point to the cluster measurement. Figure 3.19 shows a schematic representation of both residuals calculations (linear and DOCA) in a SCT end-cap module.

3.4.4.1 Pixel residuals

For Pixels, the 2-dimensional segmentation of the pixel sensor allows to define two distinct residuals: the $r\phi$-residual and η-residuals which stand respectively for the difference between the track prediction and the cluster coordinate in the short (row) and long (column) pixel directions.

3.4.4.2 SCT residuals

The SCT modules have two planes and the residuals are computed in the measurement frame of each side. Moreover, a SCT wafer is only sensitive in the coordinate across the strips as the wafers are not segmented along the strips.Thus, a measured point (**m**) in the measurement frame is given by the position x of the strip while y is set in the middle of that strip. The sensitive coordinate is also known as $r\phi$ and the non-sensitive as η.

On the other hand, the extrapolated point can be anywhere within the wafer boundaries. Then, one can think that the residual vector is simply given by $\mathbf{r} = \mathbf{m} - \mathbf{e} = (m_x - e_x,\ m_y - e_y)$ but this is not true at all. For barrel modules, the residual vector has also its two components one across the strip and one along the strip. But problems arise if strips form an angle with the y-axis of the measurement frame as in the end-cap SCT modules case which have a fan-out strip configuration. Thus, if one defines **u** and **v** for each independent strip as the unit vectors along that strip direction and orthogonally to that strip, respectively, one can compute the residual vector as a function of these unit vectors.

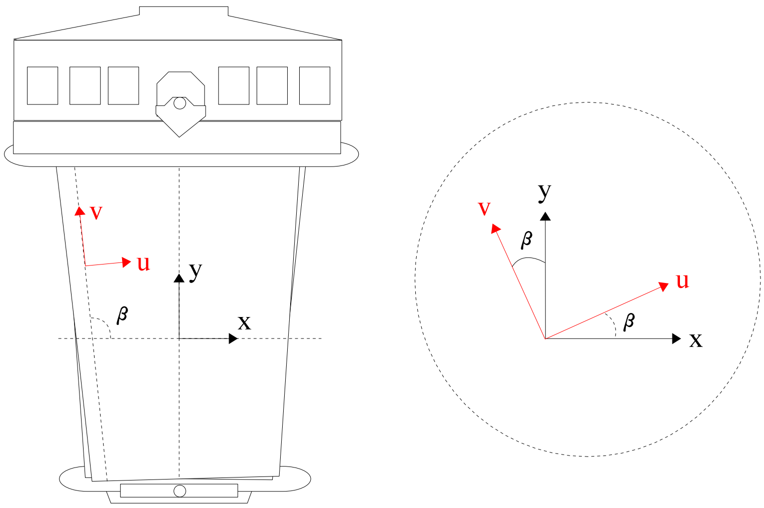

Figure 3.20: *Definition of the* **uv** *frame for a given strip (with fan-out structure) within a SCT (inner) end-cap module. The angle β is the rotation angle of the* **uv** *frame with respect the measurement frame (xy).*

Figure 3.20 shows the definition of the unit vectors **u** and **v** for a given strip (with fan-out structure) within a SCT (inner) end-cap module. β is the rotation angle of the **uv** strip frame with respect the xy measurement frame. Thus:

$$\mathbf{u} = (\cos\beta,\ \sin\beta) \quad \text{and} \quad \mathbf{v} = (-\sin\beta,\ \cos\beta)$$

Then, the residual components can be computed as:

$$r_{r\phi} = \mathbf{r}\cdot\mathbf{u} = (m_x - e_x,\ m_y - e_y)\cdot(\cos\beta,\ \sin\beta) = (m_x - e_x)\cos\beta + (m_y - e_y)\sin\beta$$

$$r_{\eta} = \mathbf{r}\cdot\mathbf{v} = (m_x - e_x,\ m_y - e_y)\cdot(-\sin\beta,\ \cos\beta) = -(m_x - e_x)\sin\beta + (m_y - e_y)\cos\beta$$

The above expressions are completely general for both, SCT barrel and SCT end-cap modules. For the barrel modules case $\beta = 0$ as all the strips are parallel, so the residuals are simply:

$$r_{r\phi} = m_x - e_x \quad \text{and} \quad r_\eta = m_y - e_y$$

3.4.5 Biased and unbiased residuals

In High Energy Physics (HEP) there are two residual concepts used for tracking and alignment purposes: "biased" and "unbiased" residuals (which are not frequently used in other fields).

- **Biased residual**: The track fit is performed with all the available hits which belong to this track, including the hit of the considered residual measurement.
- **Unbiased residual**: this time, the reconstructed track does not include the data point under test (i.e. the hit on the surface where the residual is being calculated). This means that to calculated every unbiased residual on each measuring surface one has to refit the track every time removing the hit under test. Thus, computing time for unbiased residuals is larger than for biased residuals.

One can also divide a residual by the standard deviation of the measured value and get a "normalized residual": $r_N = r/\sigma_{hit}$. Thus, normalized residuals should have a mean value of zero and a width, as measured by the standard deviation, of about 1, but not exactly 1. The value of the normalized residuals are influenced by the quality of the measured value itself but also by all other data points and by the position of the data point within the set of all data points. For example, in a straight line fit, using the "biased" residual concept, with a large number of data points the line is very accurate in the center, but not so accurate in the outer regions. A single data point in the center does not influence the accuracy of the straight line and the normalized residual will have a standard deviation close to 1, but below one. A single data point in the outer region has a larger influence on the line fit, and the residual distribution will have a standard deviation much smaller than 1. One could call this effect for the residual a "bias", because the small value of the standard deviation is caused by the influence of the data point itself. However, using the "unbiased" concept, normalized residuals of data points in the center will have also a standard deviation slightly above 1, because the line is rather accurate but in the outer region the normalized residuals will have a standard deviation much larger than 1, because the fitted line is less accurate. In addition, the "unbiased' residuals are misleading since they really introduce a bias but of opposite sign compare to the "biased" residuals. Thus the unbiased concept seems to have no advantage over the biased residuals except in special cases like single bad data points.

After considering these issues, is worth to say that the algorithm presented in this thesis will use the biased residual concept to perform the Silicon Tracker alignment.

3.4.5.1 Pull concept

The *pull* is the observable which has a true statistical significance. It is defined as the residual divided by the standard deviation of the residual, σ_r, (not of the data point, i.e. not of the hit). However, its definition depends on which type of residuals is being considered since:

$$\text{Biased residuals: } \sigma_r^2 = \sigma_{fit}^2 - \sigma_{hit}^2 \tag{3.5}$$

$$\text{Unbiased residuals:} \quad \sigma_r^2 = \sigma_{fit}^2 + \sigma_{hit}^2 \tag{3.6}$$

where σ_{fit} is the standard deviation of the track fit at the coordinate of the data point, calculated by error propagation using the full fitted parameter covariance matrix (this will be explained in section 4.2.2.1). In the biased residual case, the σ_{hit}^2 must be subtrack from σ_{fit}^2 to avoid double counting as the hit has been already included in the fit. Whilst for the unbiased residuals, the errors are a straight combination of the both quantities entering in the calculation: the measurements and the extrapolations.

Thus the pull is computed by:

$$pull = \frac{r}{\sigma_r} \tag{3.7}$$

The pulls should follow the normal distribution[4] with mean 0 and standard deviation 1 (referred as N(0,1)) and this should be valid for all data points. Any deviation from this behaviour can be due to: a bias in the data (in all data points or only in a single point), a wrongly assigned standard deviations, a wrong model, etc... i.e. that the pulls help with the systematic error hunt.

Thus, following the previous example, for a straight line fit, data points in the center will have a small value of σ_{fit}^2, and the nominator will be dominated by σ_{hit}^2 (accurate fit in the center). But in the outer region σ_{fit}^2 will not be small (no accurate line) and the standard deviation of the residual, σ_r, will be smaller than σ_{hit}.

3.4.6 Silicon Tracker survey

As it has been pointed out the goal of the alignment procedure is to determine the corrections of the 6 DoFs (three translations and three rotations) that describe the position and orientation of the module in space. Apart from the reconstructed tracks and residuals the track-based algorithms have other ingredients that can help with the alignment convergence as for example the survey measurements. This is why during the assembly of the silicon modules detailed survey data was taken to measure the precise positions of the detector elements and support structures. Obviously, these processes where done by mechanical mounting machines and robotic assemblers. Afterwards, this survey data was transformed into alignment data, i.e. into three translations in x, y and z and three rotations around these axis, α, β and γ (see figure 4.2 in chapter 4). Non-planarities of the modules, such as bows and bends, of the modules were not taken into account although there were estimated when they may be important as it will be shown.

For Pixels, the module locations on each sector were optically surveyed using a Coordinate Measurement Machine (CMM). The measuring technique uses fiducial marks in the four corners of the pixel sensors as the reference points (fiducials of Pixel wafers are similar to the fiducials of SCT wafers which can be seen on figure 3.21). Two sets of measurements are then taken, one set measuring in the sensor plane where x, y and γ (in-the-plane rotation, i.e. rotation angle around the z axis) and another set which measures 32 x, y and z points on the top side of each module allowing to calculate the remaining (out-of-plane) DoF, i.e. α, β and z. The survey precision for a pixel sector is estimated to be better than 5 μm in the plane of the module and about 13 μm in the direction perpendicular to this plane. For Pixel modules the non-planarities became

[4]The normal distribution or Gaussian distribution is a bell-shaped and continuous probability distribution with a peak at its mean. It is denoted as N(μ,σ^2) where μ represents its mean or average value and σ^2 its variance.

Alignment DoF	Pixel stave	Pixel sector	SCT stave	SCT disc
x (μm)	50	4.6	150	32
y (μm)	20	4.7	150	41
z (μm)	50	12.7	150	50
α (mrad)	1.7	0.3	2.5	1
β (mrad)	5	0.7	5	1
γ (mrad)	1.7	0.12	2.5	0.09

Table 3.5: *Summary of the estimated and systematic uncertainties (mounting precision before integration) on the survey alignment parameters for Pixels and SCT modules on staves, sectors and discs [55].*

important as it was estimated that the average module bowing is less than 50 μm, higher than the intrinsic Pixel module precision. Anyhow, the later measurements are not used nowadays in the alignment procedure but they will be used in the near future to improve the alignment precision. The Pixel staves were surveyed to a precision of 20 μm to 50 μm depending on the DoF. Table 3.5 has the survey data summary for staves and sectors and for each DoF [55]. More information about the Pixel survey can be found on reference [56].

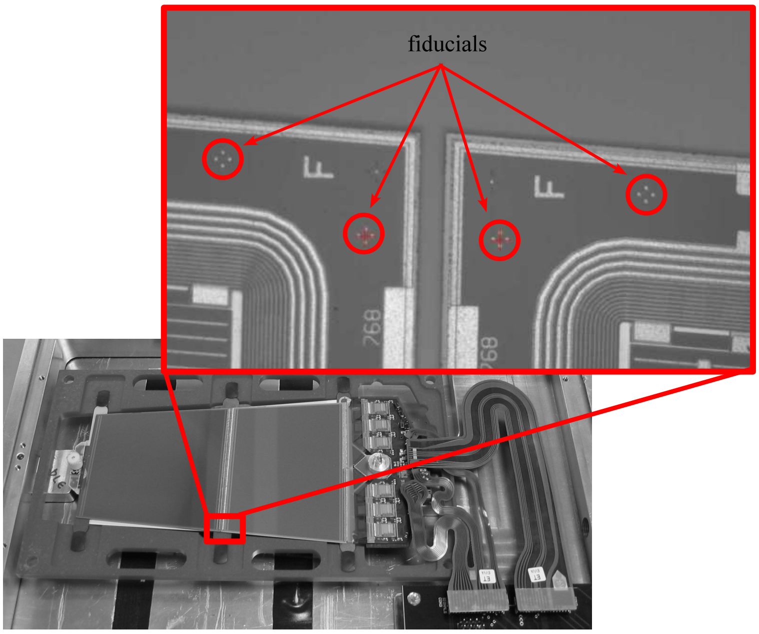

Figure 3.21: *Fiducial marks on SCT wafers for mechanical alignment purposes.*

SCT modules were assembled with mechanical precision machines which aligned both (6×6 cm^2) wafers on a particular side with micron level precision. Afterwards both sides of each particular module were assembled, aligned and rotated 40 mrad between them. This alignment was performed based on the fiducial marks, similar to the Pixels, that the SCT wafers have on the borders. Figure 3.21 shows the fiducial marks on two SCT wafers of the same side. At the end of their assembly, SCT modules where measured again after thermal tests with optical machines like the one in figure 3.22. This figure shows the metrology setup used in the SCT module survey in the IFIC's clean room which consisted in an laser interferometer device and two optical cameras. The as-built tolerances per module were $< 8\mu m$ in-plane and $< 70\mu m$ out-of-plane (bowing and thickness) and the measured RMS spread of the final module survey (after construction) was 1.6 μm in the back-to-back position of the stereo pair (measured transverse to the strips), 2.8 μm in the position of the mounting hole and slot (measured transverse to the strips) and 40 μm out-of-plane. These survey measurements tell how well are these SCT modules assembled.

SCT support structures as the one shown in figure 3.23 were survey before integration. The precision achieved for the barrel structures was 150 μm for translations and of few milliradians for rotations in the case of SCT staves. At the end-caps, the SCT discs were better mounted (higher precision) with less than 50 μm and less than a mrad. Table 3.5 summarizes the SCT survey data for staves and discs and for each DoF [55].

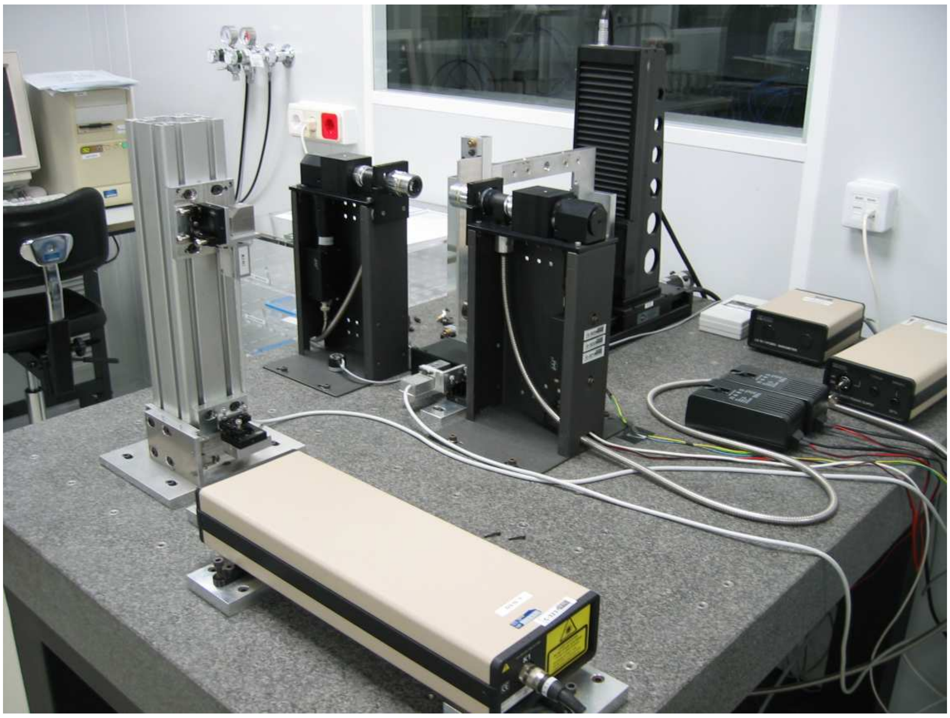

Figure 3.22: *Photograph of the metrology setup used to survey the SCT end-cap modules assembled at IFIC (Valencia).*

SCT barrel modules are much more rigid than Pixels so out of plane distortions can be neglected. On the other hand, SCT end-cap modules are less rigid and they are (more) affected

Figure 3.23: *Photograph during the assembly of one SCT End-Cap (Liverpool, UK).*

by variations of the spine thickness and bowing of the sensors. Using metrology setups as the one in figure 3.22 a common distortion profile was established for the sensors at the level of few micrometers and a module thickness variation of 15 μm. Anyhow, the position of the SCT modules was not surveyed once they were placed in their supporting structures and the SCT was integrated but it is expected to have a precision of 100 μm RMS in $r\phi$ and < 1 mm in global Z direction. It was concluded that these measurements should not be used as an input for the SCT alignment [18].

Anyhow all these survey measurements have an important handicap which is the fact they are measured before the detector integration. Thus, there are no reliable surveys done with the detector finally integrated and cold. It is expected that thermal, handling and transport effects increment the misalignment uncertainty about 50 μm. This is why it is not recommended to use the survey data in the alignment. In fact, only the Pixel survey measurements (at module level) were used as the starting alignment for producing the alignment constants using cosmic ray data (see chapter 7).

Finally, relative survey measurements were done between subdetectors. This data reveals that there is a relative misalignment of few millimeters between the Silicon Tracker and the TRT [57].

3.5 Data Streams

The ATLAS experiment uses a complex trigger strategy, as has been described in section 2.3.4, to be able to achieve the necessary EF rate output, making possible to optimize the storage and processing needs of these data. These needs are described in the ATLAS Computing Model [58], which embraces GRID concepts. The Tier-0 streaming baseline model includes four types of streams coming from the EF:

- The ***primary*** or ***physics stream*** which contains all physics events.
- The ***express stream*** which contains a subset of events ($\sim 5\%$ of the full data).
- The ***calibration stream*** for alignment and calibration purposes.
- The ***diagnostic stream*** with pathological events.

With ~ 1.6 MB per event, each SubFarm Output (SFO) at 4 Hz will fill a 2 GB file with ~ 1250 events every 5 minutes. This defines the minimum latency to start the processing of any stream. The latency of the *physics stream* is defined by the necessary time to have calibration, alignment, and other conditions data available on the Tier-0 processors based mainly on the *calibration stream*. The current goal is to be able to reconstruct the *express* and *calibration stream* within 8 hours and the primary data stream reconstruction (known as "prompt" reconstruction) beginning 24 hours after data taking.

From the alignment point of view, the *calibration stream* is obviously the most important one. This stream is composed of raw data, in byte-stream format, and contains information of the relevant parts of the detector (thanks to Partial Event Building algorithms (PEB)), in particular only the hit information of the selected tracks. This leads to a significantly improved bandwidth (~ 10 Hz) usage and storage capability. Thus, this stream will be used to derive and update the calibration and alignment constants if necessary every 24h. Processing is done using specialized algorithms running within the ATLAS software framework in dedicated Tier-0 resources, and the alignment constants will be stored and distributed using the COOL conditions database infrastructure.

The PEB algorithm of the *calibration stream* needs events with isolated tracks and the associated RoIs are used to fill the required list of ReadOut Drivers (ROBs[5]). The selection of the tracks is done running the alignment Trigger Chains, trk9i_calib and trk16i_calib, which starts respectively with HA6 and HA9i LVL1 triggers (i.e. Hadronic signatures with energy thresholds at 6 GeV and 9 GeV). At LVL2 it selects single isolated tracks inside the η-ϕ region defined by the LVL1 hadronic signatures. The associated list of ROBs from the ID is passed from LVL2 to the event builder. The desired output rate at LVL2 is of the order of 50 Hz (stream output rate should not exceed a few MB/s). For this LVL2 output rate, the pre-scales for the LVL2 objects were optimized at 40 for trk9i_calib (i.e. one event out of 40 events, fulfilling the chain, leads to an accept of the event), and 1 for trk16i_calib. This algorithm is the same used for physics and therefore no extra execution time is used. Results from preliminary tests with Cosmic ray data can be found in reference [59].

[5]The ReadOut Drivers (ROBs) are special hardware to read out the different modules of the different detectors.

3.6 ATLAS Software: *Athena*

Athena [60] is the name of the ATLAS software framework which is based on the LHCb framework known as *Gaudi* [61]. The *Athena* code is based on the C++ language and it provides a facility for various needs such as event generation, reconstruction or detector description. Thus, it consists in a huge amount of algorithms organized in packages. Moreover, it ensures that the requested algorithms are run in the correct order, and it offers common services like message logging, access to data on disc or remote disc servers (such as CASTOR) and filling of histograms and ntuples. The output of an algorithm is written to a common place in memory, called the “Transient Event Store” (TES), from where the next algorithm can retrieve the output and process it further. The output can also be written to disc, using a persistency scheme. Moreover, the framework also ensures that the data is read from disc if an algorithm requests it. Finally, the handling of input/output data as well as the usage of services and algorithms is done in so-called *jobOption* files which are written in Python, another object-orientated, interpreted scripting language.

ATLAS software is organized into a hierarchical structure of packages. Each package contains services and algorithms where each package has a defined dependency on other packages. All these packages are managed and stored in a version control repository, in particular, SVN (Subversion) software. These kind of infrastructures are mandatory needed in other to work efficiently in a so high collaborative environment as ATLAS where many scientists can be working in the same algorithm at the same time worldwide. Each package has a tag number which distinguishes between different versions. A project consists of a complete collection of tagged packages and it is identified with a release number.

Furthermore, the offline software contains a complete description of the ATLAS detector which is used by event data model for simulations and reconstructions. This part of the software has the information about the geometry and material of the detector, such as material properties, and the position and orientation of detector elements. All the simulation and reconstruction steps in ATLAS get the detector information from a common source, called GeoModel, that ensures that each step uses exactly the same information (volumes and materials), thus preventing inconsistencies. The alignment software is integrated into this framework. At the same time, the event reconstruction is performed by a collection of algorithms and tools that perform raw data reconstruction, tracking, calibrations and so on.

The last important part from the alignment point of view are the databases. Several databases are needed in order to allow the *Athena* framework succeed. Thus, for example, the numbers that define the size and position of each volume (needed by GeoModel) are stored in an Oracle database (for example, see [62] for the SCT end-cap modules description). Also, the alignment constants are stored in a conditions database which is used by the detector description to correct the nominal positions of the sensors from the previous database. It also holds the calibration constants, which are needed, for example, to convert the drift times in the TRT straws and the MDT tubes into drift radii. The calibration constants also comprise the list of dead or noisy silicon channels. Finally, an important feature of this condition database is that it implements “intervals of validity” service (IOVs). This allows that the simulation/reconstruction check which IOV corresponds to the dataset that is being simulated/reconstructed, and retrieves the alignment or calibration constants that belong to this IOV.

3.7 Track and hit selection

A good track and hit selection is generally essential for the track-based alignment algorithms. The requirements depend on the data type (collisions, cosmics, etc). The procedure is basically as follows: first, hits are selected and tracks are reconstructed with the selected ones. After that, the hits used on each track are checked to validate them as associated hits or to reject them as outliers. Finally, each track is selected based on its track parameters and number of associated hits.

- **Hit selection:** A minimum number of Pixels and SCT hits associated to a given track is required in order to be sure that the track have enough hits. By default, the Globalχ^2 algorithm uses 2 Pixel hits and 5 SCT hits, although it can require a minimum number of total hits or residuals. Moreover, it is possible to fixed a minimum number of overlap hits in total or independently for Pixels and SCT. It is also possible to select or reject tracks based on the number of holes (i.e. an expected hit where there is no hit) or shared hits (i.e. hits shared with several tracks). Finally, one can required hits in the B-layer (closer Pixel layer to the bam pipe) due to their high sensitivity to misalignments.

- **Track selection:** A basic track requirement is a transverse momentum cutoff to minimize large MCS effects. Even knowing that the trackers can estimate and take into account material effects it is desired to identify track kinks as originated from real misalignments rather than from scatterings.

The Globalχ^2 package has simple track and hit selection tools which are, in most of the cases, enough to achieve a good alignment level. Anyhow, the tracking and the alignment data model provides several tools such as the InDetAlignHitQualSelTool package [63]. This powerful tool can reject outliers (i.e. hits which are too far away of a track), edge channels and ganged pixels. It allows to cut on the maximum track incidence angle with respect the local z axis of a module in the local xz plane or on the cluster size of the hit (i.e. number of pixels/strips constituting the hit).

3.8 Track-based alignment algorithms for the ID

Nowadays, there are three independent track-based alignment algorithms for the ATLAS ID: the *Robust*, the *Local*χ^2 and the *Global*χ^2 alignment approaches. Of course, all of these methods have been developed and implemented within the *Athena* framework. Moreover, all of them make use of the residual and tracking information.

- The ***Robust*** **approach** [64] [65] is an iterative method to align planar silicon detectors by re-centring residual distributions using the module overlapping information, i.e. this method uses physical overlaps between modules to improve residual calculation. The Robust method heavily relies on iteration in order to converge, giving corrections for two or three DoF's only. This method has been tested and successfully applied in all the MC challenges [66] [67], test beams [53] and cosmic ray data taking [68] [69] up to now and although it is not as powerful as other methods it will provide very valuable cross-checks specially at the beginning of ATLAS.

- **Globalχ^2** and **Localχ^2 approaches** are both based on the minimisation of the χ^2 function. Both methods proved their principles providing good performance on simulation challenges [66] [67] and on real data challenges [53] [68] [69]. The Localχ^2 approach [54] [70] is a particular case of the Globalχ^2 approach [71]. Next chapter will detail the Globalχ^2 formalism pointing out the particular case of the Localχ^2 formalism.

3.9 Hardware-based alignment for the Silicon Tracker

There is a hardware-based alignment system integrated in the SCT subdetector. It is based on a Frequency Scanning Interferometry (FSI) [72] technology which performs 842 simultaneous real-time length measurements in-between nodes forming a geodetic grid on the SCT support structure. Figure 3.24 shows a sketch of the FSI grid where the 512 measurements lines in the barrel and 165 in both end-caps can be seen. Distance measurements between grid nodes can reach a precision of about 150 nm and a 3D grid geometry can be reconstructed to a precision of less than 5 μm in the grid line directions.

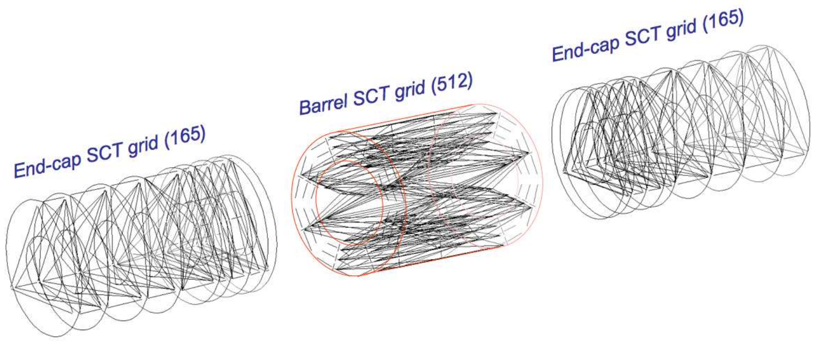

Figure 3.24: *A sketch of the FSI grid lines with its 512 measurements in the barrel and 165 in both end-caps, i.e. 842 in total.*

This system has been designed to monitor global deformations of the SCT (offering access to low spatial frequency detector deformations) quasi on real time. Because of that it will operate in conjunction with the track-based software algorithms, helping therefore to constraint these global movements and distortions. Nowadays, FSI is already installed in the ATLAS cavern and all grid lines have been successfully illuminated and read out and its data is available.

4

The Globalχ^2 algorithm

An application of the fundamental Least Squares[1] linear expansion formalism [73] is proposed as a track based offline alignment algorithm for the ATLAS Silicon Tracker system. In this chapter the Globalχ^2 algorithm [71] will be discussed with high detail, pointing out the most relevant features of the method. In addition, several types of constraints are introduced and discussed, such as track parameter and alignment parameter constraints.

4.1 The general χ^2 formalism

The most extended alignment methods for the track based algorithms of the high energy detector components (barrel, layers, modules...) are based on the Least Squares method. The minimization of a χ^2 function with respect the parameters which have to be determined is performed. The χ^2 function is defined as follows:

$$\chi^2 = \sum_{e}\sum_{t\in e}\sum_{h\in t}\left(\frac{r_{eth}}{\sigma_{eth}}\right)^2 \qquad \text{where} \qquad \forall e \in \mathbb{E} \ , \ \forall t \in \mathbb{T} \ \text{and} \ \forall h \in \mathbb{H} \tag{4.1}$$

being $\mathbb{E}$ the set of events, $\mathbb{T}$ the set of reconstructed tracks (which are not necessarily all the tracks in the event) and $\mathbb{H}$ the set of associated hits to each of the tracks (which are not necessarily all the hits in the track). r_{eht} accounts for the residual (section 3.4.4) of the h^{th} hit of track t and event e and σ_{eth} its the associated uncertainty of the measured hit (see comments on section 3.4.4). Note that the χ^2 is just a dimensionless scalar. In any case, the residuals must depend, at least, on the parameters. In case of linear dependence the solution will be exact. If the dependence is not linear, iterations will be required in order to converge to the exact solution.

[1] The method of Least Squares can be deduced directly from the Likelihood method under the assumption of Gaussian distributed random variables.

Let be, from now onwards, $\mathbf{r}$[2] the vector with all the residual components that the system can provide (see section 3.4.4), being N_{RES} the total number of residual components. For a particular track within an event, just few elements of $\mathbf{r}$ will be filled. Now, if one applies this idea to the ATLAS silicon tracker, the expresion 4.2 can be written as follows:

$$\mathbf{r} = \begin{pmatrix} r_1 \\ \vdots \\ r_{N_{RES}} \end{pmatrix} = \begin{pmatrix} r_{PIX\phi_1} \\ \vdots \\ r_{PIX\phi_{N_{pix}}} \\ r_{PIX\eta_1} \\ \vdots \\ r_{PIX\eta_{N_{pix}}} \\ r_{SCTr\phi_1} \\ \vdots \\ r_{SCTr\phi_{N_{SCT}}} \\ r_{SCTst_1} \\ \vdots \\ r_{SCTst_{N_{SCT}}} \end{pmatrix} \tag{4.2}$$

where $r_{PIX\phi_i}$ stands for the ϕ residual of the i-th pixel module and $r_{PIX\eta_i}$ stands for the η residual of the i-th pixel module. By analogy $r_{SCTr\phi_i}$ corresponds to the residual in the $r\phi$-side of the i-th SCT module and r_{SCTst_i} to the stereo-side of the same SCT module.

Obviously $\mathbf{r}$ can be defined in a more generic way in order to accommodate other detectors (e.g. TRT) or represent a generic tracking device sensor that produces residuals or alternatively use SCT space points providing local x and local y residuals for a SCT module instead of $r\phi$ and stereo side residuals. Of course, other alternative definitions of the residuals (for instance, DOCA residuals used by the Localχ^2 method [54], biased or unbiased residuals, etc...) can also be accommodated as discussed in section 3.4.4. Moreover what it is said here for the ATLAS ID can be very easily extended to accommodate other tracking devices without penalty for the generality of algebraic expressions.

Therefore, it is important to note that the order of $\mathbf{r}$ has just the total number of residuals available for a given track and it will be denoted as a column vector. In the ATLAS silicon tracker case, the order is $2(N_{pix} + N_{SCT}) \equiv N_{RES}$, so the dimension of $\mathbf{r}$ is $[N_{RES} \times 1]$. N_{pix} and N_{SCT} are the total number of Pixels and SCT modules, respectively, i.e. the total number of alignable objects. N_{RES} is twice $N_{pix} + N_{SCT}$ because the Pixels can measured two residuals per hit (so-called $r\phi$ and η residuals, respectively) and the SCT can measure one residual per hit and per side ($r\phi$) but each module has two sides ($r\phi$ side and stereo side). Then, in the SCT modules is not necessary that both residuals are measured at the same time as they come from independent hits. It is obvious that residuals will be null if the sensor that defines them has not recorded a hit for a given reconstructed track. From now onward, as a notation convention, $\mathbf{r}$ will represent the residual vector for a given track.

Furthermore, the measurement uncertainties (σ) can be written in matrix form, defining a covariance matrix. This covariance matrix, which will be denoted by V, will be diagonal, being its terms σ^2.

[2] As stated in the previous chapter, bold letters represent vectors in this thesis.

In the ATLAS Silicon Tracker case, the matrix form of V is as follows:

$$V = \begin{pmatrix} \sigma^2_{pix\phi_1} & & & & & & & \\ & \ddots & & & & (0) & & \\ & & \sigma^2_{pix\eta_1} & & & & & \\ & & & \ddots & & & & \\ & & & & \sigma^2_{SCTr\phi_1} & & & \\ & & (0) & & & \ddots & & \\ & & & & & & \sigma^2_{SCTst_1} & \\ & & & & & & & \ddots \end{pmatrix}$$

It is clear that under the assumption of independent or even uncorrelated measurements in each module, V^{-1} has all the off-diagonal elements null. This is, in fact, the current situation when one consider just the error of the intrinsic resolution of the sensors. However correlations between modules can be introduced in the formalism considering material effects. i.e. the deflection angles in the scattering planes. This issue is discussed in detail in appendix A.1 since the Globalχ^2 algorithm already uses these correlations.

Now, one has available all the ingredients to redefine the χ^2 function of expression 4.1 (assuming that V is not singular) which can be rewritten in a more generic way as follows:

$$\chi^2 = \sum_e \sum_{t \in e} \mathbf{r}^T V^{-1} \mathbf{r} \tag{4.3}$$

Using this formalism, the defined χ^2 is, as in expression 4.1, a dimensionless scalar:

$$\dim[\chi^2] = \dim[\mathbf{r}^T] \dim[V^{-1}] \dim[\mathbf{r}] = [1 \times N_{RES}][N_{RES} \times N_{RES}][N_{RES} \times 1] = [1 \times 1]$$

4.1.1 Residuals: from the detector to the χ^2 alignment function

Reached this point it is worth to reconsider how the residuals are obtained, although it was already explained in section 3.4.4. Figure 4.1 presents a scheme of the linear residual definition used in the Globalχ^2 algorithm.

The numerical value of a generic residual corresponding to a given sensitive direction was defined in expression 3.4 as:

$$\mathbf{r} = (\mathbf{m} - \mathbf{e}(\boldsymbol{\pi}, \mathbf{a}))$$

where $\mathbf{m}$ is the vector that gives the position of the measurement and $\mathbf{e}(\boldsymbol{\pi}, \mathbf{a})$ represents the vector to the extrapolated point of the track in the measurement sensor plane which follows a measurement model. Moreover, $\mathbf{e}$ depends explicitly on the track parameters (represented by $\boldsymbol{\pi}$) as well as on the alignment parameters (represented by $\mathbf{a}$), therefore $\mathbf{r}$ depends implicitly on $\boldsymbol{\pi}$ and $\mathbf{a}$.

One may argue that $\mathbf{m}$ also depends on $\mathbf{a}$. That dependence is not such as the alignment corrections can be given in the local coordinate frame. In this local system, $\mathbf{m}$ is given by the logical fired channel. Therefore, $\mathbf{m}$ is fixed in the local system and this is why $\mathbf{m}$ does not depend on $\mathbf{a}$.

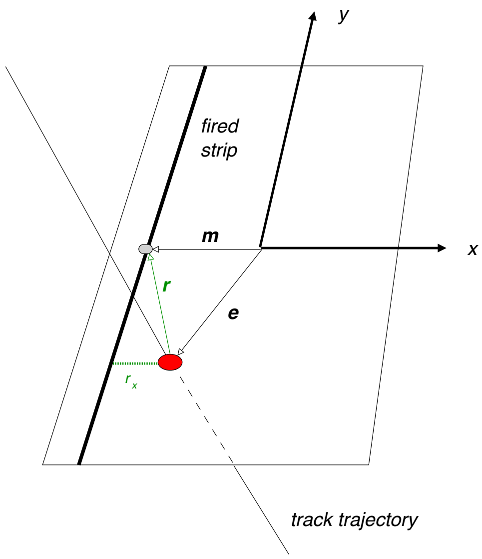

Figure 4.1: *Schematic representation of a within plane (linear residual) definition in a microstrip device (i.e. SCT plane).* **m** *is the vector to the center of the fired strip/cluster,* **e** *is the vector to the intersection between the track and the sensitive plane, whilst* **r** *is the residual vector and* r_x *is the projection of the residual vector into the x direction.*

4.1.1.1 Track parameters

In what concerns the track parameters, denoted by $\boldsymbol{\pi}$, it is convenient to use again a vector notation in order to enclose all the track parameters in a single set, so the size of this vector will be N_{TPR}.

In ATLAS tracking, a set of five track parameters (helix representation, $N_{TPR} = 5$) are used as was mentioned on section 3.4.3. These track parameters are $\boldsymbol{\pi} = \{d_0, z_0, \phi_0, cot\theta, q/p\}$.

As in certain cases one may have less than five parameters (e.g. when no B field is available, no q/p_T estimation can be done as tracks do not bend) however a general definition of the dimension of the track parameter vector will be used in this chapter (N_{TPR}).

4.1.1.2 Alignment degrees of freedom

The alignment parameters, denoted by **a**, refer to the Degrees of Freedom (DoFs) of the alignable objects. If one considers the tracking devices as rigid bodies, then one is left with six alignment DoFs per module (N_{DOF}=6), i.e. its center coordinates (T_x, T_y, T_Z) and its orientation (R_x, R_y, R_z), as it is shown in figure 4.2.

In principle, the rotations can be defined using Cardano (i.e. rotations around the nominal axis) or Euler angles. Anyhow, the ATLAS alignment model decided to use Cardano angles because the alignment corrections are suppose to be small. Then, the changes in the orientation of the measuring devices (modules) are translated into small rotations around their nominal axis. Figure 4.2 shows a scheme of this Cardano angle definition.

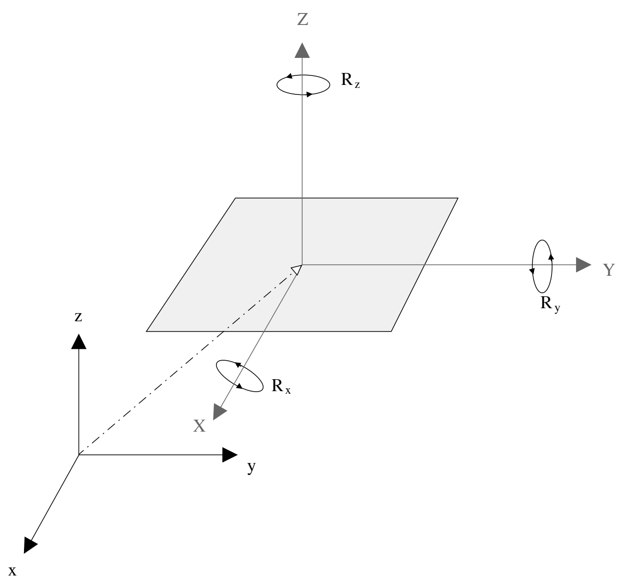

Figure 4.2: *Definition of the six degrees of freedom for a rigid body where rotations are expressed in Cardano angles, i.e. rotations around the axis.*

One may consider a subset of those parameters, but this depends on the specific application. Also, one can consider more degrees of freedom, allowing mechanical deformations such as bows or bends. Anyhow, these cases which are not yet implemented in the Globalχ^2 code, are considered as higher order corrections. So, in general, one would list **a** as a sequential list of alignment degrees of freedom (thereafter **a** will represent a column vector, in analogy to $\boldsymbol{\pi}$), and the *i*-th component of **a** would mean a given translation or rotation of any of the alignable objects. Therefore for all the ATLAS silicon modules (e.g. the SCT module case) or in general, alignable objects, their degrees of freedom under consideration can be written:

$$\mathbf{a} = \begin{pmatrix} T_{x\ 1} \\ T_{y\ 1} \\ T_{z\ 1} \\ R_{x\ 1} \\ R_{y\ 1} \\ R_{z\ 1} \\ \vdots \\ T_{x\ N_{ALI}} \\ T_{y\ N_{ALI}} \\ T_{z\ N_{ALI}} \\ R_{x\ N_{ALI}} \\ R_{y\ N_{ALI}} \\ R_{z\ N_{ALI}} \end{pmatrix} = \begin{pmatrix} T_{x\ 1_{PIX}} \\ T_{y\ 1_{PIX}} \\ T_{z\ 1_{PIX}} \\ R_{x\ 1_{PIX}} \\ R_{y\ 1_{PIX}} \\ R_{z\ 1_{PIX}} \\ \vdots \\ T_{x\ N_{SCT}} \\ T_{y\ N_{SCT}} \\ T_{z\ N_{SCT}} \\ R_{x\ N_{SCT}} \\ R_{y\ N_{SCT}} \\ R_{z\ N_{SCT}} \end{pmatrix}$$

Then, $\mathbf{a}$ is a vector of size $N_{ALI} = N_{DOF} \times (N_{pix} + N_{SCT})$ where N_{pix} and N_{SCT} are the number of Pixel and SCT modules, respectively. In other words, there are N_{ALI} degrees of freedom to align which in the ATLAS Silicon Tracker case means $N_{ALI} = 34992$.

As commented in the previous paragraph, an alignable object is not necessarily the residual provider. For instance, a SCT module can be considered as an alignable object, while the residual providers are the two sensitive sides ($r\phi$ and stereo). The SCT module is considered as a rigid body with the parameters of the $r\phi$ and stereo side linked to those of the module. Another example can be a TRT module since it provides many residuals which are linked to the straws within a TRT module. For Pixel modules, the residual provider matches the alignable object as the pixel module is made out of a single wafer.

Moreover, there are more cases where the alignable objects are not the residual providers, for instance, when super-structures are considered and residuals are projected. This topic will be carefully discussed in chapter 5.

4.2 The Globalχ^2 formalism

From the mathematical point of view, the goal of this method is to find a the set of parameters (in our case, alignment parameters which will be denoted by $\mathbf{a}$) that minimizes the χ^2 function defined in 4.3 as:

$$\chi^2 = \sum_e \sum_{t \in e} \mathbf{r}^T V^{-1} \mathbf{r}$$

This algorithm was proposed for the ATLAS Silicon Tracker [71], as well as for the ATLAS TRT [50]. Furthermore, there are also other methods as the well-known Millepede [74] algorithm which used equivalent formalism and it is used for the alignment of the CMS silicon tracker.

Therefore, one has to start from the above equation and then apply the minimum condition:

$$\frac{d\chi^2}{d\mathbf{a}} = 0 \tag{4.4}$$

In an abuse of notation which will simplify the formulas, the term $d\chi^2/d\mathbf{a}$ is a row vector, with dimension $[1 \times N_{ALI}]$, which represents the derivative of χ^2 with respect all the parameters defined in the vector $\mathbf{a}$. Expressed in a matricial way it looks like that:

$$\begin{pmatrix} \frac{d\chi^2}{d\mathbf{a}_1} & \frac{d\chi^2}{d\mathbf{a}_2} & \dots & \frac{d\chi^2}{d\mathbf{a}_{N_{ALI}}} \end{pmatrix} = \begin{pmatrix} 0 & 0 & \dots & 0 \end{pmatrix}$$

Then, the equation 4.3 together with 4.4 give:

$$\frac{d\chi^2}{d\mathbf{a}} = \frac{d}{d\mathbf{a}} \left[\sum_e \sum_{t \in e} \mathbf{r}^T V^{-1} \mathbf{r} \right] = \sum_e \sum_{t \in e} \left[\left(\frac{d\mathbf{r}}{d\mathbf{a}} \right)^T V^{-1} \mathbf{r} \right]^T + \sum_e \sum_{t \in e} \left[\mathbf{r}^T V^{-1} \frac{d\mathbf{r}}{d\mathbf{a}} \right] = 0 \tag{4.5}$$

It is worth to remind that $\mathbf{r}$ (as well as V) is defined for a single track and therefore $\sum_e \sum_{t \in e} \mathbf{r}$ will accumulate the residual contributions for all the considered tracks for all the events in a data sample. Moreover thanks to the abuse of notation, $d\mathbf{r}/d\mathbf{a}$ is a matrix and has the following dimension $[N_{RES} \times N_{ALI}]$, i.e. $d\mathbf{r}/d\mathbf{a}$ represents the derivative of each first vector element ($d\mathbf{r}_i$) with respect to the second vector element ($d\mathbf{a}_j$). In matrix form:

$$\frac{d\mathbf{r}}{d\mathbf{a}} = \begin{pmatrix} \frac{d\mathbf{r}_1}{d\mathbf{a}_1} & \cdots & \frac{d\mathbf{r}_1}{d\mathbf{a}_{N_{ALI}}} \\ \vdots & \ddots & \vdots \\ \frac{d\mathbf{r}_{N_{RES}}}{d\mathbf{a}_1} & \cdots & \frac{d\mathbf{r}_{N_{RES}}}{d\mathbf{a}_{N_{ALI}}} \end{pmatrix}$$

Of course the elements of this matrix $(d\mathbf{r}/d\mathbf{a})_{ij} = d\mathbf{r}_i/d\mathbf{a}_j$ will be null if the residual provider and the degrees of freedom are not linked. In other words, the residuals within a module are independent of the alignment degrees of freedom of another different module.

Now, taken advantage from the notation and knowing that V^{-1} is a symmetric matrix ($(V^{-1})^T = V^{-1}$), the χ^2 minimization (with respect $\mathbf{a}$) converts equation 4.5 in:

$$\frac{d\chi^2}{d\mathbf{a}} = \sum_e \sum_{t\in e} \left[\left(\frac{d\mathbf{r}}{d\mathbf{a}} \right)^T V^{-1}\mathbf{r} \right]^T + \sum_e \sum_{t\in e} \left[\mathbf{r}^T V^{-1} \frac{d\mathbf{r}}{d\mathbf{a}} \right] = 2 \sum_e \sum_{t\in e} \left[\mathbf{r}^T V^{-1} \frac{d\mathbf{r}}{d\mathbf{a}} \right] = 0 \qquad (4.6)$$

The last step uses a simple transposing rule, $(AB)^T = B^T A^T$ (being A and B matrices), therefore 4.4 condition can be expressed as:

$$\sum_e \sum_{t\in e} \mathbf{r}^T V^{-1} \frac{d\mathbf{r}}{d\mathbf{a}} = 0$$

where the previous expression is again a set of N_{ALI} equations due to the use of $d\mathbf{a}$, exactly the same as $d\chi^2/d\mathbf{a}$.

$$\dim \left[\mathbf{r}^T V^{-1} \frac{d\mathbf{r}}{d\mathbf{a}} \right] = [1 \times N_{RES}][N_{RES} \times N_{RES}][N_{RES} \times N_{ALI}] = [1 \times N_{ALI}]$$

Of course, the transpose of expression 4.4 will end up in the transpose of expression 4.6 and they can be used indistinctly, although the last option will be used in this text.

$$\sum_e \sum_{t\in e} \left(\frac{d\mathbf{r}}{d\mathbf{a}} \right)^T V^{-1}\mathbf{r} = 0 \qquad (4.7)$$

Reached this point, one needs to evaluate the total derivate of $\mathbf{r}$ with respect $\mathbf{a}$: $d\mathbf{r}/d\mathbf{a}$

4.2.1 Residual derivatives

In our case, the residuals depend on the track parameters and on the alignment parameters, i.e. $\mathbf{r} = \mathbf{r}(\pi, \mathbf{a})$, therefore, its differential is trivially given by:

$$d\mathbf{r} = \frac{\partial \mathbf{r}}{\partial \pi} d\pi + \frac{\partial \mathbf{r}}{\partial \mathbf{a}} d\mathbf{a}$$

Taking this into account, it is easy to write:

$$\frac{d\mathbf{r}}{d\pi} = \frac{\partial \mathbf{r}}{\partial \pi}\frac{d\pi}{d\pi} + \frac{\partial \mathbf{r}}{\partial \mathbf{a}}\frac{d\mathbf{a}}{d\pi} = \frac{\partial \mathbf{r}}{\partial \pi} + \frac{\partial \mathbf{r}}{\partial \mathbf{a}}\frac{d\mathbf{a}}{d\pi}$$

$$\frac{d\mathbf{r}}{d\mathbf{a}} = \frac{\partial \mathbf{r}}{\partial \pi}\frac{d\pi}{d\mathbf{a}} + \frac{\partial \mathbf{r}}{\partial \mathbf{a}}\frac{d\mathbf{a}}{d\mathbf{a}} = \frac{\partial \mathbf{r}}{\partial \pi}\frac{d\pi}{d\mathbf{a}} + \frac{\partial \mathbf{r}}{\partial \mathbf{a}} \tag{4.8}$$

Anyhow, the first expression, can be reduced as it is assumed that the sensors location do not depend on the tracks, i.e. $\mathbf{a}$ does not depend on $\boldsymbol{\pi}$. Therefore $d\mathbf{a}/d\boldsymbol{\pi} = 0$:

$$\frac{d\mathbf{r}}{d\pi} = \frac{\partial \mathbf{r}}{\partial \pi} \tag{4.9}$$

So, using expression 4.8 in expression 4.7, it can be write as follows:

$$\sum_{e}\sum_{t\in e}\left(\frac{d\mathbf{r}}{d\mathbf{a}}\right)^{T} V^{-1}\mathbf{r} = \sum_{e}\sum_{t\in e}\left(\frac{\partial \mathbf{r}}{\partial \pi}\frac{d\pi}{d\mathbf{a}} + \frac{\partial \mathbf{r}}{\partial \mathbf{a}}\right)^{T} V^{-1}\mathbf{r} = 0 \tag{4.10}$$

Now, one needs to compute $d\boldsymbol{\pi}/d\mathbf{a}$. This will require to minimize the χ^2 with respect the track parameters, or in other words to fit the track.

4.2.2 Track fitting

In the χ^2 definition (expression 4.3) there is an explicit sum over tracks and the residuals themselves depend on the track parameters (equation 3.4). So first, one has to find the solution for the track parameters for any arbitrary alignment and for every independent track. Therefore, one has to minimize the χ^2 function with respect the track parameters ($\boldsymbol{\pi}$) for a given track:

$$\chi^2 = \mathbf{r}^T V^{-1}\mathbf{r} \quad \rightarrow \quad \frac{d\chi^2}{d\pi} = 0 \quad \text{although using 4.9, one has} \quad \frac{\partial\chi^2}{\partial\pi} = 0$$

Again, $\partial\chi^2/\partial\boldsymbol{\pi}$ is a vector with dimension $[1\times N_{TPR}]$ and for the track parameters used in alignment, this vector, which is a set of N_{TPR} equations, takes the expression:

$$\left(\frac{\partial\chi^2}{\partial d_0}\ \ \frac{\partial\chi^2}{\partial z_0}\ \ \frac{\partial\chi^2}{\partial \phi_0}\ \ \frac{\partial\chi^2}{\partial \cot\theta}\ \ \frac{\partial\chi^2}{\partial q/p_T}\right) = (0\ \ 0\ \ 0\ \ 0\ \ 0)$$

and after some algebra, analogue to 4.7, but for a given track:

$$\left(\frac{\partial \mathbf{r}}{\partial \pi}\right)^{T} V^{-1}\mathbf{r} = 0 \tag{4.11}$$

The goal is to find the track parameter corrections $\delta\boldsymbol{\pi}$ which have to be applied to the initial values $\boldsymbol{\pi}_0$ to get the final track parameters: $\boldsymbol{\pi} = \boldsymbol{\pi}_0 + \delta\boldsymbol{\pi}$. Then, in order to solve expression 4.11, one may assume that the initial values $\boldsymbol{\pi}_0$ are relatively close to the solution $\boldsymbol{\pi}$ and, therefore, expand the residuals around $\boldsymbol{\pi}_0$ with the simple Taylor's rule[3]. Higher order derivatives will be neglected, $\partial^{m+n}\mathbf{r}/\partial\pi_i^m\partial\pi_j^n \rightarrow 0$, since the extrapolated points are considered linear functions of the tracks parameters (small changes). If by any chance the initial parameters are still far from

[3] The Taylor series is a representation of a function as an infinite sum of terms calculated from the values of its derivatives at a single point. It looks like:

$$f(x) = f(a) + f'(a)(x-a) + \frac{1}{2!}f''(a)(x-a)^2 + \ldots + \frac{1}{(n-1)!}f^{n-1}(a)(x-a)^{n-1} + O(n)$$

the solution, this linear approximation still holds, but one needs to iterate in order to reach the optimal results.

By using this approximation the residuals ($\mathbf{r} = \mathbf{r}(\pi, \mathbf{a})$) will change linearly around the initial track parameters ($\boldsymbol{\pi}_0$) as follows:

$$\mathbf{r}(\pi, \mathbf{a}) = \mathbf{r}(\pi_0, \mathbf{a}) + \left.\frac{\partial \mathbf{r}}{\partial \boldsymbol{\pi}}\right|_{\pi=\pi_0} \delta\pi \tag{4.12}$$

so the derivative of the residuals is computed in the neighborhood of $\boldsymbol{\pi}_0$. In what follows, the following convention will be used from now onward:

$$\left.\frac{\partial \mathbf{r}}{\partial \boldsymbol{\pi}}\right|_{\pi_0} \equiv \left.\frac{\partial \mathbf{r}}{\partial \boldsymbol{\pi}}\right|_{\pi=\pi_0} \tag{4.13}$$

Using now, the expression from equation 4.12 one can develop equation 4.11:

$$\left(\frac{\partial \mathbf{r}}{\partial \boldsymbol{\pi}}\right)^T V^{-1}\mathbf{r} = 0 \quad \rightarrow \quad \left(\left.\frac{\partial \mathbf{r}}{\partial \boldsymbol{\pi}}\right|_{\pi_0}\right)^T V^{-1}\left[\mathbf{r}(\pi_0, \mathbf{a}) + \left.\frac{\partial \mathbf{r}}{\partial \boldsymbol{\pi}}\right|_{\pi_0} \delta\pi\right] =$$

$$= \left(\left.\frac{\partial \mathbf{r}}{\partial \boldsymbol{\pi}}\right|_{\pi_0}\right)^T V^{-1}\mathbf{r}(\pi_0, \mathbf{a}) + \left(\left.\frac{\partial \mathbf{r}}{\partial \boldsymbol{\pi}}\right|_{\pi_0}\right)^T V^{-1} \left.\frac{\partial \mathbf{r}}{\partial \boldsymbol{\pi}}\right|_{\pi_0} \delta\boldsymbol{\pi} = 0 \tag{4.14}$$

and now one may define E as:

$$E \equiv \left.\frac{\partial \mathbf{r}}{\partial \boldsymbol{\pi}}\right|_{\pi_0} \tag{4.15}$$

which is a matrix defined for each track, with residuals $\mathbf{r}$ and track parameters ($\boldsymbol{\pi}$). In some literature, this matrix is called the projection matrix [50] [73]. The dimension of the matrix E is $[N_{RES} \times N_{TRP}]$.

Considering the ATLAS Silicon Tracker case, the set of track parameters (d_0, z_0, ϕ_0, $\cot\theta$, q/p_T), E (for a given track) reads as:

$$E = \begin{pmatrix} \frac{\partial r_1}{\partial d_0} & \frac{\partial r_1}{\partial z_0} & \frac{\partial r_1}{\partial \phi_0} & \frac{\partial r_1}{\partial \cot\theta} & \frac{\partial r_1}{\partial q/p_T} \\ \vdots & \vdots & \vdots & \vdots & \vdots \\ \frac{\partial r_{N_{RES}}}{\partial d_0} & \frac{\partial r_{N_{RES}}}{\partial z_0} & \frac{\partial r_{N_{RES}}}{\partial \phi_0} & \frac{\partial r_{N_{RES}}}{\partial \cot\theta} & \frac{\partial r_{N_{RES}}}{\partial q/p_T} \end{pmatrix}$$

Therefore, using the E definition from 4.15 into the track fit equation 4.14, it becomes now:

$$V^{-1}\mathbf{r}(\pi_0, \mathbf{a}) + E^T V^{-1} E\delta\boldsymbol{\pi} = 0$$

which allows to obtain the track parameters corrections $\delta\boldsymbol{\pi}$ as:

$$\delta\boldsymbol{\pi} = -(E^T V^{-1} E)^{-1} E^T V^{-1}\mathbf{r}(\pi_0, \mathbf{a}) \tag{4.16}$$

where, a $N_{TPR} \times N_{TPR}$ matrix ($\mathcal{M}_t$) and a vector of size N_{TPR} (ν_t) can be defined to compact the latter equation:

$$\mathcal{M}_t \equiv E^T V^{-1} E$$

$$\nu_t \equiv E^T V^{-1} \mathbf{r}$$

Expression 4.16, which gives the corrections to the track parameters for a track, reads as:

$$\delta\boldsymbol{\pi} = -\mathcal{M}_t^{-1} \nu_t \tag{4.17}$$

The final solution of the track parameters can be computed from $\boldsymbol{\pi} = \boldsymbol{\pi}_0 + \delta\boldsymbol{\pi}$, as:

$$\boldsymbol{\pi} = \boldsymbol{\pi}_0 - (E^T V^{-1} E)^{-1} E^T V^{-1} \mathbf{r}(\boldsymbol{\pi}_0, \mathbf{a}) = \boldsymbol{\pi}_0 - \mathcal{M}_t^{-1} \nu_t$$

In addition, $d\boldsymbol{\pi}/d\mathbf{a}$ can be now evaluated differentiating the previous expression:

$$\frac{d\boldsymbol{\pi}}{d\mathbf{a}} = \frac{d\boldsymbol{\pi}_0}{d\mathbf{a}} - \frac{d}{d\mathbf{a}}\left[(E^T V^{-1} E)^{-1} E^T V^{-1} \mathbf{r}(\boldsymbol{\pi}_0, \mathbf{a})\right] = -(E^T V^{-1} E)^{-1} E^T V^{-1} \frac{d\mathbf{r}(\boldsymbol{\pi}_0, \mathbf{a})}{d\mathbf{a}} \tag{4.18}$$

where, obviously $d\boldsymbol{\pi}_0/d\mathbf{a} = 0$ because $\boldsymbol{\pi}_0$ is constant. Also from 4.8 one has:

$$\frac{d\mathbf{r}(\boldsymbol{\pi}_0, \mathbf{a})}{d\mathbf{a}} = \frac{\partial \mathbf{r}(\boldsymbol{\pi}_0, \mathbf{a})}{\partial \boldsymbol{\pi}} \frac{d\boldsymbol{\pi}}{d\mathbf{a}} + \frac{\partial \mathbf{r}(\boldsymbol{\pi}_0, \mathbf{a})}{\partial \mathbf{a}} = \frac{\partial \mathbf{r}(\boldsymbol{\pi}_0, \mathbf{a})}{\partial \mathbf{a}}$$

due to the fact that $\partial \mathbf{r}(\boldsymbol{\pi}_0, \mathbf{a})/\partial \boldsymbol{\pi}$ is null. Therefore:

$$\frac{d\boldsymbol{\pi}}{d\mathbf{a}} = -(E^T V^{-1} E)^{-1} E^T V^{-1} \frac{\partial \mathbf{r}(\boldsymbol{\pi}_0, \mathbf{a})}{\partial \mathbf{a}} \tag{4.19}$$

4.2.2.1 Covariance matrix

Once the track parameters are determined, one needs to know their errors and correlations. Thus one needs the covariance matrix of the track parameter corrections (C). This matrix is computed as:

$$C = \mathbf{E}\left[(\delta\boldsymbol{\pi})(\delta\boldsymbol{\pi})^T\right] = \mathbf{E}\left[\left((E^T V^{-1} E)^{-1} (E^T V^{-1} \mathbf{r})\right)\left((E^T V^{-1} E)^{-1} (E^T V^{-1} \mathbf{r})\right)^T\right] =$$

$$= \mathbf{E}\left[\mathcal{M}_t^{-1} (E^T V^{-1} \mathbf{r})(\mathbf{r}^T V^{-1} E)\mathcal{M}_t^{-1}\right] = \mathcal{M}_t^{-1} (E^T V^{-1} \mathbf{E}\left[\mathbf{r}\mathbf{r}^T\right] V^{-1} E)\mathcal{M}_t^{-1} =$$

$$= \mathcal{M}_t^{-1} (E^T V^{-1} V V^{-1} E)\mathcal{M}_t^{-1} = \mathcal{M}_t^{-1} \mathcal{M}_t \mathcal{M}_t^{-1} = \mathcal{M}_t^{-1}$$

where $\mathbf{E}$ means expected value and $\mathbf{E}[\mathbf{r}\mathbf{r}^T] = V$ as is shown in [73]. Also, note, that as $\mathcal{M}_t = (E^T V^{-1} E)$ is a symmetric matrix. Therefore, the covariance matrix of the track parameters is:

$$C = \mathcal{M}_t^{-1} = (E^T V^{-1} E)^{-1}$$

i.e. the covariance matrix of the track parameters ($\boldsymbol{\pi}$) coincides with the matrix of the χ^2 fit.

4.2.3 Alignment corrections fit

In previous subsection the corrections to the track parameters were computed for any alignment parameters. In addition, $d\boldsymbol{\pi}/d\mathbf{a}$ was evaluated. Then, the way to proceed is the following, one needs first to fit the tracks from the signals on the sensors and to evaluate the residuals. Then, those tracks and their residuals are used to find the alignment parameters, by minimizing the residuals χ^2 (expression 4.4). Now, considering that our solution is calculated for $\boldsymbol{\pi}_0$, let's redefine $\mathbf{r}$ as a function of $\boldsymbol{\pi}_0$ and $\mathbf{a}$, i.e. $\mathbf{r} \equiv \mathbf{r}(\boldsymbol{\pi}_0, \mathbf{a})$. Then introducing 4.19 in 4.10:

$$\sum_e \sum_{t\in e} \left(\frac{\partial \mathbf{r}}{\partial \pi} \frac{d\pi}{d\mathbf{a}} + \frac{\partial \mathbf{r}}{\partial \mathbf{a}} \right)^T V^{-1}\mathbf{r} = \sum_e \sum_{t\in e} \left(-E\left(E^T V^{-1} E\right)^{-1} E^T V^{-1} \frac{\partial \mathbf{r}}{\partial \mathbf{a}} + \frac{\partial \mathbf{r}}{\partial \mathbf{a}} \right)^T V^{-1}\mathbf{r} =$$

$$= \sum_e \sum_{t\in e} \left(\left(I - E\left(E^T V^{-1} E\right)^{-1} E^T V^{-1} \right) \frac{\partial \mathbf{r}}{\partial \mathbf{a}} \right)^T V^{-1}\mathbf{r} = \sum_e \sum_{t\in e} \left((I - \mathcal{G}_E) \frac{\partial \mathbf{r}}{\partial \mathbf{a}} \right)^T V^{-1}\mathbf{r} = 0 \quad (4.20)$$

where the matrix $\mathcal{G}_E$ has been defined to pack the notation (it has dimension $N_{RES} \times N_{RES}$):

$$\mathcal{G}_E \equiv E(E^T V^{-1} E)^{-1} E^T V^{-1} \quad (4.21)$$

It is important to be aware that E is the essence of the Globalχ^2 method since it is the matrix that correlates different modules (through their residuals) for each track. In other words, for each track the derivatives of the residuals from different modules will be compute with respect the same track parameters. So, all modules that have signal for the same track will be correlated and their movements will be constrained. If E is null or neglected, then $\mathcal{G}_E$ is also null and the module correlations are switched off. In that case one would recover the local χ^2 regim.

One can also define what it is called the *weight matrix*, W, as it is already done in [71]:

$$W \equiv \left(I - E(E^T V^{-1} E)^{-1} E^T V^{-1} \right)^T V^{-1} = \left(V^{-1} - V^{-1} E(E^T V^{-1} E)^{-1} E^T V^{-1} \right)$$

$$\Downarrow$$

$$W \equiv (I - \mathcal{G}_E)^T V^{-1} = (I - \mathcal{G}_E^T) V^{-1} \quad (4.22)$$

which is also a $N_{RES} \times N_{RES}$ matrix. With this *weight matrix*, expression 4.20 looks as follows:

$$\sum_e \sum_{t\in e} \left(\frac{d\mathbf{r}}{d\mathbf{a}} \right)^T V^{-1}\mathbf{r} = \sum_e \sum_{t\in e} \left(\frac{\partial \mathbf{r}}{\partial \mathbf{a}} \right)^T W\mathbf{r} = 0 \quad (4.23)$$

Note, that when $E \to 0$, then $W = V^{-1}$, i.e. the *weight matrix* is just the covariance matrix.

Now the idea is basically the same as depicted in previous section. Let be $\mathbf{a}$ the set of alignment parameters, and let's assume that we have a set of initial alignment parameters $\mathbf{a}_0$. The goal is to find the corrections ($\delta\mathbf{a}$) to the latter set in such a way that $\mathbf{a} = \mathbf{a}_0 + \delta\mathbf{a}$ minimizes the χ^2.

In this way, and in complete analogy to 4.12 one may assume that the residuals will change linearly with $\delta\mathbf{a}$ around their initial values ($\mathbf{a}_0$). Therefore using a series expansion of the residuals and keeping only the first order term:

$$\mathbf{r} = \mathbf{r}(\boldsymbol{\pi}_0, \mathbf{a}_0) + \left.\frac{\partial \mathbf{r}}{\partial \mathbf{a}}\right|_{\mathbf{a}=\mathbf{a}_0} \delta\mathbf{a} \tag{4.24}$$

Let's comment on the above expression:

1. The use of $\boldsymbol{\pi}_0$ is justified as it represents the track parameters fitted with the initial set of alignment constants ($\mathbf{a}_0$). Obviously, a track fit had to be performed before the alignment procedure to build a track with track parameters $\boldsymbol{\pi}_0$.
2. Higher order terms are neglected which means: $d^{m+n}\mathbf{r}/d\mathbf{a}_i^m d\mathbf{a}_j^n \to 0$ with $m + n \geq 2$.
3. One can use the notation $D = \partial\mathbf{r}/\partial\mathbf{a}|_{a_0}$ which is a $N_{RES} \times N_{ALI}$ matrix. D is usually called the *design matrix*. In this way, the expression 4.24 can be written as: $\mathbf{r} = \mathbf{r_0} + D\delta\mathbf{a}$

Then, inserting 4.24 into 4.23 one obtains:

$$\begin{aligned}
&\sum_e \sum_{t\in e} \left(\frac{d\mathbf{r}}{d\mathbf{a}}\right)^T V^{-1}\mathbf{r} + \sum_e \sum_{t\in e} \left(\frac{d\mathbf{r}}{d\mathbf{a}}\right)^T V^{-1} \left(\frac{\partial \mathbf{r}}{\partial \mathbf{a}}\right)\delta\mathbf{a} = \\
&= \sum_e \sum_{t\in e} \left(\frac{\partial\mathbf{r}}{\partial\mathbf{a}}\right)^T W\mathbf{r} + \sum_e \sum_{t\in e} \left(\frac{\partial\mathbf{r}}{\partial\mathbf{a}}\right)^T W \left(\frac{\partial \mathbf{r}}{\partial \mathbf{a}}\right)\delta\mathbf{a} = 0
\end{aligned}$$

where $\mathbf{r}$ means $\mathbf{r}(\boldsymbol{\pi}_0, \mathbf{a}_0)$ (i.e. the initial residuals) and $\partial\mathbf{r}/\partial\mathbf{a}$ means $\partial\mathbf{r}/\partial\mathbf{a}|_{\boldsymbol{\pi}=\boldsymbol{\pi}_0,\mathbf{a}=\mathbf{a}_0}$ to simplify the notation.

Reached this point, one can proceed as in 4.16 and write:

$$\begin{aligned}
\delta\mathbf{a} &= -\left[\sum_e \sum_{t\in e} \left(\frac{d\mathbf{r}}{d\mathbf{a}}\right)^T V^{-1} \left(\frac{\partial \mathbf{r}}{\partial \mathbf{a}}\right)\right]^{-1} \sum_e \sum_{t\in e} \left(\frac{d\mathbf{r}}{d\mathbf{a}}\right)^T V^{-1}\mathbf{r} = \\
&= -\left[\sum_e \sum_{t\in e} \left(\frac{\partial\mathbf{r}}{\partial\mathbf{a}}\right)^T W \left(\frac{\partial \mathbf{r}}{\partial \mathbf{a}}\right)\right]^{-1} \sum_e \sum_{t\in e} \left(\frac{\partial\mathbf{r}}{\partial\mathbf{a}}\right)^T W\mathbf{r}
\end{aligned} \tag{4.25}$$

This would provide a solution for $\delta\mathbf{a}$ which is a column vector of dimension $[N_{ALI} \times 1]$. In other words, expression 4.25 represents a set on N_{ALI} equations, one for each parameter (degree of freedom) of each module to be aligned (~ 35k in the ATLAS Silicon Tracker case). But as in 4.17, one can write 4.25 in a more compact way by defining two blocks:

$$\begin{aligned}
\mathcal{M} &= \sum_e \sum_{t\in e} \left(\frac{d\mathbf{r}}{d\mathbf{a}}\right)^T V^{-1} \left(\frac{\partial \mathbf{r}}{\partial \mathbf{a}}\right) = \sum_e \sum_{t\in e} \left(\frac{\partial\mathbf{r}}{\partial\mathbf{a}}\right)^T W \left(\frac{\partial \mathbf{r}}{\partial \mathbf{a}}\right) = \\
&= \sum_e \sum_{t\in e} \left(\frac{\partial\mathbf{r}}{\partial\mathbf{a}}\right)^T (I - \mathcal{G}_E^T)V^{-1} \left(\frac{\partial \mathbf{r}}{\partial \mathbf{a}}\right)
\end{aligned} \tag{4.26}$$

which by construction is a $N_{ALI} \times N_{ALI}$ symmetric matrix and so-called *big-matrix* and:

$$\nu = \sum_e \sum_{t\in e} \left(\frac{d\mathbf{r}}{d\mathbf{a}}\right)^T V^{-1}\mathbf{r} = \sum_e \sum_{t\in e} \left(\frac{\partial\mathbf{r}}{\partial\mathbf{a}}\right)^T W\mathbf{r} = \sum_e \sum_{t\in e} \left(\frac{\partial\mathbf{r}}{\partial\mathbf{a}}\right)^T (I - \mathcal{G}_E^T)V^{-1}\mathbf{r} \tag{4.27}$$

which is a column vector of N_{ALI} components, so-called *big-vector*.
Now, with $\mathcal{M}$ and ν one can simply write the corrections to the alignment parameters as:

$$\delta\mathbf{a} = -\mathcal{M}^{-1}\nu \tag{4.28}$$

It is worth to point out that the matrix $\mathcal{M}^{-1}$ is in fact the covariance matrix of the alignment parameters corrections ($\delta\mathbf{a}$) as can be demonstrated in the same was it was done for the track parameters in section 4.2.2.1 with $\mathcal{M}_t^{-1}$. So, by inverting $\mathcal{M}$, one not only determines the corrections to the alignment parameters, but also their errors and their possible correlations. The latter helps to identify collective movements of the modules. This issue will be treated in the next chapter.
Finally, the alignment parameters can be obtained as:

$$\mathbf{a} = \mathbf{a}_0 + \delta\mathbf{a} = \mathbf{a}_0 - \mathcal{M}^{-1}\nu \tag{4.29}$$

where $\mathbf{a}_0$ represents the initial alignment parameter values which use to be the nominal values (i.e. $\mathbf{a}_0 = 0$) or can be the survey values (i.e. $\mathbf{a}_0 = \mathbf{a}_{survey}$). Moreover, if iterations are needed in order to converge, the solution $(\mathbf{a})_{Iter0}$ will be the initial value, $(\mathbf{a}_0)_{Iter0}$, for the next iteration, i.e. $(\mathbf{a})_{Iter1} = (\mathbf{a})_{Iter0} + (\delta\mathbf{a})_{Iter1}$. In general:

$$(\mathbf{a})_{Iter(n)} = (\mathbf{a})_{Iter(n-1)} + (\delta\mathbf{a})_{Iter(n)} \quad \text{with} \quad n \geq 1$$

4.2.3.1 Additional remarks

Some remarks should be done at this point about how the alignment corrections are technically computed, how if the nested track fit is neglected the Globalχ^2 algorithm becomes a local χ^2 approach and how to deal with material effects.

- In order to compute the alignment corrections ($\delta\mathbf{a}$) it is necessary to invert the *big-matrix*, $\mathcal{M}$. As stated above $\mathcal{M}$ is a $N_{ALI} \times N_{ALI}$ symmetric matrix. $\mathcal{M}$ must be computed from the derivative of the residuals and the track parameters (from its dependence on E).

  For large systems with many degrees of freedom (N_{ALI}), the solution of $\delta\mathbf{a} = -\mathcal{M}^{-1}\nu$ is not trivial because of the size of $\mathcal{M}$, which can require a huge amount of memory. It is not only a storage problem, it is a computational problem as well. On the one hand, the number of operations needed to invert $\mathcal{M}$ grows as N_{ALI}^3 [75] and on the other hand, the memory required is twice the original matrix size for technical reasons (this will be discussed on the next chapter). So the problem can be difficult or even unpractical from the experimental point of view. Special systems that can deal with large amount of memory and parallel processing have to be used. This problem will be discussed in section 5.3.

  Anyhow, though the size of $\mathcal{M}$ can be quite large, in a general case it is sparse. That means, many of the elements are null, specially the off-diagonal ones. Those off-diagonal elements not null are the ones that become correlated. They represent modules that participated in the reconstruction of the same track. This is the quintessence of the global approach. In this way, one can imagine that the correlation between modules that are very far one from the other in the tracking volume is null because they are not connected by any track from collisions. Though there is possibility of converting $\mathcal{M}$ in a full populated matrix by using other track collections (cosmics, for instance), introducing other correlations among modules. For instance, one can include a common vertex per event (possibility explored in section 4.5). By assuming that all the tracks are generated in the same vertex within the same event, then all modules that participated in the reconstruction of all the tracks in that event become correlated. Then after many events all modules in the tracking volume may become correlated. In this way $\mathcal{M}$ is not sparse anymore.

- In an intuitive way, the residual derivatives depend on track parameters (thanks to E) since track parameters are reconstructed from sensors positions. So there is a sort of nested dependence. One may choose to neglect it, freeze the tracks (therefore, force E to be null) and by doing so, one would end up with a local χ^2 solution as has been said before (therefore the Localχ^2 approach is a special case of the Globalχ^2). In that case, as there are no track dependencies, one looses the possible correlations between different modules that the track reconstruction introduce. Once correlations are lost, then one has two options:

  1. On the one hand, one could keep the full system notation. If this is done, then the V^{-1} and therefore $\mathcal{M}$ will be 6×6 block diagonal:

$$\mathcal{M} = \begin{pmatrix} \begin{matrix} xxx \\ xxx \end{matrix} & 0 & 0 & \dots \\ 0 & \begin{matrix} xxx \\ xxx \end{matrix} & 0 & \dots \\ 0 & 0 & \begin{matrix} xxx \\ xxx \end{matrix} & \dots \\ 0 & 0 & 0 & \dots \\ \dots & \dots & \dots & \dots \end{pmatrix} = \begin{pmatrix} \mathcal{M}_1 & 0 & 0 & \dots \\ 0 & \mathcal{M}_2 & 0 & \dots \\ 0 & 0 & \mathcal{M}_3 & \dots \\ 0 & 0 & 0 & \dots \\ \dots & \dots & \dots & \dots \end{pmatrix}$$

  2. On the other hand, one could decouple all the equations and write expression 4.25 per sensor (SCT or pixel module in our case) instead of writing it for the full system:

$$\delta \mathbf{a}_i = -\mathcal{M}_i^{-1} \nu$$

  where $i = 1, ..., N_{ALI}$, i.e. it refers to the i^{th} considered module.

Moreover, if $E \to 0$, then expressions 4.25, 4.26 and 4.27 become:

$$\delta \mathbf{a} = -\left[\sum_e \sum_{t \in e} \left(\frac{\partial \mathbf{r}}{\partial \mathbf{a}} \right)^T V^{-1} \left(\frac{\partial \mathbf{r}}{\partial \mathbf{a}} \right) \right]^{-1} \sum_e \sum_{t \in e} \left(\frac{\partial \mathbf{r}}{\partial \mathbf{a}} \right)^T V^{-1} \mathbf{r} = -\mathcal{M}^{-1} \nu$$

$$\mathcal{M} = \sum_e \sum_{t \in e} \left(\frac{\partial \mathbf{r}}{\partial \mathbf{a}} \right)^T V^{-1} \left(\frac{\partial \mathbf{r}}{\partial \mathbf{a}} \right) \quad ; \quad \nu = \sum_e \sum_{t \in e} \left(\frac{\partial \mathbf{r}}{\partial \mathbf{a}} \right)^T V^{-1} \mathbf{r}$$

In any case, one would have as many $\delta \mathbf{a}$ equations, i.e. expressions 4.28, as the number of modules to be aligned and each $\delta \mathbf{a}$ would be a $[N_{DOF} \times 1]$ column vector (6×1 in our case). From the computational point of view, the easiest solution is to computed $\delta \mathbf{a}$ for each module independently as it is faster to compute N_{ALI} (5832) small problems than one huge problem.

- It has been said that the helix representation of a track is usually described by five parameters and the associated hits to that track produce residuals resulting from propagating the track through the magnetic field volume in the absence of scattering material. In this scenario, the covariance matrix (V) of the residuals is a diagonal matrix corresponding to the measurement uncertainties. However, if material effects are considered MCS effects can be incorporated in the track model by allowing the track to kink on a finite number of scattering surfaces. In this way, one can take into account correlations between those scattering planes and between the hit measurements, because the measurement in the plane $i + 1$ depends on the scattering angle at the plane i.

  In the Globalχ^2 algorithm proposed for aligning the ATLAS Silicon Tracker, MCS effects are already accounted through a redefinition of the residual vector and covariance matrix. The new residual vector, $\bar{\mathbf{r}}$, has an extra term which accounts the zig-zagging of the track trajectory in this way:

$$\bar{\mathbf{r}} = \mathbf{r} + \frac{\partial \mathbf{r}}{\partial \boldsymbol{\theta}} \delta \boldsymbol{\theta}$$

  The derivatives $\partial \mathbf{r}/\partial \boldsymbol{\theta}$ are vectors which relates the scattering angles ($\boldsymbol{\theta}$) with the change of track extrapolation to the consecutive measurement planes.

  The new covariance matrix $\bar{V}$ incorporates the scattering effects adding an extra term as:

$$\bar{V} = V + V_{MCS} \quad \text{where} \quad V_{MCS} = \frac{\partial \mathbf{r}}{\partial \boldsymbol{\theta}} \Theta \left(\frac{\partial \mathbf{r}}{\partial \boldsymbol{\theta}} \right)^T$$

  where V describes the intrinsic resolution of the sensitive devices and it is diagonal by construction. V_{MCS} contains the MCS effects contribution through the derivatives $\partial \mathbf{r}/\partial \boldsymbol{\theta}$ and the matrix Θ. The latter is a diagonal matrix describing the expectations for the scattering angles according to Molière's theory [76] [77].

  Using these redefinitions the χ^2 minimization procedure for the alignment remains entirely unchanged. This represents one of the two possible ways to introduce MCS effects in an alignment algorithm based on residuals minimization. The full mathematical development and a detailed discussion can be found in appendix A.1.

Up to now, the basis of the Globalχ^2 algorithm has been discussed but some add-ons can be inserted to constrain the system and therefore to improve the algorithm convergence to the right minimum[4]. In the following sections these improvements will be discussed in detail.

4.3 The Globalχ^2 approach with track parameter constraints

The solution of the alignment parameters presented in this section (see expression 4.29) so far does not include any external constraints imposed on the solution, but these kind of constraints can be introduce as it will be shown in the next sections of this chapter. The reader will see that

[4]As the Globalχ^2 algorithm is based on a χ^2 minimization method, it may converge in a local minimum from several possible local minima.

there are basically two types of external constraints which can be added: first, extra χ^2 terms with different dependences for the residuals and second, Lagrange multipliers.

It is possible to include extra χ^2 terms which will constraint the system. In this section, constraints with linear dependence on the reconstructed track parameters will be considered and discussed. So, one can define a general new residual-like vector, $\mathbf{R}_\pi = \mathbf{R}_\pi(\boldsymbol{\pi})$. To simplify, this new residual will be, normally, denoted simply as $\mathbf{R}_\pi$. The size of this column vector is N_{TPR}.

Then, one has the original χ^2 plus an add-on which has the following form:

$$\chi^2 = \chi^2_{basic} + \chi^2_{trkCons} = \sum_e \sum_{t\in e} \mathbf{r}^T(\boldsymbol{\pi}, \mathbf{a}) V^{-1} \mathbf{r}(\boldsymbol{\pi}, \mathbf{a}) + \sum_e \sum_{t\in e} \mathbf{R}_\pi^T(\boldsymbol{\pi}) S^{-1} \mathbf{R}_\pi(\boldsymbol{\pi}) \tag{4.30}$$

where the second term is the contribution to the χ^2 from the track constraints. S is a matrix who defines the tolerances of the track constraints, in a similar way the covariance matrix V^{-1} does for $\mathbf{r}$. Obviously the track constraints only depend on the track parameters and not on the alignment ones. This has immediate consequences:

$$d\mathbf{R}_\pi = \frac{\partial \mathbf{R}_\pi}{\partial \pi} d\boldsymbol{\pi} \tag{4.31}$$

and therefore:

$$\frac{d\mathbf{R}_\pi}{d\mathbf{a}} = \frac{\partial \mathbf{R}_\pi}{\partial \pi}\frac{d\pi}{d\mathbf{a}} \quad \text{and} \quad \frac{d\mathbf{R}_\pi}{d\pi} = \frac{\partial \mathbf{R}_\pi}{\partial \pi} \tag{4.32}$$

where $d\mathbf{R}_\pi/d\boldsymbol{\pi}$ and $d\mathbf{R}_\pi/d\mathbf{a}$ have dimension $N_{TPR} \times N_{TPR}$ and $N_{TPR} \times N_{ALI}$, respectively.

The goal now is the usual minimization of the χ^2 with respect to the alignment parameters which requires:

$$\frac{d\chi^2}{d\mathbf{a}} = 0$$

therefore differentiating expresion 4.30 with respect to the alignment parameters and requiring the condition of minimum leads to:

$$\sum_e \sum_{t\in e} \left(\frac{d\mathbf{r}}{d\mathbf{a}}\right)^T V^{-1}\mathbf{r} + \sum_e \sum_{t\in e} \left(\frac{d\mathbf{R}_\pi}{d\mathbf{a}}\right)^T S^{-1}\mathbf{R}_\pi = 0 \tag{4.33}$$

where now $d\mathbf{R}_\pi/d\mathbf{a}$ is a $N_{TPR} \times N_{ALI}$ matrix.

Now, bringing the derivatives $d\mathbf{r}/d\mathbf{a}$ and $d\mathbf{R}_\pi/d\mathbf{a}$ into 4.33, it becomes:

$$\sum_e \sum_{t\in e} \left(\frac{\partial \mathbf{r}}{\partial \pi}\frac{d\pi}{d\mathbf{a}} + \frac{\partial \mathbf{r}}{\partial \mathbf{a}}\right)^T V^{-1}\mathbf{r} + \sum_e \sum_{t\in e} \left(\frac{\partial \mathbf{R}_\pi}{\partial \pi}\frac{d\pi}{d\mathbf{a}}\right)^T S^{-1}\mathbf{R}_\pi = 0 \tag{4.34}$$

Now one needs to determine the derivative $d\boldsymbol{\pi}/d\mathbf{a}$ term which appears above. The way to proceed is then through the track fitting as it was done in the previous section, which means to determine the correction to the track parameters ($\delta\boldsymbol{\pi}$) for an arbitrary alignment to calculate $\boldsymbol{\pi} = \boldsymbol{\pi}_0 + \delta\boldsymbol{\pi}$ and then the derivative $d\boldsymbol{\pi}/d\mathbf{a}$.

4.3.1 Track fitting with constrained track parameters

Obviously the track fitting is very similar to the one in section 4.2.2 but now with the new χ^2 as the input which has been defined in expression 4.30. So, for a given track:

$$\frac{d\chi^2}{d\boldsymbol{\pi}} = \frac{\partial\chi^2}{\partial\pi} = 0 \quad \Rightarrow \quad \left(\frac{\partial \mathbf{r}}{\partial\pi}\right)^T V^{-1}\mathbf{r} + \left(\frac{\partial \mathbf{R}_\pi}{\partial\pi}\right)^T S^{-1}\mathbf{R}_\pi = 0 \tag{4.35}$$

Using first order series expansion and neglecting second (and higher) order derivatives:

$$\mathbf{r}(\boldsymbol{\pi},\mathbf{a}) = \mathbf{r}(\boldsymbol{\pi}_0,\mathbf{a}) + \left.\frac{\partial\mathbf{r}}{\partial\boldsymbol{\pi}}\right|_{\pi=\pi_0}\delta_\pi \quad \text{and} \quad \frac{\partial^n\mathbf{r}}{\partial\pi^{\mathbf{n}}} = 0 \ \text{ with } \ n\geq 2$$

$$\mathbf{R}_\pi(\boldsymbol{\pi}) = \mathbf{R}_\pi(\boldsymbol{\pi}_0) + \left.\frac{\partial\mathbf{R}_\pi}{\partial\pi}\right|_{\pi=\pi_0}\delta_\pi \quad \text{and} \quad \frac{\partial^n\mathbf{R}_\pi}{\partial\pi^{\mathbf{n}}} = 0 \ \text{ with } \ n\geq 2$$

where one can use the definition of E given by equation 4.15 and defining a new one:

$$F_\pi \equiv \left.\frac{\partial\mathbf{R}_\pi}{\partial\pi}\right|_{\pi_0} \tag{4.36}$$

Including both series expansions in expression 4.35 together with E and F_π:

$$\begin{aligned} &E^T V^{-1}\left[\mathbf{r}(\boldsymbol{\pi}_0,\mathbf{a}) + E\delta\boldsymbol{\pi}\right] + F_\pi^T S^{-1}\left[\mathbf{R}_\pi(\boldsymbol{\pi}_0) + F_\pi\delta\boldsymbol{\pi}\right] = \\ &= E^T V^{-1}\mathbf{r}(\boldsymbol{\pi}_0,\mathbf{a}) + F_\pi^T S^{-1}\mathbf{R}_\pi(\boldsymbol{\pi}_0) + E^T V^{-1}E\delta\boldsymbol{\pi} + F_\pi^T S^{-1}F_\pi\delta\boldsymbol{\pi} = 0 \end{aligned}$$

now, grouping the terms:

$$\left(E^T V^{-1}E + F_\pi^T S^{-1}F_\pi\right)\delta\boldsymbol{\pi} + \left(E^T V^{-1}\mathbf{r}(\boldsymbol{\pi}_0,\mathbf{a}) + F_\pi^T S^{-1}\mathbf{R}_\pi(\boldsymbol{\pi}_0)\right) = 0$$

Therefore, the corrections to the track parameters fitted with the constraints are:

$$\delta\boldsymbol{\pi} = -\left(E^T V^{-1}E + F_\pi^T S^{-1}F_\pi\right)^{-1}\left(E^T V^{-1}\mathbf{r}(\boldsymbol{\pi}_0,\mathbf{a}) + F_\pi^T S^{-1}\mathbf{R}_\pi(\boldsymbol{\pi}_0)\right) \tag{4.37}$$

This expression can be rewritten as in expression 4.17. Then, defining:

$$\mathcal{M}_t \equiv E^T V^{-1}E \quad \text{and} \quad \mathcal{M}_{t_\pi} = F_\pi^T S^{-1}F_\pi \quad \text{and} \quad \tilde{\mathcal{M}}_t \equiv \mathcal{M}_t + \mathcal{M}_{t_\pi}$$

$$\nu_t \equiv E^T V^{-1}\mathbf{r}(\boldsymbol{\pi}_0,\mathbf{a}) \quad \text{and} \quad \nu_{t_\pi} = F_\pi^T S^{-1}\mathbf{R}_\pi(\boldsymbol{\pi}_0)$$

Thus:

$$\delta\boldsymbol{\pi} = -(\mathcal{M}_t + \mathcal{M}_{t_\pi})^{-1}(\nu_t + \nu_{t_\pi}) = -\tilde{\mathcal{M}}_t^{-1}(\nu_t + \nu_{t_\pi})$$

Now it is clear that if one introduces an extra term to the χ^2 with only track parameters dependence, the solution in the track fitting has the same structure adding a new matrix $\mathcal{M}_{t_\pi}$ and a new vector ν_{t_π}.

Then, the solution of the track parameters are just: $d\boldsymbol{\pi} = \boldsymbol{\pi}_0 + \delta\boldsymbol{\pi}$. One can trivially evaluate $d\boldsymbol{\pi}/d\mathbf{a}$ differentiating this solution:

$$\frac{d\pi}{d\mathbf{a}} = -\left(E^T V^{-1} E + F_\pi^T S^{-1} F_\pi\right)^{-1} E^T V^{-1} \frac{\partial \mathbf{r}(\pi_0, \mathbf{a})}{\partial \mathbf{a}} \tag{4.38}$$

where $\partial \mathbf{r}(\pi_0, \mathbf{a})/\partial \pi = 0$ and $\partial \mathbf{R}_\pi(\pi_0, \mathbf{a})/\partial \pi = 0$.

Note that the difference with respect to 4.19 is that now the track constraint covariance matrix (S) and F_π play also an important role in the derivative of the track parameters with respect to the alignment ones.

4.3.2 Alignment corrections fit with constrained tracks

After the calculation of the derivatives $d\pi/d\mathbf{a}$ one can resume the fit of the alignment corrections. Let's assume $\mathbf{r}(\pi_0, \mathbf{a})$ and $\mathbf{R}_\pi(\pi_0)$ and include 4.38 in 4.34. Then, this expression becomes:

$$\sum_e \sum_{t \in e} \left(-E(E^T V^{-1} E + F_\pi^T S^{-1} F_\pi^T)^{-1} E^T V^{-1} \frac{\partial \mathbf{r}}{\partial \mathbf{a}} + \frac{\partial \mathbf{r}}{\partial \mathbf{a}} \right)^T V^{-1} \mathbf{r} +$$

$$+ \sum_e \sum_{t \in e} \left(-F_\pi (E^T V^{-1} E + F_\pi^T S^{-1} F_\pi)^{-1} E^T V^{-1} \frac{\partial \mathbf{r}}{\partial \mathbf{a}} \right)^T S^{-1} \mathbf{R}_\pi = 0$$

Defining new "global" terms similar to the one defined in section 4.2.3:

$$\mathcal{G}'_{EF_\pi} \equiv E \mathcal{G}_{EF_\pi} \quad \text{being} \quad \mathcal{G}_{EF_\pi} \equiv (E^T V^{-1} E + F_\pi^T S^{-1} F_\pi)^{-1} E^T V^{-1}$$

the above expression becomes:

$$\sum_e \sum_{t \in e} \left(\left(I - \mathcal{G}'_{EF_\pi}\right) \frac{\partial \mathbf{r}}{\partial \mathbf{a}} \right)^T V^{-1} \mathbf{r} - \sum_e \sum_{t \in e} \left(F_\pi \mathcal{G}_{EF_\pi} \frac{\partial \mathbf{r}}{\partial \mathbf{a}} \right)^T S^{-1} \mathbf{R}_\pi =$$

$$= \sum_e \sum_{t \in e} \left(\frac{\partial \mathbf{r}}{\partial \mathbf{a}} \right)^T \left(I - \mathcal{G}'_{EF_\pi}\right)^T V^{-1} \mathbf{r} - \sum_e \sum_{t \in e} \left(\frac{\partial \mathbf{r}}{\partial \mathbf{a}} \right)^T (F_\pi \mathcal{G}_{EF_\pi})^T S^{-1} \mathbf{R}_\pi = 0$$

where $\mathcal{G}_{EF_\pi}$ depends here on E and on F_π. This dependence tells that if $E \to 0$ one enters again in the local χ^2 regim losing also the track constraint.

In terms of a new *weight matrix*: $W' \equiv \left(I - \mathcal{G}'_{EF_\pi}\right)^T V^{-1}$

$$\sum_e \sum_{t \in e} \left(\frac{\partial \mathbf{r}}{\partial \mathbf{a}} \right)^T W' \mathbf{r} - \sum_e \sum_{t \in e} \left(\frac{\partial \mathbf{r}}{\partial \mathbf{a}} \right)^T (F_\pi \mathcal{G}_{EF_\pi})^T S^{-1} \mathbf{R}_\pi = 0 \tag{4.39}$$

A series expansion for $\mathbf{r}$ and $\mathbf{R}_\pi$ is required in order to be able to solve the problem:

$$\mathbf{r}(\pi_0, \mathbf{a}) = \mathbf{r}(\pi_0, \mathbf{a}_0) + \left.\frac{\partial \mathbf{r}}{\partial \mathbf{a}}\right|_{a=a_0} \delta \mathbf{a} \quad \text{where} \quad \frac{\partial^n \mathbf{r}}{\partial \mathbf{a}^n} = 0 \quad \text{with} \quad n \geq 2$$

$$\mathbf{R}(\pi_0) = \mathbf{R}(\pi_0) + \left.\frac{\partial \mathbf{R}}{\partial \mathbf{a}}\right|_{a=a_0} \delta \mathbf{a} = \mathbf{R}(\pi_0) \quad \text{where} \quad \frac{\partial^n \mathbf{r}}{\partial \mathbf{a}^n} = 0 \quad \text{with} \quad n \geq 2$$

And the minimum condition with respect to the alignment parmeters is rewritten as:

$$\sum_e \sum_{t\in e} \left(\frac{\partial \mathbf{r}}{\partial \mathbf{a}}\right)^T W'\mathbf{r} + \sum_e \sum_{t\in e} \left(\frac{\partial \mathbf{r}}{\partial \mathbf{a}}\right)^T W' \left(\frac{\partial \mathbf{r}}{\partial \mathbf{a}}\right)\delta\mathbf{a} - \sum_e \sum_{t\in e} \left(\frac{\partial \mathbf{r}}{\partial \mathbf{a}}\right)^T (F_\pi \mathcal{G}_{EF_\pi})^T S^{-1}\mathbf{R}_\pi = 0$$

$$\Downarrow$$

$$\delta\mathbf{a} = \left(\sum_e \sum_{t\in e} \left(\frac{\partial \mathbf{r}}{\partial \mathbf{a}}\right)^T W' \frac{\partial \mathbf{r}}{\partial \mathbf{a}}\right)^{-1} \left(\sum_e \sum_{t\in e} \left(\frac{\partial \mathbf{r}}{\partial \mathbf{a}}\right)^T W'\mathbf{r} - \sum_e \sum_{t\in e} \left(\frac{\partial \mathbf{r}}{\partial \mathbf{a}}\right)^T (F_\pi \mathcal{G}_{EF_\pi})^T S^{-1}\mathbf{R}_\pi\right) = 0 \tag{4.40}$$

where, $\mathbf{r} \equiv \mathbf{r}(\boldsymbol{\pi}_0, \mathbf{a}_0)$ and $\mathbf{R}_\pi \equiv \mathbf{R}_\pi(\boldsymbol{\pi}_0)$ after the series expansion in this part of the text. Then, the new *big-matrix* and *big-vector* are defined using W':

$$\mathcal{M}_\pi = \sum_e \sum_{t\in e} \left(\frac{\partial \mathbf{r}}{\partial \mathbf{a}}\right)^T W' \left(\frac{\partial \mathbf{r}}{\partial \mathbf{a}}\right) \tag{4.41}$$

$$\nu_\pi = \sum_e \sum_{t\in e} \left(\frac{\partial \mathbf{r}}{\partial \mathbf{a}}\right)^T W'\mathbf{r} \tag{4.42}$$

and, now one has an extra *big-vector*:

$$\omega_\pi = -\sum_e \sum_{t\in e} \left(\frac{\partial \mathbf{r}}{\partial \mathbf{a}}\right)^T (F_\pi \mathcal{G}_{EF_\pi})^T S^{-1}\mathbf{R}_\pi \tag{4.43}$$

Finally, it is possible to write 4.40 in the compact way:

$$\mathcal{M}_\pi \delta\mathbf{a} + \nu_\pi + \omega_\pi = 0$$

$$\delta\mathbf{a} = -\mathcal{M}_\pi^{-1}(\nu_\pi + \omega_\pi)$$

being the final solution:

$$\mathbf{a} = \mathbf{a}_0 + \delta\mathbf{a} = \mathbf{a}_0 - \mathcal{M}_\pi^{-1}(\nu_\pi + \omega_\pi) \tag{4.44}$$

which is the general solution for $\delta\mathbf{a}$ when the χ^2 contains the contraints of the track parameters. Note, that the differences between the solution 4.28 and this one are an additional *big-vector* (ω_π) and W' (or $\mathcal{G}_{EF_\pi}$) which is present in $\mathcal{M}_\pi$ and ν_π (remind that $\mathcal{G}'_{EF_\pi} = E\mathcal{G}_{EF_\pi}$), due to their dependence of F_π and S^{-1}.

4.4 The Globalχ^2 approach with alignment parameter constraints

In analogy to the previous section, one can also consider a generic residual-like vector with just a dependence on the alignment parameters, i.e. $\mathbf{R_a} = \mathbf{R_a}(\mathbf{a})$ being its generic covariance matrix G. Here, $\mathbf{R_a}$ is a $N_{ALI} \times 1$ column vector and G is a $N_{ALI} \times N_{ALI}$ symmetric matrix. The important point here is the fact that the χ^2 term, which contains the alignment parameter constraints, should be evaluated per data sample instead of per event or track as for the same data sample the alignment parameters must to be constant. Therefore the χ^2 definition in 4.3 can be extended to:

$$\chi^2 = \chi^2_{basic} + \chi^2_{alignCons} = \sum_e \sum_{t \in e} \mathbf{r}(\pi, \mathbf{a})^T V^{-1} \mathbf{r}(\pi, \mathbf{a}) + \mathbf{R_a}(\mathbf{a})^T G^{-1} \mathbf{R_a}(\mathbf{a}) \tag{4.45}$$

where the sums are for all the considered tracks and events which belong to the data sample under consideration. It must be emphasized that the vector $\mathbf{R_a}(\mathbf{a})$ has an explicit dependence on the alignment parameters which has the following consequences:

$$\frac{d\mathbf{R_a}}{d\mathbf{a}} = \frac{\partial \mathbf{R_a}}{\partial \mathbf{a}} \quad \text{and} \quad \frac{d\mathbf{R_a}}{d\pi} = \frac{\partial \mathbf{R_a}}{\partial \pi}\frac{d\mathbf{a}}{d\pi} = 0 \tag{4.46}$$

Considering expressions 4.46, one can derive the solution to the minimization of expression 4.45 with respect the alignment corrections. The algebra is similar to the one used in the previous sections and it is fully developed in appendix A.2. Thus, the solution is:

$$\left[\sum_e \sum_{t \in e} \left(\frac{\partial \mathbf{r}}{\partial \mathbf{a}}\right)^T W \left(\frac{\partial \mathbf{r}}{\partial \mathbf{a}}\right) + F_\mathbf{a}^T G^{-1} F_\mathbf{a}\right] \delta\mathbf{a} + \sum_e \sum_{t \in e} \left(\frac{\partial \mathbf{r}}{\partial \mathbf{a}}\right)^T W\mathbf{r} + F_\mathbf{a}^T G^{-1} \mathbf{R_a} = 0 \tag{4.47}$$

where W was defined in expression 4.22 and $F_\mathbf{a}$ is:

$$F_\mathbf{a} \equiv \left.\frac{\partial \mathbf{R}}{\partial \mathbf{a}}\right|_{\mathbf{a}_0}$$

From expression 4.47, it is easy to obtain the alignment corrections ($\delta\mathbf{a}$). Furthermore, using definitions 4.26 and 4.27 together with the following definitions:

$$\mathcal{M}_\mathbf{a} = F_\mathbf{a}^T G^{-1} F_\mathbf{a} \tag{4.48}$$

$$\nu_\mathbf{a} = F_\mathbf{a}^T G^{-1} \mathbf{R_a} \tag{4.49}$$

one can give the expression of the final solution:

$$\mathbf{a} = \mathbf{a}_0 + \delta\mathbf{a} = \mathbf{a}_0 - (\mathcal{M} + \mathcal{M}_\mathbf{a})^{-1} (\nu + \nu_\mathbf{a})$$

Taking a look to the final expression, one can conclude that adding a constraint which just depends on the alignment parameters, one just has to calculate two extra terms, $\mathcal{M}_\mathbf{a}$ and $\nu_\mathbf{a}$.

As can be easily understood, this kind of constraints are global constraints in the sense that they are the same for the whole data sample and therefore there is no sum over tracks or events to accumulate statistics. Because of this, the technical implementation of these constraints is usually very straightforward.

4.5 The Globalχ^2 approach with common vertex fitting

In the Globalχ^2 formalism one has assumed that the residuals derivative depend not only on the alignment parameters but also on the track parameters. One can even go one step further and claim that all tracks in a given event are generated in a common origin, i.e. from a common point or vertex. In that case the residuals will not only depend on the alignment and on track parameters but also on the vertex coordinates.

$$\mathbf{r} = (\mathbf{m} - \mathbf{e}(\pi, \mathbf{v}, \mathbf{a})) \tag{4.50}$$

One has to be careful now with the track parameters. Actually the use of the common vertex fitting implicitly amends the list of track parameters. Considering the helix representation, the list of track parameters changes from the set $(d_0, z_0, \phi_0, \theta, q/p)$ to just $(\phi_0, \theta, q/p)$ keeping as the only degrees of freedom, the orientations and the charge over the momentum. The impact parameters (transversal (d_0) and longitudinal (z_0)) are replaced by the common vertex position parameters (or even by the beam spot parameters).

This new dependence leads to the following derivatives:

$$\frac{d\mathbf{r}}{d\pi} = \frac{\partial\mathbf{r}}{\partial\pi} \tag{4.51}$$

$$\frac{d\mathbf{r}}{d\mathbf{v}} = \frac{\partial\mathbf{r}}{\partial\pi}\frac{d\pi}{d\mathbf{v}} + \frac{\partial\mathbf{r}}{\partial\mathbf{v}} \tag{4.52}$$

$$\frac{d\mathbf{r}}{d\mathbf{a}} = \frac{\partial\mathbf{r}}{\partial\pi}\frac{d\pi}{d\mathbf{a}} + \frac{\partial\mathbf{r}}{\partial\mathbf{a}} + \frac{\partial\mathbf{r}}{\partial\mathbf{v}}\frac{d\mathbf{v}}{d\mathbf{a}} \tag{4.53}$$

In this case, the alignment formalism is to fit each track independently, then with all the tracks within an event a vertex (or several vertices) is fitted and at the end the alignment parameters are fitted event by event, considering the information given by the tracks and vertices fits.

Considering the derivatives from expressions 4.51, 4.52 and 4.53 and following an analogous procedure to the one presented in section 4.2, one can derive the alignment corrections (a full mathematical development is given at appendix A.3):

$$\delta\mathbf{a} = -\left[\sum_{e}\sum_{t\in e}\left(\frac{\partial\mathbf{r}}{\partial\mathbf{a}}\right)^T \tilde{W}\frac{\partial\mathbf{r}}{\partial\mathbf{a}}\right]^{-1} \sum_{e}\sum_{t\in e}\left(\frac{\partial\mathbf{r}}{\partial\mathbf{a}}\right)^T \tilde{W}\mathbf{r}$$

where $\tilde{W}$ is defined as:

$$\tilde{W} \equiv \left(I - WE_v(E_v^T W E_v)^{-1}E_v^T\right)W \quad \text{, being} \quad E_v \equiv \left.\frac{\partial\mathbf{r}}{\partial\mathbf{v}}\right|_{\mathbf{v}_0}$$

As in previous sections, one can define a *big-matrix* and a *big-vector*:

$$\tilde{\mathcal{M}} = \sum_{e}\sum_{t\in e}\left(\frac{\partial\mathbf{r}}{\partial\mathbf{a}}\right)^T \tilde{W}\frac{\partial\mathbf{r}}{\partial\mathbf{a}} \tag{4.54}$$

$$\tilde{\nu} = \sum_{e}\sum_{t\in e}\left(\frac{\partial\mathbf{r}}{\partial\mathbf{a}}\right)^T \tilde{W}\mathbf{r} \tag{4.55}$$

being the final solution:

$$\mathbf{a} = \mathbf{a}_0 + \delta\mathbf{a} = \mathbf{a}_0 - \tilde{\mathcal{M}}^{-1}\tilde{\nu} \tag{4.56}$$

Note that with the imposed common vertex, the solution again includes a $[N_{ALI} \times N_{ALI}]$ symmetric matrix $\tilde{\mathcal{M}}$. However, when enough statistics of tracks and vertices is used, the matrix is not sparse anymore, i.e. the matrix will be fully populated. First, due to the self-correlations between the degrees of freedom of each module, second, due to the correlations between modules due to the common tracks and to the correlations because of tracks emerging from a common vertex.

4.6 The Globalχ^2 approach with common vertex fit and vertex parameter constraints

A natural constraint can be considered to the previous case, that is, a new residual-like vector which depends only on the vertex parameters, $\mathbf{R_v} = \mathbf{R_v}(\mathbf{v})$. This residual-like vector of size N_{VTXPAR} will contain the difference of the sensitive vertex coordinates respect to the target values (of course, it is also possible to consider the beam spot coordinates to constrain the primary vertex). Then, one has the χ^2 defined in the expression 4.50 plus an add-on which has the following form:

$$\chi^2 = \chi^2 + \chi^2_{vtxCons} = \sum_e \sum_{t\in e} \mathbf{r}^T(\boldsymbol{\pi}, \mathbf{v}, \mathbf{a}) V^{-1} \mathbf{r}(\boldsymbol{\pi}, \mathbf{v}, \mathbf{a}) + \sum_e \mathbf{R_v}^T(\mathbf{v}) O^{-1} \mathbf{R_v}(\mathbf{v})$$

The derivatives of this constraint are:

$$\frac{d\mathbf{R_v}}{d\mathbf{v}} = \frac{\partial \mathbf{R_v}}{\partial \mathbf{v}} \quad , \quad \frac{d\mathbf{R_v}}{d\boldsymbol{\pi}} = \frac{\partial \mathbf{R_v}}{\partial \boldsymbol{\pi}} \frac{d\mathbf{v}}{d\boldsymbol{\pi}} = 0 \quad \text{and} \quad \frac{d\mathbf{R_v}}{d\mathbf{a}} = \frac{\partial \mathbf{R_v}}{\partial \mathbf{v}} \frac{d\mathbf{v}}{d\mathbf{a}} \tag{4.57}$$

where $d\mathbf{R_v}/d\boldsymbol{\pi} = 0$ because $d\mathbf{v}/d\boldsymbol{\pi} = 0$ (see expression 4.51). This is because the vertex position does not depend on track parameters.

Considering the new χ^2 function and the derivatives from expression 4.57 one can compute the alignment corrections as:

$$\delta\mathbf{a} = -\left[\sum_e \sum_{t\in e} \left(\frac{\partial \mathbf{r}}{\partial \mathbf{a}}\right)^T \tilde{W}_v \frac{\partial \mathbf{r}}{\partial \mathbf{a}}\right]^{-1} \left[\sum_e \sum_{t\in e} \left(\frac{\partial \mathbf{r}}{\partial \mathbf{a}}\right)^T \tilde{W}_v \mathbf{r} - \sum_e \sum_{t\in e} \left(\frac{\partial \mathbf{r}}{\partial \mathbf{a}}\right)^T \mathcal{K}^T F_v^T O^{-1} \mathbf{R_v}\right]$$

where $\tilde{W}_v$, $\mathcal{K}$ and F_v are:

$$\tilde{W}_v \equiv (I - \mathcal{K}^T E_v^T) W$$

$$\mathcal{K} \equiv (E_v^T W E_v + F_v^T O^{-1} F_v)^{-1} E_v^T W$$

$$F_v \equiv \left.\frac{\partial \mathbf{R}}{\partial \mathbf{v}}\right|_{\mathbf{v}_0}$$

A full discussion can be found in appendix A.4. Finally, one can define a *big-matrix* and two *big-vector* in analogy to the expression 4.40 in section 4.3.2:

$$\tilde{\mathcal{M}}_v = \sum_e \sum_{t\in e} \left(\frac{\partial \mathbf{r}}{\partial \mathbf{a}}\right)^T \tilde{W}_v \frac{\partial \mathbf{r}}{\partial \mathbf{a}}$$

$$\tilde{\nu}_v = \sum_e \sum_{t \in e} \left(\frac{\partial \mathbf{r}}{\partial \mathbf{a}}\right)^T \tilde{W}_v \mathbf{r}$$

$$\tilde{\omega}_v = -\sum_e \sum_{t \in e} \left(\frac{\partial \mathbf{r}}{\partial \mathbf{a}}\right)^T \mathcal{K}^T F_v^T O^{-1} \mathbf{R}_\mathbf{v}$$

Being the final solution of the alignment parameters:

$$\mathbf{a} = \mathbf{a}_0 + \delta \mathbf{a} = \mathbf{a}_0 - \tilde{\mathcal{M}}_v^{-1} (\tilde{\nu}_v + \tilde{\omega}_v)$$

This solution looks like the one in section 4.3.2, where a track parameter constraint was considered, although this case is mathematically much more complicated.

4.7 The most general solution for the Globalχ^2 approach

For completeness, the solution of the most general case will be given in this section. Therefore, the χ^2 in this section will be the basic term from expression 4.3 (where $\mathbf{r} = \mathbf{r}(\boldsymbol{\pi}, \mathbf{v}, \mathbf{a})$) plus all the extra terms considered in previous sections (where the residuals $\mathbf{R}_\pi(\boldsymbol{\pi})$, $\mathbf{R}_\mathbf{v}(\mathbf{v})$ and $\mathbf{R}_\mathbf{a}(\mathbf{a})$ are considered). Thus, the χ^2 looks like this:

$$\chi^2 = \chi^2_{basic} + \chi^2_{trkCons} + \chi^2_{vtxCons} + \chi^2_{alignCons}$$

$$\Downarrow$$

$$\chi^2 = \sum_e \left[\sum_{t \in e} \left[\mathbf{r}^T(\boldsymbol{\pi}, \mathbf{v}, \mathbf{a}) V^{-1} \mathbf{r}(\boldsymbol{\pi}, \mathbf{v}, \mathbf{a}) + \mathbf{R}_\pi^T(\boldsymbol{\pi}) S^{-1} \mathbf{R}_\pi(\boldsymbol{\pi}) \right] + \mathbf{R}_\mathbf{v}^T(\mathbf{v}) O^{-1} \mathbf{R}_\mathbf{v}(\mathbf{v}) \right] +$$

$$+ \mathbf{R}_\mathbf{a}(\mathbf{a})^T G^{-1} \mathbf{R}_\mathbf{a}(\mathbf{a}) \tag{4.58}$$

Now, considering the all the residuals, their dependences and their differentials (expressions A.41, 4.31, A.19 and A.41), one can derive the solution for the alignment corrections:

$$\delta \mathbf{a} = -\left[\sum_e \sum_{t \in e} \alpha^T W' \frac{\partial \mathbf{r}}{\partial \mathbf{a}} + F_\mathbf{a}^T G^{-1} \mathbf{R}_\mathbf{a} \right]^{-1} \cdot$$

$$\cdot \sum_e \left[\sum_{t \in e} \left[\alpha^T W' \mathbf{r} + \left(F_\pi \frac{d\boldsymbol{\pi}}{d\mathbf{a}} \right)^T S^{-1} \mathbf{R}_\pi \right] + \left(F_\mathbf{v} \frac{d\mathbf{v}}{d\mathbf{a}} \right)^T O^{-1} \mathbf{R}_\mathbf{v} \right] + F_\mathbf{a}^T G^{-1} \mathbf{R}_\mathbf{a} \tag{4.59}$$

where the following definitions has been used to compact the solution:

$$\alpha \equiv \frac{\partial \mathbf{r}}{\partial \mathbf{a}} + E_\mathbf{v} \frac{d\mathbf{v}}{d\mathbf{a}}$$

$$W' \equiv V^{-1} - V^{-1} E (E^T V^{-1} E + F_\pi^T S^{-1} F_\pi)^{-1} E^T V^{-1}$$

4.8 The Globalχ^2 approach with equality constraints: Lagrange multipliers

In addition to the previous constraints one can also consider another kind of constraints which have a slightly different philosophy. They are called *equality constraints* and the most general method to introduce them is the use of the *Lagrange multipliers* (LM). This method is a technique to determine a local extremum (maximum or minimum) of a function with simultaneous consideration of constraints.

Considering a model with m constraints, one has:

$$\sum_{\text{LM constrs}}^{m} A^T f(\mathbf{a}) - \varepsilon = 0 \tag{4.60}$$

In the LM method, an additional parameter λ, called *Lagrange multiplier*, is introduced for each constraint. Therefore, any single equality constraint is introduced by appending a term $\lambda^T(a^T f(\mathbf{a}) - \varepsilon)$ to the original χ^2 function. Thus, the χ^2 expression reads as follows:

$$\chi^2 = \sum_e \sum_{t\in e} r^T V^{-1} r + \sum_{\text{LM constrs}}^{m} \lambda^T \left[A^T f(\mathbf{a}) - \varepsilon\right] \tag{4.61}$$

This method is widely used by some algorithms, for example Millepede [74], in order to constraint undefined degrees of freedom such as global distortions which can be fixed by adding these kind of linear equality constraint equations to the χ^2.

Actually, in the Globalχ^2 algorithm for the ATLAS Silicon Tracker these constraints are already implemented although they are under test and validation. Anyhow, unconstrained degrees of freedom can be removed with Lagrange multipliers as has been said or by omitting the corresponding eigenvalue and its eigenvector from the solution to the linear system as it will be shown at the next chapter. The last option is only possible when a matrix diagonalisation is performed to invert the *big-matrix*.

A final comment have to be done about the difference between the LM and the penalty terms which were described in section B.2.2. While LM are explicit and absolute constraints on the results, the penalty terms reduce the impact to the undefined degrees of freedom within a certain precision. This generally means that the original problem is no longer being solved and as a result a biased solution is found. Imagine the case where there are 6 global movements (3 translations and 3 rotations of the whole system) which leave the χ^2 unchanged. With the LM one can specify that all translations and rotations sum to zero and then the results one gets is 100% correct but with the penalty terms, just a movement restriction for the parameters is added within a certain precision. This is why the idea is to use together both kind of constraints in the future.

5

Particular issues of the Globalχ^2 algorithm

This chapter complements the previous one in the sense that it treats the additional requirements that must be known in order to exploit the Globalχ^2 method. Topics like how to compute the derivatives of the residuals or how to align large structures will be treated in this chapter. The alignment parameter errors and how to deal the inherent problems of the method will be also discussed. Finally, a discussion about global distortions will be given.

5.1 Derivatives of the residuals

Once the mathematical basis of the Globalχ^2 algorithm has been established, the derivatives of the residuals with respect the track parameters, the alignment parameters, the vertex parameters and even the scattering angle parameters must be discussed as they appear everywhere in the formulae. Obviously, these derivatives will depend on the reference frame in which they want to be calculated, so this section will require the knowledge of section 3.3 where there was a description of the different ATLAS coordinate frames which are relevant for reconstruction and alignment. This section deals with the analytical computation of the mentioned derivatives stressing their geometrical demonstration.

5.1.1 Generalities

Generally, the derivatives depend on the reference frame in which they are calculated. The easiest is to express the residuals in the measurement frame. In that case, residuals are given in the xy plane of the measurement frame of the module whilst no measurements are given in the z direction which is considered to be out of the plane (see section 3.3).

Now, let define a generic set of parameters $\mathbf{p}$ represented in the measurement frame (being N_{PAR} the number of the parameters) and let say that $\mathbf{e}$ depends on this generic set of parameters, i.e. $\mathbf{e}(\mathbf{p})$. Then, the residual vector is written as $\mathbf{r} = (\mathbf{m} - \mathbf{e}(\mathbf{p}))$ and one can write the following derivative:

$$\frac{d\mathbf{r}}{d\mathbf{p}} = \frac{d\,(\mathbf{m} - \mathbf{e}(\mathbf{p}))}{d\mathbf{p}} = -\frac{d\mathbf{e}(\mathbf{p})}{d\mathbf{p}}$$

Thus, when one talks about the derivatives of the residuals it is equivalent to talk about the derivatives of the extrapolated track position in the measurement frame since hits are frozen in that frame (i.e. $d\mathbf{m}/d\mathbf{p} = 0$). Moreover, it is also worth to mention that $d\mathbf{r}/d\mathbf{p}$ is a $3 \times N_{PAR}$ matrix.

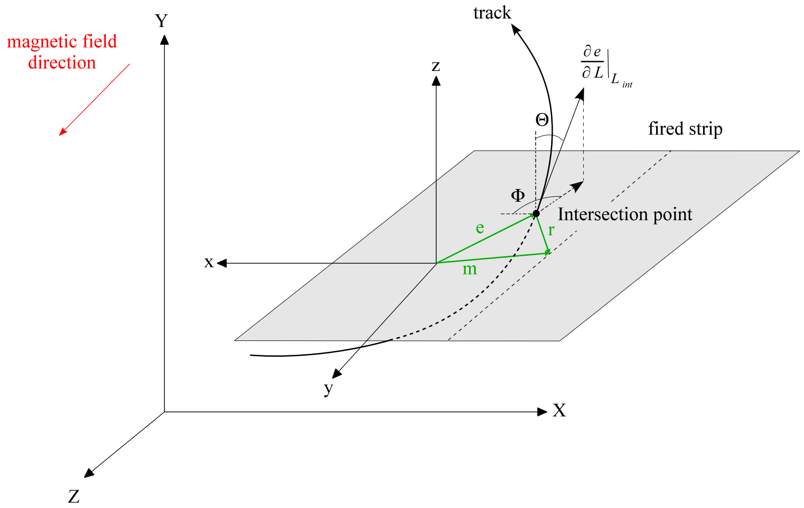

Figure 5.1: *Schematic representation of a track extrapolation into a planar detector together with the path length of this track. Both the measurement* ($\mathbf{m}$) *and the extrapolation* ($\mathbf{e}$) *are given in the measurement plane. The track has an incidence angle with respect to the xy plane which can be defined with* Φ *and* Θ.

Now, considering that the position of any point on the trajectory is parametrized by its *path length* (denoted by L), $\mathbf{e}$ will depend on this parameter (since L gives the measurement model) evaluated at the intersection point. In addition, it is obvious that L will be an implicit function of $\mathbf{p}$, therefore one can write:

$$\frac{d\mathbf{r}}{d\mathbf{p}} = -\frac{d\mathbf{e}}{d\mathbf{p}} = -\frac{\partial \mathbf{e}}{\partial \mathbf{p}} - \left(\frac{\partial \mathbf{e}}{\partial L}\frac{dL}{d\mathbf{p}}\right) \tag{5.1}$$

The problem is now how to compute $dL/d\mathbf{p}$. The solution comes from the fact that there are no measurements out of the measurement plane in the ATLAS Silicon Tracker. Then, considering there is no projection of the residual vector over the z axis (which is normal to the sensor plane), one has:

$$r_z = \mathbf{r} \cdot \hat{z} = (\mathbf{m} - \mathbf{e}(\mathbf{p})) \cdot \hat{z} = 0 \tag{5.2}$$

being $\hat{z}$ an unit vector in the direction of the z-axis.

Then, if one combines the last expression with expression 5.1 but evaluated at the intersection point (i.e. the path length evaluated at the intersection point, L_{int}), one has:

$$\frac{d\mathbf{r}}{d\mathbf{p}} \cdot \hat{z} = -\frac{\partial(\mathbf{e}\cdot\hat{z})}{\partial\mathbf{p}} - \left(\frac{\partial(\mathbf{e}\cdot\hat{z})}{\partial L}\frac{dL}{d\mathbf{p}}\right)\bigg|_{L=L_{int}} = 0$$

Then, it is trivial to isolate the derivative $(dL/d\mathbf{p})_{L=L_{int}}$:

$$\left.\frac{dL}{d\mathbf{p}}\right|_{L=L_{int}} = -\frac{\frac{\partial(\mathbf{e}\cdot\hat{z})}{\partial\mathbf{p}}}{\left.\frac{\partial(\mathbf{e}\cdot\hat{z})}{\partial L}\right|_{L=L_{int}}}$$

Using this result and considering the unit vector $\hat{k}$, which will account for the sensitive directions of the sensor under test, the residual derivative looks as follows:

$$\frac{d\mathbf{r}}{d\mathbf{p}} \cdot \hat{k} = -\left[\frac{\partial\mathbf{e}}{\partial\mathbf{p}} + \left(\frac{\partial\mathbf{e}}{\partial L}\frac{dL}{d\mathbf{p}}\right)\bigg|_{L=L_{int}}\right] \cdot \hat{k} = -\left[\frac{\partial\mathbf{e}}{\partial\mathbf{p}} - \left(\frac{\partial\mathbf{e}}{\partial L}\frac{\frac{\partial(\mathbf{e}\cdot\hat{z})}{\partial\mathbf{p}}}{\frac{\partial(\mathbf{e}\cdot\hat{z})}{\partial L}}\right)\Bigg|_{L=L_{int}}\right] \cdot \hat{k} =$$

$$= -\frac{\partial\mathbf{e}}{\partial\mathbf{p}}\left(\hat{k} - \frac{\frac{\partial(\mathbf{e}\cdot\hat{k})}{\partial L}}{\frac{\partial(\mathbf{e}\cdot\hat{z})}{\partial L}} \cdot \hat{z}\right)\Bigg|_{L=L_{int}} \quad \text{being} \quad k = x, y \tag{5.3}$$

The vector $\partial\mathbf{e}/\partial L|_{L=L_{int}}$ represents the track direction at the intersection point. Moreover, in the measurement frame, the direction of a track is defined by the angles Φ and Θ as can be seen in figure 5.1, so, one can easily write:

$$\begin{aligned} \left.\frac{\partial(\mathbf{e}\cdot\hat{x})}{\partial L}\right|_{L=L_{int}} &= cos\Phi sin\Theta \\ \left.\frac{\partial(\mathbf{e}\cdot\hat{y})}{\partial L}\right|_{L=L_{int}} &= sin\Phi sin\Theta \quad \longrightarrow \quad \frac{\partial\mathbf{e}}{\partial L} = \begin{pmatrix} cos\Phi sin\Theta \\ sin\Phi sin\Theta \\ cos\Theta \end{pmatrix} \\ \left.\frac{\partial(\mathbf{e}\cdot\hat{z})}{\partial L}\right|_{L=L_{int}} &= cos\Theta \end{aligned}$$

As it is shown, the derivative $\partial\mathbf{e}/\partial L$ is a vector of dimension 3. Then, using these geometrical results, the expression 5.3 can be written for the three components ($\hat{x}$, $\hat{y}$ and $\hat{z}$) as:

$$\begin{pmatrix} \frac{d\mathbf{r}}{d\mathbf{p}} \cdot \hat{x} \\ \frac{d\mathbf{r}}{d\mathbf{p}} \cdot \hat{y} \\ \frac{d\mathbf{r}}{d\mathbf{p}} \cdot \hat{z} \end{pmatrix} = \begin{pmatrix} -\frac{\partial\mathbf{e}}{\partial\mathbf{p}}(\hat{x} - cos\Phi tan\Theta\,\hat{z}) \\ -\frac{\partial\mathbf{e}}{\partial\mathbf{p}}(\hat{y} - sin\Phi tan\Theta\,\hat{z}) \\ 0 \end{pmatrix} = -\frac{\partial\mathbf{e}}{\partial\mathbf{p}}\begin{pmatrix} \hat{x} - cos\Phi tan\Theta\,\hat{z} \\ \hat{y} - sin\Phi tan\Theta\,\hat{z} \\ 0 \end{pmatrix} \tag{5.4}$$

Now, to simplify the notation, one can define two vectors as in reference [71] which will be the projection directions along which the change of the extrapolation is computed:

$$\mathcal{P}_x \equiv \hat{x} - cos\Phi tan\Theta\,\hat{z} = \begin{pmatrix} 1 \\ 0 \\ -cos\Phi tan\Theta \end{pmatrix} \tag{5.5}$$

$$\mathcal{P}_y \equiv \hat{y} - sin\Phi tan\Theta\,\hat{z} = \begin{pmatrix} 1 \\ 0 \\ -sin\Phi tan\Theta \end{pmatrix} \tag{5.6}$$

Using these projection vectors, expression 5.4 can be reduced to the following analytical expression:

$$\frac{d\mathbf{r}}{d\mathbf{p}} \cdot \hat{k} = -\frac{\partial \mathbf{e}}{\partial \mathbf{p}} \cdot \mathcal{P}_k \text{ being } \; k = x, y \tag{5.7}$$

This expression does not depend on any assumption about the trajectory, i.e. it is completely general. Now, the calculation of the different derivatives needed during the alignment algorithm is easier since the problem has been reduced to computed $\partial\mathbf{e}/\partial\mathbf{p}$.

5.1.2 Derivatives with respect to the track parameters

Considering the set of the track parameters, i.e. $\boldsymbol{\pi} = (d_0, \phi_0, z_0, cot\theta, q/p_T)$, one can trivially rewrite expression 5.7 as follows:

$$\frac{d\mathbf{r}}{d\boldsymbol{\pi}} \cdot \hat{k} = -\frac{\partial \mathbf{e}}{\partial \boldsymbol{\pi}} \cdot \mathcal{P}_k \text{ being } \; k = x, y$$

To compute the derivatives $\partial\mathbf{e}/\partial\boldsymbol{\pi}$, one should know the analytical dependence of the trajectory to the track parameters. Once this description is available, derivatives with respect these track parameters are easy to compute. However, a general analytical description of particle trajectories travelling inside a non-uniform magnetic field is not trivial. In order to reduce the problem, several approximations can be adopted (see references [78] and [79]).

The approximation used in the Globalχ^2 algorithm considers the path length of the trajectory from the origin, which is the perigee (since track parameters are referred to this point), to the point of intersection with the module, i.e. L_{int} (see figure 5.2), to give the analytical position of the extrapolated point **e** as follows:

$$\mathbf{e} = \begin{pmatrix} (L_{int})_T \cdot \hat{X} - d_0 sin\phi_0 \\ (L_{int})_T \cdot \hat{Y} + d_0 cos\phi_0 \\ |(L_{int})_T| cot\theta + z_0 \end{pmatrix} \tag{5.8}$$

being $(L_{int})_T$ the projection of L_{int} in the global transverse plane XY. It is worth to mention that it does not really matter in which reference frame L_{int} calculated if **e** is given in the same frame. Figure 5.2 illustrates the relation between the extrapolated point to the measuring plane **e**, the perigee **P**, $(L_{int})_T$, the radius of curvature r, the radius of the measurement from the origin of the global frame R and the sagitta s.

Expression 5.8 is an approximation that is only valid around the perigee and in addition it does not account neither for non-uniform magnetic field nor for material effects (i.e. energy loss). This implies that it is not very reliable for the end-cap regions where the non-uniformities become important (see section 3.2.4). Moreover, although it is good enough for the transverse

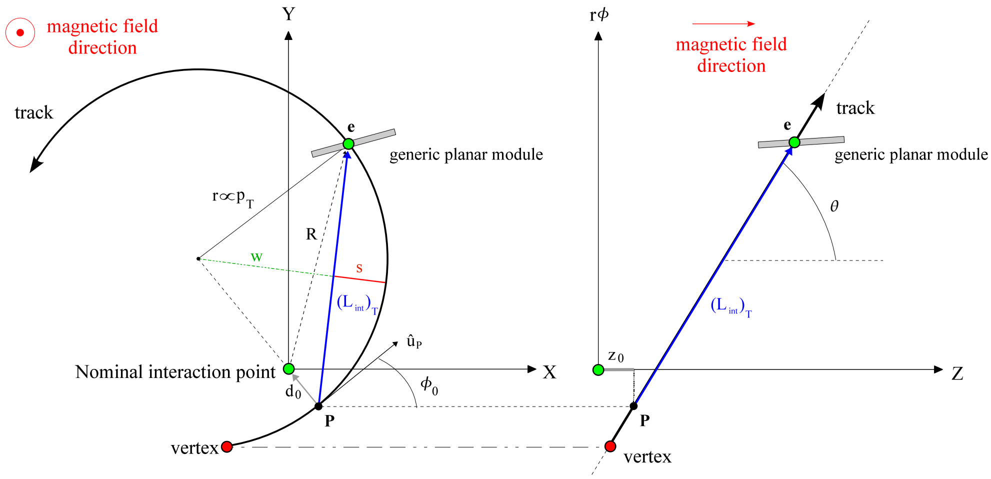

Figure 5.2: *Scheme of a particle trajectory (track) in the transverse and longitudinal planes. The relation between the extrapolated point to the measuring plane* **e**, *the perigee* **P**, *the path length of the trajectory from the origin to the perigee of intersection with the module* $(L_{int})_T$, *the radius of curvature* (r), *the radius of the measurement from the origin of global frame* (R) *and the sagitta* (s) *are shown.*

track parameters d_0, ϕ_0 and for z_0, it is not a good approximation for $cot\theta$ and q/p_T because the previous non-uniformities modify the helix parametrization and therefore degrade the validity of this approximation. Thus, numerical derivatives[1] are used for end-cap tracks as well as for parameters $cot\theta$ and q/p_T of barrel tracks. Anyhow, considering the given approximation, one can computed the derivatives for d_0, ϕ_0, z_0 and $cot\theta$ quite straight forward:

$$\frac{\partial \mathbf{e}}{\partial d_0} = \begin{pmatrix} -sin\phi_0 \\ cos\phi_0 \\ 0 \end{pmatrix} \tag{5.9}$$

$$\frac{\partial \mathbf{e}}{\partial \phi_0} = \begin{pmatrix} -d_0 cos\phi_0 \\ d_0 sin\phi_0 \\ 0 \end{pmatrix} \tag{5.10}$$

$$\frac{\partial \mathbf{e}}{\partial z_0} = \begin{pmatrix} 0 \\ 0 \\ 1 \end{pmatrix} \tag{5.11}$$

[1]Numerical derivation finds the numerical value of a derivative of a given function $f(x)$ at a given point x. The simplest approach, known as secant method, is to use finite difference approximations Δx which represents a small change in x:

$$f'(x) = \frac{f(x+\Delta x) - f(x)}{\Delta x}$$

$$\frac{\partial \mathbf{e}}{\partial cot\theta} = \begin{pmatrix} 0 \\ 0 \\ |\,(L_{int})_T\,| \end{pmatrix} \tag{5.12}$$

Finally, to compute the derivative for q/p_T a rougher approximation is used based on expression 3.1 (i.e. $p_T = 0.3qBr$) which assumes an uniform magnetic field. Firstly, let's consider the sagitta (s) as the magnitude that accounts for the deviation of the curved trajectory from a straight line (shown in figure 5.2). Using this magnitude one can write the q/p_T derivative as:

$$\frac{\partial \mathbf{e}}{\partial(q/p_T)} \approx -\frac{\partial s}{\partial(q/p_T)}\hat{\mathbf{u}}_{\mathbf{P}} \tag{5.13}$$

where $\hat{\mathbf{u}}_{\mathbf{P}} = (sin\phi_0, -cos\phi_0, 0)$ is the unit vector which gives the transverse direction to curvature radius of the track (r) at perigee.

Then, the problem can be reduced to compute $\partial s/\partial(q/p_T)$. To achieve this, one should write s as a function of p_T (or the radius of curvature, r) and the radius of measurement computed with respect the origin, R. In that sense, figure 5.2 shows that it is easy to write the following relation:

$$r = w + s \quad \text{and} \quad r^2 = w^2 + \left(\frac{R}{2}\right)^2 \quad \text{which give:} \quad s = r - \sqrt{r^2 - \left(\frac{R}{2}\right)^2}$$

This expression allows to write radius of curvature as a function of the sagitta and the radius of the measurement:

$$r = \frac{\left(\frac{R}{2}\right)^2 + s^2}{2s} = \frac{R^2}{8s} + \frac{s}{2}$$

The second term of the previous expression, i.e. $s/2$, can be neglected considering that generally $R >> s$, resulting a good approximation:

$$r = \frac{R^2}{8s} \quad \rightarrow \quad s = \frac{R^2}{8r}$$

Thus, one can introduce expression 3.1 to have s expressed as a function of the transverse momentum:

$$s = 0.3B\frac{R^2}{8}\frac{q}{p_T} \tag{5.14}$$

The previous expression is valid for straight lines. For a helix it is easy to see that R needs to be replaced by the length of trajectory which is approximated by $(L_{int})_T$, giving:

$$s = 0.3B\frac{(L_{int})_T^2}{8}\frac{q}{p_T} \tag{5.15}$$

Once one has this expression, it is possible to compute $d\mathbf{e}/d(q/p_T)$:

$$\frac{\partial \mathbf{e}}{\partial q/p_T} = -\frac{\partial s}{\partial q/p_T}\hat{\mathbf{u}}_{\mathbf{P}} = 0.3B\frac{(L_{int})^2_T}{8}\begin{pmatrix} sin\phi_0 \\ -cos\phi_0 \\ 0 \end{pmatrix} \tag{5.16}$$

Another analytic computation of these derivatives (using another representation of the track parameters, $(d_0, z_0, \phi_0, \theta, q/p)$, can be found in reference [78].

Finally, it is worth to mention that from the mathematical point of view it does not matter if the Globalχ^2 algorithm uses analytical (being always precise enough) or numerical derivatives, but from the performance point of view numerical derivation should be avoided to save computing time.

5.1.3 Derivatives with respect to the alignment parameters

The problem is just to know how module translations and rotations affect the intersection of the extrapolated track. It is trivial to write:

$$\frac{d\mathbf{r}}{d\mathbf{a}} \cdot \hat{k} = -\frac{\partial \mathbf{e}}{\partial \mathbf{a}} \cdot \mathcal{P}_k \text{ being } \quad k = x, y$$

where **a** can be divided into translations ($\mathbf{T_i}$) and rotations ($\mathbf{R_i}$), distinguishing two main cases:

- **Within plane motions**. The module plane remains the same and the extrapolated point (i.e. the intersection of the track with the module plane) stays physically the same point, only the origin of the reference frame changes and therefore the coordinates of that extrapolated point in the measurement frame.
- **Out of plane motions**. In this case the module plane changes, then the extrapolated point also changes, as well the coordinates in the new frame change. Obviously, if the extrapolated point is near to the rotation point, the change will be small and if it is far away, the change will be greater. Then, the change of the extrapolated point with the rotations will depend on the lever arm ℓ_{arm}.

$$\frac{\partial \mathbf{e}}{\partial \mathbf{a}} \longrightarrow \begin{cases} \dfrac{\partial \mathbf{e}}{\partial \mathbf{T_i}} = -\hat{\imath} \\[2ex] \dfrac{\partial \mathbf{e}}{\partial \mathbf{R_i}} = -\hat{\imath} \times \ell_{arm} \end{cases} \qquad \text{being} \quad i = x, y, z$$

Is trivial to calculate ℓ_{arm} considering the origin of the measurement frame (i.e. midpoint of the detector element (**o**)) and the intersection point of the track with the module (**e**), the lever arm is just $\ell_{arm} = (\mathbf{o} - \mathbf{e})$.

Then, the final expressions are:

$$\begin{aligned} \frac{d\mathbf{r}}{d\mathbf{T_i}} \cdot \hat{k} &= -\frac{\partial \mathbf{e}}{\partial \mathbf{T_i}} \cdot \mathcal{P}_k = \hat{\imath} \cdot \mathcal{P}_k \\ \frac{d\mathbf{r}}{d\mathbf{R_i}} \cdot \hat{k} &= -\frac{\partial \mathbf{e}}{\partial \mathbf{R_i}} \cdot \mathcal{P}_k = \left(\hat{\imath} \times \ell_{arm}\right) \cdot \mathcal{P}_k \end{aligned} \qquad \text{being} \quad k = x, y \quad \text{and} \quad i = x, y, z$$

5.1.4 Derivatives with respect to the common vertex parameters

Considering the derivates of the residuals with respect primary vertex:

$$\frac{d\mathbf{r}}{d\mathbf{v}} \cdot \hat{k} = -\frac{\partial \mathbf{e}}{\partial \mathbf{v}} \cdot \mathcal{P}_k \text{ being } \quad k = x, y$$

If the primary vertex is now given in the global frame, the derivatives $\partial\mathbf{e}/\partial\mathbf{v}$ are:

$$\frac{\partial \mathbf{e}}{\partial \mathbf{v}_j} = -\hat{\mathbf{j}} \quad \text{being} \quad j = X, Y, Z$$

Therefore, one has:

$$\frac{d\mathbf{r}}{d\mathbf{v}_j} \cdot \hat{k} = -\frac{\partial \mathbf{e}}{\partial \mathbf{v}_i} \cdot \mathcal{P}_k = \hat{\mathbf{j}} \cdot \mathcal{P}_k \text{ being } \quad k = x, y \quad \text{and} \quad j = X, Y, Z$$

being $\hat{X}$, $\hat{Y}$ and $\hat{Z}$ the unit vectors in the direction of the global X-axis, Y-axis and Z-axis respectively.

5.1.5 Derivatives with respect to the scattering angles

Finally, to compute the residual derivatives with respect the scattering angles one has to consider two scattering planes (or two modules for Pixels) a and b. This is because MCS effects occurring through plane a will affect residuals in plane b.

Thus, one has two simple cases:

- If plane a is after plane b, i.e. the track passes through plane b before plane a, then the answer is trivial: the derivatives of the residuals computed in plane b with regard to the scattering occurring later in plane a are null.

- If plane a is before plane b: following the same formalism used in the previous sections, one gets:

$$\frac{d\mathbf{r}^b}{d\boldsymbol{\psi}^a} \cdot \hat{k} = -\frac{\partial \mathbf{e}^b}{\partial \boldsymbol{\psi}^a} \cdot \mathcal{P}_k \text{ being } \quad k = x, y \text{ and } \quad \boldsymbol{\psi} = \Phi, \Theta \tag{5.17}$$

  where $\boldsymbol{\psi}^a$ represents the scattering angles and the superscripts a and b denote the corresponding plane.

  The quantity $\partial\mathbf{e}^b/\partial\boldsymbol{\psi}^a$represents the rate of the variation $\delta\mathbf{e}^b$ of the intersection point of the track with plane b, given a change in the scattering angle in plane a, $\delta\boldsymbol{\psi}^a$. It is assumed that the path length of the track is fixed.

  Changing the angle Θ^a by $\delta\Theta^a$ is equivalent to a rotation of angle $\delta\Theta^a$ about the axis u^a_ϕ whose centre is $\mathbf{e}^a$, where (u^a_r , u^a_ϕ, u^a_θ) are the local axes corresponding to the measurement frame of module a in spherical coordinates (u^a_r is along the track direction at the point $\mathbf{e}^a$). Thus, the variation of the position of the intersection point in plane b is:

$$\delta\mathbf{e}^b = \delta\Theta^a u^a_\phi \times \left(\mathbf{e}^b - \mathbf{e}^a\right) = (-sin\Theta^a\hat{x}^a + cos\Theta^a\hat{y}^a) \times \left(\mathbf{e}^b - \mathbf{e}^a\right)$$

being $\hat{x}$ and $\hat{y}$ the unit vectors in the direction of x and y in the measurement frame, respectively.

In the same way, changing the angle Φ^a by $\delta\Phi^a$ is equivalent to a rotation of angle $\delta\Phi^a$ about the axis $\hat{z}^a$ whose centre is $\mathbf{e}^a$:

$$\delta\mathbf{e}^b = \delta\Phi^a\hat{z}^a \times \left(\mathbf{e}^b - \mathbf{e}^a\right)$$

being $\hat{z}$ the unit vector in the direction of the z-axis in the measurement frame.

Using these results, expression 5.17 becomes [71]:

$$\frac{d\mathbf{r}^b}{d\Theta^a}\cdot\hat{k} = -\frac{\partial\mathbf{e}^b}{\partial\Theta^a} = -\left[(-sin\Theta^a\hat{x}^a + cos\Theta^a\hat{y}^a)\times\left(\mathbf{e}^b - \mathbf{e}^a\right)\right]\cdot\mathcal{P}_k \text{ being } k = x, y \quad (5.18)$$

$$\frac{d\mathbf{r}^b}{d\Phi^a}\cdot\hat{k} = -\frac{\partial\mathbf{e}^b}{\partial\Phi^a} = -\left[\hat{z}^a\times\left(\mathbf{e}^b - \mathbf{e}^a\right)\right]\cdot\mathcal{P}_k \text{ being } k = x, y \quad (5.19)$$

5.2 Alignment of large structures

One of most powerful feature of the track-based alignment algorithms is when large structures[2] are considered as alignable elements themselves. It is easy to understand a situation where one wants to align complex systems composed of many individual devices as for instance layers, ladders, staves, barrels, discs or whatever. This way of thinking is complete natural and it is justified because individual modules are actually mounted on large structures (as it was discussed in section 3.2).

In the particular case of the ATLAS Silicon Tracker, this approach has an important advantage as its 5832 modules (between Pixel and SCT modules) are mounted on different structures. Thus, single silicon modules are mounted on ladders and staves then they are assembled on barrel layers (in the case of the Pixels, they are grouped firstly into half-shells) and end-cap discs. After that, these layers and discs are mounted in a barrel and two end-caps, respectively and finally Pixel detector is mounted as a unique structure and the SCT as three separate structures, a barrel and two end-caps. Due to this assembling hierarchy, collective misalignments are introduced, translating into common movements for each group of modules mounted on the each structure. These structural misalignments depend on the assembling precision, being estimated to be ~ 1 mm. Comparing these misalignments with the assembling precision achieved for modules built into their structures (estimated to be $\sim 10\,\mu$m), an alignment hierarchy method based on alignment levels is justified and in fact necessary.

Therefore, knowing how the ATLAS Silicon Tracker has been built, several alignment levels have been defined in order to align the different structures before achieving the final alignment (i.e. up to module level). This technique allows, for example, to consider an alignment level where 9 Pixel structures (3 layers in the barrel and 3 discs in each end-cap) plus 22 SCT structures (4 layers in the barrel and 9 in each end-cap) are considered. In this case, one has to deal

[2] A structure consists on several sensitive elements (i.e. silicon modules in the Silicon Tracker case) arranged on barrel layers, ladders, end-cap discs, etc...

just with 31 structures that require 186 DoF, simplifying the alignment technical challenge and all the problems listed in section 5.3. Thus, table 5.1 shows all the available alignment levels that are already defined in the Globalχ^2 algorithm for the ATLAS Silicon Tracker. In that table, there are four levels marked with (*); these levels represent real physical situations for the Silicon Tracker (i.e. the real detector has been assembled within these kind of structures) while the others are used to study the collective movements of the modules.

Moreover, figures 5.3 (a), (b) and (c) show graphical models for three main alignment levels. Thus, figure 5.3 (a) shows level 1 where the Pixel detector is just one structure and the SCT is divided in three structures: the barrel and the two end-caps. Then, figure 5.3 (b) shows level 2, where the different barrel layers and end-cap discs are considered for both the Pixel and the SCT detectors. Finally, figure 5.3 (c) shows level 3 which is the finest alignment level where all the individual silicon modules are considered.

Next chapter will show that the use of the hierarchical alignment model based on these levels is the suitable strategy to align such a complex systems. Furthermore, it will discuss how using some of these levels one can have a first alignment pass where the modules can be aligned, on average, up to 100 μ precision without need of dealing with the 34992 DoFs.

To determine the alignment parameters of these structures, one has to project the residual derivatives computed for individual modules into their corresponding structures. Then, if one denotes with the vector $\mathbf{A}$ (size N_{STRU}) the alignment corrections of the considered structures, the expression 4.25 (see section 4.2.3) for the final alignment corrections $\mathbf{a}$ (at module level) can be rewritten as:

$$\delta\mathbf{A} = -\left[\sum_e \sum_{t\in e} \left(\frac{\partial \mathbf{r}}{\partial \mathbf{A}}\right)^T W \frac{\partial \mathbf{r}}{\partial \mathbf{A}}\right]^{-1} \sum_e \sum_{t\in e} \left(\frac{\partial \mathbf{r}}{\partial \mathbf{A}}\right)^T W\mathbf{r} \tag{5.20}$$

Where the only problem is that the residual providers are still the modules, not the structures. Therefore as there is an explicit dependence between the module alignment parameters $\mathbf{a}$ and the structure alignment corrections $\mathbf{A}$, one can write the following relation:

$$\frac{\partial \mathbf{r}}{\partial \mathbf{A}} = \frac{\partial \mathbf{r}}{\partial \mathbf{a}} \frac{\partial \mathbf{a}}{\partial \mathbf{A}} \tag{5.21}$$

where $\partial\mathbf{r}/\partial\mathbf{A}$ is a $N_{RES} \times N_{\text{STRU}}$ matrix and $\partial\mathbf{a}/\partial\mathbf{A}$ is the Jacobian-like matrix which performs the transformation. Then, inserting the above expression in 5.20, the later becomes:

$$\begin{aligned}
\delta\mathbf{A} &= -\left[\sum_e \sum_{t\in e} \left(\frac{\partial \mathbf{r}}{\partial \mathbf{a}}\frac{\partial \mathbf{a}}{\partial \mathbf{A}}\right)^T W \frac{\partial \mathbf{r}}{\partial \mathbf{a}}\frac{\partial \mathbf{a}}{\partial \mathbf{A}}\right]^{-1} \sum_e \sum_{t\in e} \left(\frac{\partial \mathbf{r}}{\partial \mathbf{a}}\frac{\partial \mathbf{a}}{\partial \mathbf{A}}\right)^T W\mathbf{r} = \\
&= -\left[\sum_e \sum_{t\in e} \left(\frac{\partial \mathbf{a}}{\partial \mathbf{A}}\right)^T \left(\frac{\partial \mathbf{r}}{\partial \mathbf{a}}\right)^T W \frac{\partial \mathbf{r}}{\partial \mathbf{a}}\frac{\partial \mathbf{a}}{\partial \mathbf{A}}\right]^{-1} \sum_e \sum_{t\in e} \left(\frac{\partial \mathbf{a}}{\partial \mathbf{A}}\right)^T \left(\frac{\partial \mathbf{r}}{\partial \mathbf{a}}\right)^T W\mathbf{r} = \\
&= -\left[\left(\frac{\partial \mathbf{a}}{\partial \mathbf{A}}\right)^T \mathcal{M} \frac{\partial \mathbf{a}}{\partial \mathbf{A}}\right]^{-1} \left(\frac{\partial \mathbf{a}}{\partial \mathbf{A}}\right)^T \nu = -\mathcal{M}_{\mathbf{A}}^{-1} \nu_{\mathbf{A}}
\end{aligned} \tag{5.22}$$

where:

$$\mathcal{M}_{\mathbf{A}} \equiv \left(\frac{\partial \mathbf{a}}{\partial \mathbf{A}}\right)^T \mathcal{M} \frac{\partial \mathbf{a}}{\partial \mathbf{A}} \quad \text{and} \quad \nu_{\mathbf{A}} \equiv \left(\frac{\partial \mathbf{a}}{\partial \mathbf{A}}\right)^T \nu$$

	Number of Structures			Structure description	
Level	Total (DoFs)	Pixels	SCT	Pixel structure	SCT structure
1*	4 (24)	1	3	Complete Pixel detector	1 B + 2 EC
1.5	7 (42)	4	3	2 B-HS + 2 EC	1 B + 2 EC
1.6	11 (66)	8	3	$3 \cdot 2$ B-HS + 2 EC	1 B + 2 EC
1.8*	14 (84)	8	6	$3 \cdot 2$ B-HS + 2 EC	4 B-LY + 2 EC
2	31 (186)	9	22	3 B-LY + $2 \cdot 3$ EC-D	4 B-LY + $2 \cdot 9$ EC-D
2.1	34 (204)	12	22	$3 \cdot 2$ B-HS-LY + $2 \cdot 3$ ECD	4 B-LY + $2 \cdot 9$ EC-D
2.3	184 (1104)	118	66	112 B-LD + $2 \cdot 3$ EC-D	$4 \cdot 12$ B-LY-R + $2 \cdot 9$ EC-D
2.4	67 (402)	1	66	Complete Pixel detector	$4 \cdot 12$ B-LY-R + $2 \cdot 9$ EC-D
2.5	312 (1872)	118	194	112 B-LD + $2 \cdot 3$ EC-D	176 B-LY-LD + $2 \cdot 9$ EC-D
2.6	164 (984)	114	50	112 B-LD + 2 EC	$4 \cdot 12$ B-LY-R + 2 EC
2.7*	292 (1752)	114	178	112 B-LD + 2 EC	176 B-LY-LD + 2 EC
3*	5832 (34992)	1744	4088	1456 B-MOD + $2 \cdot 144$ EC-MOD	2112 B-MOD + $2 \cdot 988$ EC-MOD

Table 5.1: *Hierarchical geometry description levels for alignment, defined in the Global*χ^2 *geometry manager algorithm for the ATLAS Silicon Tracker. In the first column (*) represents if the level is a physical situation or just an academic exercise. Several abbreviations have been used: B ≡ Barrel, B-LY ≡ Barrel Layer, B-HS ≡ Barrel Half-Shell, B-HS-LY ≡ Barrel Half-Shell Layer, B-LD ≡ Barrel Ladder, B-LY-LD ≡ Barrel Layer Ladder, B-LY-R ≡ Barrel Layer Ring, EC ≡ End-Cap, EC-D ≡ End-Cap disc, B-MOD ≡ Barrel Modules and EC-MOD ≡ End-Cap Modules.*

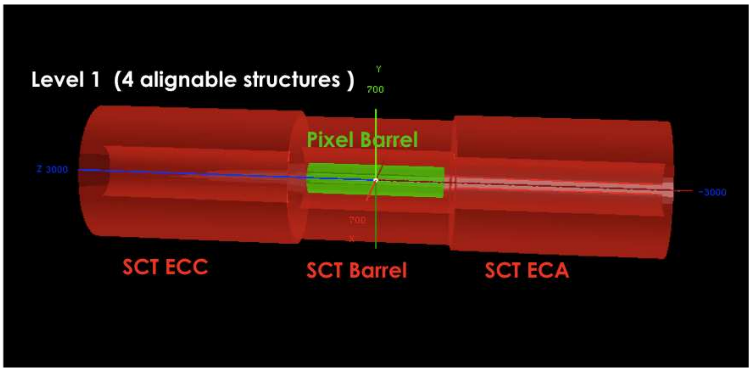

(a) *Alignment level 1 (4 alignable structures)*

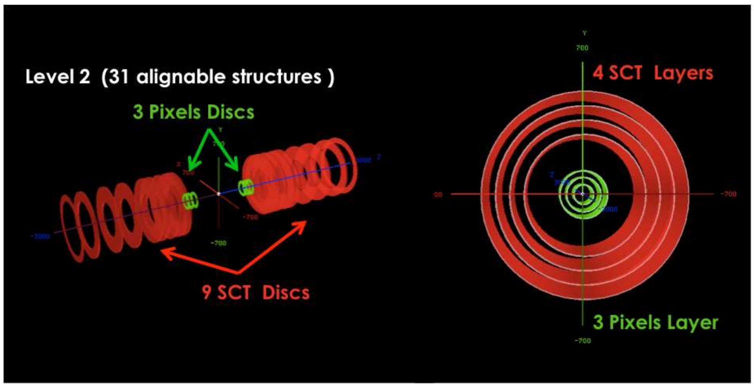

(b) *Alignment level 2 (31 alignable structures)*

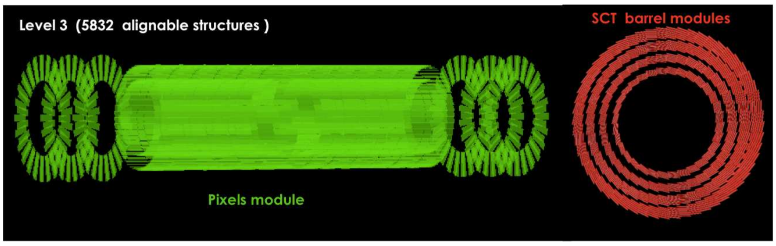

(c) *Alignment level 3 (5832 alignable modules)*

Figure 5.3: *Graphical models of three main alignment levels. Figure (a) shows level 1 where the Pixel detector is represented with just one structure and the SCT is divided in three structures (the barrel and the two end-caps). Then, figure (b) shows level 2, where the different barrel layers and end-cap discs are considered for both the Pixel and the SCT detectors. Finally, figure (c) shows level 3, which is the finest alignment level, where all the individual silicon modules are considered.*

Here, $\partial\mathbf{a}/\partial\mathbf{A}$ is not a Jacobian in a proper sense. It represents more a projection into a subspace of smaller dimensions: from N_{ALI} (module space) to N_{STRU} (structure space). Furthermore, the matrix $\mathcal{M}_{\mathbf{A}}$ has dimension $N_{ALI} \times N_{\text{STRU}}$ and vector $\nu_{\mathbf{A}}$ has size N_{STRU}. Then, now, the size of the big-matrix ($\mathcal{M}_{\mathbf{A}}$) to invert is $N_{\text{STRU}} \times N_{\text{STRU}}$ instead of $N_{ALI} \times N_{ALI}$ and this has an important advantage: the size of the problem has been drastically reduced as $N_{\text{STRU}} << N_{ALI}$.

Moreover, thanks to this projection the resulting matrix $\mathcal{M}_{\mathbf{A}}$ is not sparse (or at least not as sparse as $\mathcal{M}$), therefore this is not an issue anymore. As tracks usually produce signals in many modules in different layers or discs, when a projection into these structures is done all of them become correlated, thus making the off-diagonal elements non null.

From expression 5.22 one builds the $\mathcal{M}_{\mathbf{A}}$ matrix from $\mathcal{M}$ which is $N_{ALI} \times N_{ALI}$ i.e. $\approx$ 35k $\times$ 35k. In other words, in this case the projection is done once the $\mathcal{M}$ matrix has been processed and accumulated. This does not preserve from the matrix manipulation problems discussed in section 5.3 as one has to keep the initial matrix $\mathcal{M}$. However one does not necessarily need to define that $\mathcal{M}$ matrix in memory. Instead of projecting $\mathcal{M}$ into $\mathcal{M}_{\mathbf{A}}$, one can project directly the residuals, filling $\mathcal{M}_{\mathbf{A}}$ and $\nu_{\mathbf{A}}$ in track by track basis:

$$\mathcal{M}_{\mathbf{A}} \equiv \sum_e \sum_{t \in e} \left(\frac{\partial \mathbf{r}}{\partial \mathbf{a}} \frac{\partial \mathbf{a}}{\partial \mathbf{A}} \right)^T W \frac{\partial \mathbf{r}}{\partial \mathbf{a}} \frac{\partial \mathbf{a}}{\partial \mathbf{A}} \quad \text{and} \quad \nu_{\mathbf{A}} \equiv \sum_e \sum_{t \in e} \left(\frac{\partial \mathbf{r}}{\partial \mathbf{a}} \frac{\partial \mathbf{a}}{\partial \mathbf{A}} \right)^T W \frac{\partial \mathbf{r}}{\partial \mathbf{a}} \frac{\partial \mathbf{a}}{\partial \mathbf{A}}$$

The only point is that one has to be clever enough and for each track one has to deal only with those few elements that participate in the track reconstruction. Then, one has to perform the projection in a track by track basis into a $N_{\text{STRU}} \times N_{\text{STRU}}$ matrix and a $N_{\text{STRU}} \times 1$ vector, saving memory at the expense of CPU processing time during alignment data accumulation.

In any case, the problem of projecting either the $\mathcal{M}$ matrix or the residual derivatives consists just to compute $\partial\mathbf{a}/\partial\mathbf{A}$.

5.2.1 The projection matrix $\partial\mathbf{a}/\partial\mathbf{A}$

From section 4.1.1.2, one knows that the alignment corrections $\mathbf{a}$ denote the DoF of the alignable modules and they are generally referred by $T_x, T_y, T_z, R_x, R_y, R_z$. Here, one has two different kind of alignable objects, modules and structures, that is why the adopted notation from now will be:

- Alignment parameters for modules are denoted by $\mathbf{a}$, generic translations by $t = (x, y, z)$ and generic rotations by $r = (\alpha, \beta, \gamma)$.

- Alignment parameters for structures are denoted by $\mathbf{A}$, generic translations by $T = (X, Y, Z)$ and generic rotations by $R = (A, B, \Gamma)$.

Then, one can write $\partial\mathbf{a}/\partial\mathbf{A}$ as:

$$\frac{\partial \mathbf{a}}{\partial \mathbf{A}} = \begin{pmatrix} \frac{\partial t}{\partial T} & \frac{\partial t}{\partial R} \\ \frac{\partial r}{\partial T} & \frac{\partial r}{\partial R} \end{pmatrix} = \left(\begin{array}{ccc|ccc} \frac{\partial x}{\partial X} & \frac{\partial x}{\partial Y} & \frac{\partial x}{\partial Z} & \frac{\partial x}{\partial A} & \frac{\partial x}{\partial B} & \frac{\partial x}{\partial \Gamma} \\ \frac{\partial y}{\partial X} & \frac{\partial y}{\partial Y} & \frac{\partial y}{\partial Z} & \frac{\partial y}{\partial A} & \frac{\partial y}{\partial B} & \frac{\partial y}{\partial \Gamma} \\ \frac{\partial z}{\partial X} & \frac{\partial z}{\partial Y} & \frac{\partial z}{\partial Z} & \frac{\partial z}{\partial A} & \frac{\partial z}{\partial B} & \frac{\partial z}{\partial \Gamma} \\ \hline \frac{\partial \alpha}{\partial X} & \frac{\partial \alpha}{\partial Y} & \frac{\partial \alpha}{\partial Z} & \frac{\partial \alpha}{\partial A} & \frac{\partial \alpha}{\partial B} & \frac{\partial \alpha}{\partial \Gamma} \\ \frac{\partial \beta}{\partial X} & \frac{\partial \beta}{\partial Y} & \frac{\partial \beta}{\partial Z} & \frac{\partial \beta}{\partial A} & \frac{\partial \beta}{\partial B} & \frac{\partial \beta}{\partial \Gamma} \\ \frac{\partial \gamma}{\partial X} & \frac{\partial \gamma}{\partial Y} & \frac{\partial \gamma}{\partial Z} & \frac{\partial \gamma}{\partial A} & \frac{\partial \gamma}{\partial B} & \frac{\partial \gamma}{\partial \Gamma} \end{array}\right)$$

where four blocks can be easily seen: $\partial t/\partial T$, $\partial t/\partial R$, $\partial r/\partial T$ and $\partial r/\partial R$.

This matrix can be computed considering the relationship between a general module transformation ($\mathbf{H} = [\mathbf{T}_M, \mathbf{R}_M]$), the local movement of the given module ($\mathbf{H}_{\delta\mathbf{a}}$) and the global movement of the structure which contains this module ($\mathbf{H}_{\delta\mathbf{A}}$). A detailed mathematical development is found in appendix C. Then, after some algebra, $\partial \mathbf{a}/\partial \mathbf{A}$ is:

$$\frac{\partial \mathbf{a}}{\partial \mathbf{A}} = \begin{pmatrix} \mathbf{R}_M^{-1} & (\mathbf{T}_M \times \hat{a}) \cdot \hat{b} \\ 0 & \mathbf{R}_M^{-1} \end{pmatrix} \tag{5.23}$$

being $\hat{a} = \hat{x}, \hat{y}, \hat{z}$ and $\hat{b} = \hat{X}, \hat{Y}, \hat{Z}$ the unit vectors of the local and global frame, respectively.

5.2.2 Computing the projection of the SCT stereo side

In the case of the SCT modules another projection has to be performed since they have two sides but the alignment model assumes that both sides are linked to the same alignable object (i.e. the module). In particular, the $r\phi$ side of the SCT modules defines this alignable object. This implies that the residual derivative of the stereo side must be projected into the alignable plane. In other words, one has to compute how the alignment parameters of the stereo side change with respect the alignment parameters of the $r\phi$ side. Hence, a particular solution of expression 5.23 gives this projection, where **a** represents the stereo side and **A** represents the $r\phi$ side. In this case, one has to consider that the stereo plane is rotated around the local z axis with respect to the $r\phi$ side (therefore $\mathbf{R}(0, 0, \gamma)$) and moreover, it is shifted over the same z axis a distance z_0. An scheme can be seen on figure 5.4.

So, all the bits of the $\partial \mathbf{a}/\partial \mathbf{A}$ are computed. Joining them all together gives:

$$\frac{\partial \mathbf{a}}{\partial \mathbf{A}} = \left(\begin{array}{ccc|ccc} \cos\gamma & \sin\gamma & 0 & -z_0 \sin\gamma & z_0 \cos\gamma & 0 \\ -\sin\gamma & \cos\gamma & 0 & -z_0 \cos\gamma & -z_0 \sin\gamma & 0 \\ 0 & 0 & 1 & 0 & 0 & z_0 \\ \hline 0 & 0 & 0 & \cos\gamma & \sin\gamma & 0 \\ 0 & 0 & 0 & -\sin\gamma & \cos\gamma & 0 \\ 0 & 0 & 0 & 0 & 0 & 1 \end{array}\right)$$

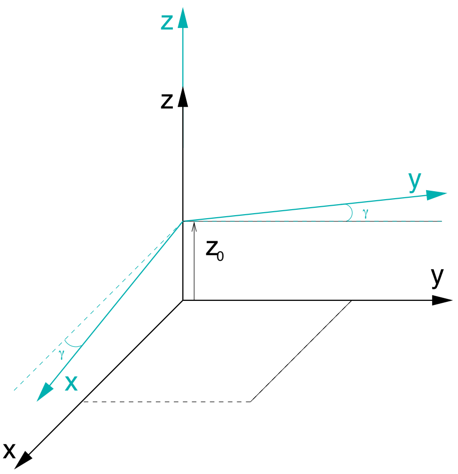

Figure 5.4: *The two planes of a SCT module are just shifted along the local z axis (a distance z_0) and rotated around the same axis to form the stereo angle (γ).*

Thus, this is the generic projection that relates a plane of a module which is shifted by z_0, and rotated around z by an angle γ. In the case of the SCT barrel modules $z_0 \approx 1.1$ mm while $\gamma = 40$ mrad.

5.2.3 Applying the alignment corrections

Another important topic to discuss is how the alignment corrections are applied to the nominal positions or iteration after iteration. In the ATLAS ID alignment model, the alignment corrections are given in terms of a transformation $\mathbf{H}_{\delta\mathbf{a}}$. The alignment corrections becomes:

$$\mathbf{H_0}' = \mathbf{H_0} \otimes \mathbf{H}_{\delta\mathbf{a}}$$

where $\mathbf{H_0}$ represents the nominal or actual positions (depending if it is the first iteration or not) and $\mathbf{H_0}'$ represents the updated positions. Obviously, not to say that this simple computation is valid either for modules and for structures, although in the first case the alignment corrections are given in the local frame and in the later case in the global frame.

5.3 Solving a large system of linear equations

Minimizing a χ^2 function with N_{ALI} parameters reduces to solving a system of N_{ALI} linear equations as it has been shown in the previous chapter. This issue is in fact the major technical challenge of the Globalχ^2 algorithm when applied on the ATLAS Silicon Tracker (section 4.2.3.1). Thus, in order to get the alignment corrections, the matrix $\mathcal{M}$ (in the alignment's jargon, *big-matrix*) must be inverted:

$$\delta\mathbf{a} = -\mathcal{M}^{-1}\nu$$

For linear systems where one has up to 1k parameters there are several options: explicit matrix inversion[3], full diagonalization (using LU decomposition, Cholesky decomposition, Gauss-Jordan elimination, etc...) and numerical iterative solving (frontal solver [80], MINRES [81], etc...). For these systems a simple explicit matrix inversion (using, for example, CLHEP matrix inversion libraries [82]) is feasible. An example of these tiny systems could be the case of the track or the vertex fits. Although the full diagonalization is quite CPU time consuming (6 times more than explicit matrix inversion) it is the technique used in the Globalχ^2 code since it provides extra information that allows to identify singularities. Anyhow, for large systems, for example to compute the alignment corrections for all the silicon modules of ATLAS (5832 modules), one has to deal with ~ 35k linear equations (i.e. ~ 35k DoFs) and therefore an explicit inversion is not practicable. In these cases, other techniques are better candidates such as the full matrix diagonalization or the numerical solution, though they also have their advantages and their limitations. Generally, there are three main technical limiting factors to achieve a matrix inversion:

- **Memory handling:** A full dense matrix of $N_{ALI} \approx 35$k needs ~ 9.8 GB of memory (generally, an alignment matrix size is N^2_{DoF} where each matrix element is defined as double precision, i.e. 8 byte or 64 bit) and at least the same amount of memory for internal computations (this is because the matrix inversion algorithms need to duplicate the matrix on memory to do their algebra). In 32-bit platforms this amount of memory is not available as they can only address a maximum of 4 GB of virtual memory. Moreover, these 4 GB are evenly divided into two parts, with 2 GB dedicated for kernel usage, and 2 GB left for application usage. Thus, each application gets its own 2 GB, but all applications have to share the same 2 GB kernel space. The 32-bit ATLAS software infrastructure allows only 2 GB of memory per job so therefore it does not permit so large matrix manipulations. This is, however, a limiting factor that can be solved nowadays using 64-bit machines which can address 512 TB. At the time of writing, the 64-bit version of the ATLAS software has not been yet certificated, so, standalone software based on diagonalization routines such as LAPACK libraries[4] [84] or ScaLAPACK libraries[5] [85] compiled in 64-bit has to be used. In particular, the Globalχ^2 algorithm uses the routines coded in the either LAPACK or ScaLAPACK libraries to perform the matrix diagonalization (where LU decomposition technique is used).

  For sparse matrices[6], there is another option which is the numerical solution. This method

[3]Being A a square matrix, if its the determinant is $|A| \neq 0$ (i.e. if A is nonsingular), A is therefore invertible and then its inverse is:

$$A^{-1} = \frac{1}{|A|}\mathrm{adj}\,(A)^T$$

[4]LAPACK is a set of routines written in Fortran90 which provides routines for solving linear systems of equations, eigenvalue problems, etc. The associated matrix factorizations (LU, Cholesky, ..) are also provided. Dense and banded matrices are handled, but not general sparse matrices. This library provides routines for real and complex matrices, in both single and double precision. Moreover, LAPACK routines are written so that as much as possible of the computation is performed by calls to the Basic Linear Algebra Subprograms (BLAS) [83].

[5]The ScaLAPACK (or Scalable LAPACK) library includes a subset of LAPACK routines redesigned for parallel/distributed computing. The fundamental building blocks of the ScaLAPACK library are a parallel version of BLAS (PBLAS) and a set of Basic Linear Algebra Communication Subprograms (BLACS) for communication tasks that arise frequently in parallel linear algebra computations.

[6]As was mentioned, in numerical analysis a sparse matrix is a matrix populated primarily with zeros although there is no formal definition in terms of number of non-zeros, patterns or properties.

will be discuss in section 5.3.2.

- **Numerical precision:** Conventional 32-bit libraries are not fully adequate for the required computational accuracy. This is because some complex numerical algorithms are limited in their precision by the errors that can creep in because not all floating point numbers can be accurately represented with a small number of bits. Thus, creeping inaccuracies can lead to incorrect results, often leading to attempts to divide by zero, or to not identify two quantities as being identical for practical purposes. The matrices of alignment problem can have large numbers which may compete with the machine precision. Therefore, special libraries have to be used in order to avoid numerical roundoff errors. These libraries were implemented [86] within the ATLAS software and they have been extensively tested and validated within the Globalχ^2 algorithm for both, the Silicon Tracker alignment and the TRT alignment. Moreover, the use of 64-bit machines together with 64-bit matrix manipulation software will solved this issue in a near future as they allow natively support for 64-bit data types and addresses.

  Several tests were done in order estimate the difference in the numerical precision between 32-bit and 64-bit architectures. But to perform these tests a combination of 32-bit and 64-bit processes were used. In particular, firstly an Athena job (compiled in 32-bit) processed events and computed contributions to matrix/vector elements and secondly, a little C program (compiled in 64-bit) received information and filled the *big-matrix* and the *big-vector* (without memory constraints due to its architecture). The communication between processes was implemented through a message queue technique. Thus, real alignment cases were studied. One of these studies used 20k events of a multimuon sample (10 muons per event) and a perfectly aligned geometry (using a small barrel fraction: 1030 modules, i.e. 6180 DoF). Then, the difference between the same elements in a matrix/vector filled in a 32-bit environment and a matrix/vector filled in 64-bit environment was $O(10^{-7})$, confirming that the alignment results were affected by the machine precision. Figure 5.6 shows the two eigenvalue spectra after a full matrix diagonalization for the first 400 eigenvectors (as known as *modes*) where the effect of the numerical precision can be easily seen. The left plot, obtained with a 32-bit machine and using LAPACK routines (in particular the *dspev* routine), shows an eigenvalue spectrum discretized in steps and the right one shows continuous values obtained with a 64-bit machine and ScaLAPACK routines (in particular the *pdsyevd* routine[7]). This is because lower modes which have the smaller eigenvalues and the larger errors are, once more, limited by machine precision in a 32-bit machine. The difference observed between the eigenvalues in both cases is $O(10^{-7})$ [87].

  Another important issue is the fact that the alignment matrices are singular by construction (due to some unconstrained global DoF), but due to numerical machine precision they are not. The null eigenvalues become very small but not null values. Thus, the eigenvalue spectrum spans over 10 orders of magnitude (i.e. the ratio of largest to smallest eigenvalue is quite large) and therefore the solution is normally numerically challenging. Then, the highest numerical precision is required.

- **Execution time:** Single-core machines take too many hours to solve large size problems as this solving time is related with the total number of operations needed to solve the sys-

[7] The routine *pdsyevd* is based on the *dspev* routine but taking advantage of parallel computing.

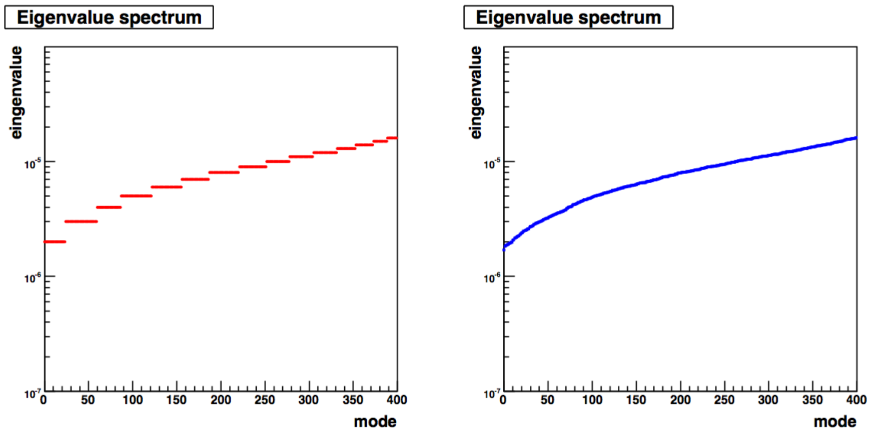

Figure 5.5: *Comparison between the eigenvalue spectrum obtained using 32-bit LAPACK (left) and using 64-bit ScaLAPACK (right). The left spectrum is discretized in steps while the right spectrum shows a continuous behavior due to the fact that the 32-bit results are affected by the machine precision [87].*

tem which are $O(N^3)$ (being N the number of linear equations, i.e. number of DoFs). The solution is to use parallel processing systems which allow the distribution of the CPU load and large size of data among various nodes together with distributed-memory libraries for matrix manipulation. Five years ago, the most powerful technique was to use several single-core machines or several servers (with two or more single-core CPUs) linked with dedicated high performance connections (Myrinet [88], InfiniBand [89] or similar technologies). The problem was that each machine had their own memory and the different processes had to talk each other through external network links which were obviously much slower that direct memory access (due to the latency of data transfers). Nowadays, multicore machines are used to parallelize these kind of tasks within a single machine with a common and shared high speed memory. This option is much more efficient as all the cores have internal high speed access to the same memory avoiding bottleneck problems.

Special libraries have to be used to exploit parallel processing such as the ScaLAPACK library which includes a subset of LAPACK routines redesigned for distributed memory parallel computers. It is currently based on a Single-Program-Multiple-Data style which uses explicit message passing for interprocessor communication. Thus it can be used in any computer that supports Message Passing Interface standards (MPI) [90].

Several clusters have been used during these years in order to perform numerical tests with the Globalχ^2 and of course to align the ATLAS Silicon Tracker at module level. Thus, the first cluster used was the Beowulf cluster located at the Rutherford Appleton Laboratory (RAL) known as SCARF. It consisted in a 128-node dual CPU 64-bit AMD Opteron 248 2.2 GHz cluster running on Red Hat Enterprise Linux 3.0. The great majority of the nodes had 4 GB of memory while 16 of them had 8 GB. AMD Core Math Library (ACML) plus ScaLAPACK libraries compiled in 64-bit and MPI specification for message-passing were used. The performance and

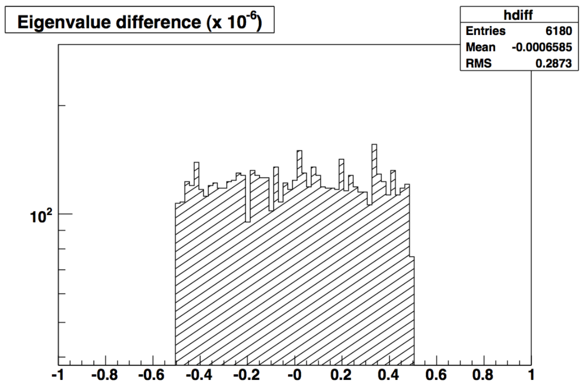

Figure 5.6: *Difference between the eigenvalues for 6180 DoF, obtained using 32-bit LAPACK and using 64-bit ScaLAPACK. As can be seen this difference is $O(10^{-7})$ [87].*

achieved precision of the 64-bit parallel cluster was demonstrated to largely improve the results with respect to the 32-bit architecture. Tests and their results are described in reference [75].

Then, in 2007, a dedicated server for alignment was acquired by IFIC's Computing Center, named *Alineator* [91]. It is a server with two AMD Dual-Core Opteron 2218 (64-bit) working at 2.6 GHz (i.e. 4 cores) with 32 GB of shared memory with embebed Error Checking and Correction (ECC) algorithms. It runs on Scientific Linux IFIC 4[8] in 64-bit mode and the 64-bit ScaLAPACK library is installed together with MPI for message-passing between the different cores. Moreover, the ACML libraries are also used in order to optimize the performance for AMD cores. As it is a dedicated server for alignment purposes it has spearheaded the full ATLAS Silicon Tracker alignment when a full alignment solution has been required at module level with error estimation, i.e. using the diagonalization method (see next section).

Figure 5.7 shows the full solving time to diagonalize a matrix (including the harddisk drive i/o times) as a function of its number of DoF for a 32-bit (triangles) and a 64-bit (circles) machines. In particular, the 32-bit machine was a Pentium IV Dual Core running at 3 GHz with 3 GB of memory an using the LAPACK library compiled in 32-bit (although, this machine had already two cores, the LAPACK routine just run on one of the two cores). The 64-bit machine was the mentioned *Alineator* using the ScaLAPACK library compiled in 64-bit and using its 4 cores together thanks to the MPI protocol. The matrix inversion with 32-bit LAPACK is shown to be applicable to problems with more or less 10k parameters (dashed line in figure 5.7) and although LAPACK library [75] could be compiled in 64-bit to remove memory constraints, 64-bit ScaLAPACK routine has to be used in order to parallelize the problem and to tackle the full system solution. The performance and achieved precision of the 64-bit parallel server was demonstrated to largely improve the results with respect to the 32-bit single core architecture. However, as has been commented the computation time grows approximately with the third power of the dimension of the problem making even the step from 10k to the actual 35k parameters in the ATLAS alignment nontrivial.

[8] Scientific Linux IFIC 4 (SLI4) is based on Scientific Linux CERN 4 (SLC4).

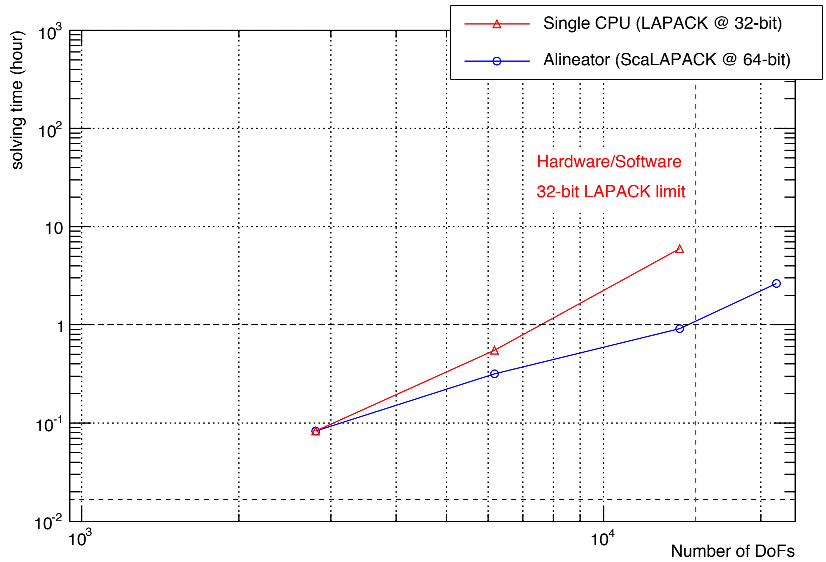

Figure 5.7: *Comparison between a single core process using LAPACK compiled in 32-bit (triangle) and a multicore machine (*Alineator*: 4 cores) using ScaLAPACK compiled in 64-bit (circles). The vertical dashed line illustrates the hardware and software 32-bit limits for LAPACK.*

Anyhow, the results from figure 5.7 are the solving times from the diagonalization technique and as has been said there are two techniques which can be used in order to solve large system of equations: diagonalization or numerical iterative techniques. Both methods are implemented and tested in the Globalχ^2 code. In the next subsections, both techniques will be discussed and the main advantages and problems will be pointed out.

5.3.1 Diagonalization method

The matrix diagonalization is the process of taking a squared, dense and symmetric real matrix ($\mathcal{M}$ in our case) and converting it into a diagonal matrix which shares the same fundamental properties that the original matrix. It is equivalent to perform a change of basis where the initial matrix takes its canonical form (i.e. diagonal form). Technically, diagonalizing a matrix is also equivalent to finding the matrix's eigenvalues. Similarly, the eigenvectors form the matrix which allows the change of basis to the corresponding diagonal matrix. Due to this change of basis, the diagonalization of the matrix allows to recognize the singularities which correspond to undefined or weakly defined DoFs. Then, the diagonalization of $\mathcal{M}$ is expressed as:

$$\mathcal{M} = UDU^{-1}$$

where D is a diagonal matrix constructed from the corresponding eigenvalues of $\mathcal{M}$ and U is an orthogonal matrix (i.e. $U^{-1} = U^T$, and therefore $UU^T = U^TU = I$) which columns are the eigenvectors of $\mathcal{M}$. Since $\mathcal{M}$ is symmetrical, the eigenvalues will be real numbers. The rank of $\mathcal{M}$ is the number of non-zero eigenvalues. The matrix $\mathcal{M}$ is invertible only if all eigenvalues are non-zero, i.e. if its rank is equal to its dimension N_{ALI}. Then, the inverse of $\mathcal{M}$ is:

$$\mathcal{M}^{-1} = UD^{-1}U^{-1} \tag{5.24}$$

The eigenvalues, denoted by λ_i (where $i = 1, ..., N_{ALI}$), appear in D as:

$$D = \begin{pmatrix} \lambda_1 & 0 & 0 & 0 \\ 0 & \lambda_2 & 0 & 0 \\ 0 & 0 & \ddots & 0 \\ 0 & 0 & 0 & \lambda_{N_{ALI}} \end{pmatrix} \quad \rightarrow \quad D = [diag(\lambda_i)] : \quad \lambda_1 \leq \lambda_1 \leq ... \leq \lambda_{N_{ALI}}$$

Then, the matrix D can be trivially inverted as it is just:

$$D^{-1} = \begin{pmatrix} 1/\lambda_1 & 0 & 0 & 0 \\ 0 & 1/\lambda_2 & 0 & 0 \\ 0 & 0 & \ddots & 0 \\ 0 & 0 & 0 & 1/\lambda_{N_{ALI}} \end{pmatrix} \quad \rightarrow \quad D^{-1} = \left[diag\left(\frac{1}{\lambda_i}\right)\right]$$

Hence, $\mathcal{M}$ can be inverted thanks to expression 5.24 using several methods such as LU decomposition, Cholesky decomposition, Gauss-Jordan elimination, etc... Once $\mathcal{M}$ has been diagonalized, the alignment corrections are:

$$\delta\mathbf{a} = -UD^{-1}U^T\nu \tag{5.25}$$

The final solution can be also expressed in the diagonal basis which are called *eigenmodes* in the alignment jargon ($\delta\mathbf{b}$). Considering a simple change of basis, these modes can be written as:

$$\delta\mathbf{b} = -D^{-1}\nu_D \quad \text{where} \quad \nu_D = U\nu \tag{5.26}$$

The advantage is that one can always choose a basis in the alignment parameters space in which the $\mathcal{M}$ matrix is diagonal. The usual way to find this new basis is by the straight diagonalization of $\mathcal{M}$, where the technical problems discussed at the beginning of this section appear. This can be trivially demonstrated considering a simple change of basis (which is at the end the diagonalization) as will be shown in the next subsection.

5.3.1.1 Change of basis in the alignment parameters space

As the diagonalization implies a change of basis, let's consider a simple transformation. One can find a vector $\delta\mathbf{b}$ (dimension N_{ALI}) and an unitary matrix B (size $N_{ALI} \times N_{ALI}$) such:

$$\delta\mathbf{a} = B\delta\mathbf{b} \qquad \delta\mathbf{b} = B^{-1}\delta\mathbf{a}$$

and as B is a change of basis matrix (orthonormal): $B^T = B^{-1}$.

Let be f a generic function that depends on the alignment parameters (either $\mathbf{a}$ or $\mathbf{b}$):

$$df = \frac{\partial f}{\partial \mathbf{a}}\delta\mathbf{a} = \frac{\partial f}{\partial \mathbf{b}}\delta\mathbf{b} = \frac{\partial f}{\partial \mathbf{b}}B^{-1}\delta\mathbf{a} \quad \text{therefore:} \quad \frac{\partial f}{\partial \mathbf{a}} = \frac{\partial f}{\partial \mathbf{b}}B^{-1} \quad \text{and} \quad \frac{\partial f}{\partial \mathbf{a}}B = \frac{\partial f}{\partial \mathbf{b}} \tag{5.27}$$

One can compute the alignment corrections in the new basis and compute $\delta\mathbf{b}$ instead of $\delta\mathbf{a}$. From equation 4.25 and using 5.27, one can write:

$$\delta\mathbf{a} = B\delta\mathbf{b} = -\left[\sum_{e}\sum_{t\in e}\left(\frac{\partial\mathbf{r}}{\partial\mathbf{b}}B^{-1}\right)^T W\frac{\partial\mathbf{r}}{\partial\mathbf{b}}B^{-1}\right]^{-1}\sum_{e}\sum_{t\in e}\left(\frac{\partial\mathbf{r}}{\partial\mathbf{b}}B^{-1}\right)^T W\mathbf{r} =$$

$$= -\left[\sum_{e}\sum_{t\in e}B\left(\frac{\partial\mathbf{r}}{\partial\mathbf{b}}\right)^T W\frac{\partial\mathbf{r}}{\partial\mathbf{b}}B^{-1}\right]^{-1}\sum_{e}\sum_{t\in e}B\left(\frac{\partial\mathbf{r}}{\partial\mathbf{b}}\right)^T W\mathbf{r} =$$

$$= -\left[B\mathcal{M}_b B^{-1}\right]^{-1}B\nu_b = -B\mathcal{M}_b^{-1}B^{-1}B\nu_b = -B\mathcal{M}_b^{-1}\nu_b \quad\longrightarrow\quad \delta\mathbf{b} = -\mathcal{M}_b^{-1}\nu_b$$

where the *big-matrix* and the *big-vector*, expressed in the new basis, are:

$$\mathcal{M}_b \equiv \sum_{e}\sum_{t\in e}\left(\frac{\partial\mathbf{r}}{\partial\mathbf{b}}\right)^T W\frac{\partial\mathbf{r}}{\partial\mathbf{b}} \quad\text{and}\quad \nu_b \equiv \sum_{e}\sum_{t\in e}\left(\frac{\partial\mathbf{r}}{\partial\mathbf{b}}\right)^T W\mathbf{r}$$

These results obtained with this change of basis were already expected. But usually one would compute the $\mathcal{M}$ matrix and the ν vector using the derivatives of the residuals with respect to the DoF of the physical modules ($\mathbf{a}$). Now, in order to compute the new matrix ($\mathcal{M}_b$) and vector (ν_b) one has to apply the expression 5.27. Then M_b can be written as:

$$\mathcal{M}_b = \sum_{e}\sum_{t\in e}\left(\frac{\partial\mathbf{r}}{\partial\mathbf{b}}\right)^T W\left(\frac{\partial\mathbf{r}}{\partial\mathbf{b}}\right) = B^{-1}\left[\sum_{e}\sum_{t\in e}\left(\frac{\partial\mathbf{r}}{\partial\mathbf{a}}\right)^T W\left(\frac{\partial\mathbf{r}}{\partial\mathbf{a}}\right)\right]B = B^{-1}\mathcal{M}B$$

and for ν_b as:

$$\nu_b = \sum_{e}\sum_{t\in e}\left(\frac{\partial\mathbf{r}}{\partial\mathbf{b}}\right)^T W\mathbf{r} = \sum\left(\frac{\partial\mathbf{r}}{\partial\mathbf{a}}B\right)^T W\mathbf{r} = B^{-1}\left[\sum_{e}\sum_{t\in e}\left(\frac{\partial\mathbf{r}}{\partial\mathbf{a}}\right)^T W\mathbf{r}\right] = B^{-1}\nu$$

5.3.1.2 Error of the alignment parameters

The alignment correction must come with their errors as they are physical measurements. As it was discussed in section 4.2.2.1 the covariance matrix (C) of the considered parameters is the inverse of $\mathcal{M}$ (i.e. $C = \mathcal{M}^{-1}$). Then, if one considers the alignment corrections in the diagonal basis, the covariance matrix and the errors of the parameters are:

$$C_b = D^{-1} \quad\longrightarrow\quad [\varepsilon(\delta\mathbf{b})]^2 = D^{-1} = \begin{pmatrix} 1/\lambda_1 & 0 & 0 & 0 \\ 0 & 1/\lambda_2 & 0 & 0 \\ 0 & 0 & \ddots & 0 \\ 0 & 0 & 0 & 1/\lambda_{N_{ALI}} \end{pmatrix}$$

And, in the physical basis (i.e. non-diagonal basis), this result looks like this:

$$\varepsilon(\delta\mathbf{a}) = U\varepsilon(\delta\mathbf{b}) = U\begin{pmatrix} \sqrt{1/\lambda_1} & 0 & 0 & 0 \\ 0 & \sqrt{1/\lambda_2} & 0 & 0 \\ 0 & 0 & \ddots & 0 \\ 0 & 0 & 0 & \sqrt{1/\lambda_{N_{ALI}}} \end{pmatrix}$$

Thus, this expression relates the eigenvalues ($D = [diag(\lambda_i)]$) and the eigenvectors (U) of with the errors of the alignment parameters. From it one can easily see that small eigenvalues lead to large errors of the alignment parameters. In the other hand large eigenvalues mean small errors and therefore well determined alignment parameters. This allows to identify eigenmodes that are weakly constrained (i.e. eigenmodes for which the algorithm has very low sensitivity).

In the extreme case of null eigenvalues ($\lambda_i = 0$) the errors become infinite which means that one is not sensitive to the movements along the direction (given by its eigenvector) of that parameter. In this case, D would become singular. That is one of the goodness of diagonalizing the matrix $\mathcal{M}$ and performing the change of basis where one can deal with the singularity just by discarding those null eigenvalues and their associated eigenvectors and work just with the rest (the non null eigenvalues), extracting from them the well-defined alignment corrections. In the Globalχ^2 algorithm an eigenvalue cut (actually based on a cut on the mode number) is performed before giving the final alignment corrections, removing the degeneracies of the system.

In principle there would be 12 global DoF's of the entire system which leave the χ^2 unchanged (6 movements over each DoF, 3 scales or expansions over X, Y and Z and 3 deformations over XY, XZ and YZ). For instance one can just move or rotate the whole system as a rigid body. Internally the system would notice nothing and the same tracks will be reconstructed and they would have the same residuals and the same χ^2. Of course the tracks will be reconstructed with different parameters (specially the space track parameters, d_0 and so on) reflecting the spatial shift of the system, but the momentum of the particle should remain the same (as far as the displacements are not to big and one avoids entering in the non uniform region of the magnetic field of the tracking system). Theoretically, if no constraints are used, the eigenvalues associated to the 12 global DoF should be null. In practice one has to compute the $\mathcal{M}$ matrix, find its diagonal form (D) and from there one extracts its eigenvalues. As results of those operations the eigenvalues do not come up exactly null but very small. But as already stated, small eigenvalues mean large errors in the alignment parameters which actually mean the parameters are not precisely determined. Thus, the best is to remove the very small eigenvalues and their associated eigenvectors from the calculations setting them to zero in the D matrix. So, apart from the first 12 DoF, it is envisageable to remove also those DoF which their estimated shifts ($\delta\mathbf{b}$) are smaller than their errors. Considering the *i-th* term:

$$\delta\mathbf{b}_i = -\left(\frac{1}{\lambda_i}\right)\nu_{D_i} = -\left[\varepsilon(\delta\mathbf{b})_i\right]^2 \nu_{D_i}$$

then requiring that the shift must be larger than its error:

$$\left|\frac{\delta\mathbf{b}_i}{\varepsilon(\delta\mathbf{b})_i}\right| \geq 1 \quad \text{then} \quad \left|\frac{\delta\mathbf{b}_i}{\varepsilon(\delta\mathbf{b})_i}\right| = \varepsilon(\delta\mathbf{b}_i)\nu_{D_i} = \left(\sqrt{\frac{1}{\lambda_i}}\right)\nu_{D_i} \geq 1$$

At the end, the eigenvalues (λ_i) to be considered are the ones satisfying:

$$\nu_{D_i} \geq \sqrt{1/\lambda_i} \quad \text{with i} = 1, ..., N_{ALI} \tag{5.28}$$

So, this is a possible criteria to select only those DoFs that are well determined. This criteria is already coded in the Globalχ^2 algorithm and it demands that the determined eigenvalues fulfills the above expression.

5.3.2 Iterative numerical methods

On the other hand, there are some cases where the matrix $\mathcal{M}$ is sparse (in our case, the occupancy should not be higher than $\sim 3\%$). As has been commented in the previous chapter this could be due because the sample used (collision data, cosmics, etc...) does not correlate enough silicon modules. In these cases, there are other king of algorithms which can solve the system $\mathcal{M}\delta\mathbf{a} = -\nu$ without neither an explicit inversion nor a diagonalization. They solve the system searching iteratively for a solution $\delta\mathbf{a}$ that minimizes the "distance" d defined as:

$$d = |\mathcal{M}\delta\mathbf{a} + \nu| \tag{5.29}$$

Historically, the first algorithm of this kind was MINRES [81] dating from 70's. More modern algorithms are MA27 [92], MA57 [93] and PARDISO [94] that are even faster and less sensitive to initial conditions. The MA27 is already integrated in the Globalχ^2 code and it has been intensively used and tested. While using these solvers, soft constraints (see appendix B.2.2) have to be used in order to converge as no eigenvectors/eigenvalues are determined and therefore it is not possible to remove undefined modes. Anyhow, these algorithms can be combined with the ARPACK [95] algorithm to calculate a limited number of eigenvalues and eigenvectors of $\mathcal{M}$ which it is useful for the suppression of global distortions. ARPACK has not been tested with the Globalχ^2 algorithm yet.

On one hand, the main advantage of these methods is their speed (the number of operations needed to solve a system is $k\mathcal{O}(N^2)$) and this is why they are known as *fast solvers*. In fact, they are extremely fast, improving the solving time by several orders of magnitudes with respect the diagonalization methods. Some tests done with MINRES report that it is able to obtain a solution with 10k DoFs in approximately 30 s being almost 1 hour in *Alineator*. In our tests using MA27 within the Globalχ^2 code, the alignment corrections for all the ATLAS silicon modules (i.e. 35k DoFs) using a sample that produces a sparse matrix are obtained in 10 minutes in a 32-bit single core machine. Another advantage is that they can make optimally use of the fact that $\mathcal{M}$ is sparse, saving a considerably amount of memory. Hence, the memory handling and the execution time problems commented before are not an issue.

On the other hand, a limitation is the fact that if the matrix is not sparse enough, the solving time could be even longer than the other methods due to the factor k that dominates the number of operations. Another limitation is that, in principle, one has no control neither on the weakly defined movements nor on the error estimation. Anyhow, adding additional χ^2 terms to constraint the system as for example *softmode cuts* (see appendix B.2.2) the errors can be limited and global distortions can be controlled. Millepede II algorithm, which is used to align the CMS tracker, uses MINRES [96] together with the Lagrange Multipliers in order to avoid divergences and the global distortions. The Globalχ^2 algorithm, used for the ATLAS Silicon Tracker, uses MA27 with penalty terms (see section B.2.2).

5.3.3 Weak Modes

Track-based alignment algorithms are intrinsically blind to global distortions that leave the χ^2 of the reconstructed tracks unchanged. Such distortions are known as *weak modes*. They introduce biases in the track parameters, presenting a serious threat to the physics performance of the ID. Figure 5.8 summarizes in a 3×3 grid the most important *weak modes* of the ID and their potential impact on physics. Some of the systematic deformations have been already simulated and studied [97]. The final goal is to understand and determine the most dangerous *weak modes* and how they can be detected, avoided and eliminated using real data.

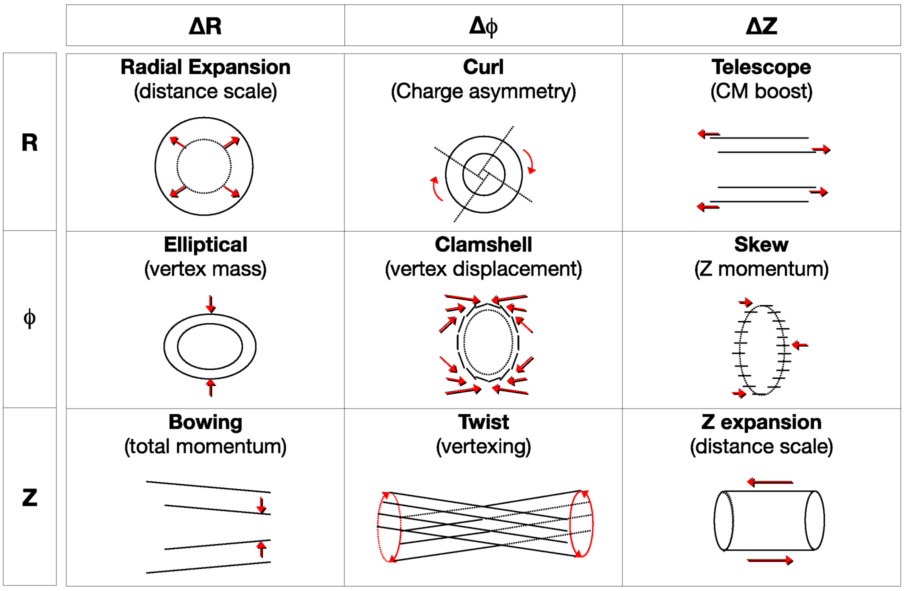

Figure 5.8: *Summary of possible systematic deformations.*

Despite the limited sensitivity of the track-based algorithms, the Globalχ^2 has several ways to minimize the impact of these *weak modes*:

- On the one hand, computing the alignment corrections through the diagonalization of the *big-matrix* allows to recognize singularities. Zero and small positive eigenvalues correspond to undefined or weakly defined DoFs and therefore their corresponding linear combinations can be suppressed as it is done in the method discussed in section 5.3.1. These eigenvalues are used to write the solution as is shown in expression 5.25, so if one does not consider a particular eigenvalue, the associated movement in the diagonal basis will be removed as the corresponding eigenvector will be also neglected. Hence, as the eigenvectors are just the rows of the change of basis, i.e. the U matrix, these eigenvectors would be of tremendous help in order to identify the direction of the movements in the new basis. For instance, one may find that in the new basis, a particular movement corresponds to a global X shift, or rotation or an uniform movement of the whole set of modules in a layer.

- On the other hand, several kind of constraints can be used to limit the impact of these *weak modes*. For example, the inclusion of penalty terms as additional χ^2 terms is widely used within the Globalχ^2 algorithm to limit the ranges of the alignment corrections. Appendix B.2.2 discusses this topic.

Also, Lagrange multipliers are often used to control the *weak modes* as was commented in section 4.8.

Even using the advantages that the diagonalization provides, the previous constraints and a very large number of collision tracks, *weak modes* could be extremely hard to remove or even detect. The combination of the previous techniques with the use of tracks with different topologies is the actual golden solution.

- Collision tracks coming from the interaction point will normally constitute the bulk of the sample of tracks used for alignment. Constraining the track parameters to the average position of the beam spot will help to eliminate certain *weak modes*, specially, the sagitta and clocking distortions. The description of this kind of constraint is done in appendix B.1.1. Also, the primary vertex of each event can be considered to constrain the tracks as it discussed in section 4.3.

- Cosmic ray tracks, which have the advantage of providing a continuous helicoidal trajectory across the whole ID, thereby mimicking a pair of opposite-sign, equal-momentum and back-to-back tracks, when they pass close to the interaction point. In addition, a large fraction of the cosmic ray tracks will cross the ID far from the beam axis, providing additional constraints to eliminate for example telescope distortions. Despite their advantages, cosmic ray tracks help to constrain basically the barrel as they arrive mostly vertically.

- Tracks from beam halo events will help to constrain the alignment of the end-caps as these tracks travel almost parallel to the beam line, complementing the constrains provided by cosmic ray tracks.

- Tracks passing through the overlap regions of adjacent modules. These tracks constrain the circumference of cylindrical geometries (radial expansion) and thus improve the determination of the average radial position of the modules.

- Track pairs from Z and J/Ψ decays. Fitting these tracks to a common decay vertex and to a known invariant mass will provide sensitivity to systematic correlations between different detector elements. This constrain is discussed in appendix B.1.2.

- Finally, additional constraints are provided by the information from survey measurements, which are, however, limited in practice to the relationships between nearby detector elements connected by rigid support structures.

During the alignment of the Silicon Tracker, which will be presented in chapters 6 and 7, most of these tools have been used in order to minimize the impact of the *weak modes* in the final alignment corrections.

6

ATLAS Silicon Tracker alignment performance and results with simulated data

The performance of the Globalχ^2 method has been extensively tested, evaluated and validated using simulated data and, thanks to this, the algorithm has been debugged and tuned within the *Athena* framework. The alignment performance studies and results achieved with the Globalχ^2 algorithm using MC data will be discussed in this chapter.

6.1 Introduction

Several MC challenges have been proposed in parallel to the ATLAS assembly, integration and commissioning but the so-called Computing System Commissioning (CSC) challenge was the first realistic exercise that tested the full ATLAS software system. It included subdetector misalignments, distorted material and distorted magnetic field. The CSC main goal was to validate all aspects of the computing model, from generators to physics analysis, starting thus from a blind knowledge of the geometry misalignments to finally derive the alignment constants that were used for reconstruction. Thus, several CSC physics analyses were performed using the derived alignment constants in order to study the ATLAS physics performance.

The later exercises, the so-called Full Dress Rehearsal (FDR), tested not only the full ATLAS software chain but also the ATLAS computing model. Thus, their aim was to emulate the full data processing chain from the trigger SFO disks at ATLAS Point-1 (see figure 2.2) to the end-user (i.e. through the complete Tier hierarchy) data distribution and physics analysis. But from the alignment point of view, the main goal was to test the capability to produce alignment constants for the reconstruction of physics events within 24h after data taking.

6.2 Computing System Commissioning

The CSC challenge provided full-scale simulations of the ATLAS detector response with the novelty of introducing geometry distortions, the so-called *as-built* geometry, together with distorted materials and a tilted and shifted magnetic field. Large numbers of simulation samples were produced for physics, calibration and alignment purposes. The CSC provided an important operational test of the ATLAS software system and essential results, allowing to estimate the expected ATLAS detector performance for early data [7]. In addition, the processing (reconstruction and analysis) was distributed world-wide over the ATLAS Grid facilities (see section 2.2.3) and hence provided a preliminary, although important, test of the ATLAS computing system and the ATLAS Distributed Data Management (DDM). Thus, the CSC was an important milestone towards the ATLAS data taking, as it represented the typical scenario of what can be expected with initial data.

Although a preliminary CSC alignment was already presented in a previous PhD. thesis [40] this work is extended to the full detector. Finally, a validation of the final set of alignment constants is given, based on physics observables.

6.2.1 Realistic detector description

The *as-built* geometry was implemented within GeoModel infrastructure (see section 3.6). A detector description layer mechanism was designed in order to deal with the different detector geometry distortions levels which could be introduced while building and assembling the detector. This geometry description levels were the same geometry levels already defined as level 1, 2 and 3 in section 5.2. This description does not account for module distortions like bows, bends, etc as the silicon modules are assumed to have planar geometry. Anyhow, the Globalχ^2 algorithm can not deal yet with these fine module misalignments.

The introduced deformations were based on the expected mounting uncertainties during the construction of the various detector components, not taking into account possible improvements based on survey measurements, leading therefore to movements up to several millimeters. Table 6.1 summarizes the introduced misalignments. For more details see reference [98].

<table>
<tr><th>Level</th><th>Detector</th><th>Frame</th><th>Translations (μm)</th><th>Rotations (mrad)</th></tr>
<tr><td>1</td><td>All</td><td>Global</td><td>$O(1000)$</td><td>$O(0.1)$</td></tr>
<tr><td rowspan="2">2</td><td>Pixel and SCT Barrel layers
and SCT end-cap discs</td><td rowspan="2">Global</td><td>$O(100)$</td><td>$O(0.5)$</td></tr>
<tr><td>Pixel end-cap discs</td><td>$O(150)$ for X and Y
$O(200)$ for Z</td><td>$O(1)$</td></tr>
<tr><td>3</td><td>Pixel modules
SCT modules</td><td>Local</td><td>$O(50)$
$O(150)$</td><td>$O(0.1)$</td></tr>
</table>

Table 6.1: *Summary of the introduced misalignments in the CSC* as-built *geometry. Rotations are around the global or local axis of the superstructure or module, respectively (i.e. they are Cardano rotations).*

Finally, the misalignments contained a limited number of systematic deformations like a sagitta effect based on the movement of a complete Silicon barrel layer and a clocking effect from a systematic rotation of the Silicon barrel layers, leading to biased measurements of the momentum which are source of systematic errors.

Moreover, additional material was added in different locations of the ID and in front of the ECAL. The increased values were always larger than the estimated uncertainties to be in the worst case. In particular, material corresponding to an increase of 1-3% of a radiation length (X_0) was added just behind the first Pixel layer, and just behind the second SCT layer. Also in the end-caps, adjacent to one of the end-cap Pixel discs and adjacent to two of the end-cap SCT discs. Within the active tracking volume, the material in regions of service routing was increased by 1-5% of a radiation length. For services outside the active tracking volume the material was increased by up to 15% of a radiation length.

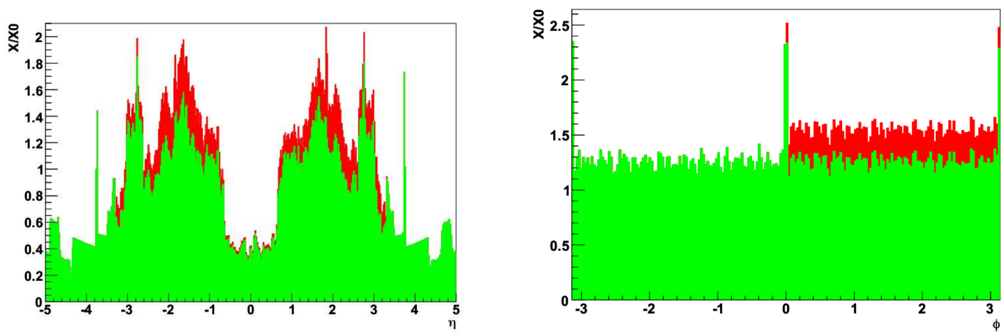

(a) X/X_0 *Vs* η

(b) X/X_0 *Vs* ϕ

Figure 6.1: *Total radiation length in the ID (integrated over* $0 < \phi < \pi$*) as a function of* η *(a) and total radiation length at* η *= 1.5 as a function of* ϕ *(b). In both plots, the perfect and extra-material description are respectively shown in light and dark color. The spikes at* ϕ *= 0 and* π *on the right histogram correspond to the ID support rails (extracted from reference [98]).*

Figure 6.1 (a) shows the total radiation length for the ID integrated over $-\pi < \phi < \pi$. It should be noted that for the ID, the extra material was only added in one half of the azimuthal angle ($0 < \phi < \pi$), as figure 6.1 (b) shows, to allow for a straightforward study of the difference in calibration and performance with single particles.

Furthermore, a distorted magnetic field configuration was introduced, where the symmetry axis of the field did not coincide with the beam axis.

Finally, different geometry tags were created in order to simulate or reconstruct with a realistic detector description. Thus, these tags contain the nominal geometry as well as the *as-built* geometry. Also tags with the shifted/tilted magnetic field and distorted material were available. Moreover, tags with different sets of alignment constants were also defined.

Straight reconstruction with this realistic detector description resulted in a low track reconstruction efficiency, with large track parameter distortions. This translates in, for example, the expected mass peak for $Z \rightarrow \mu\mu$ decays was not visible prior the alignment. This made from the *as-built* geometry the perfect testbed for alignment. Much more details can be found on references [98], [7], [18] and [40].

6.2.2 Data samples

Two different samples were used to align the Silicon Detector within the CSC challenge, collision-like and cosmic ray simulations. The collision sample consisted in an "academic" sample specially produced for alignment purposes called "multimuon sample". On the other hand, two cosmic ray samples were simulated, with and without the presence of the ID magnetic field, to study the impact and usefulness of this kind of data.

- **The multimuon sample** consisted of almost 100k events simulated with the *as-built* geometry and produced using the full ATLAS simulation chain. The simulation and digitization was done with *Athena* release 12.0.31 and the sample was generated as one of the ID calibration samples of the CSC exercise. Each event contained 10 muons. Positively and negatively charged muons alternated from one event to the next. The track parameters p_T, η and ϕ for the muon tracks were chosen to be flat with the following track parameter ranges: p_T = [2, 50] GeV/c, η = [-2.7, 2.7] and ϕ = [0, 2π] rad. All tracks within an event where produced at the same primary vertex. Moreover, the primary event vertex distribution was generated using gaussian distributions centered around zero with widths of: $\sigma_x = \sigma_y = \sqrt{2} \cdot 15\ \mu m$ and $\sigma_z = \sqrt{2} \cdot 56$ mm. Figure 6.2 shows the generated primary vertex profiles.

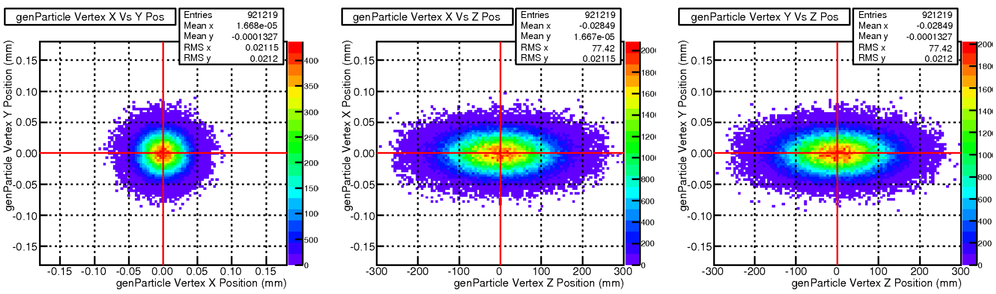

Figure 6.2: *Generated primary vertex distribution of the multimuon sample.*

- **The cosmic ray samples.** Two different cosmic samples were produced with the *as-built* geometry. Moreover, these simulations considered that the ATLAS detector was located on its cavern (i.e. ~100 m of rocks on top of ATLAS were simulated). One of the sample contained ~53k tracks simulated without an active magnetic field (i.e. tracks were straight tracks) and the other one contained ~5k and it was simulated with the ID solenoidal B-field at its nominal value (i.e. 2 T). The production of these samples used *Athena* release 13.0.10 and 13.0.20 and the `CosmicGenerator` [99] as the particle generator.

  As was already commented on section 5.3.3, cosmic ray data is used to constrain some weak modes as cosmic tracks are complementary to collision tracks. Cosmic tracks may pass twice through the same barrel layer. Moreover, cosmic ray tracks are mainly off-axis tracks correlates different modules than can not be connected with collision tracks. This is why cosmic ray data is very important for a good alignment quality.

6.2.3 CSC alignment strategy

The Globalχ^2 algorithm was run iteratively to align the Silicon Tracker, starting from the nominal geometry description until the convergence was found. The multimuon sample was the main sample used although the cosmic ray samples were added in the last iteration to provide additional constraints.

As commented in section 3.7, a track and hit selection was needed in order to filter the really useful information for alignment. In this case, the selection cuts applied were different for collision data and for cosmic ray data. Thus, for the multimuon data at least 7 silicon hits associated to each track were required, where at least 2 of them had to be Pixel hits. For cosmics, the minimum number of total hits required per track was incremented up to 9, where the minimum number of SCT hits was 7.

For collision data, tracks with transverse momenta above 10 GeV/c were constrained to be consistent with the beam spot assumed at (0,0) in the XY plane (see appendix B.1.1 for track constraints within the Globalχ^2 algorithm). The tracks were constrained to the beam spot with an error 10 times larger than the error on their transverse impact parameter (d_0) obtained from the track fit. The impact of this constraint will be discussed in later sections.

The strategy which was followed in the CSC alignment was a combination of a level 2 and a level 3 alignment (see table 5.1). The sequence was: first, four iterations at level 2 (i.e. involving the silicon barrel cylinders and end-cap discs with 186 DoFs), then, two iterations at level 3 (involving the entire set of 34.922 DoFs of the ATLAS silicon system), after that, two more iterations at level 2 to confirm the convergence and to align out any residual distortions that might had been introduced. Finally, an extra iteration was performed which combined multimuon tracks with cosmic tracks.

In level 2 iterations, a full matrix diagonalisation was done as few DoFs were considered. Moreover, the first four eigenmodes were removed which corresponded to the four near-singular modes of the solution, i.e. the three rotations and the translation along Z of the whole system. Note, that the freedom of the X and Y translations were removed by the beam spot constraint. To process the level 3, the sparse matrix representation was used and the solution was obtained using the MA27 solver (see section 5.3.2). As was discussed in the previous chapter, direct solvers cannot deal with ill-defined or explicitly singular problems and as there is no diagonalisation (i.e. neither eigenvectors nor eigenvalues), one has no control over the statistical error of the solution. Then, in order to overcome these difficulties penalty terms (see appendix B.2.2) were introduced in the χ^2 limiting the magnitude of the individual DoF uncertainties and corrections. The assumed constraint (softmode cuts) corresponds closely to the allowed statistical error on the correction (motivated by the CSC misalignments themselves): translations of $O(10)$ μm for Pixel modules and $O(50)$ μm for SCT modules and rotations of $O(0.3)$ μm for both silicon modules.

These constraints meant that for example any mode leading to error on the local x corrections in Pixels larger than 10 μm are down weighted.

It is also worth to mention that an *error scaling* was introduced during the reconstruction of first iterations with the goal of inflating the hit errors (generally represented by σ), maintaining thus the track efficiency in the track fit. This scaling was introduced simply as $\sigma_{scaled} = a\sigma \oplus c$, where a is a scaling factor and c is a residual misalignment (added in quadrature to the scaled hit uncertainty). The values used are summarized in table 6.2. More information can be found in reference [98].

System	Residual type	Scale factor (a)	Offset (c)
Pixel Barrel	rϕ	1.030	0.058
Pixel Endcap		1.050	0.087
Pixel Barrel	η	0.974	0.071
Pixel Endcap		1.080	0.087
SCT Barrel	rϕ	0.776	0.074
SCT Endcap		0.863	0.067

Table 6.2: *Error scaling values used for the CSC exercise when a nominal detector description is used.*

The silicon alignment achieved with this procedure, together with a TRT alignment and a relative alignment between both subdetectors will be referred as *CSC alignment* set and it was the alignment used to evaluate the CSC performance in reference [7].

6.2.4 CSC alignment performance

6.2.4.1 Number of reconstructed tracks and associated hits

One of the largest impacts of misalignments in the detector performance is the track and hit (associated to the tracks) reconstruction efficiency. Obviously, the goal is that after alignment this efficiency should be completely recovered. These two facts can be seen in figures 6.3 as they show together the performance of the nominal geometry (dashed line), the perfect geometry (pointed line) and the aligned geometry (solid line). Thus, figure 6.3 (a) shows the total number of reconstructed tracks. One can easily see that for the nominal geometry, i.e. before alignment, the number of reconstructed tracks is on average just 4 per event, which means that the detector is very inefficient. Comparing this result with the reconstruction average with the perfect geometry (almost 9 tracks per event), the degradation is very substantial in the nominal case. Then, after aligning the nominal geometry, the track reconstruction performance is recovered and the number of tracks is the same as the perfect case. Similar results can be seen for the total number of Pixel and SCT hits (see figures 6.3 (b) and (c), respectively), where a poor hit reconstruction efficiency exists for the nominal geometry. After alignment the total hit efficiency is totally recovered for both subdetectors.

Moreover, figure 6.4 show the number of silicon hits separately for the different Pixel and SCT barrel layer and end-cap discs. From those plots one can see the degradation for the nominal geometry and that the hit efficiency is totally recovered for all the structures with the underlying alignment, being comparable to the perfectly aligned geometry.

6.2.4.2 Residuals

Residual distributions are widely degrade when misalignments are present and as was already commented in section 3.8, track-based alignment techniques are based on the minimization of

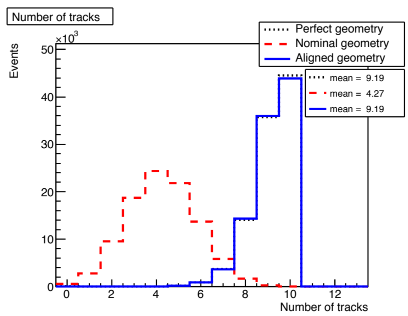

(a) *Number of tracks*

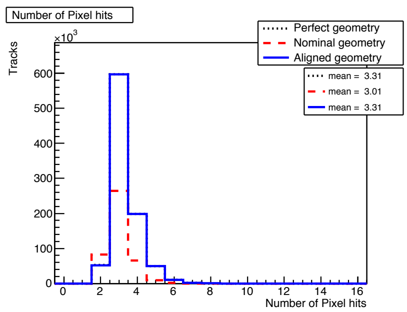

(b) *Number of Pixel hits*

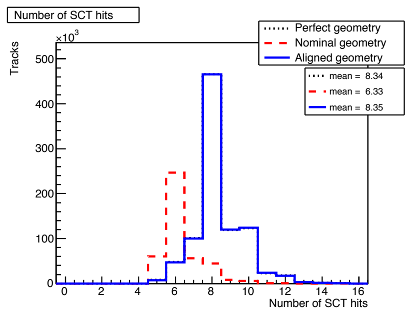

(c) *Number of SCT hits*

Figure 6.3: *Total number of tracks (a), Pixel hits (b) and SCT hits (c), containing the nominal geometry (dashed line), perfect geometry (pointed line) and* CSC alignment *(solid line). The hits are just the ones associated to the tracks.*

those residuals. Hence, residual distributions should be completely recovered after alignment. Figures 6.5 show the biased residual distributions for the Pixel and SCT barrel and end-caps and for the nominal geometry (dashed line), perfect geometry (pointed line) and aligned geometry (solid line). For the nominal geometry, distribution are broad and awful and no peaks can even be seen. After alignment, the distributions are practically the same as for the perfectly aligned detector as it was expected.

On the other hand, figure 6.6 (a) and (b) show the average of the rϕ residuals as a function of the iteration, for each barrel layer of the Pixel and SCT detectors, respectively. They show that after the third iteration the residuals are centered at zero for all silicon barrel layers. Moreover, figure 6.7 shows the RMS of the rϕ residuals for the barrel modules of the Pixel and SCT detectors as a function of the iteration. Initially, the averaged RMS are 40 μm for the Pixels and 70 μm for the SCT and after alignment, these values are very close to the expected ones for each subdetector. Even, the alignment transition between level 2 and level 3 is clearly shown from

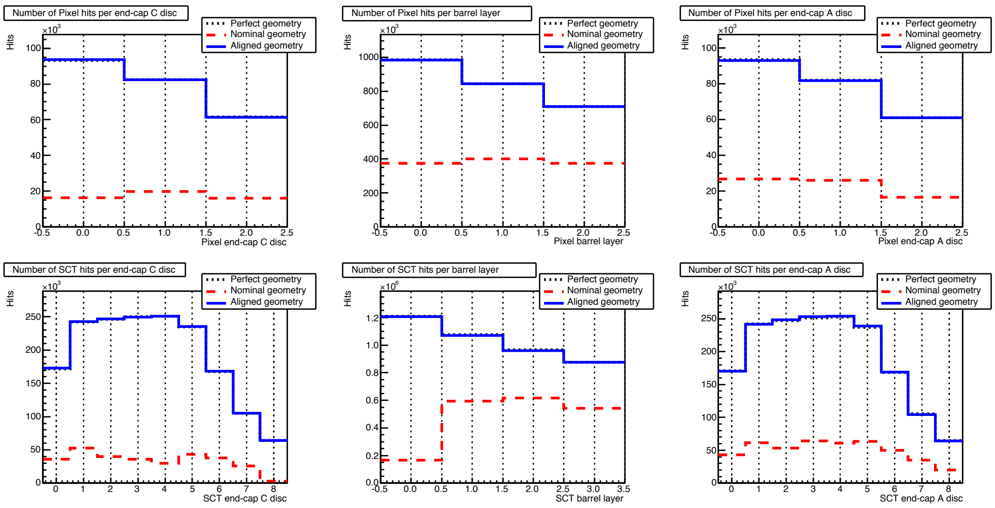

Figure 6.4: *Number of silicon hits (associated to the tracks) for each barrel layer and end-cap disc containing the nominal geometry (dashed line), perfect geometry (pointed line) and* CSC *alignment (solid line). The upper row shows the Pixel setup while lower row shows the SCT setup (from left to right: end-cap C, barrel and end-cap A).*

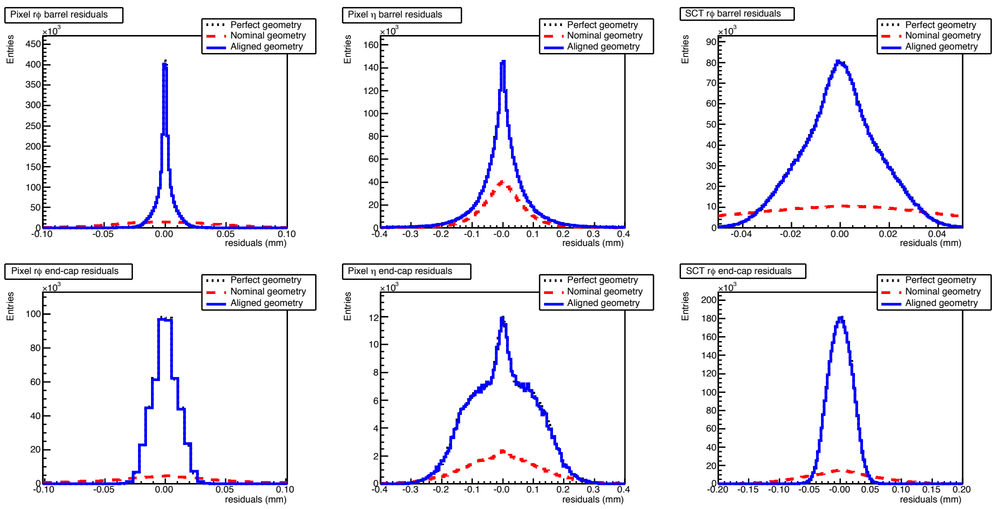

Figure 6.5: *Biased residuals for silicon barrels and end-caps, containing the nominal geometry (dashed line), perfect geometry (pointed line) and* CSC *alignment (solid line). The upper row shows the Pixel $r\phi$ and η residuals and SCT $r\phi$ residuals for the barrel region while the lower row shows the analogous plots for the end-cap region.*

iteration 3 to 4, as a qualitative step.

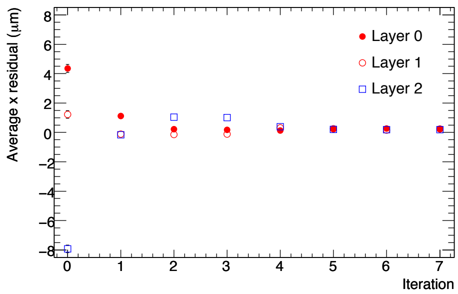

(a) *Average Pixel local x residuals Vs iteration*

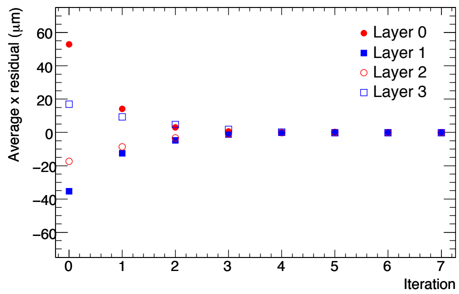

(b) *Average SCT local x residuals Vs iteration*

Figure 6.6: *Average of the local x (i.e. $r\phi$) residuals as a function of the iteration, for each barrel layer of the Pixel (a) and SCT (b) detectors. Iteration 0 corresponds to the nominal geometry while iteration 7 represents the results produced thanks to the* CSC alignment *constants.*

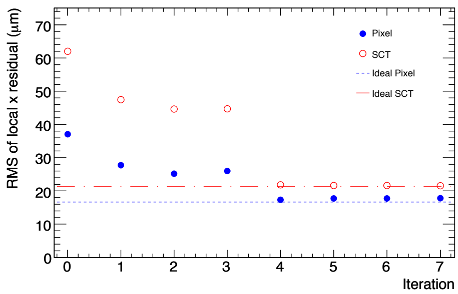

Figure 6.7: *RMS of the $r\phi$ residuals for the barrel modules of the Pixel (solid circle) and SCT (unfilled circle) detectors as a function of the iteration.*

This reveals how the Globalχ^2 method is doing its job perfectly, i.e. it minimizes residual distributions. But, if fact, one can assert that even if any track-based alignment algorithm leads a perfect residual distributions after alignment, this does not mean that the given geometry is the correct one (it this case, this does not mean that the final geometry is the *as-built* CSC geometry). This only means that the χ^2 minimization has converged but not necessary to the right minimum. Then, the tool to evaluate the quality of the alignment constants are the track parameters as it will be shown.

6.2.4.3 Track parameters

As it was already commented, track parameters are also quite degraded because of misalignments. This degradation can be seen in figure 6.8, where the dashed lines show the distributions for the nominal geometry. These plots also show superimposed the same distributions for the perfectly aligned geometry (pointed line) and for the *CSC alignment* (solid line). Generally, from those plots one can state that the reconstruction performance has been recovered after alignment. Despite of this apparent good agreement, a small mismatch can be observed in the transverse impact parameter (d_0) meaning that a residual misalignment still remains. Figure 6.9 shows the χ^2 distribution and the χ^2 as a function of ϕ_0 and η. From these plots one can just say that almost a perfect recovering is achieved after alignment (i.e. the track fit quality is near to be perfect).

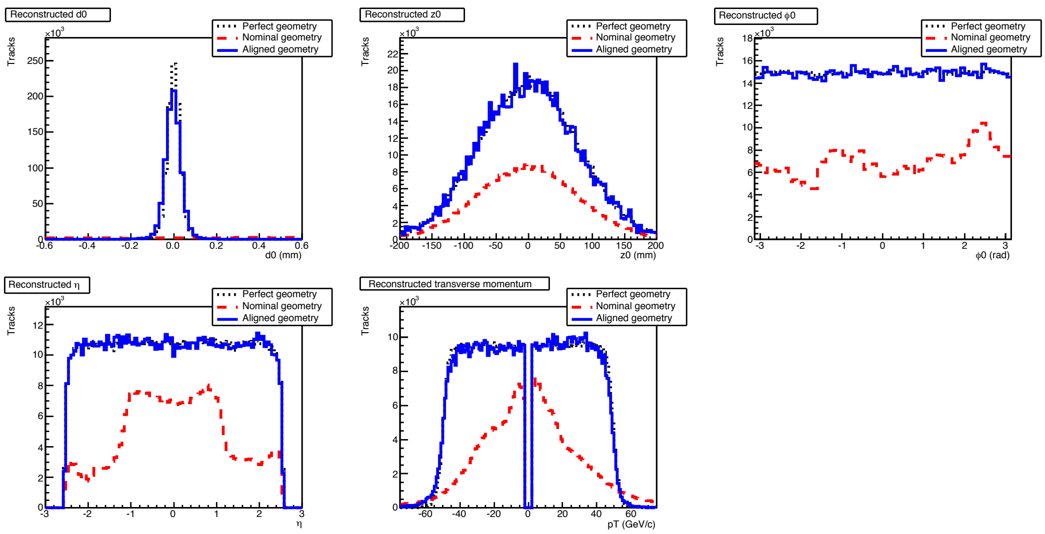

Figure 6.8: *Track parameters for nominal geometry (dashed line), perfect geometry (pointed line) and aligned geometry (solid line).*

This residual misalignment can be spotted in figures 6.10 where the difference between the reconstructed and the truth track parameters is shown. Those plots show that all the track parameters, specially ϕ_0, have a residual bias after alignment. One can suspect that a global rotation around the Z axis is one of the main contributors to this bias.

The track parameter distributions are a powerful tool to detect the presence of weak modes and residual misalignments. In fact, they give much more information, specially, their correlations, as it will be shown now.

Impact track parameter correlations

Both impact parameter distributions give a lot of information about the global position of the detector. Thus, the transverse impact parameter gives relevant information about global

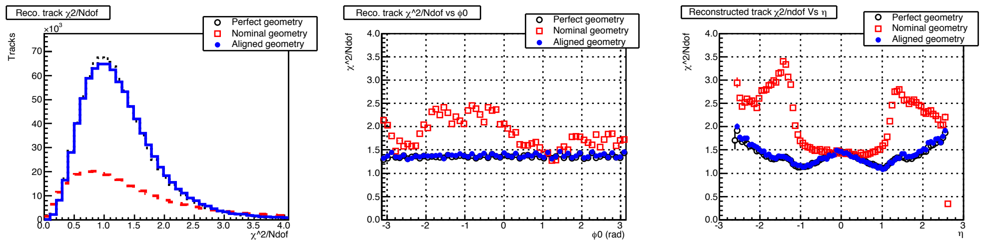

Figure 6.9: *χ^2 distribution and its correlations with ϕ_0 and η for nominal geometry (dashed line/squares), perfect geometry (pointed line/empty circles) and aligned geometry (solid line/solid circles). It can be observed how the χ^2 varies with η at the overlap regions between barrel and end-cap structures and how the chi^2 increases at large η.*

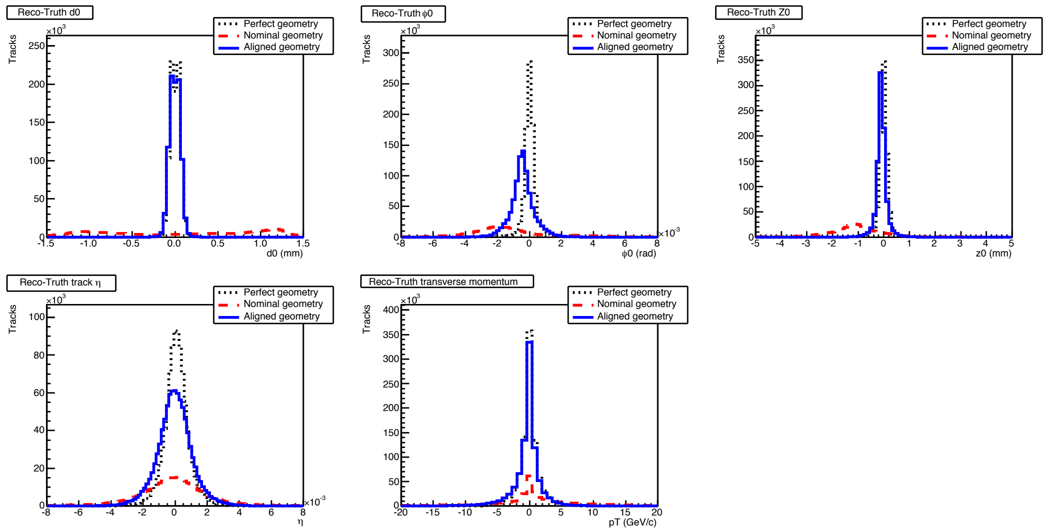

Figure 6.10: *Difference between the reconstructed and the truth track parameters for nominal geometry (dashed line), perfect geometry (pointed line) and aligned geometry (solid line).*

displacements in the transverse plane (i.e. XY). Figure 6.11 (a) shows how the d_0 distribution looks like if the detector is shifted with respect the beam spot (i.e. origin of the global frame). This non gaussian distribution is due to the fact that the track parameters are given at the perigee computed with respect to the origin of the global frame, which in this case does not match with the detector origin. If the perigee is computed with respect the primary vertex, d_0 would be a gaussian distribution. On the other hand, figure 6.11 (b) shows the typical gaussian-like distribution for d_0 using the final aligned geometry, where the global detector position has been corrected in such a way that its origin matches with the origin of the global frame. But how can this shift be computed?

To compute the detector position with respect to the beam spot, one can use the correlation

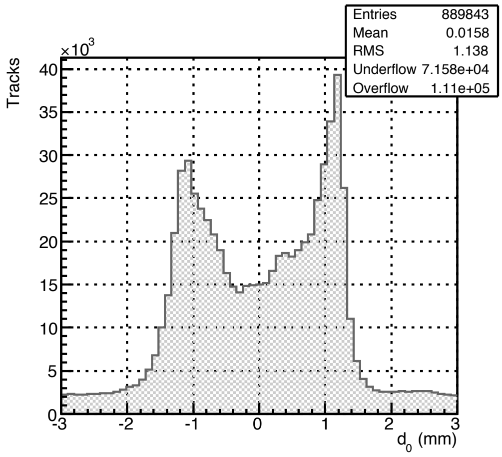

(a) d_0 *distribution for a displaced geometry*

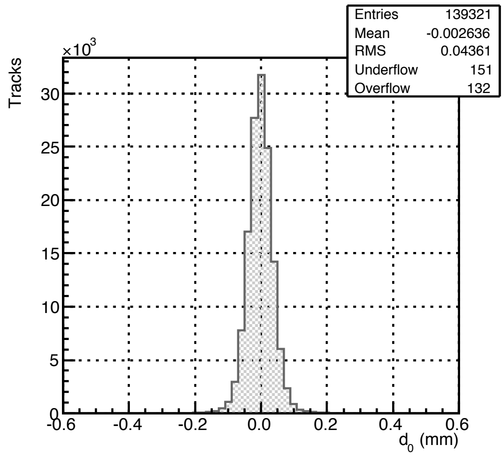

(b) d_0 *distribution for a centered geometry*

Figure 6.11: *Figure (a) shows the transverse impact parameter distribution with respect the global frame origin (ideally, the beam spot) where the detector is shifted and figure (b) the same but when the origin of the detector matches the beam spot. Figure (a) has been produced using 100k events while figure (b) just using 15k. In both cases,* d_0 *was given at the perigee.*

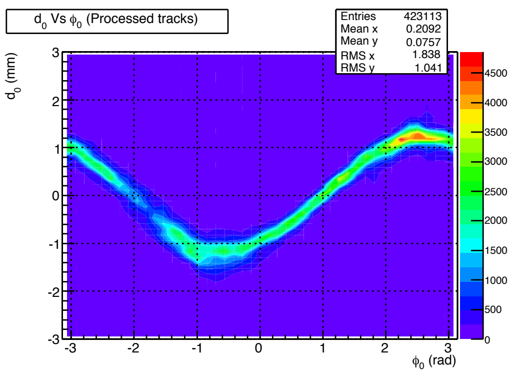

(a) d_0 *Vs* ϕ_0 *for a displaced geometry*

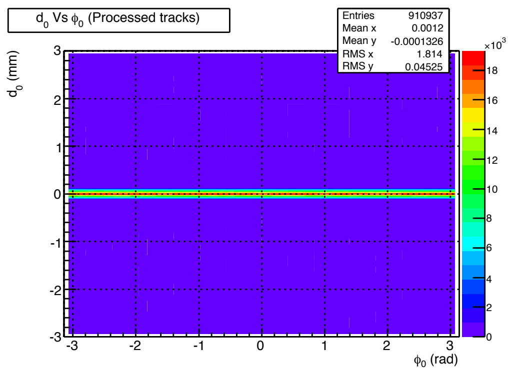

(b) d_0 *Vs* ϕ_0 *for a centered geometry*

Figure 6.12: *Transverse impact parameter as a function of* ϕ_0 *when the detector is shifted with respect the beam spot (left plot) and when the detector's origin fits with the beam spot. In the first case, a characteristic sinusoidal shape appears.*

between d_0 and ϕ_0. Figure 6.12 (a) shows this correlation for the nominal case and its characteristic sinusoidal shape due to this shift can be seen. Then, considering that the transverse impact parameter can be expressed as (based on reference [100]):

$$d_0 = -(X_{BS} + m_X\, z_0)\, sin\phi_0 + (Y_{BS} + m_Y\, z_0)\, cos\phi_0 \tag{6.1}$$

where X_{BS} and Y_{BS} are the average transverse positions of the beam spot given in the global frame and m_X and m_Y are the average slopes of the beam in the XZ and YZ planes, respectively. Then, one could fit the correlation shown in figure 6.12 (a) and obtain these average values as it is done in figure 6.13 for a fixed z_0 value.

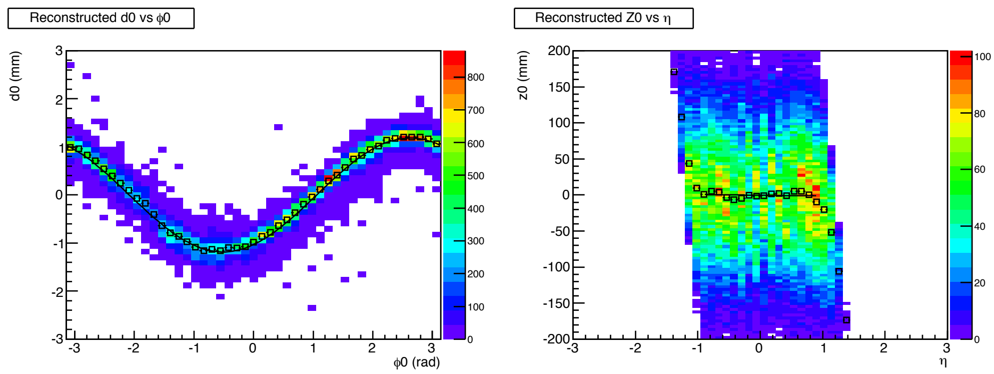

Figure 6.13: *Determination of the position and orientation of the beam spot. The transverse components are extracted from the correlation between d_0 and ϕ_0 (and z_0) and using expression 6.1 as the fit function. The longitudinal beam line component is computed from the correlation between z_0 and η. In both cases, just the barrel information is used.*

Moreover, a similar procedure can be followed in order to determine the Z detector position with respect the whole detector. In this case, the correlation between z_0 and η is used, following the next expression:

$$z_0 = m\,\eta + Z_{BS} \tag{6.2}$$

where Z_{BS} represents the average Z position of the beam spot in the global frame. Then, an simple linear fit is enough to extract the longitudinal average position of the beam spot (z_0 Vs η is less fit range dependent than z_0 Vs θ). This correlation can be seen in figure 6.13 as well as the linear fit (plot on the right). The results of both fits are summarized in table 6.3.

Of course, the misalignments limit the precision of the method. However it can provide a beam spot position even if misalignments are large. Alternatively, this method can be used to determine the level 1 alignment. In fact, comparing the numbers on table 6.3, the computed average beam spot position matches with the level 1 of the CSC *as-built* geometry for the Pixel structure. Anyhow, in principle one does not know if the detector has its origin at the global frame origin and is the beam spot the one that is shifted or viceversa, i.e. the beam spot matches with the global frame origin and the detector origin is shifted. This was, in fact, the strategy followed in the FDR challenge.

Vertex parameter	**Average position of the Beam Spot estimated from track correlations**	**Pixel level 1 of the CSC *as-built* geometry**
X_{BS} (mm)	0.62 ± 0.03	0.600
Y_{BS} (mm)	1.04 ± 0.03	1.050
Z_{BS} (mm)	1.08 ± 0.3	1.150
m_X (mrad)	-0.12 ± 0.3	-0.10
m_Y (mrad)	0.34 ± 0.3	0.25

Table 6.3: *Summary table of the computed average beam spot position for the nominal geometry within the CSC exercise. Statistical errors are shown. Level 1 of the Pixel structure is shown to allow comparisons.*

For the CSC alignment, this discussion was settled as the beam spot was assumed to be known and since tracks were constrained to it. Thus, the whole detector was moved globally with respect the global frame origin.

Momentum correlations

Analogously to the previous section, momentum correlations are tremendously useful to spot sagitta and clocking distortions. From the wide discussion on reference [40], one knows that clocking[1] affects the curvature of positively and negatively charged particles by an equal but opposite amount (i.e. an offset is observed), while a sagitta[2] produces an effect in the transverse momentum which is not constant with ϕ_0 (i.e. appearing the sinusoidal shape). Thus, plotting q/p_T as a function of ϕ_0 allows to monitor these two weak modes. Figure 6.14 shows this distribution for positive (left) and negative (right) charged tracks, separately. An offset of ~ 0.02 GeV^{-1} is observed for the nominal geometry (squares) as well as the sinusoidal shape, telling the existence of the previous commented weak modes.

Thanks, mainly to cosmic ray tracks, these weak modes can be under control as it can be seen looking the results on the previous figure for the aligned geometry (it was already proven in reference [101]). These results also show slight differences with respect the perfectly aligned detector which indicate that small residual misalignments are still present. Thus, to completely remove these misalignments additional constraints should be used as overlap hits, more event topologies (as already claimed on section 5.3.3), external constraints, etc...

Finally, in order to evaluate the ultimate and real impact of the observed residual misalignments, physics samples and observables must be use to give the ultimate performance.

6.2.5 Achieved alignment performance

The real performance of the *CSC alignment* set, which includes the Silicon Tracker alignment described above, a TRT alignment and a relative alignment between both subdetectors, was validated using several physics samples. This validation is widely discussed on references [66] and [18] but a brief summary will be given here.

[1]The clocking effect, also known as rotational sagitta, appears when layers are progressively rotated about the Z axis. Thus it can be characterized as: $\Delta r\phi(r) \sim ar^2 + br + c$

[2]The sagitta effect, also known as translational sagitta, is when layers are progressively translated along the XY axes proportionally to the radius r as: $\Delta XY(r) \sim dr^2 + er + f$

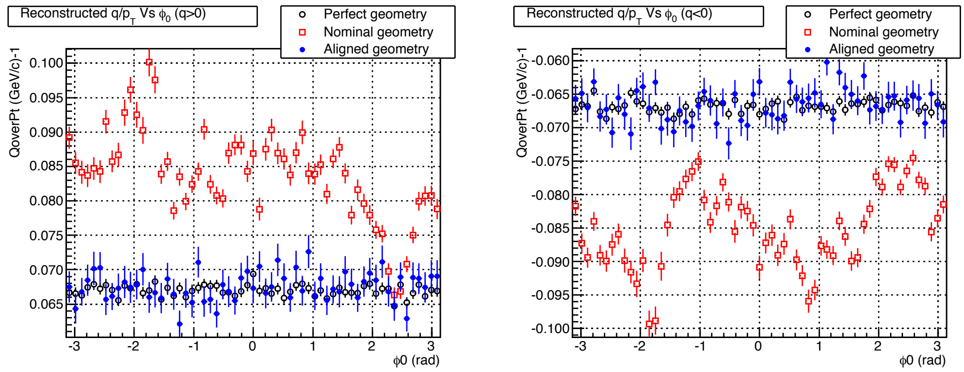

Figure 6.14: *Correlation between q/p_T and ϕ_0 for positive (left) and negative (right) charged tracks, separately. The nominal geometry (squares), perfect geometry (empty circles) and aligned geometry (solid circles) are shown.*

It is known that achieving the expected residual, hit efficiency and track parameters distributions is a necessary criterion for the alignment validation but not sufficient to guarantee the correct convergence of the track-based alignment algorithms. In other words, the presence of possible residual systematic misalignments and biases (i.e. weak modes) were verified using external alignment tools and physics samples. For that purpose, independent monitoring tools were developed to check the alignment sets, in particular the InDetAlignmentMonitoring package [102]. It is nowadays part of the standard *Athena* monitoring tools which can be run online or offline during data reconstruction to monitor data quality. It can display generic alignment and tracking information like hit efficiencies, track distributions, residual distributions, different correlations but also invariant mass of resonances, like J/Ψ, Υ or Z, properties of long lived particles, electrons, muons reconstructed in the muon spectrometer, cosmics, primary and secondary vertices and the reconstructed beam line, etc.

The CSC validation did not show a hit efficiency degradation compared with the perfectly aligned geometry, which meant that the pattern recognition was not affected by the *CSC alignment*. However, although generally all the barrel layers have residual distributions centered at zero, the outer SCT layer show the presence of small misalignments. Moreover, as it was expected, the track parameter distributions showed slight deterioration in their resolution, with small biases.

In parallel, figure 6.15 (a) shows the effect of the known residual misalignments on the reconstructed invariant mass from dimuon tracks, reconstructed only in the ID, from $Z \to \mu\mu$ events for an integrated luminosity of about 14 pb^{-1}. Fitting the reconstructed $Z \to \mu\mu$ mass distributions to gaussian functions, the given widths are 2.6 GeV/c^2 for the perfectly aligned detector and 3.3 GeV/c^2 after the *CSC alignment*. This illustrates how sensitive are mass precision measurements to ID misalignments. Furthermore, figure 6.15 (b), which shows the normalized difference of number of reconstructed negatively and positively charged muons from $Z \to \mu\mu$ events, shows an asymmetry and a bias that depends on the charge and on the transverse momentum. This indicates the presence of a weak mode, probing the usefulness of using resonances for validation.

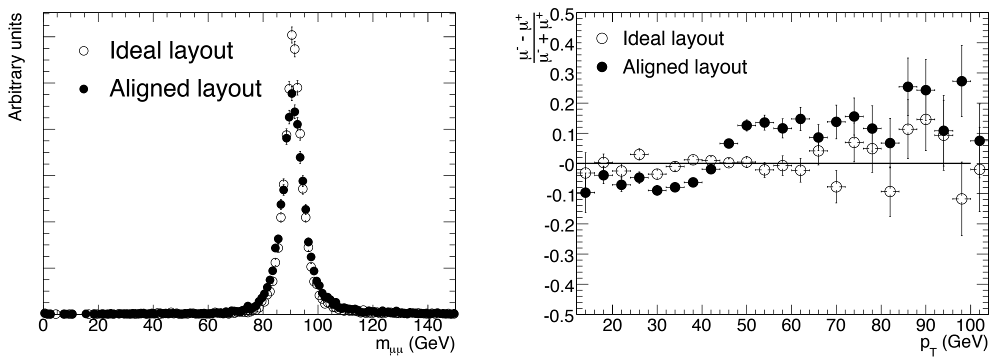

(a) *Invariant mass of the muon pair*

(b) *Muon number ratio Vs p_T*

Figure 6.15: *Figure (a) shows the invariant mass of the muon pairs coming $Z \rightarrow \mu\mu$ events for the perfectly aligned detector and for the* CSC alignment. *On the other hand, figure (b) shows the normalized difference of number of reconstructed negatively and positively charged muons for the same events and for both geometries. Taken from reference [66].*

Another important source which definitely helps in the alignment validation are electron measurements. Specially, as it is expected that the ratio of energy over momentum (E/p) of an electron or positron is centered in one, with tails, caused by bremsstrahlung, any deviation will indicate a problem. Moreover, any difference between positrons and electrons would be a direct measure of sagitta distortions (independent of whether one has understood all the material effects on E/p). This is due to the fact that the calorimeter response and material effects should be the same for electrons and positrons while tracking can be different for positive and negative particles. These issues are monitored by InDetAlignmentMonitoring. Figure 6.16 (a) shows the E/p charge asymmetry as a function of the inverse momentum and the charge asymmetry as a function of E/p for electrons from $Z \rightarrow ee$ events for an integrated luminosity of about 70 pb^{-1}. Both plots are independent of an absolute calorimeter calibration. It is only required that E/p be independent of the particle's charge, which is given, neglecting the level of a few MeV. Both plots indicate the presence of residual systematic misalignments, confirming what is shown in figure 6.15.

All these points tell that an alignment validation based on physics performance is mandatory.

6.3 Full Dress Rehearsal

During 2008, several tests were performed to exercise the overall ATLAS data taking chain and the ATLAS computing model. These challenges were known as FDRs and it consisted in several exercises (FDR1, FRD2 and its follow-ups) where the ID calibration stream was used to align the full ID detector within 24h after data taking starting from a blind knowledge of the

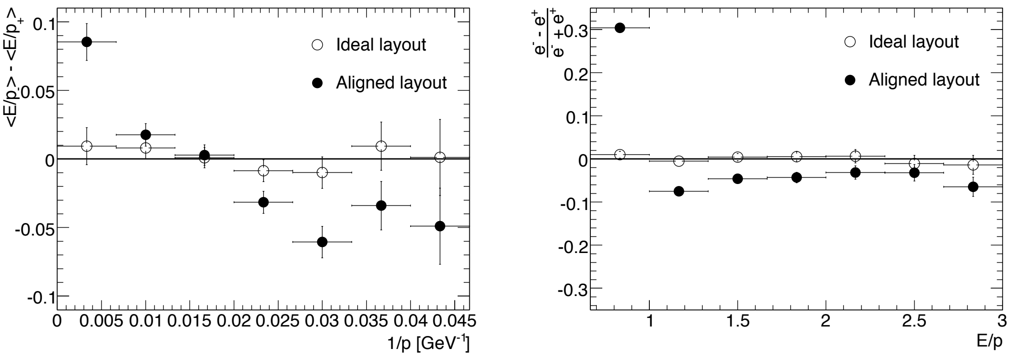

(a) *E/p charge asymmetry Vs 1/p*

(b) *Charge asymmetry Vs E/p*

Figure 6.16: *Figure (a) shows the E/p charge asymmetry as a function of 1/p (which is related with the curvature through expression 3.1) for electrons from Z → ee events. Figure (b) shows the charge asymmetry as a function of E/p for the same events. In both cases, the perfectly aligned geometry and for the* CSC alignment *is shown. Taken from reference [66].*

detector misalignments.

For the different FDR exercises, the calibration stream (see section 3.5) was not given by the PEB algoritm (see section 3.5), but it was emulated by stripping single tracks from existing simulated samples or directly simulating particular single tracks events. About 1M collision tracks were written out to the ID calibration stream in a byte-stream format, where the event was only partially stored. For example, for the FDR1 a dijet sample with $p_T > 17$ GeV/c (JF17) was used and tracks with $p_T < 5$ GeV/c were rejected and for the FDR2, a single pion sample was used. For cosmic tracks, raw data objects (RDO) were converted to byte-stream format without PEB.

6.3.1 FDR alignment strategy

One of the novelties introduced in this challenge was the fact that the full ID alignment procedure was performed almost automatically using dedicated python scripts. As it is illustrated in figure 6.17, the full ID alignment chain started with a first pass beam spot determination using the calibration stream. Then, knowing the average beam spot position, the silicon alignment was computed with the Globalχ^2 algorithm using that beam spot position to constraint the track parameters. The final silicon alignment was a combination of the three alignment levels 1, 2 and 3 from table 5.1.

After, the silicon alignment a new algorithm was implemented which computed the center of gravity (CoG) of the system. The purpose of the CoG algorithm [67] is to correct back any

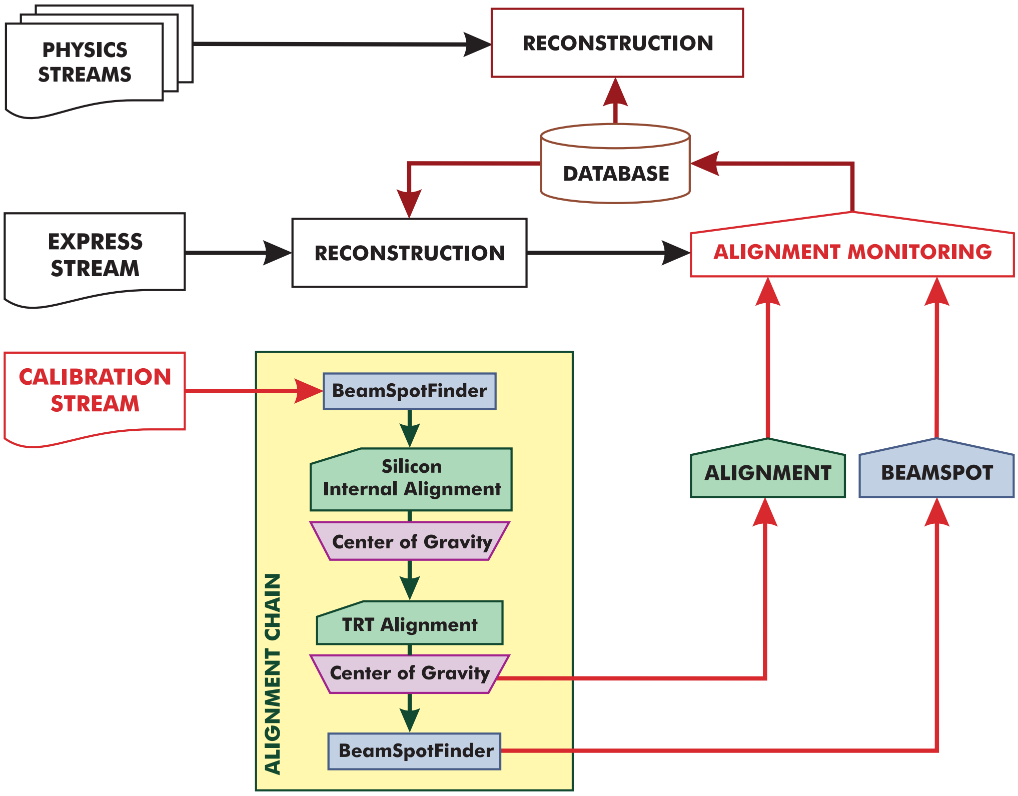

Figure 6.17: *Integration of the ID alignment chain into the overall ATLAS data taking diagram.*

effective change of the generalised centre of gravity [3] of the detector system as an artifact of the unconstrained alignment[4]. In a second step the TRT alignment was performed with respect to the silicon detectors and at the end, the center of gravity was calculated again but using both systems, the Silicon Tracker and the TRT. Finally, the express stream was processed with the computed alignment constants and the beam spot was determined this time estimating the uncertainty on the beam spot position (due that a vertex-based beam spot algorithm was used).

The full alignment chain was processed on the CERN Analysis Facilities (CAF) where 10 hosts[5] were available exclusively for the alignment. Several steps of the alignment chain (reconstruction, accumulation of the alignment variables, monitoring, etc) were performed in parallel, distributing each task between the available hosts and merging all the outputs at the end.

[3]Understood as the "average position and orientation" in the 6 DoFs in space.

[4]Note that when the silicon standalone alignment is performed, track-based alignment algorithms are (ideally) insensitive to the 6 global DoFs (i.e. global translations and global rotations).

[5]Each host was composed by a Intel Xeon CPU E5345 at 2.33 GHz with 8 cores and 16 GB of RAM memory, meaning 2 GB of memory by core.

6.3.2 FDR alignment performance

The FDR alignment performance was evaluated based on the same criteria followed at the CSC exercise. Residual distributions as well as hit and track efficiencies were almost as the perfectly aligned case, as expected, with distributions similar to the ones shown in figures 6.5, 6.3 and 6.4. Talking about correlations figure 6.18 shows the mean of the SCT residuals per barrel layer as a function of the transverse momentum. As in the CSC case, the nominal geometry (squares), perfect geometry (empty circles) and aligned geometry (solid circles) are shown. It is clear that the initial bias and momentum dependence are removed after alignment.

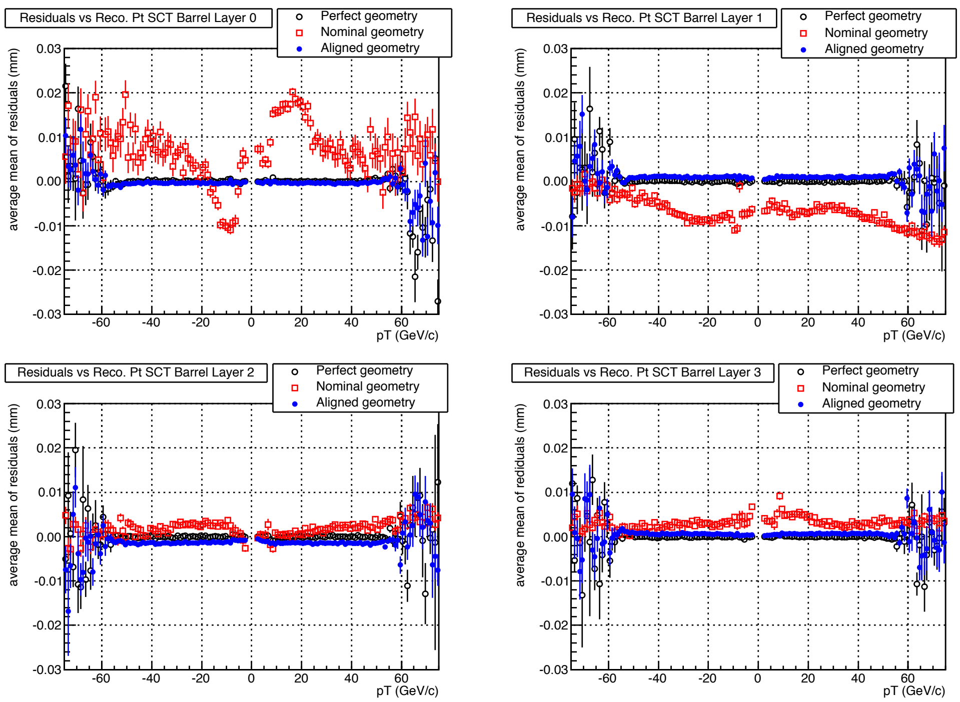

Figure 6.18: *Average mean of the SCT residuals per barrel layer as a function of the transverse momentum where the nominal geometry (squares), perfect geometry (empty circles) and aligned geometry (solid circles) are shown altogether.*

Moreover, figure 6.19 shows the correlation between q/p_T and ϕ_0 for positive (left) and negative (right) charged tracks, separately. Then, thanks to the fact that a minimum transverse momentum cut exists, an offset of ~ 0.015 GeV^{-1} is observed for the nominal geometry (squares) as well as the sinusoidal shape. This confirms the existence of the both weak modes, the sagitta and the clocking, which were intrinsic from the CSC *as-built* geometry. After alignment, the weak modes are almost under control although the achieved weak mode control is smaller than in the CSC case. Please remind that during the FDR, the alignment was run in a 24h loop.

Finally, 6.20 shows transverse impact parameter as a function of ϕ_0. For the nominal case, the characteristic sinusoidal shape appears as it is expected. On the other hand, in this case, the

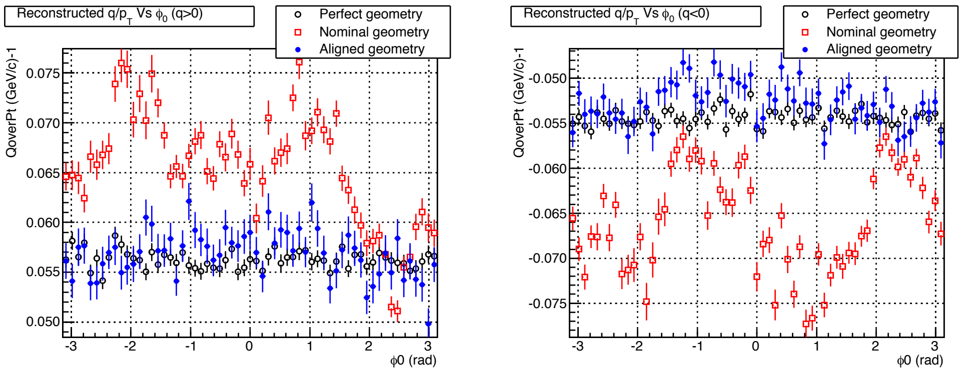

Figure 6.19: *Correlation between q/p_T and ϕ_0 for positive (left) and negative (right) charged tracks, separately. The nominal geometry (squares), perfect geometry (empty circles) and aligned geometry (solid circles) are shown.*

combination of constraining the tracks to the determined beam spot and the CoG algorithm lead to no dependence between d_0 and ϕ_0 for the aligned geometry.

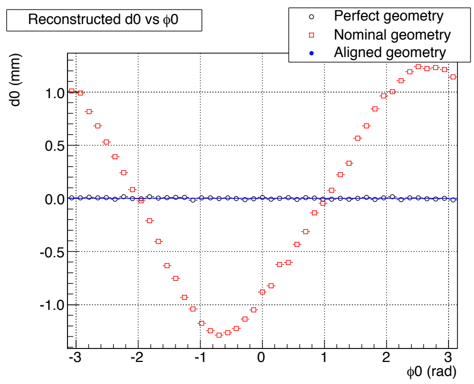

Figure 6.20: *Transverse impact parameter as a function of ϕ_0. In this figure the nominal geometry (squares), perfect geometry (empty circles) and aligned geometry (solid circles) are shown altogether. For the nominal case, the characteristic sinusoidal shape appears.*

6.4 Conclusions

The CSC was the first challenge that provided full-scale simulations of the ATLAS detector response using an *as-built* geometry, together with a distorted material and a tilted and shifted magnetic field [98]. Some weak modes were incorporated on purpose to have a really realistic detector. During CSC exercise, a set of alignment constants was released, including the internal

Silicon Tracker alignment, a TRT alignment and a relative alignment between both subdetectors. The quality of the derived constants was evaluated using hit/track efficiencies, residuals and track parameters together with their correlations. Moreover, several physics samples were used by external alignment monitoring tools. Residual misalignments were observed, mainly due to weak modes which were not completely removed. Anyhow, the achieved alignment performance was good enough for the initial physics analysis with early data.

On the other hand, the FDR was a challenge that served to test and exercise the software of the complete ATLAS data taking chain, starting from the trigger SFO to the physics analysis of the taken data. The calibration stream was used to align the full ID detector within 24h after data taking starting from a blind knowledge of the detector misalignments. In fact, one of the goals of this challenge was to evaluate the readiness of this capability as it was an ATLAS computing model requirement.

Alignment constants were delivered on time (24h loop). Several important lessons, specially technical ones, were learnt and the I/O reliability was truthfully estimated under pseudo-data taking. Moreover, these exercises allowed to perform several important alignment improvements such the CoG algorithm or the beam spot finder and of course, to test the final alignment infrastructure.

7

ATLAS Silicon Tracker alignment performance and results with real data

Once the expected detector performance based on MC studies has been presented, it is time to discussed the alignment performance based on real data. This chapter will discussed the alignment results achieved with the Globalχ^2 algorithm using real cosmic data. The result of this work was a set of alignment constants that was successfully used to reconstruct the first ever LHC collision events on November 2009. Finally, preliminary results based on the first LHC collisions are presented.

7.1 Introduction

The performance of the Globalχ^2 algorithm within the alignment data model has been extensively tested and validated using MC as it has been shown in the chapter 6. However, the true alignment challenge is to used real data to achieve the optimal detector performance. Thus, during the commissioning phase of ATLAS, an alignment using the Globalχ^2 algorithm of the Silicon Tracker was performed with cosmic rays recorded during several data taking periods. The first ever LHC collisions were reconstructed with a set of alignment constants obtained from cosmic ray data. Finally, the LHC era has started and therefore collision data is now being used to align the ID.

7.2 SR1 Cosmics test

In spring 2006, several operational and combined performance tests were carried out as the final stage of SCT and TRT integration prior to their installation in the ATLAS cavern. These tests were performed at the CERN ID integration facility at ATLAS SR1 surface building with the fully assembled SCT and TRT barrel. They represented the first tests of hardware and software of the combined tracker. The performance checks consisted in a series of noise and cross-talk tests with random triggers and calibration-mode noise tests [68], followed by data taking to record cosmic ray tracks. The main goal of the data taking was to prove the full ATLAS offline software chain to reconstruct tracks, then analyze and verify the basic tracker performance parameters like efficiency and spatial resolution in combined operation. Key parts of the software were tested on real data for the first time, being nowadays used regularly for collision data, such as the monitoring, the reconstruction chain, and the calibration and alignment algorithms.

7.2.1 SR1 setup

The SCT and TRT barrels were partially instrumented. The connected sectors comprised 12 TRT modules and 468 modules of the SCT barrel (i.e. 22% and 13% of the SCT and TRT barrel, respectively), in a conical section of a 20 degrees tilted geometry covering about 30 degrees of the azimuthal ϕ slice. Figure 7.1 illustrates the setup used during the SR1 test data taking. The pixel detector did not participate in this test.

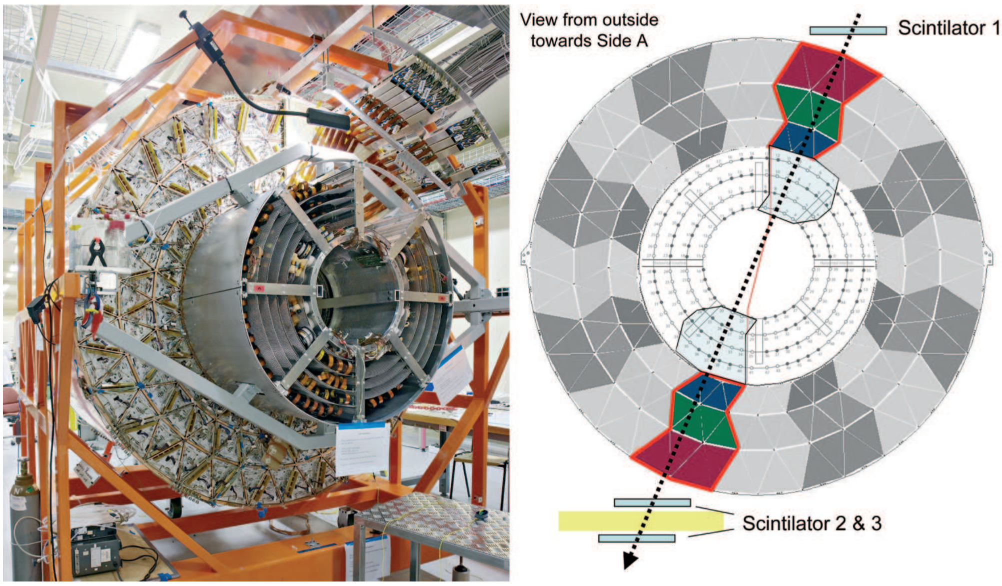

Figure 7.1: *Photograph of the ID Barrel setup for the cosmic test (left) and a scheme of the configuration of module groups chosen for this test (right). Just 22% SCT and 13 % TRT barrel modules were read out. Trigger was perform with three scintillators located as shown [68].*

The SR1 setup did not have a magnetic field and consequently, the momentum of the muons traversing the detector could not be measured. Each reconstructed track was fitted without accounting neither for MCS nor material effects, which is equivalent to fitting the track as if it had infinite momentum. As the momentum of the cosmic rays peaks at low values [103], the residual resolutions were dominated by MCS effects.

Cosmic ray events were triggered using a setup of three scintillators of dimension 144 × 40 × 2.5 cm^3 and they were arranged so that a wide angular distribution of the cosmic ray muons would hit the scintillators as well as the instrumented sectors of the TRT and SCT. One of the scintillators was placed above the detector, one of them below it and another under the concrete floor as figure 7.1 illustrates.The events were triggered by demanding coincidences of the top and middle scintillators, providing a trigger rate of about 2.4 Hz. The separation of the two lower scintillators by 15 cm of concrete effectively introduced a momentum cut-off of about 200 MeV/c.

Additionally, it was estimated that time resolution for time of flight (TOF) measurements was of 0.5 ns. Thus, using the TOF from the top scintillator to the bottom scintillator, one could perform a rough momentum selection, cutting away noise events (i.e., false triggers) which can be recognized by an unphysical value of the computed TOF [68].

The data reconstruction was done within the *Athena* framework using release 12.0.1 although some fixes and adaptations were required in some algorithms in order to take into account the fact that particles were not produced in the center of the detector and that they were not synchronized with the readout clock but arrived randomly.

7.2.2 SR1 alignment strategy

The Globalχ^2 algorithm was used to analyze 133k cosmic ray events and finally a set of alignment constants was determined for the SCT within the SR1 test. Due to the SR1 geometry there was poor uniformity on the barrel layers illumination and therefore a hit cut was needed in order to reject modules with too few hits. This decision came from the fact that the statistical uncertainty on the alignment corrections is related with the number of hits as figure 7.2 shows. Then, a hit cut was applied, requiring at least 200 hits per module. Thus, 16 modules were rejected (from 468) which were located mainly at the horizontal edges of the barrel. Figure 7.3 shows the hitmaps of the SCT barrel layer 3 after alignment where the non-uniform illumination is shown.

A simple track selection was applied, requiring at least 5 SCT hits on track. Thus, with this requirement, nine iteration were done at level 3[1] considering 6 DoFs per module (i.e. 2712 DoFs in total). A nice alignment convergence was observed. Figure 7.4 shows the evolution of two of the local alignment corrections (Tx and Ty) as a function of the iteration number for the full alignment procedure.

Moreover, no track constraints were used and therefore the first six eigenmodes were removed which corresponded to the six near-singular modes of the solution, i.e. the three rotations and three translation of the whole system.

7.2.3 SR1 alignment performance

Due to the specifications of the SR1 setup, the study of the alignment performance was rather difficult. On the one hand the special SR1 geometry restricted the information that could be extracted from the track parameter distributions and from their correlations. On the other hand, the available simulated data did not account for cosmic shower effects (at particle generator level) and its description lacks the distribution of material surrounding the detector. Moreover,

[1] It was done just at level 3 because the other alignment levels were not implement yet.

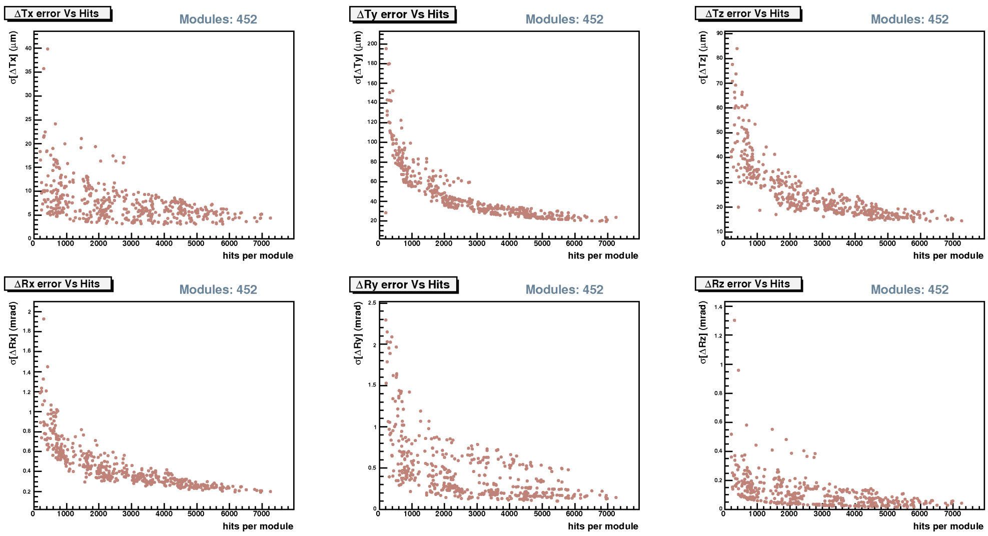

Figure 7.2: *Alignment constant uncertainties as a function of the number of hits for the given modules. The upper and lower rows contain the uncertainty on the translations and rotations, respectively.*

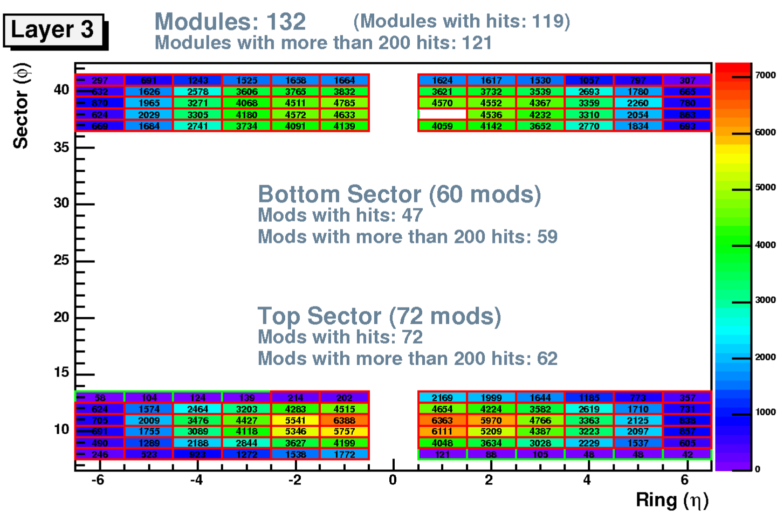

Figure 7.3: *Hitmap of the SCT barrel layer 3 after alignment. The poor uniformity on the module illumination, specially at the barrel edges, can be observed.*

although random misalignments were introduced at reconstruction level they do not achieved the realistic estimation considered in the CSC *as-built* description. These issues made difficult a quantitative comparison between data and simulated events due to the difference in track mul-

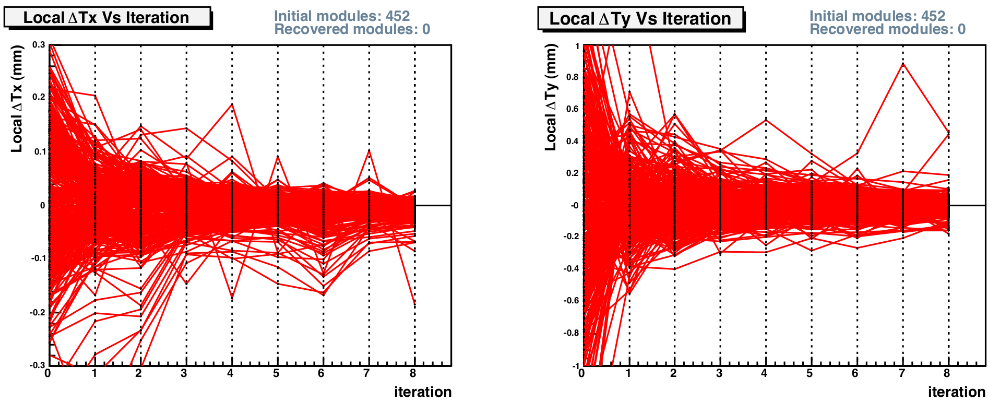

Figure 7.4: *Flow of the alignment corrections Tx and Ty for the SR1 alignment procedure, showing their convergence.*

tiplicity and the large uncertainty in the momentum distribution. Anyhow, a discussion and a qualitative comparison can be found on reference [68].

Thus, the alignment performance was based on residual and pull distributions as well as on hit efficiency studies. Figure 7.5 shows the difference of the biased residuals between the nominal geometry and the aligned one. It is clearly visible that the residual distributions are distorted before the alignment and that after the alignment the mean for all layers is centered around zero and the widths of the residual distributions are smaller. Moreover, figure 7.6 shows the mean and the widths of the residual (upper row) and pull (lower row) distributions as a function of the iteration number. Those plots show that the average widths of the residuals before alignment was of $O(90)$ μm, while after alignment it was of $O(50)$ μm. As already commented, the widths of the residuals distributions were dominated by MCS, therefore, the residual misalignment is hardly visible. In addition, the contribution to the track uncertainty originating from the track fit was largely underestimated, since the MCS contribution was not calculated, leading to the fact that, generally, widths of pull distributions were too broad, being $\sigma_{pull} \sim 1.45$.

As a performance test, the hit efficiency was computed using using some quality hit cuts (track with 10 or more SCT hits, χ^2/ndof ≤ 24, etc...) and requiring that the hit must be found within a certain road-width around the predicted hit position. Then, in order to neglect MCS effects (and based on simulation studies), a cut of 2 mm was chosen to compute the final efficiencies from real data. The efficiency performance is shown in figure 7.7 where after alignment the unbiased hit efficiency[2] in all barrel layers was measured to be within specifications (> 99%).

The obtained alignment corrections suggested a twist distortion of the SCT barrel [104]. Comparisons with photogrammetry measurements were not conclusive due to systematic uncertainties, so, no independent confirmation was possible. It could be a weak mode of the alignment.

Finally, the mechanical survey of the SCT and TRT barrel revealed a horizontal displacement of ΔX=0.3 mm and a rotation around the Y axis of 0.221 mrad of the SCT with respect to the

[2]Unbiased hit efficiency means that the hit located on the SCT barrel layer under investigation was removed for computing the track. In other words, a track refit was then performed excluding these hits and then, the efficiency was computed.

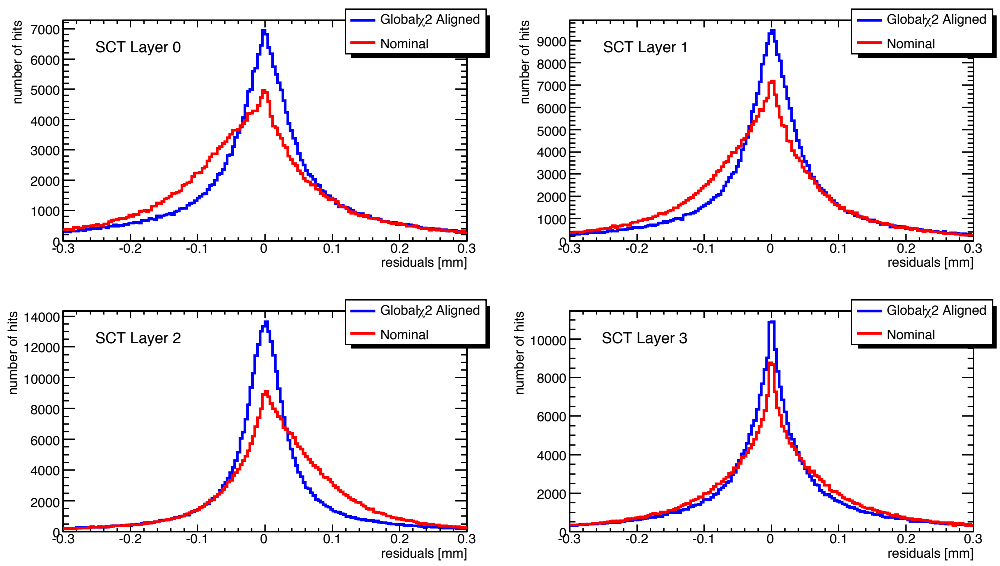

Figure 7.5: *Biased residual distributions for each SCT barrel layer before and after alignment.*

TRT barrel. It is worth to say that the relative alignment between the SCT and the TRT was consistent with these survey measurements [68].

7.3 Cosmic ray commissioning runs

Since 2008, many performance studies have been carried on the ATLAS detector as part of its commissioning. From all of them, the golden tests have been the technical runs with cosmic rays which were carried out to operate together all subsystems, to test the TDAQ and DCS systems, the data transfer from the SFO disks at ATLAS Point-1, the data processing and re-processing at Tier0 and Tier1 respectively and of course to obtain the first track-based alignment and calibration constants for the full and real detector. All these issues led to gain experience with the ATLAS tracker hardware and its performance even before LHC collisions were recorded.

Two major cosmic data taking periods were carried out with full detector:

- **Autumn 2008**: More than 200 million events were registered, reconstructed and processed during this period with different detector and magnet configurations. Figure 7.8 (a) shows the integrated cosmic data rate versus the run number. It shows that almost 7 millon events with tracks traversing the ID were recorded. Collected data went through two reprocessing cycles at Tier1's centers to further improve the quality of the data, using improved calibration and alignment constants, tuned reconstruction software, etc.

- **June/July 2009**: More than 90 million events were collected with different detector and

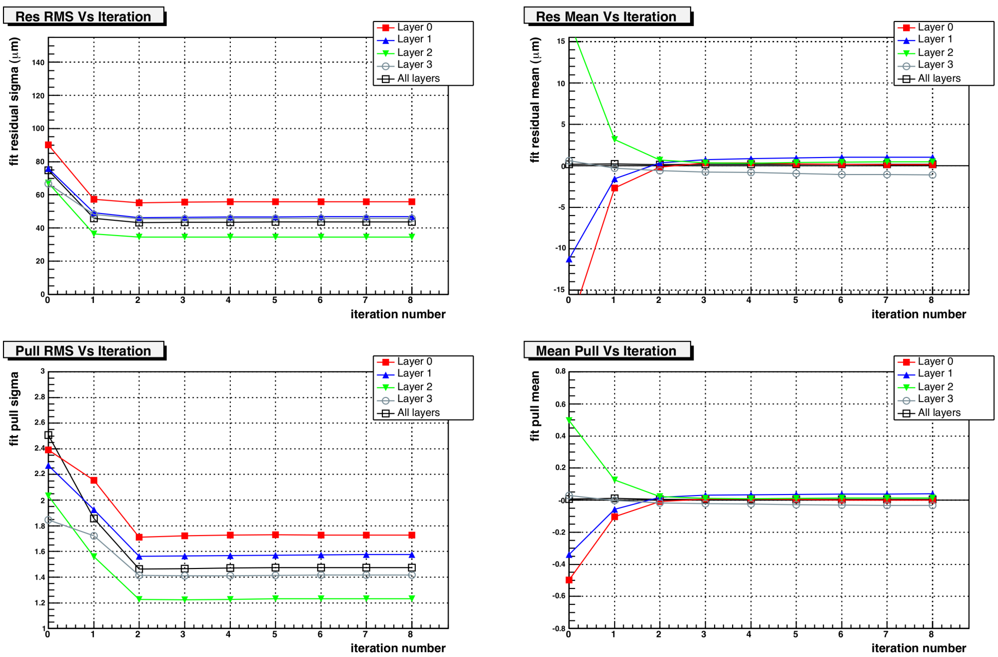

Figure 7.6: *Averaged means and the widths of the residual (upper row) and pull (lower row) distributions per SCT barrel layer as a function of the iteration number.*

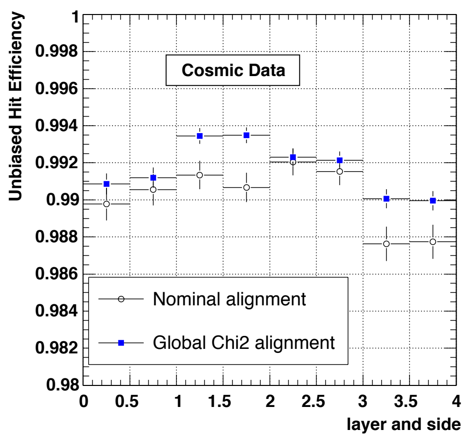

Figure 7.7: *The unbiased hit efficiency measured for the different barrel layers and sides from cosmic data, before and after alignment.*

magnet configurations. Figure 7.8 (b) shows the integrated cosmic data rate versus the run number for this period. It shows that about 20 millon events with tracks traversing the

ID were collected. This time just one reprocessing was done, firstly to unify the reconstruction software release and secondly to apply an improved calibration and alignment constant set.

During these cosmic ray runs, the full ATLAS software and hardware chains were exercised with a trigger rate from $O(1)$ Hz to $O(700)$ Hz (depending on the subdector size and location). From the trigger point of view these events were primarily collected using level-1 muon triggers, but also calorimetry-based triggers. In fact, cosmic rays allowed the first real cross-check that the energy measured by the calorimeter trigger is consistent with what is observed via the full calorimeter readout [105]. Events collected with level-1 trigger allowed the verification and training of the software algorithms, mainly tracking and muon reconstruction, running in the HLT. Moreover, level-2 trigger was actively used to select/reject events based on track reconstruction in the ID to maximize statistics of events crossing all detectors.

Furthermore, the detector performance was explicitly measured for the ID detector. For the silicon detectors the hit efficiency was $> 99\%$ while for the TRT was $\sim 97\%$ (in good agreement with MC) and the noise occupancy was low [106]: $\sim 10^{-10}$ for Pixels (i.e., less than 1 noisy pixel hit per event), $\sim 10^{-5}$ for the SCT (measured at 150V) and $\sim 2\%$ for the TRT. Moreover, combined tests showed no evidence of cross-talk between ID subdetectors. Finally, also the continuity of the electrical and optical services was verified.

Muon reconstruction was specially exercised on the same events both in the HLT and offline, demonstrating the excellent agreement between the two reconstructions and also the ability to perform offline-like reconstruction in real time at the ATLAS Event Filter [107] [108]. Figures 7.9 (a) and (b) show the distributions of the track parameters ϕ_0 and θ_0, respectively, reconstructed with the ID. On the one hand, ϕ_0 should be a gaussian-like distribution peaking around $-\pi/2$, meaning that cosmic rays were coming mainly from the zenith. This was not the case since all the RPC chambers, which gave the main trigger, were not available, explaining therefore the ϕ_0 distribution shown in figure (a). On the other hand, figure (b) shows two peaks in the θ_0 distribution that correspond with the two main access shafts of the ATLAS cavern. Furthermore, independent measurements with the ID and the muon spectrometer were compared as figure 7.10 shows. It was also demonstrated that the energy lost by muons traversing the material between the two detectors (which includes the calorimeters and the solenoid coil) is, on average, 3 GeV/c^2. This is shown in figure 7.11 where the distribution of the difference between the momentum measured by the ID and the muon spectrometer for bottom tracks (i.e. tracks reconstructed with the lower half detector) peaks at +3 GeV/c. Moreover, simulated data, discussed in the next section, is also shown on the same plot for comparisons and a good agreement is observed.

Finally, it is worth to mention that much more studies were carried out such: as electron (produced via ionisation), photon and tau identification, jet and missing energy studies.

7.3.1 Monte Carlo simulations

Simulations were also produced within the *Athena* framework and based on the Geant4 toolkit [110]. Moreover, a cosmic MC generator [111] was used for simulating muons from cosmic ray events, based on flux calculations from reference [112] and in the standard cosmic ray momentum spectrum [5]. Single muons were generated across a large area (600×600 m^2) at the surface, with an energy range of 10 GeV to 5 TeV. Only those muons pointing to a sphere of

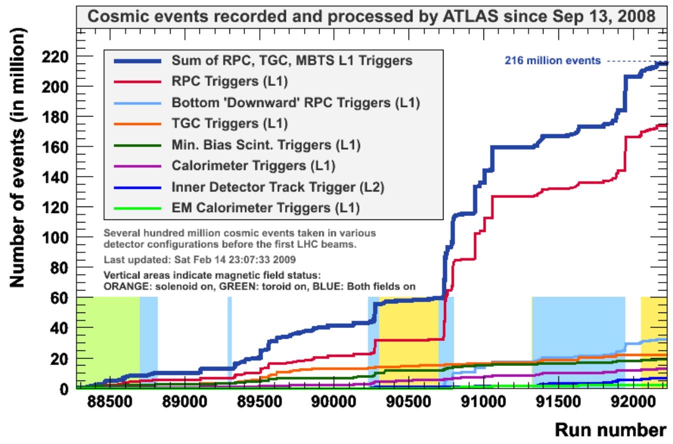

(a) *Period: Autumn 2008*

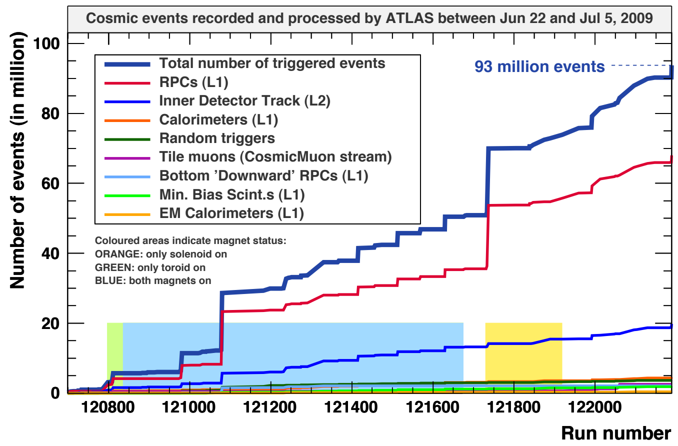

(b) *Period: June and July 2009*

Figure 7.8: *Figure (a) shows the integrated cosmic data rate versus the run number since September 13, 2008 (i.e., after short single beam runs). Moreover, the magnetic field status is illustrated with vertical colored areas: yellow color: only solenoid on, green color: only toroid on (including barrel and endcaps), blue color: all magnet systems on. Figure (b) shows the same plot for the data taken during June and July 2009. Due to the inclusive streaming model, the overall sum of the events in all streams exceeds the total number of accepted events. The sum of RPC, TGC and MBTS triggers approximates to good precision the full cosmic rate taken.*

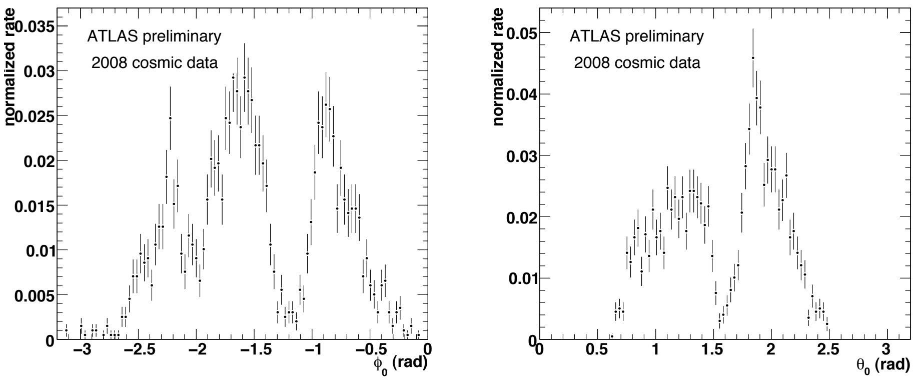

(a) ϕ_0 *distribution* (b) θ_0 *distribution*

Figure 7.9: *Distributions of track parameters ϕ_0 (a) and θ_0 (b) measured in the ID. The ϕ_0 distribution is affected by the trigger configuration which was mainly given by the RPC chambers (being not all of them available). Figure (b) shows two peaks that correspond with the two cavern's shafts.*

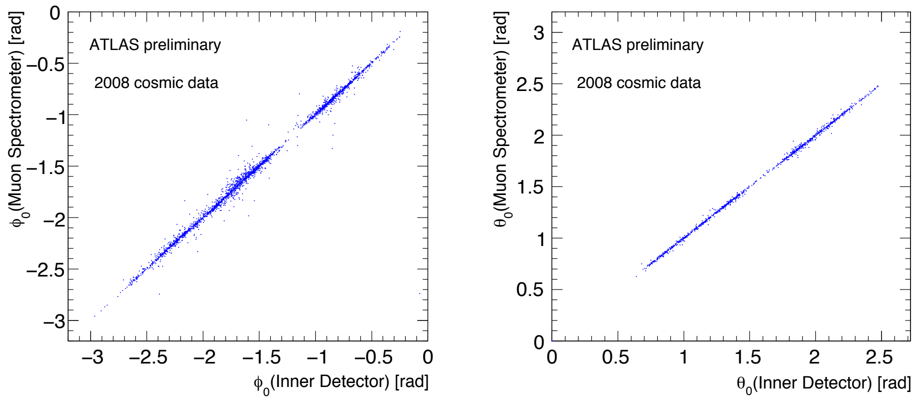

(a) ϕ_0 *correlation* (b) θ_0 *correlation*

Figure 7.10: *Correlation between track parameters ϕ_0 (a) and θ_0 (b) measured in the ID and the muon spectrometer. The good correlation observed for parameters measured with both subdetectors implies that they are well synchronized [109].*

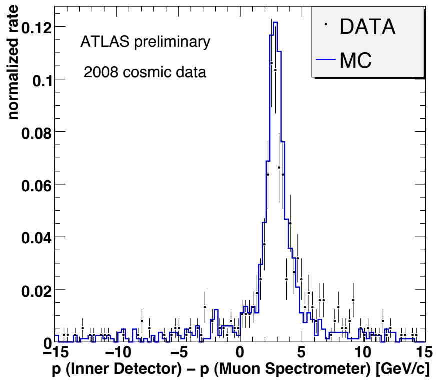

Figure 7.11: *Distribution of the difference between the momentum measured in the ID and the muon spectrometer for tracks reconstructed with the lower half detector. A mean value of about 3 GeV/c is observed for both data and MC [109].*

radius about 20 m representing the inside of the ATLAS cavern were initially selected. Then, the Geant4 simulation propagated the muons through ~ 100 m of rock, emulating the position where the ATLAS detector lies. Once in the cavern, a second filter level was applied in order to reduce the simulation time and therefore to increase the efficiency. Thus, only events with at least one hit in a given volume inside of the ATLAS detector were selected. The emulation of the electronics was adapted from the one used for collision events in order to take into account the difference in the timing. Finally, several MC samples were produced with different detector geometry configurations and with and without the presence of both magnetic fields (solenoid and toroids).

Even with this high detailed simulation, comparison with real data should be taken with care as the MC does not model some details of the special geometry, cosmic trigger configuration and timing. For example, although it includes the two main access shafts, it does not include the two lift shafts. On the other hand, in the simulation, the whole detector was assumed to be readout and the three trigger levels were not simulated. Also, the ratio of positive and negative charged generated muons was larger than the measured value [5]. Therefore, comparisons with MC should be interpreted with care. In that sense, offline performance studies has provided direct feedback for simulation verification and fine tuning. Much more information can be found in reference [109].

7.3.2 Alignment strategy

Two different sets of alignment constants were produced for both cosmic ray data taking periods, which will be denoted here as *Cosmic08 alignment* and *Cosmic09 alignment*. Each alignment set is accessible via the conditions database selecting the tags InDet_Cosmic_2008_08 and InDet_Cosmic_2009_01, respectively.

In both cases a combination of the data taken with and without the presence of the solenoid magnetic field was used. The starting geometry used the Pixel module survey whilst SCT modules were placed at their nominal values and not the nominal geometry as in the CSC or FDR exercises. It will be referred with the *Initial geometry* label.

7.3.2.1 Pixel Survey

The Pixel modules were surveyed once assembled on the staves as was already described in section 3.4.6. This recorded information was used and translated to assume how the individual Pixel modules were mounted with respect to their stave neighbours (this corresponds to level 3 in the geometry hierarchy), being these positions the starting geometry for present alignment strategies. Figure 7.12 shows the final local alignment correction distributions, obtained from the survey measurements [55], for each DoF (translations and rotations) and independently for the barrel and end-cap Pixel modules (0 means no correction with respect its nominal value).

A detailed discussion can be found on references [55] and [56] which give a detailed analysis. The accuracy of the end-cap survey was also confirmed by the alignment (using the Robust approach) of one of the two end-caps in SR1 test [68].

7.3.2.2 Cosmic08 alignment strategy

The strategy to produce the *Cosmic08 alignment* used runs without and with the solenoid field and it had to evolve with time as more cosmic ray data was collected. Thus, the first iterations used 1 million of events (which corresponds to ~ 200k useful tracks) without magnetic field (i.e. the existing data at this moment) while the latest combined events with and without magnetic field.

The *Athena* framework release used to process and derive the *Cosmic08 alignment* set was 15.0.0 at the beginning and 15.5.1.6 for the latest iterations (both cases used the built project: AtlasTier0). It is also worth to mention that CTB tracking [78] was the tracker used to reconstruct the cosmic ray trajectories.

A simple track quality selection was applied based on a transverse momentum cut, $p_T > 2$ GeV/c, for events with magnetic field. For events without magnetic field straight tracks were reconstructed and material effects were not taken into account in the track fit as no momentum estimation was available. This was translated into wide residual distributions. Furthermore, tracks with less than 10 SCT hits were rejected. This track and hit selection cuts will be denoted as standard quality cuts in this section. In addition, when the alignment was done at stave level (i.e. level 2.7), the requirement was strengthen by asking for at least one overlap (either in SCT or Pixels) in order to enhance the stave correlation, keeping the hit statistics still high.

As claimed before, alignment strategy was started from the geometry provided by the *Initial geometry* (iteration 0) and the following iterations have been summarized in table 7.1. In that table, the number of events as well as the run type are shown. Also the alignment level and the track and hit quality selection cut, defined in table 5.1, are given. Finally, it also contains the alignment DoF considered in each iteration.

It can be observed that this strategy has been proposed to cover, i.e. to align, all the real assembled structure units although with a limited accuracy: full structures (level 1), Pixel half-shells (level 1.5 and 1.8), staves (level 2.7), barrel layers and end-cap discs (level 2) and modules (level 3). The last three iterations were done just to check convergence.

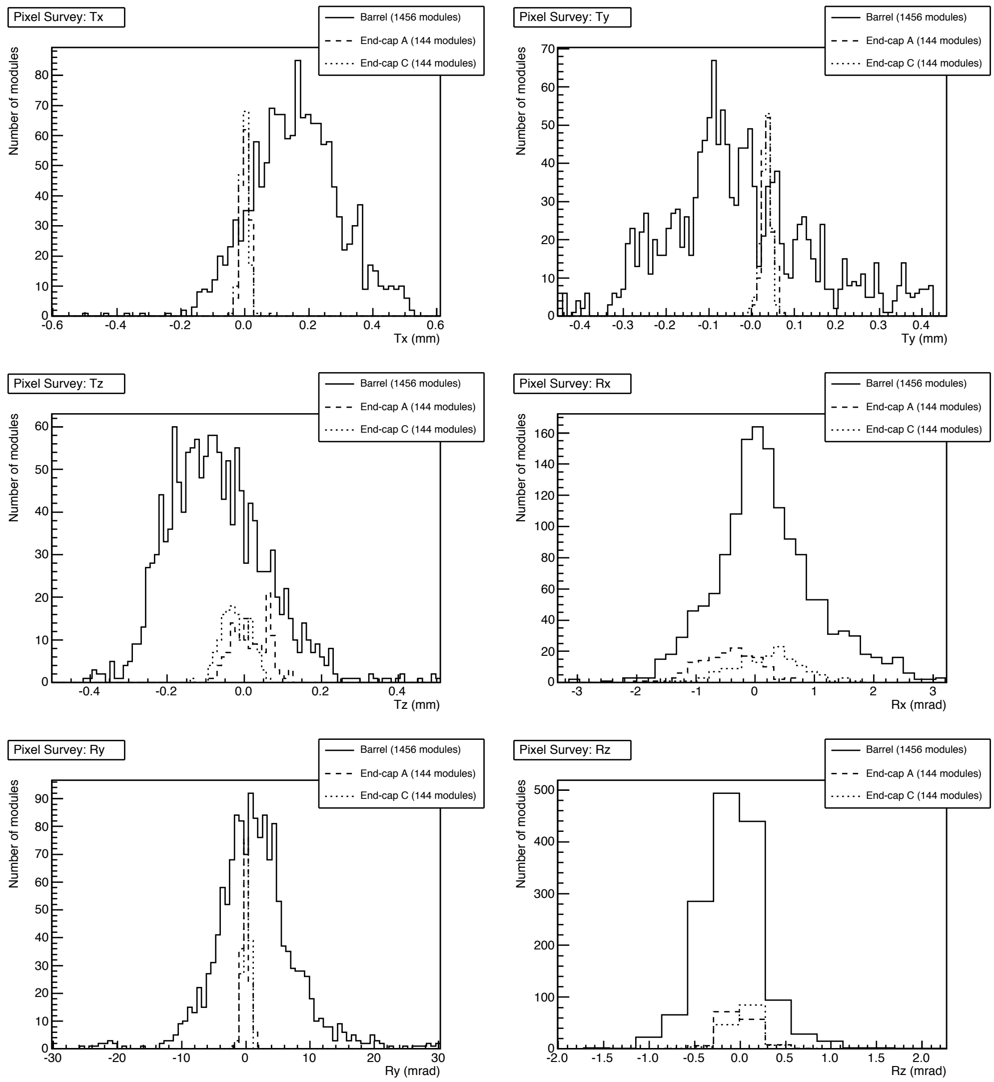

Figure 7.12: *Alignment correction distributions obtained from the Pixel survery [55] for each DoF (translations and rotations). All figures contain independent distributions for barrel (solid line) and end-cap Pixel modules (end-cap A: dashed line and end-cap C: dotted line).*

Finally, the first six eigenmodes were removed in all iterations. This was possible since a matrix diagonalization was performed to solve the system.

Events	**Mag. field**	**Alignment level**	**Number of iterations**	**Track/Hit quality selection cuts**	**DoF**
1M	Off	1	4	standard	6
1M	Off	1.5	4	standard	6
1M	Off	1.8	4	standard	6
4M	Off	2.7	4	standard + + ≥1 overlap Pixel/SCT	6
210k 383k	Off On	3	5	standard	Tx, Rz
210k 383k	Off On	2	5	standard	Tx, Ty, Rz
210k 383k	Off On	2.7	2	standard + + ≥1 overlap Pixel/SCT	6
210k 383k	Off On	1.8	1	standard	6
210k 383k	Off On	1	1	standard	6

Table 7.1: *Summary table of the alignment strategy followed to derive the* Cosmic08 alignment. *Here, the alignment level (see table 5.1), the number of events, the presence of the ID magnetic field as well as the number of iteration of each level are written out. Finally, it also contains the alignment DoF considered in each level.*

7.3.2.3 Cosmic09 alignment strategy

The strategy followed to produce the *Cosmic09 alignment* benefited from the experience gained with the *Cosmic08 alignment*. Each iteration used a mixture between ∼1.7 millon of events without any magnetic field and ∼1.5 million of events with the ID solenoid switched on. This can be translate into ∼440k and ∼52k useful cosmic ray tracks, respectively. The starting geometry used the Pixel module survey and SCT nominal positions as in the previous case.

Athena release 15.5.1.6 (built project: AtlasTier0) was used to process and produce this alignment set and as in the previous case, CTB tracking [78] was the tracker used to reconstruct the cosmic ray trajectories.

A track quality selection was applied based on a transverse momentum cut, $p_T > 2$ GeV/c, for events with magnetic field. In this case, for events without magnetic field, the material effects were estimated inside the tracking code, assuming that all tracks had $p = 10$ GeV/c. Moreover, the InDetAlignHitQualSelTool package (see section 3.7) was used and after the selection, tracks with less than 12 SCT hits were rejected. This track and hit selection cuts will be denoted as standard quality cuts. Even more, when the alignment was done at stave level (i.e. level 2.7), it was required at least one overlap (either in SCT or Pixels), with the idea of enriching the sample with tracks with overlaps.

In addition, an *error scaling* was introduced in some iterations, specially at the beginning when the detector was quite inefficient in tracking terms because of the large misalignments.

The alignment strategy has been summarized in table 7.2. There, the alignment level as well as the number of iteration of each level is written out. The number of DoF which are defined by the given alignment level which are summarized in table 5.1. Also the hit and track quality selection requirements and the *error scaling* used appear in this table. Finally, it also contains the alignment DoF considered in each level.

It can be observed that this strategy has also tried to align all the real assembled structure units but this time with more accuracy (i.e. considering more aligning DoF) than the *Cosmic08*: full structures (level 1), Pixel half-shells (level 1.8), staves (level 2.7), barrel layers and end-cap discs (level 2) and modules (level 3). Few iterations using each level were needed to reach convergence and the last three iterations were performed just to check the right convergence and indeed the correlations were very small ($O(1)$ μm).

Alignment level	Number of iterations	Error Scaling	Hit quality selection cuts	DoF
1	3	$a = 1, c$=0.2	standard	6
1.8	3	$a = 1, c$=0.2	standard	6
1.8	3	$a = 1, c$=0.1	standard + HitQualSelTool	6
2.7	4	$a = 1, c$=0.05	standard + HitQualSelTool + + ≥1 overlap Pixel/SCT	Tx, Ty, Tz, Rx, Rz
3	4	-	standard + HitQualSelTool	Tx, Ty, Tz, Rz
2	1	$a = 1, c$=0.0 (just end-caps)	standard + HitQualSelTool	6 (for barrel) Tx, Ty, Rz (for end-caps)
	2	-		
2.7	1	-	standard	Tx, Ty, Tz, Rx, Rz
1.8	1	-	standard	6
1	1	-	standard	6

Table 7.2: *Summary table of the alignment strategy followed to derive the* Cosmic09 alignment. *In this table the alignment level as well as the number of iterations of each level is given. The number of DoF which are defined by the given alignment level which are summarized in table 5.1. Moreover, an* error scaling *($\sigma_{scaled} = a\sigma \oplus c$) was used in some iterations (being σ the intrinsic hit error). Finally, it also contains the alignment DoF considered in each level.*

Finally, similarly to the *Cosmic08* strategy, this one removed the first six eigenmodes in all iterations.

7.3.3 Performance with the alignment based on cosmic ray data

Once both strategies have been presented, the performance achieved with each alignment set will be discussed. A comparison between the two alignments will be given together with the initial performance that the starting geometry (Pixel survey and the SCT nominal positions) provides. Plots will be normalized to the number of tracks which have passed the quality cuts to allow comparisons. It is expected that the alignment sets improve, generally, the performance of the Silicon Tracker although one can predict some problems at the sides of the barrel and at the end-caps since a poor alignment quality is expected in those regions. For example, figure 7.13 shows the hitmaps for the four SCT barrel layers where the non-uniformity in the illumination can be observed and specially the small number of hits at the horizontal edges of the barrel (barrel sides correspond to sectors with less than 200 hits).

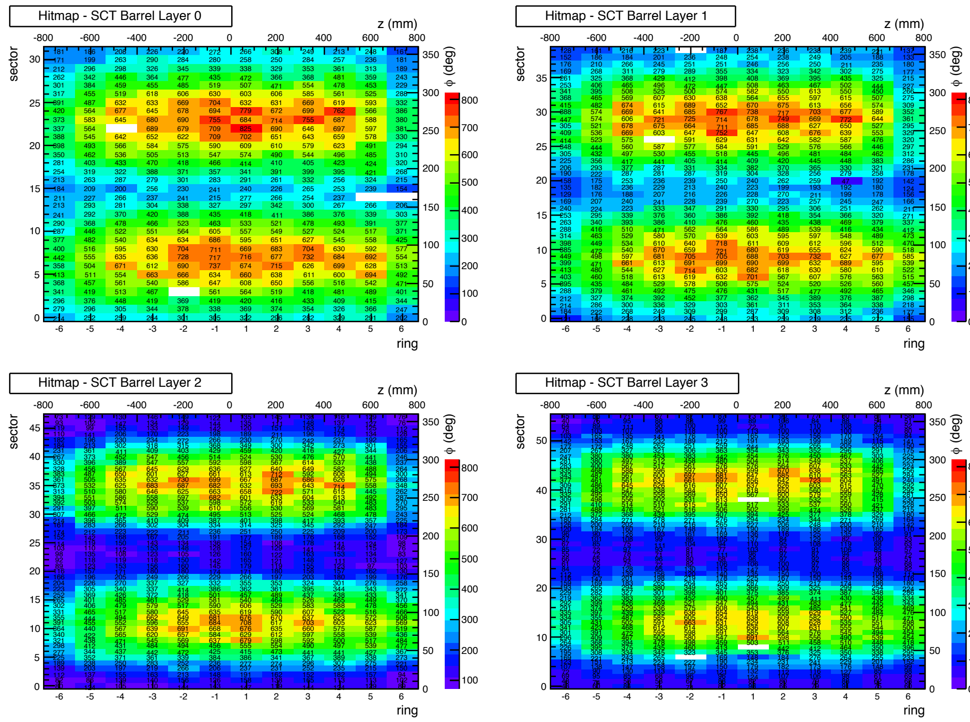

Figure 7.13: *Hitmaps from cosmic ray data collected in 2008 for the four SCT barrel layers using the initial geometry provided by the Pixel module survey and the SCT modules at their nominal positions. These hitmaps show the dependence with the sector number, which translates into a non-uniformity in the barrel layer illumination.*

Starting now to discuss the basic distributions, figures 7.14 and 7.15 show the biased residual distributions for the Pixel and SCT barrel layers, respectively. Moreover, these plots shows results for the *Initial geometry* (dotted line), *Cosmic08 alignment* (dashed line) and *Cosmic09 alignment* (solid line) to allow comparisons. Thus, a great improvement is shown for $r\phi$ residuals for both subdetectors, with all distributions centered around zero and widths of $O(14)\ \mu m$.

In the Pixel case, the *Cosmic09 alignment* produces slightly worse $r\phi$ residuals than the *Cosmic08 alignment* but narrower η residuals. On the other hand, for the SCT case, the improvement due to both alignment sets is also spectacular compare with the initial geometry. Comparing both sets, one can conclude that the performance is at the same level, with biased residuals of width of $O(19)\ \mu m$.

Furthermore, figures 7.16 show the average biased $r\phi$ and η residual distributions for the Pixel end-cap, respectively. From those plots, a great improvement is observed in both cases.

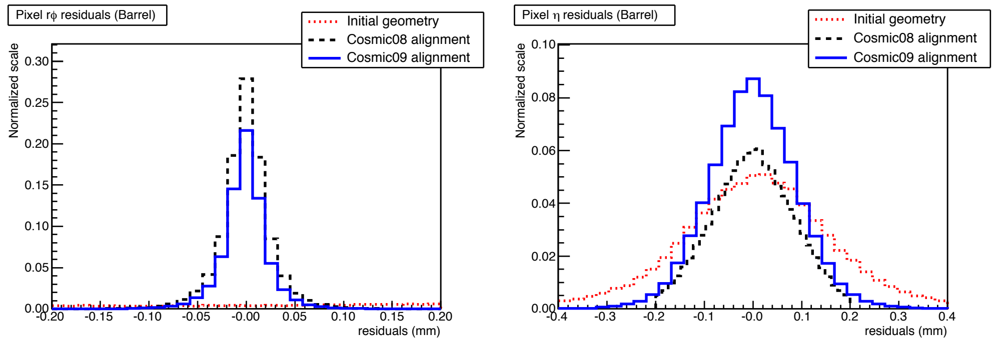

Figure 7.14: *Biased $r\phi$ and η residuals for Pixel barrel layers using the* Initial geometry *(dotted line),* Cosmic08 *(dashed line) and* Cosmic09 alignment *(solid line). Plot normalized to the number of tracks which have passed the quality cuts.*

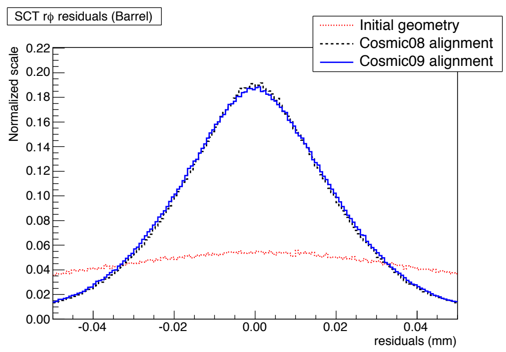

Figure 7.15: *Biased $r\phi$ residual distributions for SCT barrel layers using the* Initial geometry *(dotted line),* Cosmic08 alignment *(dashed line) and* Cosmic09 alignment *(solid line). Plot normalized to the number of tracks which have passed the quality cuts.*

Anyhow, the performance is better with the *Cosmic09 alignment*, specially looking at the η residual distribution.

To finish with the residual discussion, figures 7.17 (a) and (b) show the $r\phi$ residual distributions for the SCT end-cap A and C, respectively. In particular, residuals provided by the modules on disc 4 are given as a representative sample of the each end-cap behaviour. Again, both alignment sets improve these residuals with respect the starting geometry though the achieved performance is quite poor, specially for the *Cosmic08 alignment*. Moreover, end-cap A looks better aligned than end-cap C.

Another nice performance estimator is given by the χ^2 correlations. Figure 7.18 shows the χ^2 as a function of ϕ_0 (left) and η (right). Generally, lower χ^2 values are shown for both alignment sets compared with the starting geometry, being quite similar in both cases. After alignment, the correlation with ϕ_0 is quite flat but it shows a little valley at $\pi/2$. This effect is due that cosmic

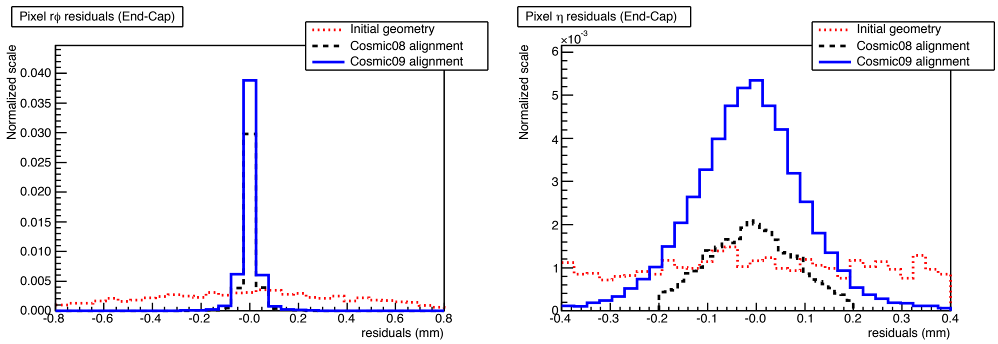

Figure 7.16: *Biased $r\phi$ (left) and η (right) residual distributions for the Pixel end-caps using the* Initial geometry *(dotted line),* Cosmic08 *(dashed line) and* Cosmic09 alignment *(solid line). Plots are normalized to the number of track passing the quality cuts.*

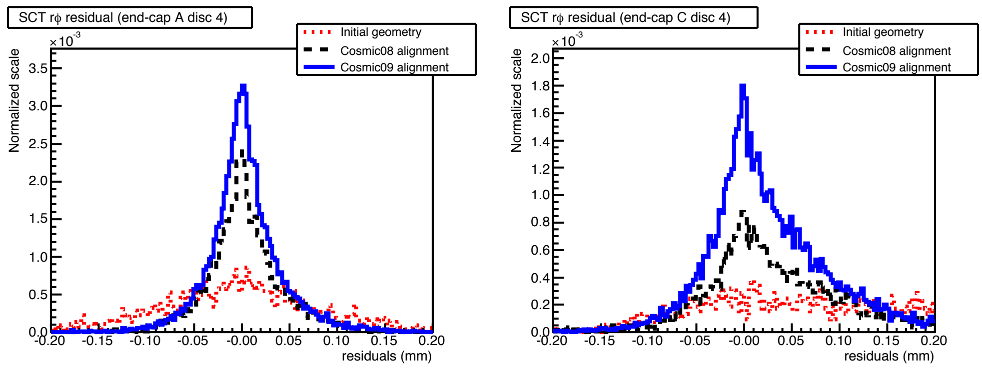

(a) *SCT end-cap A (disc 4)*

(b) *SCT end-cap C (disc 4)*

Figure 7.17: *Biased $r\phi$ residual distributions for disc 4 and SCT end-cap A (a) and C (b), using the* Initial geometry *(dotted line),* Cosmic08 alignment *(dashed line) and* Cosmic09 alignment *(solid line). Plots are normalized to the number of track passing the quality cuts.*

ray tracks with vertical incidence angle with respect ATLAS are better determined as they have more associated hits. The η correlation shows how the barrel region has lower χ^2 values than the end-cap regions since the first is better aligned.

Finally, correlations between the residuals and the reconstructed p_T do not show any dependence after alignment which is a good sign. Figures 7.19 (a) and (b) show the behaviour of these correlations for the layer 0 of Pixel and SCT barrels, respectively. These plots are representative for the rest of the barrel layers of each subdetector.

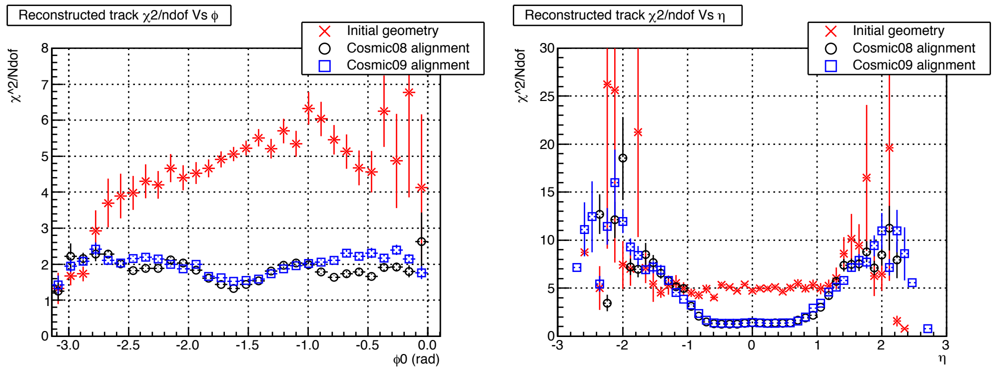

Figure 7.18: χ^2 *value as a function of* ϕ_0 *(left) and* η *(right) for cosmic ray data with the presence of the ID magnetic field and using the* Initial geometry *(crosses),* Cosmic08 alignment *(circles) and* Cosmic09 alignment *(squares).*

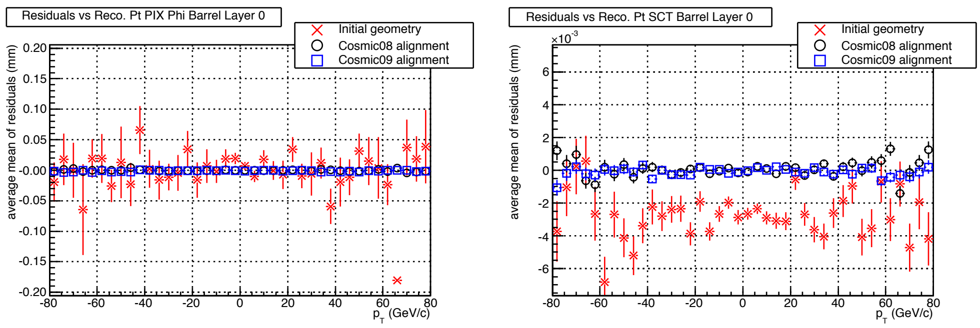

(a) *Residuals Vs pT (Pixel Barrel, layer 0)*

(b) *Residuals Vs pT (SCT Barrel, layer 0)*

Figure 7.19: *Average of the biased* $r\phi$ *residuals for Pixels (a) and SCT (b) as a function of the reconstructed transverse momentum for cosmic ray data with the presence of the ID magnetic field. The* Initial geometry *(crosses),* Cosmic08 alignment *(circles) and* Cosmic09 alignment *(squares) are shown.*

7.3.3.1 Validation of the *Cosmic08 alignment* set

The *Cosmic08 alignment* set was also studied by the alignment monitoring group where comparisons with MC simulations were performed. Tracks were selected to have $p_T > 2$ GeV, $|d_0| <$ 50 mm, $|z_0| < 400$ mm (i.e. tracks were required to go through the Pixel layer 0). Figures 7.20 (a) and (b) show the unbiased $r\phi$ and η residuals integrated over all hits-on-tracks for the Pixel barrel for the nominal geometry (squares), the *Cosmic08 alignment* (filled circles) and for a perfect aligned and simulated detector (empty circles). Figure 7.20 (c) shows the unbiased $r\phi$ residual distribution for the SCT barrel. Narrower residuals for the perfect aligned MC geometry reveal that there is a 20 μm residual misalignment. This value is computed comparing the residual widths provided by MC data and real data[3] [113]. This indicates a very good barrel alignment, at least for being based just on cosmic ray data and at that stage of the experiment.

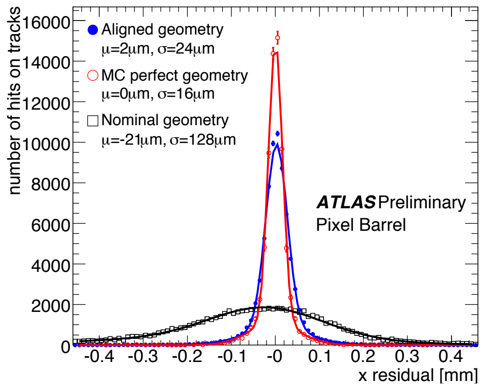

(a) *Pixel rϕ residuals*

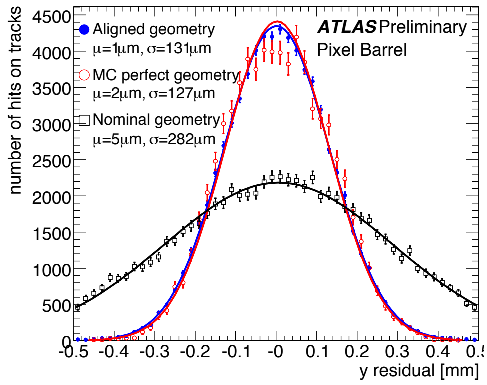

(b) *Pixel η residuals*

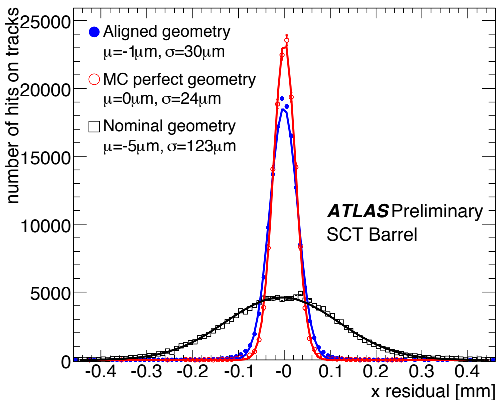

(c) *SCT rϕ residuals*

Figure 7.20: *Unbiased rϕ and η residuals integrated over all hits-on-tracks for the Pixel barrel (a) and (b) and for the SCT barrel (c). Results using the nominal geometry (squares), the* Cosmic08 alignment *(filled circles) and for a perfect aligned and simulated detector (empty circles) are shown. These plots are official and they have been approved by the ATLAS Collaboration [114].*

Moreover, track parameter resolutions were studied by means of track segments. The fact

[3]The residual misalignment for the cosmic based alignment was computed comparing the ideal residuals given by MC data and the initial residuals given by the real cosmic ray data: $\sigma^2_{res\ misal} = \sigma^2_{MC} - \sigma^2_{data} = 20\mu m$.

is that cosmics muons traverse the whole ID and thus leave hits in the upper and lower parts of the detector. By dividing the track to its upper and lower half according to the value of the y coordinate of hits on track and refitting both hit collections, two track segments originated from the same cosmic muon are obtained. Then, track parameter resolutions can be obtained by comparing the difference of the track segment parameters at the perigee point. Since both tracks have an associated error, the quoted resolution is the RMS of the residual distribution of the particular track parameter divided by $\sqrt{2}$. Unexpected dependences or asymmetries of the track parameter resolutions with p_T or the d_0 of these tracks can be a sign of systematic detector deformations. Thus, figures 7.21 (a) and (b) show the d_0 resolution as a function of p_T and d_0, respectively. Both plots show comparisons using the full ID (filled triangles), only the Silicon Tracker (empty triangles) and the full ID from cosmic simulations (stars).

Figure (a) illustrates that in the low p_T region, the resolution is dominated by MCS effects and that at higher values, the resolution is flat. Moreover, is shown that taking into account the TRT information improves the resolution. Finally, the discrepancy with the MC curve indicates a remaining misalignment. On the other hand, figure (b) shows that the resolution is better in the central d_0 region due to more Pixel layers crossed and less spread clusters in the Pixel detector. Taking a closer look, dips are seen if the d_0 of the tracks equal the radii of the pixel layers (indicated by dashed lines). Since the d_0 is in these cases very close to a hit on a Pixel layer, the extrapolation to the perigee point is very small and the resolution improves. The MC distributions confirms the observed behaviour although some discrepancies can be observed. Thus, generally, the resolution for full ID tracks is better.

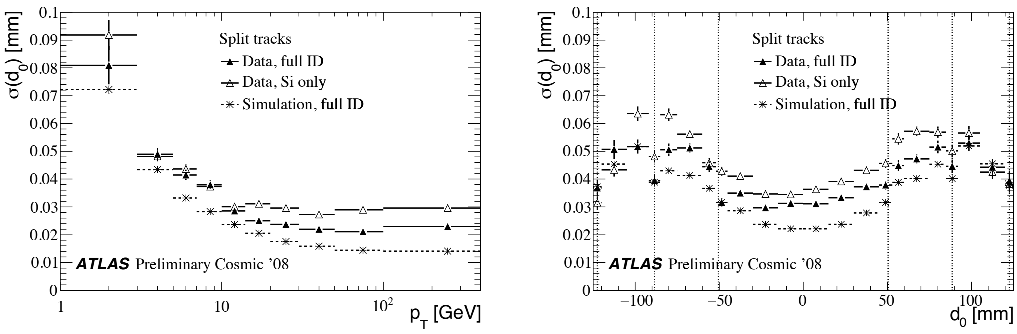

(a) $\sigma(d_0)$ *Vs* p_T (b) $\sigma(d_0)$ *Vs* d_0

Figure 7.21: *d_0 resolution as a function of p_T (a) and d_0 (b). In the low p_T region, the resolution is dominated by MCS effects. At higher values, the resolution is flat. The difference to the MC curve indicates a remaining misalignment. In general the resolution for full ID tracks is better. [114].*

Although much more studies were performed they will not be shown here. In fact, thanks to this validation is was decided that the *Cosmic08* constants were used to reconstruct the first LHC collisions [114].

7.3.3.2 Detector details for module level alignment

The module level alignment revealed several interesting geometry details such as bowing on the Pixel staves. Figures 7.22 shows the alignment corrections, Tx (circles) and Rz (squares), for two Pixel staves as a function of the global Z coordinate of each stave. The observed dependences indicate a bow in the transverse global plane in these staves. Thus, the correlations between Tx (circles) and Rz (squares) in figure (a) corresponds to the scheme (a) in figure 7.23 and the one in figure (b) corresponds to the scheme (b).

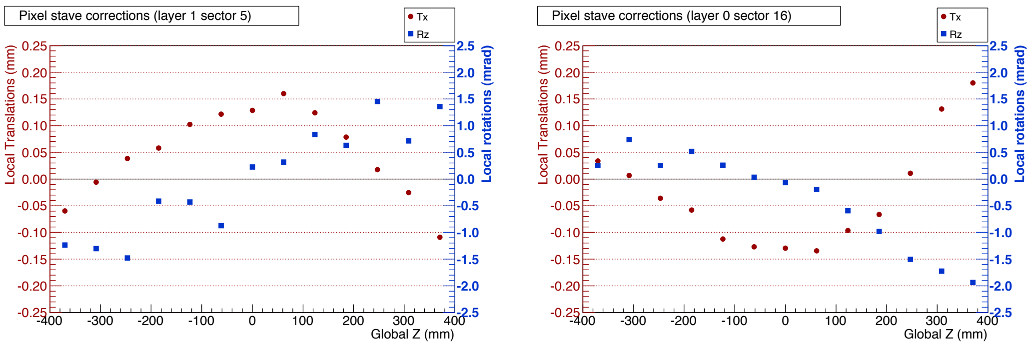

(a) *Positive bowing in XY*

(b) *Negative bowing in XY*

Figure 7.22: *Tx (circles) and Rz (squares) alignment corrections for two different Pixel staves as a function of the global Z coordinate of each stave. The correlation of the Tx and Ry indicates a bow deformation of the stave under study.*

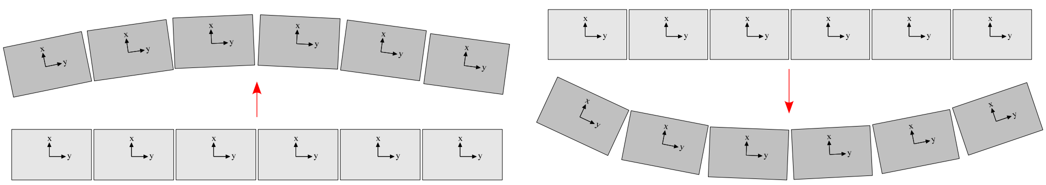

(a) *Positive bowing in XY*

(b) *Negative bowing in XY*

Figure 7.23: *Schemes of positive and negative stave bows in the XY global plane.*

Other structure distortions were observed such as bows over local z direction [115]. The presence of these alignment corrections are expected when a good alignment quality is reached, thus they indicate that the alignment model and in particular the Globalχ^2 algorithm can provide a good detector performance.

7.3.4 Reconstructed tracks from the first ever LHC collisions

In November 23rd, 2009, ATLAS recorded the first proton-proton collision events during the beam commissioning of the LHC. Tracks were reconstructed using the silicon alignment constants derived from the *Cosmic08 alignment*[4], discussed previously. Figure 7.24 shows proudly the first collision candidate event (run 140541).

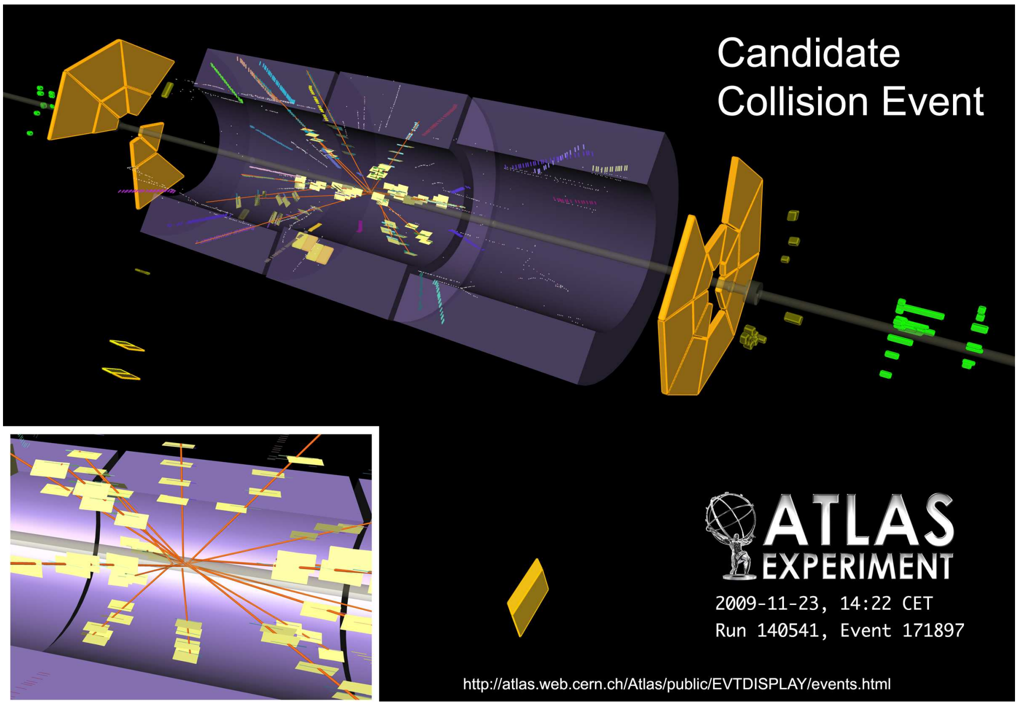

Figure 7.24: *Event Display of the first 900 GeV candidate collision event (run 140541, event 171897) from November 2009. The* Cosmic08 alignment *was used to perform the bulk reconstruction of those events. Straight tracks are shown here as no magnetic field was present.*

To conclude, one can state that the silicon alignment obtained with the Globalχ^2 algorithm using cosmic ray events has worked well for the first LHC collision tracks.

7.4 Aligning with the first LHC collisions at 900 GeV

Since late November early December 2009, collision data is being recorded by all the LHC experiments. This event announced the new LHC era and opened great expectations towards new and amazing physics knowledge.

The LHC's first run has allowed that ATLAS recorded almost 1 million collision candidates at 900 GeV (~ 500k during stable beams) and about 34k collision candidates at 2.35 TeV. Then,

[4] As the *Cosmic09 alignment* validation was not complete it was decided that the *Cosmic08 alignment* had to be used.

the total integrated luminosity recorded by ATLAS was 20 μb^{-1} (12 μb^{-1} considering just the runs with stable beams) and 1 μb^{-1}, respectively, with estimated systematic uncertainties of up to 30% in these numbers. Figure 7.25 shows the cumulative number of events for all runs and just for those with stable beams, since the beginning of data taking in December. Events were triggered by the Minimum Bias Trigger Scintillators (MBTS) and it is expected that this trigger is contaminated by background from unpaired bunches between 1% and 20%, depending on the run conditions.

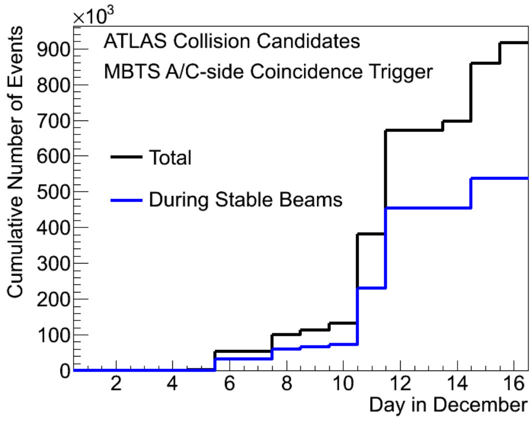

Figure 7.25: *Cumulative number of events triggered by the Minimum Bias Trigger Scintillators (MBTS) since early December 2009. The LVL1 trigger chain used requires at least one hit on either side of ATLAS (A and C). Shown in the figure are the total number of recorded events (black line) and the number of recorded events during LHC stable-beam periods (blue). [116].*

From the ATLAS experiment point of view, the detector response was really great, with an almost perfect operation. Thus, for the ID detector, the operational fraction was 97.9%, 99.3% and 98.2% for Pixels, SCT and TRT respectively.

Finally, although this collision data was the result of the LHC beam commissioning program, stable runs (i.e. events at 900 GeV) have been used to improve the alignment and calibration of the different ATLAS subdetectors. At the end, a preliminary set of alignment constants has been prepared using the first LHC collisions, so-called InDet_Collisions_2009_01 in the database.

7.4.1 Alignment strategy

Starting from the *Cosmic08 alignment* set, collision data was exploited in order to improve the existing Silicon Tracker alignment, specially at the SCT end-caps. Thus, runs 141749 and 141811 which contained about 58k minimum bias events from collisions at 900 GeV have been used. These runs are the first LHC runs with stable beams. It is obvious that these events are not the optimal ones for alignment purposes but they lead to exercise the alignment data model with the first LHC collisions.

The followed strategy was: 1 iteration at level 1 and 8 iterations just at level 2, fixing the full Pixel detector and the SCT barrel (i.e. just the SCT end-caps were aligned). Level 1 provided small corrections of the super structures (in the global frame) as can be seen in table 7.3.

Detector structure	**Translations (mm)**			**Rotations (mrad)**		
	Tx	**Ty**	**Tz**	**Rx**	**Ry**	**Rz**
Pixel	-0.020	-0.005	0.032	0.042	-0.041	-0.143
SCT end-cap A	0.004	0.042	0.110	-0.069	0.058	-0.096
SCT barrel	-0.010	-0.005	0.094	-0.021	0.080	0.018
SCT end-cap C	0.006	-0.010	-0.241	-0.035	0.062	0.222

Table 7.3: *Summary table of the derived level 1 alignment corrections obtained with the first LHC collisions. The statistical uncertainty is given by the last digit.*

Then, these small level 1 corrections together with used level 2 strategy imply that either the Pixel end-caps and the sides of silicon barrel remain still "poorly" aligned (i.e. it can be improved with collision data). Moreover, only just 3 DoFs have been considered at level 2, Tx,Ty and Rz, leading translations of about 250 μm and rotation around the global Z axis of about 1.5 mrad. Furthermore, basic hit and track quality selection cuts have been applied: 7 silicon hits on track together a track momentum cut of $p_T > 1$ GeV/c. Furthermore, an *error scaling* was introduced for the end-caps to inflate hit errors ($a = 1$ and $c = 200$ μm) during the first iterations, maintaining thus the track efficiency in the track fit. Finally, the first six eigenmodes were removed after the matrix solving.

Furthermore, even a simulation was produced in order to compare these early results. PYTHIA was used to simulate minimum bias events coming from collisions at 900 GeV, using the full ATLAS detector description (i.e. full simulation). Comparisons with MC are on going thanks to the alignment monitoring [117] and some of those will be discussed in the next subsection.

Finally, it is worth to say that the full procedure has been performed using *Athena* release 15.5.3.9 (built project: AtlasTier0).

7.4.2 Alignment performance

As was discussed in the section 7.3.3, aligning the full silicon tracker using just cosmics has its problems and limitations, specially at the end-caps because the small cross section of the end-cap modules to record cosmic ray (leading a very low statistics in those regions). To cure some of these problems and limitations collision data must be used (and also beam halo tracks, etc...) as has been preliminary done.

This section will give a comparison between the *Cosmic08 alignment* (which has been the staring geometry in this exercise) and the new alignment derived using the first LHC collisions, i.e. *Collision09 alignment*. In both cases, collision data is reconstructed. Since different statistics have been used to construct each alignment set, plots are normalized to the number of tracks which have passed the quality cuts to allow comparisons.

The average number of hits have uniform behaviour with respect ϕ for both alignment sets but differences appear with respect η. Figure 7.26 shows the average number of Pixel and SCT hits as a function of η. These plots show that the barrel region remains practically the same (as expected) and that the new alignment introduces a big improvement in the SCT end-caps, specially in end-cap C ($\eta < -1.1$ region).

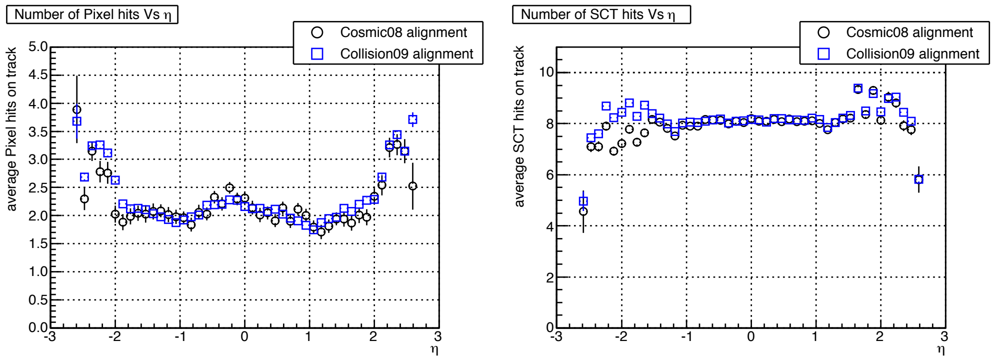

Figure 7.26: *Average number of Pixel and SCT hits as a function of η. Circles represent the* Cosmic08 alignment *while the squares represent the* Collision09 alignment.

Figure 7.27 takes a closer look to the number of hits for each silicon substructure. It can easily seen that the SCT end-caps have recovered missing hits on track, specially on the SCT end-cap C, where disc 4 was known to be misaligned. Moreover, with the new alignment, both SCT end-cap hit distributions are almost equal, as expected. On the other hand, the silicon barrel keeps almost the same distributions, with marginal improvements.

Figures 7.28, 7.29, 7.30 (a) and (b) show the biased residual distributions for some particular the Pixel and SCT end-cap discs, respectively, where initial and final alignment are shown together.

In the first two figures, it can be seen how the Pixel rϕ residuals are greatly improved for disc 1, being narrower with the *Collision09 alignment*. Distributions of the other Pixel end-cap discs look similar to disc 1. This could be expected as combined tracks (i.e. tracks with hits in the Pixel and SCT end-caps) produce now better residuals. This improvement will be commented later on.

Figures 7.30 (a) and (b) show the average of the biased residual distributions of disc 4 of the SCT end-cap A and C, respectively. The selected disc represents the general misalignment level of each SCT end-cap although it is, in fact, the most misaligned disc. From these figures, one can conclude that SCT end-cap A had, generally, better initial alignment (based on cosmic ray data) than SCT end-cap C (already known from section 7.3). After alignment, disc 4 is centered around zero (on average) and its performance is higher, specially for SCT end-cap C.

The improvement provided by the new alignment based on collisions can be seen much better in figures 7.31 and 7.32 where the mean and the width of the residuals for each individual module (side 0) are given as residual maps, using the *Cosmic08 alignment* (a) and the *Collision09 alignment* (b). The modules of these figures are assembled in disc4 of SCT end-cap C. Before the new alignment the residual maps show that just few modules have their residual distributions centered at zero and with widths narrower than 50 μm (black represents out of scale). After alignment, the opposite situation is given since most of the modules have their residuals centered around zero and with widths narrower than 40 μm. As already said, the results of this end-cap disc represents the general behaviour of both SCT end-caps.

Thus, generally, this preliminary alignment produces gaussian-like residual distributions cen-

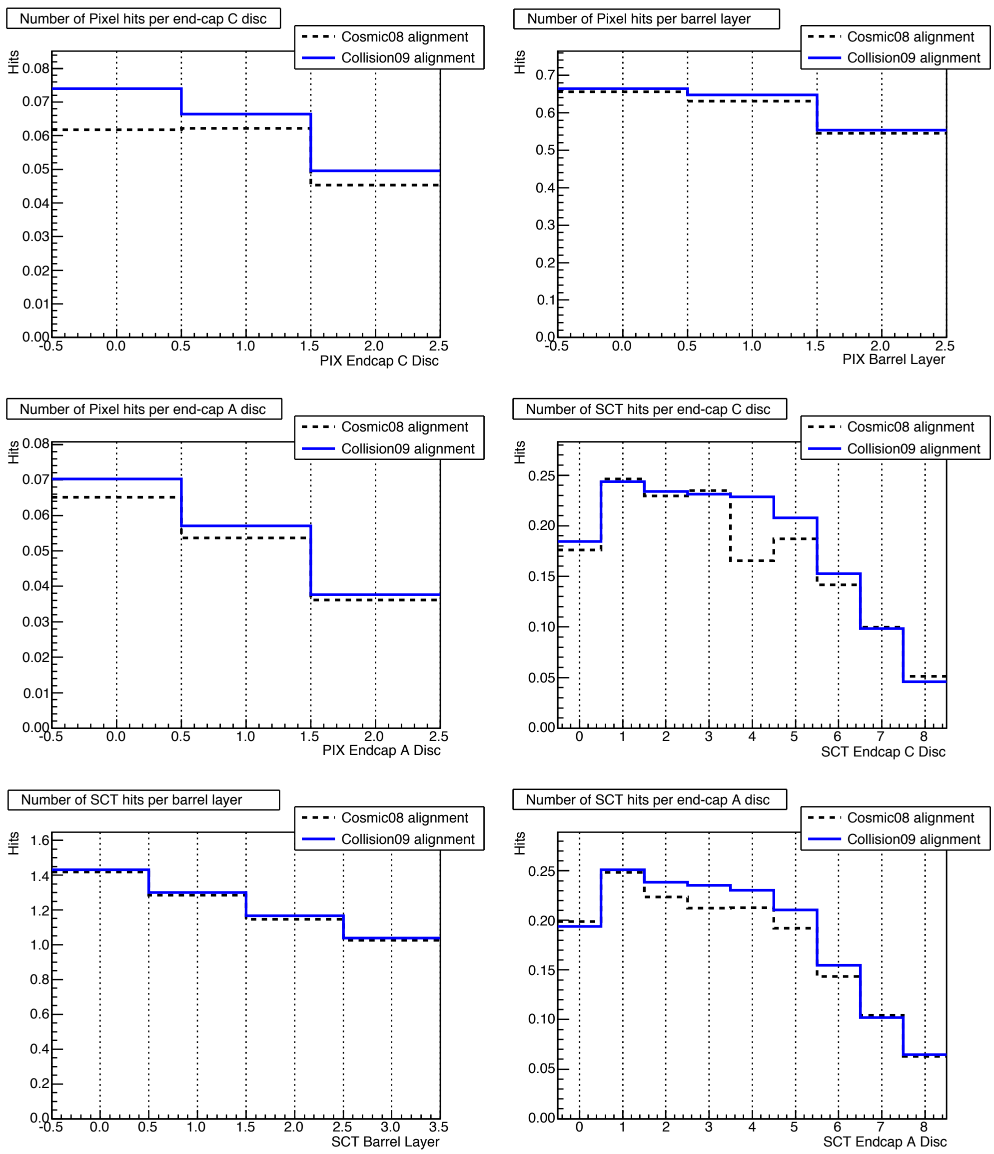

Figure 7.27: *Average of the number of hits per barrel layer or end-cap disc. Dash line represents the* Cosmic08 alignment *while the solid line represents the* Collision09 alignment. *A big improvement is observed at the end-caps, specially at SCT end-cap C. Plots are normalized to the number of track passing the quality cuts.*

tered around zero for both silicon end-caps though module level alignment was not attempted yet. Barrel residual distributions, which have not been shown, remain practically the same al-

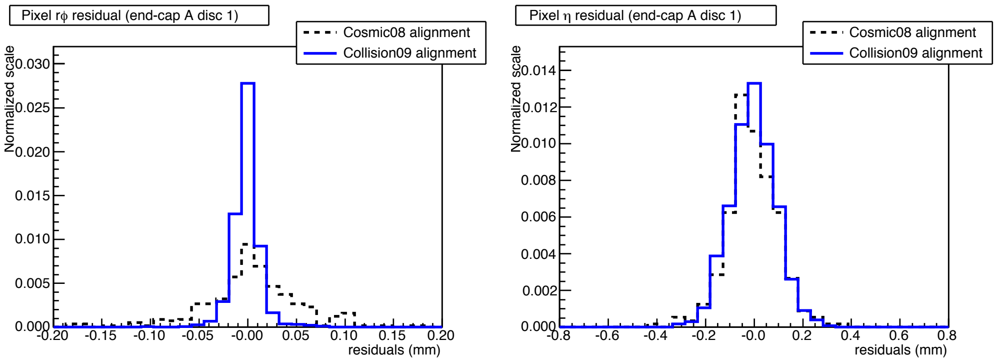

Figure 7.28: *Biased $r\phi$ and η residual distributions of the Pixel end-cap A disc 1. Dash line represents the* Cosmic08 alignment *while the solid line represents the* Collision09 alignment. *Plots are normalized to the number of track passing the quality cuts.*

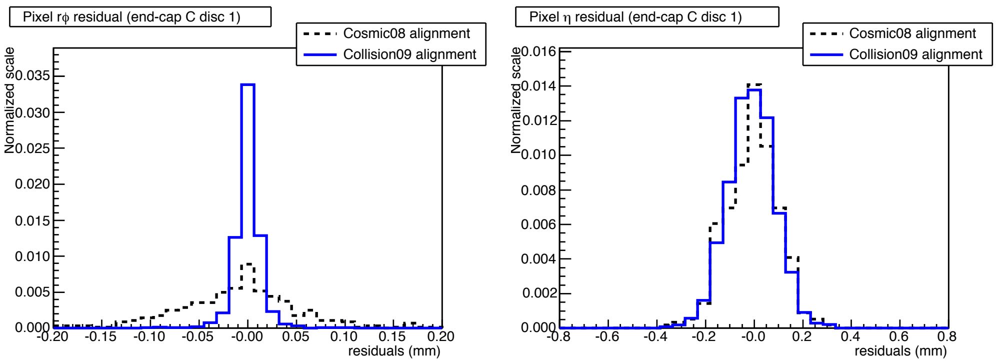

Figure 7.29: *Biased $r\phi$ and η residual distributions of the Pixel end-cap C disc 1. Dash line represents the* Cosmic08 alignment *while the solid line represents the* Collision09 alignment. *Plots are normalized to the number of track passing the quality cuts.*

though marginal changes have been introduced. This issue will be also discussed later on.

Anyhow, one knows that residual distributions as well as hit/track distributions should be accompanied and complemented with other distributions than can help to identify problems like wrong momentum reconstruction or other distortions. Although these issues are still under study and this alignment represents the first preliminary contact with real collision data, some distributions can be shown.

In such a way, figure 7.33 shows χ^2 distribution as a function of ϕ and η for both, the *Cosmic08 alignment* (circles) and the *Collision09 alignment* (squares). On the one hand, an uniform behaviour is shown over ϕ_0 in both cases, with slightly more flat shape for the collision based alignment. Larger error bars appear for the *Cosmic08 alignment* data because lower statistics was used in that case. On the other hand, the average value of the χ^2 as a function of η is lower

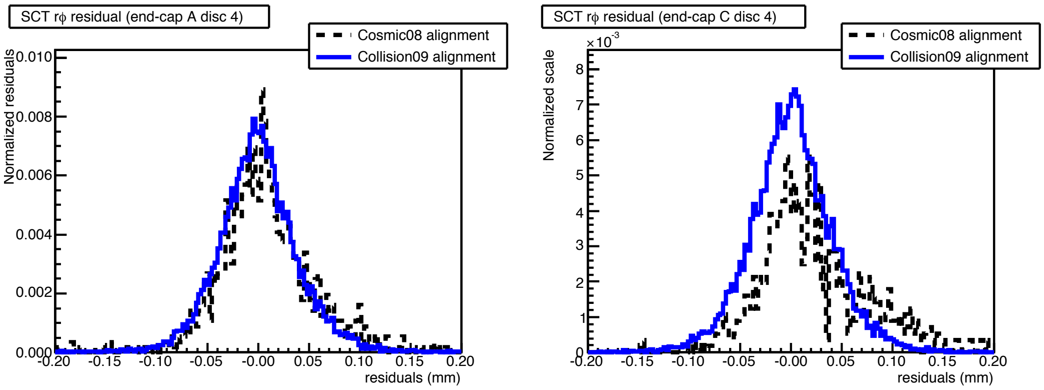

(a) *SCT end-cap A* (b) *SCT end-cap C*

Figure 7.30: *Biased residual distributions of disc 4 of the SCT end-cap A (a) and C (b). Dash line represents the* Cosmic08 alignment *while the solid line represents the* Collision09 alignment*. Plots are normalized to the number of track passing the quality cuts.*

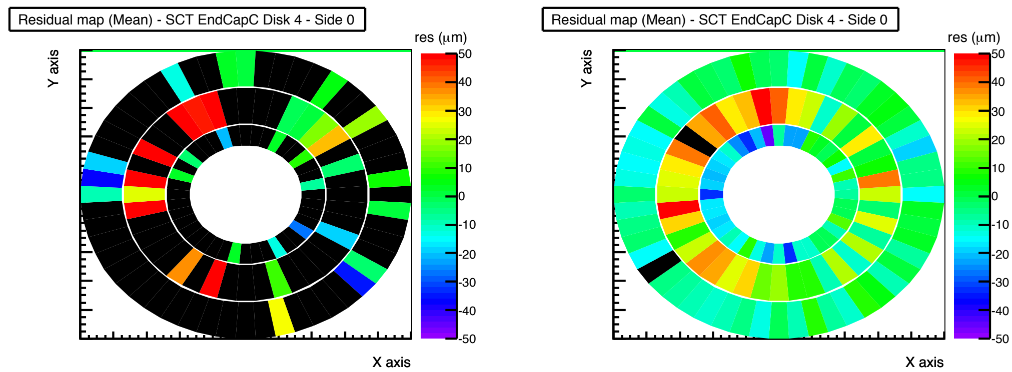

(a) *Using* Cosmic08 alignment (b) *Using* Collision09 alignment

Figure 7.31: *Residual maps showing the mean of each module for disc 4 of SCT end-cap C (side 0). Figure (a) gives the results using the* Cosmic08 alignment *while figure (b) gives the results using the* Collision09 alignment. *Black modules represent out of scale modules.*

for the *Collision09 alignment* . Moreover, the χ^2 is lower at the end-cap regions since an *error scaling* was introduced.

Finally, one important issue is to have a good momentum reconstruction performance. This

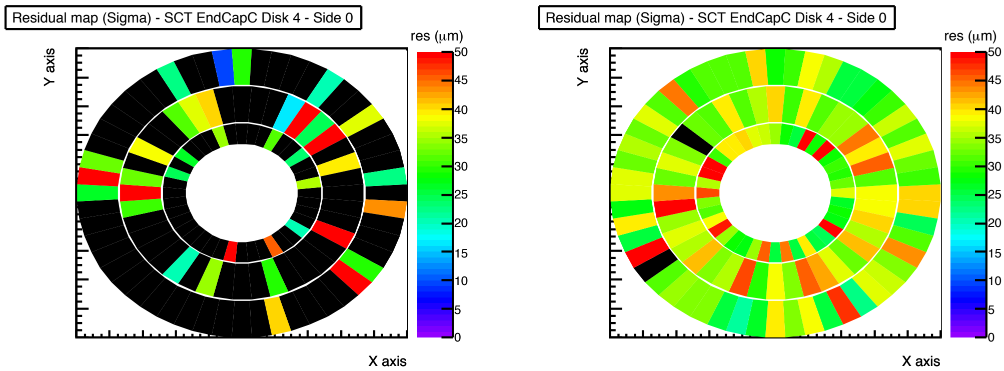

(a) *Using* Cosmic08 alignment

(b) *Using* Collision09 alignment

Figure 7.32: *Residual maps showing the width of each module for disc 4 of SCT end-cap C (side 0). Figure (a) gives the results using the* Cosmic08 alignment *while figure (b) gives the results using the* Collision09 alignment. *Black modules represent out of scale modules*.

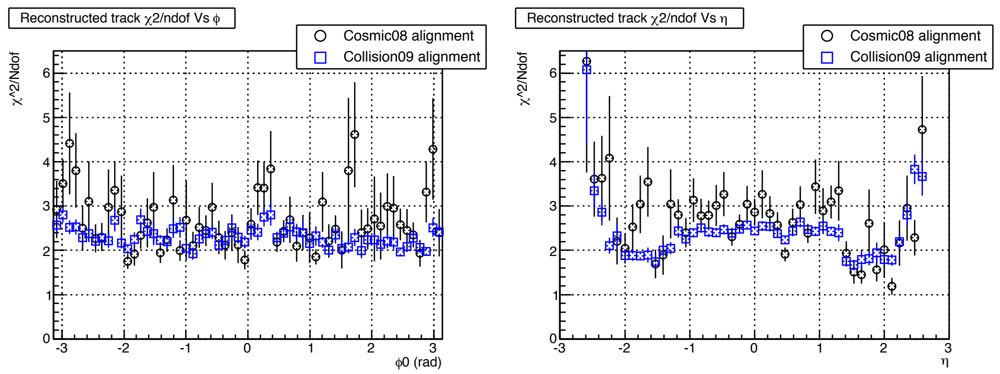

Figure 7.33: χ^2 *distribution as a function of* ϕ *and* η *for both, the* Cosmic08 alignment *(circles) and the* Collision09 alignment *(squares). Larger error bars appear for the* Cosmic08 alignment *data since lower statistics was used in that case. The* χ^2 *is lower at the end-cap regions since an* error scaling *was introduced for the residuals of those modules*.

performance is highly related with weak modes as it was discussed on section 6.2.4.3, which can be identify as dependences with ϕ. Thus, figure 7.34 shows the average of the transverse momentum as a function of ϕ for positive (left) and negative (right) tracks. Circles show the *Cosmic08 alignment* and how there is an asymmetry between negative and positive tracks. On the other hand, squares represent the *Collision09 alignment*. With the new constants, the average p_T peaks at 2 GeV/c in both cases (i.e. there is no offset) and it is also flat over ϕ in both cases, indicating that there is neither a clocking nor a sagitta distortion (at least at the momentum scale).

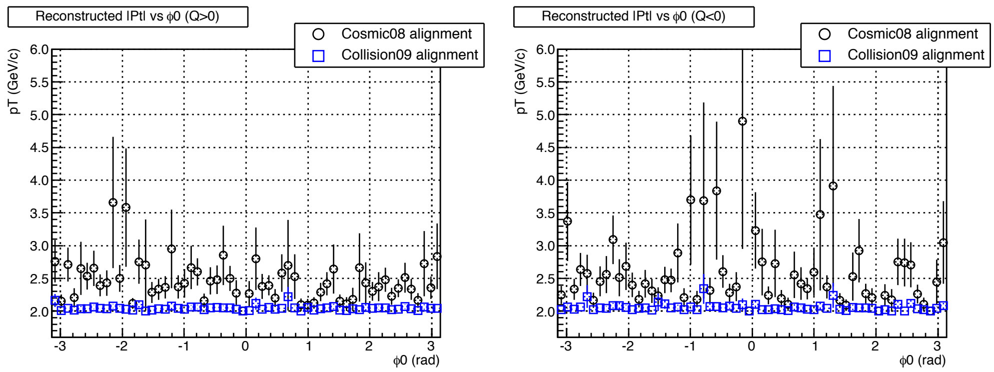

Figure 7.34: *Average of the transverse momentum as a function of ϕ for positive (left) and negative (right) tracks. Circles represent the* Cosmic08 alignment *while squares represent the* Collision09 alignment.

7.4.3 MC comparisons with minimum bias data

The alignment monitoring, i.e. the InDetAlignmentMonitoring package introduced in section 6.2.5, is studying the performance achieved by this preliminary alignment based on collision data. To enrich the study, it also adds a MC comparison where minimum bias events are reconstructed using a perfectly aligned geometry in order to estimate the goodness of this new alignment set and what is its performance.

Figure 7.35 shows the average unbiased rϕ residual distributions for the Pixel and SCT end-caps. In all of these plots, three results are shown: MC sample with perfect alignment (solid blue), collision data using the alignment based on cosmic rays (open black squares) and the actual preliminary alignment using collision data (open red circles). On the one hand, the first row shows that the Pixel end-cap performance can be improved compared with MC although in fact, end-cap C has really done it. It is easy to think that when a Pixel end-cap alignment is performed this residuals will be improved. On the other hand, the lower row, shows the SCT end-cap unbiased residual distributions. Comparing the new alignment with MC, one can conclude that there is still a residual misalignment, but comparing with the initial alignment a big improvement is observed, specially in end-cap C, as has been said before. Then, the new alignment leads, on average, unbiased residual widths of 28 μm for Pixels and ~ 86 μm for SCT end-cap modules. Comparing these numbers with MC, i.e. unbiased residuals of 24 μm for Pixels and ~ 46 μm for the SCT, the difference can be attributed to the lack of level 3 alignment of the end-cap module.

Moreover, figure 7.36 shows the barrel unbiased residuals for both, Pixel (a) and SCT (b). It can be observed that marginal differences exist between the previous and the new alignment in those distributions. As claimed before, this is expected as no silicon barrel alignment has been performed apart from a level 1, which has produced quite small corrections. Thus, the *Collision09 alignment* leads, on average, unbiased residual widths of 34 μm for the Pixel barrel

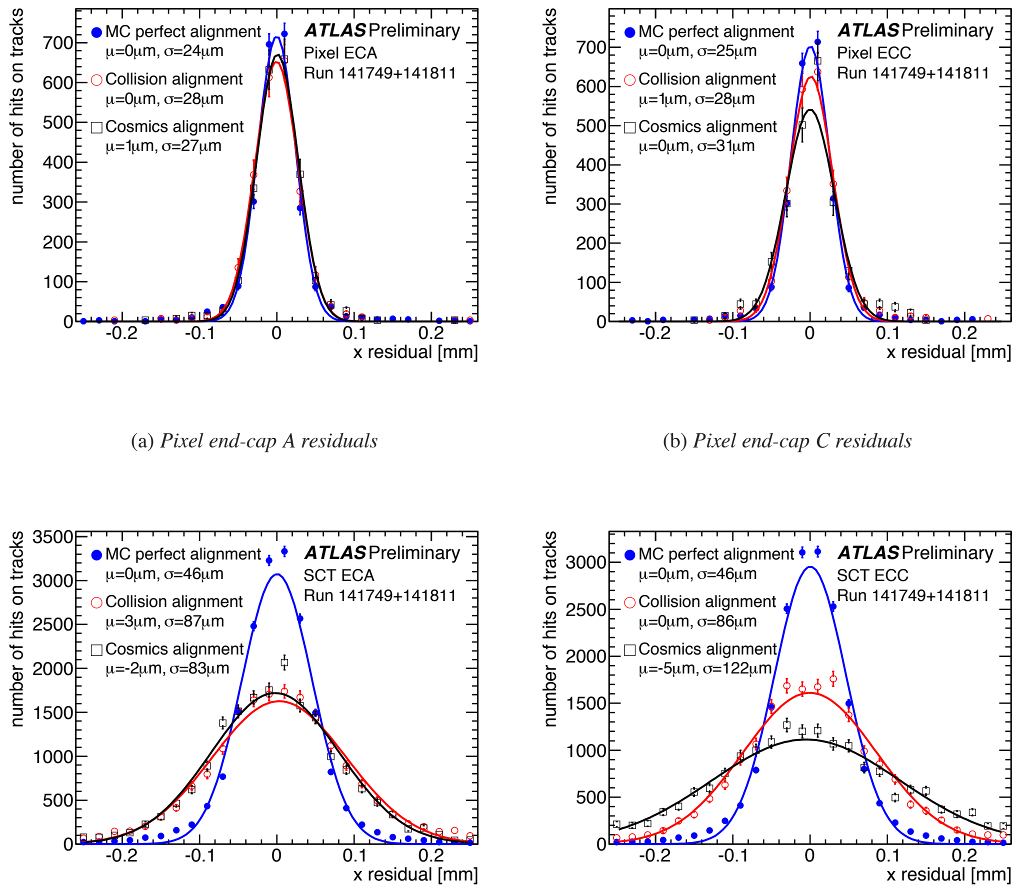

(a) *Pixel end-cap A residuals*

(b) *Pixel end-cap C residuals*

(c) *SCT end-cap A residuals*

(d) *SCT end-cap C residuals*

Figure 7.35: *Unbiased local x residuals (i.e. $r\phi$ residuals) for a minimum bias MC sample with perfect alignment (solid blue), collision data using the alignment based on cosmic rays (open black squares) and the actual preliminary alignment using collision data (open red circles) [118].*

and $\sim 43\ \mu m$ for SCT barrel modules while the perfectly aligned MC leads widths of 22 μm and $\sim 36\ \mu m$, for Pixels and SCT, respectively. This points to a necessary level 3 alignment.

Hit efficiency studies are on going using all the runs with stable beams, comparing them also with MC. They show that the SCT end-cap C has been really improved but as they are too preliminary they will not be shown here. More information can be found on reference [117].

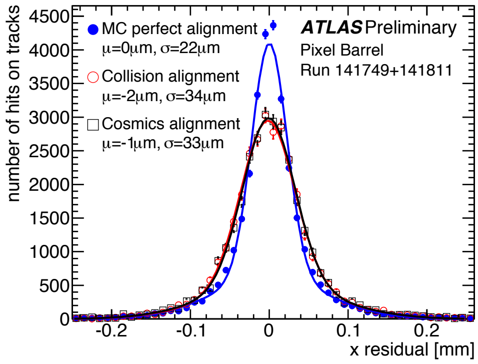

(a) *Pixel barrel residuals*

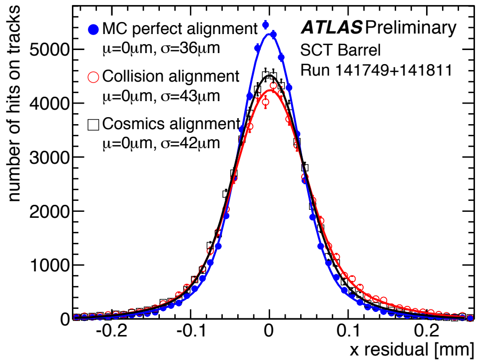

(b) *SCT barrel residuals*

Figure 7.36: *Pixel (a) and SCT (b) barrel local x residuals (i.e. $r\phi$ residuals) for a minimum bias MC sample with perfect alignment (solid blue), collision data using the alignment based on cosmic rays (open black squares) and after a first update using collision data (open red circles) [118].*

7.4.4 Beam spot reconstruction

Finally, it is worth to mention that the beam spot is also being reconstructed as the average mean and width of the primary vertices distributions and monitored either online (within the L2 HLT algorithms) and offline. Figure 7.37 illustrates the reconstruction of the primary vertices for a given luminosity block using events with more than two tracks. The beam spot position is given at (-0.215, 1.066, 1.05) mm in the global frame with a width of (0.335, 0.428, 1.05) mm [118]. It has been also seen small drifts of the beam spot within a given run. These shifts are just of tens micrometers, which in fact is already a very good sign of the stability of the beams.

7.4.5 Early physics with first collisions

Even first basic physics results have appeared with the first LHC collision candidates such as: electron/gamma conversion studies, jet reconstruction and missing energy studies, kaon mass analysis, etc...

Then, to summarize one can say that this early and preliminary alignment using collision data have produced large improvements over the kick-off alignment which was based on cosmic rays. These results suggest a very promising and high quality alignment of the ATLAS Silicon Tracker based on the Globalχ^2 algorithm, in a near future.

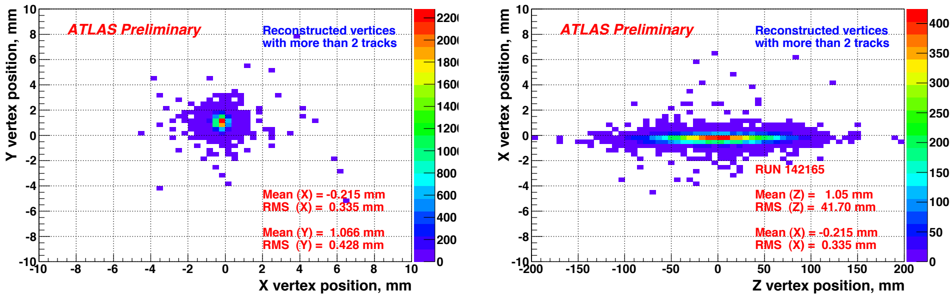

(a) *Reconstructed primary vertices (XY plane)* (b) *Reconstructed primary vertices (XZ plane)*

Figure 7.37: *XY (a) and XZ (b) distributions of the reconstructed primary vertices for the run 142165. The p_T cut for incoming tracks is lowered to 100 MeV to have enough statistics. Tracks contributing less than χ^2 value of 15 (per two degrees of freedom) to the reconstructed vertex are accepted to the fit. The beam spot position is given at (-0.215, 1.066, 1.05) mm with a width of (0.335, 0.428, 1.05) mm [118].*

7.5 Conclusions

This chapter has presented the alignment results and achievements using real cosmic ray data and even the first LHC collision data at 900 GeV. It has been discussed how the SR1 test in 2006 was the first testbed of the Globalχ^2 algorithm with real data, although this data was cosmic rays and just the SCT barrel was used. The alignment convergence was shown and the residual distributions were improved, giving widths of $\mathcal{O}$ (50) μm. In addition, performance studies revealed that the hit efficiency was within specifications after alignment (>99%).

It was also extensively discussed the cosmic ray data taking periods during the ATLAS commissioning in 2008 and 2009. During these periods the ATLAS software and hardware chains were fully exercised. The alignment model was also tested and the two alignment set of constants were derived based on cosmic rays and one of these sets was used to reconstruct the first tracks produced by LHC collisions in December 2009. Both sets were produced starting from the detector survey measurements although using different number of events and magnets configurations as well as different alignment strategy. In parallel, a detailed MC simulation was also performed, considering ATLAS on its cavern, 100 m below the surface. Anyhow, simulation of the exact operation conditions was not achieved. On the other hand, it was the first time that the geometry level hierarchy model was used in the alignment procedure using real data and it produced very good results. The alignment performance provided large improvements on the residual distributions, specially in the barrel region, leading residuals widths of $\mathcal{O}$ (24) μm for Pixels and $\mathcal{O}$ (30) μm for the SCT. Individual module corrections were performed, revealing stave bows in the Pixel barrel and showing a good Globalχ^2 performance. A poor alignment was observed and verified at the edges of the barrel and at the end-caps. This feature was anticipated and it is just due to the incident angle of the cosmic rays over the modules and the poor illumination of the end-cap discs. But, as it has been emphasized in this thesis, a combination of different track topologies must be used in order to provide the best alignment performance without the presence of weak modes.

Finally, the first attempt to improve the existing alignment using LHC collision data was performed and although it consisted in a preliminary exercise, the SCT end-cap disc alignment had a spectacular improvement. The achieved performance proved that the near future Silicon Tracker alignment based on collision data and using the Globalχ^2 algorithm is very promising.

8
Top quark reconstruction

This and the following chapters summarize the top quark mass analysis performed for this thesis, with the novelty of introducing the Globalχ^2 algorithm for the fit. The work presented here has been based on fully simulated data within the CSC challenge [7] assuming 1 fb^{-1} of accumulated data at low luminosity (10^{33} cm^{-2} s^{-1}) and at the nominal LHC energy ($\sqrt{s}$ = 14 TeV). Moreover, the semileptonic decay channel of the $t\bar{t}$ pair has been used since it constitutes the best compromise between a high branching ratio ($\sim 44\%$) and a high signal over background ratio as the lepton of the final state, which is relatively easy to trigger experimentally, allows a good rejection of the QCD background.

8.1 Introduction

The top quark was discovered by the Tevatron experiments, CDF and DØ, at Fermilab in 1995 [119] [120]. Hence, with the discovery of the most massive of known elementary particles and with the later discovery of the ν_τ in summer of 2000 by the DONUT collaboration (also at Fermilab) [121], the three generation structure of the SM was directly observed and therefore finally completed. From that moment, the top quark physics was born. In principle one can see the top quark as just another SM quark. However the top quark appears to be a rather interesting species because of its large mass which is intriguingly close to the scale of EW symmetry breaking. Moreover, it interacts primarily by the strong interaction (QCD) but it can only decay, as the rest of the quarks, through the weak force since it is the only interaction that allows flavour changing. In addition, due to the fact that its lifetime is roughly short, $5 \cdot 10^{-25}$ s (SM prediction), i.e. it is about 20 times shorter than the timescale of the strong interaction, it decays before hadronizing.

In the SM, the relevant CKM coupling V_{tb} is already determined by the (three-generation) unitarity of the CKM matrix and the Branching Ratio (BR) of the top quark decay channels:

$BR(t \to Wb)/BR(t \to Wq) = |V_{tb}|^2$. And the predicted BRs of the top quark decays are: $BR(t \to Wd) \approx 0.006\%$, $BR(t \to Ws) \approx 0.17\%$ and $BR(t \to Wb) \approx 99.9\%$. The later is therefore the golden decay.

Despite the large top quark mass (~ 35 times larger than the bottom quark), the key issue is that the its mass is of the same order of the scale of EW symmetry breaking which raises a number of interesting theoretical questions:

- Is the top quark mass generated by the Higgs mechanism as predicted by the SM?
- Does the top quark play a fundamental role in the EW symmetry breaking mechanism?
- If there are new particles lighter than the top quark, does the top quark decay into them?
- Could non-SM physics first manifest itself in non-standard couplings of the top quark which show up as anomalies in top quark production and decays?

Precise top quark mass measurements will constrain the Higgs boson mass and will increase the sensitivity to physics beyond the SM. Therefore, an important tool for testing the consistency of any theory (SM or its extensions) consists in comparing the measurements of the EW precision observables with the theoretical predictions provided by the model under consideration. In particular, the top quark mass (M_t) enters the EW precision observables via powers of M_t, contrary to the other particles of the SM which provide lower contributions. In particular, M_t is related to the W boson mass (M_W) via radiative corrections ($\Delta\mathcal{R}$) [122]:

$$M_W = \left(\frac{\pi\alpha}{\sqrt{2}G_F}\right)^{1/2} \frac{(1-\Delta\mathcal{R})}{sin\theta_W} \tag{8.1}$$

At one loop order, $\Delta\mathcal{R}$ is quadratic in M_t via a term proportional to M_t^2/M_Z^2 while its dependence on the Higgs mass is only logarithmic via a term proportional to $\log(M_H/M_Z)$. Therefore, an accurate measurement of the top quark mass is required to provide tighter constraints on the W boson mass and the weak mixing angle θ_W which are already very precisely measured. Moreover, the precise knowledge of both M_t and M_W leads to a theoretical mass window for the still hypothetical Higgs boson and additional contributions to $\Delta\mathcal{R}$ arise in various extensions of the SM (SUSY, etc...).

Of course, the study of the quark properties will give answers to these questions. Up to now, several properties of the top quark have already been examined at the Tevatron which include studies of the kinematical properties of top production, the measurements of its mass [9], of its production cross section [123], the reconstruction of $t\bar{t}$ pairs in the fully hadronic final states, the study of τ decays of the top quark, the reconstruction of hadronic decays of the W boson from top decays, the search for flavour changing neutral current (FCNC) decays, the measurement of the W helicity in top decays and bounds on $t\bar{t}$ spin correlations. Anyhow, Tevatron measurements are limited by the statistics and this is why it will pass the baton to the LHC.

In hadron colliders the top quark are predominantly produced through strong interactions: gluon-gluon and quark-antiquark annihilation. The Feynman diagrams at tree level of the $t\bar{t}$ pair production modes can be seen in figure 8.1. As the relative importance of both amplitudes depends on the center of mass energy of the collision and on the nature of the beams, at the Tevatron, $t\bar{t}$ pairs are produced predominantly through quark-antiquark annihilation (85%) while the gluon-gluon fusion is much less probable (15%). On the contrary, at the LHC, $t\bar{t}$ pairs will be mainly produced by gluon-gluon fusion (90%) while the quark-antiquark annihilation has a very lower probability (10%).

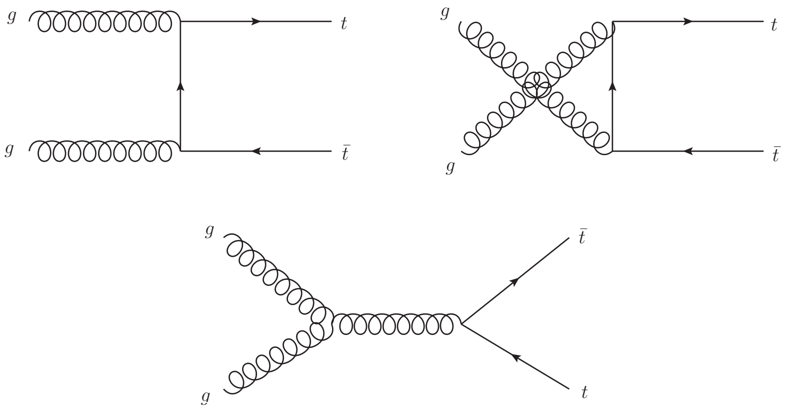

(a) *gluon-gluon fusion: $gg \to t\bar{t}$*

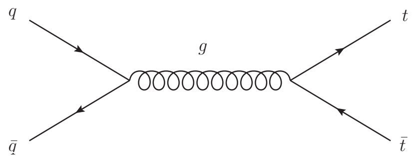

(b) *quark-antiquark annihilation: $q\bar{q}' \to t\bar{t}$*

Figure 8.1: *Feynman diagrams at tree level for the $t\bar{t}$ pair production modes. At the LHC, the $t\bar{t}$ pair production is expected (from SM predictions) predominantly by gluon-gluon fusion (90 %) while the quark-antiquark annihilation mode has lower probability (10%).*

The LHC will be a top factory when operates at 14 TeV. At low luminosity (10^{33} cm^{-2} s^{-1}) and with an integrated luminosity of 10 fb^{-1}, a cross section of ~ 800 pb, ~ 8 million $t\bar{t}$ pairs will be produced. Therefore one can expect that top quark properties may be studied with significant precision at the LHC. Since numerous single (anti-)top quark events are produced via EW interactions, the top quark properties, such as the V_{tb} coupling, will be examined with high precision during the first years of LHC running. Entirely new measurements can be contemplated on the basis of the large available statistics.

From the empirical point of view, the understanding of the experimental top quark event signatures involves most parts of the ATLAS detector and even a very good alignment (due to its impact on b quark identification). Consequently, it is essential to achieve a good understanding of the top event reconstruction in order to perform high precision measurements and claim potential discoveries of new physics. The present and the following chapter of thesis have two goals: firstly, introduce the Globalχ^2 algorithm to measure the top quark mass and secondly, contribute to the studies of the ATLAS potential by measuring the top quark mass with high precision.

8.1.1 Top quark mass

For the time being, real top quarks are produced in the proton-antiproton collisions delivered by the Tevatron collider at center of mass energies of $\sqrt{s}$ = 1.96 TeV during the Run 2. At the end of the year 2008, this collider delivered an integrated luminosity of 5.5 fb^{-1} and its two experiments, CDF and DØ, collected 4.5 fb^{-1} and 4.7 fb^{-1} respectively. From the combination of the latest top quark physics analyses which considered an integrated luminosity of 3.6 fb^{-1} it has been established that the current measurement of the top quark mass is M_t = 173.1 $\pm$ 0.6 (stat.) $\pm$ 1.1 (syst.) GeV/c^2 [9] (using combined data from CDF and DØ). Adding these errors in quadrature yields a total uncertainty of 1.3 GeV/c^2 which corresponds to a relative precision ($\Delta M_t/M_t$) of 0.75% on the top quark mass. Figure 8.2 shows the history of the top quark mass measurements from combined studies within the Tevatron experiments, i.e. CDF and DØ.

From MC studies within the CSC challenge [7], the total expected uncertainty in ATLAS with 1 fb^{-1} of integrated luminosity is of the order of 1 to 3.5 GeV/c^2, assuming an uncertainty on the jet energy scale of 1 to 5%.

The $t\bar{t}$ cross section calculated at the Next to Leading Order (NLO) including Next to Leading Logarithm (NLL) soft gluon resummation at the LHC nominal energy (i.e. $\sqrt{s}$ = 14 TeV) is $\sigma_{t\bar{t}} = 833 \pm 100$ pb [124] (a factor ~ 100 larger than at the Tevatron which is O(7 pb); for precise quotations consulte reference [125] [126] [127]), where the uncertainty reflects the theoretical error obtained from varying the renormalisation scale by a factor of two [128]. Therefore, it is going to be possible to collect large samples of $t\bar{t}$ pairs at the LHC as has been spotted before. In order to minimize the statistical uncertainty, earlier measurements of the mass concentrated on preserving as much of the signal as possible, then, stringent requirements can be imposed to the signal. In this way one can restrict the measurement to regions in which the systematic uncertainties can be under control. It is expected that with 1 fb^{-1} of data, the measurement will already be completely dominated by systematic uncertainties O(1 GeV) [7]. The dominant contribution to the systematic uncertainty of the mass measurement is expected to be the Jet Energy Scale (JES). In-situ calibration methods will allow the light jet energy scale to be known to the percent level precision after 1 fb^{-1} of collected data. This high precision can be partially translated to the b-jet energy scale. Detailed studies with LHC data will be necessary to reach the desired precision.

Usually the top quark mass measurements are based on kinematic studies and in trying to find the peak in the invariant mass distribution of the final state products: W boson decay particles and a b-jet, coming from the hadronization of a b quark. This closely corresponds to the pole mass of the top quark. Because of fragmentation effects, it is believed that the top quark mass determination in a hadronic environment is inherently ambiguous by an amount proportional to Λ_{QCD} (i.e. O(100 MeV)). In addition, it is also possible to measure the top quark mass from the $t\bar{t}$ production cross section, allowing a better theoretical definition of the energy scale and of the theoretical uncertainties.

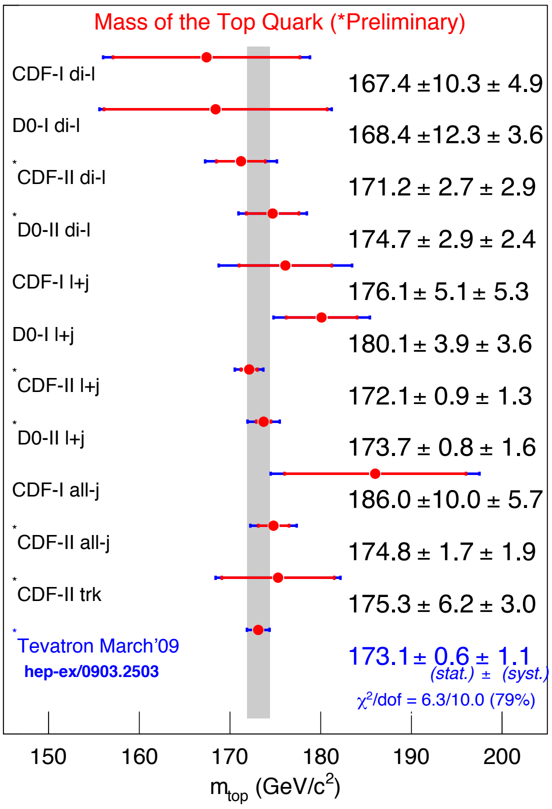

Figure 8.2: *Top quark mass measurements history from combined studies within CDF and DØ experiments. The latest result is achieved using the data from both experiments and it represents, up to now, the current top quark mass value [9].*

8.1.2 First Measurements and Possible Discoveries

Before ATLAS can realise its discovery potential, the SM must be "rediscovered" in the LHC environment. As it is shown in table 8.1, the rates for the W, Z and $t\bar{t}$ production (with lepton plus jets decay) processes (so-called "standard candles") will be far higher at the LHC compared to previous and existing machines. These processes will allow the initial performance of ATLAS to be quickly improved towards the design limits, but of course once the detector has been understood in terms of alignment, calibration and performance.

The LHC expectations in the first year of data taking are quite modest as the LHC will not be at its design potential. According to the current schedule, the LHC accelerator started its operations at 450 GeV per beam (i.e. $\sqrt{s}$ = 900 GeV). It is expected that $\sqrt{s}$ = 7 TeV will be the collision energy during 2010 and 2011. A beam energy of 7 TeV means that the $t\bar{t}$ cross section will be reduced by more than half of the one estimated for 14 TeV. In fact, the estimated $t\bar{t}$ cross section at 7 TeV is ~ 170 pb^{-1} [129]. This applies roughly to all background processes

Process	Events/100 pb^{-1}	Total events from LEP/Tevatron
$Z \to e^+e^-$ $Z \to \mu^+\mu^-$	$\sim 10^5$	$\sim 10^6$ LEP $\sim 10^5$ Tevatron
$W \to e\nu$ $W \to \mu\nu$	$\sim 10^6$	$\sim 10^4$ LEP $\sim 10^6$ Tevatron
$t\bar{t}$ (lepton plus jets decay)	$\sim 10^4$	$\sim 10^4$ Tevatron

Table 8.1: *Number of W, Z and $t\bar{t}$ (lepton plus jets decay) events expected in ATLAS with the first 100 pb^{-1} of data, which would correspond to just a few days of data taking at low luminosity (10^{32} cm^{-2} s^{-1}). For comparison, the total statistics available from LEP and Tevatron are also shown.*

as well.

Although we are currently working with simulations within this early environment [130], all the studies presented in this thesis were carried out at the design LHC energy ($\sqrt{s}$ = 14 TeV) and low luminosity (10^{33} cm^{-2} s^{-1}) as the present studies are based on the CSC simulations [7].

The expected performance on day one of nominal LHC operation are shown on Table 8.2. From the ID alignment point of view, the alignment constants used will come from cosmic data, beam gas/halo events, or from a combination of them [131], so these measurements are somehow related with the results from chapter 6. Calorimeter calibrations will also used cosmics together with physics samples such us $Z \to \ell\ell$ while the JES will use physics samples such as $W \to jj$, $\gamma + jets$, di-jets and multi-jet events. In fact, at the end, collision data at 7 TeV will be used to optimize the detector calibration for higher energy collision data.

System	Expected precision on day "1"
Tracker alignment	$\mathcal{O}(20)$ μm in $r\phi$ (barrel region)
ECAL uniformity	1-2%
Electron energy scale	$\sim 2\%$
HCAL uniformity	$\sim 2\%$
Jet energy scale	$< 10\%$

Table 8.2: *ATLAS detector performance at LHC start-up.*

With this preliminary performance ATLAS should measure the Z and W cross sections to about 10% with 100 pb^{-1} of data, dominated by the uncertainty on the luminosity. Another early measurement will be the top quark mass and $t\bar{t}$ production cross section through the lepton plus jets channel $t\bar{t} \to b\ell\nu_\ell bjj$ where ℓ means a lepton (i.e. $\ell = e$ or μ (see section 8.2.1)) and ν_ℓ (or just ν) means the neutrino (the subscript denotes the lepton flavour). This channel benefits from the high trigger efficiency accompanying the isolated charged lepton coupled with a small QCD background compared to the fully hadronic (multijet) channel. A simple analysis can be performed even with an imperfect detector, without requiring b-tagging (see performance without b-tagging in reference [7]), by selecting events with an isolated electron or muon, missing transverse energy[1] (E_T^{miss}) and exactly four jets, two of which must have an invariant mass compatible with the W mass. Simply plotting the invariant mass of the three jets with the largest p_T should reveal a clear top signal in 100 pb^{-1} of data, with the mass and cross section measured with 20% uncertainty, dominated by the luminosity measurement and the jet energy scale resolution. Moreover, the $t\bar{t}$ events will be used to improve the jet energy scale using the $W \to jj$ component of the events.

Whilst the early data has an invaluable role to play in the detector commissioning, it should not be forgotten that the very first LHC collisions represent uncharted territory, where new discoveries are waiting to be made. For example, there is currently significant disparity between the different models (PYTHIA, PHOJET, etc...) describing "minimum bias" events at LHC energies. A sample of 10^4 events, representing just a few hours of data taking at low luminosity, would provide adequate statistics to discriminate between the different models. Also, earlier top quark mass measurements will contribute significantly to the SM Higgs hunting through EW precision tests as was commented in chapter 1. In fact, this is one of the motivation to perform precise top quark mass measurements. Figure 8.3 shows the correlation between the top quark mass and the Higgs mass. The solid line represents the allowed correlation from the SM fit at 65% CL using High-Q^2 results (i.e. results from LEP, SLC and Tevatron) [10]. Moreover, experimental excluded regions (at 95% CL given by direct searches) by LEP ($M_H <$ 114 GeV/c^2) [132] and Tevatron ($160 < M_H < 170$ GeV/c^2) [13] are shown together with the latest Tevatron measurement on the top quark mass.

Finally, even hints of SUSY could appear with as little as 100 pb^{-1} of data, though here, as well as in the search for the Higgs boson, considerably more time will be required to control the backgrounds.

8.2 Top quark event reconstruction

This section will define the "signal" topology to measure the top quark mass and the physics backgrounds which have the same final state objects.

8.2.1 Top decays

The top quark decays almost exclusively (>99%) to a W boson plus a b quark. Then, as the b quark will always hadronize generating a jet of particles, the top quark decay classification at Leading Order (LO) (i.e. at tree level) will depend on the W boson decay mode (hadronically $W \to q\bar{q}'$ where the two resulting quarks have different flavour or leptonically $W \to \ell\nu_\ell$ where both have the same flavour) and this classification will be the same for t and $\bar{t}$. Obviously, NLO corrections as well as Initial State Radiation (ISR) and Final State Radiation (FSR) will modify the final event topology because of the gluon radiation and additional jet production. However a simple classification is proposed. Moreover, this LO classification is done irrespectively of the

[1]The missing transverse energy E_T^{miss} is computed summing all the measured energy deposits:

$$E_T^{miss} = \sqrt{\left(\sum E_T cos\phi\right)^2 + \left(\sum E_T sin\phi\right)^2}$$

where E_T is the energy in the transverse plane to the beam direction and ϕ is the azimuthal angle.

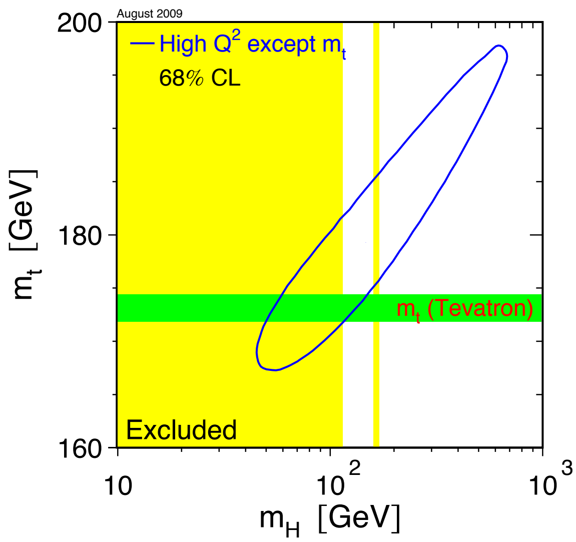

Figure 8.3: *Consistency SM test where the correlation between the top quark mass and the Higgs mass is shown [10]. The solid line represents the allowed correlation from the SM fit at 65% CL using High-Q^2 results. Moreover, lower (LEP: M_H < 114 GeV/c^2) and upper (Tevatron: 160 < M_H < 170 GeV/c^2) experimental excluded regions are shown together with the latest Tevatron measurement on the top quark mass.*

quark flavour. Thus, one can divide the $t\bar{t}$ events (based on the final state objects) into three main channels whose tree level Feynman diagrams can be seen on figure 8.4:

1. **Dileptonic:** $2\ \ell + 2\ \nu + b\bar{b}$ (producing two b-jets). This mode is quite clean and in principle can be easily identified by requiring two high p_T leptons and the presence of missing transverse energy (E_T^{miss}). However, its main problem is due to the two neutrinos at the final state which limit the reconstruction efficiency and performance of ATLAS to measure the top quark mass.

2. **Semileptonic:** $1\ \ell + 1\ \nu + b\bar{b}q\bar{q}'$ (i.e. producing the light quarks[2] two light jets and the b quarks two b-jets). The presence of just one high p_T lepton in the final state allows to suppress the QCD background. Moreover, this channel is quite easy to trigger due to its lepton.

3. **Fully hadronic:** $b\bar{b} + q\bar{q}' + q''\bar{q}'''$ (i.e. producing four light jets and two b-jets). In this case, there are no leptons to trigger on, and the signal is not easily distinguishable from the abundant SM QCD multijets production, which is expected to be orders of magnitude higher than the signal (before any selection cuts). Furthermore, from the technical

[2] The "light quark" term refers the u, d, c or s quarks.

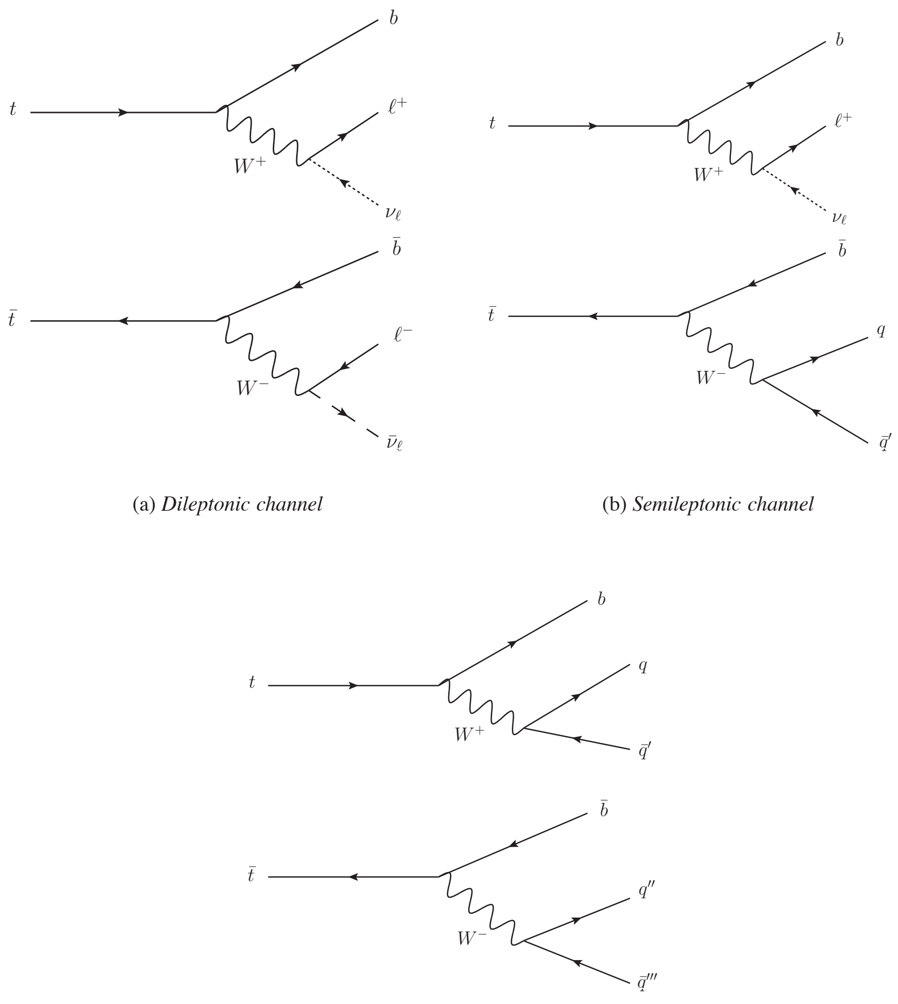

(a) *Dileptonic channel* (b) *Semileptonic channel*

(c) *Fully hadronic*

Figure 8.4: *Feynman diagrams at tree level of the top-antitop pair decay modes. These channels are classified irrespectively of the quark flavour.*

point of view, the presence of a high combinatorial background (see section 8.2.4 for the definition) is another challenging problem for the reconstruction of the top quark mass.

On the one hand, the W^- boson may decay into $e^-\nu, \mu^-\nu, \tau^-\nu$, $3 \times u\bar{d}$ and $3 \times c\bar{s}$ (being the "3" factor due to the degree of freedom of the color charge). On the other hand, the W^+ boson decay into the conjugate modes. Then, each charged W boson has 9 decay modes and combining these modes one has $9 \times 9 = 81$ as figure 8.5 illustrates. In principle, since the W boson mass is larger than sum its product masses, these channels have the same decay probability as it is shown in table 8.3. Kinematic corrections, due to the difference of the product masses, do not change significantly the BRs.

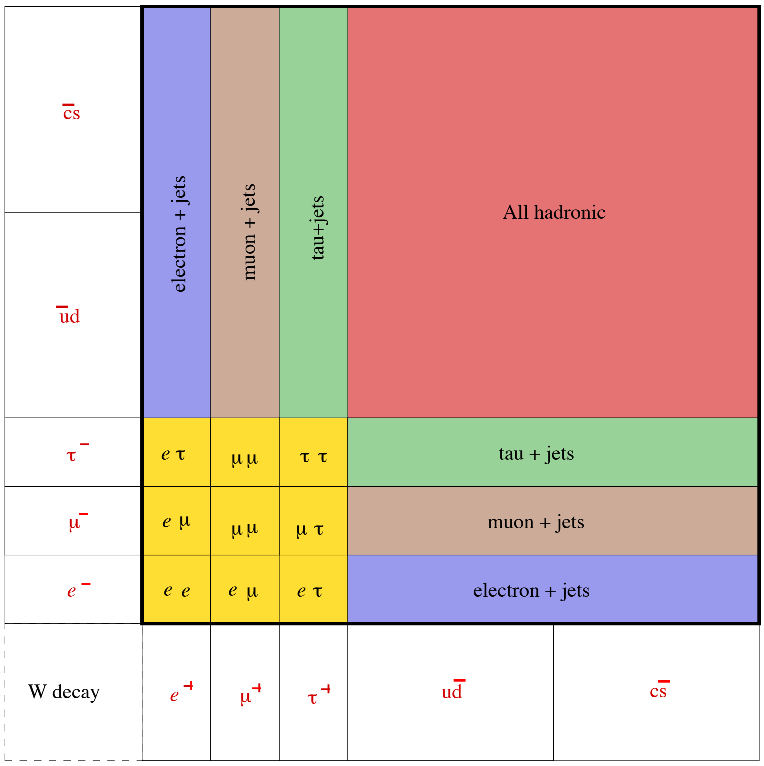

Figure 8.5: *Graphical representation of the $t\bar{t}$ decay channels.*

It is worth to say that the τ-dileptonic decay channel is somewhat special as the τ lepton decays hadronically or leptonically, so then the final state objects change.

Finally, considering that total $t\bar{t}$ cross section at $\sqrt{s} = 14$ TeV is 833 pb (see section 8.1.1) and considering each decay channel probability, i.e. their BRs, the cross sections for the different channels can be estimated. Thus, the considered cross sections for the different channels are in table 8.4.

8.2.2 Semileptonic signal

The channel selected to be studied in this thesis has been the semileptonic decay channel, i.e. $t\bar{t} \to \ell\nu$ + jets where ℓ is e, μ or τ. It is the most promising channel since it constitutes the best compromise between a high BR ($\sim 44\%$) and a high signal over background ratio as the lepton of the final state, which is relatively easy to trigger experimentally, allows a good rejection of

Category	Decay Mode	Branching Ratio (BR)	
e/μ- Dileptonic	$t\bar{t} \to e\nu_e b\ e\nu_e\bar{b}$	1/81	4/81 (~ 5%)
	$t\bar{t} \to \mu\nu_\mu b\ \mu\nu_\mu\bar{b}$	1/81	
	$t\bar{t} \to e\nu_e b\ \mu\nu_\mu\bar{b}$	2/81	
τ- Dileptonic	$t\bar{t} \to e\nu_e b\ \tau\nu_\tau\bar{b}$	2/81	5/81 (~ 6%)
	$t\bar{t} \to \mu\nu_\mu b\ \tau\nu_\tau\bar{b}$	2/81	
	$t\bar{t} \to \tau\nu_\tau b\ \tau\nu_\tau\bar{b}$	1/81	
Semileptonic	$t\bar{t} \to e\nu_e b\ q\bar{q}'\bar{b}$	12/81	36/81 (~ 44%)
	$t\bar{t} \to \mu\nu_\mu b\ q\bar{q}'\bar{b}$	12/81	
	$t\bar{t} \to \tau\nu_\tau b\ q\bar{q}'\bar{b}$	12/81	
Fully hadronic	$t\bar{t} \to q\bar{q}'b\ q''\bar{q}'''\bar{b}$	36/81	36/81 (~ 44%)

Table 8.3: *Top quark pair decay channels.*

Category	Decay Mode	Estimated cross section (pb)
$t\bar{t}$	$t\bar{t} \to Wb\ Wb$	833
Dileptonic ($\ell = e, \mu$ or τ)	$t\bar{t} \to \ell\nu_\ell b\ \ell\nu_\ell\bar{b}$	92
Dileptonic ($\ell = e$ or μ)	$t\bar{t} \to \ell\nu_\ell b\ \ell\nu_\ell\bar{b}$	42
τ - Dileptonic ($\ell = e$ or μ)	$t\bar{t} \to \ell\nu_\ell b\ \tau\nu_\tau\bar{b}$	50
Semileptonic ($\ell = e, \mu$ or τ)	$t\bar{t} \to \ell\nu_\ell b\ q\bar{q}'\bar{b}$	370
Semileptonic ($\ell = e$ or μ)	$t\bar{t} \to \ell\nu_\ell b\ q\bar{q}'\bar{b}$	250
τ - Semileptonic	$t\bar{t} \to \tau\nu_\tau b\ q\bar{q}'\bar{b}$	125
Fully hadronic	$t\bar{t} \to q\bar{q}'b\ q''\bar{q}'''\bar{b}$	370

Table 8.4: *Estimated cross sections summary table based on the BRs from table 8.3 for the different $t\bar{t}$ decay channels. All channels have been computed at NLO+NLL and at the LHC nominal energy ($\sqrt{s}$ = 14 TeV).*

the QCD background. Moreover, the presence of E_T^{miss} which comes from the ν is a source of rejection. Thus, this channel is usually called the "Golden Channel" and it is expected that ATLAS will record ~ 2.5 million events per year.

The semileptonic channel has a cross section of 370 pb according to its BR. However not all the semileptonic events within this classification will be considered as " semileptonic signal" in this analysis. In fact, events where the W bosons decay into τ's are a little bit special, just the events where the τ's decay leptonically will be consider as "signal". On the other hand, events with τ's decaying hadronically will be classified as fully hadronic decays. The hadronic τ reconstruction is more complex due to the variety of objects in the final state. This is basically because the trigger is performed from electrons or muons. Then, if there is pion coming from the decay of the τ, this will not be considered as "signal". Anyhow, the presence of ν_τ makes more difficult the event reconstruction. Then, considering that the leptonic τ decay has a BR of ~ 35% (17.9% to $e\nu_e$ and 17.4% to $\mu\nu_\mu$), the considered "signal" will have a cross section of 370 - (65% × 125) = 289 pb. The objects that should be reconstructed in the final state are the following:

- One lepton.

- E_T^{miss} (as the neutrinos are invisible to ATLAS, their indirect detection is based on estimating the missing energy in each event).
- Two jets labelled as b-jets (due to the hadronization of the b quarks).
- Two jets not labelled as b-jets (due to the hadronization of the light quarks which come from the W boson hadronic decay).

8.2.3 Physics backgrounds

There are some physics channels that have exactly the same final topology as the semileptonic signal and therefore they can not be distinguished *a priori*. Moreover, there are other physics channels that in some cases can lead, for different reasons, to the same final topology as the signal. All these physics channels constitute the physics background. For the present studies, they can be classified in six groups:

- $t\bar{t}$ events themselves which are not semileptonic signal, i.e. fully hadronic channel, dileptonic channel and semileptonic channel where the lepton is a τ decaying hadronically. In these cases, sometimes one of the b quarks of a fully hadronic channel can decay into a lepton. On the other hand, together with the leptonic channel can appear extra jets (gluon radiation, etc...) not being labelled as b-jets and one of the two leptons can escape being undetected. The cross sections for these $t\bar{t}$ backgrounds are 370 pb, 92 pb and 81 pb, respectively. The problem with these events is, as they are not genuinely semileptonic, that the reconstruction will bias the event observables such as the top quark mass.
- Single top production: Wt, s and t channels. These channels will be important backgrounds, specially the t channel at the LHC (contrary to the Tevatron) as they have high cross sections [7]: σ_{Wt} = 25.5 pb, σ_{sch} = 2.3 pb and σ_{tch} = 81.3 pb. As $t\bar{t}$, the production rate of the single top processes will also be larger by a factor around 100 compared to the Tevatron. As can be seen in figure 8.6, the LO final topologies of these three channels are similar to that of the requested signal, since some light jets can be produced by final state radiation (FSR).
- W+partons production with $W \to \ell\nu$. This is a QCD background and its signal/background relationship is lower than the previous backgrounds. Figure 8.7 shows the tree level Feynman diagram of this channel and taking into account the flavour of the lepton and the number of jets in the final state this background can be classified into 12 sub-channels: $e\nu_e + X$ jets, $\mu\nu_\mu + X$ jets and $\tau\nu_\tau + X$ jets, with $X = 2, 3, 4$ or 5.

  Not all of these sub-channels have been considered in this analysis as the simulation of some of them was not available (see section 8.2.5). The cross sections of each sub-channel, found on reference [7], can be found in table 8.5.
- W+$b\bar{b}$+partons and W+$c\bar{c}$+partons where $W\to\ell\nu$. Figure 8.8 (a) and (b) show the Feynman diagrams at tree level of these two QCD backgrounds. As in the previous case several sub-channels can be defined as a function of their number of final jets (0,1,2 or 3). Table 8.5 contains the cross sections of all these sub-channels extracted from reference [7].

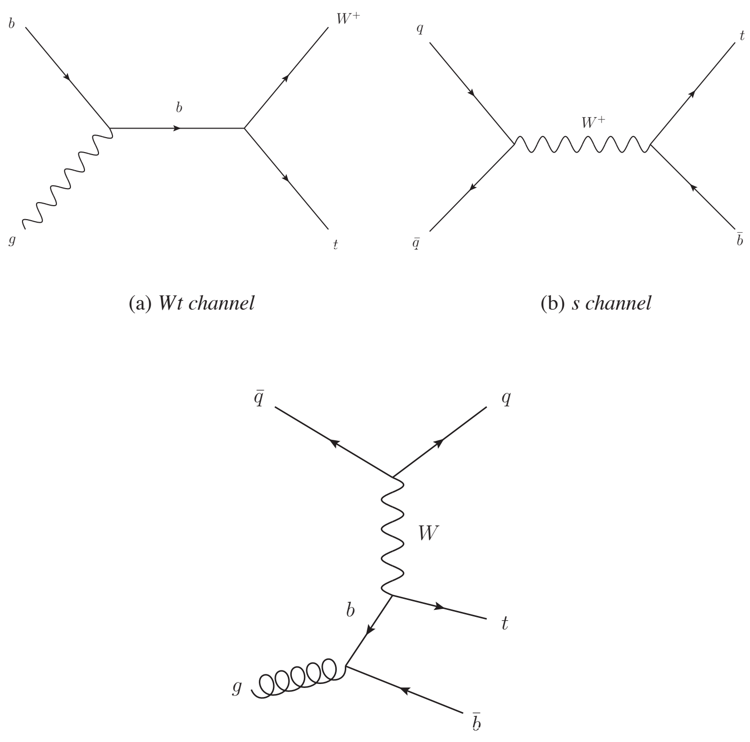

(a) *Wt channel*

(b) *s channel*

(c) *t channel*

Figure 8.6: *Feynman diagrams at tree level for single top production.*

- Gauge boson pair production: WW, WZ and ZZ (see figure 8.9 for their tree level Feynman diagrams). These channels are also classified as expected backgrounds although they have much smaller contributions than the previous backgrounds [133] and they have not been considered in this analysis.

- Z+ partons events with $Z \to \ell\ell$ (see figure 8.10 for its Feynman diagram at tree level). As in the previous case, the contribution can be neglected [133]. Therefore, this background has not been evaluated here.

- QCD multijet events and $b\bar{b}$ productions are also expected. These channels have not been included in the present analysis as simulation studies have revealed that these backgrounds are negligible after leptonic cuts in the event selection [133].

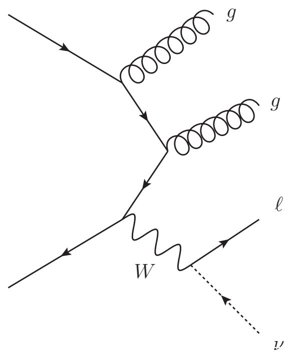

Figure 8.7: *Feynman diagram a tree level of W+partons production with $W \to \ell\nu$.*

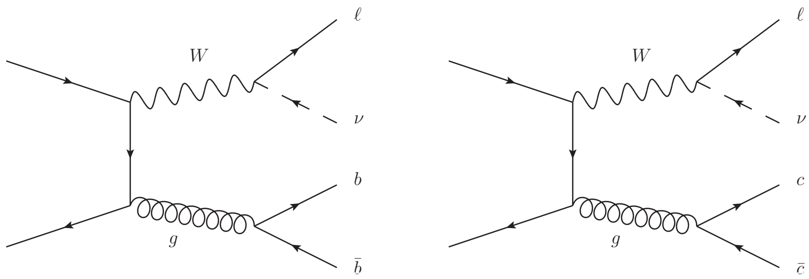

(a) *$W + b\bar{b}$ channel* (b) *$W + c\bar{c}$ channel*

Figure 8.8: *Feynman diagrams at tree level for $W + b\bar{b}$ and $W + c\bar{c}$ backgrounds.*

8.2.4 Combinatorial background

When using MC samples, one can match the reconstructed objects with the truth information at parton level, determining if the jets selected as light jet candidates in an event are really jets originated from light quarks hadronization. Moreover, one can even inspect if those light quarks stemmed from the quarks produced by the W decay. Also one can determine if the selected b-jets truthfully correspond to each of the two b-jets which come from the corresponding b quarks (hadronic side or leptonic side).

In that sense, one can always find out if the selected object candidates at reconstruction level (jets and leptons) are really the right ones and when at least one of these choices is detected as wrong, the event can be classified as Combinatorial Background. For events where all the selected candidates match with the genuine partons, will be labelled as Good Combinations. Therefore, these good combinations would constitute the perfect and clean requested "signal".

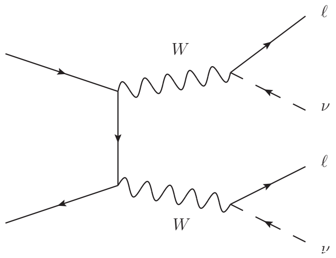

(a) *WW channel*

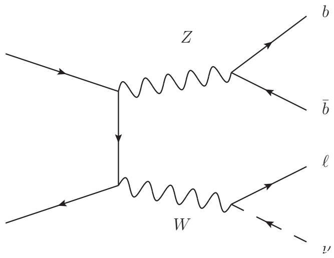

(b) *WZ channel*

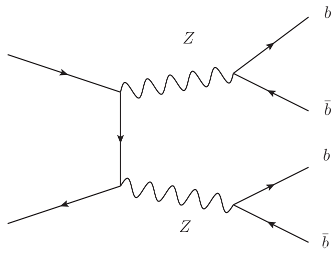

(c) *ZZ channel*

Figure 8.9: *Feynman diagrams at tree level for the gauge boson pair production (WW, WZ and ZZ).*

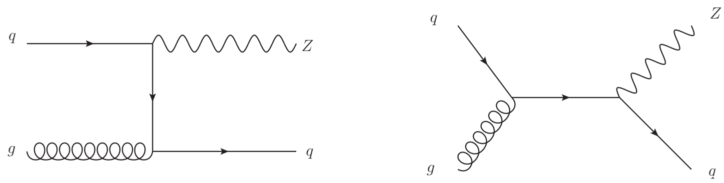

Figure 8.10: *Feynman diagram at tree level of Z+partons events with Z $\rightarrow \ell\ell$.*

8.2.5 Datasets

The present studies have been done using MC samples based on the official TopView ntuples generated within *Athena* framework (release 12.14.0.3) for the CSC challenge. All samples were processed with the full ATLAS detector simulation (based on Geant4 [110]) and reconstruction software. Some of the characteristics of these datasets are [134]:

- Simulation with detector description ATLAS-CSC-01-02-00 [135]. This includes a magnetic field description based on the map *bmagatlas04_test1.data* with initial displacements

Category	Decay Mode	Cross section (pb)
$t\bar{t}$ (fully hadronic)	$t\bar{t} \rightarrow q\bar{q}b\ q\bar{q}b$	370
	$t\bar{t} \rightarrow q\bar{q}b\ \tau\nu_\tau b$	81
$t\bar{t}$ (dileptonic)	$t\bar{t} \rightarrow \ell\nu_\ell b\ \ell\nu_\ell b$	92
Single top	Wt	25.5
	t channel	81.3
	s channel	2.3
W $\rightarrow \mu\nu_\mu + X$ partons	W + 2 partons	16
	W + 3 partons	65
	W + 4 partons	36
	W + 5 partons	20
W $\rightarrow \tau\nu_\tau + X$ partons	W + 2 partons	88
	W + 3 partons	87
	W + 4 partons	46
	W + $\geq$5 partons	21
W + $b\bar{b}$ + X partons	W + $b\bar{b}$ + 0 partons	6.26
	W + $b\bar{b}$ + 1 partons	6.97
	W + $b\bar{b}$ + 2 partons	3.92
	W + $b\bar{b}$ + 3 partons	2.77
W + $c\bar{c}$ + X partons	W + $c\bar{c}$ + 0 partons	6.72
	W + $c\bar{c}$ + 1 partons	7.49
	W + $c\bar{c}$ + 2 partons	4.36
	W + $c\bar{c}$ + 3 partons	2.45

Table 8.5: *Cross sections summary table for the different background samples computed at the LHC energy ($\sqrt{s}$ = 14 TeV) [7].*

and misaligned geometry (CSC realistic distorted geometry: OFLCOND-CSC-00-01-00 [136]) with material distortion for ID and LAr.

- Reconstruction done with detector description ATLAS-CSC-01-00-00 [135] which includes a magnetic field description based on the map *bmagatlas04_test1.data* with no displacements, perfect geometry (i.e. location of the modules perfectly known: OFLCOND-CSC-00-00-00 [136]) with calibration constants.

The datasets for the $t\bar{t}$ semileptonic signal, the $t\bar{t}$ dileptonic background and the $t\bar{t}$ fully hadronic background contain events with $t\bar{t}$ decays at NLO (produced with the MC@NLO generator) i.e. ISR and FSR are considered. For these NLO samples, one must consider the *event weight* (in the ntuple: EventWeight@NLO). These weights can be +1 or -1 and they come from NLO calculations performed by the event generator and from the inclusion of the HERWIG "parton showers". Because of the complicated computations, there is an excess of events i.e. sometimes there is a "double counting" in an given event and that is why this event has to have weight set to -1. Therefore, the *event weight* affects the calculation of cross section and must be use in order to weight all histograms made from this kind of samples. Much more information about this issue can be found in references [137] [138]. The other physics backgrounds contain events with LO decays, where the *event weight* value is always +1. Appendix D contains more information about the datasets used to perform the present study.

For all the datasets a generated fixed top mass (M_t^{gen}) equal to 175 GeV/c^2. The width of the top was not used at generator level and all the samples assume $\Gamma_t = 0$ GeV/c^2.

8.3 Reconstruction and selection of physics objects

Once the required signal has been established, the reconstruction of the final state physics objects has to be discussed. Thus, this section presents the reconstruction performance for leptons (electrons and muons separately), missing transverse energy and jets based on MC data (i.e. the truth information from generation is used as reference). This performance study will include efficiencies, purities, resolutions, linearities and uniformities of the reconstructed physics objects. But first at all, one has to define these quantities:

- **Efficiency (ε):**

$$\varepsilon(\Delta R) \equiv \frac{\#\text{ of matches of truth } e\,/\,\mu\,/\text{ jets with reconstructed e}\,/\,\mu\,/\text{ jets } (\Delta R)}{\#\text{ of truth } e\,/\,\mu\,/\text{ jets}} \tag{8.2}$$

  This quantity depends on the isolation $\Delta R = \sqrt{\Delta\eta^2 + \Delta\phi^2}$ as this is the matching rule to link reconstructed objets with truth objects. This is done based on information from EM calorimeters and tracking variables. Thus, the matching between truth and reconstructed objects ($\Delta R(truth, reco)$) is the criterion used to study the efficiency.

- **Purity (P):**

$$P(\Delta R) \equiv \frac{\#\text{ of reconstructed } e\,/\,\mu\,/\text{ jets with truth e}\,/\,\mu\,/\text{ jets } (\Delta R)}{\#\text{ of reconstructed } e\,/\,\mu\,/\text{ jets}} \tag{8.3}$$

  The purity also depends on the same ΔR criterion as the efficiency.

- **Energy linearity:**

$$\frac{E_{reco} - E_{truth}}{E_{truth}} \;\text{ Vs }\; E_{reco} \tag{8.4}$$

- **Energy uniformity:**

$$\frac{E_{reco} - E_{truth}}{E_{truth}} \;\text{ Vs }\; \phi_{reco}, \eta_{reco} \tag{8.5}$$

- **Energy resolution:**

$$\sigma\left(\frac{E_{reco} - E_{truth}}{E_{truth}}\right) \;\text{ Vs }\; E_{reco}, \phi_{reco}, \eta_{reco} \tag{8.6}$$

Then, once these quantities have been defined, one can start with the different studies for each reconstructed object type.

8.3.1 Electron reconstruction performance

The electron signature from the reconstruction point of view is the energy deposited in the ECAL and a track pointing at the energy deposition, being its momentum consistent with its energy at the ECAL. The standard algorithm for electron reconstruction is: a seeded EM tower with $E_T > 3$ GeV plus one ID track (not belonging to a γ conversion) with $E/p < 10$. Moreover, this track is required to match the cluster within a $\Delta\eta \times \Delta\phi$ window of 0.05×0.10. If these requirements are satisfied, the candidate is labelled as an electron [7].

Furthermore, some electron "identification cuts" for the reconstructed particles are applied in order to remove background:

- $p_T > 25$ GeV/c.
- $|\eta| < 2.5$ and outside the transition region between the EM barrel and the EM end-caps, i.e. $1.37 < |\eta| < 1.52$.
- Isolation cut based on ECAL energy: additional E_T in a cone with radius $\Delta R = 0.2$ around the electron < 6 GeV.

In simulated events, true electrons, from W leptonic decays, can easily be selected thanks to the truth persistency.

Once, both signatures (reco and truth) are established, one can start the performance studies. Firstly, electron reconstruction efficiency as a function of the p_T, ϕ and η are shown in figures 8.11 (a), (b) and (c) . As pointed before, the efficiency depends on the truth-reconstruction matching (based on the ΔR criterion) then, events where no reconstructed electron is associated to a true electron, are not included in the efficiency study.

From these figures one can say that the efficiency of electron reconstruction reaches up to 60%. A little degradation is found on $\eta = 0$ due to the identification cuts. The efficiency drops up to 40% for large $|\eta|$ values, i.e. at the ECAL end-caps ($|\eta| < 1.52$) and at the overlap region between barrel and end-cap calorimeters (these transition regions are also known as "cracks"), i.e. $1.37 < |\eta| < 1.52$. Finally, as it is expected no asymmetries are observed over ϕ.

Moreover, figures on 8.12 show the purity as a function of p_T, ϕ and η, where one can see how the purity increases up to 100% for high p_T electrons and how stable is over ϕ and η (therefore, there is no geometrical dependence as expected). Thus, on these plots, the purity is $\sim$94% (i.e. the "pollution" is $\sim$6%) due to the fact that the plotted values are the average of all p_T values as a function of ϕ or η. Generally, it is better to have a good purity with low efficiency than viceversa.

Figure 8.13 shows the energy linearity for electrons where a small departure from linearity is observed (up to 0.5%). This is probably due to the additional material in front of the calorimeters (it is worth to remind that the alignment/calibration constants were provided for the as-built geometry without material distortions) [7].

Another important parameter is the energy uniformity which can be seen in figures 8.14 (a) and (b), for ϕ and η respectively. Small fluctuations can be seen in both plots from the ideal case (i.e. a flat line just over zero) which probably are due to additional material effects as in the previous case [7]. Moreover, in figure 8.14 (b) the EM cracks ($1.37 < |\eta| < 1.52$) break the uniformity as it is expected, explaining the loss of efficiency in these regions.

To finalize, figure 8.15 (a) shows the energy resolution of the reconstructed electrons as a function of the reconstructed energy and as it is expected (i.e. $\sigma_E/E \sim 1/\sqrt{E}$. See section 2.3.2)

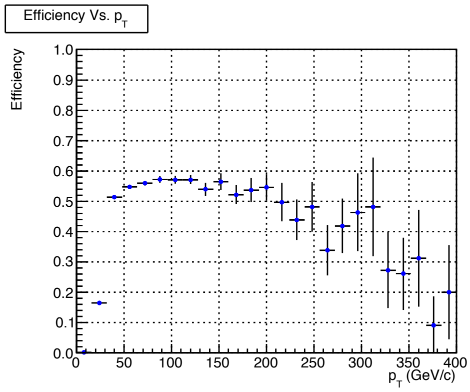

(a) *Efficiency Vs p_T*

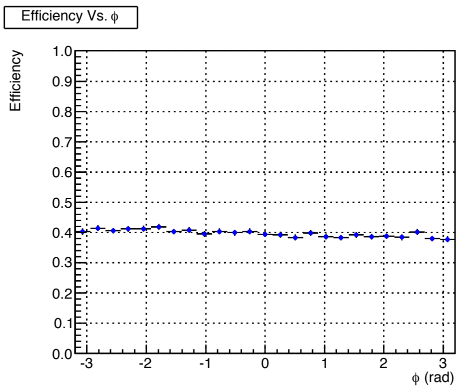

(b) *Efficiency Vs ϕ*

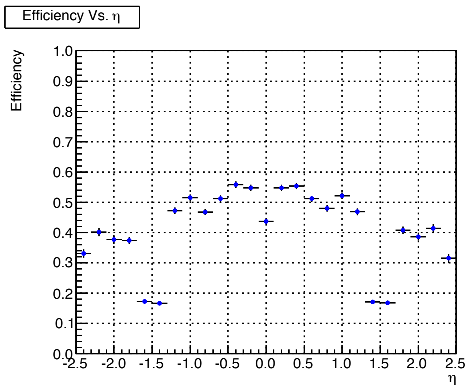

(c) *Efficiency Vs η*

Figure 8.11: *Electron reconstruction efficiency as a function of p_T (a), ϕ (b) and η (c) for the $t\bar{t}$ semileptonic sample.*

this resolution is better for high energy electrons. Moreover, figures 8.15 (b) and (c) show the energy resolution uniformity over ϕ and η. Once more, as it is expected, there are no relevant fluctuations over ϕ (with the exception of the ones due to material effects) and there is an increase of the value of the resolution (i.e. the resolution gets worse) around the calorimeter cracks.

The conclusion is that inefficiencies and fluctuations are just observed along η, fact that is expected since the detector is continuous and homogeneous along ϕ but not along η.

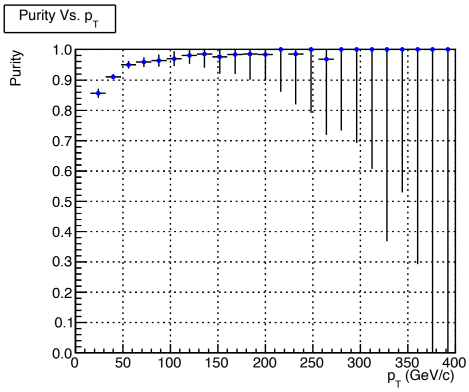

(a) *Purity Vs p_T*

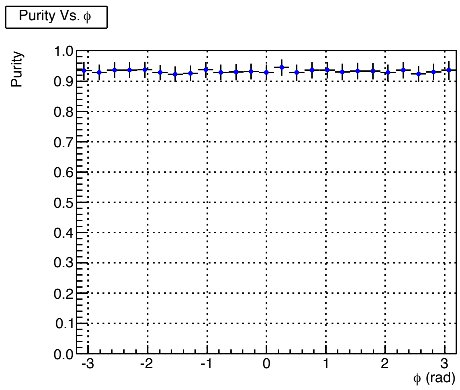

(b) *Purity Vs ϕ*

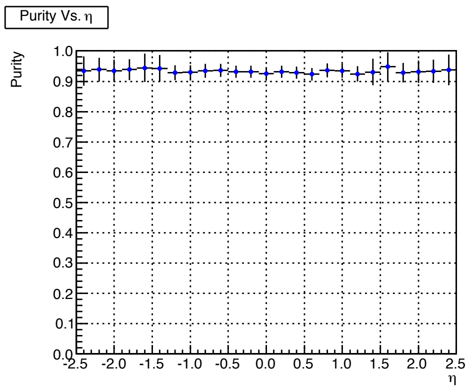

(c) *Purity Vs η*

Figure 8.12: *Electron reconstruction purity as a function of p_T (a), ϕ (b) and η (c) for the $t\bar{t}$ semileptonic sample.*

8.3.2 Muon reconstruction performance

Naively the muon reconstruction is expected to perform better than the electron reconstruction since muons are minimum ionizing particles (mip's[3]). This means that generally material effects will be much less important for muons than for electrons, i.e. muon tracks will be slightly

[3] Generally, when a charged particle passes through matter, it ionizes or excites the atoms or molecules that it encounters, losing energy in small steps. The mean rate at which this crossing particle loses energy depends on the material, the own nature of that particle and also its momentum. Thus, a minimum ionizing particle (or mip) is a particle whose mean energy loss rate through matter is close to the minimum where good examples are muons.

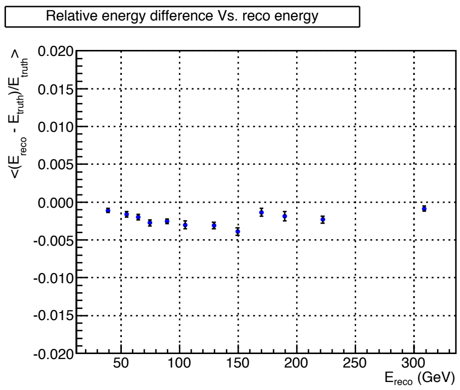

Figure 8.13: *Electron reconstruction linearity for the $t\bar{t}$ semileptonic sample. A small departure from linearity is observed, probably, due to the additional material in front of the calorimeters.*

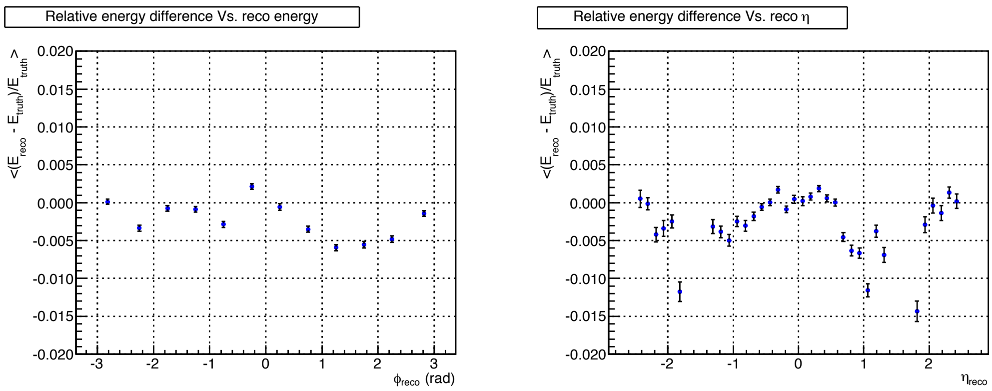

(a) *Uniformity Vs ϕ*

(b) *Uniformity Vs η*

Figure 8.14: *Electron reconstruction uniformity as a function of ϕ and η for the $t\bar{t}$ semileptonic sample. Small fluctuations can be seen, probably, also to the additional material in front of the calorimeters.*

affected by MCS and energy losses. A muon signature is as follows: muon track in the ID, (minimum) energy deposition at the ECAL and at the end, a track in the muon chambers.

The muon reconstruction is performed by the STACO algorithm [139]. This algorithm uses the Muon Spectrometer to perform the tracking and the Muonboy algorithm [139] to extrapolate the reconstructed tracks to the ID. This task is not trivial since the muons travel firstly through a magnetic field generated by a solenoid in the ID and secondly through a magnetic field generated by the toroid system in the Muon system. The first magnetic field bend muons in the transverse plane while the second magnetic field bend muons in the longitudinal plane, being the later not

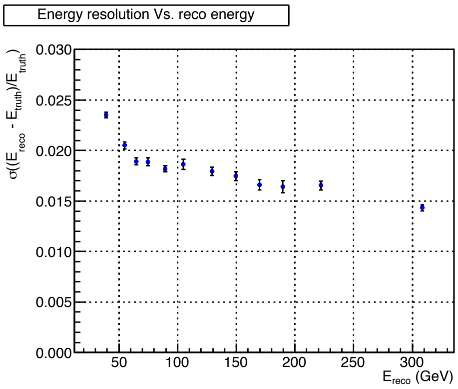

(a) *Resolution Vs E*

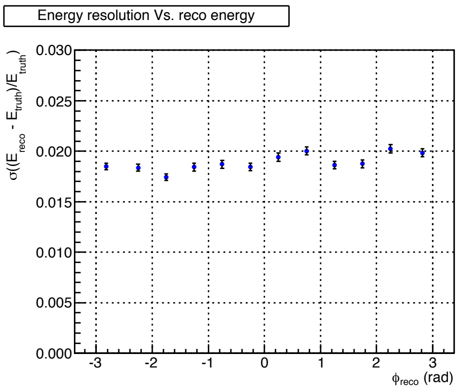

(b) *Resolution Vs ϕ*

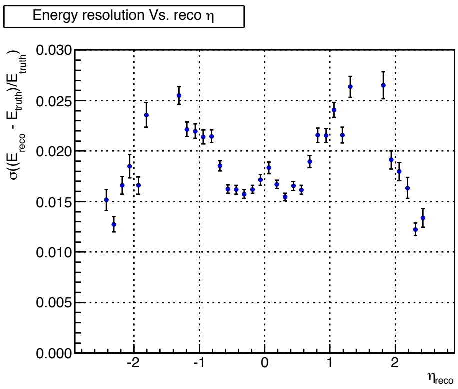

(c) *Resolution Vs η*

Figure 8.15: *Energy resolution and resolution uniformity for electron reconstruction for the $t\bar{t}$ semileptonic sample.*

uniform. The algorithm is based on a χ^2 criterion for the matching. The extrapolation accounts for MCS effects and energy loss in calorimeters considering the crossed material.

As in the previous case, some "identification cuts" are used:

- $p_T > 20$ GeV/c.
- $|\eta| < 2.5$ and outside the transition region between the EM barrel and the EM end-caps, i.e. $1.37 < |\eta| < 1.52$.
- Isolation cut based on ECAL energy: additional E_T in a cone with radius $\Delta R = 0.2$ around

the muon < 6 GeV.

- Remove muons if there is a good jet within $\Delta R = 0.3$.

For muons, the matching criterion to link reconstructed muons with the MC genuine muons from the W decay is as follows:

$$D_{ref} = \sqrt{\left[\frac{\phi_{reco} - \phi_{truth}}{0.005}\right]^2 + \left[\frac{\eta_{reco} - \eta_{truth}}{0.005}\right]^2 + \left[\frac{p_T^{reco} - p_T^{truth}/p_T^{truth}}{0.03}\right]^2} < 100 \tag{8.7}$$

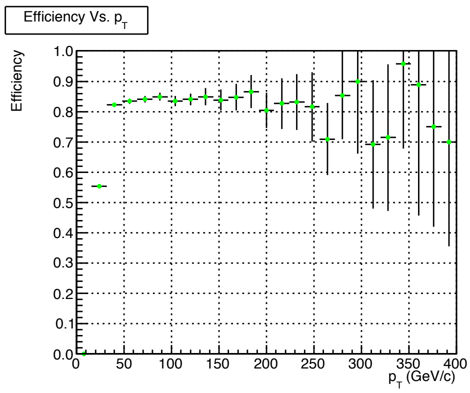

(a) *Efficiency Vs p_T*

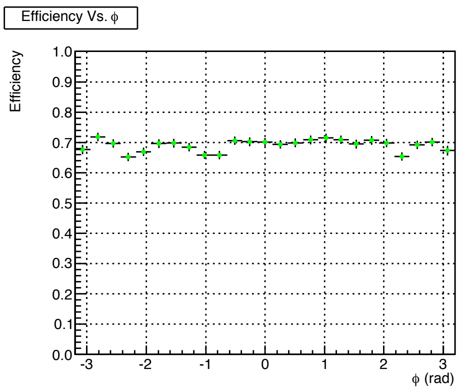

(b) *Efficiency Vs ϕ*

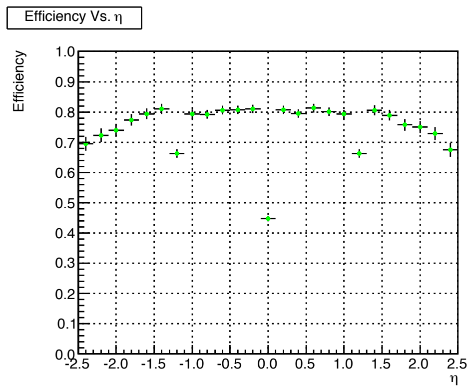

(c) *Efficiency Vs η*

Figure 8.16: *Muon reconstruction efficiency as a function of p_T (a), ϕ (b) and η (c) for the $t\bar{t}$ semileptonic sample.*

where D is the distance measured from true muon to the reconstructed muon. This implies the matched muons must be within a distance of 0.5 in η and ϕ and have the same charge sign with $p_T^{reco} > 0.25\ p_T^{truth}$ or opposite sign with $p_T^{reco} > 0.50\ p_T^{truth}$ [7].

Figures 8.16 (a), (b) and (c) show the muon reconstruction efficiency as a function of the p_T, ϕ and η, respectively. The upper one shows that the efficiency reaches up to 85% for $p_T > 70$ GeV/c. Rather small fluctuations can be observed over ϕ, being already expected since the ϕ coverage of the muon spectrometer is not completely homogeneous. Over η, one can see that on average the efficiency in the barrel region is 80% and it decreases in the end-cap regions. A substantial degradation can be observed at $\eta = 0$ which is due to a detector coverage hole and once more a large degradation appears at the transition between end-caps and barrel.

The muon reconstruction purity just depends on the p_T as can be seen in figure 8.17 (a) and it increases up to 100% with the momentum as expected. Moreover, from figures 8.17 (b) and (c) one can say that the average purity is about 92%.

Good linearity and uniformity in ϕ and η is the conclusion from figures 8.18, 8.19 (a) and (b), respectively. Negligible fluctuations are shown in figure 8.19 (a) while non-uniformities are observed (as expected) in end-cap regions (see figure 8.19 (b)).

The full ATLAS tracker (ID and muon spectrometer) is used to measure the energy of muons (assuming that the muon mass is known). According to expression 3.2 ($\sigma(p_T)/p_T \sim p_T$), the energy resolution is better for low energy muons than for high energy muons as figure 8.20 (a) shows. Moreover, in this figure one can see that the resolution is also worse in the transition region $1.2 < |\eta| < 1.7$, which is expected due to the barrel to end-cap transition. Figure 8.20 (b) shows the resolution over ϕ where small fluctuations can be appreciated. Finally, as in the previous case, in the transition regions between the EM barrel and end-caps there is a large degradation of the resolutions as it is shown in figure 8.20 (c).

8.3.3 E_T^{miss} reconstruction performance

Once the lepton reconstruction performance has been presented, it is time now to look for the neutrinos in the final state. The problem is that the neutrino is an invisible particle for ATLAS and therefore, no direct reconstruction performance can be done. The signal that neutrinos produced in the detector is in fact a lack of signal, becoming apparently as an unbalanced p_T. Then, the solution is to study the reconstructed missing energy which is estimated based on physical laws such as the conservation of energy and conservation of momentum. Thus, missing energy is generally attributed to particles which escape the detector, although apparent missing energy may be caused by instrumental effects:[4] mismeasurements and resolution effects.

In hadron colliders, the initial momentum of the colliding partons along the beam axis is not known as the energy of each hadron is split between its constituents. Also, ISR and FSR effects contribute to make this problem more complicated. However, it is assumed that the initial energy in particles travelling transverse to the beam axis (XY plane) is zero, so any net momentum in the transverse direction indicates missing transverse energy (MET or E_T^{miss}), i.e. must be compensated. Thus, the reconstructed E_T^{miss} is used as an estimate of the neutrino transverse momentum. The reconstruction algorithm, RefMET, is based on the energy deposited in the

[4]Generally all HEP detectors have a limited geometrical acceptance and therefore it is possible that particles escape without being detected. In the case of ATLAS, it has a full coverage over ϕ but a limited coverage over η (moreover, the later is different for each subdetector as was discussed in section 2.3). This is the reason why the missing energy at low η values does not contribute to the E_T^{miss}.

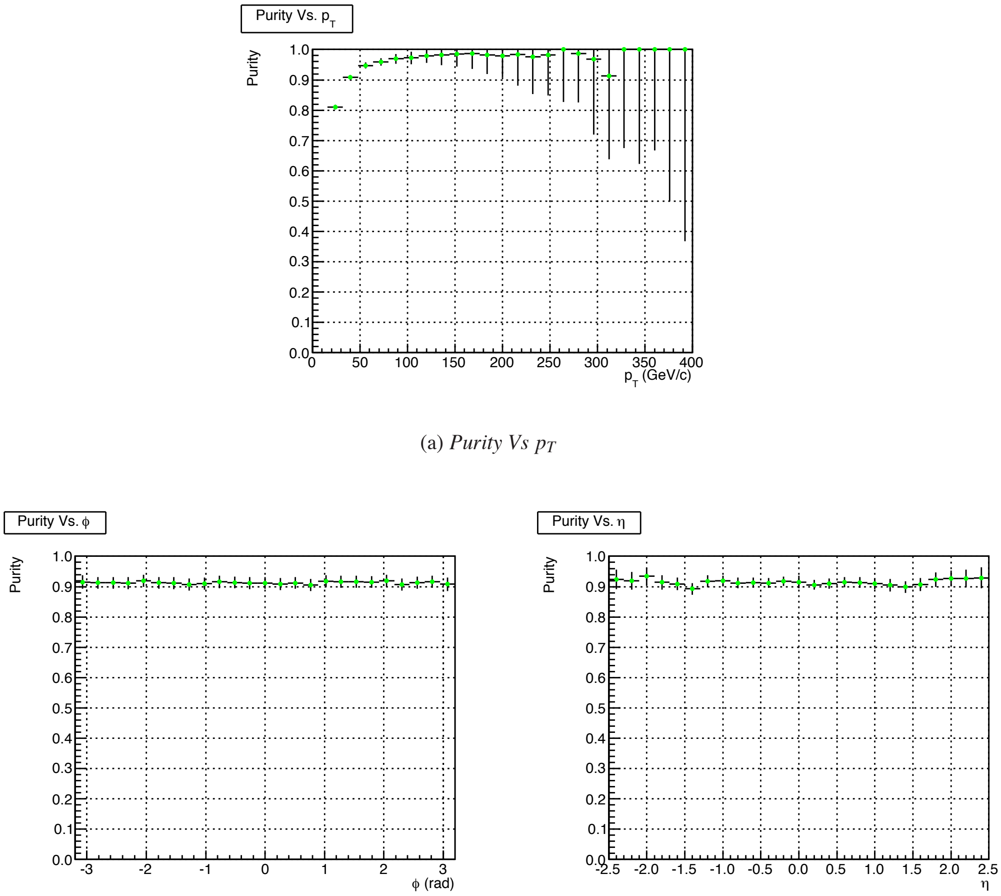

(a) *Purity Vs p_T*

(b) *Purity Vs ϕ*

(c) *Purity Vs η*

Figure 8.17: *Muon reconstruction purity as a function of p_T (a), ϕ (b) and η (c) for the $t\bar{t}$ semileptonic sample.*

calorimeter cells, reconstructed muon tracks and in the estimation of energy lost in the cryostat between the ECAL and the HCAL. The X and Y components of the final E_T^{miss} can be defined as:

$$(E_T^{miss})_{XY}^{final} = (E_T^{miss})_{XY}^{Calo} + (E_T^{miss})_{XY}^{Cryo} + (E_T^{miss})_{XY}^{Muon} \tag{8.8}$$

where $(E_T^{miss})^{Calo}$, $(E_T^{miss})^{Cryo}$ and $(E_T^{miss})^{Muon}$ are referred as calorimeter, cryostat and muon terms. Firstly, estimating the calorimeter term involves two steps. The first step is to select calorimeter cells that are primarily from signal and not noise. The second step is to calibrate these cells to account for differences in electromagnetic and hadronic showers. For this kind of

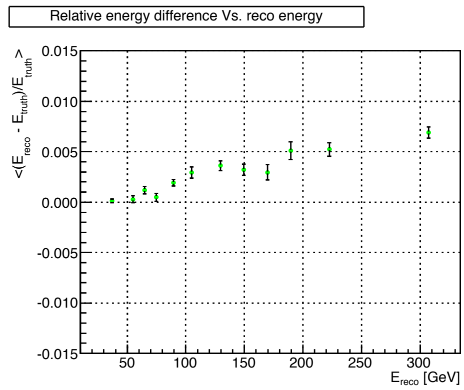

Figure 8.18: *Muon reconstruction linearity for the $t\bar{t}$ semileptonic sample. Small fluctuations can be seen.*

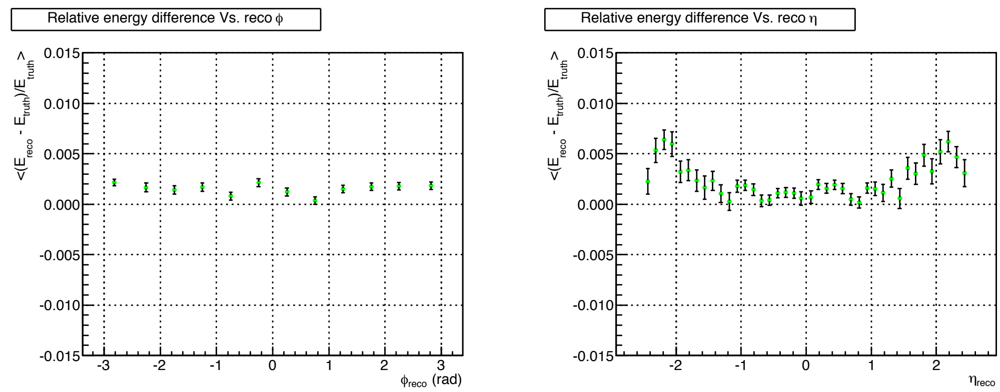

(a) *Uniformity Vs ϕ*

(b) *Uniformity Vs η*

Figure 8.19: *Muon reconstruction uniformity as a function of ϕ and η for the $t\bar{t}$ semileptonic sample. Small fluctuations can be seen, probably, also to the additional material in front of the calorimeters.*

calculations it is also important to take into account the energy lost in dead materials, thus the cryostat term corrects for the cryostat material between the electromagnetic and the hadronic calorimeters. The muon term is calculated from the energies of the reconstructed muons. The $(E_T^{miss})^{final}$ resolution is dominated by the calorimeter term [140] and although the muon term does not contribute much to the $(E_T^{miss})^{final}$ resolution, unmeasured, bad-measured, fake muons and punch through pions can be a source of fake E_T^{miss}.

On the other hand, the truth E_T^{miss} (MET$_{truth}$ in the plots) is calculated from the contribution of all stable and non-interacting particles (neutrinos, the Lightest Supersymmetric Particle in SUSY models, etc) in the final state.

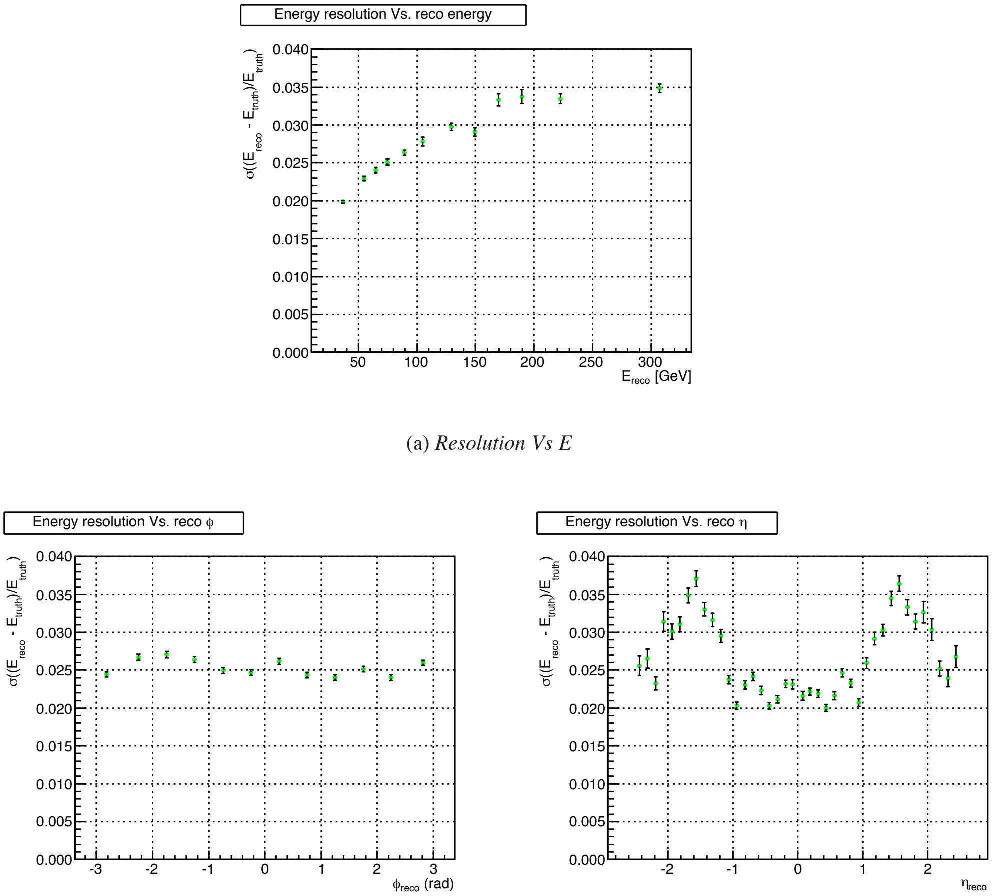

(a) *Resolution Vs E*

(b) *Resolution Vs ϕ*

(c) *Resolution Vs η*

Figure 8.20: *Energy resolution and resolution uniformity for muon reconstruction for the $t\bar{t}$ semileptonic sample.*

Figure 8.21 (a) shows the linearity of the E_T^{miss} where an excellent linearity exists for $E_T^{miss} >$ 50 GeV. For $E_T^{miss} <$ 50 GeV there is a linearity deviation because E_T^{miss} is in fact poorly determined (a detailed explanation of this fact can be found on these references [140] [7]).

Finally, figure 8.21 (b) shows the E_T^{miss} resolution where its dependence with the reconstructed E_T^{miss} can be observed. This dependence is $\sigma(E_T^{miss}) \propto \sqrt{\sum E_T} \sim \sqrt{E_T^{miss}}$ as the E_T^{miss} is mainly measured by the calorimeters and it increases up to 7%. For $E_T^{miss} <$ 20 GeV the resolution is very poor especially due to the resolution effects and this is one of the motivations to perform a 20 GeV cut for event selection as it will be discussed in section 8.3.8.

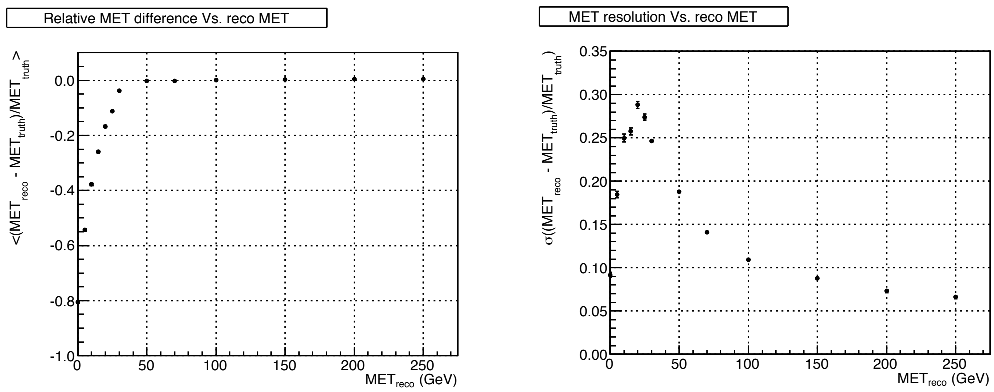

(a) E_T^{miss} *linearity*

(b) E_T^{miss} *resolution*

Figure 8.21: *Figure (a) shows the* E_T^{miss} *linearity while figure (b) shows the* E_T^{miss} *resolution, both for the* $t\bar{t}$ *semileptonic sample.*

8.3.4 Jets

Once the performance of the isolated lepton and the neutrino (through the E_T^{miss}) have been studied, the jet reconstruction performance is considered. A jet is intuitively a narrow cone of hadrons and other particles produced by the hadronization of a quark (with the exception of the top quark that decays before hadronize) or gluon in a high energy physics experiment. This hadronization is due to the QCD confinement (see chapter 1). As particles carrying a color charge, such as quarks, cannot exist in free form, they fragment into colorless (i.e. color singlets) hadrons stemming out in jets. Thus, the signals measured in the detectors must be studied in order to determine the properties of the original quark. Then, one observes the jets as the materialization of their original partons and the following assumption is made: the properties of the jets (energy and direction) are directly related to the same properties of the original partons. This is equivalent to a LO approximation of the final event topology. In other words, the jet of particles must be reconstructed and calibrated back to parton level in order to study the physics of the event. For that some effects must be considered:

- Detector effects: dead material, electric noise, energy leakage, non-uniformities, magnetic field effects...
- Physics effects: jet types (light quarks, gluons, b-jet or τ-jet), parton shower and fragmentation, underlying events, ISR and FSR, pileup from minimum bias events, etc...
- Clusterization effects: imperfections of the algorithm to associate all partons to the jets.

Several algorithms are implemented within the *Athena* framework such as Cone, KT, etc to perform these tasks. Basically these algorithms start from calorimeter cells and apply some jet finding methods, which cluster calorimeter towers within different cones, to produce uncalibrated jet candidates. After that, they incorporate detector effects to produce calibrated jets. But to achieve this reconstruction, a deep detector knowledge is required. The aim of this study is to measure the top quark mass and not to study the jet reconstruction, then the jet calibration effects were removed by performing a jet calibration to parton level using the MC information. This allows to disentangle the jet calibration from other effects on the top quark mass measurement such as selection cuts, reconstruction or measurement methods.

8.3.5 Jet reconstruction

The jet reconstruction was done using the fixed cone jet finder algorithm, known as Cone or Cone4TowerJets. In this algorithm the jet is delivered using calorimeter towers within a cone of selectable radius. The finding depends on the jet radius as it is shown on figure 8.22 (a) and (b), where different jet radii lead to reconstruct just one jet or two jets. For the present analysis the selected radius was R_{cone} =0.4 ($R_{cone} = \sqrt{\Delta\eta^2 + \Delta\phi^2}$) as in the official CSC analysis [7].

Finally, at reconstruction level the current ATLAS default b-tagger (IP3D + SV1) [141] was used on top of the selected jets to tag *b-jets* (technical requirement: weight>6). This method combines two algorithms that use the fact that the b hadrons have a long lifetime ($c\tau$ = 450 μm) and therefore, they decay a little far away from the primary vertex as can be seen on figure 8.23. The first algorithm uses the 3-dimensional impact parameter (IP) of tracks associated to the jet. Thus, the IP values of the tracks from those b quarks are larger than for primary tracks and therefore, those tracks can be tagged as b-jets. The second algorithm is based on secondary vertices as the probability to find a secondary vertex in a b-jet is much higher than to find it in a light jet.

8.3.6 Jet calibration

With MC samples, one can compare the energy of the reconstructed jets with the parton energy. This implies that a calibration must be done. For that purpose, an algorithm which matches reconstructed jets to partons before radiation was developed. It requires ΔR (parton,jet) < 0.3 and then derives the difference between the reconstructed jet energy and the parton energy as a function of the parton energy. To do this, three levels of jets are defined:

- **Parton Level:** each parton is taken as a different jet.
- **Truth Particle Jets:** built from stable (true) particles after the hadronization and without detector effects. At this level, neutrinos generated from the primary collisions are excluded.
- **Reconstructed Jets:** built from calorimeter towers defined as massless pseudo-particles corrected by detector effects. At this level, the algorithm applies some cuts:
  - Transverse momentum cut: $p_T > 20$ GeV
  - Within the tracking detector acceptance, i.e. $|\eta| < 2.5$
  - Jets coinciding within $\Delta R < 0.2$ with reconstructed electrons are removed.

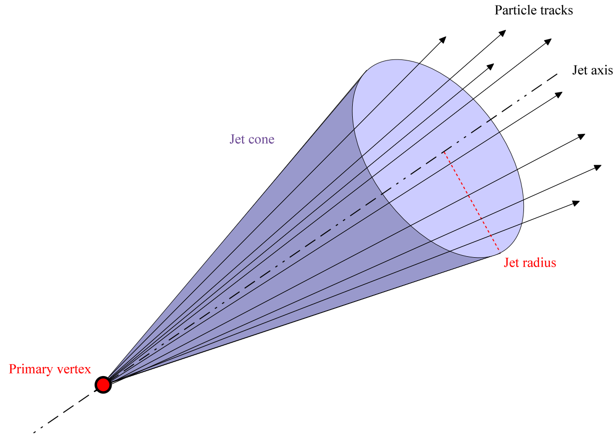

(a) *Large radius for jet finding*

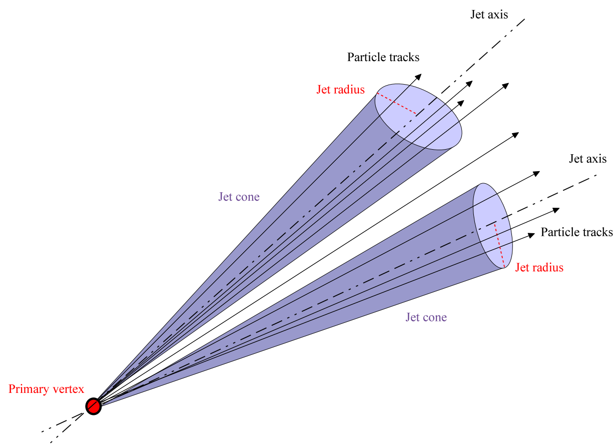

(b) *Small radius for jet finding*

Figure 8.22: *Schematics of the jet finding algorithm based on variable radius. With larger radius all particles can be clustered in one jet whilst with smaller radius some jets can show their internal structure.*

The three levels are consecutive in the sense that the first level (quark level) cannot be directly matched with the third level (reconstructed jet level). Thus, jets are associated to their original partons, step by step, based on the minimum ΔR distance for the combinatorial selection and requiring $\Delta R < 0.3$. The disadvantage is that one has to apply theoretical corrections at fragmentation level though detector effects are the dominant ones in real life.

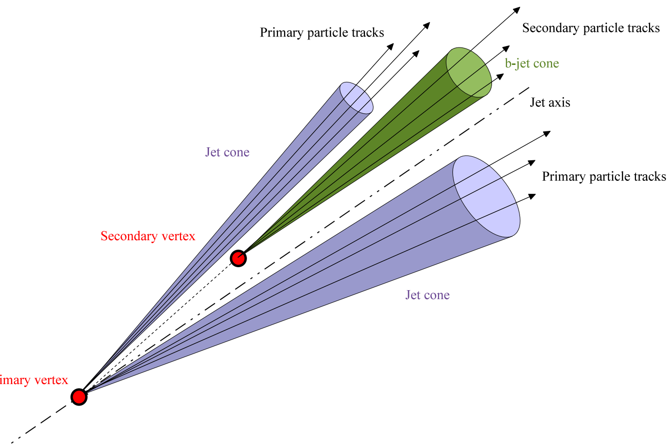

(a) *b-hadron tagging*

Figure 8.23: *Schematics of the b-hadron tagging based on the three-dimensional impact parameter and on secondary vertices.*

The jet calibration performed for the present analysis was based on the MC information of the semileptonic signal events. Thus, expecting that the reconstructed jet energy (E_{reco}) and the jet resolution should depend on the energy and on η values, the energy correction factors $\alpha_E \equiv E_{truth}/E_{reco}$ and the resolution values $\sigma_E(E_{reco} - E_{truth})$ were computed for binned energy and η regions as it is detailed on appendix E.

The energy correction factors are given as maps for light jets and for b-jets without muon decays and as fixed values for b-jets with muon decays (see figures E.1 and E.2). From section E.1, one can summarize that α_E decreases with the energy and increases with η, and its values are always slightly higher than one which indicates some reconstructed energy fault.

The resolutions are firstly computed as maps but it order to improve the energy dependence a parametrization is done. In this case, $\sigma_E(E_{reco} - E_{truth})$ is plotted as a function of the energy (for a given η region) and then it is fitted to $\sigma_E = a\sqrt{E} + bE$ (being a and b two free parameters). Further details can be found on section E.2.2. To summarize, one can say that the resolutions are $\mathcal{O}$(10-20 GeV) though the exact fit parameters and some discussion can be found on the same appendix.

8.3.7 Jets reconstruction performance

Once jets have been calibrated, the performance of the jet reconstruction is studied. Figures 8.24 (a), (b) and (c) show the efficiency[5] as a function of the energy, ϕ and η respectively, for light jets (circles) and b-jets (triangles). As can be seen on these figures, the efficiency is higher

[5]The computed efficiency evaluates the reconstruction of jets and the correct association between those reconstructed jets and their corresponding primary quarks.

for light jets than for b-jets. Figure 8.24 (a) shows that for light jets the efficiency grows with the transverse momentum of the light jets up to 90% while for b-jets the efficiency grows up to 65% but just up to $p_T \sim 200$ GeV/c. This difference is because the b-jet efficiency contains two folded factors: firstly, jet reconstruction and b-quark association and secondly, the reconstructed jet must be tagged as such. Moreover, for higher momenta, the reconstruction efficiency for b-jets decreases due to the fact that b-jets are much more collimated due to the high momentum (i.e. their boosts) which makes that the b-tagging algorithms lose jet separation performance. On the other hand, figure 8.24 (b) shows that the efficiency does not depend on ϕ for both types of jets. Finally figure 8.24 (c) shows that efficiency have the same behaviour over η for light jets and b-jets. One can also see that the efficiency is quite stable in the barrel region and it decreases for higher η. Moreover, the transition regions between the barrel and the extended barrel (i.e. $|\eta| \sim 1.5$) can be observed on this plot.

On figures 8.25 (a), (b) and (c) one can find the purity, computed following expression 8.3, as a function of p_T, ϕ and η respectively. The figures show how the purity is higher for b-jets (triangles) than for light jets (circles), in particular, b-jet purity reach up to 92% while the higher purity for light jets is 52%. This difference is mainly due to the fact that b-jets have been b tagged and this step requires the existence of b quarks. In other words, the denominator for the light jet purity includes all the b-jets. Moreover, ISR and FSR effects give additional light jets which can escape at high η values and therefore can not be associated with tree level truth partons (at LO), decreasing the light jet purity. Another contribution to this difference comes from reconstruction because there are cases where several jets are reconstructed from a single parton, degrading the identification. It is also observed that the purity decreases with p_T and this is because as the jet collimation grows with p_T, the jet isolation/identification becomes trickier (increment of fake jets). Figure 8.25 (b) does not show any ϕ dependence as expected and figure 8.25 (c) shows an almost flat purity over η for b-jets and how the purity decrease for $|\eta| > 1$ in the case of light jets.

To study the linearity, the uniformity and the resolution, light jets and b-jets have been represented in two different plots for the sake of clarity. Figures 8.26 (a) and (b) show the linearity for light jets and b-jets respectively. It can be seen that the linearity has some fluctuations for both types of jets and this is basically due to the dependence between the reconstruction performance and the energy, though the used calibration (see previous section) could have its impact. On the other hand, figures 8.27 (a) and (b) show a good uniformity over ϕ where the slight distortions (asymmetry between $\phi > 0$ and $\phi < 0$ regions) are understood in terms of the material effects. Furthermore, figures 8.28 (a) and (b) show a quite good uniformity for the barrel region and lager fluctuations at high η values, especially at the crack regions.

Finally, the figures 8.29 (a) and (b) show the energy resolution and the uniformity resolution for both, light jets and b-jets separately. The energy resolution becomes better when the energy of the jets increase, as expected, with a $1/\sqrt{E}$ dependence. See section 2.3.2). From these plots, one can say that the behaviour is quite similar in both cases, although the energy resolution is slightly better for light jets than for b-jets. Finally, figures 8.30 (a) and (b) do not show any apparent resolution dependence with ϕ and figures 8.31 (a) and (b) show the expected increase of the energy resolution in the crack regions and around the coverage hole $\eta = 0$.

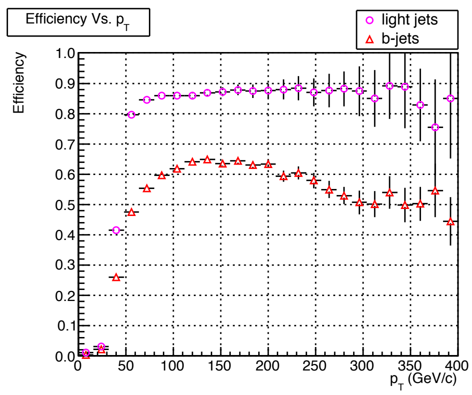

(a) *Efficiency Vs E*

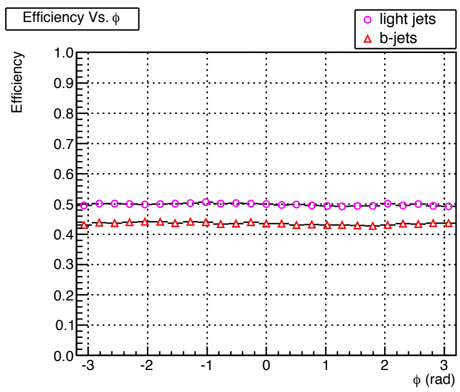

(b) *Efficiency Vs* ϕ

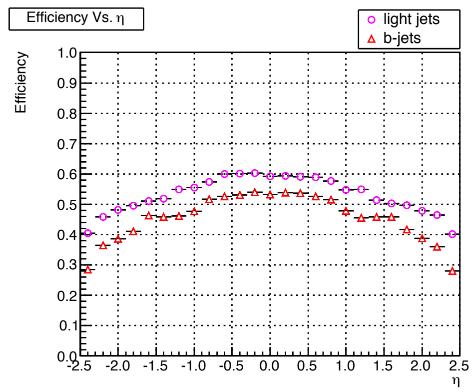

(c) *Efficiency Vs* η

Figure 8.24: *Jet reconstruction for the* $t\bar{t}$ *semileptonic sample: efficiency as a function of* p_T *(a),* ϕ *(b) and* η *(c). On these plots, two different set of points exist, one for light jets (circles) and another for b-jets (triangles).*

8.3.8 Semileptonic $t\bar{t}$ event selection

After studying the reconstruction performance and in order to maximize the signal over the background ratio (S/B), an event and trigger selection have to be applied.

8.3.8.1 Trigger

The proposed signal has to be triggered using lepton triggers at EF level to select interesting events that contain evidences of the topology one is interested on. Thus, there are two trigger

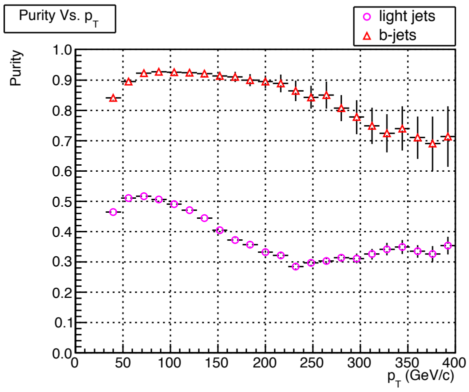

(a) *Purity Vs E*

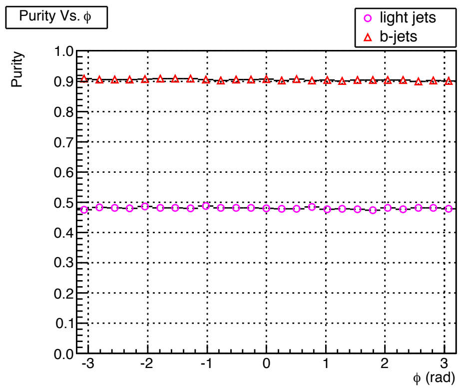

(b) *Purity Vs ϕ*

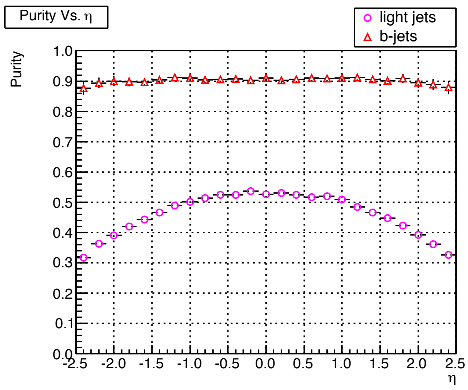

(c) *Purity Vs η*

Figure 8.25: *Jet reconstruction for the $t\bar{t}$ semileptonic sample: purity as a function of p_T (a), ϕ (b) and η (c). On these plots, two different set of points exist, one for light jets (circles) and another for b-jets (triangles).*

menus for this purpose:

- e22i: at least one isolated electron with p_T greater than 25 GeV/c.
- mu20: at least one isolated muon with p_T greater than 20 GeV/c.

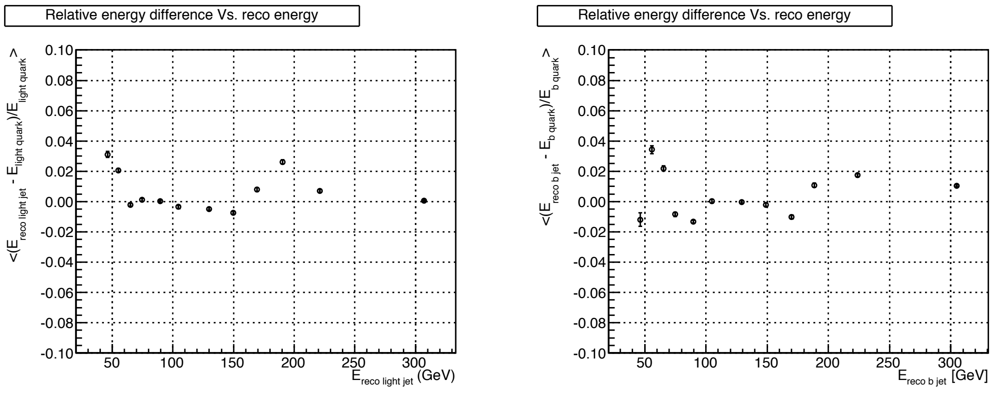

(a) *Light jets* (b) *b-jets*

Figure 8.26: *Jet reconstruction for the $t\bar{t}$ semileptonic sample: energy linearity as a function of p_T for light jets (a) and b-jets (b).*

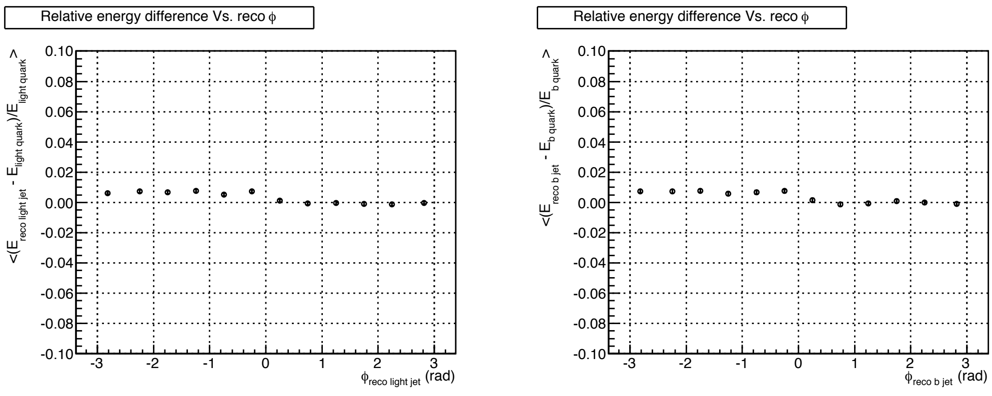

(a) *Light jets* (b) *b-jets*

Figure 8.27: *Jet reconstruction for the $t\bar{t}$ semileptonic sample: energy uniformity as a function of ϕ for light jets (a) and b-jets (b).*

8.3.8.2 Event selection cuts

Once the interesting events have been selected by the trigger a sequence of consecutive cuts is applied in order to retain the signal and to discard background events:

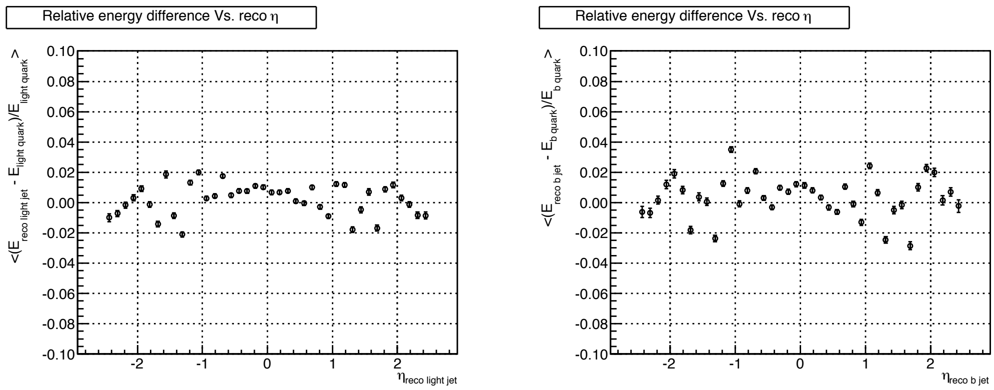

(a) *Light jets* (b) *b-jets*

Figure 8.28: *Jet reconstruction for the $t\bar{t}$ semileptonic sample: energy uniformity as a function of η for light jets (a) and b-jets (b).*

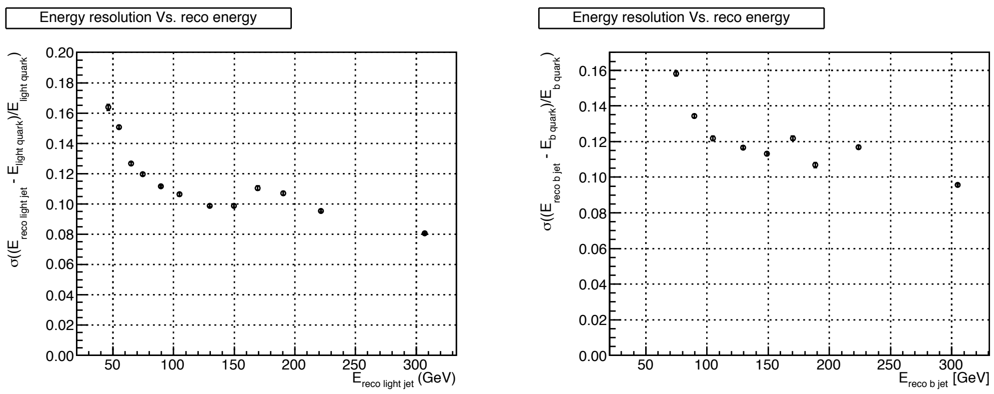

(a) *Light jets* (b) *b-jets*

Figure 8.29: *Energy resolution for light jet (a) and b-jet (b) reconstruction.*

- Exactly one isolated lepton within $|\eta| < 2.5$ with $p_T > 25$ GeV/c or $p_T > 20$ GeV/c if the lepton is a e or a μ, respectively as from the trigger selection. Table 8.6 shows that this cut rejects most of the $t\bar{t}$ fully hadronic events (99.4%). Some of the $t\bar{t}$ fully hadronic events still remain because the leptonic decays of the b quarks sometimes mimic the semileptonic signal. Moreover, this selection also reduces the QCD backgrounds as

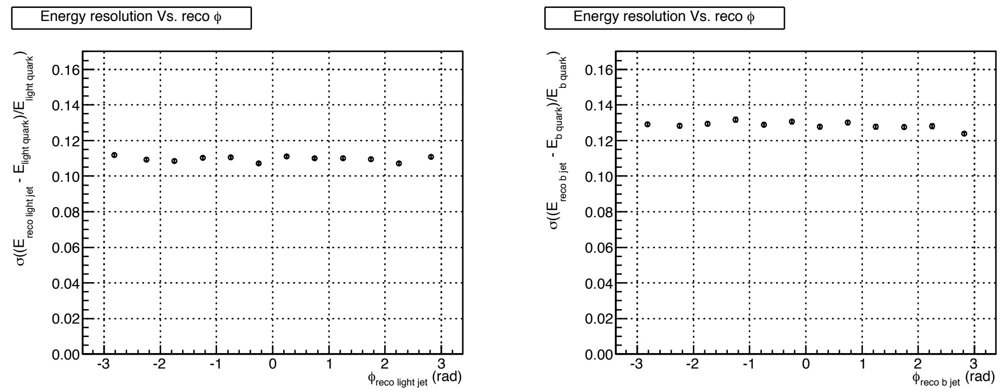

(a) *Light jets* (b) *b-jets*

Figure 8.30: *Uniformity resolution (ϕ) for light jet (a) and b-jet (b) reconstruction, both for the $t\bar{t}$ semileptonic sample.*

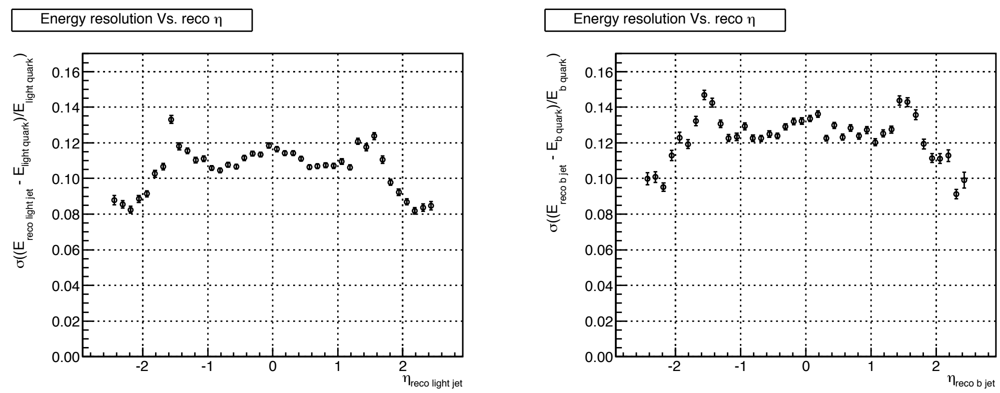

(a) *Light jets* (b) *b-jets*

Figure 8.31: *Uniformity resolution (η) for light jet (a) and b-jet (b) reconstruction, both for the $t\bar{t}$ semileptonic sample.*

one lepton is required.

- E_T^{miss} > 20 GeV. This cut requires missing transverse energy which should has its origin in the produced neutrino from the leptonically decay of the W. Together with the previous cut, helps to reject QCD backgrounds, as genuine QCD events that do not produce high energetic neutrinos.

- At least four jets with $p_T > 40$ GeV/c within $|\eta| < 2.5$. Below 40 GeV/c, jets are known to be less precisely calibrated. This cut is quite tight as can be seen in table 8.6 as only $\sim 34\%$ of W which decay hadronically have both jets satisfying this requirement [7].

- Exactly two tagged b-jets are required to perform the top quark mass measurements in this thesis.

From the third and the fourth selection cut, one can see that two or more light jets are required but there is no upper limit in the number of light jets in an event. This is due to the fact that events with gluon radiation (ISR and FSR) are considered here and therefore 31.6% of the signal events have more than two light jets as is shown in figure 8.32 where the number of light jets, i.e. the jets not tagged as b-jets, are displayed for events passing the selection cuts.

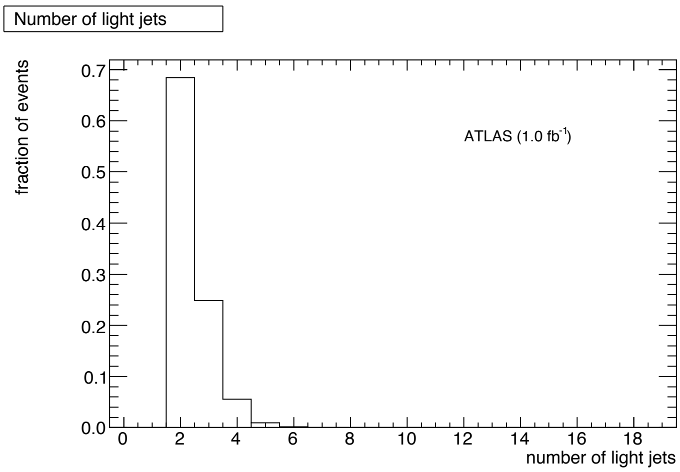

Figure 8.32: *Normalized distribution of the number of jets no tagged as b-jets, i.e. light jets, in the $t\bar{t}$ semileptonic sample.*

Table 8.6 shows the number of events (including *event weights*) normalized at luminosity of 1 fb^{-1}, before and after each selection cut, for the semileptonic $t\bar{t}$ signal and for the main backgrounds. The normalizations of each sample were computed using the cross sections (estimated for $\sqrt{s} = 14$ TeV) written in the different tables of section 8.2.1. About 4.6% of the semileptonic $t\bar{t}$ signal events pass all the selection cuts. Moreover, the S/B ratio before any cut is, quite low, 0.13 (just 11% is signal) (considering just the backgrounds on the table)[6] and after all the selection cuts is 5.7 ($\sim 85\%$ is signal), which is enough to perform the mass measurement. The semileptonic signal purity, i.e. comparing the combinatorial background with the total number of signal events, is just 35%. Additional cuts will be added in order to clean the signal, decreasing the efficiency but increasing the S/B ratio and the semileptonic signal purity. Finally,

[6] In the table, some W + jets samples were not considered as their datasets were not available but considering the numbers from reference [142], the S/B ratio before any of the proposed cuts decreases to 0.11 ($\sim 10\%$ is signal).

although after the selection cuts the total reconstruction efficiency is just 0.6%, it is expected that ATLAS will collected enough data to neglect the statistical error compared with the systematics.

Process	**Number of events at 1 fb^{-1} (including weights)**				
	Before cuts	**1 isolated lepton** (p_T > **25 (20) GeV/c**)	E_T^{miss} **> 20 GeV**	**≥4 jets** (p_T > **40 GeV/c**)	**2 b-jets**
semileptonic $t\bar{t}$ signal	289000	143657	129104	38424	13161
fully hadronic	370000	2152	1063	570	103
fully had (τ decay)	81000	446	421	107	18
dileptonic	91000	43257	40794	3623	1331
single top (Wt)	25500	10394	9114	875	216
single top (t-ch)	81300	29048	25790	1658	409
single top (s-ch)	2300	766	679	14	6
W$b\bar{b}$ + 0 partons	6260	2011	1733	2	1
W$b\bar{b}$ + 1 partons	6969	2011	1723	13	7
W$b\bar{b}$ + 2 partons	3920	1125	969	57	22
W$b\bar{b}$ + 3 partons	2770	840	740	208	65
W$c\bar{c}$ + 0 partons	6719	2111	1797	0	0
W$c\bar{c}$ + 1 partons	7490	2319	2011	23	0
W$c\bar{c}$ + 2 partons	4360	1290	1095	76	3
W$c\bar{c}$ + 3 partons	2770	805	703	190	11
W $\to \mu\nu_\mu$ + 3 parts	65000	35474	31564	530	5
W $\to \mu\nu_\mu$ + 4 parts	36000	18990	16706	1473	22
W $\to \mu\nu_\mu$ + 5 parts	20000	10872	9716	2676	72
W $\to \tau\nu_\tau$ + 2 parts	88000	4989	4033	8	0
W $\to \tau\nu_\tau$ + 3 parts	87000	4972	4109	53	0
W $\to \tau\nu_\tau$ + 4 parts	46000	2848	2552	272	8
WW [133]	17100	1820	1820	1	1
WZ [133]	3400	1830	1830	0	0
ZZ [133]	9200	258	258	1	1
Z + partons [133]	1200000	40000	40000	23	0

Table 8.6: *Number of events (including* event weights*) normalized at 1 fb^{-1} for semileptonic $t\bar{t}$ signal and main backgrounds before and after each consecutive event selection cut. The cross sections were estimated assuming* $\sqrt{s}$ = 14 *TeV. The diboson and the Z + jets backgrounds numbers are from [133], where the first and the second cut are applied as a unique "leptonic cut" and the b-jets cut is done before the light jets cut.*

9

Top quark mass measurement using the Globalχ^2 algorithm

This chapter presents the top quark mass measurement performed with a Kinematic Fit (KF) based on the Globalχ^2 formalism. It uses the LO final state reconstructed objets of the semileptonic channel as it has been already described in the previous chapter. In the present study b-tagging has been required, therefore a good b-jet reconstruction performance is assumed. Obviously this will not be the case for the early LHC days. Of course, one may even try this KF without requiring b-tagging (which of course is somewhat a bit more difficult) but as one of the main goals of this thesis is to introduce the Globalχ^2 algorithm within this framework, a fully commissioning analysis of the top quark mass measurement has not been considered here. Anyhow, work is on progress with these kind of studies, specially using MC08 data [143] ($\sqrt{s}$ = 10 GeV) for near future publications.

KF methods use a χ^2 function that accounts all the reconstructed objects and some extra information. The composition of this χ^2 is important since some of its terms can introduce strong constraints to the solution. There are three options to minimize a χ^2 function: The first would be to fit all possible parameters at once (KF methods). The second would consist in performing firstly a fit with limited set of parameters (for instance, hadronic W boson parameters) and then introducing the results directly (i.e. fixing the energy corrections of the light jets) to the global fit. And finally, the third option would be to follow the Globalχ^2 philosophy, where a nested fit is performed and its results are considered as correlations in the final global fit. The latter case ensures that the hadronic W boson and the top quark fits are simultaneously at their minima.

In the Globalχ^2 formalism, the energy scale factors are determined by the same means as the other KFs but the light jet energy scale factors become more constrained. Anyhow, as the b-jet energy scale is the main source of systematic uncertainty for the top quark mass determination, the Globalχ^2 should have the almost same systematic uncertainty as other χ^2 methods. Besides, more than the χ^2 fit type, the systematics come from the observable terms used in the χ^2.

9.1 The Globalχ^2 algorithm within the $t\bar{t}$ context

The Globalχ^2 formalism was introduced in section 4.1 to solve alignment problems but this section will migrate this formalism in order to measure the top quark mass.

9.1.1 Introduction

One of the methods to compute the top quark mass from the reconstructed objects in $t\bar{t}$ events is the use of χ^2 methods [142] [7]. In particular the so-called KF defines a χ^2 function which uses explicitly the knowledge of the event topology, i.e. it uses the particle decay model. Then, a simple χ^2 can be defined as:

$$\chi^2 = \sum_{\text{i = jets+lepton}} \left(\frac{E_i^m - E_i^f}{\sigma_{E_i}}\right)^2 + \left(\frac{M_{jj} - M_W^{ref}}{\Gamma_W^{ref}}\right)^2 + \left(\frac{M_{l\nu} - M_W^{ref}}{\Gamma_W^{ref}}\right)^2 + \\ + \left(\frac{M_{jjb_H} - M_{top}^f}{\sigma_{top_H}}\right)^2 + \left(\frac{M_{\ell\nu b_\ell} - M_{top}^f}{\sigma_{top_L}}\right)^2 \tag{9.1}$$

This χ^2 has several terms with different meanings. Thus, the first term compares the measured and corrected energy (E_i^m) with the expected energy (E_i^f). In fact, $E_i^f = \alpha_{E_i} E_i^m$ where α_{E_i} is the fine energy scale correction of the i object and the parameters to be determined. These scaling factors should not be confused with the JES factors which are provided by the calibration (see section 8.3.6). Then, the numerator of this χ^2 term can be written as $E_i^m(1-\alpha_{E_i})$, i.e. the energy scale factors are compared to 1. In other words, this term allows an fine correction of the current calibration for the four jets and for the lepton separately. The next two χ^2 factors constrain the invariant mass of two light jets and the lepton plus the neutrino to the pole mass of the reference W boson (M_W^{ref}), the first for the hadronic W decay and the second for the leptonic W decay. Finally, the latest two terms allow to computed the top quark mass from the hadronic and the leptonic top quark decays. As can be see, M_{top}^f must be the same for t and $\bar{t}$. Then, as this χ^2 contains terms built with kinematic information of the $t\bar{t}$ decay, the procedure is known as KF.

From the mathematical point of view, the goal of the KF methods is just to find the best parameter values which minimize the χ^2 function from 9.1. Now is more convenient and elegant to use a matrix notation analogously to the one used in chapter 4, so the expression 9.1 can be rewritten as:

$$\chi^2 = \mathbf{r}^T V^{-1}\mathbf{r} + \mathbf{R_W}^T S^{-1}\mathbf{R_W} \tag{9.2}$$

where in the first term, $\mathbf{r}$ represents a column vector containing all the observable residuals considered and therefore it has a dimension N_{RES} (in this particular case, $N_{RES} = 7$). Here, $\mathbf{r}$ depends on the set of parameters parameters used in the hadronic W boson fit (energy scale corrections of the light jets) and on the set of parameters used in the top quark fit (M_{top} and energy scale corrections). These sets will be referred as $\mathbf{W}$ and $\mathbf{t}$, respectively. Formally, $\mathbf{W}$ are the local parameters and $\mathbf{t}$ the global parameters. Thus, one can write $\mathbf{r} = \mathbf{r}(\mathbf{W}, \mathbf{t})$. In the second term appears the column vector $\mathbf{R_W} = \mathbf{R_W}(\mathbf{W})$ with dimension N_{RES_W} (here, $N_{RES_W} = 2$) which are the observable residuals containing the kinematic constraints. Thus, one has:

$$\mathbf{r} = \begin{pmatrix} r_1 \\ \vdots \\ r_{N_{RES}} \end{pmatrix} \longrightarrow \mathbf{r} = \begin{pmatrix} E^m_{j_1} - E^f_{j_1} \\ E^m_{j_2} - E^f_{j_2} \\ E^m_{b_H} - E^f_{b_H} \\ E^m_{b_\ell} - E^f_{b_\ell} \\ E^m_{\ell} - E^f_{\ell} \\ M_{jjb_H} - M^f_{top} \\ M_{\ell\nu b_\ell} - M^f_{top} \end{pmatrix} = \begin{pmatrix} E^m_{j_1} - \alpha_{E_{j_1}} E^m_{j_1} \\ E^m_{j_2} - \alpha_{E_j 2} E^m_{j_2} \\ E^m_{b_H} - \alpha_{E_{b_H}} E^m_{b_H} \\ E^m_{b_L} - \alpha_{E_{b_\ell}} E^m_{b_L} \\ E^m_{\ell} - \alpha_{E_\ell} E^m_{\ell} \\ M_{jjb_H} - M^f_{top} \\ M_{\ell\nu b_\ell} - M^f_{top} \end{pmatrix} = \begin{pmatrix} E^m_{j_1}(1 - \alpha_{E_{j_1}}) \\ E^m_{j_2}(1 - \alpha_{E_{j_2}}) \\ E^m_{b_H}(1 - \alpha_{E_{b_H}}) \\ E^m_{b_L}(1 - \alpha_{E_{b_\ell}}) \\ E^m_{\ell}(1 - \alpha_{E_\ell}) \\ M_{jjb_H} - M^f_{top} \\ M_{\ell\nu b_\ell} - M^f_{top} \end{pmatrix}$$

$$\mathbf{R_W} = \begin{pmatrix} R_1 \\ \vdots \\ R_{N_{RES_W}} \end{pmatrix} \longrightarrow \mathbf{R_W} = \begin{pmatrix} M_{jj} - M^{ref}_W \\ M_{\ell\nu} - M^{ref}_W \end{pmatrix}$$

On the other hand, V and S represent the covariance matrices (with dimension $[N_{RES} \times N_{RES}] = [7 \times 7]$ and $[N_{RES_W} \times N_{RES_W}] = [2 \times 2]$ respectively) for each case. Generally, a covariance matrix can be fully populated, but here correlations between different jets and the lepton, and between the different constraints are neglected as they are almost independent objects, so one finally has the following covariance matrices:

$$V^{-1} = \begin{pmatrix} 1/\sigma^2_{E_{j_1}} & 0 & 0 & 0 & 0 & 0 & 0 \\ 0 & 1/\sigma^2_{E_{j_2}} & 0 & 0 & 0 & 0 & 0 \\ 0 & 0 & 1/\sigma^2_{E_{b_H}} & 0 & 0 & 0 & 0 \\ 0 & 0 & 0 & 1/\sigma^2_{E_{b_L}} & 0 & 0 & 0 \\ 0 & 0 & 0 & 0 & 1/\sigma^2_{E_\ell} & 0 & 0 \\ 0 & 0 & 0 & 0 & 0 & 1/\sigma^2_{top_H} & 0 \\ 0 & 0 & 0 & 0 & 0 & 0 & 1/\sigma^2_{top_L} \end{pmatrix}$$

$$S^{-1} = \begin{pmatrix} 1/(\Gamma^{ref}_W)^2 & 0 \\ 0 & 1/(\Gamma^{ref}_W)^2 \end{pmatrix}$$

Here, it is worth to mention that the S matrix has to be interpreted with care. For this covariance matrix, its diagonal elements are not built from gaussian-like uncertainty distributions, they are built from the reference W boson decay width (Γ^{ref}_W) which obey a Breit-Wigner distribution[1] So, to be more realistic a Breit-Wigner distribution convoluted with a gaussian (accounting for the detector resolution and for the experimental uncertainties) should be used. Anyhow, this refinement is not applied here, and it will be postpone for further studies.

[1]The Breit-Wigner distribution is used to model resonances (i.e., unstable particles) in high energy physics. It is defined as:

$$BW(E) = \frac{\Gamma}{2\pi\left[(E - M)^2 + \left(\frac{\Gamma}{2}\right)^2\right]}$$

where E is the center-of-mass energy that produces the resonance, M is the mass of the resonance, and Γ is the resonance's decay width. Any particle with a finite lifetime (τ) has a mass distribution of non-zero width, explained by the Heisenberg uncertainty principle ($\tau = \hbar/\Gamma$). Thus, the Γ is in fact the Full Width at Half Maximum (FWHM) of that Breit-Wigner mass distribution.

9.2 Globalχ^2 formalism

Now, once the χ^2 function has been proposed, one can apply the Globalχ^2 formalism. To do this, one has to fix with respect which parameters the χ^2 should be minimize. In that sense, the idea is to minimize the previous χ^2 (expression 9.2) with respect the set of parameters used for the top quark fit, represented by the vector $\mathbf{t} = \{M_{top}, ...\}$. Therefore, one has to apply the minimum condition:

$$\frac{d\chi^2}{d\mathbf{t}} = 0 \tag{9.3}$$

where the term $d\chi^2/d\mathbf{t}$ is a row vector, which represents the derivative of the χ^2 function with respect $\mathbf{t}$. This is a clear abuse of notation which will simplify the formulae. Then, the dimension of this vector is $[1 \times N_t]$ and expressed in a matricial way it looks like that:

$$\left(\frac{d\chi^2}{d\mathbf{t}_1}, \frac{d\chi^2}{d\mathbf{t}_2}, \ldots, \frac{d\chi^2}{d\mathbf{t}_{N_t}}\right) = (0, 0, \ldots, 0) \tag{9.4}$$

Then, the equation 9.2 together with 9.4 give:

$$\frac{d\chi^2}{d\mathbf{t}} = \frac{d}{d\mathbf{t}}\left[\mathbf{r}^T V^{-1}\mathbf{r} + \mathbf{R_W}^T S^{-1}\mathbf{R_W}\right] =$$

$$= \left[\left(\frac{d\mathbf{r}}{d\mathbf{t}}\right)^T V^{-1}\mathbf{r}\right]^T + \left[\mathbf{r}^T V^{-1}\frac{d\mathbf{r}}{d\mathbf{t}}\right] + \left[\left(\frac{d\mathbf{R_W}}{d\mathbf{t}}\right)^T S^{-1}\mathbf{R_W}\right]^T + \left[\mathbf{R_W}^T S^{-1}\frac{d\mathbf{R_W}}{d\mathbf{t}}\right] = 0 \tag{9.5}$$

Now, taken advantage from the notation and that V^{-1} and S^{-1} are diagonal matrices (let A be a diagonal matrix, therefore $(A^{-1})^T = A^{-1}$), the χ^2 minimization (with respect $\mathbf{t}$) converts equation 9.5 in:

$$\frac{d\chi^2}{d\mathbf{t}} = 2\left[\mathbf{r}^T V^{-1}\frac{d\mathbf{r}}{d\mathbf{t}}\right] + 2\left[\mathbf{R_W}^T S^{-1}\frac{d\mathbf{R_W}}{d\mathbf{t}}\right] = 0$$

The last step uses a simple transposing rule, $(AB)^T = B^T A^T$, therefore condition 9.3 can be expressed as:

$$\mathbf{r}^T V^{-1}\frac{d\mathbf{r}}{d\mathbf{t}} + \mathbf{R_W}^T S^{-1}\frac{d\mathbf{R_W}}{d\mathbf{t}} = 0$$

and this expression is again a set of N_t equations. For convenience, it can be rewritten in its transposed form:

$$\left(\frac{d\mathbf{r}}{d\mathbf{t}}\right)^T V^{-1}\mathbf{r} + \left(\frac{d\mathbf{R_W}}{d\mathbf{t}}\right)^T S^{-1}\mathbf{R_W} = 0 \tag{9.6}$$

9.2.1 Derivatives

Now, one should consider how $d\mathbf{r}/d\mathbf{t}$ can be calculated. In our case, $\mathbf{r} = \mathbf{r}(\mathbf{W}, \mathbf{t})$ and $\mathbf{R_W} = \mathbf{R_W}(\mathbf{W})$, therefore:

$$d\mathbf{r} = \frac{\partial \mathbf{r}}{\partial \mathbf{W}} d\mathbf{W} + \frac{\partial \mathbf{r}}{\partial \mathbf{t}} d\mathbf{t}$$

$$d\mathbf{R_W} = \frac{\partial \mathbf{R_W}}{\partial \mathbf{W}} d\mathbf{W}$$

leading the following derivatives:

$$\frac{d\mathbf{r}}{d\mathbf{W}} = \frac{\partial \mathbf{r}}{\partial \mathbf{W}} \quad \text{and} \quad \frac{d\mathbf{r}}{d\mathbf{t}} = \frac{\partial \mathbf{r}}{\partial \mathbf{W}} \frac{d\mathbf{W}}{d\mathbf{t}} + \frac{\partial \mathbf{r}}{\partial \mathbf{t}}$$

$$\frac{d\mathbf{R_W}}{d\mathbf{W}} = \frac{\partial \mathbf{R_W}}{\partial \mathbf{W}} \quad \text{and} \quad \frac{d\mathbf{R_W}}{d\mathbf{t}} = \frac{\partial \mathbf{R_W}}{\partial \mathbf{W}} \frac{d\mathbf{W}}{d\mathbf{t}}$$

An important point is to assume that the top quark parameters ($\mathbf{t}$) should not depend on the W boson parameters ($\mathbf{W}$) as the top quark parameters are the ones that fix the event kinematics, i.e. $\mathbf{t}$ parameters do not depend on $\mathbf{W}$ parameters just because the top quarks decay into the W's and not viceversa. Therefore $d\mathbf{t}/d\mathbf{W} = 0$.

So, with these residuals, expression 9.6 can be write as follows:

$$\left(\frac{\partial \mathbf{r}}{\partial \mathbf{W}} \frac{d\mathbf{W}}{d\mathbf{t}} + \frac{\partial \mathbf{r}}{\partial \mathbf{t}} \right)^T V^{-1} \mathbf{r} + \left(\frac{\partial \mathbf{R_W}}{\partial \mathbf{W}} \frac{d\mathbf{W}}{d\mathbf{t}} \right)^T S^{-1} \mathbf{R_W} = 0 \tag{9.7}$$

Now, the only problem is how to obtain the derivative $d\mathbf{W}/d\mathbf{t}$. Actually, this is the novelty of the Globalχ^2 method with respect other χ^2 fits and it will introduce the correlations between the W boson parameters and the top quark parameters. To get it, one needs to find the solution of the W boson parameters for any arbitrary top quark parameters. Then, this requires to minimize the χ^2 function from 9.2 with respect the W boson parameters ($\mathbf{W}$).

Reached to this point it is worth to establish a parallelism with the alignment problem. The role of the local parameters in the alignment is played by the track parameters, while here, one uses the $\mathbf{W}$ parameters. On the other hand, the global parameters are the alignment parameters themselves, but the top fit parameters in the current case.

9.2.2 W boson parameters fitting

Considering a minimization of the χ^2 function with respect the $\mathbf{W}$, one has:

$$\frac{d\chi^2}{d\mathbf{W}} = 0 \quad \longrightarrow \quad \left(\frac{d\mathbf{r}}{d\mathbf{W}} \right)^T V^{-1} \mathbf{r} + \left(\frac{d\mathbf{R_W}}{d\mathbf{W}} \right)^T S^{-1} \mathbf{R_W} = 0$$

therefore, using the previous derivatives:

$$\left(\frac{\partial \mathbf{r}}{\partial \mathbf{W}} \right)^T V^{-1} \mathbf{r} + \left(\frac{\partial \mathbf{R_W}}{\partial \mathbf{W}} \right)^T S^{-1} \mathbf{R_W} = 0 \tag{9.8}$$

In order to solve 9.8, one can assume that the initial values $\mathbf{W}_0$ are relatively close to the solution $\mathbf{W}$ (if not, this linear approximation holds but iterations should be required) and, because of that, expand the residuals around these values $\mathbf{W}_0$ with the simple Taylor's rule. Moreover, only the first linear term will be used, i.e. higher order derivatives will be neglected, $\partial^{m+n}\mathbf{r}/\partial\mathbf{W}_i^m\partial\mathbf{W}_j^n \to 0$, because the extrapolated points are considered as linear functions of the W boson parameters (small changes). Therefore, $\mathbf{W} = \mathbf{W}_0 + \delta\mathbf{W}$ being $\delta\mathbf{W}$ a set of linear corrections to the initial W boson parameters.

By using this approximation the $\mathbf{W}$ residuals will change linearly from those computed with $\mathbf{W}_0$ by:

$$\mathbf{r} = \mathbf{r}(\mathbf{W}_0, \mathbf{t}) + \left.\frac{\partial\mathbf{r}}{\partial\mathbf{W}}\right|_{W=W_0} \delta\mathbf{W} \tag{9.9}$$

$$\mathbf{R_W} = \mathbf{R_W}(\mathbf{W}_0, \mathbf{t}) + \left.\frac{\partial\mathbf{R_W}}{\partial\mathbf{W}}\right|_{W=W_0} \delta\mathbf{W} \tag{9.10}$$

so the derivative of the residuals is computed in the neighborhood of W_0. Moreover, in what follows, the following convention will be used:

$$\frac{\partial\mathbf{r}(\mathbf{W}_0, \mathbf{t})}{\partial\mathbf{W}} \equiv \left.\frac{\partial\mathbf{r}}{\partial\mathbf{W}}\right|_{W_0} \equiv \left.\frac{\partial\mathbf{r}}{\partial\mathbf{W}}\right|_{W=W_0}$$

In addition, as has been stated above, second order (and higher) derivatives of the residuals are neglected. Then, one can just write:

$$\begin{aligned} &\left(\frac{\partial\mathbf{r}}{\partial\mathbf{W}}\right)^T V^{-1}\mathbf{r} + \left(\frac{d\mathbf{R_W}}{d\mathbf{W}}\right)^T S^{-1}\mathbf{R_W} = \\ &= \left(\frac{\partial\mathbf{r}(\mathbf{W}_0,\mathbf{t})}{\partial\mathbf{W}}\right)^T V^{-1}\mathbf{r}(\mathbf{W}_0,\mathbf{t}) + \left(\frac{\partial\mathbf{r}(\mathbf{W}_0,\mathbf{t})}{\partial\mathbf{W}}\right)^T V^{-1} \left.\frac{\partial\mathbf{r}}{\partial\mathbf{W}}\right|_{W_0} \delta\mathbf{W} + \\ &+ \left(\frac{\partial\mathbf{R_W}(\mathbf{W}_0)}{\partial\mathbf{W}}\right)^T S^{-1}\mathbf{R_W}(\mathbf{W}_0) + \left(\frac{\partial\mathbf{R_W}(\mathbf{W}_0)}{\partial\mathbf{W}}\right)^T S^{-1} \left.\frac{\partial\mathbf{R_W}}{\partial\mathbf{W}}\right|_{W_0} \delta\mathbf{W} = 0 \end{aligned} \tag{9.11}$$

and now one may define:

$$E \equiv \left.\frac{\partial\mathbf{r}}{\partial\mathbf{W}}\right|_{W_0} \tag{9.12}$$

$$F_\mathbf{W} \equiv \left.\frac{\partial\mathbf{R_W}}{\partial\mathbf{W}}\right|_{W_0} \tag{9.13}$$

where $dim[E] = [N_{RES} \times N_W]$ and $dim[F_\mathbf{W}] = [N_{RES_W} \times N_W]$ (being N_W the number of W boson parameters, i.e. the α's for two light jets. See expression 9.1).

These matrices are very important because they correlate the different observable residuals for each W boson. Therefore, using the E and $F_\mathbf{W}$ definitions from 9.12 and 9.13 into the W boson fit equation 9.11, it becomes now:

$$E^T V^{-1}\mathbf{r}(\mathbf{W}_0,\mathbf{t}) + E^T V^{-1} E\delta\mathbf{W} + F_\mathbf{W}^T S^{-1}\mathbf{R_W}(\mathbf{W}_0) + F_\mathbf{W}^T S^{-1} F_\mathbf{W}\delta\mathbf{W} = 0$$

which allows to obtain the W boson parameters corrections $\delta\mathbf{W}$ as:

$$\delta\mathbf{W} = -\left(E^T V^{-1} E + F_\mathbf{W}^T S^{-1} F_\mathbf{W}\right)^{-1} \left(E^T V^{-1}\mathbf{r}(\mathbf{W}_0,\mathbf{t}) + F_\mathbf{W}^T S^{-1}\mathbf{R_W}(\mathbf{W}_0)\right) \tag{9.14}$$

Therefore, equation 9.14 can be written in a very compact way:

$$\delta\mathbf{W} = -\mathcal{M}_W^{-1}\left(\nu_W + \nu_{F_W}\right)$$

where:

$$\mathcal{M}_W^{-1} \equiv \left(E^T V^{-1} E + F_{\mathbf{W}}^T S^{-1} F_{\mathbf{W}}\right)^{-1}$$

and:

$$\nu_W \equiv E^T V^{-1}\mathbf{r} \quad \text{and} \quad \nu_{F_W} \equiv F_{\mathbf{W}}^T S^{-1}\mathbf{R}_{\mathbf{W}}$$

which in its turn can be used to find the final W boson parameters as: $\mathbf{W} = \mathbf{W}_0 + \delta\mathbf{W}$.

$$\mathbf{W} = \mathbf{W}_0 - \mathcal{M}_W^{-1}\left(\nu_W + \nu_{F_W}\right)$$

Finally, one is able to evaluate $d\mathbf{W}/d\mathbf{t}$ using the previous expression:

$$\frac{d\mathbf{W}}{d\mathbf{t}} = -\left(E^T V^{-1} E + F_{\mathbf{W}}^T S^{-1} F_{\mathbf{W}}\right)^{-1} E^T V^{-1} \frac{\partial \mathbf{r}(\mathbf{W}_0, \mathbf{t})}{\partial \mathbf{t}} \tag{9.15}$$

where:

$$\frac{d\mathbf{r}(\mathbf{W}_0, \mathbf{t})}{d\mathbf{t}} = \frac{\partial \mathbf{r}(W_0, \mathbf{t})}{\partial \mathbf{W}} \frac{d\mathbf{W}}{d\mathbf{t}} + \frac{\partial \mathbf{r}(W_0, \mathbf{t})}{\partial \mathbf{t}} = \frac{\partial \mathbf{r}(W_0, \mathbf{t})}{\partial \mathbf{t}}$$

$$\frac{d\mathbf{R}_{\mathbf{W}}(\mathbf{W}_0)}{d\mathbf{t}} = \frac{\partial \mathbf{R}(W_0)}{\partial \mathbf{W}} \frac{d\mathbf{W}}{d\mathbf{t}} = 0$$

9.2.3 Top quark parameters fitting

Previous subsection was necessarily introduced in order to find the corrections to the W boson parameters for any top quark parameters and therefore to evaluate $d\mathbf{W}/d\mathbf{t}$. In other words, one needs first to fit the W boson which has been produced. Then, those residuals are used to fit the top quark parameters, by minimizing the residuals χ^2 as it is presented in eq. 9.3. Therefore, considering that our solution is calculated for W_0 (let redefine again $\mathbf{r}$, since now, $\mathbf{r} \equiv \mathbf{r}(\mathbf{W}_0, \mathbf{t})$) and then introducing 9.15 in 9.7:

$$\left(\frac{\partial \mathbf{r}}{\partial \mathbf{W}}\frac{d\mathbf{W}}{d\mathbf{t}} + \frac{\partial \mathbf{r}}{\partial \mathbf{t}}\right)^T V^{-1}\mathbf{r} + \left(\frac{\partial \mathbf{R}_{\mathbf{W}}}{\partial \mathbf{W}}\frac{d\mathbf{W}}{d\mathbf{t}}\right)^T S^{-1}\mathbf{R}_{\mathbf{W}} =$$

$$\left(-E\left(E^T V^{-1} E + F_{\mathbf{W}}^T S^{-1} F_{\mathbf{W}}\right)^{-1} E^T V^{-1} \frac{\partial \mathbf{r}}{\partial \mathbf{t}} + \frac{\partial \mathbf{r}}{\partial \mathbf{t}}\right)^T V^{-1}\mathbf{r} +$$

$$+\left(-F_{\mathbf{W}}\left(E^T V^{-1} E + F_{\mathbf{W}}^T S^{-1} F_{\mathbf{W}}\right)^{-1} E^T V^{-1} \frac{\partial \mathbf{r}}{\partial \mathbf{t}}\right)^T S^{-1}\mathbf{R}_{\mathbf{W}} = 0$$

Now, defining a "global" term ($\mathcal{G}_{EF_W}$) like in section 4.3.2:

$$\mathcal{G}_{EF_W} \equiv \left(E^T V^{-1} E + F_{\mathbf{W}}^T S^{-1} F_{\mathbf{W}}\right)^{-1} E^T V^{-1}$$

One can write:

$$\left(\frac{\partial \mathbf{r}}{\partial \mathbf{t}}\right)^T (I - E\mathcal{G}_{EF_W})^T V^{-1}\mathbf{r} - \left(\frac{\partial \mathbf{r}}{\partial \mathbf{t}}\right)^T (F_\mathbf{W}\mathcal{G}_{EF_W})^T S^{-1}\mathbf{R_W} = 0$$

Or even, defining:

$$\mathcal{W}' \equiv \left(I - E\left(E^T V^{-1} E + F_\mathbf{W}^T S^{-1} F_\mathbf{W}\right)^{-1} E^T V^{-1}\right)^T V^{-1} = (I - E\mathcal{G}_{EF_W})^T V^{-1}$$

the previous expression can be rewritten as:

$$\left(\frac{\partial \mathbf{r}}{\partial \mathbf{t}}\right)^T \mathcal{W}'\mathbf{r} - \left(\frac{\partial \mathbf{r}}{\partial \mathbf{t}}\right)^T (F_\mathbf{W}\mathcal{G}_{EF_W})^T S^{-1}\mathbf{R_W} = 0 \tag{9.16}$$

Now the idea is basically the same as depicted in section 4.3.2. Let be $\mathbf{t}$ the set of top quark parameters, and let assume that one has a set of initial parameters $\mathbf{t}_0$. The goal is to find the corrections ($\delta\mathbf{t}$) to the later set in such a way that: $\mathbf{t} = \mathbf{t}_0 + \delta\mathbf{t}$.

In this way, and in complete analogy to 9.9 one may assume that the residuals will change with $\delta\mathbf{t}$ around their values for $\mathbf{t}_0$. Therefore using a series expansion of the residuals and keeping only the first order term, one has:

$$\mathbf{r} = \mathbf{r}(\mathbf{W}_0, \mathbf{t}_0) + \left.\frac{\partial \mathbf{r}}{\partial \mathbf{t}}\right|_{\mathbf{t}=\mathbf{t}_0} \delta\mathbf{t} \tag{9.17}$$

Now, two comments on the above expression:

1. the use of W_0 is justified as it represents the W boson parameters fitted with the initial set of top quark parameters ($\mathbf{t}_0$).

2. Higher order terms are neglected which means that: $d^2\mathbf{r}/d\mathbf{t}_i d\mathbf{t}_j \to 0$.

Then, inserting 9.17 into 9.16 one obtains:

$$\left(\frac{\partial \mathbf{r}}{\partial \mathbf{t}}\right)^T \mathcal{W}'\mathbf{r} + \left(\frac{\partial \mathbf{r}}{\partial \mathbf{t}}\right)^T \mathcal{W}'\frac{\partial \mathbf{r}}{\partial \mathbf{t}}\delta\mathbf{t} - \left(\frac{\partial \mathbf{r}}{\partial \mathbf{t}}\right)^T (F_\mathbf{W}\mathcal{G}_{EF_W})^T S^{-1}\mathbf{R_W} = 0$$

Reached this point, one can proceed as in 9.14 and write:

$$\delta\mathbf{t} = -\left[\left(\frac{\partial \mathbf{r}}{\partial \mathbf{t}}\right)^T \mathcal{W}'\frac{\partial \mathbf{r}}{\partial \mathbf{t}}\right]^{-1} \left[\left(\frac{\partial \mathbf{r}}{\partial \mathbf{t}}\right)^T \mathcal{W}'\mathbf{r} - \left(\frac{\partial \mathbf{r}}{\partial \mathbf{t}}\right)^T (F_\mathbf{W}\mathcal{G}_{EF_W})^T S^{-1}\mathbf{R_W}\right] = 0 \tag{9.18}$$

This would provide a solution for $\delta\mathbf{t}$ which is a column vector of dimension $[N_t \times 1]$ (being N_t the number of parameters associated to the top quark). However one can draw few remarks. In an intuitive way, the fact is that residual derivatives depend on W boson parameters (thanks to E, and in these expressions through $\mathcal{W}'$) because those parameters are reconstructed from top quarks. So there is a nested dependence. Then, this equation is the general solution to the top quark parameters (equivalent to the equation 9.14 for the W boson parameters) and represents a set on N_t equations, one for each parameter (degree of freedom) of the top quark.

Furthermore, one can write 9.18 in a more compact way by defining three blocks:

$$\mathcal{M} = \left(\frac{\partial \mathbf{r}}{\partial \mathbf{t}}\right)^T \mathcal{W}' \frac{\partial \mathbf{r}}{\partial \mathbf{t}}$$

which by construction is a $N_t \times N_t$ symmetric matrix (and so-called *big-matrix* in the alignment jargon). And:

$$\nu = \left(\frac{\partial \mathbf{r}}{\partial \mathbf{t}}\right)^T \mathcal{W}' \mathbf{r}$$

$$\nu_{\mathbf{W}} = -\left(\frac{\partial \mathbf{r}}{\partial \mathbf{t}}\right)^T (F_{\mathbf{W}} \mathcal{G}_{EF_W})^T S^{-1} \mathbf{R_W}$$

which are column vectors of N_t components (so-called *big-vectors*). Then, with $\mathcal{M}$, ν and $\nu_{\mathbf{W}}$ one can simply write:

$$\delta\mathbf{t} = -\mathcal{M}^{-1}(\nu + \nu_{\mathbf{W}}) \tag{9.19}$$

Therefore, as in the alignment problem, in order to compute the top quark corrections ($\delta\mathbf{t}$) it is necessary to invert the matrix $\mathcal{M}$. In addition, one of the benefits is that $\mathcal{M}^{-1}$ is the covariance matrix of the top parameters fit (as already explained in section 4.2.2.1).

Finally, just one comment that was extensively discussed on chapter 4.1: if one chooses to neglect the correlations that the hadronic W decay can introduce doing $E \to 0$ and freezing $\mathbf{W}'$, one would end up with a "local" or traditional χ^2 solution where all the parameters are fitted at once.

9.2.4 Implementation

This formalism has been coded into a standalone ROOT [144] class which can be found in the following link: https://svnweb.cern.ch/trac/atlasgrp/browser/Institutes/IFIC-Valencia/IFIC/trunk/TopPhysics/TopMassAnalysis/VKiFi

A software package called TopViewAna, which is based on the official TopView[2] [145], has been prepared as interface to read and prepare the objects for the KF. Finally, just to say that the input files were the ntuples contained in the datasets summarized in appendix D.

9.3 Strategy

Once the mathematical basis of the Globalχ^2 method has been established, one has to present the strategy to perform the present analysis, which is as follows:

- First at all, event selection cuts from section 8.3.8 must be applied in order to have an enriched sample of semileptonic $t\bar{t}$ events. After this selection, assuming that b-tagging[3], there are mainly two problems within this analysis: select the light jets candidates and to estimate the neutrino four-momentum.

[2]TopView is an application of EventView analysis framework specialized in top quark physics. It was developed between the ATLAS physics analysis group and the ATLAS top working group.

[3]The b-tagging performance problem is beyond the scope of this work and therefore requiring exactly two jets tagged as b-jets allow to neglect this issue.

- As the selected channel is the lepton plus jets (where there is no upper limit for the number of light jets), one has to select the two light jets candidates which will build the hadronic W boson from all the possible jet pairings. Extra light jets come from gluon radiations, etc. Thus, the policy to select the two light jets will be based on a χ^2 minimization for just the hadronic side of the $t\bar{t}$ decay. Though some rework may be done at a later stage.

- Then, once the two light jet candidates have been selected, one of the two b-jets must be associated in order to fix the three final objects for the hadronic side. The initial assumption is done by choosing the closest b-jet to the hadronic W boson candidate (i.e. to the light jet pair) by means of the ΔR distance.

- The other issue is to estimate the neutrino four-momentum as this particle is not detected. As it will be show, the p_T^{ν} is just estimated assuming that the E_T^{miss} within an event is due to the neutrino of the leptonic side of the $t\bar{t}$ decay. Assuming the latter, the p_T component is trivially computed but the problem comes trying to compute the longitudinal momentum component. As it will be discussed, it will be estimated using the kinematics of the leptonic W boson decay.

- After that, the last piece is to associate the other b-jet to the leptonic side of the $t\bar{t}$ decay. The easiest way is just to assign the b-jet which has not been associated before. Instead of following the previous criterion, one can gain some efficiency using the fact that the difference between the invariant masses for both reconstructed tops (the hadronic and the leptonic) should be minimum. Therefore if the initial b-jet association does not obey this requirement, a b-jet association swapping is performed.

- Finally, with the six final object candidates, the Globalχ^2 algorithm can be applied to measure the top quark mass. Obviously, the fit strategy has to be performed in an event by event basis. Although there is also the possibility to accumulate all the events and then fit the whole sample.

9.4 Reconstruction of the hadronic decay side

9.4.1 Hadronic W boson mass reconstruction

The event selection from section 8.3.8 ends with pre-calibrated events which have at least four jets, two of them not labelled as b-jets, above the p_T threshold of 40 GeV/c. In particular, figure 8.32 showed that $\sim 32\%$ of those events have more than two light jet candidates. Following the strategy presented in the previous section, the first problem to be solved is to pair correctly the two light jet candidates which come from the hadronically-decaying W boson ($W \rightarrow jj$) for those events where several pairing combinations are possible. Within this work, the two candidates are extracted selecting the pair that gives the lowest χ^2 value after the minimization[4].

The χ^2 function which is minimized reads as follows:

[4]Other methods can be used, as for instance the geometric method which consists in choosing the two closest light jets [7]. Or even methods which choose the two light jets that give the mass closest to the known mass of the W boson [146] but none of these methods are considered here.

$$\chi^2 = \sum_{\mathrm{j = light\ jets}} \left(\frac{E_j^m - E_j^f}{\sigma_{E_j}} \right)^2 + \left(\frac{M_{jj} - M_W^{ref}}{\Gamma_W^{ref}} \right)^2 = \sum_{\mathrm{j = light\ jets}} \left(\frac{E_j^m (1 - \alpha_j)}{\sigma_{E_j}} \right)^2 + \left(\frac{M_{jj} - M_W^{ref}}{\Gamma_W^{ref}} \right)^2 \quad (9.20)$$

The first term sums over the two light jets ($j = j_0, j_1$). This is the usual χ^2 term for an fine tuning the energy scale of the corresponding jet energy through a multiplicative constant α_j. σ_{E_j} is the light jet energy uncertainty which is derived from the MC information (see appendix E) is $\mathcal{O}$(5-30 GeV) and it depends on the energy and η as was commented on section 8.3.6. Then, the aim of this term is to do an *in-situ* calibration of the hadronic decay side, event by event. This *in-situ* calibration does not correct the bulk of the detector and resolution effects. It represents a fine tuning correction that correlates the energy correction of the two light jets stemmed from the W boson. The second term constrains the jet pair mass M_{jj} to a reference W boson mass, with an associated uncertainty given also by a reference W boson decay width which has to be taken with care as was already commented in section 9.1.1. In this case, the reference W boson has been extracted from the simulation, i.e. from a Breit-Wigner fit to the true W boson (see figure 9.1).

$$M_W^{ref} = 80.416 \pm 0.002\ \mathrm{GeV/c^2} \quad \text{and} \quad \Gamma_W^{ref} = 2.128 \pm 0.004\ \mathrm{GeV/c^2}$$

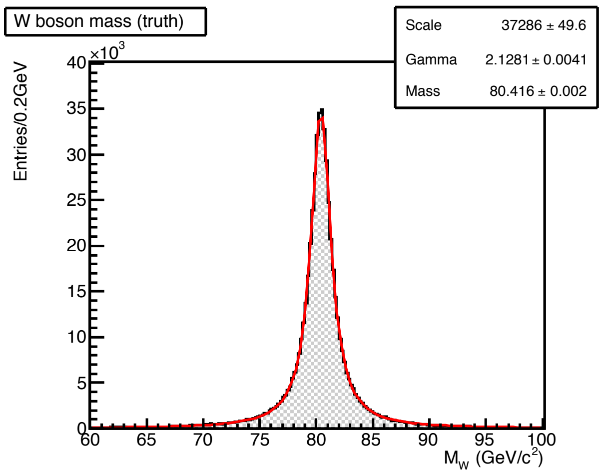

Figure 9.1: *W boson mass distribution from the truth information, fitted to a Breit-Wigner function.*

This reference W boson mass was obviously compatible with the PDG value when the simulation was done, which can be found on reference [147].

Then, expression 9.20 is minimized for all the possible light jet pair combinations within an event and the pair with the smallest χ^2 is kept.

Once the pair candidates are selected, two preliminary cuts are applied in order to reject really bad pair combinations or bad events (if there is no pair passing these preliminary cuts the event is rejected). These two preliminary cuts are based on simple kinematic variables which are the distance between the two light jet candidates ($\Delta R = \sqrt{\Delta\phi^2 + \Delta\eta^2}$) and the invariant mass of the pair ($M_{jj} = \sqrt{(E_{j_0} + E_{j_1})^2 + (\mathbf{p}_{j_0} + \mathbf{p}_{j_1})^2}$), respectively. Figures 9.2 (a) and (b) show these two variables for the best pair of light jet candidates in each event. They show, as all the plots in this chapter, good and bad combinations for the semileptonic signal events (defined in the previous chapter) based on the truth-reco matching, the contribution of physics backgrounds and the selected events which are all these events that have passed the event selection cuts (i.e. the sum of the semileptonic signal and the physics backgrounds). In other words, the label "selected events" emulates the final distribution one would observe with real data.

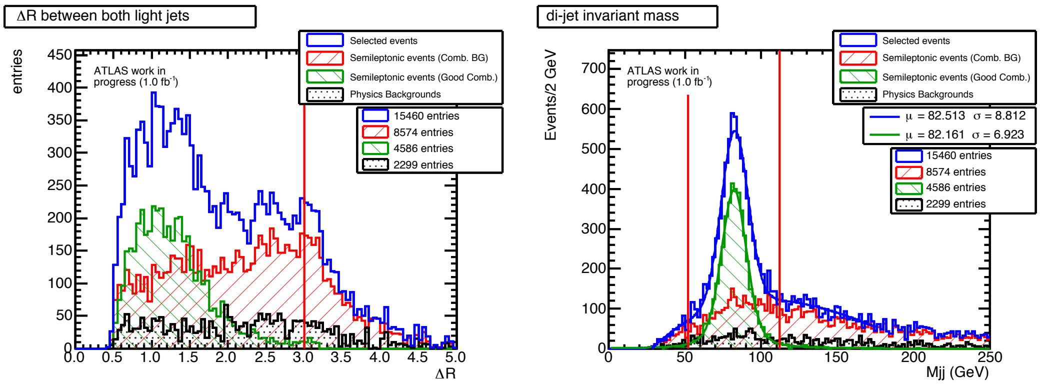

(a) *PreCut 0:* $\Delta R < 3.0$

(b) *PreCut 1:* $|M_{jj} - M_{jj}^{peak}| < 30$ *GeV/c*^{2}

Figure 9.2: *Distribution of the* ΔR *distance between the two best light jet candidates (a) and of the invariant mass of the pair (b) for simulated events. Moreover, proposed cuts are drawn on each histogram.*

From these figures it is easy to propose the following cuts:

- **PreCut 0:** The first cut comes from figure 9.2 (a), where a cut $\Delta R < 3.0$ will reject mainly combinatorial background events. Although this cutting value is quite conservative, the semileptonic signal purity rises from 35% up to 41%, although the $t\bar{t}$ semileptonic reconstruction efficiency drops from 4.6% to $\sim 3.8\%$.

- **PreCut 1:** The next cut comes from figure 9.2 (b) which consists on keeping just the pairs with an invariant mass within a mass window of 30 GeV/c^2 around the peak value of this distribution, that is $M_{jj}^{peak} = 82.5 \pm 0.2$ GeV/c^2 (to fit the "Selected events" distribution a Gauss plus a third degree polynomial function has been used while to fit "Good Comb." distribution a Breit-Wigner convoluted with a gaussian function was used). In fact, events with higher invariant mass values than 100 GeV/c^2 are mainly combinatorial background events and physics background, then this cut will clean the sample more than the previous case and therefore the purity will rise again. Thanks to this cut, semileptonic signal purity increases up to 61% while its reconstruction efficiency decreases up to $\sim 2.5\%$.

Besides, both cuts are quite loose in order to avoid biases.

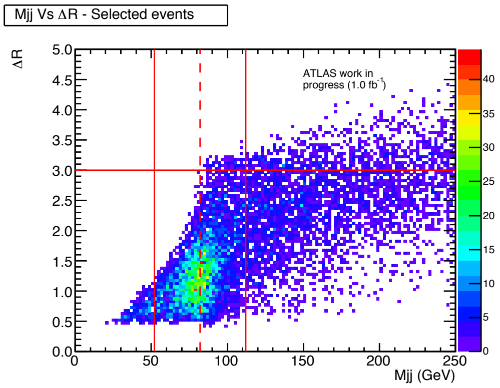

(a) *Selected events*

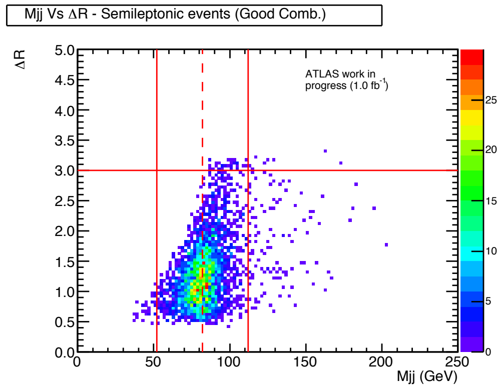

(b) *Semileptonic events (good comb.)*

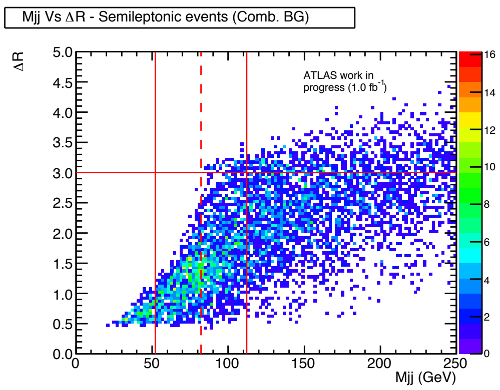

(c) *Semileptonic events (comb. background)*

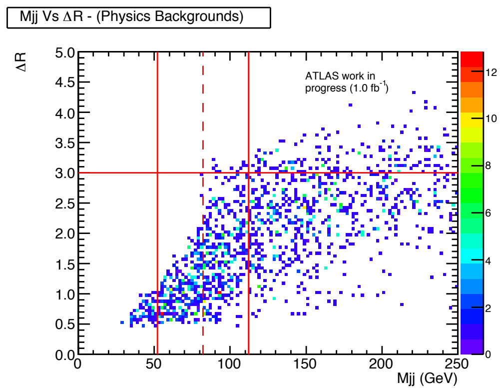

(d) *Physics background events*

Figure 9.3: *Correlation between ΔR and the invariant mass of the best light jet pair candidates.*

How well these two cuts clean the sample is shown in figures 9.3 (a), (b), (c) and (d), where one has the correlation between ΔR and the invariant mass of the pair for the selected events, the semileptonic events (good and wrong combinations) and physics backgrounds, respectively. Both cuts are represented with solid horizontal and vertical lines on these plots and can be seen how they preserve the good combinations of the semileptonic events (see figure (b)) while most of the combinatorial and physics background are rejected. The semileptonic signal efficiency drops from 4.6% to 2.5% while the S/B ratio increases from 5.7 ($\sim$85% is signal) up to 9.0 (90% is signal). Finally, the semileptonic signal purity has been increased from 35% to 61%.

After considering these two cuts, the minimization procedure gives the corresponding energy correction factors (α_0 and α_1). Their distributions can be found on figures 9.4 (a) and (b). From a gaussian fit, one can extract two conclusions: firstly, since both distributions peak almost at 1, it means that the calibration was very good and secondly the widths of these distributions tell that some jets can be better calibrated. The latter is performed through this fine tuning *in-situ* calibration. Finally, it is worth to mention that the fact that figure (a) is narrower than figure (b) is because jets are always sorted from higher to lower p_T, i.e. j_0 has always higher p_T than j_1 within an event.

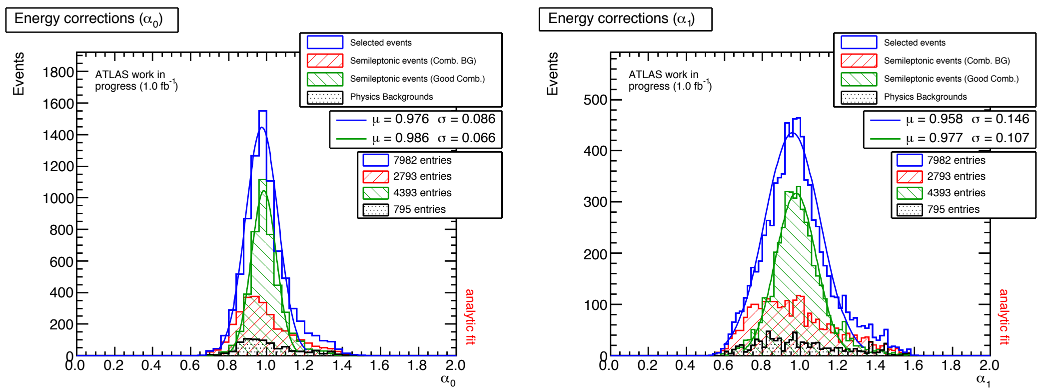

(a) *Energy correction factors for jet 0* (b) *Energy correction factors for jet 1*

Figure 9.4: *Energy correction factors estimated in-situ by the χ^2 minimization for the hadronic W boson decay. Distributions are fitted to a gaussian function.*

Figures 9.5 (a) and (b) show the overall behaviour of the *in-situ* energy correction factors as a function of the energy and η.

These energy correction factors lead to a very narrow W boson mass distribution as can be seen in figure 9.6. Fitting this distribution to a Breit-Wigner convoluted with a gauss function (although it really has asymmetric tails) gives M_W = 80.686 $\pm$ 0.013 (stat.) GeV/c^2 and σ_W = 0.738 $\pm$ 0.017 (stat.) GeV/c^2, where the later result corresponds to the measurement uncertainty (the uncertainty due to the detector resolution is assumed to be gaussian-like). These results are compatible with the ones on reference [5].

Further on, a cut can be applied to the fitted W boson mass distribution in order to clean the sample:

- **Cut C0:** Only hadronic W boson candidates with $\chi^2 < 6$ are kept (see figure 9.7 (a)). This χ^2 value was chosen to preserve the 80% of the efficiency as can be seen in figures 9.7 (b). With this other cut the S/B ratio increase up to 10.9 (92% is signal) while the purity of the semileptonic signal is 68%. Moreover, the asymmetric tails from figure 9.6 have almost disappear thanks to this cut as can be seen in figure 9.8. The fit results for the W boson mass are M_W = 80.622 $\pm$ 0.002 (stat.) GeV/c^2 and σ_W = 0.665 $\pm$ 0.001 (stat.) GeV/c^2. Then, these W boson candidates are the one that will be used further on to reconstruct the

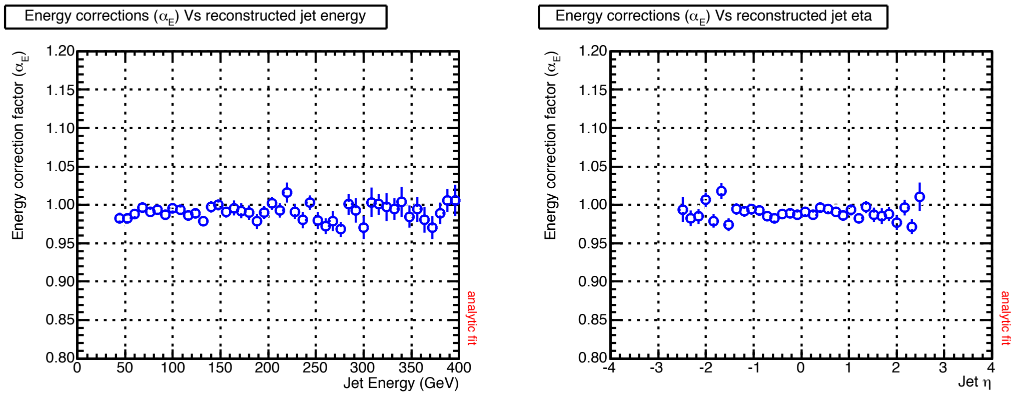

(a) *Energy corrections Vs Energy* (b) *Energy corrections Vs η*

Figure 9.5: *Energy correction factors as a function of Energy (a) and η (b) for the hadronic W boson decay minimization.*

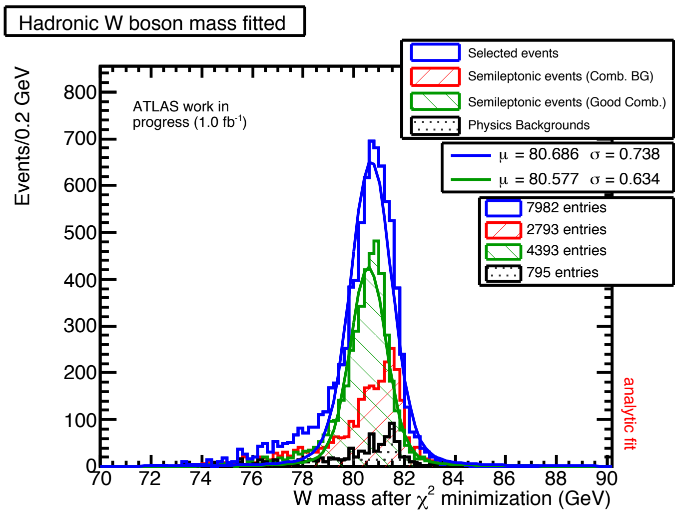

Figure 9.6: *Hadronic W boson mass after the χ^2 minimization without any additional cut. Distributions are fitted to a Breit-Wigner convoluted with a Gauss function.*

hadronic top quark mass.

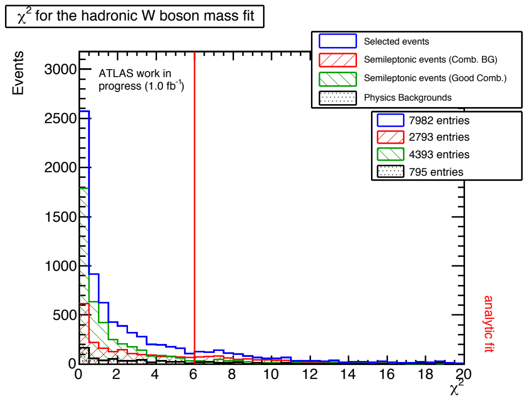

(a) χ^2 *distribution after the minimization*

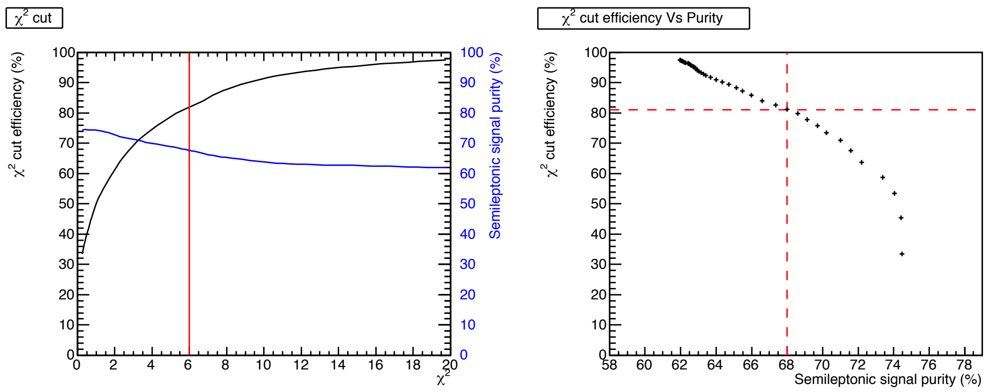

(b) *Cut efficiency Vs* χ^2 *and Vs the semileptonic signal purity*

Figure 9.7: *The upper plot shows the* χ^2 *distribution after the hadronic W boson fit and the proposed cut C0 (i.e.* $\chi^2 < 6$*) is drawn as a vertical solid line. This cut preserves the 80% of the reconstruction efficiency increasing the semileptonic signal purity up to 68%.*

9.4.2 Hadronic b-jet association

Once the light jet pair candidate has been selected, one of the two existing b-jets must be associated to the hadronic decay side. This association is performed based on the ΔR distance between the reconstructed hadronic W boson and the corresponding b-jet. Thus, the closest b-jet is the chosen one at the first instance.

Other selection methods can also be used as the one that chooses the b-jet that maximizes the hadronic top quark transverse momentum or the method which chooses the b-jet furthest from

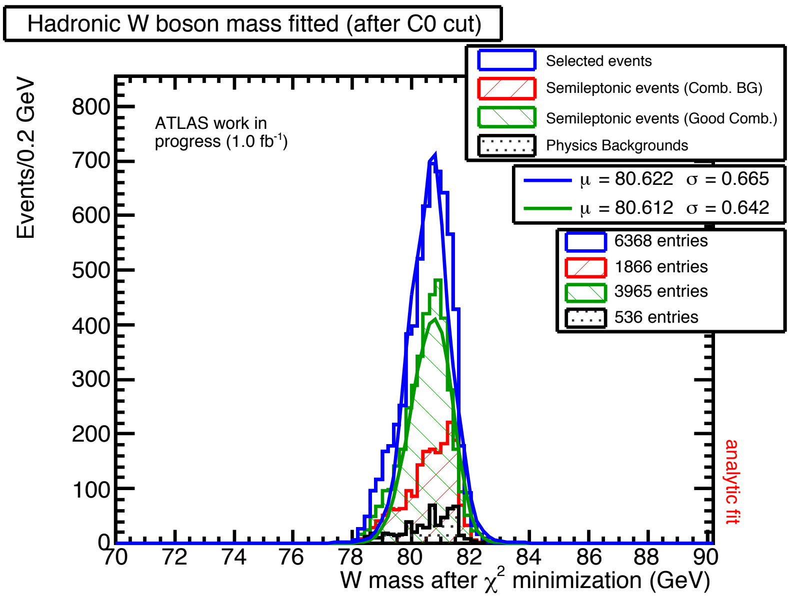

Figure 9.8: *Hadronic W boson mass after applying the cut C0 (i.e. $\chi^2 < 6$) for simulated $t\bar{t}$ events. Distributions are fitted and the results for "Selected events" are $M_W^{had} = 80.622 \pm 0.002$ (stat.) GeV/c^2 and $\sigma_W^{had} = 0.665 \pm 0.001$ (stat.) GeV/c^2.*

the leptonic W boson, but the actual method has proven to deliver a slightly higher purity (as it is claimed on reference [7]).

9.4.3 Hadronic top quark mass reconstruction

Now, one can build the hadronic top quark with the hadronic W boson fitted in section 9.4.1 and the reconstructed b-jet. Figure 9.9 shows the reconstructed hadronic top quark mass where it is fitted to the sum of a gaussian and a third degree polynomial. The gaussian peak for the "Selected events" distribution has its mean at $M_t^{had} = 174.5 \pm 0.3$ (stat.) GeV/c^2 and a width of $\sigma_t^{had} = 11.7 \pm 0.3$ (stat.) GeV/c^2 which leads a relative statistical precision on the top quark mass of 0.17%. It must be said that the fit function does not totally reproduce the top quark mass distribution for low masses. Considering just the good combinations of the semileptonic signal, one gets $M_t^{had} = 174.3 \pm 0.2$ (stat.) GeV/c^2 and a width of $\sigma_t^{had} = 11.17 \pm 0.14$ (stat.) GeV/c^2 from a Breit-Wigner convoluted with a gaussian fit as can be seen on that figure. In this case, the fit is quite good and the semileptonic signal purity is 52% (this value includes the b-jet purity).

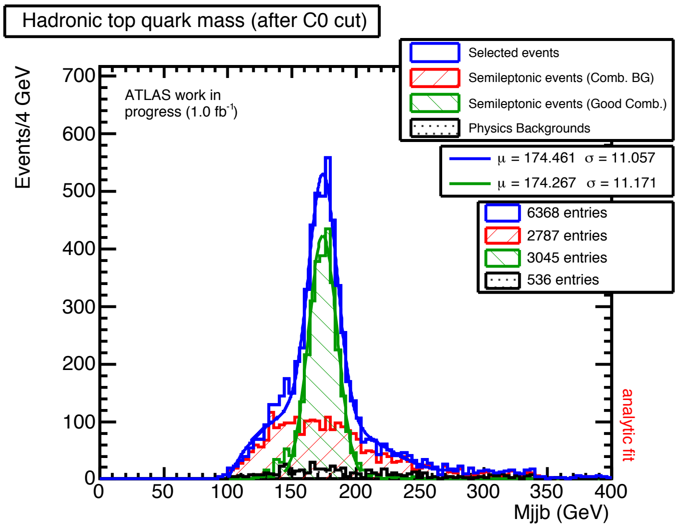

Figure 9.9: *Reconstructed top quark mass, after cut C0, for the hadronic decay side of simulated $t\bar{t}$ events. The distribution is fitted to the sum of a gaussian and a polynomial (third degree). The gaussian peak has its mean at M_t^{had} = 174.5 $\pm$ 0.3 (stat.) GeV/c^2 for "Selected events".*

9.5 Reconstruction of the leptonic decay side

9.5.1 Leptonic W boson mass reconstruction

The leptonic W boson decay ($W \rightarrow \ell\nu$) reconstruction posses a difficult challenge which comes from the kinematics of the neutrino. This is because the neutrino escapes undetected and even if the lepton can be accurately reconstructed, the kinematics of the W decay is in principle not fully defined. In order to find a solution to this dilemma, the most common assumption is that the missing transverse energy (denoted by MET or E_T^{miss}) of the event corresponds to the one of the undetected neutrino (i.e. as the neutrino is massless, $E_T^{miss} \equiv p_T^{\nu}$). Although it is true that the neutrino is the main contributor to the E_T^{miss} at LO, there are more contributors, such as extra neutrinos (from B hadron and τ decays), additional p_T contributions (ISR/FSR effects, etc), miscalibration of E_T^{miss}, fake missing E_T^{miss} due to the detector energy resolution and acceptance, etc. For instance, the semileptonic decay of B hadrons ($B \rightarrow X\ell\nu$) produces also genuine neutrinos that should be considered as part of the E_T^{miss} and although they are softer than the ones coming directly from the $t\bar{t}$ decay their contribution can not be disentangled.

9.5.2 Determination of the neutrino p_z

From the $W \to \ell\nu$ decay, the four-momentum[5] conservation $p^W = p^\ell + p^\nu$ (W, ℓ and ν stand for the W boson, for the lepton and for the neutrino, respectively) gives:

$$(p^W)^2 = (p^\ell + p^\nu)^2 \quad \to \quad M_W^2 = m_\ell^2 + 2(E_\ell, \mathbf{p}^\ell)(E_\nu, \mathbf{p}^\nu) = m_\ell^2 + 2(E_\ell E_\nu - \mathbf{p}^\ell \cdot \mathbf{p}^\nu) \qquad (9.21)$$

where the neutrino mass has been neglected ($m_\nu = 0$). Now, using the hypothesis that transverse energy in the center of mass of the collision is equal to zero, then the E_T^{miss} in the detector can be approximated as due just for the neutrino, i.e. $E_T^{miss} = p_T^\nu$. Figure 9.10 illustrates this approximation where the reconstructed $E_T^{miss}/p_T^{MC\nu}$ ratio is shown. The maximum of the selected event distribution (and also the semileptonic signal) is almost at 1, which means that the main contributor to the E_T^{miss} is that neutrino (which is the one coming from the leptonic W boson decay). Moreover, the asymmetric tails tell that there are more contributions. Finally, it is worth to mention that the entries on the first bin in this plot correspond to background events without neutrinos (since any true neutrino can be associated with the E_T^{miss}) or with more one true neutrinos (since it is not possible to decide which amount of the E_T^{miss} corresponds to each neutrino). In that cases, a truth matching is not performed for simplicity and $E_T^{miss}/p_T^{MC\nu} = 0$ is simply done.

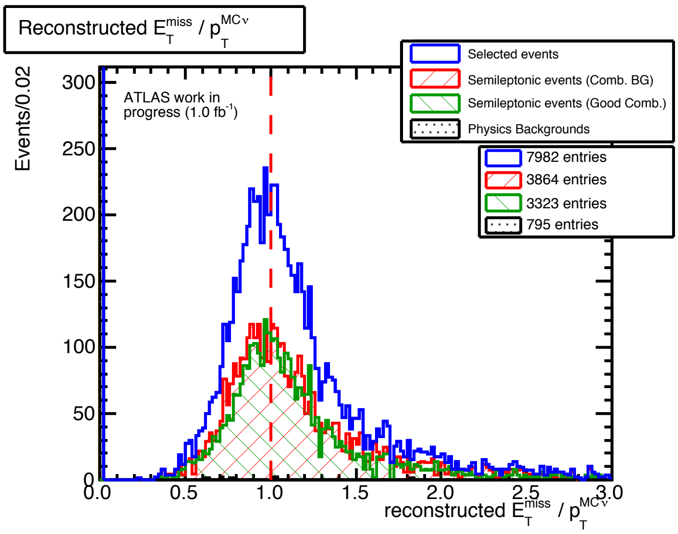

Figure 9.10: *Reconstructed $E_T^{miss}/p_T^{MC\nu}$ ratio can be seen. The maximum of these distributions is almost at 1, which means that the main contributor to the E_T^{miss} is the neutrino which comes from the leptonic W boson decay. Moreover, the asymmetric tails tell that there are more contributions.*

Following with the kinematics, the neutrino energy can be expressed as:

[5] The four-momentum, also known as the invariant mass, is a four-vector defined as $p = (E, \mathbf{p})$ where E is the energy and $\mathbf{p} = (p_x, p_y, p_z)$ is the three-momentum of the given particle of mass m, respectively. Moreover, the square of the four-momentum is $p^2 \equiv E^2 - |\mathbf{p}|^2 = m^2$ (in natural units).

$$E_\nu = (p_x^\nu)^2 + (p_y^\nu)^2 + (p_z^\nu)^2 = (p_T^\nu)^2 + (p_z^\nu)^2 = \sqrt{E_T^{miss\,2} + (p_z^\nu)^2}$$

and its transverse momentum components are given by: $p_x^\nu = E_T^{miss} \cos\phi_{\ E_T^{miss}}$ and $p_y^\nu = E_T^{miss} \sin\phi_{\ E_T^{miss}}$. Therefore the M_w^2 from expression 9.21 becomes:

$$M_W^2 = m_\ell^2 + 2E_\ell E_\nu - 2\left(p_x^\ell p_x^\nu + p_y^\ell p_y^\nu + p_z^\ell p_z^\nu\right) =$$

$$= m_\ell^2 + 2E_\ell \sqrt{E_T^{miss\,2} + (p_z^\nu)^2} - 2\left(E_T^{miss}(p_x^\ell \cos\phi_{\ E_T^{miss}} + p_y^\ell \sin\phi_{\ E_T^{miss}}) + p_z^\ell p_z^\nu\right) \tag{9.22}$$

Using a reference mass value for M_W, the only unknown quantity left of the above equation is the neutrino longitudinal momentum (p_z^ν). Then one can work out p_z^ν from expression 9.22 which leads a quadratic expression for p_z^ν:

$$a(p_z^\nu)^2 + bp_z^\nu + c = 0 \quad \rightarrow \quad \begin{cases} a = E_\ell^2 - (p_z^\ell)^2 \\ \\ b = p_z^\ell\left(-M_W^2 + m_\ell^2 - 2(p_x^\ell p_x^\nu + p_y^\ell p_y^\nu)\right) \\ \\ c = E_\ell^2 E_T^{miss\,2} - \frac{1}{4}\left(M_W^2 - m_\ell^2 + 2(p_x^\ell p_x^\nu + p_y^\ell p_y^\nu)\right)^2 \end{cases}$$

Thus p_z^ν has two solutions which are as follow:

$$p_z^\nu = \frac{-p_z^\ell\left(-M_W^2 + m_\ell^2 - 2(p_x^\ell p_x^\nu + p_y^\ell p_y^\nu)\right)}{2(E_\ell^2 - (p_z^\ell)^2)} \pm$$

$$\pm \sqrt{E_\ell^2\left[\left(M_W^2 - m_\ell^2 + 2(p_x^\ell p_x^\nu + p_y^\ell p_y^\nu)\right)^2 + 4(E_T^{miss})^2(-E_\ell^2 + (p_z^\ell)^2)\right]} \tag{9.23}$$

The discriminant, denoted as Δ, of this expression is defined as:

$$\Delta \equiv E_\ell^2\left[\left(M_W^2 - m_\ell^2 + 2(p_x^\ell p_x^\nu + p_y^\ell p_y^\nu)\right)^2 + 4(E_T^{miss})^2(-E_\ell^2 + (p_z^\ell)^2)\right]$$

Although equation 9.23 offers two posible solutions to the neutrino p_z^ν, those solutions rely on the assumption that the neutrino is the only contributor to the E_T^{miss} and as discussed earlier, this is not always the case. Thus, there are some cases where equation 9.23 has no solution, i.e. when $\Delta < 0$. This is because of the overestimation of p_z^ν, i.e. because E_T^{miss} has additional contributors.

If that happens, there two options to cure the problem:

- On the one hand, one could decrease E_T^{miss} (i.e. p_T^ν) step by step until a solution is found. This decreasing can be done within the E_T^{miss} resolution using the MC information as it is done in reference [142] or using the restriction that the transverse W boson mass has to remain below 90 GeV as in reference [7] (see *Top Quark Mass Measurements* section).
- On the other hand, one can find for which values of the E_T^{miss} the Δ term becomes positive (or at least 0). By doing so, one just scales E_T^{miss} but preserves its direction $(\cos\phi_{\ E_T^{miss}}, \sin\phi_{\ E_T^{miss}})$. Therefore one can do $\Delta = 0$ and solve the new quadratic equation this time in terms of $(E_T^{miss})'$. Of course, this equation has two solutions which are:

$$(E_T^{miss})' = \frac{-(-M_W^2 + m_\ell^2)(p_x^\ell \cos\phi_{\ E_T^{miss}} + p_y^\ell \sin\phi_{\ E_T^{miss}}) \pm (-M_W^2 + m_\ell^2)\sqrt{E_\ell^2 - (p_z^\ell)^2}}{2\left[E_\ell^2 - (p_z^\ell)^2 - (p_x^\ell \cos\phi_{\ E_T^{miss}} + p_y^\ell \sin\phi_{\ E_T^{miss}})^2\right]}$$

From the two solutions the positive one is selected as the negative solution has no physical meaning.

Once the $\Delta < 0$ problem has been solved, one has two solutions for p_z^ν and the choice among these two solutions is performed using the W bosons with their associated b-jet candidates. Thus, the combination giving the smaller difference between the hadronic and the leptonic top quark masses ($|\Delta M| \equiv |M_{jjb_{had}} - M_{\ell\nu b_{lept}}|$) is kept.

Obviously, the leptonic W boson mass reconstructed using this p_z^ν solution is a Dirac delta distribution, i.e. exactly the M_W^{ref}, as one is computing the neutrino four-momentum which gives this reference mass for the given lepton, event by event. This is complete artificial as it is well known that the W boson has a given life time (i.e. its decay width is not zero as has been commented on at the beginning of this chapter) but this result is coherent with the proposed approximation done in this section. Therefore, this should be one of the sections that should be improved in next analysis (see future thesis).

Once this has been solved, the leptonic b-jet association should be done.

9.5.3 Leptonic b-jet association

The leptonic b-jet association should be trivial as exactly two b-jets have been required per event and one of them has been already associated to the hadronic side. However, the early association could be wrong. Moreover, it has been said that the solution of p_z^ν is selected based on which give the minimum value of the difference $|\Delta M| \equiv |M_{jjb_{had}} - M_{\ell\nu b_{lept}}|$. Thus, once more, if the initial association was wrong, the latter decision would lead to a wrong mass reconstruction.

Then, a simple trick can be performed in order to solve this problem and by the way to recover a small fraction of wrong hadronic b-jet associations done through the previous ΔR method. The idea is to combine the hadronic W boson and the leptonic W boson, first with their b-jets associated in previous steps and measure $|\Delta M|$. Then, a b-jet association swapping is done and the quantity $|\Delta M|$ is again measured with these candidates. Finally, the smaller top quark mass difference from the four combinations is kept. Thus, if this trick indicates that the initial b-jet association was wrong, a re-association is performed and used in the KF. This recovers $\sim 1\%$ of wrong associations.

9.5.4 Leptonic top quark mass reconstruction

Finally, figure 9.11 shows the reconstructed top quark mass for the leptonic decay side for those events passing cut C0. The main source of uncertainty comes from the b-jet calibration as the leptonic W boson is fixed.

The mass distribution is fitted to the sum of a gaussian and a third degree polynomial. The gaussian peak has its mean at $M_t^{lep} = 174.9 \pm 0.4$ (stat.) GeV/c^2 and a width of $\sigma_t^{lep} = 15.4 \pm 0.5$ (stat.) GeV/c^2 (i.e. slightly wider than the hadronic side) which leads a relative statistical

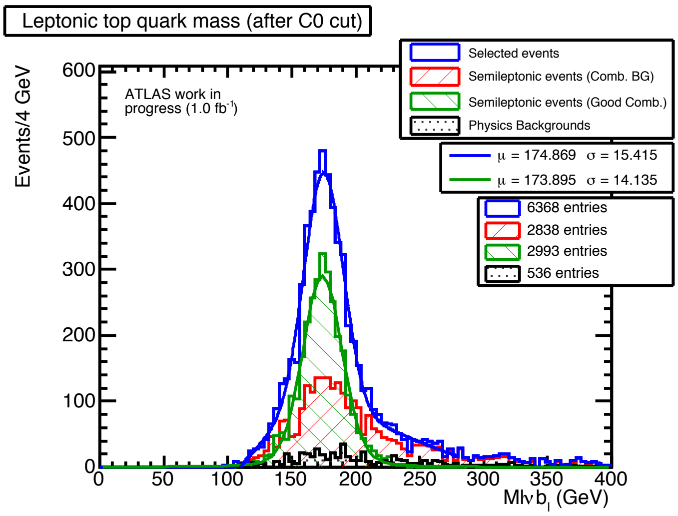

Figure 9.11: *Reconstructed leptonic top quak mass, after cut C0. The main source of uncertainty comes from the b-jet calibration as the leptonic W boson mass becomes fixed due to the neutrino determination method.*

precision on the top quark mass of 0.23%. Finally, the semileptonic signal purity for the leptonic top quark distribution is 51%. Considering just the good combinations of the semileptonic signal, one gets M_t^{lep} = 173.9 ± 0.3 (stat.) GeV/c^2 and a width of σ_t^{lep} = 14.1 ± 0.5 (stat.) GeV/c^2 from a Breit-Wigner convoluted with a gaussian fit as can be seen on that figure.

9.6 Additional cuts

Once, all the final objects have been selected some extra additional cuts can be applied in order to increase the purity of the sample (i.e. to increment the combinatorial and physics background rejection). Thus, they are defined as:

- **Cut C1:** the invariant mass of the hadronic W boson and the b-jet associated to the leptonic W boson must be greater than 200 GeV as shown in figure 9.12 (a). The vertical solid line represents this cut, i.e. $M_{jjb_\ell} > 200$ GeV/c^2.

- **Cut C2:** the invariant mass of the lepton and the b-jet associated to the leptonic W boson must be lower than 160 GeV as shown in figure 9.12 (b). Analogously to the previous case, the vertical solid line represents this cut, i.e. $M_{\ell b_\ell} < 160$ GeV/c^2.

These cuts reduce the efficiency but increase the semileptonic signal purity from 52 % to 66% while the S/B ratio is shown in section 9.8. Table 9.1 summarizes the cuts applied after the event selection cuts in the present analysis. In this table, the purity given for the three first cuts is for the W boson mass distribution while the purity for the later three cuts is for the top quark mass distribution (i.e. matching also the associated b-jet).

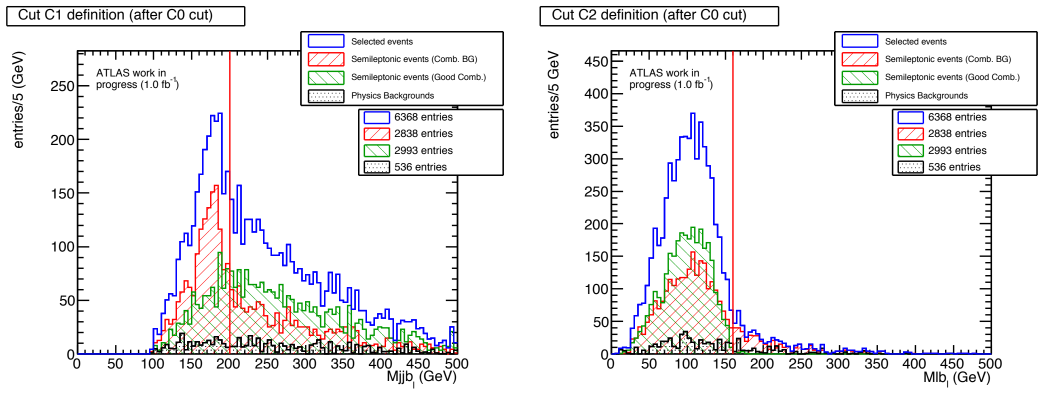

(a) *Cut C1: M_{jjb_ℓ} > 200 GeV/c^2* (b) *Cut C2: $M_{\ell b_\ell}$ < 160 GeV/c^2*

Figure 9.12: *Invariant mass of the hadronic W boson and the leptonic b-jet (a) and invariant mass of the lepton and the b-jet associated to the leptonic W boson (b). Both distributions for events passing the cut C0.*

Cut Label	**Impact**	**Description**	**Semilept. purity (%)**	**Semilept. eff (%)**
Evt. Sel.	All	see section 8.3.8	35	4.6
PreCut 0	Light jets	ΔR(j,j)< 3.0	40	2.4
PreCut 1	Light jets	$\lvert\Delta M_{jj}\rvert$ < 30 GeV/c^2	61	2.5
Cut C0	Had. W	$\chi^2_{min} < 6$	68	2.0
Cut C1	All	M_{jjb_ℓ} > 200 GeV/c^2	62	1.2
Cut 2	All	$M_{\ell b_\ell}$ < 160 GeV/c^2	66	1.2

Table 9.1: *Summary of all cuts proposed and used within this analysis. The semileptonic purities from the forth cut is for the top quark mass distributions while for the other cuts is for the W boson mass distributions (i.e. the b-jet purity is also included in the later ones). This explains the jump from 68% to 61% in purity. In the third row, $|\Delta M_{jj}| = |M_{jj} - 82.6$ GeV/c$^2| < 30$ GeV/c^2.*

9.7 Kinematic fit using the Globalχ^2 algorithm

As discussed on section 9.1, the top quark mass can be extracted from a KF using the Globalχ^2 algorithm. The method uses the 6 final state objects of the semileptonic $t\bar{t}$ decay channel at tree level. The χ^2 which will be minimized was already defined by expression 9.1:

$$\chi^2 = \sum_{\text{i = jets+lepton}} \left(\frac{E_i^m - E_i^f}{\sigma_{E_i}}\right)^2 + \left(\frac{M_{jj} - M_W^{ref}}{\Gamma_W^{ref}}\right)^2 + \left(\frac{M_{l\nu} - M_W^{ref}}{\Gamma_W^{ref}}\right)^2 +$$

$$+\left(\frac{M_{jjb_H} - M_{top}^f}{\sigma_{top_H}}\right)^2 + \left(\frac{M_{\ell\nu b_\ell} - M_{top}^f}{\sigma_{top_\ell}}\right)^2$$

The first term simply allows an *in-situ* fine-tuning scaling of the corresponding jet or lepton energy through a multiplicative constant α_E. This rescaling is done independently for the two light jets, the two b-jets and the lepton, event by event. The energy uncertainties used in these term has been extracted from MC information and they depend on the energy and η as already discussed in appendix E.2. The next two terms constrain the reconstructed W boson mass to the pole mass M_W^{ref}, i.e. they constrain the energy of the light jets and of the lepton, for the hadronic and the leptonic terms, respectively. For the W boson uncertainties, Γ_W^{ref} is used as a fixed value in both terms. Finally, in the later two terms M_{jjb_H} and $M_{\ell\nu b_\ell}$ refer to the invariant mass of the sum of the four-momenta of the particles associated to the hadronic and the leptonic sides, respectively. The M_{top}^f is a free parameter to be determined by the KF. One should note that since the KF aims to minimize the difference between the top quark masses measured separately with the hadronic and leptonic objects, this may introduce a bias on different the top quark masses (i.e. for the reconstructed M_{jjb_H} and $M_{\ell\nu b_\ell}$) due to the p_T cut of jets, which can act differently on each side [142]. Then, as the top quark mass is constrained to be the same for t and $\bar{t}$, one will consider different top quark uncertainties to account for the different detector resolution on each side. Thus, the top quark uncertainties, σ_{top_H} and σ_{top_ℓ}, are the fixed values of the fit widths coming from results on section 9.4.3 (figure 9.9) and section 9.5.4 (figure 9.11), respectively, for the hadronic and the leptonic terms.

Thus, using the formalism described on section 9.2, one can build the final top quark mass distribution which is shown on figure 9.13. This distribution is built for those events passing all the proposed cuts on table 9.1 and it is fitted to the sum of a gaussian and a third degree polynomial, giving a top quark mass of M_{top}^{fit} = 174.1 ± 0.3 (stat.) GeV/c^2 and a width of σ_t^{fit} = 10.7 ± 0.4 (stat.) GeV/c^2, leading a relative statistical precision on the top quark mass of 0.17%.

In parallel, as one obtains the energy rescaled input objects from the KF, it is possible to reconstruct separately the hadronic and the leptonic W boson masses from those objects. Thus, figures 9.14 (a) and (b) shows these distributions for each reconstructed W boson mass, fitted to gaussian functions. The hadronic W boson, fixed by the nested fit of the Globalχ^2 procedure, is M_W^{had} = 80.54 ± 0.02 (stat.) GeV/c^2 and σ_W^{had} = 0.75 ± 0.01 (stat.) GeV/c^2 which is compatible with the reference value (see section 9.4.1). Moreover, as it was expected, the leptonic W boson mass is almost a Dirac delta distribution with mean M_W^{lep} = 80.456 ± 0.003 (stat.) GeV/c^2, which is also compatible with the pole mass of the reference, M_W^{ref}. Once more, this distributions is non-physical but it is coherent with the proposed approximation discussed on section 9.5.2.

Analogously, one can also reconstruct separately the hadronic and the leptonic top quark masses from the final rescaled objects as can be seen on figures 9.15 (a) and (b).

In this case, both distributions have been fitted to the sum of a gaussian and a third degree polynomial. The mean of the gaussian peak for the hadronic side is M_{top}^{had} = 174.6 ± 0.3 (stat.) GeV/c^2 and for the leptonic side is M_{top}^{lep} = 174.4 ± 0.4 (stat.) GeV/c^2. Both distribution give widths compatible with the previous sections, i.e. σ_{top}^{had} = 10.4 ± 0.3 (stat.) GeV/c^2 and σ_{top}^{lep} = 13.8 ± 0.6 (stat.) GeV/c^2, being the leptonic width wider than the hadronic one.

It is also important to say some words about the energy correction factors given by this KF. Figures 9.16 (a) and (b) shows the α_E distributions for the two light jets. The same behaviour

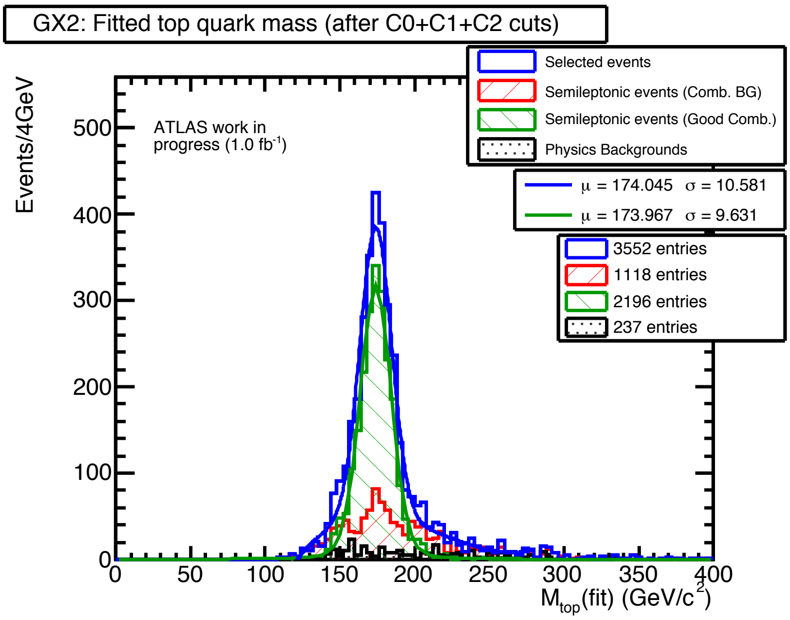

Figure 9.13: *Top quark mass extracted with the Globalχ^2 algorithm in the KF, after applying all the cuts summarized on table 9.1. Performing a fit to the sum of a gaussian and a third degree polynomial, for "Selected events" one has M_{top}^{fit} = 174.1 ± 0.3 (stat.) GeV/c^2.*

than the energy scale factors in section 9.4.1 is observed here, i.e. both peak almost at 1 but slightly below this value: α_{J0} = 0.991 ± 0.001 (stat.) and α_{J1} = 0.981 ± 0.002 (stat.). Furthermore, figure (a) is narrower than figure (b). In this case, this effect is also due the fact that jets are always sorted from higher to lower p_T.

On the other hand, figures 9.16 (c) and (d) shows the α_E distributions for the two b-jets. Taking a look to the fit results, i.e. α_{b_H} = 0.999 ± 0.001 (stat.) and α_{b_ℓ} = 1.002 ± 0.001 (stat.), one could say that the energy of the b-jets were slightly better calibrated than the energy for the light jets but in reality this cannot be stated from the χ^2 used as it does not constraint the b-jets directly as it is done for the light jets (thanks to the second and the third term of expression 9.1). Then, these energy corrections come as the result of a soft and indirect constraint imposed by the fact that the reconstructed hadronic and leptonic top quark masses should lead the same final top quark mass.

Finally, the energy rescaling factor for the lepton shown in figure 9.16 (e) is 1.003 ± 0.001 which is the expected value after the pre-calibration, due to two reasons. First, because isolated leptons are usually very well measured and secondly because of the approximation used to determine the neutrino four-momentum.

The final χ^2 distribution of the KF is shown in figure 9.17 (a). Earlier studies (see reference [146]) showed that the accuracy of the determination of the top quark mass depends on the χ^2. For events in which the b-jets are well measured and ISR/FSR effects are negligible, the χ^2 of the fit is close to 0. That produces a top quark mass value reflecting the MC input top quark mass.

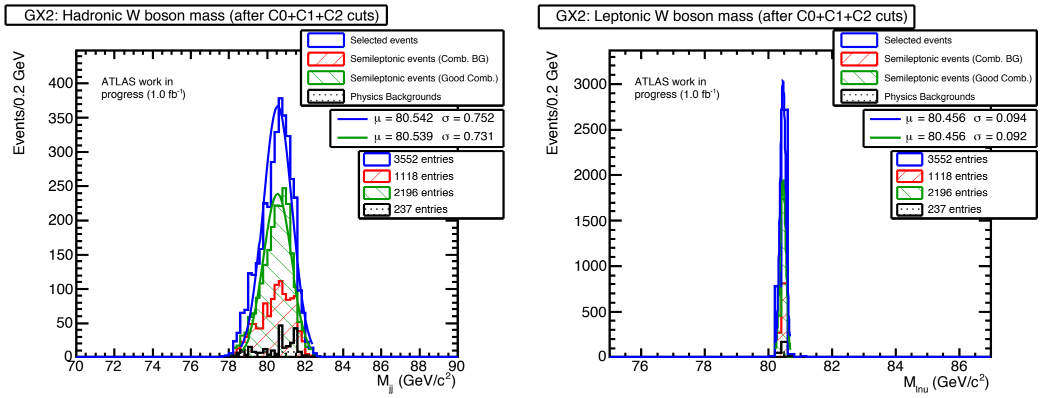

(a) *Hadronic W boson mass* (b) *Leptonic W boson mass*

Figure 9.14: *W boson masses reconstructed from the hadronic and the leptonic objects extracted with the Globalχ^2 algorithm in the KF. From fits, M_W^{had} = 80.54 ± 0.02 (stat.) GeV/c^2 and M_W^{lep} =* 80.456 ± *0.003 (stat.) GeV/c^2, respectively.*

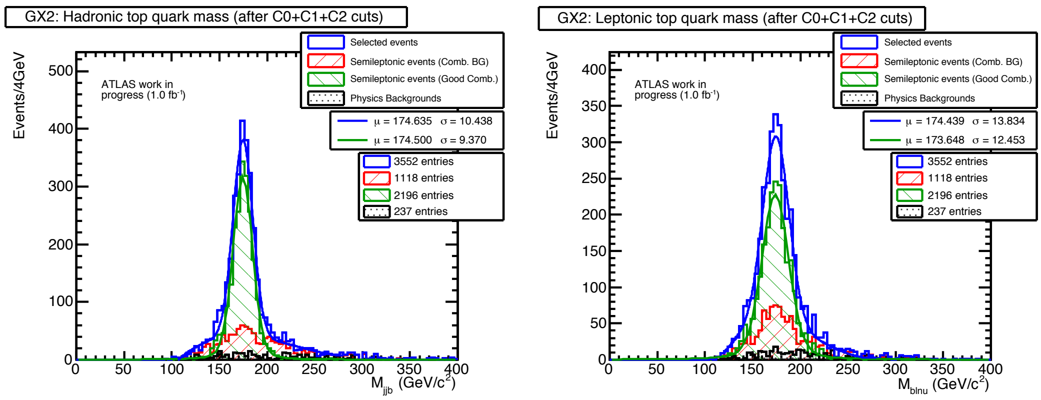

(a) *Hadronic top quark mass* (b) *Leptonic top quark mass*

Figure 9.15: *Top quark masses reconstructed from the hadronic and the leptonic objects extracted with the Globalχ^2 algorithm in the KF. From fits, M_{top}^{had} =* 174.6 ± *0.3 (stat.) GeV/c^2 and M_{top}^{lep} =* 174.4 ± *0.4 (stat.) GeV/c^2, respectively.*

For larger χ^2 value, the top quark mass value decreases (see “Good Comb.” label on figure 9.17 (b)) while the fraction of b-quarks with a large gluon radiation increases. This observation is

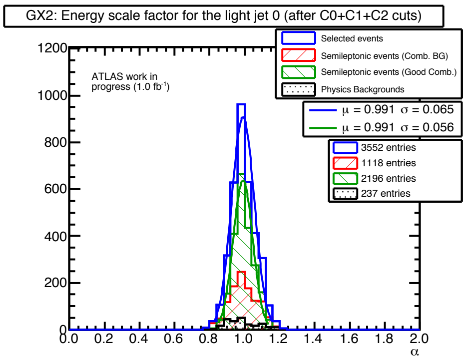

(a) *Energy scaling factor for the light jet 0*

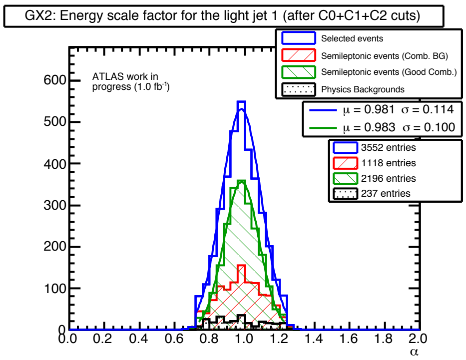

(b) *Energy scaling factor for the light jet 1*

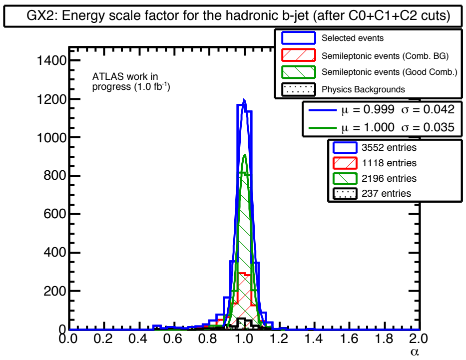

(c) *Energy scaling factor for the hadronic b-jet*

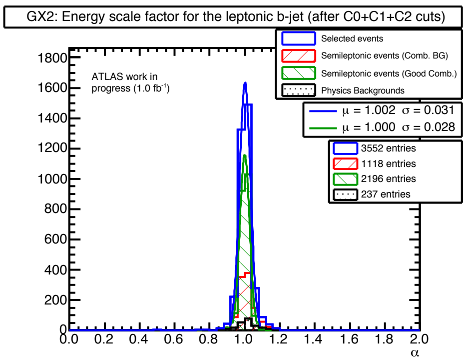

(d) *Energy scaling factor for the leptonic b-jet*

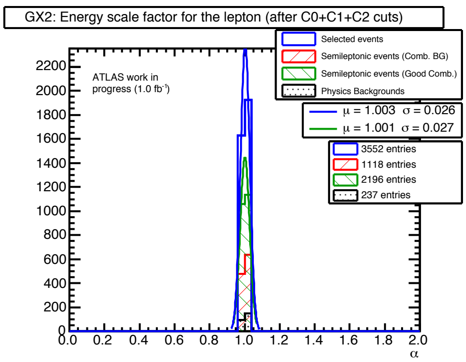

(e) *Energy scaling factor for the lepton*

Figure 9.16: *Energy scaling factors resulting from the KF using the Globalχ^2 formalism for the light jets, the b-jets and the lepton.*

used in some references, as for example reference [7], for performing a linear fit to the extracted top quark mass as a function of the χ^2. In this case, for the "Selected events", this fit gives a top quark mass of $M_{top} = 175.8 \pm 0.5$ (stat.) GeV/c^2 extrapolating that linear fit to $\chi^2 = 0$. This procedure should lead to a lower sensitivity to final state radiation effects of the extracted top quark mass as it is claimed on reference [7]. That case will be theoretically the LO term, where there are 6 jets and everything is perfectly well reconstructed.

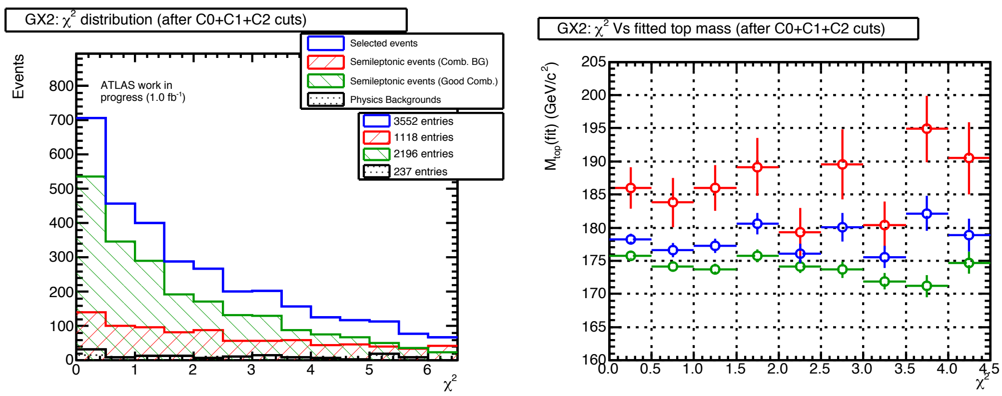

(a) χ^2 *distribution*

(b) *Top quark mass fitted Vs* χ^2 *distribution*

Figure 9.17: *χ^2 distribution resulting from the KF (a) and the fitted top quark mass as a function of the χ^2. On the right plot, blue, red and green marks represent the Selected events, the Combinatorial Background events and the Good Combination events, respectively.*

9.8 Physics background rejection

The number of remaining events after each cut, for the semileptonic signal and for the main backgrounds, are shown in table 9.2. As can be seen the Globalχ^2 kinematic method together with the different cuts improves significatively the ratio S/B which was $\sim$5.7 (after the event selection cuts) up to $\sim$13.7. The $t\bar{t}$ dileptonic decay channel and the single top processes are the most important backgrounds for this analysis at the LHC. The Wt channel (single top) is especially important since it has two W bosons in the final state.

9.9 Stability of the method

In order to check the stability and linearity of the method, the top quark mass measurement using the Globalχ^2 algorithm has been performed for several values of the generated top quark mass: 160 GeV/c^2, 165 GeV/c^2, 170 GeV/c^2, 180 GeV/c^2, 185 GeV/c^2 and 190 GeV/c^2. These samples were simulated using the AcerMC generator at LO level (see appendix 8.2.5). All the

Process	Number of events at 1 fb^{-1} (including weights) after cut...				
	Event selection (S/B)	PreCuts (S/B)	Cut C0 (S/B)	Cut C1 (S/B)	Cut C2 (S/B)
semileptonic $t\bar{t}$ signal	13161 (-)	7187 (-)	5831 (-)	3559 (-)	3314 (-)
fully hadronic	121 (109)	78 (92)	66 (88)	44 (81)	33 (100)
dileptonic	1331 (10)	410 (18)	250 (23)	154 (23)	101 (33)
single top	631 (21)	224 (32)	169 (21)	128 (28)	91 (36)
W$b\bar{b}$ + partons	95 (139)	20 (359)	15 (389)	10 (356)	3 (1104)
W$c\bar{c}$ + partons	14 (940)	4 (1797)	2 (2916)	2 (1780)	2 (1657)
W $\rightarrow \ell\nu_\ell$ + partons	107 (123)	59 (122)	29 (201)	14 (254)	7 (473)
Total S/B	6.3	9.0	10.9	10.1	14.0
Total S/(S+B) (%)	86	90	92	91	93

Table 9.2: *Number of reconstructed events (including* event weights *which were introduced in section 8.2.5) after each selection cut for 1 fb^{-1} of integrated luminosity.*

proposed cuts on table 9.1 were applied in order to reproduce the previous analysis for each generated top mass. The major problem to perform this study was the incompleteness of these datasets, leading a very low statistics for each generated top quark mass.

Thus, figure 9.18 shows reconstructed top quark mass using the Globalχ^2 algorithm as a function of the generated top quark mass. Results were fitted to a first degree polynomial, telling that the method is stable and there is a good linearity, with a slope very close to one (0.99 ± 0.05). As can be seen some mass points have large errors associated to them. The large statistical errors compared with the main 175 GeV/c^2 sample are due to the low statistics available for the particular datasets.

9.10 Systematic uncertainties

Due to the expected $t\bar{t}$ cross section at 14 TeV, the statistical uncertainty on the top quark mass would be negligible with a few fb^{-1} of collected data, and therefore the total uncertainty will be dominated by the systematic uncertainties. Unfortunately, a detailed systematic study is beyond the scope of this work, as its aim is basically to introduce the Globalχ^2 method within the top mass measurement context. However, one can mention the main source of systematics:

- **JES:** The top quark mass measurement relies essentially on the reconstruction of jets of particles arising from quarks and gluons and this is why the JES is the dominant source of systematic uncertainty on the top quark mass. From previous studies [142], it is known that the resulting top quark mass depends linearly on these rescaling factor. Thus, the related systematic uncertainty can be expressed as a percentage of the light jet and b-jet energy scale miscalibration.

  CSC studies to measure the top quark mass requiring exactly 2 b-jets [7] estimated that the JES uncertainty in light jets produces an uncertainty in the top quark mass of 0.2

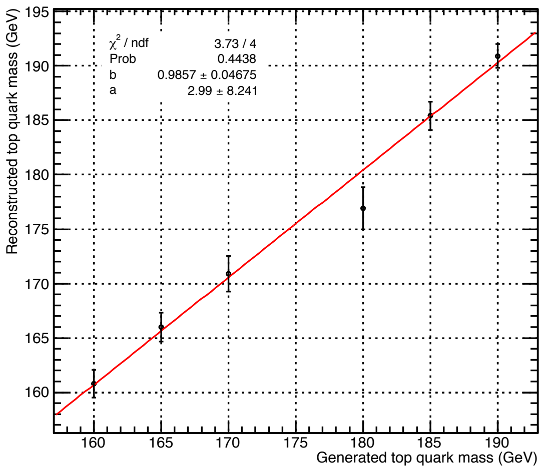

Figure 9.18: *Reconstructed top quark mass using the Globalχ^2 algorithm as a function of the generated input top quark mass.*

GeV/% while the JES uncertainty in b-jets produces an uncertainty of 0.7 GeV/%. If just one b-jet is required or there is any b-tagging requirement, the JES uncertainty for light jets increase up to 0.3 GeV/% or 0.4 GeV/%, respectively. The JES uncertainty for b-jets remains the same.

The lower dependence of light jets is due to the W boson mass constraint in the KF. As has been claimed, the b-jets are poorly constrained in expression 9.1, but should be possible to improve it and therefore to reduce the b-jet uncertainty. Future work will follow these ideas. Meanwhile, for early data, the b-jet scale will be derived from the measured light jet scale together with a MC correction term modeling the difference between the two jet energy scales. once, there is enough statistics the b-jet scale will be determined with data from Z+ jets.

Therefore, expecting that the jet energy scale would be known with a precision of 1-5% with 1 fb^{-1} of accumulated data, the corresponding uncertainty on the top quark mass would be 1-3.6 GeV (requiring two b-jets).

- **ISR/FSR:** Preliminary studies show an impact of the ISR/FSR effects on the top quark mass measurement, estimating a systematic uncertainty of $\sim$0.3 GeV (for two b-jets requirement) [7]. Additional jets coming from ISR are more energetic that the ones from FSR. Moreover, the jets which arise from particles undergone FSR are less boosted and therefore they are liable not to pass the event selection cuts (i.e. the p_T cut). Then, ISR should be *a priori* a larger source of combinatorial background than FSR. Finally, although ISR does not modify the invariant mass of the $t\bar{t}$ pair, an overestimation of the top quark mass measurement could be observed as one of the additional jets could be reconstructed together with a regular jet of the final state. Therefore, ISR and FSR may introduce some unbalanced p_T or E_T^{miss} as not all the transverse energy is due to the $t\bar{t}$ decay.

Either way, collision data will be needed to determine the contribution to the systematic uncertainty more accurately. For example, the jet multiplicity could help to determine the size of the ISF and FSR contribution.

- **b quark fragmentation:** This effect is usually estimated by varying the Peterson parameter (ε_b) [148] within its uncertainty. Studies performed with fast simulation have revealed that the expected uncertainty should be lower than 0.1 GeV [146].

- E_T^{miss}**:** People used to say that the JES and the b-tagging should be the two main sources of systematics, specially for early data. But determining the E_T^{miss} is as difficult as the previous tasks. Moreover, if ISR/FSR effects modify the final energy balance, increasing therefore the E_T^{miss} which would be associated to the neutrino coming from the $t\bar{t}$ semileptonic decay, this will bias significatively the reconstructed top quark mass. In fact, in reference [142] is claimed that the incidence of the E_T^{miss} scale on the top quark mass is equal to 0.6 GeV%.

- **Physics Background:** Physics background is negligible as a source of systematic uncertainty, specially compared with the previous sources. From figure 9.13 one can sense that physics background does not have a clear dependence with the reconstructed top quark mass as in the case of the combinatorial background, that clearly peaks on the top quark mass. Moreover, in reference [7] is argued that variations in the size of the background did not have noticeable effect on the computed top quark mass.

- **Method itself:** The different approximations considered in the present analysis (performing analysis at tree level over NLO processes, the neutrino four-momentum determination, χ^2 with poor constrained b-jets, etc...) have to lead to systematic uncertainties which should be reducible. The top quark mass determined is M_{top}^{fit} = 174.1 ± 0.3 (stat.) GeV/c^2 which is 3σ away from the input mass (175 GeV/c^2). This discrepancy could be mainly due because this analysis should be performed at NLO instead of at LO. Thus, it is expected that future improvements should reduce this contribution.

9.11 Conclusions

The Globalχ^2 algorithm has been introduced as a novel method to perform an accurate top quark mass measurement with 1 fb^{-1} of collected data using the $t\bar{t}$ semileptonic decay channel, using MC samples. This analysis has followed a clear strategy, requiring two jets tagged as b-jets and some standard event selection cuts. The final S/B ratio is 14, which means that the expected physics background is under control. The top quark mass determined by the KF of the Globalχ^2 algorithm is M_{top}^{fit} = 174.1 ± 0.3 (stat.) GeV/c^2, being this value 3σ away from the input mass (175 GeV/c^2).

With 1 fb^{-1} of integrated luminosity the present analysis of the top quark mass is not statistically limited. The estimated statistical error is 0.3 GeV/c^2, and as it was expected the total uncertainty will be dominated by systematics. Although a systematic uncertainty study has not been done in this thesis, a brief overview has been presented. The conclusion of this summary is that the precision on the top quark mass will mainly rely on the JES uncertainty, being the b-jet uncertainty the larger one. Actually, assuming a jet energy scale uncertainty of 1 to 5%, the expected precision would be of the order of 1 to 3.6 GeV with 1 fb^{-1} of accumulated data [7].

Finally, as has been said, several issues should be tackle in order to improved on this analysis. Thus, one of the weak points has been the poor constraints applied to the b-jets. Another, is the approximation done to reconstruct the neutrino four-momentum. And last but not least, provisions should be made to perform the analysis beyond the LO approximations. Therefore, improvements based on these ideas will be the guidelines to continue working on this topic and, of course, for next publications.

10 Conclusions

This thesis has been divided in two parts where the link between these parts has been the use of a Globalχ^2 algorithm in order to fit the distributions and to obtain the fit parameter values. The first part has been focused to discuss the alignment results and performance of the ATLAS Silicon Tracker using MC data as well as real data. The second part has been dedicated to the ATLAS potential for measuring the top quark mass, introducing the Globalχ^2 formalism as the main novelty.

The Globalχ^2 algorithm is the actual baseline algorithm for the ATLAS Silicon Tracker alignment. Chapters 6 and 7 have presented all the performance studies carried out using simulation data, real cosmic ray data and the first real collision data. In that sense, the CSC exercise was the first alignment challenge that provided full-scale simulations of the ATLAS detector. This exercise introduced a realistic detector description with an *as-built* geometry together with a tilted and shifted magnetic field and a distorted material. This implied that CSC was an important milestone towards the ATLAS data taking. The quality of the derived alignment constants was evaluated using hit/track efficiencies, residuals and track parameters together with their correlations. Furthermore, several physics samples were used by external alignment monitoring tools. Residual misalignments were observed, mainly due to weak modes which could not be completely removed. Anyhow, the achieved alignment performance was good enough to estimate the expected ATLAS performance for early data.

FDR exercises were the other challenge based on MC data that served to test and exercise the software of the complete ATLAS data taking chain, starting from the trigger SFO to the physics analysis of the taken data. Its main goal was to evaluate the readiness of this capability as it was an ATLAS computing model requirement. The calibration stream was used to align the full ID detector and the alignment constants were delivered on time within the 24h calibration-loop starting from a blind knowledge of the detector misalignments. Although they were of lower quality compared with the CSC alignment, they were of decent quality for its start-up scenario and delivered on time (24h loop). Several important lessons were learnt and the I/O reliability was truthfully estimated under pseudo-data taking. These exercises allowed to set the final alignment integration within the ATLAS calibration loop.

In addition the alignment achievements using real cosmic ray data and the first LHC collision data were presented. The SR1 test in 2006 was the first testbed of the Globalχ^2 algorithm with real cosmic ray data. The alignment convergence was shown and the residual distributions were improved, giving widths of O (50) μm. Moreover, performance studies revealed that the hit efficiency was within specifications after alignment, being greater than 99%.

Cosmic ray data taking periods during the ATLAS commissioning in 2008 and 2009 have allowed to exercise the software and hardware chains. The alignment model was also tested and the two alignment set of constants were derived based on real cosmic rays and one of these sets was used to reconstruct the first ever tracks produced by LHC collisions in November 2009. Both sets were produced starting from the available detector survey measurements although using different number of events and magnets configurations. At the same time, a detailed MC simulation was also produced, considering ATLAS on its cavern. On the other hand, it was the first time that the geometry level hierarchy model was used in the alignment procedure using real data and it produced very good results. As expected, large residual improvements were observed after alignment, specially in the barrel region, with final residual widths of O (24) μm for Pixels and O (30) μm for the SCT. Individual module corrections were performed, revealing bows in the Pixel barrel staves. These misalignments were corrected.

At the end of this part, the first attempt to improve the existing alignment using LHC collision data at 900 GeV was performed. The preliminary alignment improved the SCT end-cap disc alignment. The performance achieved with this alignment set proved that the near future Silicon Tracker alignment based on collision data and using the Globalχ^2 algorithm is very promising.

The second part was dedicated to the top quark mass measuring with the ATLAS detector. Simulated data within the CSC challenge was used in chapter 9, assuming 1 fb^{-1} of accumulated data at low luminosity (10^{33} cm^{-2} s^{-1}) and at the nominal LHC energy ($\sqrt{s}$ = 14 TeV). This part had two main goals, on the one hand, to contribute to the ATLAS potential by measuring with high precision the top quark mass. On the other hand, to introduced the Globalχ^2 method as a novel method to perform an accurate top quark mass measurement using the $t\bar{t}$ semileptonic decay channel. This analysis has followed a clear strategy, requiring two jets tagged as b-jets and some standard event selection cuts. The final S/B ratio is 14, which means that the expected physics background is under control. The top quark mass determined by the KF is M_{top}^{fit} = 174.1 ± 0.3 (stat.) GeV/c^2, being this value 3σ away from the input mass (175 GeV/c^2). The statistical uncertainty on the final top quark mass measurement with this analysis and for 1 fb^{-1} of integrated luminosity is 0.3 GeV/c^2, and as it was expected the total uncertainty will be dominated by systematics. No systematic uncertainty study was done in this thesis, though a brief overview was presented. The precision on the top quark mass will mainly rely on the jet energy scale uncertainty, being the b-jet uncertainty the larger one. In fact, assuming a JES uncertainty of 1 to 5%, the expected precision would be of the order of 1 to 3.6 GeV with 1 fb^{-1} of accumulated data [7].

Resumen

11.1 Introducción

El CERN [16] es en la actualidad el mayor centro de investigación de Física de Partículas del mundo. El complejo de aceleradores del CERN consiste un gran número de aceleradores interconectados que van aumentando la energía de los haces de partículas progresivamente hasta llegar al último eslabón, el LHC (ver figura 2.1). Hoy por hoy, el LHC es el mayor proyecto científico internacional del mundo. Este proyecto incluye el acelerador de hadrones más potente jamás construido, cuatro enormes detectores en sus cuatro puntos de colisión y el proyecto de computación distribuida Grid.

El LHC es un colisionador circular de 27 km de longitud por el que se acelerarán dos haces de protones (aunque también se acelerarán iones de plomo) en sentidos opuestos, alcanzando una energía de 7 TeV por haz y una luminosidad de 10^{34} cm^{-1} s^{-1} [17]. Gracias a las energías alcanzadas en las colisiones, el LHC explorará a fondo la escala energética del TeV. Los haces no son contínuos, sino que están formados por paquetes de protones (o iones de Pb) separados espacio-temporalmente unos de otros. Cada paquete contendr hasta $1.1 \cdot 10^{11}$ protones. Las colisiones se producirán a una frecuencia de 40 MHz (es decir, hadrá una colisión cada 25 ns). En la tabla 2.1 se recogen todos los parámetros relevantes del LHC. Se espera que esta máquina realice medidas de alta precisión de observables ya conocidos del Modelo Estandar así como que proporcione respuestas a preguntas como el origen de la masa de las partículas a través del bosón de Higgs. También buscará pruebas experimentales de nuevas y emocionantes teorías más allá del Modelo Estandar, como son SuperSimetría o Dimensiones Extras. Por todos estos motivos, es comprensible que los físicos se refieran al LHC como “la máquina de los descubrimientos”, ya que ha sido diseñado para explorar nuevas fronteras del conocimiento.

Tal y como muestra la figura 2.4, el LHC alberga cuatro grandes detectores localizados en los cuatro puntos de colisión del acelerador, aunque en realidad se llevan a cabo seis experimentos:

- **A Toroidal LHC ApparatuS (ATLAS)** [18]: Detector de propósito general que realizará medidas de alta precisión dentro del Modelo Estándar y buscará el bosón de Higgs y evidencias de nueva física. Es el detector más grande, con 44 m de largo y 25 m de alto y un peso de 7000 toneladas. Posee dos imanes, uno solenoidal de 2 T envolviendo el detecotr interno y uno toroidal que genera hasta 6 T/m en el espectrómetro de muones.

- **Compact Muon Solenoid (CMS)** [19]: Es otro detector de propósito general que posee en mismo potencial que ATLAS aunque un diseño distinto. Es más pequeño (21 m de largo y 15 m de alto) pero más pesado que el primero, con 12500 toneladas. Posee un único imán que genera un campo magnético no lineal de hasta 4 T.

- **Large Hadron Collider beauty (LHCb)** [20]: Este detector está diseñado para estudiar violación de $\mathcal{CP}$ en interacciones de hadrones B. El LHCb es un espectrómetro lineal de 20 m de longitud dispuesto en la misma dirección que el haz, es decir, con sus subdetectores situados unos detrás de otros como si fueran libros en una estantería.

- **A Large Ion Collider Experiment (ALICE)** [21]: Este detector está dedicado al estudio colisiones de iones pesados y del plasma quark-gluon.

- **Total Cross Section, Elastic Scattering and Diffraction Dissociation (TOTEM)** [22]: El objetivo de este experimento es la medición de secciones eficaces, procesos difractivos y dispersiones inelásticas a ángulos bajos. Está situado en el mismo punto que CMS.

- **Large Hadron Collider forward (LHCf)** [23]: Es un experimento especial para el estudio de piones neutros producidos en las regiones hacia delante de las colisiones. Comparte caverna con ATLAS y está situado 140 m a ambos lados del punto de interacción.

Por último el proyecto de computación Grid aporta la infraestructura necesaria para el análisis y el almacenamiento de los datos producidos por el LHC y recogidos por sus detctores. Se estima que se recogeran unos 15 PB de datos al año, los cuales serán distribuidos alrededor del mundo para ser analizados por miles de físicos al mismo tiempo (ver figure 2.5). Para poder hacer frente a tales demandas, la filosofía de la tecnología Grid es que los análisis se procesen en los lugares donde se encuentren los datos requeridos, minimizando las grandes transferencias de datos.

11.1.1 ATLAS

ATLAS es un detector de geometría cilíndrica formado por distintas capas concéntricas de subdetectores. La figura 11.1 muestra una representación tridimensional de ATLAS en la que se puede apreciar su configuración final, compuesta por tres sistemas principales:

- **Detector de trazas:** El sistema más cercano al haz es el detector de trazas, por eso se conoce también con el nombre de Detector Interno. Éste está inmerso en un campo magnético de 2 T y se compone de subdetectores basados en silicio y en tubos de deriva. A su vez, posee dos tecnologías diferentes para los detectores de silicio, estando una de ellas basadas en píxeles y la otra en microbandas. Con este subdetector se asegura una reconstrucción precisa del momento, la carga y los vértices primarios y secundarios de las partículas cargadas, así como la capacidad de identificación de piones.

- **Calorímetros:** Fuera del solenoide del detector interno se encuentran los calorímetros. En primer lugar, está el calorímetro electromagnético que utiliza argón líquido como medio de ionización y posee una geometría en forma de acordeón. Este subdetector permite la identificación y medición de electrones y fotones. Rodeándolo se encuentra el calorímetro hadrónico que usa una tecnología de tejas centelleadoras para medir *jets* hadrónicos y ayudar en la determinación de la energía trasversa faltante (fundamentalmente, energía que se llevan los neutrinos y que no es detectada).

- **Espectrómetro de muones:** Finalmente, en la parte más exterior de ATLAS se encuentra el espectrómetro de muones, inmerso en un campo magnético generado por un toroide, que mide el momento de los muones y da el *trigger*.

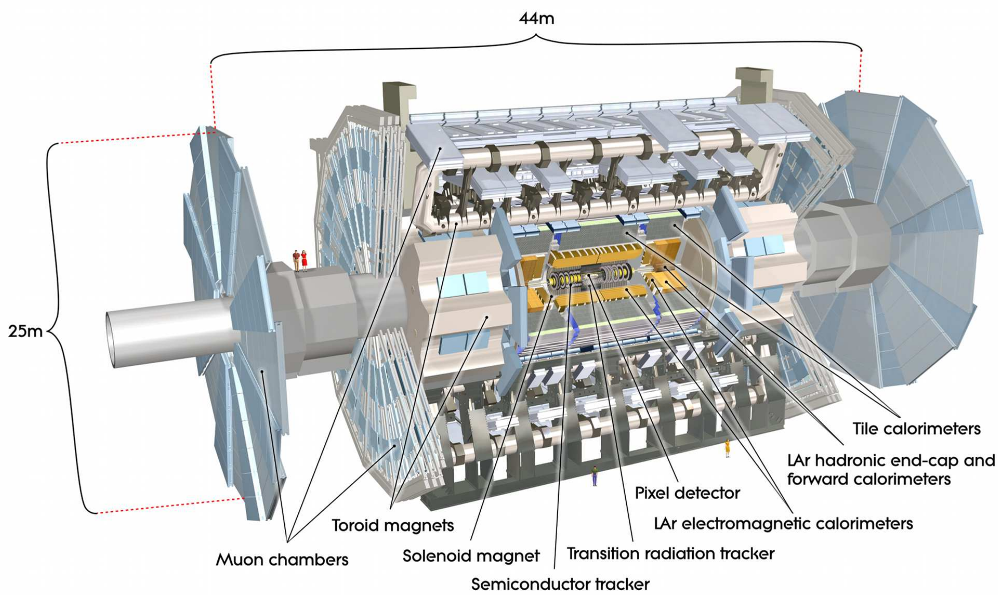

Figure 11.1: *Representación tridimensional del detector ATLAS en el que se observan todos sus subdetectores. Además, se han añadido varias figuras humanas para tener una referencia del tamaño de este detector.*

Por último conviene mencionar el sistema de *trigger* de ATLAS. Este sistema discrimina los eventos interesantes desde el punto de vista físico, reduciendo la necesidad de almacenar los 40 millones de eventos por segundo a tan sólo unos 100. Este sistema está estructurado en varios niveles. El primer nivel (LVL1) se realiza a nivel hardware y es responsable de la primera selección de eventos usando básicamente la información de los calorímetros y de las cámaras de muones. Los siguientes dos niveles están basados en software y el conjunto de ambos se llama HLT. Primero el LVL2 decide si los eventos tienen que ser o no descartados basándose en regiones de interés predefinidas en todos los subdetectores. Por último, el EF utiliza algoritmos *offline* para realizar una selección fina de los eventos que pasaron los anteriores niveles de selección.

11.1.2 Detector de trazas de silicio

El detector de trazas de silicio es el subdetector para el cual se ha desarrollado el algoritmo de alineamiento presentado en esta tesis. Es por esto que necesitamos conocer en detalle este subdetector, cuya tarea fundamental es la de reconstruir las trayectorias de las partículas cargadas que se producen en las colisiones del LHC. Su diseño proporciona una excelente resolución en la reconstrucción del momento de las partículas así como de sus vértices primarios y secundarios. Tiene una covertura espacial de $|\eta| < 2.5$ y los detectores que posee son resistentes a altas dosis de radiación [18]. Esto último es indispensable debido a la alta luminosidad que el LHC alcanzará, 10^{34} cm^{-1} s^{-1}.

Este subdetector está en el interior de un solenoide que genera un campo magnético de 2 T, lo que hace posible la medida del momento de las partículas cargadas a partir de la curvatura de sus trayectorias (expresión 3.1): $p_T = 0.3qBr$.

El subdetector de píxeles es el más próximo al punto de interacción, siendo éste motivo por el cual es el que más radiación debe de soportar (158 kGy/año). Pero es precisamente esa posición privilegiada la que le permite realizar medidas precisas así como detectar partículas de vida relativamente larga como pueden ser *quarks* b o leptones τ. Estructuralmente, el detector se compone de una parte barril y dos *end-caps*. El barril posee 3 capas y cada *end-caps* 3 discos situados a cada lado del barril. A su vez, cada capa del barril está construida en dos partes llamadas *half-shells* (ver figura 3.7) y éstas a su vez en tiras llamadas *staves* donde van montados finalmente los módulos de los píxeles tal y como se aprecia en la figura 3.6. Por su parte, los discos de los *end-caps* están formados por distintos sectores con tres módulos por sector, como se aprecia en la fotografía de la figura 3.8. Por último, cada módulo está formado por una única oblea de silicio dotada de implantes n^+ sobre un substrato de tipo n. La conexión pn se encuentra en el plano de detrás. Estos módulos proporcionan medidas (*hits*) bidimensionales del paso de las partículas. Todos los detalles se pueden ver en la figura 3.5. Para más información consultar la referencia [41].

El subdetector de microbandas de silicio, tambien llamado SCT, está situado inmediatamente después del de los píxeles. Su principal objetivo es el de complementar al anterior subdetector, dado que al estar situado a una mayor distancia del punto de interacción la precisión en el cálculo de vertices secundarios es menor pero aportando la ventaja de tener un mayor brazo de palanca a la hora de calcular el momento y la trayectoria de las partículas cargadas. Estructuralmente se compone de un barril (figura 3.10) y dos *end-caps* (figura 3.11). El barril está formado por 4 capas donde van montados los módulos. Por su parte, los *end-caps* poseen 9 discos cada uno, en los cuales se montan los módulos. Tal y como puede apreciarse en la figura 3.12, los módulos del SCT están formados por 2 caras pegadas espalda con espalda con una rotación relativa entre ellas de 40 mrad. Cada cara tiene 2 obleas de silicio unidas por uno de sus extremos para duplicar su longitud en la dirección de sus microbandas. Cada oblea tiene 768 microbandas de silicio, separadas de media unas 80 μm, de tipo p^+ sobre un substrato tipo n. Estos módulos proporcionan una medida (*hit*) unidimensiomal por cara. La combinación de ambas medidas independientes y la posición de dicho módulo en el espacio da la posibilidad de reconstruir un punto tridimensional llamado *space-point*. Existen 5 topologías diferentes según se trate de módulos montados en la parte barril o en los *end-caps*. La figura 3.13 muestra estos cinco tipos. Para más información consultar la referencia [27].

11.2 Alineamiento del detector de trazas de silicio de ATLAS

Tal y como se ha discutido en el capítulo anterior, el detector ATLAS ha sido construido utilizando dispositivos de reconstrucción de posición y energía de alta resolución aunque éstos deben estar adecuadamente calibrados y alineados para poder exprimir todas sus características. Si nos centramos en el detector de trazas de silicio podemos afirmar que cualquier desalineamiento de sus elementos (es decir, sus módulos) degradará significativamente las medidas de las trayectorias de las partículas cargadas, así como el reconocimiento de patrones usado en la búsqueda de trazas. Además, esto repercutirá negativamente en el rendimento general de ATLAS y en su potencial de descubrimientos. Es por este motivo por el cual el principal objetivo del alineamiento es el de conocer la posición de cada uno de los módulos que componen el detector de trazas de silicio hasta una precisión en la que el deterioro en la resolución de los parámetros de las trazas sea inferior al 20% con respecto a su resolución intríseca [26]. Esto se traduce en que la precisión alcanzada por el alineamiento debe ser de unas 7 μm para los módulos de los píxeles y unas 12 μm para los módulos del SCT [34]. Por estos motivos, para asegurar un rendimiento excelente tanto a nivel de física como a nivel del propio detector interno es necesario alcanzar los siguientes objetivos [35]:

- Alcanzar un nivel de precisión del orden de 10 μm en el plano transverso con respecto la dirección de los haces.
- Entender el campo magnético generado por el solenoide a un nivel del 0.02%, para calcular correctamente el momento.
- Describir correctamente el material hasta una precisión del $\sim 1\%$, con el fin de calcular correctamente los efectos de dispersión múltiple.
- Entender la resolución del momento transverso hasta una precisión del 1%.

Para resolver este tema es por lo que se desarrollan los algoritmos de alineamiento basados en trazas, siendo el algoritmo Globalχ^2 el método de referencia en estos momentos para el alineamiento del detector interno de ATLAS.

11.2.1 Algoritmo Globalχ^2

El algoritmo Globalχ^2 se basa en la minimización de una función χ^2 definida como:

$$\chi^2 = \sum_e \sum_{t \in e} \mathbf{r}^T V^{-1} \mathbf{r}$$

donde $\mathbf{r}$ es el vector que contiene todos los residuos *biased* que el sistema de medición (en nuestro caso, el detector de trazas de silicio de ATLAS) puede proporcionar. Es decir, que el tamaño del vector $\mathbf{r}$ es $N_{RES} = 2N_{PIX} + N_{SCT}$, siendo N_{PIX} y N_{SCT} el número de residuos que los píxeles y el SCT pueden proporcionar, respectivamente. Estos residuos se pueden calcular como $\mathbf{r} = (\mathbf{m} - \mathbf{e}(\boldsymbol{\pi}, \mathbf{a}))$, donde $\mathbf{m}$ es el vector que contiene las posiciones del *hit* y $\mathbf{e}$ es el vector que contiene las posiciones de los puntos de intersección de las trazas con los planos de sus correspondientes módulos. A su vez $\mathbf{e}$ depende de $\boldsymbol{\pi}$ que representa los parámetros de las trazas (tamaño N_{TPR}) y de $\mathbf{a}$ que son los parámetros de alineamiento (tamaño N_{ALI}). V es la matriz de covarianzas de los *hits* medidos. Esta matriz es simétrica y tiene en los elementos de la diagonal los errores intrínsecos en las medidas de los *hits*. Los elementos fuera de la diagonal describen las correlaciones entre los *hits* de los distintos módulos. Estas correlaciones las dan los distintos *hits* medidos en distintos módulos pero asociados a una misma traza. Los efectos de dispersiones debidos a efectos del material también estan incluidos en estos elementos.

El objetivo de este algoritmo es obtener los parámetros de alineamiento óptimos para todos los módulos de silicio. Para conseguir esto, el Globalχ^2 hace uso del hecho de que los residuos dependen tanto de los parámetros de las trazas como de los parámetros de alineamiento. De modo que el χ^2 es minimizado primero con respecto $\boldsymbol{\pi}$ y luego con respecto $\mathbf{a}$, pero incorporando la información que la primera minimización nos proporciona. Esto permite encontrar el mínimo de la función χ^2 para ambos conjuntos de parámetros simultáneamente.

La solución para los parámetros de una sóla traza y para unos parámetros de alineamiento arbitrarios, se consigue imponiendo la condición de mínimo:

$$\sum_e \sum_{t\in e} \frac{d\chi^2}{d\boldsymbol{\pi}} = \sum_e \sum_{t\in e} \frac{\partial\chi^2}{\partial\boldsymbol{\pi}} = \sum_e \sum_{t\in e} \left(\frac{\partial\mathbf{r}}{\partial\boldsymbol{\pi}}\right)^T V^{-1}\mathbf{r} = 0$$

En general tenemos que: $\boldsymbol{\pi} = \boldsymbol{\pi}_0 + \delta\boldsymbol{\pi}$, siendo $\boldsymbol{\pi}_0$ los valores iniciales. Usando esta expresión podemos ver que es posible calcular las correcciones a los parámetros de las trazas realizando un desarrollo en serie de $\boldsymbol{\pi}$ alrededor de $\boldsymbol{\pi}_0$. Despreciando derivadas de orden dos en adelante, tenemos:

$$\mathbf{r}(\boldsymbol{\pi},\mathbf{a}) = \mathbf{r}(\boldsymbol{\pi}_0,\mathbf{a}) + E\delta\boldsymbol{\pi} \quad \text{definiendo} \quad E \equiv \left.\frac{\partial\mathbf{r}}{\partial\boldsymbol{\pi}}\right|_{\boldsymbol{\pi}=\boldsymbol{\pi}_0}$$

donde la matriz E es de dimensión $N_{RES} \times N_{TPR}$. Esta matriz que depende del número de *hits* asociados a cada traza y del número de trazas, es la matriz que correlaciona los diferentes módulos que comparten trazas, por lo que es la esencia del algoritmo Globalχ^2 . Además, $\mathbf{r}$ está ahora evaluado en $\boldsymbol{\pi}_0$, es decir, $\mathbf{r} = (\mathbf{m} - \mathbf{e}(\boldsymbol{\pi}_0,\mathbf{a}))$. Usando estos últimos resultados, tenemos:

$$\delta\boldsymbol{\pi} = -(E^T V^{-1} E)^{-1} E^T V^{-1}\mathbf{r}(\boldsymbol{\pi}_0,\mathbf{a})$$

donde el término $(E^T V^{-1} E)$ es la matriz de covarianzas de las correcciones de los parámetros de las trazas.

De forma similar, podemos realizar la minimización del χ^2 con respecto los parámetros de las trazas:

$$\sum_e \sum_{t\in e} \frac{d\chi^2}{d\mathbf{a}} = \sum_e \sum_{t\in e} \left(\frac{d\mathbf{r}}{d\boldsymbol{\pi}}\right)^T V^{-1}\mathbf{r} = \sum_e \sum_{t\in e} \left(\frac{\partial\mathbf{r}}{\partial\boldsymbol{\pi}}\frac{d\boldsymbol{\pi}}{d\mathbf{a}} + \frac{\partial\mathbf{r}}{\partial\mathbf{a}}\right)^T V^{-1}\mathbf{r} = 0$$

Llegados a este punto, también podemos realizar un desarrollo en serie de $\mathbf{a}$ y quedándonos a primer orden se obtiene:

$$\sum_e \sum_{t\in e} \left(\frac{d\mathbf{r}}{d\mathbf{a}}\right)^T V^{-1}\mathbf{r} + \sum_e \sum_{t\in e} \left(\frac{d\mathbf{r}}{d\mathbf{a}}\right)^T V^{-1} \left(\frac{\partial\mathbf{r}}{\partial\mathbf{a}}\right)\delta\mathbf{a} =$$

$$= \sum_e \sum_{t\in e} \left(\frac{\partial\mathbf{r}}{\partial\boldsymbol{\pi}}\frac{d\boldsymbol{\pi}}{d\mathbf{a}} + \frac{\partial\mathbf{r}}{\partial\mathbf{a}}\right)^T V^{-1}\mathbf{r} + \sum_e \sum_{t\in e} \left(\frac{\partial\mathbf{r}}{\partial\boldsymbol{\pi}}\frac{d\boldsymbol{\pi}}{d\mathbf{a}} + \frac{\partial\mathbf{r}}{\partial\mathbf{a}}\right)^T V^{-1} \left(\frac{\partial\mathbf{r}}{\partial\mathbf{a}}\right)\delta\mathbf{a} = 0$$

donde ahora $\mathbf{r}$ está también evaluado en $\mathbf{a}_0$ (parámetros de alineamiento iniciales), es decir, $\mathbf{r} = (\mathbf{m} - \mathbf{e}(\boldsymbol{\pi}_0,\mathbf{a}_0))$. Por simplificar, también se ha considerado que $\partial\mathbf{r}/\partial\mathbf{a}$ significa $\partial\mathbf{r}/\partial\mathbf{a}|_{\boldsymbol{\pi}_0,\mathbf{a}_0}$.

El problema es cómo calcular la derivada $d\boldsymbol{\pi}/d\mathbf{a}$. La solución es simplemente, recuperar la expresión de $\delta\boldsymbol{\pi}$ y derivarla con respecto los parámetros de las trazas. Haciendo esto se obtiene:

$$\frac{d\boldsymbol{\pi}}{d\mathbf{a}} = -(E^T V^{-1} E)^{-1} E^T V^{-1} \frac{\partial\mathbf{r}}{\partial\mathbf{a}}$$

Juntando estos dos últimos resultados y despejando $\delta\mathbf{a}$ se obtiene fácilmente:

$$\delta\mathbf{a} = -\left[\sum_e \sum_{t\in e} \left(\frac{d\mathbf{r}}{d\mathbf{a}}\right)^T V^{-1} \left(\frac{\partial\mathbf{r}}{\partial\mathbf{a}}\right)\right]^{-1} \sum_e \sum_{t\in e} \left(\frac{d\mathbf{r}}{d\mathbf{a}}\right)^T V^{-1}\mathbf{r} =$$

$$= -\left[\sum_e \sum_{t\in e} \left(\frac{\partial \mathbf{r}}{\partial \mathbf{a}}\right)^T (I - \mathcal{G}_E^T) V^{-1} \left(\frac{\partial \mathbf{r}}{\partial \mathbf{a}}\right)\right]^{-1} \sum_e \sum_{t\in e} \left(\frac{\partial \mathbf{r}}{\partial \mathbf{a}}\right)^T (I - \mathcal{G}_E^T) V^{-1} \mathbf{r}$$

habiendo definido: $\mathcal{G}_E \equiv E(E^T V^{-1} E)^{-1} E^T V^{-1}$.

Por último, es conveniente destacar que la expression de las correcciones a los parámetros de alineamiento pueden compactarse, definiendo una matriz y un vector:

$$\delta\mathbf{a} = -\mathcal{M}^{-1}\nu$$

donde:

$$\mathcal{M} = \sum_e \sum_{t\in e} \left(\frac{d\mathbf{r}}{d\mathbf{a}}\right)^T V^{-1} \left(\frac{\partial \mathbf{r}}{\partial \mathbf{a}}\right) = \sum_e \sum_{t\in e} \left(\frac{\partial \mathbf{r}}{\partial \mathbf{a}}\right)^T (I - \mathcal{G}_E^T) V^{-1} \left(\frac{\partial \mathbf{r}}{\partial \mathbf{a}}\right)$$

$$\nu = \sum_e \sum_{t\in e} \left(\frac{d\mathbf{r}}{d\mathbf{a}}\right)^T V^{-1}\mathbf{r} = \sum_e \sum_{t\in e} \left(\frac{\partial \mathbf{r}}{\partial \mathbf{a}}\right)^T (I - \mathcal{G}_E^T) V^{-1} \mathbf{r}$$

$\mathcal{M}$ es la matriz de covarianzas de las correcciones de los parámetros de alineamiento de dimensión $N_{ALI} \times N_{ALI}$.

Finalmente, el cálculo de los nuevos parámetros de alineamiento son:

$$\mathbf{a} = \mathbf{a}_0 + \delta\mathbf{a} = \mathbf{a}_0 - \mathcal{M}^{-1}\nu$$

Esta última expresión puede extenderse fácilmente en el caso de que se requieran n iteraciones para que los parámetros de alineamiento convergan:

$$(\mathbf{a})_{Iter(n)} = (\mathbf{a})_{Iter(n-1)} + (\delta\mathbf{a})_{Iter(n)} \quad \text{with} \quad n \geq 1$$

Este es el formalismo básico, sin imponer restricciones ni a unos parámetros ni a otros. Sin embargo, es posible añadir restricciones para poder controlar la evolución y convergencia del método. En el capítulo 4 y los apéndices A y B se detalla todo el formalismo.

Para finalizar, es importante remarcar que si no se consideraran correlaciones entre los distintos módulos, es decir, si hicieramos $E = 0$, entonces se entraría en el régimen local y las correcciones de los parámetros de las trazas serían símplemente:

$$\delta\mathbf{a} = -\left[\sum_e \sum_{t\in e} \left(\frac{\partial \mathbf{r}}{\partial \mathbf{a}}\right)^T V^{-1} \left(\frac{\partial \mathbf{r}}{\partial \mathbf{a}}\right)\right]^{-1} \sum_e \sum_{t\in e} \left(\frac{\partial \mathbf{r}}{\partial \mathbf{a}}\right)^T V^{-1} \mathbf{r}$$

En este régimen, todo el potencial del método se perdería y los módulos se alinearian de forma independiente.

11.2.2 Resultados usando el Globalχ^2

El algoritmo Globalχ^2 ha sido desarrollado, depurado, probado, evaluado, afinado y finalmente validado usando tanto datos de simulación MC como datos reales de rayos cósmicos e incluso con datos de las primeras colisiones del LHC a 900 GeV. Además, todo esto ha sido implementado dentro del software oficial de ATLAS, conocido con el nombre de *Athena*.

11.2.2.1 Resultados con datos simulados

Durante los años previos a la instalación e integración de ATLAS en su caverna, únicamente se dispuso de simulaciones MC para poder estimar y evaluar las prestaciones de todos los sistemas y subdetectores trabajando al unísono. Estas simulaciones fueron cruciales para preparar y depurar los algoritmos que luego se aplicarían en la vida real. Además, estas simulaciones no sólo se usan cuando no se dispone físicamente del detector, sino que son una fuente de información con la que comparar los datos experimentales reales. Al mismo tiempo, la propia simulación se modifica y actualiza para modelizar lo más fielmente posible la realidad. Este capítulo presenta dos ejercicios de simulación que se realizaron durante la puesta a punto de ATLAS:

- **Computing System Commissioning (CSC):** en este ejercicio se introdujo por primera vez una descripción realista del detector ATLAS. Específicamente para el detector interno, esta descripción incluyó desplazamientos de los detectores a distintos niveles a nivel de simulación (a nivel de reconstrucción ya se había realizado en simulaciones previas), lo que se conoce como geometría *as-built*, material adicional en distintas zonas del detector interno y un campo magnético distorsionado (desplazado e inclinado). Por supuesto, todo esto constituyó un banco de pruebas perfecto para la puesta a punto de los algoritmos de alineamiento y de su validación de cara a la toma de datos reales.

  Para realizar los estudios de rendimiento y prestaciones de los algoritmos de alineamiento se generó una muestra específica que tenía las siguientes características: 10 muones por evento, p_T = [2, 50] GeV/c, η = [-2.7, 2.7] y ϕ = [0, 2π]. Además, todas las trazas dentro de un mismo evento se generaban en un mismo vértice primario y este vértice cambiaba de evento a evento con unas características promedio de: $\sigma_x = \sigma_y = \sqrt{2} \cdot 15\ \mu m$ y $\sigma_z = \sqrt{2} \cdot 56$ mm. Obviamente, en la realidad uno no se iba a encontrar con este tipo de eventos, pero constituía una muestra que minimizaba todo posible *bias* que pueden introducir ciertas muestras reales de física. Esto permitió concentrar todos los esfuerzos en el alineamiento.

  Además de la muestra anterior, también se dispuso de la simulación de rayos cósmicos en la caverna de ATLAS. Se simularon dos tipos de muestras, una con la presencia del campo magnético en el detector interno a su valor nominal (2 T) y otra muestra sin campo magnético. La primera muestra permitía la medida del momento de los rayos a partir de su curvatura y la segunda muestra permitía tener trazas completamente rectas atravesando el detector de arriba hacia abajo. De este modo cada muestra tenía sus pros y sus contras, pero ambas proporcionaba información fundamental para diversos estudios de alineamiento.

  En la estrategia para alinear el detector de silicio con el algoritmo Globalχ^2 se introdujo por primera vez la estructura de niveles de alineamiento. Esta estrategia consistía en alinear colectivamente los módulos considerando las estructuras en las cuales éstos estaban físicamente montados. De este modo, primero se realizó un alineamiento a nivel 1, que consiste en considerar todo el detector de los píxeles como un solo objeto y el SCT como tres objetos (el barril y los dos *end-caps*). Después se procedió a alinear el nivel 2, en el cual se consideraban los capas de los barriles y los discos de los *end-caps* como los objetos a alinear. Por último, se realizó un nivel 3 en el que se alineaba a nivel de módulo. En esta estrategia también se incluyo un término extra en el χ^2 para restringir los parámetros de las trazas.

Las distribuciones de residuos mejoraron de forma espectacular consiguiéndose unas prestaciones comparables a un alineamiento perfecto. No obstante, se confirmó que el obtener un rendimiento óptimo en esta distribuciones era un factor necesario pero no suficiente para evaluar el alineamiento del detector interno. Para ello, a parte de las distribuciones "clásicas" (*hits*, trazas, residuos, parámetros de las trazas, etc...) se utilizaron multitud de correlaciones entre distintos parámetros así como muestras reales de física para evaluar los resultados. La figura 11.2 (a) muestra la masa invariante del canal $Z \rightarrow \mu\mu$ tanto para el caso en el que el detector interno está idealmente alineado y para el alineamiento conseguido por el algoritmo Globalχ^2. En dicha figura se ve que aunque el rendimiento alcanzado es muy bueno no es óptimo. Por otra parte la figura 11.2 (b) muestra la proporción de muones positivos y negativos reconstruidos en función de su momento transverso. Puede observarse que existen diferencias apreciables entre un alineamiento real y el obtenido, lo que nos dice que el alineamiento realizado se podría mejorar.

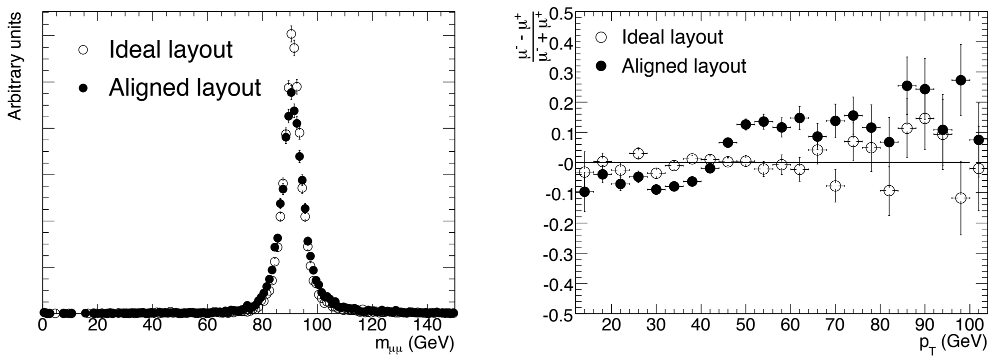

(a) *Masa invariante del par $\mu\mu$*

(b) *Relación del número de μ^+ y μ^- Vs p_T*

Figure 11.2: *La figura (a) muestra la masa invariante del canal $Z \rightarrow \mu\mu$. La figura (b) muestra la proporción de muones positivos y negativos reconstruidos en función de su momento transverso. En ambos casos se muestran los resultados para un alineamiento ideal y para el obtenido con el algoritmo Globalχ^2 [66].*

- **Full Dress Rehearsal (FDR):** este ejercicio evaluó y puso a prueba todo el sistema de adquisición, reconstrucción, procesado y análisis de datos de ATLAS usando datos simulados. Desde el punto de vista del alineamiento, constituía la prueba final en la que todo el modelo se tenía que integrar en la cadena anterior y obtener resultados en ciclos de 24 horas. La figura 11.3 muestra un esquema de la integración del modelo de alineamiento del detector interno dentro de la cadena de toma de datos de ATLAS.

  La simulación utilizada fué similar a la del CSC y se generaron unas muestras reales de

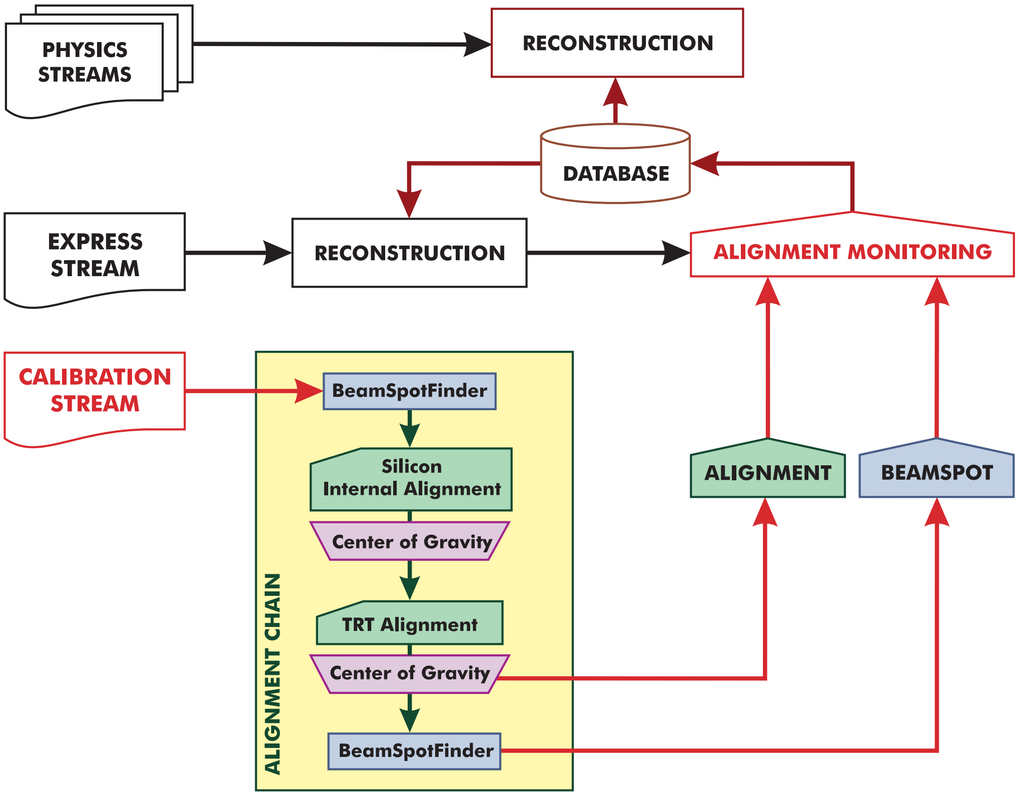

Figure 11.3: *Esquema de la integración del modelo de alineamiento del detector interno dentro de la cadena de toma de datos de ATLAS.*

física para emular datos de colisiones. Además, estos datos fueron filtrados por el sistema de *trigger* para aumentar el realismo del ejercicio.

Las prestaciones alcanzadas fueron muy buenas y las constantes de alineamiento fueron publicadas dentro de cada ciclo de 24 horas. Este ejercicio permitió comprobar la validez del modelo de alineamiento así como su estrategia basada en niveles.

11.2.2.2 Resultados con datos reales

Una vez presentado el alineamiento basado en datos simulados, es el momento de discutir los resultados obtenidos a partir de datos reales, usando tanto rayos cósmicos como las primeras colisiones del LHC a 900 GeV.

- **Pruebas con rayos cósmicos en el SR1:** En primavera de 2006, se realizaron una serie de pruebas en el laboratorio SR1 del CERN para comprobar el correcto funcionamiento del barril del SCT y del TRT antes de bajarlos a la caverna de ATLAS. Fué la primera vez que se probaban estos dos subdetectores de forma combinada. Se realizaron pruebas de ruido electrónico y de *cross-talk* usando *triggers* aleatorios [68]. Como prueba final se configuró el sistema para la adquisición de rayos cósmicos. De este modo se evaluó toda la cadena hardware/software de reconstrucción, calibración y alineamiento.

La configuración del detector fué algo peculiar debido a que tanto el barril del SCT como el del TRT estaban parcialmente alimentados. Únicamente 12 módulos del TRT y 468 módulos del SCT (es decir, un 22% del TRT y un 13% del SCT) estaban operativos. La figura 7.1 ilustra dicha configuración, donde los píxeles no estaban presentes. El sistema tampoco estaba inmerso en ningún campo magnético por lo que no fué posible realizar ninguna medida del momento de los muones ni estimar los efectos del material.

La figura 11.4 muestra la evolución de las correcciones de los parámetros de alineamiento para las traslaciones Tx y Ty. Se observa una buena convergencia del sistema. Por otro lado, la figura 11.5 muestra la evolución de los promedios de la media y de la anchura de las distribuciones de los residuos de todos los módulos del barril del SCT, agrupados por capas. Además, también se muestra la evolución de sus *pulls*. En todos los casos, la convergencia se alcanza a partir de la segunda iteración y se pasan de unas anchuras del orden de 90 μm a unas del orden de 50 μm. Esto nos indica una gran mejora en las prestaciones y en el rendimeinto del detector.

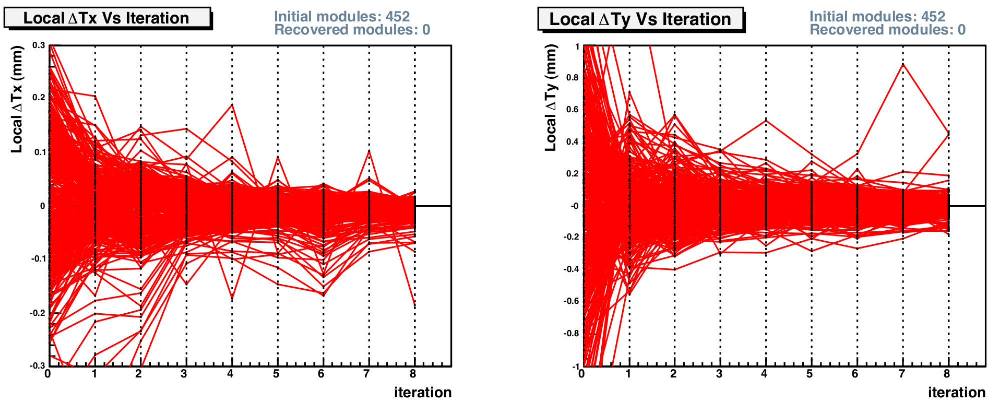

Figure 11.4: *Evolución de las correcciones de los parámetros de alineamiento iteración tras iteración. En concreto se muestran las correcciones a las traslaciones Tx y Ty y se observa su convergencia*

Los resultados se compararon con la simulación que se había realizado.

- **Pruebas con rayos cósmicos en el pozo de ATLAS:** En 2008 comenzó la fase de puesta a punto de ATLAS. Con el detector instalado en su caverna, la prueba más ambiciosa fué la de configurar todo el detector para realizar varios periodos contínuos de toma de datos de rayos cósmicos. Esto permitió probar y depurar todos los sistemas, desde el software de control y adquisición de datos, pasando por los sistemas de transferencia (hardware) hasta llegar a la cadena de reconstrucción *offline*. Entre todas estas pruebas, se realizó el alineamiento del detector interno.

  Hubo dos periodos de toma de datos:

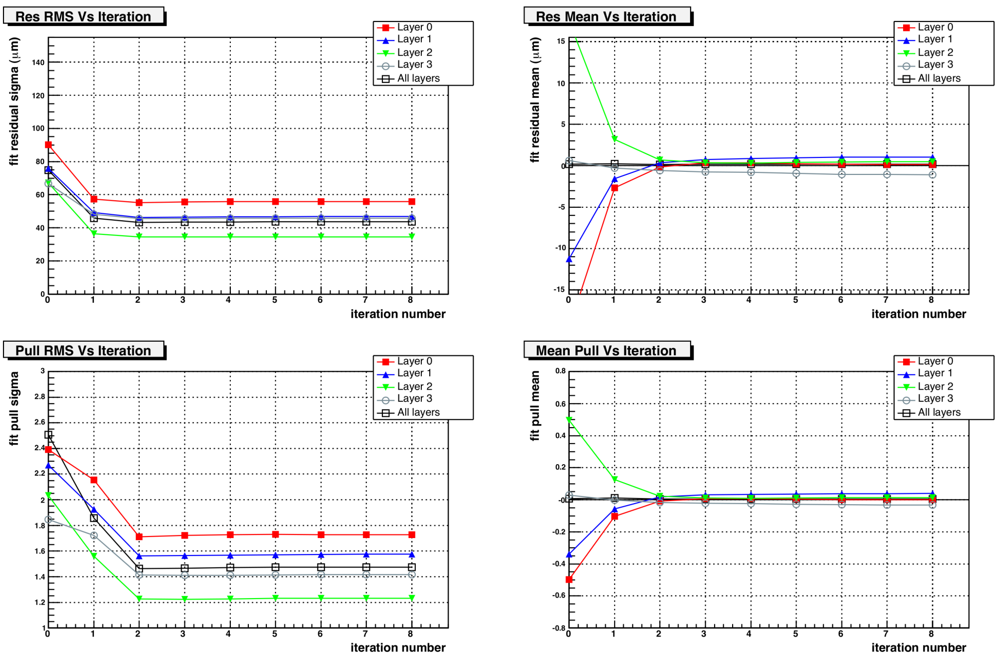

Figure 11.5: *Evolución de los promedios de la media y de la anchura de las distribuciones de los pulls (izquierda) y de los residuos (derecha) de todos los módulos del barril del SCT, agrupados por capas.*

- **Agosto de 2008:** Se recogieron más de 200 millones de eventos, existiendo periodos con distintas configuraciones de los subdetectores así como temporadas con y sin campo magnético. En la figura 11.6 (a) se encuentran los datos recogidos e integrados en función del número de *run*. Se puede ver que el detector interno registró casi 7 millones de eventos.
- **Junio y Julio de 2009:** Durante este periodo se recogieron más de 90 millones de eventos, también con distintas configuraciones de los subdetectores y de los imanes, repartidos en diferentes periodos. En la figura 7.8 (b) se muestra, al igual que antes, los datos recogidos e integrados en función del número de *run*. En este caso, el detector interno detectó unos 20 millones de eventos.

Se realizarón diversas simulaciones para poder tener con qué comparar los datos reales y aunque se incorporaron multitud de detalles no se llegó al nivel de precisión exigido para poder publicar dichas comparativas.

Se calcularon dos conjuntos de constantes de alineamiento, uno para cada uno de los periodos siendo etiquetados como *Cosmic08 alignment* y *Cosmic09 alignment*. En ambos casos se partió de los datos del *survey* para los píxeles y de las posiciones nominales para el SCT. Esta geometría de partida se etiquetó como *Initial geometry*.

Las estrategias seguidas en ambos periodos fueron ligeramente distintas, aprovechando en

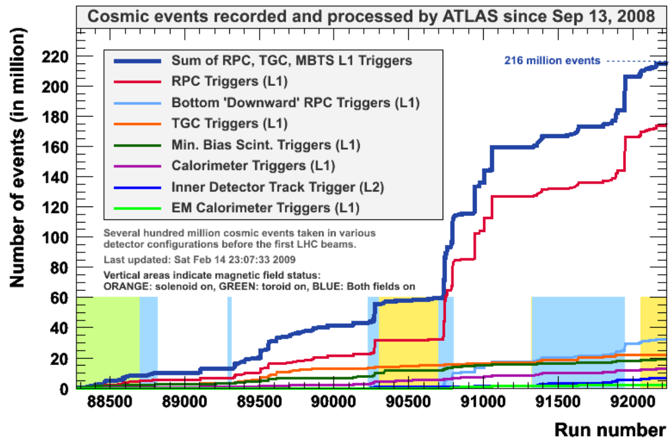

(a) *Periodo: Agosto 2008*

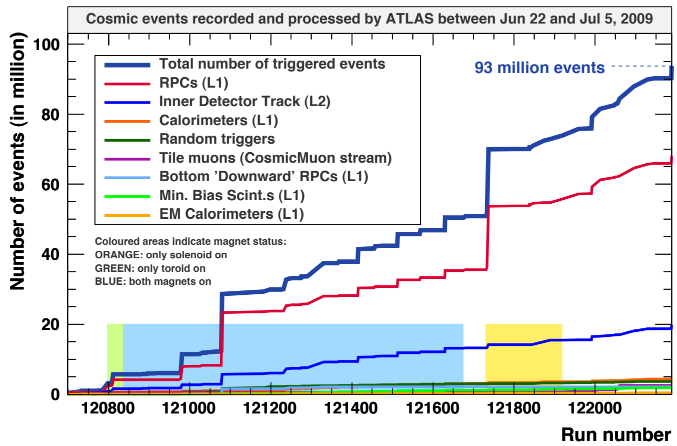

(b) *Periodo: Junio y Julio 2009*

Figure 11.6: *Las figuras (a) y (b) muestran los datos recogidos e integrados en función del número de run para el 2008 y el 2009 respectivamente.*

el 2009 todo el conocimiento y la experiencia aquiridas en el 2008. El número de eventos usados en cada periodo también fué diferente ya que en cada caso se recogió una cantidad de datos distinta. Por un lado, la tabla 7.1 muestra un resumen de la estrategia seguida en 2008 y por otro lado, la tabla 7.2 muestra lo mismo para el periodo de 2009. En ambos casos, se optó por alinear primero las estructuras (alineando colectivamente los módulos) hasta llegar al nivel de módulo individial, como ya se hizo con datos simulados en los ejercicios CSC y FDR. Esta estrategia resultó ser la adecuada, consiguiéndose unos muy buenos resultados.

Tal y como se esperaba, las prestaciones alcanzadas en el barril fueron muy superiores a las alcanzadas en los *end-caps*. Esto se debe fundamentalmente a que se registran los rayos cósmicos que vienen principalmente del zenit de ATLAS, siendo sus trazas bastantes paralelas a los discos de los *end-caps*. El resultado es una muy baja estadística en los *end-caps* y una calidad de las trazas inferior a las trazas en el barril. Las figuras 11.7 (a) y (b) muestran los residuos $r\phi$ del disco 4 del *end-cap* A y C del SCT, respectivamente. Puede verse que aunque el alineamiento de 2009 es mejor que el del 2008, las prestaciones de los *end-caps* necesitan ser mejoradas con más estadística y principalmente, con otra topología de trazas, concretamente con datos de colisiones y *beam halo*.

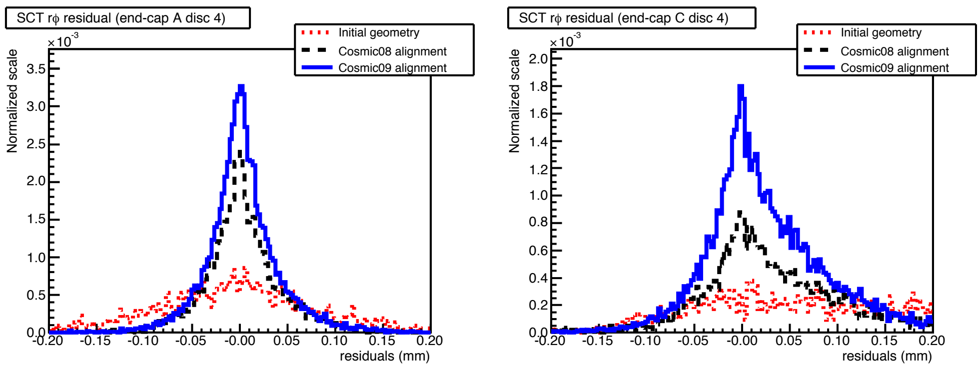

(a) *End-cap A del SCT (disco 4)*

(b) *End-cap C del SCT (disco 4)*

Figure 11.7: *Distribuciones de residuos $r\phi$ del disco 4 del* end-cap *A (a) y C (b) del SCT. En la leyenda tenemos, Initial geometry con línea de puntos, Cosmic08 alignment con línea discontínua y Cosmic09 alignment con línea contínua.*

Para el barril, las prestaciones alcanzadas fueron bastantes buenas. Las figuras 11.8 (a) y (b) muestran el promedio de la media de los residuos $r\phi$ en el barril para los píxeles y el SCT, respectivamente, en función del momento transverso reconstruido. Se puede apreciar cómo ambos conjuntos de constantes de alineamiento (círculos para el alineamiento del 2008 y triángulos para el del 2009) mejoran notablemente los residuos respecto al alineamiento inicial (cruces).

La validación de ambos alineamientos se realizó de forma independiente y externa por el grupo de *monitoring* de alineamiento. La figura 11.9 muestra la resolución del parámetro d_0 en función de p_T (a) y de él mismo (b). Se puede ver que a bajo momento transverso la resolución está dominada por efectos de dispersión debidos al material. Para altos valores del momento transverso la resolución es plana. La diferencia con el MC indica desalineamiento residuales. También se aprecia que la resolución es mejor utilizando todo

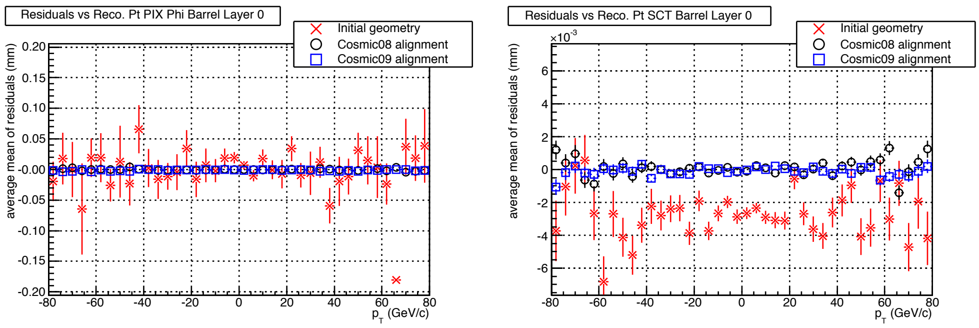

(a) *Residuos Vs pT (barril de los píxeles, capa 0)*

(b) *Residuos Vs pT (barril del SCT, capa 0)*

Figure 11.8: *Promedio de la media de los residuos para los píxeles (a) y el SCT (b) en función del momento transverso reconstruido para rayos cósmicos en presencia del campo magnético del detector interno. En la leyenda tenemos, Initial geometry con cruces, Cosmic08 alignment con círculos y Cosmic09 alignment con triángulos.*

el detector interno que usando únicamente el detector de trazas de silicio.

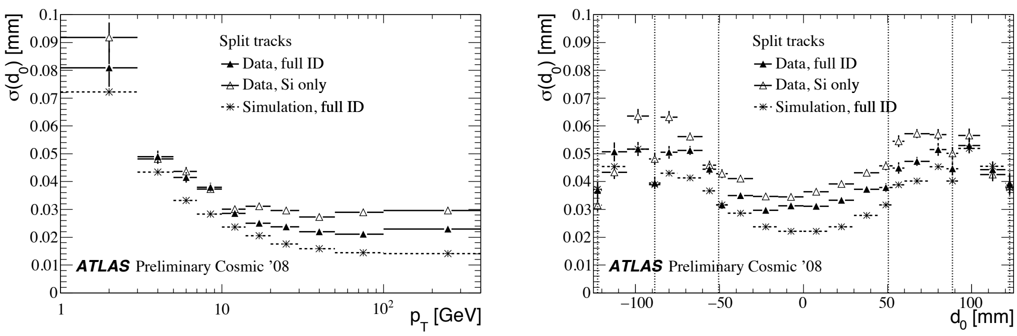

(a) $\sigma(d_0)$ *en función de* p_T

(b) $\sigma(d_0)$ *en función de* d_0

Figure 11.9: *Resolución del parámetro* d_0 *en función de* p_T *(a) y de él mismo (b) [114].*

Vale la pena mencionar que gracias al nivel de precisión alcanzado, se observaron y corrigieron curvaturas en los *staves* de los píxeles.

- **Pruebas con los primeros datos de colisiones del LHC a 900 GeV:** En noviembre de 2009, ATLAS comenzó a registrar las primeras colisiones del LHC. Pasado un tiempo, con los primeros haces estables a 900 GeV llegaron los primeros datos útiles desde el punto de vista de alineamiento. Estos datos se usaron para actualizar las constantes de alineamiento obtenidas a partir de datos reales de rayos cósmicos. De este modo, aunque se realineó todo el detector de trazas de silicio, la estrategia seguida se centró en mejorar los *end-caps* del SCT. Las figuras 11.10 (a) y (b) muestran las distribuciones de residuos para el disco 4 de los *end-caps* A y C respectivamente. En ambas figuras hay tres conjuntos de datos, uno para el caso de alineamiento ideal usando MC (círculos rellenos), otro para el alineamiento basado en cósmicos (cuadrados) y otro para la mejora del alineamiento a partir de los datos de colisiones (círculos vacíos). Puede verse que las constantes obtenidas usando colisiones mejoran estas distribuciones aunque como se esperaba aún hay camino por recorrer.

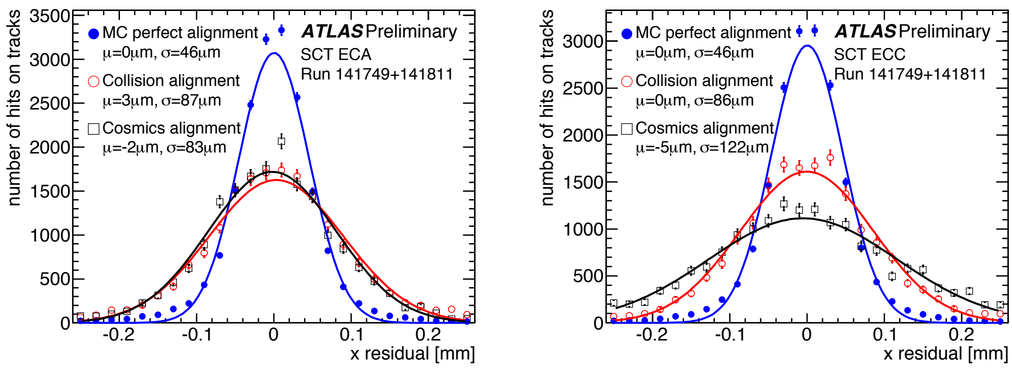

(a) *Residuos del end-cap A del SCT*

(b) *Residuos del end-cap C del SCT*

Figure 11.10: *Residuos rφ de una muestra simulada de minimum bias., donde tres conjuntos de datos están representados: alineamiento perfecto (círculo sólido), alineamiento basado en rayos cósmicos (cuadrados abiertos) y alineamiento basado en cósmicos y datos de colisiones (círculos abiertos) [118].*

Estos resultados preliminares auguran un futuro prometedor para las prestaciones que se alcanzarán a nivel de alineamiento mediante el algoritmo Globalχ^2 .

11.3 Medida de la masa del quark top

El *quark* top fué descubierto en los experimentos de Tevatron, CDF y DØ, en Fermilab en 1995 [119] [120]. Este *quark* posee unas interesantes propiedades que no poseen los demás *quarks* debido fundamentalmente a que su masa es muy parecida a la escala de rotura de simetría. Además, su vida media es muy corta $5 \cdot 10^{-25}$ s (predicción del Modelo Estandar), por lo que se desintegra (con cambio de sabor) antes de hadronizar.

Este capítulo resume el trabajo realizado para la medida de la masa del *quark* top, donde la principal novedad ha sido la introducción del algoritmo Globalχ^2 dentro de este contexto. En este trabajo se utilizó datos simulados dentro del ejercicio CSC [7] asumiendo una luminosidad integrada de 1 fb^{-1} a baja luminosidad (10^{33} cm^{-2} s^{-1}) y a la energía nominal del LHC ($\sqrt{s}$ = 14 TeV). Además, se escogió el canal de desintegración semileptónico, $t\bar{t} \rightarrow \ell\nu_\ell$ + jets con $\ell = e, \mu, \tau$, por ser el canal que tenía un mayor compromiso entre su BR ($\sim$44%) y su relación señal/ruido. Esto último se debe fundamentalmente a la presencia de un leptón en el estado final, el cual permite discriminar el fondo de QCD. Se estima que este canal tiene una sección eficaz de 370 pb a 14 TeV.

La selección de este canal se realiza por medio de una serie de cortes secuenciales en los que se exige la reconstrucción de ciertos observables, que son los siguientes:

- Un único lepton en el estado final con $|\eta| < 2.5$ y $p_T > 25$ (20) GeV/c (para e y μ, respectivamente).
- $E_T^{miss} > 20$ GeV, ya que el neutrino del estado final no se detectará.
- Al menos 4 *jets* con $|\eta| < 2.5$ y $p_T > 40$ GeV/c.
- Exactamente 2 *jets* etiquetados como *b-jets*

La tabla 8.6 muestra el número de eventos (normalizados a 1 fb^{-1}) antes y después de cada corte, tanto para la señal semileptónica como para los fondos. La relación señal/ruido incial es del $\sim$11% mientras que después de aplicar los cortes es del $\sim$85%. Sin embargo, únicamente un 4.6% de los eventos semileptónicos pasan los todos cortes, por lo que la estadística se reduce bastante.

11.3.1 Formalismo del Globalχ^2 en este contexto

Los métodos para medir la masa del *quark* top se basan en el uso de los objetos del estado final de la desintegración de $t\bar{t}$ a nivel árbol. En particular los llamados ajustes cinemáticos definen una función χ^2 que utiliza explícitamente la información de la topología de dicha desintegración. La función χ^2 que se usará es:

$$\chi^2 = \sum_{\text{i = jets+lepton}} \left(\frac{E_i^m - E_i^f}{\sigma_{E_i}}\right)^2 + \left(\frac{M_{jj} - M_W^{ref}}{\Gamma_W^{ref}}\right)^2 + \left(\frac{M_{l\nu} - M_W^{ref}}{\Gamma_W^{ref}}\right)^2 + \\ + \left(\frac{M_{jjb_H} - M_{top}^f}{\sigma_{top_H}}\right)^2 + \left(\frac{M_{\ell\nu b_\ell} - M_{top}^f}{\sigma_{top_L}}\right)^2$$

De modo que introducir el formalismo del Globalχ^2 en este contexto resulta bastante sencillo teniendo en cuenta ciertas ideas. Definiendo dos vectores de residuos, $\mathbf{r} = \mathbf{r}(\mathbf{W}, \mathbf{t})$ y $\mathbf{R_W} = \mathbf{R_W}(\mathbf{W})$ y sus matrices de covarianzas V y S de este modo:

$$\mathbf{r} = \begin{pmatrix} E_{j_1}^m(1 - \alpha_{E_{j_1}}) \\ E_{j_2}^m(1 - \alpha_{E_{j_2}}) \\ E_{b_H}^m(1 - \alpha_{E_{b_H}}) \\ E_{b_L}^m(1 - \alpha_{E_{b_\ell}}) \\ E_\ell^m(1 - \alpha_{E_\ell}) \\ M_{jjb_H} - M_{top}^f \\ M_{\ell\nu b_\ell} - M_{top}^f \end{pmatrix} \quad \text{y} \quad \mathbf{R_W} = \begin{pmatrix} M_{jj} - M_W^{ref} \\ M_{\ell\nu} - M_W^{ref} \end{pmatrix}$$

$$V^{-1} = \begin{pmatrix} 1/\sigma^2_{E_{j_1}} & 0 & 0 & 0 & 0 & 0 & 0 \\ 0 & 1/\sigma^2_{E_{j_2}} & 0 & 0 & 0 & 0 & 0 \\ 0 & 0 & 1/\sigma^2_{E_{b_H}} & 0 & 0 & 0 & 0 \\ 0 & 0 & 0 & 1/\sigma^2_{E_{b_L}} & 0 & 0 & 0 \\ 0 & 0 & 0 & 0 & 1/\sigma^2_{E_\ell} & 0 & 0 \\ 0 & 0 & 0 & 0 & 0 & 1/\sigma^2_{top_H} & 0 \\ 0 & 0 & 0 & 0 & 0 & 0 & 1/\sigma^2_{top_L} \end{pmatrix}$$

$$S^{-1} = \begin{pmatrix} 1/(\Gamma_W^{ref})^2 & 0 \\ 0 & 1/(\Gamma_W^{ref})^2 \end{pmatrix}$$

donde $\mathbf{W}$ representa los parámetros de la desintegración hadrónica del bosón W y $\mathbf{t}$ representan los parámetros del *quark* top.

Hecho esto podemos escribir la función χ^2 como:

$$\chi^2 = \mathbf{r}^T V^{-1}\mathbf{r} + \mathbf{R_W}^T S^{-1}\mathbf{R_W}$$

Aplicando el formalismo del Globalχ^2 llegamos a que las correcciones a los parámetros del *quark* top son los siguientes:

$$\delta\mathbf{t} = -\left[\left(\frac{\partial\mathbf{r}}{\partial\mathbf{t}}\right)^T \mathcal{W}' \frac{\partial\mathbf{r}}{\partial\mathbf{t}}\right]^{-1} \left[\left(\frac{\partial\mathbf{r}}{\partial\mathbf{t}}\right)^T \mathcal{W}'\mathbf{r} - \left(\frac{\partial\mathbf{r}}{\partial\mathbf{t}}\right)^T (F_\mathbf{W}\mathcal{G}_{EF_W})^T S^{-1}\mathbf{R_W}\right] = -\mathcal{M}^{-1}(\nu + \nu_\mathbf{W})$$

siendo:

$$\mathcal{W}' \equiv \left(I - E\left(E^T V^{-1} E + F_\mathbf{W}^T S^{-1} F_\mathbf{W}\right)^{-1} E^T V^{-1}\right)^T V^{-1}$$

$$E \equiv \left.\frac{\partial\mathbf{r}}{\partial\mathbf{W}}\right|_{W_0} \quad \text{y} \quad F_\mathbf{W} \equiv \left.\frac{\partial\mathbf{R_W}}{\partial\mathbf{W}}\right|_{W_0}$$

Una vez presentado el formalismo sólo resta empezar con el análisis.

11.3.2 Estrategia a seguir

La estrategia a seguir es la siguiente:

- Realizar una serie de cortes de selección para tener una muestra enriquecida de eventos semileptónicos. Estos cortes se presentan en la sección 8.3.8.

- Como el canal seleccionado tiene un leptón más *jets* en el estado final sin restricción superior en el número *light jets*, se debe elegir la mejor pareja de *light jets* que reconstruyan el bosón W. Para ello se usa la minimización de una función χ^2. La combinación que dé un menor valor del χ^2 es la elegida en cada evento.

- Una vez se tiene los *light jets* de la desintegración del bosón W, se asocia el *b-jet* más cercano en $\phi \times \eta$ al W reconstruido. Con esto ya tenemos la parte hadrónica de la desintegración del sistema $t\bar{t}$.

- Para reconstruir la parte leptónica hace falta estimar el cuadrimomento del neutrino del estado final, que no se detecta. Esto se hace asumiendo que toda la E_T^{miss} del evento es debida a dicho neutrino. Por lo tanto la E_T^{miss} es la componente transversal del momento del neutrino. La componente longitudinal hay que calcularla como veremos.

- Ahora solo resta asociar el *b-jet* que falta a la parte leptónica. No obstante, es posible incrementar la eficiencia simplemente asociando los *b-jets* de forma que la diferencia entre masas invariantes de los *quarks* tops reconstruidos sea mínima.

- Siguiendo estos pasos ya tendríamos los cuadrimomentos de los 6 objetos del estado final. Es entonces cuando es posible realizar el ajuste cinemático usando el algoritmo Globalχ^2 .

11.3.3 Reconstrucción de la parte hadrónica

Como no hay restricción superior en el número *light jets*, se debe elegir la mejor pareja de *light jets* que reconstruyan el bosón W que se desintegra hadrónicamente. Para ello se realizan todas las combinaciones posibles de parejas de *light jets* y se minimiza la función χ^2 siguiente:

$$\chi^2 = \sum_{\text{j = light jets}} \left(\frac{E_j^m - E_j^f}{\sigma_{E_j}}\right)^2 + \left(\frac{M_{jj} - M_W^{ref}}{\Gamma_W^{ref}}\right)^2 = \sum_{\text{j = light jets}} \left(\frac{E_j^m(1-\alpha_j)}{\sigma_{E_j}}\right)^2 + \left(\frac{M_{jj} - M_W^{ref}}{\Gamma_W^{ref}}\right)^2$$

La combinación que dé un menor valor del χ^2 es la elegida en cada evento. La figura 11.11 muestra la masa invariante de la mejor pareja de *light jets* que reconstruye el bosón W, después de aplicar el corte $\chi^2 < 6$ (corte C0). El valor de la masa del bosón W para la señal es de $M_W^{had} = 80.622 \pm 0.002$ (stat.) GeV/c^2 y $\sigma_W^{had} = 0.665 \pm 0.001$ (stat.) GeV/c^2.

Una vez asociado el *b-jet* más cercano al W reconstruido obtenemos la reconstrucción de la masa del *quark* top hadrónico tal y como muestra la figura 11.12. La distribución es ajustada a la suma de una gausiana y un polinómio de tercer grado (para el fondo), siendo la media de dicha gausiana $M_t^{had} = 174.5 \pm 0.3$ (stat.) GeV/c^2 para la señal.

11.3.4 Reconstrucción de la parte leptónica

El p_T del neutrino se asume que es la E_T^{miss} y la componente longitudinal del momento se calcula mediante siguente expresión:

$$p_z^\nu = \frac{-p_z^\ell\left(-M_W^2 + m_\ell^2 - 2(p_x^\ell p_x^\nu + p_y^\ell p_y^\nu)\right)}{2(E_\ell^2 - (p_z^\ell)^2)} \pm$$

$$\pm\sqrt{E_\ell^2\left[\left(M_W^2 - m_\ell^2 + 2(p_x^\ell p_x^\nu + p_y^\ell p_y^\nu)\right)^2 + 4(E_T^{miss})^2(-E_\ell^2 + (p_z^\ell)^2)\right]}$$

Una vez calculado el cuadrimomento del neutrino ya se puede proceder a asociar los *b-jets* a cada parte (tanto a la parte hadrónica como a la parte leptónica) exigiendo que la diferencia entre masas invariantes de los *quarks* tops reconstruidos sea mínima. Una vez hecho esto, podemos reconstruir la masa del *quark* top de la parte leptónica tal y como muestra la figura 11.13.

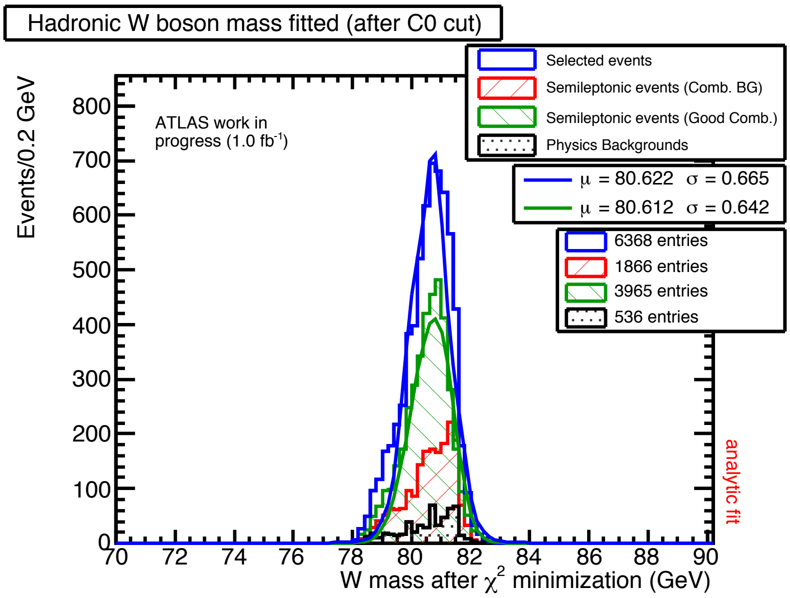

Figure 11.11: *Masa invariante de la mejor pareja de* light jets *que reconstruye el bosón W, después de aplicar el corte* $\chi^2 < 6$ *(corte C0). El valor de la masa del W para la señal es de* $M_W^{had} = 80.622 \pm 0.002$ *(stat.)* GeV/c^2 *y* $\sigma_W^{had} = 0.665 \pm 0.001$ *(stat.)* GeV/c^2.

11.3.5 Ajuste cinemático usando el algoritmo Globalχ^2

Una vez tenemos los cuadrimomentos de los 6 objetos del estado final podemos realizar el ajuste cinemático usando el algoritmo Globalχ^2 , donde la función χ^2 es la siguente:

$$\chi^2 = \sum_{i=\text{jets+lepton}} \left(\frac{E_i^m - E_i^f}{\sigma_{E_i}}\right)^2 + \left(\frac{M_{jj} - M_W^{ref}}{\Gamma_W^{ref}}\right)^2 + \left(\frac{M_{l\nu} - M_W^{ref}}{\Gamma_W^{ref}}\right)^2 +$$
$$+ \left(\frac{M_{jjb_H} - M_{top}^f}{\sigma_{top_H}}\right)^2 + \left(\frac{M_{\ell\nu b_\ell} - M_{top}^f}{\sigma_{top_\ell}}\right)^2$$

La figura 11.14 muestra la distribución final de la masa del *quark* top obtenida a partir del ajuste cinemático usando el algoritmo Globalχ^2 . Esta distribución ha sido obtenida después de aplicar una serie de cortes definidos en la tabla 9.1. Ajustando dicha distribución (sólo para los eventos seleccionados) a la suma de una gausiana y un polinomio de tercer grado se obtiene: $M_{top}^{fit} = 174.1 \pm 0.3$ (stat.) GeV/c^2

11.3.6 Discusión cualitativa de los errores sistemáticos

Debido a la sección eficaz esperada a 14 TeV para el canal $t\bar{t}$, el error total de la masa del *quark* va a estar dominado por el error sistemático a partir de unos pocos fb^{-1} de luminosidad

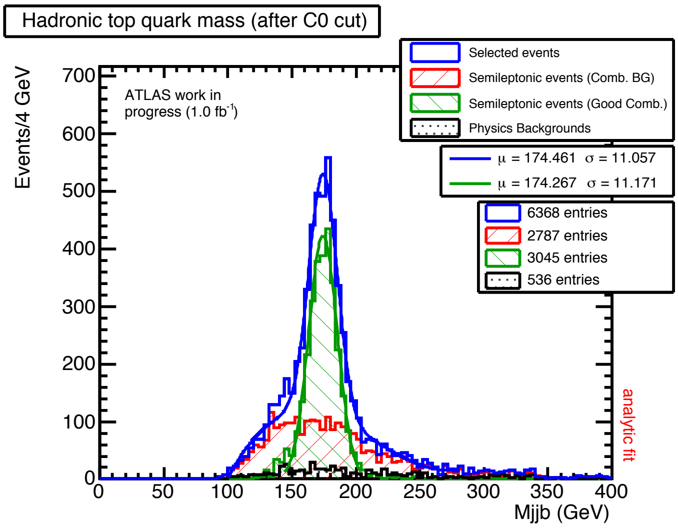

Figure 11.12: *Reconstrucción de la masa del* quark *top hadrónico, después del corte C0. La distribución es ajustada a la suma de una gausiana y un polinómio de tercer grado (para el fondo), siendo la media de dicha gausiana* M_t^{had} *= 174.5 ± 0.3 (stat.) GeV/*c^2 *para la señal.*

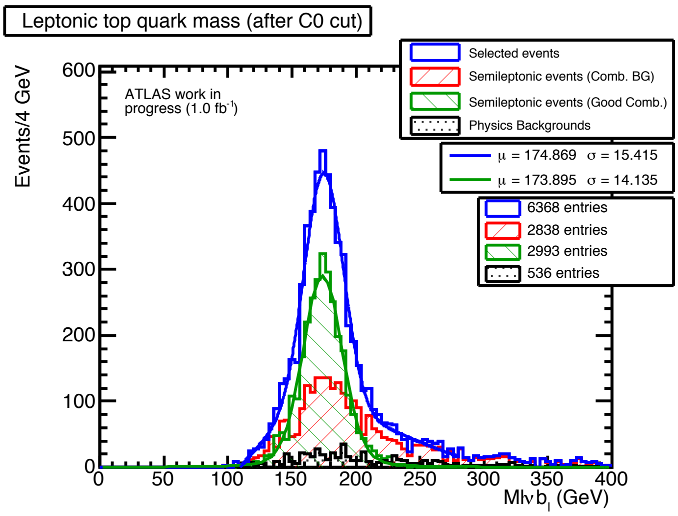

Figure 11.13: *Reconstrucción de la parte leptónica de la masa del quark después del corte C0.*

integrada. Aunque no se ha estimando cuantitativamente el error sistemático en esta tesis, sí que se enumeran cualitativamente todas sus contribuciones:

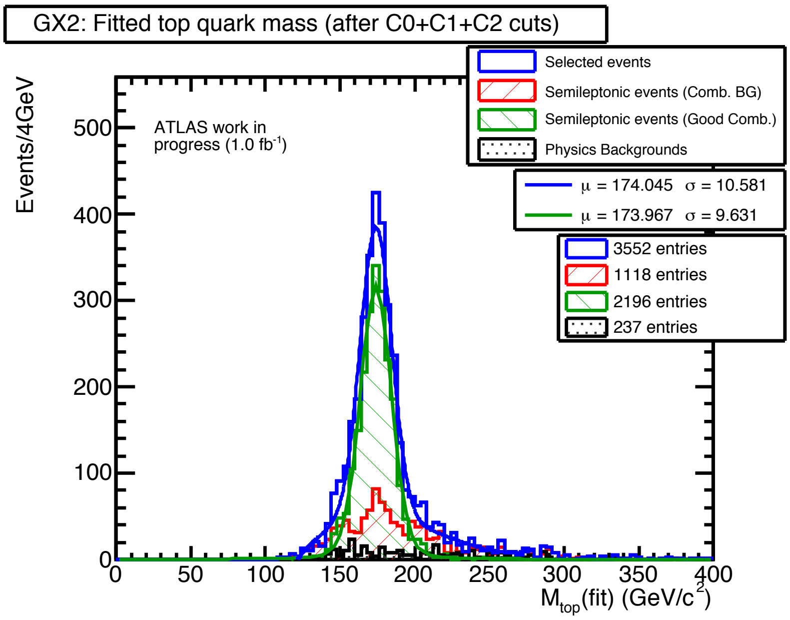

Figure 11.14: *Distribución final de la masa del* quark *top obtenida a partir del ajuste cinemático usando el algoritmo Global*χ^2 *. Ajustando dicha distribución (sólo para los eventos seleccionados) a la suma de una gausiana y un polinomio de tercer grado se obtiene:* M_{top}^{fit} = 174.1 ± *0.3 (stat.) GeV/c*^{2}.

- **JES:** Ya que la medida de la masa del *quark* top recae sobre la medida de los *jets* reconstruidos, una fuente importante de errores sistemáticos vendrá de la escala de energía de estos *jets*. Se estima que alcanzando una precisión de entre el 1 y el 5% en la escala de energía de los *jets* y teniendo 1 fb^{-1} de datos acumulados, el error sistemático será de entre 1 y 3.6 GeV.

- **ISR/FSR:** Se estima que la contribución al error sistemático de los efectos ISR/FSR sea de $\sim$0.3 GeV.

- **Fragmentación del quark b:** Estudios realizados con simulación rápida revelan que el impacto será inferior a 0.1 GeV [146].

- E_T^{miss}**:** En la referencia [142] se dice que el error en la escala de la E_T^{miss} introducirá un error del 0.6 GeV%.

- **Fondos:** Se ha estimado que los fondos son una fuente despreciable de errores sistemáticos [7].

- **El propio método:** Las diferentes aproximaciones realizadas en este trabajo son una fuente de errores sistemáticos nada despreciable. Aunque no se han estimado cuantitativamente, el hecho de realizar un estudio a nivel árbol (es decir, a LO) en vez de a NLO podría afectar significativamente. De este modo, se trabajará en futuras mejoras para reducir la contribución del propio método.

11.4 Conclusiones

Esta tesis se ha dividido en dos partes siendo el denominador común el algoritmo Globalχ^2 . La primera parte está enfocada a la discusión de los resultados del alineamiento del detector de trazas de silicio de ATLAS así como de su rendimiento y prestaciones usando tanto datos simulados con técnicas MC como con datos reales. La segunda parte esta dedicada a estudiar el potencial de ATLAS para medir la masa del *quark* top, siendo la principal novedad la introducción del formalismo Globalχ^2 en este contexto.

El algoritmo Globalχ^2 es el método de referencia usado actualmente para el alineamiento del detector de trazas de ATLAS. En las secciones 11.2.2.1 y 11.2.2.2 se han presentado todos los resultados de los estudios realizados con datos simulados y con datos reales tanto de rayos cósmicos, como con las primeras colisiones del LHC. En este sentido, el ejercicio CSC constituyó la primera simulación a gran escala y totalmente detallada del detector ATLAS. Este ejercicio introdujo una descripción realista del detector, considerando incluso un campo magnético inclinado y desplazado así como una distribución de material distorsionado. Además, algunos desplazamientos globales y desalineamientos fueron incorporados a propósito para completar dicha descripción geométrica. Esto tuvo implicaciones importantes a la hora de tener listo el software de ATLAS para la toma de datos. La calidad de las constantes de alineamiento calculadas fueron evaluadas usando las eficiencias de los *hits*/trazas, los residuos y los parámetros de las trazas junto con sus correlaciones. Adicionalmente, varias muestras de física se usaron para monitorear y evaluar de forma externa el alineamiento realizado. Esto permitió observar un desalineamiento residual, principalmente debido a la presencia de algunos *weak modes* que no pudieron ser completamente eliminados. De todas maneras, las prestaciones alcanzadas por el alineamiento obtenido fueron suficientemente buenas como para estimar el rendimiento de ATLAS frente a los primeros datos reales de colisiones.

Los ejercicios FDR, basados en datos MC, sirvieron para probar y ejercitar toda la cadena de recogida y procesado de datos de ATLAS. Esta serie de ejercicios pusieron a prueba desde la salida de datos del *trigger* en las SFO hasta el análisis final. Su objetivo principal fue evaluar el rendimiento de toda la infraestructura de adquisición de datos, ya que era uno de los requisitos fundamentales del modelo de computación de ATLAS. El *calibration stream* se usó para alinear todo el detector interno en las 24 horas posteriores a la toma de datos, partiendo de un desconocimiento total de los desalineamientos del detector. A pesar de que las constantes de alineamiento obtenidas para los ejercicios FDR fueron de menor calidad en comparación con las obtenidas para el ejercicio CSC, éstas proporcionaron unas prestaciones bastante decentes para haber sido procesadas y publicadas en tan sólo 24 horas desde la puesta en marcha de estos ejercicios. Varias lecciones importantes fueron aprendidas, siendo la fiabilidad del sistema de adquisición puesto a prueba con éxito en un entorno pseudo real de toma de datos. Por último, el otro gran éxito fué la integración del modelo de alineamiento dentro del modelo de calibración y toma de datos de ATLAS.

Además de todo lo anterior, también se han presentado los logros usando datos reales, tanto con rayos cósmicos como con los primeros datos de las colisiones del LHC a 900 GeV. La primera de estas pruebas fué el *run* llevado a cabo en el SR1 durante el 2006. Éste constituyó el primer banco de pruebas con datos reales de rayos cósmicos para el algoritmo Globalχ^2 . Fué mostrada la buena convergencia de las constantes de alineamiento así como las distribuciones de los residuos antes y después del alineamiento, mostrando una notable mejora de los residuos, con anchuras del orden de 50 μm. Además, estos estudios revelaron que la eficiencia de los módulos del SCT se encontraba dentro de las especificaciones después del alineamiento, siendo superior al 99%.

Los datos de rayos cósmicos recogidos durante los periodos de puesta a punto de ATLAS en 2008 y 2009 permitieron probar y ejercitar con muy buenos resultados las cadenas de software y hardware. También se probó el modelo de alineamiento y dos conjuntos de constantes de alineamiento fueron obtenidas como resultado del estudio con estos datos. Fué precisamente con las constantes obtenidas a partir de los datos de 2008 con las que se reconstruyeron las primeras colisiones del LHC en 2009. Ambos conjuntos de constantes fueron obtenidas partiendo de las mediciones mecánico-ópticas de las posiciones de los dectores, siendo las diferencias fundamentales la estadística usada en cada caso y la estrategia. Al mismo tiempo, el poseer una detallada simulación MC permitió realizar comparativas entre datos reales y simulación. Por otra parte, fué la primera vez que se usó el modelo de alineamiento basado en niveles geométricos jerárquizados con datos reales, produciendo muy buenos resultados. Como era de esperar, se obtuvieron grandes mejoras en las distribuciones de los residuos, especialmente en la región del barril, con anchuras del orden de 24 μm para píxeles y de 30 μm para el SCT. Al final del procesos, se realizaró un alineamiento de cada módulo a nivel individual observándose que los *staves* de los píxeles estaban arqueados. Estos desalineamientos fueron corregidos.

Al final de esta parte, se presentó el primer intento de mejorar el alineamiento existente a partir de los primeros datos de las colisiones del LHC con una energía de 900 GeV. Un alineamiento preliminar dió como resultado la mejorar significativa de los discos de los *end-caps* del SCT. El rendimiento conseguido en esta prueba reveló que el nivel de precisión en el alineamiento del detector de trazas de silicio de ATLAS que se podía llegar a alcanzar era muy prometedor.

La segunda parte de la tesis está dedicada a la medida de la masa del *quark* top usando el detector ATLAS. En esta parte únicamente se usaron datos simulados, concretamente datos procesados dentro del ejercicio CSC. Además, se asumió una luminosidad integrada de 1 fb^{-1} para una baja luminosidad (10^{33} cm^{-2}s^{-1}) y para la energía nominal del LHC ($\sqrt{s}$ = 14 TeV). Esta parte tuvo como objetivos principales, por un lado, estimar el potencial de ATLAS para realizar medidas de precisión de la masa del *quark* top y por otra parte introducir el algoritmo Globalχ^2 como un novedoso método para llevar a cabo dicha medida. Para ello se escogió el canal semileptónico de desintegración del sistema $t\bar{t}$. Tal y como se presentó, este análisis siguió una estrategia clara, requiriendo dos *jets* etiquetados como *b-jets* y algunos cortes estándar para la selección de los eventos interesantes. Al final del análisis, la relación señal/ruido que se obtuvo fue de 14, lo que significa que el fondo está bajo control. La masa del *quark* top que se determinó fué de M_{top}^{fit} = 174.1 ± 0.3 (stat.) GeV/c^2, estando este resultado a 3σ de la masa de entrada (175 GeV/c^2).

Tal y como se esperaba, la incertidumbre estadística en la medida del *quark* top fué realmente pequeña (0.3 GeV/c^2), estando el error total dominado por los errores sistemáticos. No se realizaron estudios de errores sistemáticos, aunque se presentó una breve descripción de cuáles podrían ser los factores y contribuciones a considerar. De hecho, el factor que más influye en la incertidumbre es la escala de energía de los *jets*, siendo la más importante las de los *b-jets*. Suponiendo un error del 1 al 5 % en la scala de energía de los *jets*, la precisión esperada sería del orden de 1 a 3,6 GeV, siempre considerando una luminosidad integrada de 1 fb $^{-1}$ [7].

Appendices

A

Full development of the Globalχ^2 formalism for alignment

This appendix will be an extension of chapter 4.1 since it contains the full mathematical development of sections that were not detailed. Section A.1 will discuss how the material effects can be introduced in the Globalχ^2 formalism. Section A.2 contains the Globalχ^2 approach with alignment parameter constraints. Section A.3 gives the full discussion of the Globalχ^2 formalism with common vertex fitting and section A.4 extends the later adding vertex parameter constraints. Finally, section A.5 constrains the most general solution for the Globalχ^2 approach.

A.1 Material effects within the Globalχ^2 formalism

If material effects want to be considered MCS effects can be incorporated in the track model by allowing the track to kink on a finite number of scattering surfaces. In this way, one can take into account correlations between those scattering planes (and therefore between the hit measurements).

To introduce the MCS contribution two approaches can be followed: an explicit or an implicit approach. In both cases the residuals will also depend (explicitly or implicitly) on the scattering angles ($\boldsymbol{\theta}$), i.e. $\mathbf{r} = \mathbf{r}(\boldsymbol{\pi}, \boldsymbol{\theta}, \mathbf{a})$.

A.1.1 First approach: explicit scattering effects dependence

In the first option, the χ^2 is redefined and an extra χ^2 term is added:

$$\chi^2 = \chi^2_{basic} + \chi^2_{MCS} = \sum_e \sum_{t \in e} \mathbf{r}^T V^{-1} \mathbf{r} + \sum_e \sum_{t \in e} \mathbf{R}_{\theta}^T \Theta^{-1} \mathbf{R}_{\theta} \tag{A.1}$$

where the first term is the basic χ^2 (where, now, the residuals ($\mathbf{r}$) depend explicitly on the scattering angles ($\boldsymbol{\theta}$)) and the second χ^2 term represents the contribution from the expected scattering angles. In this term, $\mathbf{R}_{\boldsymbol{\theta}} = (\boldsymbol{\theta}_m - \boldsymbol{\theta}_e(\boldsymbol{\theta}))$ represents the residual vector for the scattering angles ($\boldsymbol{\theta}_e$ is the expected value and $\boldsymbol{\theta}_m$ the measured value) with dimension N_{scat} (i.e. the total number of scattering angles). $\Theta = \sigma_{\boldsymbol{\theta}}\sigma_{\boldsymbol{\theta}}^T$ is the covariance matrix of dimension $[N_{scat} \times N_{scat}]$ for the MCS contribution which is diagonal as the expectations for the scattering angles are independent and their elements can be estimated according to Molière's theory [76] [77]:

$$\sigma_{\boldsymbol{\theta}} = \frac{13.6MeV}{\beta cp} Z' \sqrt{\frac{l}{X_0}} \left(1 + 0.038 \, ln \frac{l}{X_0}\right) \tag{A.2}$$

in this formula, l is the thickness of the material layer, X_0 is the radiation length, βc the velocity of the traversing particle, Z' its charge number and p its momentum. Of course, for low momentum tracks these effects will be important as $\sigma_{\boldsymbol{\theta}} \sim 1/p$. If no momentum determination can be done then there is no option to apply this formula. This is the case where magnetic field is not present as the track curvature can not be measured. In the figure A.1 one can see how the MCS effects affect the out-coming trajectory for a charged particle crossing a material. It is also shown the expected out-coming trajectory when MCS effects are not considered in the tracking model. In that case, kinks are not expected and therefore the incoming and out-coming track directions are the same (i.e. $\theta_i' = \theta_f'$). Thus, when material effects are included in the tracking, expression A.2 is used to estimated deflection angles at each material surface. Obviously, in that case, $\theta_i' \neq \theta_f'$ as is also shown in that figure.

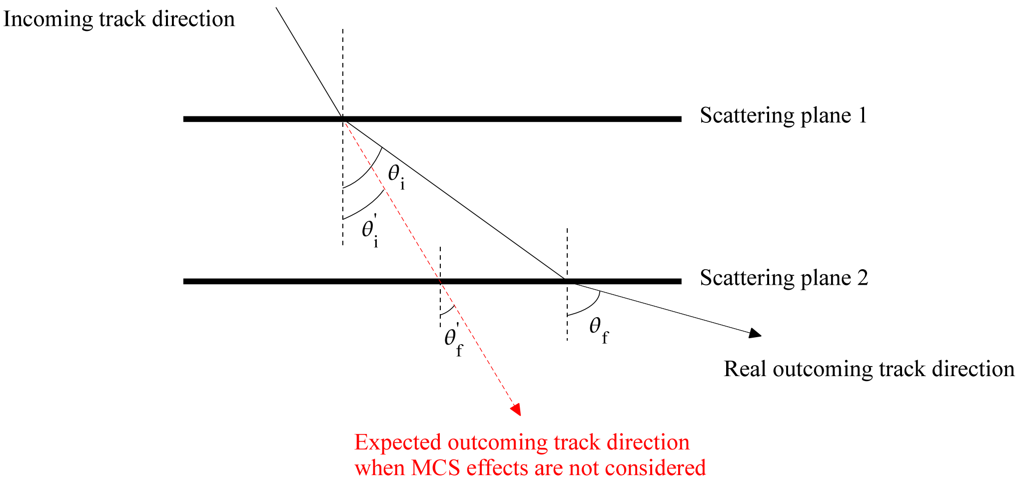

Figure A.1: *Scheme showing how the MCS effects affect the out-coming trajectory for a charged particle crossing a material. It is also shown the expected out-coming trajectory when MCS effects are not considered in the tracking model. On the one hand, when no MCS effects are considered, kinks are not expected and therefore, the incoming track direction is assumed for the out-coming track direction (i.e. $\theta_i' = \theta_f'$). On the other hand, when MCS effects are considered, kinks are estimated based on expression A.2 and therefore the out-coming track is better estimated. In this case, $\theta_i' \neq \theta_f'$ because the incoming track direction is not the out-coming track direction after crossing any material.*

So, in this approach both covariance matrices, V and Θ, remain diagonal but now, in the track fit the χ^2 has to be minimized for the track parameters ($\boldsymbol{\pi}$) and for the scattering angles ($\boldsymbol{\theta}$), simultaneously. Anyhow, the χ^2 minimization procedure for the alignment discussed above remains entirely unchanged.

In this formalism some objects can be redefined in order to pack the expressions and thereby the χ^2, so:

$$\boldsymbol{\pi} \rightarrow \tilde{\boldsymbol{\pi}} = \begin{pmatrix} \boldsymbol{\pi} \\ \boldsymbol{\theta} \end{pmatrix}, \quad \mathbf{r}(\boldsymbol{\pi}, \boldsymbol{\theta}, \mathbf{a}) \rightarrow \tilde{\mathbf{r}}(\tilde{\boldsymbol{\pi}}, \mathbf{a}) = \begin{pmatrix} \mathbf{r}(\tilde{\boldsymbol{\pi}}, \mathbf{a}) \\ \mathbf{R}_{\theta}(\boldsymbol{\theta}) \end{pmatrix} \quad \text{and} \quad V \rightarrow \tilde{V} = \begin{pmatrix} V & 0 \\ 0 & \Theta \end{pmatrix} \tag{A.3}$$

$$\Downarrow$$

$$\chi^2 = \sum_{e} \sum_{t \in e} \tilde{\mathbf{r}}^T \tilde{V}^{-1} \tilde{\mathbf{r}} \quad \text{where} \quad \tilde{\mathbf{r}} = \tilde{\mathbf{r}}(\tilde{\boldsymbol{\pi}}, \mathbf{a}) \tag{A.4}$$

This approach is used by the ATLAS TRT alignment algorithm [50] and by some ATLAS ID trackers (for instance, the Globalχ^2 fitter [149] [78]) where a track is not defined just by the five parameters of its helix but also by a sequence of two scattering angles attributed to each scattering plane it traverses (there is the possibility to include also an energy loss term like in [149]).

A.1.2 Second approach: implicit scattering effects dependence

There is an alternative approach which eliminates the scattering angles from the χ^2 minimization by assimilating their contribution in the covariance matrix. In this case, the non-diagonal matrix elements of this covariance matrix are not null anymore. This is, in fact, the approach used in the Globalχ^2 algorithm. Therefore the χ^2 used is the one in 4.3 where $\bar{V}$ is used instead of V. This $\bar{V}$ is written as a simple sum of two terms:

$$\bar{V} = V + V_{MCS} \quad \text{where} \quad V_{MCS} = \frac{\partial \mathbf{r}}{\partial \boldsymbol{\theta}} \Theta \left(\frac{\partial \mathbf{r}}{\partial \boldsymbol{\theta}} \right)^T \tag{A.5}$$

where V describes the intrinsic resolution of the sensitive devices and it is diagonal by construction. V_{MCS} contains the scattering effects contribution. Then, $\partial \mathbf{r}/\partial \boldsymbol{\theta}$ are vectors with the derivatives relating the deflection angles ($\boldsymbol{\theta}$) to the change of track extrapolation to the consecutive measurement planes and Θ is, as before, a diagonal matrix describing the expectations for the scattering angles which follow the expression A.2.

At the same time the apparent residuals have to be redefined to accomodate the zig-zagging track trajectory:

$$\bar{\mathbf{r}} = \mathbf{r} + \frac{\partial \mathbf{r}}{\partial \boldsymbol{\theta}} \delta \boldsymbol{\theta} \tag{A.6}$$

therefore, the new residuals have a $\boldsymbol{\theta}$ dependence, i.e. $\bar{\mathbf{r}} = \bar{\mathbf{r}}(\boldsymbol{\pi}, \boldsymbol{\theta}, \mathbf{a})$, although this dependence is, in fact, hidden in the implicit dependence through expression A.6. Anyhow, as in the previous approach, the χ^2 minimization procedure for the alignment remains again entirely unchanged. In other words, the residuals $\mathbf{r}(\boldsymbol{\pi}, \boldsymbol{\theta}, \mathbf{a})$ are the ones used in the algorithm but they are corrected with $\partial\mathbf{r}/\partial\boldsymbol{\theta}$ and the covariance matrix $\bar{V}$ is used instead of V in order to consider the proper scattering surfaces associated to the proper measurements:

$$\chi^2 = \sum_e \sum_{t\in e} \bar{\mathbf{r}}^T \bar{V}^{-1} \bar{\mathbf{r}} \tag{A.7}$$

Note that this χ^2 will replace the one defined in 4.3 in the Globalχ^2 algorithm considered for the ATLAS Silicon Tracker alignment.

A.1.3 Equivalence between approaches

The mathematical equivalence of both approaches can be demonstrated. Let's remind the χ^2 from expression A.1 for a given track within an event:

$$\chi^2 = \mathbf{r}^T V^{-1} \mathbf{r} + \mathbf{R}_\theta^T \Theta^{-1} \mathbf{R}_\theta$$

Then, considering $\mathbf{r} = \mathbf{r}(\boldsymbol{\pi}, \boldsymbol{\theta})$[1] one has:

$$d\mathbf{r} = \frac{\partial\mathbf{r}}{\partial\boldsymbol{\pi}} d\boldsymbol{\pi} + \frac{\partial\mathbf{r}}{\partial\boldsymbol{\theta}} d\boldsymbol{\theta} \quad\longrightarrow\quad \frac{d\mathbf{r}}{d\boldsymbol{\pi}} = \frac{\partial\mathbf{r}}{\partial\boldsymbol{\pi}} + \frac{\partial\mathbf{r}}{\partial\boldsymbol{\theta}}\frac{d\boldsymbol{\theta}}{d\boldsymbol{\pi}} \text{ and } \frac{d\mathbf{r}}{d\boldsymbol{\theta}} = \frac{\partial\mathbf{r}}{\partial\boldsymbol{\theta}} \tag{A.8}$$

$$d\mathbf{R}_\theta = \frac{\partial\mathbf{R}_\theta}{\partial\boldsymbol{\theta}} d\boldsymbol{\theta} \quad\longrightarrow\quad \frac{d\mathbf{R}_\theta}{d\boldsymbol{\pi}} = \frac{\partial\mathbf{R}_\theta}{\partial\boldsymbol{\theta}}\frac{\partial\boldsymbol{\theta}}{\partial\boldsymbol{\pi}} \text{ and } \frac{d\mathbf{R}_\theta}{d\boldsymbol{\theta}} = \frac{\partial\mathbf{R}_\theta}{\partial\boldsymbol{\theta}} \tag{A.9}$$

The crucial point here is that $d\boldsymbol{\pi}/d\boldsymbol{\theta} = 0$ because there is an assumption that track parameters do not depend on the scattering angles. In this case, expression 4.11 from section 4.2.2, where $d\chi^2/d\boldsymbol{\pi} = 0$ has been applied, becomes:

$$\left(\frac{d\mathbf{r}}{d\boldsymbol{\pi}}\right)^T V^{-1}\mathbf{r} + \left(\frac{d\mathbf{R}_\theta}{d\boldsymbol{\pi}}\right)^T \Theta^{-1}\mathbf{R}_\theta = 0$$

$$\Downarrow$$

$$\left(\frac{\partial\mathbf{r}}{\partial\boldsymbol{\pi}} + \frac{\partial\mathbf{r}}{\partial\boldsymbol{\theta}}\frac{d\boldsymbol{\theta}}{d\boldsymbol{\pi}}\right)^T V^{-1}\mathbf{r} + \left(\frac{\partial\mathbf{R}_\theta}{\partial\boldsymbol{\theta}}\frac{d\boldsymbol{\theta}}{d\boldsymbol{\pi}}\right)^T \Theta^{-1}\mathbf{R}_\theta = 0 \tag{A.10}$$

So, in analogy to the case of $d\boldsymbol{\pi}/d\mathbf{a}$ in expression 4.10, one has to obtain $d\boldsymbol{\theta}/d\boldsymbol{\pi}$ through a scattering angle fit, i.e. minimizing the χ^2 with respect to $\boldsymbol{\theta}$ for a given scattering angle:

$$\frac{d\chi^2}{d\boldsymbol{\theta}} = \frac{\partial\chi^2}{\partial\boldsymbol{\theta}} = 0 \;\rightarrow\; \left(\frac{\partial\mathbf{r}}{\partial\boldsymbol{\theta}}\right)^T V^{-1}\mathbf{r} + \left(\frac{\partial\mathbf{R}_\theta}{\partial\boldsymbol{\theta}}\right)^T \Theta^{-1}\mathbf{R}_\theta = 0 \tag{A.11}$$

Now, expanding the residuals around $\boldsymbol{\theta}_0$ and considering the linear approximation ($\partial^n\mathbf{r}/\partial\boldsymbol{\theta}^n = 0$ with $n \geq 2$):

$$\mathbf{r}(\boldsymbol{\pi}, \boldsymbol{\theta}) = \mathbf{r}(\boldsymbol{\pi}, \boldsymbol{\theta}_0) + \left.\frac{\partial\mathbf{r}}{\partial\boldsymbol{\theta}}\right|_{\theta_0} \delta\boldsymbol{\theta} \quad\text{and}\quad \mathbf{R}_\theta(\boldsymbol{\theta}) = \mathbf{R}_\theta(\boldsymbol{\theta}_0) + \left.\frac{\partial\mathbf{R}_\theta}{\partial\boldsymbol{\theta}}\right|_{\theta_0} \delta\boldsymbol{\theta}$$

where the notation from 4.13 should be reminded. Moreover, defining S and P:

[1] To develop this demonstration and for simplicity, the alignment parameters dependence will not be taken into account (i.e. $\mathbf{r} = \mathbf{r}(\boldsymbol{\pi}, \boldsymbol{\theta})$) as they do not play any role here as a given track is being considered. Anyhow, everything is completely valid if one wants to consider for alignment parameter dependence, i.e $\mathbf{r} = \mathbf{r}(\boldsymbol{\pi}, \boldsymbol{\theta}, \mathbf{a})$.

$$S \equiv \left.\frac{\partial \mathbf{r}}{\partial \boldsymbol{\theta}}\right|_{\theta_0} \quad \text{and} \quad P \equiv \left.\frac{\partial \mathbf{R}_\theta}{\partial \boldsymbol{\theta}}\right|_{\theta_0} \tag{A.12}$$

Then, expression A.11 reads as follows:

$$S^T V^{-1}\mathbf{r}(\pi, \boldsymbol{\theta}_0) + S^T V^{-1} S\,\delta\boldsymbol{\theta} + P^T \Theta^{-1}\mathbf{R}_\theta(\boldsymbol{\theta}_0) + P^T \Theta^{-1} P\delta\boldsymbol{\theta} = 0 \tag{A.13}$$

Now, working out $\delta\boldsymbol{\theta}$:

$$\delta\boldsymbol{\theta} = -\left(S^T V^{-1} S + P^T \Theta^{-1} P\right)^{-1}\left(S^T V^{-1}\mathbf{r}(\pi, \boldsymbol{\theta}_0) + P^T \Theta^{-1}\mathbf{R}_\theta(\boldsymbol{\theta}_0)\right) = -\mathcal{M}_\theta^{-1}\nu_\theta \tag{A.14}$$

where one has defined:

$$\mathcal{M}_\theta \equiv \left(S^T V^{-1} S + P^T \Theta^{-1} P\right) \quad \text{and} \quad \nu_\theta \equiv S^T V^{-1}\mathbf{r}(\pi, \boldsymbol{\theta}_0) + P^T \Theta^{-1}\mathbf{R}_\theta(\boldsymbol{\theta}_0)$$

Finally, one is able to evaluate $d\boldsymbol{\theta}/d\pi$ derivating the solution for the scattering angles, i.e. $\boldsymbol{\theta} = \boldsymbol{\theta}_0 + \delta\boldsymbol{\theta}$:

$$\frac{d\boldsymbol{\theta}}{d\pi} = -\left(S^T V^{-1} S + P^T \Theta^{-1} P\right)^{-1} S^T V^{-1}\frac{\partial \mathbf{r}(\pi, \boldsymbol{\theta}_0)}{\partial \pi} \tag{A.15}$$

where, obviously:

$$\frac{d\mathbf{r}(\pi, \boldsymbol{\theta}_0)}{d\pi} = \frac{\partial \mathbf{r}(\pi, \boldsymbol{\theta}_0)}{\partial \pi} \quad \text{and} \quad \frac{d\mathbf{R}_\theta(\boldsymbol{\theta}_0)}{d\pi} = 0.$$

Reached this point, one can do an assumption which can simplify the problem. The residuals of the scattering angles which were generally defined as $\mathbf{R}_\theta = (\boldsymbol{\theta}_m - \boldsymbol{\theta}_e(\boldsymbol{\theta}))$ can be written as $\mathbf{R}_\theta = (\boldsymbol{\theta}_m - \boldsymbol{\theta})$, i.e. $\boldsymbol{\theta}_e(\boldsymbol{\theta}) = \boldsymbol{\theta}$. Moreover, at this point $\mathbf{R}_\theta(\boldsymbol{\theta}_0) = \boldsymbol{\theta}_m - \boldsymbol{\theta}_0$, i.e. $\mathbf{R}_\theta(\boldsymbol{\theta}_0) = \delta\boldsymbol{\theta}$. This implies that the derivative P becomes:

$$P = \left.\frac{\partial \mathbf{R}_\theta}{\partial \boldsymbol{\theta}}\right|_{\theta_0} = \left.\frac{\partial(\boldsymbol{\theta}_m - \boldsymbol{\theta}_e(\boldsymbol{\theta}))}{\partial \boldsymbol{\theta}}\right|_{\theta_0} = -\left.\frac{\partial \boldsymbol{\theta}_e(\boldsymbol{\theta})}{\partial \boldsymbol{\theta}}\right|_{\theta_0} = -\left.\frac{\partial \boldsymbol{\theta}}{\partial \boldsymbol{\theta}}\right|_{\theta_0} = -I$$

So, A.15 is now written as:

$$\frac{d\boldsymbol{\theta}}{d\pi} = -(S^T V^{-1} S + \Theta^{-1})^{-1} S^T V^{-1}\frac{\partial \mathbf{r}(\pi, \boldsymbol{\theta}_0)}{\partial \pi} \tag{A.16}$$

and now, using the identity [50]:

$$(S^T V^{-1} S + \Theta^{-1})^{-1} S^T V^{-1} \equiv \Theta^T S^T (V + S\Theta S^T)^{-1}$$

One can finally write:

$$\frac{d\boldsymbol{\theta}}{d\pi} = -\Theta^T S^T (V + S\Theta S^T)^{-1}\frac{\partial \mathbf{r}(\pi, \boldsymbol{\theta}_0)}{\partial \pi} \tag{A.17}$$

Including this result in equation A.10 and using $\mathbf{R}_\theta(\boldsymbol{\theta}_0) = \delta\boldsymbol{\theta}$ and $P = \partial R_\theta/\partial\boldsymbol{\theta} = -I$:

$$\left(\frac{\partial \mathbf{r}}{\partial \pi} + S\frac{d\boldsymbol{\theta}}{d\pi}\right)^T V^{-1}\mathbf{r} - \left(\frac{d\boldsymbol{\theta}}{d\pi}\right)^T \Theta^{-1}\delta\boldsymbol{\theta} = 0$$

$$\Downarrow$$

$$\left(\frac{\partial \mathbf{r}}{\partial \pi} - S\Theta^T S^T (V + S\Theta S^T)^{-1} \frac{\partial \mathbf{r}}{\partial \pi}\right)^T V^{-1}\mathbf{r} + \left(\Theta^T S^T (V + S\Theta S^T)^{-1} \frac{\partial \mathbf{r}}{\partial \pi}\right)^T \Theta^{-1}\delta\boldsymbol{\theta} =$$

$$= \left(\frac{\partial \mathbf{r}}{\partial \pi}\right)^T V^{-1}\mathbf{r} - \left(\frac{\partial \mathbf{r}}{\partial \pi}\right)^T (V + S\Theta S^T)^{-1} S\Theta S^T V^{-1}\mathbf{r} + \left(\frac{\partial \mathbf{r}}{\partial \pi}\right)^T (V + S\Theta S^T)^{-1} S\Theta\Theta^{-1}\delta\boldsymbol{\theta} =$$

$$= \left(\frac{\partial \mathbf{r}}{\partial \pi}\right)^T \left(V^{-1} - (V + S\Theta S^T)^{-1} S\Theta S^T V^{-1}\right)\mathbf{r} + \left(\frac{\partial \mathbf{r}}{\partial \pi}\right)^T (V + S\Theta S^T)^{-1} S\delta\boldsymbol{\theta} = 0$$

Now, using the identity [50]:

$$V^{-1} - (V + S\Theta S^T)^{-1} S\Theta S^T V^{-1} \equiv (V + S\Theta S^T)^{-1}$$

Then,

$$\left(\frac{\partial \mathbf{r}}{\partial \pi}\right)^T (V + S\Theta S^T)^{-1}\mathbf{r} + \left(\frac{\partial \mathbf{r}}{\partial \pi}\right)^T (V + S\Theta S^T)^{-1} S\delta\boldsymbol{\theta} = \left(\frac{\partial \mathbf{r}}{\partial \pi}\right)^T (V + S\Theta S^T)^{-1}(\mathbf{r} + S\delta\boldsymbol{\theta}) = 0$$

Now, comparing this expression with expression 4.11, i.e. with the standard track fit of the Globalχ^2 (section 4.2.2), it is easy to identify $\bar{\mathbf{r}} = \mathbf{r} + S\delta\boldsymbol{\theta}$ and $\bar{V} = V + S\Theta S^T$ which were already defined in expressions A.6 and A.5. Therefore, one can write:

$$\left(\frac{\partial \bar{\mathbf{r}}}{\partial \pi}\right)^T (\bar{V})^{-1}\bar{\mathbf{r}} = 0 \tag{A.18}$$

Then, it has been demonstrated that with the substitution of $\mathbf{r}$ and V with $\bar{\mathbf{r}}$ and $\bar{V}$, one can incorporate MCS contributions to the Globalχ^2 method without introducing an extra χ^2 term. Moreover, it has been verified that the fit results using the two formalisms lead to the same track perigee parameters and therefore both methods are completely equivalent and valid to extract the alignment parameters corrections.

Finally, a practical point of view of this section is given in appendix B.1 where some real applications are discussed.

A.2 The Globalχ^2 approach with alignment parameter constraints

In analogy to the previous section, one can also consider a generic residual-like vector with just a dependence on the alignment parameters, i.e. $\mathbf{R_a} = \mathbf{R_a}(\mathbf{a})$ being its generic covariance matrix G. Here, $\mathbf{R_a}$ is a $N_{ALI} \times 1$ column vector and G is a $N_{ALI} \times N_{ALI}$ symmetric matrix. The important point here is the fact that the χ^2 term, which contains the alignment parameter constraints, should be evaluated per data sample instead of per event or track as for the same data sample the alignment parameters must to be constant. Therefore the χ^2 definition in 4.3 can be extended to expression 4.45:

$$\chi^2 = \chi^2_{basic} + \chi^2_{alignCons} = \sum_e \sum_{t\in e} \mathbf{r}(\pi, \mathbf{a})^T V^{-1}\mathbf{r}(\pi, \mathbf{a}) + \mathbf{R_a}(\mathbf{a})^T G^{-1}\mathbf{R_a}(\mathbf{a})$$

where the sums are for all the considered tracks and events which belong to the data sample under consideration. It must be emphasized that the vector $\mathbf{R_a}(\mathbf{a})$ has an explicit dependence on the alignment parameters and therefore its differential is:

$$d\mathbf{R_a} = \frac{\partial \mathbf{R_a}}{\partial \mathbf{a}} d\mathbf{a} \tag{A.19}$$

and consequently expressions 4.46 appear:

$$\frac{d\mathbf{R_a}}{d\mathbf{a}} = \frac{\partial \mathbf{R_a}}{\partial \mathbf{a}} \quad \text{and} \quad \frac{d\mathbf{R_a}}{d\boldsymbol{\pi}} = \frac{\partial \mathbf{R_a}}{\partial \boldsymbol{\pi}} \frac{d\mathbf{a}}{d\boldsymbol{\pi}} = 0$$

where $d\mathbf{R_a}/d\boldsymbol{\pi} = 0$ because $d\mathbf{a}/\boldsymbol{\pi} = 0$ as it was argued in section 4.2.1 (i.e. the sensors locations do not depend on the tracks). Accordingly, the dimension of the covariance matrix G is $[N_{ALI} \times N_{ALI}]$.

Once more, the goal is the usual minimization of the χ^2 with respect to the alignment parameters which requires:

$$\frac{d\chi^2}{d\mathbf{a}} = 0$$

therefore differentiating expression 4.45 leads to:

$$\frac{d\chi^2}{d\mathbf{a}} = 2\left(\sum_e \sum_{t\in e} \left[\mathbf{r}^T V^{-1} \left(\frac{d\mathbf{r}}{d\mathbf{a}}\right)\right] + \mathbf{R}_\mathbf{a}^T G^{-1} \left(\frac{d\mathbf{R_a}}{d\mathbf{a}}\right)\right) = 0$$

just remember that the above is a matrix equation, thus its transposed is also null. Then, using the transposed of the previous expression and adding equations A.19 and 4.46 to the minimum condition reads as:

$$\begin{aligned} &\sum_e \sum_{t\in e} \left[\left(\frac{d\mathbf{r}}{d\mathbf{a}}\right)^T V^{-1}\mathbf{r}\right] + \left(\frac{d\mathbf{R_a}}{d\mathbf{a}}\right)^T G^{-1}\mathbf{R_a} = \\ &= \sum_e \sum_{t\in e} \left[\left(\frac{\partial \mathbf{r}}{\partial \boldsymbol{\pi}}\frac{d\boldsymbol{\pi}}{d\mathbf{a}} + \frac{\partial \mathbf{r}}{\partial \mathbf{a}}\right)^T V^{-1}\mathbf{r}\right] + \left(\frac{\partial \mathbf{R_a}}{\partial \mathbf{a}}\right)^T G^{-1}\mathbf{R_a} = 0 \end{aligned} \tag{A.20}$$

where now $d\mathbf{R_a}/d\mathbf{a}$ is a $[N_{ALI} \times N_{ALI}]$ matrix. Once more, $d\boldsymbol{\pi}/d\mathbf{a}$ has to be estimated within the track fitting section as in the previous sections.

A.2.1 Track fitting with constrained alignment parameters

This time, as $\mathbf{R_a} = \mathbf{R_a}(\mathbf{a})$ and therefore $d\mathbf{R_a}/d\boldsymbol{\pi} = 0$, there is no extra contribution to the track fitting, so all the results, specially equation 4.19, in section 4.2.2 are completely valid here.

A.2.2 Alignment corrections fit with constrained alignment parameters

Considering expression 4.10, equation A.20 can be rewritten as:

$$\sum_e \sum_{t\in e} \left(\frac{\partial \mathbf{r}}{\partial \mathbf{a}}\right)^T W\mathbf{r} + \left(\frac{\partial \mathbf{R_a}}{\partial \mathbf{a}}\right)^T G^{-1}\mathbf{R_a} = 0 \tag{A.21}$$

where in the previous formula $\mathbf{r}$ means $\mathbf{r}(\pi_0, \mathbf{a})$ to simplify since a track parameter solution for an arbitrary alignment has been used. Now, in order to solve equation A.21 one has to expand in series both, $\mathbf{r}(\pi_0, \mathbf{a})$ and $\mathbf{R_a}(\mathbf{a})$ around $\mathbf{a}_0$. For $\mathbf{r}$ it was done in expression 4.24 and for $\mathbf{R}$ one has:

$$\mathbf{r} = \mathbf{r}(\pi_0, \mathbf{a}_0) + \left.\frac{\partial \mathbf{r}}{\partial \mathbf{a}}\right|_{\mathbf{a}_0} \delta\mathbf{a}$$

$$\mathbf{R_a}(\mathbf{a}) = \mathbf{R_a}(\mathbf{a}_0) + \left.\frac{\partial \mathbf{R}}{\partial \mathbf{a}}\right|_{\mathbf{a}_0} \delta\mathbf{a} = \mathbf{R_a}(\mathbf{a}_0) + F_{\mathbf{a}}\delta\mathbf{a} \tag{A.22}$$

where $d^n\mathbf{r}/da^n = 0$ with $n \geq 2$ and where $F_{\mathbf{a}}$ has been defined as:

$$F_{\mathbf{a}} \equiv \left.\frac{\partial \mathbf{R}}{\partial \mathbf{a}}\right|_{\mathbf{a}_0}$$

Using, then, expressions 4.24 and A.22 and inserting them into A.21:

$$\sum_e \sum_{t\in e} \left(\frac{\partial \mathbf{r}}{\partial \mathbf{a}}\right)^T W\mathbf{r} + \sum_e \sum_{t\in e} \left(\frac{\partial \mathbf{r}}{\partial \mathbf{a}}\right)^T W\frac{\partial \mathbf{r}}{\partial \mathbf{a}}\delta\mathbf{a} + F_{\mathbf{a}}^T G^{-1}\mathbf{R_a} + F_{\mathbf{a}}^T G^{-1} F_{\mathbf{a}}\delta\mathbf{a} = 0$$

and $\mathbf{r}$ and $\mathbf{R_a}$ mean $\mathbf{r}(\pi_0, \mathbf{a}_0)$ and $\mathbf{R_a}(\mathbf{a}_0)$ to simplify the notation. Therefore the above expression can be rewritten as expression 4.47:

$$\left[\sum_e \sum_{t\in e} \left(\frac{\partial \mathbf{r}}{\partial \mathbf{a}}\right)^T W\frac{\partial \mathbf{r}}{\partial \mathbf{a}} + F_{\mathbf{a}}^T G^{-1} F_{\mathbf{a}}\right]\delta\mathbf{a} + \sum_e \sum_{t\in e} \left(\frac{\partial \mathbf{r}}{\partial \mathbf{a}}\right)^T W\mathbf{r} + F_{\mathbf{a}}^T G^{-1}\mathbf{R_a} = 0$$

using definitions 4.26 and 4.27:

$$\mathcal{M} = \sum_e \sum_{t\in e} \left(\frac{\partial \mathbf{r}}{\partial \mathbf{a}}\right)^T W\frac{\partial \mathbf{r}}{\partial \mathbf{a}}$$

$$\nu = \sum_e \sum_{t\in e} \left(\frac{\partial \mathbf{r}}{\partial \mathbf{a}}\right)^T W\mathbf{r}$$

and the new following definitions (4.48 and 4.49):

$$\mathcal{M}_{\mathbf{a}} = F_{\mathbf{a}}^T G^{-1} F_{\mathbf{a}}$$

$$\nu_{\mathbf{a}} = F_{\mathbf{a}}^T G^{-1}\mathbf{R_a}$$

expression 4.47 can be finally compacted as:

$$\delta\mathbf{a} = -\left(\mathcal{M} + \mathcal{M}_{\mathbf{a}}\right)^{-1}\left(\nu + \nu_{\mathbf{a}}\right) \tag{A.23}$$

where, obviously the final solution of the alignment parameters is:

$$\mathbf{a} = \mathbf{a}_0 + \delta\mathbf{a} = \mathbf{a}_0 - \left(\mathcal{M} + \mathcal{M}_{\mathbf{a}}\right)^{-1}\left(\nu + \nu_{\mathbf{a}}\right) \tag{A.24}$$

Taking a look to the final expression, one can conclude that adding a constraint which just depends on the alignment parameters ($\mathbf{a}$), the results from the general formalism (expression 4.28) can be used directly and one just has to calculate two extra terms, $\mathcal{M}_\mathbf{a}$ and $\nu_\mathbf{a}$.

As can be easily understood, this kind of constraints are global constraints in the sense that they are the same for the whole data sample and therefore there is no sum over tracks or events to accumulate statistics. Because of this, the technical implementation of these constraints is usually very straightforward. Finally, two real applications of this constraint are discussed in appendix B.2.

A.3 The Globalχ^2 approach with common vertex fitting

In the Globalχ^2 formalism one has assumed that the residuals derivative depend not only on the alignment parameters but also on the track parameters. One can even go one step further and claim that all tracks in a given event are generated in a common origin, i.e. from a common point or vertex. In that case the residuals will not only depend on the alignment and on track parameters but also on the vertex coordinates as expression 4.50 illustrates.

$$\mathbf{r} = (\mathbf{m} - \mathbf{e}(\pi, \mathbf{v}, \mathbf{a}))$$

One has to be careful now with the track parameters. Actually the use of the common vertex fitting implicitly amends the independent track parameters. Considering the helix representation, the list of track parameters changes from the set $(d_0, z_0, \phi_0, \theta_0, q/p)$ to just $(\phi_0, \theta_0, q/p)$ keeping as the only degrees of freedom, the orientations and the charge over the momentum. The impact parameters (transversal (d_0) and longitudinal (z_0)) are replaced by the common vertex position parameters which would be ordinarily given by a column vector with just 3 components such as:

$$\mathbf{v} = \begin{pmatrix} x_v \\ y_v \\ z_v \end{pmatrix}$$

although its size would be normally 3, one could think also in terms of beam spot (BS) and then it would require to define at least 5 parameters [100] per data sample instead of per event:

$$\mathbf{v}_{BS} = \begin{pmatrix} x_{BS} \\ y_{BS} \\ z_{BS} \\ \tan\alpha_{BS} \\ \tan\beta_{BS} \end{pmatrix}$$

So, this is why a generic notation will be use and therefore $\mathbf{v}$ will be a vector of size N_{VTX}.

For simplicity, the existence of just one vertex per event will be considered, i.e. all the track within an event will come from a common point, although it is, of course, possible to have more than one vertex per event (secondary vertices).

In order to solve the alignment, one would start with the χ^2 definition as given in expression 4.3, then one should impose the minimum condition with respect the alignment parameters as in 4.4 which leads to the well known expression 4.7:

$$\chi^2 = \sum_e \sum_{t \in e} \mathbf{r}^T V^{-1} \mathbf{r} \;\Rightarrow\; \frac{d\chi^2}{d\mathbf{a}} = 0 \;\Rightarrow\; \sum_e \sum_{t \in e} \left(\frac{d\mathbf{r}}{d\mathbf{a}} \right)^T V^{-1} \mathbf{r} = 0 \tag{A.25}$$

Once one has the above expression, the next step it is just to consider the new residual derivates.

A.3.1 Residual derivatives with vertex dependence

As already stated the residuals ($\mathbf{r}$), now, depends on the track parameters ($\boldsymbol{\pi}$), on the vertex position ($\mathbf{v}$) and on the alignment parameters ($\mathbf{a}$). Therefore:

$$d\mathbf{r} = \frac{\partial \mathbf{r}}{\partial \boldsymbol{\pi}} d\boldsymbol{\pi} + \frac{\partial \mathbf{r}}{\partial \mathbf{v}} d\mathbf{v} + \frac{\partial \mathbf{r}}{\partial \mathbf{a}} d\mathbf{a} \tag{A.26}$$

which implies expressions 4.51, 4.52 and 4.53:

$$\frac{d\mathbf{r}}{d\boldsymbol{\pi}} = \frac{\partial \mathbf{r}}{\partial \boldsymbol{\pi}}$$

$$\frac{d\mathbf{r}}{d\mathbf{v}} = \frac{\partial \mathbf{r}}{\partial \boldsymbol{\pi}} \frac{d\boldsymbol{\pi}}{d\mathbf{v}} + \frac{\partial \mathbf{r}}{\partial \mathbf{v}}$$

$$\frac{d\mathbf{r}}{d\mathbf{a}} = \frac{\partial \mathbf{r}}{\partial \boldsymbol{\pi}} \frac{d\boldsymbol{\pi}}{d\mathbf{a}} + \frac{\partial \mathbf{r}}{\partial \mathbf{a}} + \frac{\partial \mathbf{r}}{\partial \mathbf{v}} \frac{d\mathbf{v}}{d\mathbf{a}}$$

where, as the alignment parameters, the vertex position do not depend on the track parameters, one has $d\mathbf{v}/d\boldsymbol{\pi} = 0$ and $d\mathbf{a}/d\boldsymbol{\pi} = 0$. Moreover, the alignment parameters do not depend on the vertex position, therefore $d\mathbf{a}/d\mathbf{v} = 0$. Thus inserting expression 4.53 in equation A.25 one may write:

$$\sum_e \sum_{t \in e} \left(\frac{\partial \mathbf{r}}{\partial \boldsymbol{\pi}} \frac{d\boldsymbol{\pi}}{d\mathbf{a}} + \frac{\partial \mathbf{r}}{\partial \mathbf{a}} \right)^T V^{-1} \mathbf{r} + \sum_e \left(\frac{\partial \mathbf{r}}{\partial \mathbf{v}} \frac{d\mathbf{v}}{d\mathbf{a}} \right)^T V^{-1} \mathbf{r} = 0 \tag{A.27}$$

Now, one needs to calculate the derivates $d\boldsymbol{\pi}/d\mathbf{a}$ and $d\mathbf{v}/d\mathbf{a}$ and to do it one needs to find a solution of the track parameters and on the vertex parameters for any arbitrary alignment parameters, i.e. a minimization with respect the track parameters and on the vertex parameters is needed.

A.3.2 Track fitting with common vertex fitting

The first derivative ($d\boldsymbol{\pi}/d\mathbf{a}$) was already computed in section 4.2.2 and was given in equation 4.18 but now there is a novelty which is $\mathbf{r} = \mathbf{r}(\boldsymbol{\pi}_0, \mathbf{v}, \mathbf{a})$. This term comes from the track fit which in its turn requires the χ^2 minimization: $d\chi^2/d\boldsymbol{\pi} = 0$. However that expression must be amended to account for the common vertex effects. As one needs to compute the plain $d\boldsymbol{\pi}/d\mathbf{a}$ for a given track and evaluated with the initial track parameters ($\boldsymbol{\pi}_0$), one has to use expression 4.18 for just one track:

$$\frac{d\boldsymbol{\pi}}{d\mathbf{a}} = -(E^T V^{-1} E)^{-1} E^T V^{-1} \frac{d\mathbf{r}(\boldsymbol{\pi}_0, \mathbf{v}, \mathbf{a})}{d\mathbf{a}}$$

which, together with equation 4.53 evaluated at $\boldsymbol{\pi}_0$ ($\partial\mathbf{r}(\boldsymbol{\pi}_0, \mathbf{v}, \mathbf{a})/\partial\boldsymbol{\pi} = 0$), should be rewritten as:

$$\frac{d\boldsymbol{\pi}}{d\mathbf{a}} = -(E^T V^{-1} E)^{-1} E^T V^{-1} \left(\frac{\partial \mathbf{r}}{\partial \mathbf{a}} + \frac{\partial \mathbf{r}}{\partial \mathbf{v}} \frac{d\mathbf{v}}{d\mathbf{a}} \right) \tag{A.28}$$

Comparing this expression with expression 4.19, an extra term has been introduced.

Finally, it is also useful to consider $d\boldsymbol{\pi}/d\mathbf{v}$ as it would be needed in the vertex fit, which is the following step.

$$\frac{d\boldsymbol{\pi}}{d\mathbf{v}} = -(E^T V^{-1} E)^{-1} E^T V^{-1} \frac{d\mathbf{r}}{d\mathbf{v}} = -(E^T V^{-1} E)^{-1} E^T V^{-1} \frac{\partial \mathbf{r}}{\partial \mathbf{v}} \tag{A.29}$$

where has been used expression 4.52 evaluated around $\boldsymbol{\pi}_0$:

$$\frac{d\mathbf{r}(\boldsymbol{\pi}_0, \mathbf{v}, \mathbf{a})}{d\mathbf{v}} = \frac{\partial \mathbf{r}}{\partial \mathbf{v}}$$

A.3.3 Vertex fitting

The next step is to find the solution of the vertex parameters by fitting the vertex. In the current scenario, the vertex fit should be done in an event by event basis, as tracks originated in different events are not necessarily produced at the same point (common primary vertex). However, one can focus on a slightly different scenario where no fit of the primary vertex per event is done and where all tracks are constrained to the *beam spot*, assuming that they come from the same region. This issue was treated in appendix B.1.1 and it is however a completely different situation.

The starting point is now the χ^2 function defined in equation A.25. One has to minimize the χ^2 with respect to the vertex parameters for a given vertex (i.e. for a given event):

$$\frac{d\chi^2}{d\mathbf{v}} = 0 \longrightarrow \left(\frac{d\mathbf{r}}{d\mathbf{v}} \right)^T V^{-1} \mathbf{r} = 0 \tag{A.30}$$

where, generally:

$$\frac{d\chi^2}{d\mathbf{v}} = \begin{pmatrix} \frac{d\chi^2}{dv_1} & \frac{d\chi^2}{dv_2} & \dots & \frac{d\chi^2}{dv_{N_{VTX}}} \end{pmatrix} = \begin{pmatrix} 0 & 0 & \dots & 0 \end{pmatrix}$$

Following the same procedure as in the previous sections, one has to include 4.52 in A.30:

$$\sum_{t \in e} \left(\frac{\partial \mathbf{r}}{\partial \boldsymbol{\pi}} \frac{d\boldsymbol{\pi}}{d\mathbf{v}} \right)^T V^{-1} \mathbf{r} + \left(\frac{\partial \mathbf{r}}{\partial \mathbf{v}} \right)^T V^{-1} \mathbf{r} = \left(\sum_{t \in e} \frac{\partial \mathbf{r}}{\partial \boldsymbol{\pi}} \frac{d\boldsymbol{\pi}}{d\mathbf{v}} + \frac{\partial \mathbf{r}}{\partial \mathbf{v}} \right)^T V^{-1} \mathbf{r} = 0 \tag{A.31}$$

then, one can find the solution to the vertex fit in a similar way as for the track fit. Let's consider the residual series expansion around $\mathbf{v}_0$ up to first order in terms of the vertex parameters:

$$\mathbf{r} = \mathbf{r}(\boldsymbol{\pi}_0, \mathbf{v}_0, \mathbf{a}) + \left. \frac{\partial \mathbf{r}}{\partial \mathbf{v}} \right|_{v=v_0} \delta\mathbf{v} = \mathbf{r}_0 + E_v \delta\mathbf{v}$$

where, $\mathbf{r}$ means $\mathbf{r} = \mathbf{r}(\boldsymbol{\pi}_0, \mathbf{v}_0, \mathbf{a})$ and being $\delta\mathbf{v}$ the correction to the initial vertex parameters. Moreover one has made use of the following definition:

$$E_v \equiv \left.\frac{\partial \mathbf{r}}{\partial \mathbf{v}}\right|_{\mathbf{v}_0} \qquad \text{where} \qquad \dim[E_v] = [N_{RES} \times N_{VTX}] \tag{A.32}$$

So, importing this expansion in A.30 and also using the defined E, one obtains:

$$\left(\sum_{t\in e} E\frac{d\pi}{d\mathbf{v}} + E_v\right)^T V^{-1}\mathbf{r} + \left(\sum_{t\in e} E\frac{d\pi}{d\mathbf{v}} + E_v\right)^T V^{-1}E_v\delta\mathbf{v} = 0$$

Now one needs to deal with the term $d\pi/d\mathbf{v}$, which was calculated and can be found in equation A.29

$$\sum_{t\in e}\left(E_v - E(E^TV^{-1}E)^{-1}E^TV^{-1}E_v +\right)^T V^{-1}\mathbf{r} + \sum_{t\in e}\left(E_v - E(E^TV^{-1}E)^{-1}E^TV^{-1}E_v + E_v\right)^T V^{-1}E_v\delta\mathbf{v} = 0$$

which can be compacted using the already defined $\mathcal{G}_E \equiv E(E^TV^{-1}E)^{-1}E^TV^{-1}$ (expression 4.21) and the weight matrix $W \equiv (I - \mathcal{G}_E)^T\, V^{-1}$ (expression 4.22). With some simple operations can be obtained:

$$\sum_{t\in e} E_v^T\,(I-\mathcal{G}_E)^T\, V^{-1}\mathbf{r} + \sum_{t\in e} E_v^T\,(I-\mathcal{G}_E)^T\, V^{-1}E_v\delta\mathbf{v} = \sum_{t\in e} E_v^T W\mathbf{r} + \sum_{t\in e} E_v^T W E_v\delta\mathbf{v} = 0$$

and therefore:

$$\delta\mathbf{v} = -\left(\sum_{t\in e} E_v^T W E_v\right)^{-1} \sum_{t\in e} E_v^T W\mathbf{r} = -\mathcal{M}_v^{-1}\nu_v \tag{A.33}$$

where again, one has defined:

$$\mathcal{M}_v = \sum_{t\in e} E_v^T W E_v \tag{A.34}$$

which is a symmetric matrix of dimension $N_{VTX} \times N_{VTX}$. While the term:

$$\nu_v = \sum_{t\in e} E_v^T W\mathbf{r} \tag{A.35}$$

is a column vector with N_{VTX} components.
Finally, the vertex fit result is simply given by:

$$\mathbf{v} = \mathbf{v}_0 + \delta\mathbf{v} = \mathbf{v}_0 - \mathcal{M}_v^{-1}\nu_v \tag{A.36}$$

All these calculations serve to evaluate the derivative $d\mathbf{v}/d\mathbf{a}$:

$$\frac{d\mathbf{v}}{d\mathbf{a}} = -\sum_{t\in e}\left(E_v^T W E_v\right)^{-1} E_v^T W\frac{\partial \mathbf{r}}{\partial \mathbf{a}} \tag{A.37}$$

where:

$$\frac{d\mathbf{r}(\pi_0, \mathbf{v}_0, \mathbf{a})}{d\mathbf{a}} = \frac{\partial \mathbf{r}}{\partial \mathbf{a}}$$

A.3.4 Alignment corrections fit with common vertex fitting

Reached this point, one has all the ingredients to solve A.27. First, let's complete equation A.28 (for one track) inserting equation A.37:

$$\frac{d\pi}{d\mathbf{a}} = -(E^T V^{-1} E)^{-1} E^T V^{-1} \left(\frac{\partial \mathbf{r}}{\partial \mathbf{a}} + E_v \frac{d\mathbf{v}}{d\mathbf{a}} \right) =$$

$$= -(E^T V^{-1} E)^{-1} E^T V^{-1} \left(\frac{\partial \mathbf{r}}{\partial \mathbf{a}} - E_v (E_v^T W E_v)^{-1} E_v^T W \frac{\partial \mathbf{r}}{\partial \mathbf{a}} \right) =$$

$$= -(E^T V^{-1} E)^{-1} E^T V^{-1} \left(I - E_v (E_v^T W E_v)^{-1} E_v^T W \right) \frac{\partial \mathbf{r}}{\partial \mathbf{a}} \tag{A.38}$$

Using the above expression and expression A.37 for a given event, equation A.27 can be written as:

$$\sum_e \sum_{t \in e} \left(E \frac{d\pi}{d\mathbf{a}} + \frac{\partial \mathbf{r}}{\partial \mathbf{a}} \right)^T V^{-1} \mathbf{r} + \sum_e \left(E_v \frac{d\mathbf{v}}{d\mathbf{a}} \right)^T V^{-1} \mathbf{r} =$$

$$= \sum_e \sum_{t \in e} \left[-E (E^T V^{-1} E)^{-1} E^T V^{-1} \left(\frac{\partial \mathbf{r}}{\partial \mathbf{a}} - E_v (E_v^T W E_v)^{-1} E_v^T W \frac{\partial \mathbf{r}}{\partial \mathbf{a}} \right) + \frac{\partial \mathbf{r}}{\partial \mathbf{a}} \right]^T V^{-1} \mathbf{r} +$$

$$+ \sum_e \sum_{t \in e} \left(-E_v (E_v^T W E_v)^{-1} E_v^T W \frac{\partial \mathbf{r}}{\partial \mathbf{a}} \right)^T V^{-1} \mathbf{r} =$$

$$= \sum_e \sum_{t \in e} \left[\frac{\partial \mathbf{r}}{\partial \mathbf{a}} - E (E^T V^{-1} E)^{-1} E^T V^{-1} \frac{\partial \mathbf{r}}{\partial \mathbf{a}} + E (E^T V^{-1} E)^{-1} E^T V^{-1} E_v (E_v^T W E_v)^{-1} E_v^T W \frac{\partial \mathbf{r}}{\partial \mathbf{a}} \right]^T V^{-1} \mathbf{r} +$$

$$+ \sum_e \sum_{t \in e} \left(-E_v (E_v^T W E_v)^{-1} E_v^T W \frac{\partial \mathbf{r}}{\partial \mathbf{a}} \right)^T V^{-1} \mathbf{r} =$$

$$= \sum_e \sum_{t \in e} \left(\frac{\partial \mathbf{r}}{\partial \mathbf{a}} \right)^T W \mathbf{r} + \sum_e \sum_{t \in e} \left(\mathcal{G}_E E_v (E_v^T W E_v)^{-1} E_v^T W \frac{\partial \mathbf{r}}{\partial \mathbf{a}} \right)^T V^{-1} \mathbf{r} +$$

$$+ \sum_e \sum_{t \in e} \left(-E_v (E_v^T W E_v)^{-1} E_v^T W \frac{\partial \mathbf{r}}{\partial \mathbf{a}} \right)^T V^{-1} \mathbf{r} =$$

$$= \sum_e \sum_{t \in e} \left(\frac{\partial \mathbf{r}}{\partial \mathbf{a}} \right)^T W \mathbf{r} - \sum_e \sum_{t \in e} \left(\frac{\partial \mathbf{r}}{\partial \mathbf{a}} \right)^T W E_v (E_v^T W E_v)^{-1} E_v^T (I - \mathcal{G}_E)^T V^{-1} \mathbf{r} =$$

$$= \sum_e \sum_{t \in e} \left(\frac{\partial \mathbf{r}}{\partial \mathbf{a}} \right)^T W \mathbf{r} - \sum_e \sum_{t \in e} \left(\frac{\partial \mathbf{r}}{\partial \mathbf{a}} \right)^T W E_v (E_v^T W E_v)^{-1} E_v^T W \mathbf{r} =$$

$$= \sum_e \sum_{t \in e} \left(\frac{\partial \mathbf{r}}{\partial \mathbf{a}} \right)^T \left(I - W E_v (E_v^T W E_v)^{-1} E_v^T \right) W \mathbf{r} = \sum_e \sum_{t \in e} \left(\frac{\partial \mathbf{r}}{\partial \mathbf{a}} \right)^T \tilde{W} \mathbf{r} = 0 \tag{A.39}$$

where, $\tilde{W}$ has been defined for convenience[2]:

$$\tilde{W} \equiv \left(I - WE_v(E_v^T W E_v)^{-1} E_v^T\right) W$$

To conclude, one has to perform a series expansion of the residuals around the initial alignment parameters ($\mathbf{a}_0$) and keep only the first order term:

$$\mathbf{r} = \mathbf{r}(\pi_0, \mathbf{v}_0, \mathbf{a}_0) + \left.\frac{\partial \mathbf{r}}{\partial \mathbf{a}}\right|_{\mathbf{a}=\mathbf{a}_0} \delta\mathbf{a}$$

Inserting the above expression into equation A.39, one has:

$$\sum_e \sum_{t\in e} \left(\frac{\partial \mathbf{r}}{\partial \mathbf{a}}\right)^T \tilde{W}\mathbf{r} + \sum_e \sum_{t\in e} \left(\frac{\partial \mathbf{r}}{\partial \mathbf{a}}\right)^T \tilde{W} \frac{\partial \mathbf{r}}{\partial \mathbf{a}} \delta\mathbf{a} = 0 \tag{A.40}$$

Finally, the alignment corrections ($\delta\mathbf{a}$) are given by:

$$\delta\mathbf{a} = -\left[\sum_e \sum_{t\in e} \left(\frac{\partial \mathbf{r}}{\partial \mathbf{a}}\right)^T \tilde{W} \frac{\partial \mathbf{r}}{\partial \mathbf{a}}\right]^{-1} \sum_e \sum_{t\in e} \left(\frac{\partial \mathbf{r}}{\partial \mathbf{a}}\right)^T \tilde{W}\mathbf{r}$$

As in previous sections, one can define the new *big-matrix* and the new *big-vector* (expressions 4.54 and 4.55):

$$\tilde{\mathcal{M}} = \sum_e \sum_{t\in e} \left(\frac{\partial \mathbf{r}}{\partial \mathbf{a}}\right)^T \tilde{W} \frac{\partial \mathbf{r}}{\partial \mathbf{a}}$$

$$\tilde{\nu} = \sum_e \sum_{t\in e} \left(\frac{\partial \mathbf{r}}{\partial \mathbf{a}}\right)^T \tilde{W}\mathbf{r}$$

being the final solution (expression A.56):

$$\mathbf{a} = \mathbf{a}_0 + \delta\mathbf{a} = \mathbf{a}_0 - \tilde{\mathcal{M}}^{-1}\tilde{\nu}$$

Note that with the imposed common vertex, the solution again includes a $[N_{ALI} \times N_{ALI}]$ symmetric matrix $\tilde{\mathcal{M}}$. However, when enough statistics of tracks and vertices is used, the matrix is not sparse anymore, i.e. the matrix will be fully populated. First, due to the self-correlations between the degrees of freedom of each module, second, due to the correlations between modules due to the common tracks and now due to the correlations because of tracks emerging from a common vertex.

A.4 The Globalχ^2 approach with common vertex fit and vertex parameter constraints

The previous extension of the Globalχ^2 formalism is very powerful thanks to the fact that the residuals depend on the vertex parameters. Following the previous formalism, there is a natural

[2]If one compares these expression with the ones in reference [71], it is worth to say that this $\tilde{W}$ is not the one defined in that reference.

constraint to be considered. Therefore, a new residual-like vector which depends only on the vertex parameters, $\mathbf{R_v} = \mathbf{R_v}(\mathbf{v})$ is introduced. This residual-like vector of size N_{VTXPAR} will contain the difference of the sensitive vertex coordinates respect to the target values (of course, it is also possible to consider the beam spot coordinates to constrain the primary vertex).

The differential of this new residual is:

$$d\mathbf{R_v} = \frac{\partial \mathbf{R_v}}{\partial \mathbf{v}} d\mathbf{v} \tag{A.41}$$

and, of course, its derivatives are:

$$\frac{d\mathbf{R_v}}{d\mathbf{v}} = \frac{\partial \mathbf{R_v}}{\partial \mathbf{v}} \quad , \quad \frac{d\mathbf{R_v}}{d\pi} = \frac{\partial \mathbf{R_v}}{\partial \pi}\frac{d\mathbf{v}}{d\pi} = 0 \quad \text{and} \quad \frac{d\mathbf{R_v}}{d\mathbf{a}} = \frac{\partial \mathbf{R_v}}{\partial \mathbf{v}}\frac{d\mathbf{v}}{d\mathbf{a}}$$

where $d\mathbf{R_v}/d\pi = 0$ because $d\mathbf{v}/d\pi = 0$ (see expression 4.51). This is because the vertex position does not depend on track parameters. Accordingly, the dimension of the covariance matrix will be $[N_{VTXPAR} \times N_{VTXPAR}]$.

Then, one has the χ^2 defined in the expression 4.50 plus an add-on which has the following form:

$$\chi^2 = \chi^2 + \chi^2_{vtxCons} = \sum_e \sum_{t \in e} \mathbf{r}^T(\pi, \mathbf{v}, \mathbf{a}) V^{-1} \mathbf{r}(\pi, \mathbf{v}, \mathbf{a}) + \sum_e \mathbf{R}^T_\mathbf{v}(\mathbf{v}) O^{-1} \mathbf{R_v}(\mathbf{v}) \tag{A.42}$$

being O the covariance matrix of the vertex constraint, $\mathbf{R_v}(\mathbf{v})$. The residual derivatives are the ones discussed in section A.3.1, therefore equations 4.51, 4.52 and 4.53 will be used in this section. And then the minimum condition $d\chi^2/d\mathbf{a} = 0$ can be written as:

$$\sum_e \sum_{t \in e} \left(\frac{\partial \mathbf{r}}{\partial \pi}\frac{d\pi}{d\mathbf{a}} + \frac{\partial \mathbf{r}}{\partial \mathbf{a}} \right)^T V^{-1} \mathbf{r} + \sum_e \left(\frac{\partial \mathbf{r}}{\partial \mathbf{v}}\frac{d\mathbf{v}}{d\mathbf{a}} \right)^T V^{-1} \mathbf{r} + \sum_e \left(\frac{\partial \mathbf{R_v}}{\partial \mathbf{v}}\frac{d\mathbf{v}}{d\mathbf{a}} \right)^T O^{-1} \mathbf{R_v} = 0 \tag{A.43}$$

A.4.1 Track fitting with constrained vertex parameters

As $\mathbf{R_v} = \mathbf{R_v}(\mathbf{v})$ (and therefore $d\mathbf{R_v}/d\pi = 0$) there is no contribution to the track fitting. Thus, all the results in section 4.2.2 are completely valid here. Therefore, the needed equations for a given track are A.28 and A.29 from section A.3.2:

$$\frac{d\pi}{d\mathbf{a}} = -(E^T V^{-1} E)^{-1} E^T V^{-1} \left(\frac{\partial \mathbf{r}}{\partial \mathbf{a}} + \frac{\partial \mathbf{r}}{\partial \mathbf{v}}\frac{d\mathbf{v}}{d\mathbf{a}} \right)$$

$$\frac{d\pi}{d\mathbf{v}} = -(E^T V^{-1} E)^{-1} E^T V^{-1} \frac{\partial \mathbf{r}}{\partial \mathbf{v}}$$

where, one has to remind that $\mathbf{r}$ means $\mathbf{r} = \mathbf{r}(\pi_0, \mathbf{v}, \mathbf{a})$ due to the track fit and the series expansion.

A.4.2 Vertex fitting with constrained vertex parameters

In this case, one has to apply the minimum condition to the expression A.42 for a given vertex (i.e. event):

$$\frac{d\chi^2}{d\mathbf{v}} = 0 \quad \longrightarrow \quad \sum_{t\in e} \left(\frac{d\mathbf{r}}{d\mathbf{v}}\right)^T V^{-1}\mathbf{r} + \left(\frac{d\mathbf{R_v}}{d\mathbf{v}}\right)^T O^{-1}\mathbf{R_v} = 0 \tag{A.44}$$

Then, following the same procedure as in the previous sections, one has to include 4.52 and 4.57 in A.44:

$$\sum_{t\in e} \left(\frac{\partial \mathbf{r}}{\partial \boldsymbol{\pi}}\frac{d\boldsymbol{\pi}}{d\mathbf{v}}\right)^T V^{-1}\mathbf{r} + \left(\frac{\partial \mathbf{r}}{\partial \mathbf{v}}\right)^T V^{-1}\mathbf{r} + \left(\frac{\partial \mathbf{R_v}}{\partial \mathbf{v}}\right)^T O^{-1}\mathbf{R_v} = 0 \tag{A.45}$$

as it has been done before, one can find the solution to the vertex fit considering the residual series expansion around the initial values of the vertex parameters ($\mathbf{v}_0$) up to first order:

$$\mathbf{r} = \mathbf{r}(\boldsymbol{\pi}_0, \mathbf{v}_0, \mathbf{a}) + \left.\frac{\partial \mathbf{r}}{\partial \mathbf{v}}\right|_{\mathbf{v}_0} \delta\mathbf{v} \quad \text{and} \quad \mathbf{R_v} = \mathbf{R_v}(\mathbf{v}_0) + \left.\frac{\partial \mathbf{R}}{\partial \mathbf{v}}\right|_{\mathbf{v}_0} \delta\mathbf{v} \tag{A.46}$$

where now, $\mathbf{r}$ means $\mathbf{r} = \mathbf{r}(\boldsymbol{\pi}_0, \mathbf{v}_0, \mathbf{a})$ and $\mathbf{R_v}$ means $\mathbf{R_v} = \mathbf{R_v}(\mathbf{v}_0)$.
Moreover, one can use the previous defined $E = \partial\mathbf{r}/\partial\boldsymbol{\pi}|_{\mathbf{v}_0}$ and $E_v = \partial\mathbf{r}/\partial\mathbf{v}|_{\mathbf{v}_0}$ together with a new one:

$$F_v \equiv \left.\frac{\partial \mathbf{R}}{\partial \mathbf{v}}\right|_{\mathbf{v}_0}$$

So, importing these expressions and A.46 into A.45, one obtains:

$$\left(\sum_{t\in e} E\frac{d\boldsymbol{\pi}}{d\mathbf{v}} + E_v\right)^T V^{-1}\mathbf{r} + \left(\sum_{t\in e} E\frac{d\boldsymbol{\pi}}{d\mathbf{v}} + E_v\right)^T V^{-1}E_v\delta\mathbf{v} + F_v^T O^{-1}\mathbf{R_v} + F_v^T O^{-1}F_v\delta\mathbf{v} = 0$$

importing also $d\boldsymbol{\pi}/d\mathbf{v}$:

$$\sum_{t\in e}(-E(E^TV^{-1}E)^{-1}E^TV^{-1}E_v + E_v)^T V^{-1}\mathbf{r} +$$

$$+ \sum_{t\in e}(-E(E^TV^{-1}E)^{-1}E^TV^{-1}E_v + E_v)^T V^{-1}E_v\delta\mathbf{v} + F_v^T O^{-1}\mathbf{R_v} + F_v^T O^{-1}F_v\delta\mathbf{v} =$$

$$= \sum_{t\in e} E_v^T W\mathbf{r} + \sum_{t\in e} E_v^T W E_v\delta\mathbf{v} + F_v^T O^{-1}\mathbf{R_v} + F_v^T O^{-1}F_v\delta\mathbf{v} = 0$$

where the *weight matrix* W have been used to compact the formulas.
Then:

$$\delta\mathbf{v} = -\left[\sum_{t\in e} E_v^T W E_v + F_v^T O^{-1}F_v\right]^{-1}\left(\sum_{t\in e} E_v^T W\mathbf{r} + F_v^T O^{-1}\mathbf{R_v}\right) \tag{A.47}$$

Now, using the already defined $\mathcal{M}_{v_v}$ and ν_{v_v} in A.34 and A.35, respectively, and with the following two new definitions:

$$\mathcal{M}_{\nu_v} = F_v^T O^{-1} F_v \tag{A.48}$$

$$\nu_{\nu_v} = F_v^T O^{-1} \mathbf{R_v} \tag{A.49}$$

is trivial to write:

$$\delta\mathbf{v} = -\left(\mathcal{M}_v + \mathcal{M}_{\nu_v}\right)^{-1}\left(\nu_v + \nu_{\nu_v}\right) \tag{A.50}$$

and now, one can evaluate the missing $d\mathbf{v}/d\mathbf{a}$ deriving $\mathbf{v} = \mathbf{v}_0 + \delta\mathbf{v}$ since $\delta\mathbf{v}$ is known and :

$$\frac{d\mathbf{v}}{d\mathbf{a}} = -\left[\sum_{t\in e} E_v^T W E_v + F_v^T O^{-1} F_v\right]^{-1}\left(\sum_{t\in e} E_v^T W \frac{\partial\mathbf{r}}{\partial\mathbf{a}}\right) \tag{A.51}$$

where one has to remind:

$$\frac{d\mathbf{r}(\boldsymbol{\pi}_0, \mathbf{v}_0, \mathbf{a})}{d\mathbf{a}} = \frac{\partial\mathbf{r}}{\partial\mathbf{a}} \quad \text{and} \quad \frac{d\mathbf{R}(\mathbf{v}_0)}{d\mathbf{a}} = \frac{\partial\mathbf{R}(\mathbf{v}_0)}{\partial\mathbf{a}}\frac{d\mathbf{v}}{d\mathbf{a}} = 0$$

A.4.3 Alignment corrections fit with constrained vertex parameters

Now, one has all the ingredients to solve A.43. First, let's complete equation A.28 (for one track) inserting equation A.51:

$$\frac{d\boldsymbol{\pi}}{d\mathbf{a}} = -(E^T V^{-1} E)^{-1} E^T V^{-1}\left(\frac{\partial\mathbf{r}}{\partial\mathbf{a}} + E_v\frac{d\mathbf{v}}{d\mathbf{a}}\right) =$$

$$= -(E^T V^{-1} E)^{-1} E^T V^{-1}\left(\frac{\partial\mathbf{r}}{\partial\mathbf{a}} - E_v(E_v^T W E_v + F_v^T O^{-1} F_v)^{-1}\left(E_v^T W \frac{\partial\mathbf{r}}{\partial\mathbf{a}}\right)\right) = 0 \tag{A.52}$$

Then, inserting the above expression and with A.51 again for one event, equation A.43 can be resolved:

$$\sum_e\sum_{t\in e}\left(E\frac{d\boldsymbol{\pi}}{d\mathbf{a}} + \frac{\partial\mathbf{r}}{\partial\mathbf{a}}\right)^T V^{-1}\mathbf{r} + \sum_e\left(E_v\frac{d\mathbf{v}}{d\mathbf{a}}\right)^T V^{-1}\mathbf{r} + \sum_e\left(F_v\frac{d\mathbf{v}}{d\mathbf{a}}\right)^T O^{-1}\mathbf{R_v} =$$

$$= \sum_e\sum_{t\in e}\left(-\mathcal{G}_E\left(\frac{\partial\mathbf{r}}{\partial\mathbf{a}} - E_v(E_v^T W E_v + F_v^T O^{-1} F_v)^{-1} E_v^T W\frac{\partial\mathbf{r}}{\partial\mathbf{a}}\right) + \frac{\partial\mathbf{r}}{\partial\mathbf{a}}\right)^T V^{-1}\mathbf{r} +$$

$$+ \sum_e\sum_{t\in e}\left(-E_v(E_v^T W E_v + F_v^T O^{-1} F_v)^{-1} E_v^T W\frac{\partial\mathbf{r}}{\partial\mathbf{a}}\right)^T V^{-1}\mathbf{r} +$$

$$+ \sum_e\sum_{t\in e}\left(-F_v(E_v^T W E_v + F_v^T O^{-1} F_v)^{-1} E_v^T W\frac{\partial\mathbf{r}}{\partial\mathbf{a}}\right)^T O^{-1}\mathbf{R_v} =$$

$$= \sum_e\sum_{t\in e}\left(-\mathcal{G}_E\left(\frac{\partial\mathbf{r}}{\partial\mathbf{a}} - E_v\mathcal{K}\frac{\partial\mathbf{r}}{\partial\mathbf{a}}\right) + \frac{\partial\mathbf{r}}{\partial\mathbf{a}}\right)^T V^{-1}\mathbf{r} +$$

$$+\sum_e \sum_{t\in e}\left(-E_v\mathcal{K}\frac{\partial \mathbf{r}}{\partial \mathbf{a}}\right)^T V^{-1}\mathbf{r} + \sum_e \sum_{t\in e}\left(-F_v\mathcal{K}\frac{\partial \mathbf{r}}{\partial \mathbf{a}}\right)^T O^{-1}\mathbf{R_v} = 0$$

where the already defined $\mathcal{G}_E$ have been used together with a new definition $\mathcal{K}$:

$$\mathcal{G}_E \equiv E(E^T V^{-1} E)^{-1} E^T V^{-1}$$

$$\mathcal{K} \equiv (E_v^T W E_v + F_v^T O^{-1} F_v)^{-1} E_v^T W$$

let's compact the above expressions:

$$\begin{aligned}
&\sum_e \sum_{t\in e}\left(-\mathcal{G}_E\frac{\partial \mathbf{r}}{\partial \mathbf{a}} + \mathcal{G}_E E_v\mathcal{K}\frac{\partial \mathbf{r}}{\partial \mathbf{a}} + \frac{\partial \mathbf{r}}{\partial \mathbf{a}}\right)^T V^{-1}\mathbf{r} - \\
&-\sum_e \sum_{t\in e}\left(\frac{\partial \mathbf{r}}{\partial \mathbf{a}}\right)^T (E_v\mathcal{K})^T V^{-1}\mathbf{r} - \sum_e \sum_{t\in e}\left(\frac{\partial \mathbf{r}}{\partial \mathbf{a}}\right)^T (F_v\mathcal{K})^T O^{-1}\mathbf{R_v} = \\
&= \sum_e \sum_{t\in e}\left(\frac{\partial \mathbf{r}}{\partial \mathbf{a}}\right)^T (I-\mathcal{G}_E)^T V^{-1}\mathbf{r} + \left(\frac{\partial \mathbf{r}}{\partial \mathbf{a}}\right)^T (\mathcal{G}_E E_v\mathcal{K})^T V^{-1}\mathbf{r} - \\
&-\sum_e \sum_{t\in e}\left(\frac{\partial \mathbf{r}}{\partial \mathbf{a}}\right)^T (E_v\mathcal{K})^T V^{-1}\mathbf{r} - \sum_e \sum_{t\in e}\left(\frac{\partial \mathbf{r}}{\partial \mathbf{a}}\right)^T (F_v\mathcal{K})^T O^{-1}\mathbf{R_v} = \\
&= \sum_e \sum_{t\in e}\left(\frac{\partial \mathbf{r}}{\partial \mathbf{a}}\right)^T W\mathbf{r} - \left(\frac{\partial \mathbf{r}}{\partial \mathbf{a}}\right)^T \mathcal{K}^T E_v^T W\mathbf{r} - \sum_e \sum_{t\in e}\left(\frac{\partial \mathbf{r}}{\partial \mathbf{a}}\right)^T \mathcal{K}^T F_v^T O^{-1}\mathbf{R_v} = \\
&= \sum_e \sum_{t\in e}\left(\frac{\partial \mathbf{r}}{\partial \mathbf{a}}\right)^T (I-\mathcal{K}^T E_v^T)W\mathbf{r} - \sum_e \sum_{t\in e}\left(\frac{\partial \mathbf{r}}{\partial \mathbf{a}}\right)^T \mathcal{K}^T F_v^T O^{-1}\mathbf{R_v} = \\
&= \sum_e \sum_{t\in e}\left(\frac{\partial \mathbf{r}}{\partial \mathbf{a}}\right)^T \mathcal{P}\mathbf{r} - \sum_e \sum_{t\in e}\left(\frac{\partial \mathbf{r}}{\partial \mathbf{a}}\right)^T \mathcal{K}^T F_v^T O^{-1}\mathbf{R_v} = 0
\end{aligned} \tag{A.53}$$

where, the matrix $\tilde{W}_v$ have been defined for convenience:

$$\tilde{W}_v \equiv (I - \mathcal{K}^T E_v^T) W$$

Note that expression A.53 looks similar to expression 4.39.

To conclude, one has to perform a series expansion of the residuals around the initial values of the alignment parameters ($\mathbf{a}_0$) and keep only the first order term:

$$\mathbf{r}(\boldsymbol{\pi}_0, \mathbf{v}_0, \mathbf{a}) = \mathbf{r}(\boldsymbol{\pi}_0, \mathbf{v}_0, \mathbf{a}_0) + \left.\frac{\partial \mathbf{r}}{\partial \mathbf{a}}\right|_{a=a_0} \delta\mathbf{a} \quad \text{where} \quad \frac{\partial^n \mathbf{r}}{\partial \mathbf{a}^n} = 0 \quad \text{with} \quad n \geq 2$$

$$\mathbf{R_v}(\mathbf{v}_0) = \mathbf{R_v}(\mathbf{v}_0) + \left.\frac{\partial \mathbf{R_v}}{\partial \mathbf{a}}\right|_{a=a_0} \delta\mathbf{a} = \mathbf{R_v}(\mathbf{v}_0) \quad \text{where} \quad \frac{\partial^n \mathbf{r}}{\partial \mathbf{a}^n} = 0 \quad \text{with} \quad n \geq 1$$

as usual, since this moment, $\mathbf{r}$ and $\mathbf{R_v}$ will mean $\mathbf{r} = \mathbf{r}(\boldsymbol{\pi}_0, \mathbf{v}_0, \mathbf{a}_0)$ and $\mathbf{R_v} = \mathbf{R_v}(\mathbf{v}_0)$, respectively. Inserting the above expression into equation A.53:

$$\sum_e \sum_{t\in e} \left(\frac{\partial \mathbf{r}}{\partial \mathbf{a}}\right)^T \tilde{W}_v \mathbf{r} + \sum_e \sum_{t\in e} \left(\frac{\partial \mathbf{r}}{\partial \mathbf{a}}\right)^T \tilde{W}_v \frac{\partial \mathbf{r}}{\partial \mathbf{a}} \delta\mathbf{a} - \sum_e \sum_{t\in e} \left(\frac{\partial \mathbf{r}}{\partial \mathbf{a}}\right)^T \mathcal{K}^T F_v^T O^{-1} \mathbf{R_v} = 0 \tag{A.54}$$

Finally, the alignment corrections $\delta\mathbf{a}$ are given by:

$$\delta\mathbf{a} = -\left[\sum_e \sum_{t\in e} \left(\frac{\partial \mathbf{r}}{\partial \mathbf{a}}\right)^T \tilde{W}_v \frac{\partial \mathbf{r}}{\partial \mathbf{a}}\right]^{-1} \left[\sum_e \sum_{t\in e} \left(\frac{\partial \mathbf{r}}{\partial \mathbf{a}}\right)^T \tilde{W}_v \mathbf{r} - \sum_e \sum_{t\in e} \left(\frac{\partial \mathbf{r}}{\partial \mathbf{a}}\right)^T \mathcal{K}^T F_v^T O^{-1} \mathbf{R_v}\right] \tag{A.55}$$

where, as in all the previous sections, one can define a *big-matrix* and two *big-vector* in analogy to the expression 4.40 in section 4.3.2:

$$\tilde{\mathcal{M}}_v = \sum_e \sum_{t\in e} \left(\frac{\partial \mathbf{r}}{\partial \mathbf{a}}\right)^T \tilde{W}_v \frac{\partial \mathbf{r}}{\partial \mathbf{a}}$$

$$\tilde{\nu}_v = \sum_e \sum_{t\in e} \left(\frac{\partial \mathbf{r}}{\partial \mathbf{a}}\right)^T \tilde{W}_v \mathbf{r}$$

$$\tilde{\omega}_v = -\sum_e \sum_{t\in e} \left(\frac{\partial \mathbf{r}}{\partial \mathbf{a}}\right)^T \mathcal{K}^T F_v^T O^{-1} \mathbf{R_v}$$

so, the final solution of the alignment parameters is:

$$\mathbf{a} = \mathbf{a}_0 + \delta\mathbf{a} = \mathbf{a}_0 - \tilde{\mathcal{M}}_v^{-1}(\tilde{\nu}_v + \tilde{\omega}_v) \tag{A.56}$$

As it has been pointed out, this solution looks like the one in section 4.3.2, where a track parameter constraint was considered, although this case is mathematically much more complicated.

A.5 The most general solution for the Globalχ^2 approach

For completeness, the solution of the most general case, i.e. considering the previous constraints all together, will be described in this section. Therefore, the χ^2 in this section will be the basic term from expression 4.3 (where $\mathbf{r} = \mathbf{r}(\boldsymbol{\pi}, \mathbf{v}, \mathbf{a})$) plus all the extra terms considered in previous sections (where the residuals $\mathbf{R}_\pi(\boldsymbol{\pi})$, $\mathbf{R_v}(\mathbf{v})$ and $\mathbf{R_a}(\mathbf{a})$ are considered). Thus, the χ^2 looks like expression 4.58:

$$\chi^2 = \chi^2_{basic} + \chi^2_{trkCons} + \chi^2_{vtxCons} + \chi^2_{alignCons}$$

$$\Downarrow$$

$$\chi^2 = \sum_e \left[\sum_{t\in e} \left[\mathbf{r}^T(\boldsymbol{\pi}, \mathbf{v}, \mathbf{a}) V^{-1} \mathbf{r}(\boldsymbol{\pi}, \mathbf{v}, \mathbf{a}) + \mathbf{R}_\pi^T(\boldsymbol{\pi}) S^{-1} \mathbf{R}_\pi(\boldsymbol{\pi})\right] + \mathbf{R_v}^T(\mathbf{v}) O^{-1} \mathbf{R_v}(\mathbf{v})\right] +$$

$$+\mathbf{R_a}(\mathbf{a})^T G^{-1} \mathbf{R_a}(\mathbf{a})$$

Now, considering the previous residuals and their dependences (see expressions 4.31, A.19 and A.41):

$$d\mathbf{r} = \frac{\partial \mathbf{r}}{\partial \pi} d\pi + \frac{\partial \mathbf{r}}{\partial \mathbf{v}} d\mathbf{v} + \frac{\partial \mathbf{r}}{\partial \mathbf{a}} d\mathbf{a}$$

$$d\mathbf{R}_\pi = \frac{\partial \mathbf{R}_\pi}{\partial \pi} d\pi \quad , \quad d\mathbf{R}_\mathbf{a} = \frac{\partial \mathbf{R}_\mathbf{a}}{\partial \mathbf{a}} d\mathbf{a} \quad , \quad d\mathbf{R}_\mathbf{v} = \frac{\partial \mathbf{R}_\mathbf{v}}{\partial \mathbf{v}} d\mathbf{v}$$

Now, the minimum condition with respect the alignment parameters has to be proposed:

$$\frac{d\chi^2}{d\mathbf{a}} = 0$$

$$\Downarrow$$

$$\sum_e \left[\sum_{t\in e} \left[\left(\frac{d\mathbf{r}}{d\mathbf{a}}\right)^T V^{-1}\mathbf{r} + \left(\frac{d\mathbf{R}_\pi}{d\mathbf{a}}\right)^T S^{-1}\mathbf{R}_\pi \right] + \left(\frac{d\mathbf{R}_\mathbf{v}}{d\mathbf{a}}\right)^T O^{-1}\mathbf{R}_\mathbf{v} \right] + \left(\frac{d\mathbf{R}_\mathbf{a}}{d\mathbf{a}}\right)^T G^{-1}\mathbf{R}_\mathbf{a} = 0 \tag{A.57}$$

As in all the previous sections, the next step is just to replace the total derivatives with the partial ones using the chain rule. All of these expressions have been already discussed in the previous sections (see expressions 4.53, 4.32, 4.57 and 4.46), so one can write:

$$\sum_e \left[\sum_{t\in e} \left[\left(\frac{\partial \mathbf{r}}{\partial \pi}\frac{d\pi}{d\mathbf{a}} + \frac{\partial \mathbf{r}}{\partial \mathbf{a}}\right)^T V^{-1}\mathbf{r} + \left(\frac{\partial \mathbf{R}_\pi}{\partial \pi}\frac{d\pi}{d\mathbf{a}}\right)^T S^{-1}\mathbf{R}_\pi \right] + \left(\frac{\partial \mathbf{r}}{\partial \mathbf{v}}\frac{d\mathbf{v}}{d\mathbf{a}}\right)^T V^{-1}\mathbf{r} + \left(\frac{\partial \mathbf{R}_\mathbf{v}}{\partial \mathbf{v}}\frac{d\mathbf{v}}{d\mathbf{a}}\right)^T O^{-1}\mathbf{R}_\mathbf{v} \right] +$$
$$+ \left(\frac{\partial \mathbf{R}_\mathbf{a}}{\partial \mathbf{a}}\right)^T G^{-1}\mathbf{R}_\mathbf{a} = 0 \tag{A.58}$$

Now, the problem is to obtain the derivatives $d\pi/d\mathbf{a}$ and $d\mathbf{v}/d\mathbf{a}$. One has to calculate the solution of the track parameters and the one for the vertex parameters for any arbitrary alignment parameters, i.e. a χ^2 minimization with respect the track and with respect the vertex parameters has to be done, respectively.

A.5.1 Track fitting for the most general solution

The solution of the track parameters for a given track is really straightforward as the only residuals which contribute are $\mathbf{r}$ and $\mathbf{R}_\pi$. So, the corrections to the solution of track parameters can be written using the results from previous sections, in particular equation 4.37 (and using the definition of F_π from 4.36), but here with $\mathbf{r} = \mathbf{r}(\pi_0, \mathbf{v}, \mathbf{a})$:

$$\delta\pi = -\left(E^T V^{-1} E + F_\pi^T S^{-1} F_\pi\right)^{-1} \left(E^T V^{-1}\mathbf{r}(\pi_0, \mathbf{v}, \mathbf{a}) + F_\pi^T S^{-1}\mathbf{R}_\pi(\pi_0)\right) =$$
$$= -\tilde{\mathcal{M}}_t^{-1} \left(E^T V^{-1}\mathbf{r}(\pi_0, \mathbf{v}, \mathbf{a}) + F_\pi^T S^{-1}\mathbf{R}_\pi(\pi_0)\right) \tag{A.59}$$

where the already defined $E = \partial\mathbf{r}/\partial\pi|_{\pi_0}$ and $F_\pi = \partial\mathbf{R}_\pi/\partial\pi|_{\pi_0}$ have been used (see expressions 4.15 and 4.36) together with $\tilde{\mathcal{M}}_t$ which has been defined to compact the formula (as in section 4.3.1):

$$\tilde{\mathcal{M}}_t \equiv E^T V^{-1} E + F_\pi^T S^{-1} F_\pi$$

Therefore, derivating the solution $\boldsymbol{\pi} = \boldsymbol{\pi}_0 + \delta\boldsymbol{\pi}$, one trivially has one of the requested derivatives:

$$\frac{d\boldsymbol{\pi}}{d\mathbf{a}} = -\tilde{\mathcal{M}}_t^{-1} E^T V^{-1} \left(\frac{\partial \mathbf{r}(\boldsymbol{\pi}_0, \mathbf{v}, \mathbf{a})}{\partial \mathbf{a}} + \frac{\partial \mathbf{r}(\boldsymbol{\pi}_0, \mathbf{v}, \mathbf{a})}{\partial \mathbf{v}} \frac{d\mathbf{v}}{d\mathbf{a}} \right) \tag{A.60}$$

and the following useful derivative:

$$\frac{d\boldsymbol{\pi}}{d\mathbf{v}} = -\tilde{\mathcal{M}}_t^{-1} E^T V^{-1} \frac{\partial \mathbf{r}(\boldsymbol{\pi}_0, \mathbf{v}, \mathbf{a})}{\partial \mathbf{v}} \tag{A.61}$$

where $\partial \mathbf{r}(\boldsymbol{\pi}_0, \mathbf{v}, \mathbf{a})/\partial \boldsymbol{\pi} = 0$ and $\partial \mathbf{R}_\pi(\boldsymbol{\pi}_0)/\partial \boldsymbol{\pi} = 0$.

Once one has these derivatives, the solution for the vertex parameters has to be found to calculate the last required derivative ($d\mathbf{v}/d\mathbf{a}$).

A.5.2 Vertex fitting for the most general solution

To calculate $d\mathbf{v}/d\mathbf{a}$, one has to obtain the solution of the vertex parameters for a given vertex and for any arbitrary alignment parameters, so one can use the expression A.44 but considering that $\mathbf{R}_\pi$ will introduce another term:

$$\frac{d\chi^2}{d\mathbf{v}} = 0 \longrightarrow \sum_{t\in e} \left[\left(\frac{d\mathbf{r}}{d\mathbf{v}} \right)^T V^{-1} \mathbf{r} + \left(\frac{d\mathbf{R}_\pi}{d\mathbf{v}} \right)^T S^{-1} \mathbf{R}_\pi \right] + \left(\frac{d\mathbf{R}_\mathbf{v}}{d\mathbf{v}} \right)^T O^{-1} \mathbf{R}_\mathbf{v} = 0 \tag{A.62}$$

and therefore, using F_π which is already defined:

$$\sum_{t\in e} \left[\left(E \frac{d\boldsymbol{\pi}}{d\mathbf{v}} \right)^T V^{-1} \mathbf{r} + \left(F_\pi \frac{d\boldsymbol{\pi}}{d\mathbf{v}} \right)^T S^{-1} \mathbf{R}_\pi \right] + \left(\frac{\partial \mathbf{r}}{\partial \mathbf{v}} \right)^T V^{-1} \mathbf{r} + \left(\frac{\partial \mathbf{R}_\mathbf{v}}{\partial \mathbf{v}} \right)^T O^{-1} \mathbf{R}_\mathbf{v} = 0 \tag{A.63}$$

Now, instead of develop the full expression step by step, one can compare the later equation with expression A.45, use its results and infer the solution to this equation, just solving the differences, which are the following:

- The first difference is the most trivial one, there is an extra term:

$$\sum_{t\in e} \left[\left(F_\pi \frac{d\boldsymbol{\pi}}{d\mathbf{v}} \right)^T S^{-1} \mathbf{R}_\pi \right]$$

So, considering just this term and introducing equation A.61, this term can be written as:

$$-\sum_{t\in e} \left[\left(F_\pi \tilde{\mathcal{M}}_t^{-1} E^T V^{-1} \frac{\partial \mathbf{r}}{\partial \mathbf{v}} \right)^T S^{-1} \mathbf{R}_\pi \right] = -\sum_{t\in e} \left[\left(F_\pi \tilde{\mathcal{M}}_t^{-1} E^T V^{-1} E_v \right)^T S^{-1} \mathbf{R}_\pi \right] \tag{A.64}$$

where, the definitions $E_v = \partial \mathbf{r}/\partial \mathbf{v}|_{\mathbf{v}_0}$ (see equation A.32) and $\tilde{\mathcal{M}}_t$ have been used.

Now, taking the residual series expansion around the initial values of the vertex parameters ($\mathbf{v}_0$) up to first order from A.46 and also for the new residual $\mathbf{R}_\pi(\boldsymbol{\pi}_0)$ which is simply this value, i.e. $\mathbf{R}_\pi(\boldsymbol{\pi}_0)$, then the previous stays unchanged.

- Focusing in the similarities between expressions A.45 and A.63, one has to point out that now $d\boldsymbol{\pi}/d\mathbf{v}$, i.e. expression A.61, is not exactly the same as expression A.29.

$$\frac{d\boldsymbol{\pi}}{d\mathbf{v}} = -(E^TV^{-1}E)^{-1}E^TV^{-1}\frac{\partial\mathbf{r}}{\partial\mathbf{v}} \longrightarrow \frac{d\boldsymbol{\pi}}{d\mathbf{v}} = -(E^TV^{-1}E + F_\pi^TS^{-1}F_\pi)^{-1}E^TV^{-1}\frac{\partial\mathbf{r}}{\partial\mathbf{v}}$$

This implies that expression A.47, which represents the vertex corrections, holds if one changes W with W' (already defined and used in section 4.3.2) accordingly with the previous difference, where:

$$\begin{aligned} W' &\equiv V^{-1} - V^{-1}E(E^TV^{-1}E + F_\pi^TS^{-1}F_\pi)^{-1}E^TV^{-1} = \\ &= V^{-1} - V^{-1}E\tilde{\mathcal{M}}_tE^TV^{-1} = (I - V^{-1}E\tilde{\mathcal{M}}_tE^T)V^{-1} \end{aligned}$$

Then, expression A.47 is rewritten here as:

$$\delta\mathbf{v} = -\left[\sum_{t\in e} E_v^TW'E_v + F_v^TO^{-1}F_v\right]^{-1}\left(\sum_{t\in e} E_v^TW'\mathbf{r} + F_v^TO^{-1}\mathbf{R}_\mathbf{v}\right) \tag{A.65}$$

Now, collecting up the two previous results, i.e. A.64 and A.65, one can easily write the corrections $\delta\mathbf{v}$:

$$\delta\mathbf{v} = -\left[\sum_{t\in e} E_v^TW'E_v + F_v^TO^{-1}F_v\right]^{-1}\left(\sum_{t\in e}\left[E_v^TW'\mathbf{r} - E_v^TV^{-1}E\tilde{\mathcal{M}}_t^{-1}F_\pi^TS^{-1}\mathbf{R}_\pi\right] + F_v^TO^{-1}\mathbf{R}_\mathbf{v}\right)$$

where, once more, one has abused of the notation because $\mathbf{r}$, $\mathbf{R}_\pi$ and $\mathbf{R}_\mathbf{v}$ mean in fact $\mathbf{r}(\boldsymbol{\pi}_0, \mathbf{v}_0, \mathbf{a})$, $\mathbf{R}_\pi(\boldsymbol{\pi}_0)$ and $\mathbf{R}_\mathbf{v}(\mathbf{v}_0)$.

So, derivating the solution of the vertex parameters, i.e. $\mathbf{v} = \mathbf{v}_0 + \delta\mathbf{v}$, with respect the alignment parameters one obtains:

$$\frac{d\mathbf{v}}{d\mathbf{a}} = -\left[\sum_{t\in e} E_v^TW'E_v + F_v^TO^{-1}F_v\right]^{-1}\sum_{t\in e} E_v^TW'\frac{\partial\mathbf{r}}{\partial\mathbf{a}} = -\mathcal{M}_\mathbf{v}^{-1}\sum_{t\in e} E_v^TW'\frac{\partial\mathbf{r}}{\partial\mathbf{a}} \tag{A.66}$$

where $\mathcal{M}_\mathbf{v}^{-1}$ has been introduce in order to establish a parallelism with the results in [71]. Obviously, this matrix represents the covariance matrix of the final vertex parameters, as it has been emphasized in similar results.

$$\mathcal{M}_\mathbf{v}^{-1} \equiv \left[\sum_{t\in e} E_v^TW'E_v + F_v^TO^{-1}F_v\right]^{-1}$$

Note that wanted derivative, expression A.66, is at the end the same expression as A.51 but now with $W' = (I - V^{-1}E\tilde{\mathcal{M}}_tE^T)V^{-1}$ instead of $W = (I - V^{-1}E\mathcal{M}_t^{-1}E^T)V^{-1}$.

A.5.3 Alignment corrections for the most general solution

Reached to this point, one can introduce A.60 and A.66 in A.58 to calculate the final solution for the alignment parameters just using matrix manipulation methods. But before doing this a new term called α will be introduced in order to be consistent with the reference [71]:

$$\alpha \equiv \frac{\partial \mathbf{r}}{\partial \mathbf{a}} + E_{\mathbf{v}} \frac{d\mathbf{v}}{d\mathbf{a}}$$

Thus, one can write expression A.60 using this α:

$$\frac{d\pi}{d\mathbf{a}} = -\tilde{\mathcal{M}}_t^{-1} E^T V^{-1} \alpha$$

So, starting from expression A.58:

$$\sum_e \left[\sum_{t\in e} \left[\left(E\frac{d\pi}{d\mathbf{a}} + \frac{\partial \mathbf{r}}{\partial \mathbf{a}} \right)^T V^{-1}\mathbf{r} + \left(F_\pi \frac{d\pi}{d\mathbf{a}} \right)^T S^{-1} \mathbf{R}_\pi \right] + \left(E_\mathbf{v} \frac{d\mathbf{v}}{d\mathbf{a}} \right)^T V^{-1}\mathbf{r} + \left(F_\mathbf{v} \frac{d\mathbf{v}}{d\mathbf{a}} \right)^T O^{-1} \mathbf{R}_\mathbf{v} \right] +$$
$$+ F_\mathbf{a}^T G^{-1} \mathbf{R}_\mathbf{a} = 0 \tag{A.67}$$

Now, as this expression is quite complicated, it is easier to consider firstly just the terms which come with $\mathbf{r}$:

$$\sum_e \left[\sum_{t\in e} \left(E\frac{d\pi}{d\mathbf{a}} + \frac{\partial \mathbf{r}}{\partial \mathbf{a}} \right)^T V^{-1}\mathbf{r} + \left(E_\mathbf{v} \frac{d\mathbf{v}}{d\mathbf{a}} \right)^T V^{-1}\mathbf{r} \right] =$$
$$= \sum_e \left[\sum_{t\in e} \left(-E\tilde{\mathcal{M}}_t^{-1} E^T V^{-1} \frac{\partial \mathbf{r}}{\partial \mathbf{a}} + \frac{\partial \mathbf{r}}{\partial \mathbf{a}} \right)^T V^{-1}\mathbf{r} + \sum_{t\in e} \left(-E\tilde{\mathcal{M}}_t^{-1} E^T V^{-1} E_\mathbf{v} \frac{d\mathbf{v}}{d\mathbf{a}} \right)^T V^{-1}\mathbf{r} + \left(E_\mathbf{v} \frac{d\mathbf{v}}{d\mathbf{a}} \right)^T V^{-1}\mathbf{r} \right] =$$
$$= \sum_e \left[\sum_{t\in e} \left(\frac{\partial \mathbf{r}}{\partial \mathbf{a}} \right)^T W'\mathbf{r} + \sum_{t\in e} \left(-E\tilde{\mathcal{M}}_t^{-1} E^T V^{-1} E_\mathbf{v} \frac{d\mathbf{v}}{d\mathbf{a}} + E_\mathbf{v} \frac{d\mathbf{v}}{d\mathbf{a}} \right)^T V^{-1}\mathbf{r} \right] =$$
$$= \sum_e \left[\sum_{t\in e} \left(\frac{\partial \mathbf{r}}{\partial \mathbf{a}} \right)^T W'\mathbf{r} + \sum_{t\in e} \left(E_\mathbf{v} \frac{d\mathbf{v}}{d\mathbf{a}} \right)^T W'\mathbf{r} \right] = \sum_e \sum_{t\in e} \alpha^T W'\mathbf{r}$$

And introducing this result in the previous expression, one has:

$$\sum_e \left[\sum_{t\in e} \left[\alpha^T W'\mathbf{r} + \left(F_\pi \frac{d\pi}{d\mathbf{a}} \right)^T S^{-1} \mathbf{R}_\pi \right] + \left(F_\mathbf{v} \frac{d\mathbf{v}}{d\mathbf{a}} \right)^T O^{-1} \mathbf{R}_\mathbf{v} \right] + F_\mathbf{a}^T G^{-1} \mathbf{R}_\mathbf{a} = 0 \tag{A.68}$$

One would continue with the derivative replacement in the rest of the terms, but to be consistent with the final result shown in [71], no more replacements will be done for the moment.

Then, in order to solve this equation, a series expansion is required around the initial values of the alignment parameters ($\mathbf{a}_0$). In this section, as there are only two residuals, $\mathbf{r}$ and $\mathbf{R}_\mathbf{a}$, which depend on the alignment parameters, they are the ones to be expanded:

$$\mathbf{r}(\pi, \mathbf{v}, \mathbf{a}) = \mathbf{r}(\pi_0, \mathbf{v}_0, \mathbf{a}_0) + \left.\frac{\partial \mathbf{r}}{\partial \mathbf{a}}\right|_{\mathbf{a}_0} \delta\mathbf{a} \quad \text{where} \quad \frac{\partial^n \mathbf{r}}{\partial \mathbf{a}^n} = 0 \quad \text{with} \quad n \geq 2$$

$$\mathbf{R_a}(\mathbf{a}) = \mathbf{R_a}(\mathbf{a}_0) + F_{\mathbf{a}}\delta\mathbf{a} \quad \text{where} \quad \frac{\partial^n \mathbf{R}}{\partial \mathbf{a}^n} = 0 \quad \text{with} \quad n \geq 2$$

Thus, the previous equation looks now like this:

$$\sum_e \sum_{t\in e} \alpha^T W' \frac{\partial \mathbf{r}}{\partial \mathbf{a}} \delta\mathbf{a} + F_{\mathbf{a}}^T G^{-1} \mathbf{R_a} \delta\mathbf{a} +$$

$$+ \sum_e \left[\sum_{t\in e} \left[\alpha^T W' \mathbf{r} + \left(F_\pi \frac{d\boldsymbol{\pi}}{d\mathbf{a}} \right)^T S^{-1} \mathbf{R}_\pi \right] + \left(F_{\mathbf{v}} \frac{d\mathbf{v}}{d\mathbf{a}} \right)^T O^{-1} \mathbf{R_v} \right] + F_{\mathbf{a}}^T G^{-1} \mathbf{R_a} = 0 \tag{A.69}$$

where $\mathbf{r} = \mathbf{r}(\boldsymbol{\pi}_0, \mathbf{v}_0, \mathbf{a}_0)$, $\mathbf{R}_\pi = \mathbf{R}_\pi(\boldsymbol{\pi}_0)$, $\mathbf{R_v} = \mathbf{R_v}(\mathbf{v}_0)$, $\mathbf{R_a} = \mathbf{R_a}(\mathbf{a}_0)$.
Therefore, the alignment corrections are:

$$\delta\mathbf{a} = - \left[\sum_e \sum_{t\in e} \alpha^T W' \frac{\partial \mathbf{r}}{\partial \mathbf{a}} + F_{\mathbf{a}}^T G^{-1} \mathbf{R_a} \right]^{-1} \cdot$$

$$\cdot \sum_e \left[\sum_{t\in e} \left[\alpha^T W' \mathbf{r} + \left(F_\pi \frac{d\boldsymbol{\pi}}{d\mathbf{a}} \right)^T S^{-1} \mathbf{R}_\pi \right] + \left(F_{\mathbf{v}} \frac{d\mathbf{v}}{d\mathbf{a}} \right)^T O^{-1} \mathbf{R_v} \right] + F_{\mathbf{a}}^T G^{-1} \mathbf{R_a}$$

In other words:

$$\delta\mathbf{a} = -\mathcal{M}_{\text{mg}}^{-1} \nu_{\text{mg}}$$

where, the *big-matrix* for the most general case is:

$$\mathcal{M}_{\text{mg}} = \sum_e \sum_{t\in e} \alpha^T W' \frac{\partial \mathbf{r}}{\partial \mathbf{a}} + F_{\mathbf{a}}^T G^{-1} \mathbf{R_a} \tag{A.70}$$

and the *big-vector* for the most general case is:

$$\nu_{\text{mg}} = \sum_e \left[\sum_{t\in e} \left[\alpha^T W' \mathbf{r} + \left(F_\pi \frac{d\boldsymbol{\pi}}{d\mathbf{a}} \right)^T S^{-1} \mathbf{R}_\pi \right] + \left(F_{\mathbf{v}} \frac{d\mathbf{v}}{d\mathbf{a}} \right)^T O^{-1} \mathbf{R_v} \right] + F_{\mathbf{a}}^T G^{-1} \mathbf{R_a} \tag{A.71}$$

In order to compare the *big-matrix* from expression A.70 and the one defined in [71], one has to take into account the following identity:

$$\sum_e \sum_{t\in e} \alpha^T W \alpha = \sum_e \sum_{t\in e} \left[\alpha^T W \frac{\partial \mathbf{r}}{\partial \mathbf{a}} - \left(\frac{d\mathbf{v}}{d\mathbf{a}} \right)^T O^{-1} \frac{d\mathbf{v}}{d\mathbf{a}} \right]$$

To finish, it is worth to point out the fact that this *big-matrix* is also the covariance matrix for the alignment corrections as it was demonstrated for the track parameters corrections in section 4.2.2.1.

B

Applications of constraints within the Globalχ^2 formalism for alignment

Once the theory of the method have been proposed in chapter 4.1, some particular applications should be detailed, as they have been already implemented in the Globalχ^2 code. The goal of this appendix is to discuss briefly the applications where the track parameters and the alignment parameters are constrained. This is done is sections B.1.1 and B.2, respectively.

B.1 Applications of track parameters constraints

This section will discuss how the track parameters are constrained to the truth (of course, just for simulations), to the beam spot (even without an explicit beam spot determination), to an external tracking system (external momentum determination thanks to the TRT or to the Muon Chambers) or to physical observables (using mass resonances, charge symmetries, etc...).

B.1.1 Track Parameters constrained on external models

The simplest case is to consider a residual like $\mathbf{R}_\pi(\boldsymbol{\pi}) = (\boldsymbol{\pi} - \hat{\boldsymbol{\pi}})$ where $\hat{\boldsymbol{\pi}}$ would be external tracker measurements, estimations or even assumptions (as could be the true track parameters) and $\boldsymbol{\pi}$ means the original tracks measured with the devices to be align (in our case the ATLAS Silicon Tracker). Considering the tracks with its helix parameters representation, $\mathbf{R}_\pi$ reads as follows:

$$\mathbf{R}_\pi(\boldsymbol{\pi}) = \begin{pmatrix} d_0 - \widehat{d_0} \\ z_0 - \widehat{z_0} \\ \phi_0 - \widehat{\phi_0} \\ \cot\theta - \widehat{\cot\theta} \\ q/p_T - \widehat{q/p_T} \end{pmatrix} \tag{B.1}$$

where, of course, the track parameters $\boldsymbol{\pi}$ are considered as independent.

Moreover, if one considers the $\boldsymbol{\pi}$ dependence as $\boldsymbol{\pi} + \varepsilon$, where ε is just a matrix with track parameter offsets, one introduces a bias in the corresponding track parameter contraint which can be again very useful for testing purposes.

The covariance matrix will look like this one:

$$S^{-1} = \begin{pmatrix} 1/\sigma^2_{d_0} & 0 & 0 & 0 & 0 \\ 0 & 1/\sigma^2_{z_0} & 0 & 0 & 0 \\ 0 & 0 & 1/\sigma^2_{\phi_0} & 0 & 0 \\ 0 & 0 & 0 & 1/\sigma^2_{\cot\theta} & 0 \\ 0 & 0 & 0 & 0 & 1/\sigma^2_{q/p_T} \end{pmatrix}$$

where correlation factor ρ is null for the off-diagonal values and the unit for the diagonal values (i.e. $\rho_{ii} = 1$ and $\rho_{ij} = 0$ if $i \neq j$). Its dimension is $[N_{TPR} \times N_{TPR}]$. In this matrix, σ_π is the error on the determination of the corresponding track parameter. One can even add a weight factor (ς) to the covariance matrix, something like $S^{-1} \to \varsigma S^{-1}$. This is useful for testing purposes since it allows an overweighting or an underweighting of this constraint.

The mathematical problem is simpler in this case because $\partial\mathbf{R}_\pi/\partial\boldsymbol{\pi}$ is the identity matrix:

$$F_\pi = \frac{\partial\mathbf{R}_\pi}{\partial\boldsymbol{\pi}} = \frac{\partial(\boldsymbol{\pi} - \hat{\boldsymbol{\pi}})}{\partial\boldsymbol{\pi}} = \frac{\partial\boldsymbol{\pi}}{\partial\boldsymbol{\pi}} = \begin{pmatrix} \frac{\partial d_0}{\partial d_0} & \frac{\partial d_0}{\partial z_0} & \frac{\partial d_0}{\partial \phi_0} & \frac{\partial d_0}{\partial \cot\theta} & \frac{\partial d_0}{\partial q/p_T} \\ \frac{\partial z_0}{\partial d_0} & \frac{\partial z_0}{\partial z_0} & \frac{\partial z_0}{\partial \phi_0} & \frac{\partial z_0}{\partial \cot\theta} & \frac{\partial z_0}{\partial q/p_T} \\ \frac{\partial \phi_0}{\partial d_0} & \frac{\partial \phi_0}{\partial z_0} & \frac{\partial \phi_0}{\partial \phi_0} & \frac{\partial \phi_0}{\partial \cot\theta} & \frac{\partial \phi_0}{\partial q/p_T} \\ \frac{\partial \cot\theta}{\partial d_0} & \frac{\partial \cot\theta}{\partial z_0} & \frac{\partial \cot\theta}{\partial \phi_0} & \frac{\partial \cot\theta}{\partial \cot\theta} & \frac{\partial \cot\theta}{\partial q/p_T} \\ \frac{\partial q/p_T}{\partial d_0} & \frac{\partial q/p_T}{\partial z_0} & \frac{\partial q/p_T}{\partial \phi_0} & \frac{\partial q/p_T}{\partial \cot\theta} & \frac{\partial q/p_T}{\partial q/p_T} \end{pmatrix} = I \tag{B.2}$$

Considering, then, all the previous arguments, the formulas can be written as:

$$\mathcal{G}_{EF_\pi} = (E^T V^{-1} E + S^{-1})^{-1} E^T V^{-1}$$

and finally, the new *big-vector*:

$$\omega_\pi = -\sum_e \sum_{t \in e} \left(\frac{\partial\mathbf{r}}{\partial\mathbf{a}}\right)^T \mathcal{G}^T_{EF_\pi} S^{-1} \mathbf{R}_\pi = 0$$

therefore, the implementation of this kind of constraints is very straightforward.

In the Globalχ^2 there are several flavours of this kind of constraints:

- The MC information can be used to constrain the track parameters when running over simulated (for testing purposes, this could be quite useful to study the right convergence of the algorithm). In this case, $\hat{\pi}$ are simply the track parameter values from the truth.

- The Beam Spot information can also be used to constrain the track parameters if one considers the impact parameter (specially the transverse one) as a function of the beam spot parameters [100] [40]. So, one can write:

$$d_0 = -(x_{BS} + z_0\alpha_{BS})\, sin\phi_0 + (y_{BS} - z_0\beta_{BS})\, cos\phi_0 \tag{B.3}$$

  where x_{BS} and y_{BS} are the two global coordinates of the Beam Spot (BS) and α_{BS} and β_{BS} are the tilts with respect the X and Y axis of the global coordinates system of the BS.

  In this case, d_0 and ϕ_0 are correlated and therefore $\partial\mathbf{R}_\pi/\partial\boldsymbol{\pi}$ is not the identity matrix anymore (as it was in B.2):

$$F_\pi = \frac{\partial\mathbf{R}_\pi}{\partial\boldsymbol{\pi}} = \begin{pmatrix} 1 & \frac{\partial d_0}{\partial z_0} & \frac{\partial d_0}{\partial \phi_0} & 0 & 0 \\ 0 & 1 & 0 & 0 & 0 \\ 0 & 0 & 1 & 0 & 0 \\ 0 & 0 & 0 & 1 & 0 \\ 0 & 0 & 0 & 0 & 1 \end{pmatrix}$$

  where these off-diagonal derivatives should be properly calculated:

$$\frac{\partial d_0}{\partial z_0} = -\alpha_{BS}\, sin\phi_0 - \beta_{BS}\, cos\phi_0$$

$$\frac{\partial d_0}{\partial \phi_0} = -(x_{BS} + z_0\alpha_{BS})\, cos\phi_0 - (y_{BS} - z_0\beta_{BS})\, sin\phi_0$$

  One could also consider to constrain the track parameter z_0 to the z coordinate of the beam spot although due to the poor resolution it is not recommended.

  This constraint will be discussed in the next chapter as well as its results.

- Finally, in the Globalχ^2 code, it is possible to constrain the momentum (specifically q/p) to the TRT momentum. In that sense, the $\widehat{q/p}$ value in the residual from expression B.1 should come from the reconstructed momentum using just the TRT and q/p should be the reconstructed momentum using the Silicon Tracker. Also the $\sigma_{q/p}$ has to be changed to include the error on the momentum determination with the TRT. By doing this, one has also to consider the correlations between the TRT q/p and the silicon z_0 and θ.

  Another possibility could be to use the calorimetry information, in particular, one could use the E/P measurement to constraint the the momentum of the silicon tracks (or the ID tracks) but this feature is not yet implemented in the Globalχ^2 code.

B.1.2 Track Parameters constrained on physical observables

One can envisage the use of some physical samples that allow to apply constraints on track parameters thanks to its event observables. The idea is to constraint on the mass of a known resonance, for instance the Z or the J/Ψ resonances can be used through their decays $Z \to \mu^+\mu^-$ and $J/\Psi \to \mu^+\mu^-$, respectively. Of course, the reconstructed muons will be the ones used to define the extra χ^2 term as defined in 4.30. In other words, one can introduce an event constraint which requires that the invariant mass of the muon pair has to be compatible with the Z or J/Ψ mass. In general, the extra χ^2 term will be:

$$\chi^2_{trkCons} = \sum_e \left(\frac{m_{reco} - M_{reso}}{\sigma_{reso}} \right)^2$$

being M_{reso} the mass of the resonance and σ_{reso} the experimental resolution on the mass[1] of this resonance and m_{reco} the invariant mass of the reconstructed products in each event, and the sum extends to all the events in the sample. Moreover one can use the matrix notation for the above expression which after defining the covariance matrix S^{-1} as $1/\sigma^2_{reso}$ becomes:

$$\chi^2_{trkCons} = \sum_e \mathbf{R}_\pi^T(\pi) S^{-1} \mathbf{R}_\pi(\pi) = \sum_e (m_{reco} - M_{reso})^T S^{-1} (m_{reco} - M_{reso})$$

where, generally, $\mathbf{R}_\pi = (m_{reco} - M_{reso})$ will be a vector of size N_{PHYS} and S will be a diagonal matrix of dimension $[N_{PHYS} \times N_{PHYS}]$

Furthermore, one can introduce more constrains as for instance that both muons in the event should be generated in the same space point, and due to the extremely short life of the resonance it must be the collision point where the primary vertex is. Therefore, both impact parameters: transversal (d_0) and longitudinal (z_0) of both muons should be distributed accordingly to the intrinsic resolution in each parameter (σ_{d_0} and σ_{z_0}). Therefore, one can define a sort of residual vector for event related observables. Considering the Z resonance, one has:

$$\mathbf{R}_\pi = \begin{pmatrix} m_{\mu\mu} - M_Z \\ d_0(\mu^+) - d_0(\mu^-) \\ z_0(\mu^+) - z_0(\mu^-) \end{pmatrix}$$

where and a sort of covariance matrix S that in this particular case may look something like:

$$S = \begin{pmatrix} \sigma_Z^2 & 0 & 0 \\ 0 & \sigma_{d_0}^2 & 0 \\ 0 & 0 & \sigma_{z_0}^2 \end{pmatrix} \Rightarrow S^{-1} = \begin{pmatrix} 1/\sigma_Z^2 & 0 & 0 \\ 0 & 1/\sigma_{d_0}^2 & 0 \\ 0 & 0 & 1/\sigma_{z_0}^2 \end{pmatrix}$$

with all the off-diagonal elements being null.

Finally, in the formulas of section 4.3 one has to identify:

[1]The experimental resolution of the resonance mass (σ_{reso}) has to be properly calculated as the quadratic sum of the decay width of the resonance (σ_{width}), which should be estimated (it is not Γ_{reso}) and the experimental error on the reconstructed invariant mass (σ_{reco}) from the decay particles:

$$\sigma_{reso} = \sqrt{\sigma^2_{reco} + \sigma^2_{width}}$$

$$F_\pi \equiv \left.\frac{\partial \mathbf{R}_\pi}{\partial \pi}\right|_{\pi_0} = \left.\frac{\partial m_{reco}}{\partial \pi}\right|_{\pi_0}$$

and then, expression 4.44 is the final solution of the alignment parameters using this constraint.

It is worth to say that these kind constraints are not yet officially implemented in the Globalχ^2 nowadays although they have been already tested [150].

B.1.3 Track Parameters constrained on the q/p symmetries

One can also impose a constraint considering the symmetry between positive and negative tracks. In this case, the extra χ^2 will contain residuals built as the sum of all the track parameters, in particular all the q/p parameters. Then, the χ^2 will look like this:

$$\chi^2 = \sum_e \sum_{t\in e} \mathbf{r}^T(\pi, \mathbf{a}) V^{-1} \mathbf{r}(\pi, \mathbf{a}) + \mathbf{R}_\pi^T(\pi_1, ..., \pi_N) S^{-1} \mathbf{R}_\pi(\pi_1, ..., \pi_N) \tag{B.4}$$

where the $\mathbf{R}_\pi$ is built as a linear combination of each track parameters for all tracks:

$$\mathbf{R}_\pi(\pi_1, \pi_2, ..., \pi_N) \equiv \sum_e \sum_{t\in e}^{N} \mathbb{C}\boldsymbol{\pi} = \sum_e \sum_{t\in e}^{N} \pi \tag{B.5}$$

where $\mathbb{C}$ is a matrix which can introduce correlations between different track parameters although in this particular implementation it is the identity matrix, $\mathbb{C} = I$ in this case.

Moreover, $\mathbf{R}_\pi$ is going to be defined as a column vector of dimension $[N_{BIN} \times 1]$ where N_{BIN} are the number of bins. These bins will allow to establish the behaviour of the reconstructed momentum at different energies:

$$\mathbf{R}_\pi = \begin{pmatrix} \mathbf{R}_1 \\ \mathbf{R}_2 \\ \vdots \\ \mathbf{R}_{N_{BIN}} \end{pmatrix}$$

For instance, one could expect the same number of positive and negative charged particles in a given momentum range in a particular sample[2].

Then, the covariance matrix S is then a symmetric matrix $[N_{BIN} \times N_{BIN}]$.

$$d\mathbf{R}_\pi = \sum_e \sum_{t\in e} \frac{\partial \mathbf{R}_\pi}{\partial \pi} d\boldsymbol{\pi} \tag{B.6}$$

and S should be statistics dependent, so:

$$S = \frac{1}{\sqrt{N}} S_0$$

[2]This is a thorny topic because as in the LHC one will have p-p collisions, there would be some bias towards positive charges.

Then, equation 4.38 is still valid, where S_0 is a template covariance matrix with the intrinsic momentum resolution of each considered bin (or energy range) and N is the total number of tracks (total statistics).

$$\frac{d\mathbf{R}_\pi}{d\mathbf{a}} = \sum_e \sum_{t\in e} \frac{\partial \mathbf{R}_\pi}{\partial \pi} \frac{d\pi}{d\mathbf{a}} \quad \text{and} \quad \frac{d\mathbf{R}_\pi}{d\pi} = \sum_e \sum_{t\in e} \frac{\partial \mathbf{R}_\pi}{\partial \pi} \tag{B.7}$$

where $d\mathbf{R}_\pi/d\mathbf{a}$ is a matrix of dimension $[N_{BIN} \times N_{ALI}]$ and $d\mathbf{R}_\pi/d\pi$ is another matrix of dimension $[N_{BIN} \times N_{TPR}]$

For a given track, $S = S_0$:

$$\frac{d\pi}{d\mathbf{a}} = -\left(E^T V^{-1} E + F_\pi^T S_0^{-1} F_\pi\right)^{-1} \left(E^T V^{-1} \frac{\partial \mathbf{r}}{\partial \mathbf{a}}\right) \tag{B.8}$$

Note, that one do not need $\mathbf{R}_\pi$ to evaluate $d\pi/d\mathbf{a}$ because it is done by track, $F_\pi = (\partial \mathbf{R}_\pi)_i/(\partial \pi)_i = q_i$, being i the considered track.

Then, one ends up with the same M_π and ν_π from expressions 4.41 and 4.42 respectively, and the extra ω_π in equation 4.43 can be written as:

$$\omega_\pi = -\left(\sum_e \sum_{t\in e} \left(\frac{\partial \mathbf{r}}{\partial \mathbf{a}}\right)^T (F_\pi \mathcal{G}_{EF_\pi})^T\right) S^{-1} \mathbf{R}_\pi = 0 \tag{B.9}$$

where $\mathbf{R}_\pi$ and S^{-1} can be built considering the full statistics.

B.2 Applications of the alignment parameters constraints

The applications of this kind of constraint are basically two: constrain the alignment parameters to the survey data and introduce penalty terms to the alignment parameters. Both constraints have been used in the Globalχ^2 method and are commented below.

B.2.1 Survey measurements as constraints

An important application for a χ^2 with the alignment parameters constrained is when the information obtained from the detector survey is considered. In section B.2.1 the survey measurements of the Pixel and SCT detectors were presented, so this information could be implemented here. In that sense, if survey measurements are done at module level, being all its DoF measured independent, the constraints can be added straightforward with the following extra χ^2 term (another possibility is when the survey measurements of the structures are converted to module positions):

$$\chi^2_{survey} = (\mathbf{a} - \hat{\mathbf{a}})^T G^{-1}_{survey} (\mathbf{a} - \hat{\mathbf{a}}) \tag{B.10}$$

where $\mathbf{R_a} = (\mathbf{a} - \hat{\mathbf{a}})$ is the residual, $\hat{\mathbf{a}}$ represents the survey measurement and $\mathbf{a}$ is the alignment paramater to be determined. In this situation:

$$\frac{d\mathbf{R_a}}{d\mathbf{a}} = \frac{\partial \mathbf{R_a}}{\partial \mathbf{a}} = I$$

The covariance matrix G accounts the uncertainty in the survey measurements, considering all the measurement correlations due to common physical anchors between modules. Therefore, expressions 4.48 and 4.49 can be written as:

$$\mathcal{M}_{\mathbf{a}} = G^{-1}_{survey} \quad \text{and} \quad \nu_{\mathbf{a}} = G^{-1}_{survey}(\mathbf{a}_0 - \hat{\mathbf{a}}) \tag{B.11}$$

Anyhow, sometimes, the survey measurements are expressed as linear combination of the modules (or structures) DoF, i.e. $\mathbf{R_a}(\mathbb{C}\mathbf{a})$ where $\mathbb{C}$ is a $[N_{ALI} \times N_{ALI}]$ matrix which introduces the correlations.

$$\chi^2_{survey} = \mathbf{R_a}(\mathbb{C}\mathbf{a})^T G^{-1}_{survey} \mathbf{R_a}(\mathbb{C}\mathbf{a}) \tag{B.12}$$

where, generally, G^{-1}_{survey} will not be diagonal anymore and $d\mathbf{R_a}/d\mathbf{a}$ will not be the identity matrix:

$$\frac{d\mathbf{R_a}}{d\mathbf{a}} = \frac{\partial \mathbf{R_a}}{\partial \mathbf{a}} = \frac{\partial \mathbb{C}\mathbf{a}}{\partial \mathbf{a}} = \mathbb{C}$$

So, expressions 4.48 and 4.49 read as:

$$\mathcal{M}_{\mathbf{a}} = \mathbb{C}^T G^{-1}_{survey} \mathbb{C} \quad \text{and} \quad \nu_{\mathbf{a}} = \mathbb{C}^T G^{-1}_{survey}(\mathbf{a}_0 - \hat{\mathbf{a}}) \tag{B.13}$$

Obviously, when $\mathbb{C} = I$, the results from B.11 are recovered.

This formalism is equivalent to the fact the one could start the alignment procedure form the survey values without this extra χ^2 term instead of from the nominal positions using this constraint, i.e. $\mathbf{a}_0 = \hat{\mathbf{a}}$ using the χ^2 from expression 4.3.

Anyhow, the problem is not as simple since the survey measurements involve combinations of alignment parameters where relative positions and a mixture of structures are measured, such as relative position differences between modules, staves, barrels or discs. Therefore, the problem is how one can translate these complex measurements to individual DoF of each module. In the ATLAS Silicon Tracker case, survey data exists for the SCT End-Cap and for the Pixel detector (Barrel and End-Cap), being the End-Cap data more precise (see table 3.5). This problem is widely discussed in reference [55].

It is not yet clear how useful the survey data is for a real application in the alignment procedure. For instance, Pixel and SCT survey measurements were recorded while detector was at a much higher temperature than at which it will be operated for data taking. Another important issue, specially for the SCT, is the fact that the detectors might have moved during installation. Up to now, the Pixel survey data has been used as the start-up geometry for a Silicon Tracker alignment based on cosmic rays. This will be discussed on chapter 7.

B.2.2 Alignment parameters constrained using χ^2 penalty terms

It is also possible to add constraints to the alignment parameters in such a way that they represent χ^2-penalties, also known as *softmode cuts*. In this case, the residuals are just $\mathbf{R_a} = (\mathbf{a} - \mathbf{a}_0) = \delta\mathbf{a}$ and the covariance matrix is $G^{-1}_{penalty} = 1/\sigma^2_{penalty}$ which is diagonal. With these residuals:

$$\frac{d\mathbf{R_a}}{d\mathbf{a}} = \frac{\partial \mathbf{R_a}}{\partial \mathbf{a}} = I$$

therefore, expressions 4.48 and 4.49 can be written as:

$$\mathcal{M}_{\mathbf{a}} = G^{-1}_{penalty} \quad \text{and} \quad \nu_{\mathbf{a}} = 0 \tag{B.14}$$

where $\nu_{\mathbf{a}} = 0$ because $\mathbf{R_a}(\mathbf{a}_0) = (\mathbf{a}_0 - \mathbf{a}_0) = 0$. This means that implementing this constraint is trivial, and the final solution is just the same as without constraint but where a diagonal matrix ($G^{-1}_{penalty}$) has been added to $\mathcal{M}$:

$$\mathbf{a} = \mathbf{a}_0 + \delta\mathbf{a} = \mathbf{a}_0 - \left(\mathcal{M} + G^{-1}_{penalty}\right)^{-1} \nu \tag{B.15}$$

Moreover, one can consider to apply this penalties to combinations of the alignment parameters, for instance, one could constraint the same rotation for two discs in an end-cap. This extension is also almost trivial because just a correlation matrix (with dimension $[N_{ALI} \times N_{ALI}]$) has to be introduce: $\mathbf{R_a}(\mathbb{C}\mathbf{a})$. With this add-on (as in the previous case) one has:

$$\frac{d\mathbf{R_a}}{d\mathbf{a}} = \frac{\partial \mathbf{R_a}}{\partial \mathbf{a}} = \frac{\partial \mathbb{C}\mathbf{a}}{\partial \mathbf{a}} = \mathbb{C}$$

and therefore the final solution is simply:

$$\mathbf{a} = \mathbf{a}_0 + \delta\mathbf{a} = \mathbf{a}_0 - \left(\mathcal{M} + \mathbb{C}^T G^{-1}_{penalty} \mathbb{C}\right)^{-1} \nu \tag{B.16}$$

Again, when $\mathbb{C} = I$, the results from B.14 are recovered.

These kind of constraints are very useful and used to solve ill-defined or explicit singular problems as they fill te diagonal matrix elements. This topic will be explained in section 5.3 of the next chapter.

C

Computing the projection matrix for aligning structures

In section 5.2.1, the projection matrix $\partial\mathbf{a}/\partial\mathbf{A}$ is given in order to compute the alignment corrections of the structures where the modules are assembled. This appendix contains the full mathematical development.

C.1 The generic projection

It is obvious that $\partial\mathbf{a}/\partial\mathbf{A}$ represents how the local alignment parameters $\mathbf{a}$ of a module vary due to the global movements $\mathbf{A}$ of the supporting structure in which the module is mounted. No need to say that if a module is not mounted in a supporting structure then $\partial\mathbf{a}/\partial\mathbf{A} = 0$. Let's consider a local to global transformation which will account for the projection of the residuals given in the local frame into the global frame. Thus, $\mathbf{H}_M$ will be a general operator that transforms a space point from the local module system ($\vec{l}$) to the global reference system ($\vec{\mathcal{G}}$) (see figure C.1):

$$\vec{\mathcal{G}} = \mathbf{H}_M \vec{l}$$

For a given module, $\mathbf{H}_M$ is given by the translation of its origin and rotation of its axis (i.e. its local frame) with respect to the global frame: $\mathbf{H}_M = [\mathbf{T_0},\ \mathbf{R}(\alpha,\beta,\gamma)]$, being $\mathbf{T} = (x_0,\ y_0,\ z_0)$ (i.e. the origin of the local module frame) and α being the rotation around the local x axis, β around local y axis and γ around the local z axis.

Imagine, now, a shift in the local frame of the module which is generally represent by new alignment corrections. Then, the goal is to find the size of the shifts in the local reference frame ($\mathbf{H}_{\delta\mathbf{a}}$) so the new module position ($\mathbf{H}'_M$) can be given as:

$$\mathbf{H}'_M = \mathbf{H}_M \otimes \mathbf{H}_{\delta\mathbf{a}}$$

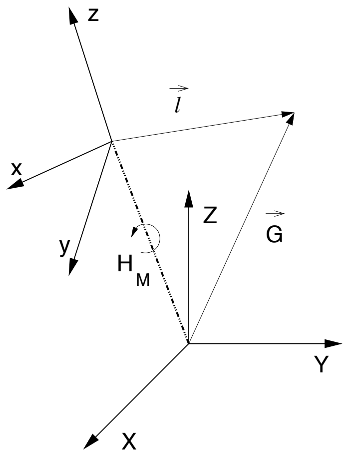

Figure C.1: *Change of reference system. A given point in the global reference frame is denoted by the vector $\vec{\mathcal{G}}$, whilst the same point seen from a local reference point is $\vec{l}$. Both systems are related by the $\mathbf{H}_M$ transformation which contains a translation and a rotation of the axis orientation.*

Then, consider that the local shift of the module is due to a global movement of the supporting structure ($\mathbf{H}_{\delta\mathbf{A}}$), one has:

$$\mathbf{H}'_M = \mathbf{H}_{\delta\mathbf{A}} \otimes \mathbf{H}_M$$

which leads to:

$$\mathbf{H}_{\delta\mathbf{a}} = \mathbf{H}_M^{-1} \otimes \mathbf{H}_{\delta\mathbf{A}} \otimes \mathbf{H}_M \tag{C.1}$$

This provides the relationship between the movements of the supporting structure ($\delta\mathbf{A}$) and the local ones ($\delta\mathbf{a}$). Knowing the position and orientation of a given module, one can compute how the shifts or rotations of the supporting structure affect the local shifts or rotations of a module. So one has to introduce one by one small changes for each of the $\mathbf{A}$ parameters and by virtue of C.1 those shifts will translate in changes in the $\mathbf{a}$ parameters. Hence, this provides a method to compute $\mathbf{H}_{\delta\mathbf{a}}$ (i.e. $\partial\mathbf{a}/\partial\mathbf{A}$).

First, let's consider the generic transformation $\mathbf{H}_M$ which consists in a generic translation matrix $\mathbf{T}_M$ and in a generic rotation matrix $\mathbf{R}_M(\alpha,\beta,\gamma)$. This rotation matrix is given by $\mathbf{R}(\alpha,\beta,\gamma) = R_x(\alpha)R_y(\beta)R_z(\gamma)$, i.e. it is applied first around z, then around y and finally around x, being the individual rotation matrices:

$$R_x(\alpha) = \begin{pmatrix} 1 & 0 & 0 \\ 0 & \cos\alpha & -\sin\alpha \\ 0 & \sin\alpha & \cos\alpha \end{pmatrix} \quad ; \quad R_y(\beta) = \begin{pmatrix} \cos\beta & 0 & \sin\beta \\ 0 & 1 & 0 \\ -\sin\beta & 0 & \cos\beta \end{pmatrix}$$

$$R_z(\gamma) = \begin{pmatrix} \cos\gamma & -\sin\gamma & 0 \\ \sin\gamma & \cos\gamma & 0 \\ 0 & 0 & 1 \end{pmatrix}$$

Hence, the transformation $\mathbf{H}_M$ can be written as:

$$\mathbf{H}_M = [\mathbf{T}_M, \mathbf{R}_M(\alpha,\beta,\gamma)] =$$

$$= \left[\begin{pmatrix} x_0 \\ y_0 \\ z_0 \end{pmatrix}, \begin{pmatrix} \cos\beta\cos\gamma & -\cos\beta\sin\gamma & \sin\beta \\ \cos\alpha\sin\gamma + \sin\alpha\sin\beta\cos\gamma & \cos\alpha\cos\gamma - \sin\alpha\sin\beta\sin\gamma & -\sin\alpha\cos\beta \\ \sin\alpha\sin\gamma - \cos\alpha\sin\beta\cos\gamma & \sin\alpha\cos\gamma + \cos\alpha\sin\beta\sin\gamma & \cos\alpha\cos\beta \end{pmatrix} \right] \tag{C.2}$$

where $\mathbf{T}_M = (x_0, y_0, z_0)$ indicates the position of the origin of the local reference frame in global coordinates, and the $\mathbf{R}(\alpha,\beta,\gamma)$ the relative orientation of local x, y and z axis with respect to the global ones (see figure C.1).

Now, its inverse[1] transformation $\mathbf{H}_M^{-1}$ is:

$$\mathbf{H}_M^{-1} = [-\mathbf{R}^{-1}\mathbf{T}, \mathbf{R}^{-1}] =$$

$$= \left[\begin{pmatrix} -x_0\cos\beta\cos\gamma - y_0(\cos\alpha\sin\gamma + \sin\alpha\sin\beta\cos\gamma) - z_0(\sin\alpha\sin\gamma - \cos\alpha\sin\beta\cos\gamma) \\ x_0\cos\beta\sin\gamma - y_0(\cos\alpha\cos\gamma - \sin\alpha\sin\beta\sin\gamma) - z_0(\sin\alpha\cos\gamma + \cos\alpha\sin\beta\sin\gamma) \\ -x_0\sin\beta + y_0\sin\alpha\cos\beta - z_0\cos\alpha\cos\beta \end{pmatrix}, \right.$$

$$\left. \begin{pmatrix} \cos\beta\cos\gamma & \cos\alpha\sin\gamma + \sin\alpha\sin\beta\cos\gamma & \sin\alpha\sin\gamma - \cos\alpha\sin\beta\cos\gamma \\ -\cos\beta\sin\gamma & \cos\alpha\cos\gamma - \sin\alpha\sin\beta\sin\gamma & \sin\alpha\cos\gamma + \cos\alpha\sin\beta\sin\gamma \\ \sin\beta & -\sin\alpha\cos\beta & \cos\alpha\cos\beta \end{pmatrix} \right] \tag{C.3}$$

And finally, considering that the transform $\mathbf{H}_{\delta\mathbf{A}}$ is produced by small global translations and rotations ($A \to 0$, $B \to 0$ and $\Gamma \to 0$), one can approximate this transform as:

$$\mathbf{H}_{\delta\mathbf{A}} = \left[\begin{pmatrix} T_x \\ T_y \\ T_z \end{pmatrix}, \begin{pmatrix} 1 & -\Gamma & B \\ \Gamma & 1 & -A \\ -B & A & 1 \end{pmatrix} \right] \tag{C.4}$$

where the cosines have been replace by 1 and the sines by its angle. Note, that in the most general case, $\mathbf{H}_{\delta\mathbf{a}}$ should be similar to expression C.2.

Now, one can easily compute $\mathbf{H}_{\delta\mathbf{a}}$ thanks to expression C.1: $\mathbf{H}_{\delta\mathbf{a}} = \mathbf{H}_M^{-1}\mathbf{H}_{\delta\mathbf{A}}\mathbf{H}_M$. Anyhow, due to the complexity of the resulting transformation, translations and rotations will be considered separately:

- **Translations:** concerning the local translations of $\mathbf{H}_{\delta\mathbf{a}}$, one has:

[1] Being a transformation $\mathbf{H} = [\mathbf{T}, \mathbf{R}]$, two consecutive transformations $\mathbf{H}_1$ and $\mathbf{H}_2$ work as:

$$\mathbf{H}_1 \otimes \mathbf{H}_2 = [\mathbf{T}_1, \mathbf{R}_1] \otimes [\mathbf{T}_2, \mathbf{R}_2] = [\mathbf{T}_1 + \mathbf{R}_1\mathbf{T}_2, \mathbf{R}_1\mathbf{R}_2]$$

then, its inverse $\mathbf{H}^{-1} = [\mathbf{T}^{-1}, \mathbf{R}^{-1}]$ is simply:

$$\mathbf{H}^{-1} \otimes \mathbf{H} = \mathbf{H}_I \quad \to \quad \mathbf{H}^{-1} = [-\mathbf{R}^{-1}\mathbf{T}, \mathbf{R}^{-1}] \text{ where the identity transformation is: } \mathbf{H}_I = [0, \mathbf{R}_I]$$

$$\mathbf{T}_{\delta\mathbf{a}} = \left(\mathbf{T}_M^{-1} + \mathbf{R}_M^{-1}\mathbf{T}_{\delta\mathbf{A}}\right) + \mathbf{R}_M^{-1}\mathbf{R}_{\delta\mathbf{A}}\mathbf{T}_M = \left(\begin{array}{l} (T_x - \Gamma y_0 + Bz_0)\cos\beta\cos\gamma + \\ (T_y + \Gamma x_0 - Az_0)(\cos\alpha\sin\gamma + \sin\alpha\sin\beta\cos\gamma) + \\ (T_z - Bx_0 + Ay_0)(\sin\alpha\sin\gamma - \cos\alpha\sin\beta\cos\gamma) \\ \\ -(T_x - \Gamma y_0 + Bz_0)\cos\beta\sin\gamma + \\ (T_y + \Gamma x_0 - Az_0)(\cos\alpha\cos\gamma - \sin\alpha\sin\beta\sin\gamma) + \\ (T_z - Bx_0 + Ay_0)(\sin\alpha\cos\gamma + \cos\alpha\sin\beta\sin\gamma) \\ \\ (T_x - \Gamma y_0 + Bz_0)\sin\beta + \\ (-T_y - \Gamma x_0 + Az_0)\sin\alpha\cos\beta + \\ (T_z - Bx_0 + Ay_0)\cos\alpha\cos\beta \end{array}\right)$$

therefore, the derivative $\partial t/\partial T$ is:

$$\frac{\partial t}{\partial T} = \begin{pmatrix} \cos\beta\cos\gamma & (\cos\alpha\sin\gamma + \sin\alpha\sin\beta\cos\gamma) & (\sin\alpha\sin\gamma - \cos\alpha\sin\beta\cos\gamma) \\ -\cos\beta\sin\gamma & (\cos\alpha\cos\gamma - \sin\alpha\sin\beta\sin\gamma) & (\sin\alpha\cos\gamma + \cos\alpha\sin\beta\sin\gamma) \\ \sin\beta & -\sin\alpha\cos\beta & \cos\alpha\cos\beta \end{pmatrix}$$

where one can see that this matrix is in fact $\mathbf{R}_M^{-1}$. On the other hand, using the unit vectors of the local module frame axis:

$$\hat{x} = \begin{pmatrix} \cos\beta\cos\gamma \\ \cos\alpha\sin\gamma + \sin\alpha\sin\beta\cos\gamma \\ \sin\alpha\sin\gamma - \cos\alpha\sin\beta\cos\gamma \end{pmatrix} \; ; \; \hat{y} = \begin{pmatrix} -\cos\beta\sin\gamma \\ \cos\alpha\cos\gamma - \sin\alpha\sin\beta\sin\gamma \\ \sin\alpha\cos\gamma + \cos\alpha\sin\beta\sin\gamma \end{pmatrix}$$

$$\hat{z} = \begin{pmatrix} \sin\beta \\ -\sin\alpha\cos\beta \\ \cos\alpha\cos\beta \end{pmatrix}$$

one can write:

$$\frac{\partial t}{\partial T} = \begin{pmatrix} \hat{x}^T\cdot\hat{X} & \hat{x}^T\cdot\hat{Y} & \hat{x}^T\cdot\hat{Z} \\ \hat{y}^T\cdot\hat{X} & \hat{y}^T\cdot\hat{Y} & \hat{y}^T\cdot\hat{Z} \\ \hat{z}^T\cdot\hat{X} & \hat{z}^T\cdot\hat{Y} & \hat{z}^T\cdot\hat{Z} \end{pmatrix} = \hat{a}^T\cdot\hat{b} \quad \text{where} \quad a = x, y, z \text{ and } \; b = X, Y, Z$$

where $\hat{X}$, $\hat{Y}$ and $\hat{Z}$ are just the unit vectors of the global frame axis:

$$\hat{X} = \begin{pmatrix} 1 \\ 0 \\ 0 \end{pmatrix} \; ; \; \hat{Y} = \begin{pmatrix} 0 \\ 1 \\ 0 \end{pmatrix} \quad \text{and} \quad \hat{Z} = \begin{pmatrix} 0 \\ 0 \\ 1 \end{pmatrix}$$

In what concerns the terms $\partial t/\partial R$ one can write them as:

$$\frac{\partial t}{\partial R} = \begin{pmatrix} y_0\hat{x}_z - z_0\hat{x}_y & z_0\hat{x}_x - x_0\hat{x}_z & x_0\hat{x}_y - y_0\hat{x}_x \\ -z_0\hat{y}_y + y_0\hat{y}_z & -z_0\hat{y}_x + x_0\hat{y}_z & -y_0\hat{y}_x + x_0\hat{y}_y \\ z_0\hat{z}_y + y_0\hat{z}_z & z_0\hat{z}_x - x_0\hat{z}_z & -y_0\hat{z}_x - +x_0\hat{z}_y \end{pmatrix}$$

or considering the vectorial products:

$$\frac{\partial t}{\partial R} = \begin{pmatrix} (\mathbf{T}_M \times \hat{x}) \cdot \hat{X} & (\mathbf{T}_M \times \hat{x}) \cdot \hat{Y} & (\mathbf{T}_M \times \hat{x}) \cdot \hat{Z} \\ (\mathbf{T}_M \times \hat{y}) \cdot \hat{X} & (\mathbf{T}_M \times \hat{y}) \cdot \hat{Y} & (\mathbf{T}_M \times \hat{y}) \cdot \hat{Z} \\ (\mathbf{T}_M \times \hat{z}) \cdot \hat{X} & (\mathbf{T}_M \times \hat{z}) \cdot \hat{Y} & (\mathbf{T}_M \times \hat{z}) \cdot \hat{Z} \end{pmatrix}$$

or simply:

$$\frac{\partial t_a}{\partial R_b} = (\mathbf{T}_M \times \hat{a}) \cdot \hat{b} = (\hat{b} \times \mathbf{T}_M) \cdot \hat{a} \quad \text{where } a = x, y, z \text{ and } b = X, Y, Z$$

- **Rotations:** In what concerns the local rotations of $\mathbf{H}_{\delta\mathbf{a}}$, one has:

$$\mathbf{R}_{\delta\mathbf{a}} = \mathbf{R}_M^{-1} \mathbf{R}_{\delta\mathbf{A}} \mathbf{R}_M =$$

$$= \begin{pmatrix} 1 & \begin{matrix} A(-\sin\beta)+ \\ B\sin\alpha\cos\beta+ \\ \Gamma(-\cos\alpha\cos\beta) \end{matrix} & \begin{matrix} A(-\cos\beta\sin\gamma)+ \\ B(\cos\alpha\cos\gamma - \sin\alpha\sin\beta\sin\gamma)+ \\ \Gamma(\sin\alpha\cos\gamma + \cos\alpha\sin\beta\sin\gamma) \end{matrix} \\ \begin{matrix} A(\sin\alpha)+ \\ B(-\sin\alpha\cos\beta) \\ \Gamma(\cos\alpha\cos\beta) \end{matrix} & 1 & \begin{matrix} A(-\cos\beta\cos\gamma)+ \\ B(-\cos\alpha\sin\gamma - \sin\alpha\sin\beta\cos\gamma)+ \\ \Gamma(-\sin\alpha\sin\gamma + \cos\alpha\sin\beta\cos\gamma) \end{matrix} \\ \begin{matrix} A(\cos\beta\sin\gamma)+ \\ B(-\cos\alpha\cos\gamma + \sin\alpha\sin\beta\sin\gamma)+ \\ \Gamma(-\sin\alpha\cos\gamma - \cos\alpha\sin\beta\sin\gamma) \end{matrix} & \begin{matrix} A(\cos\beta\cos\gamma)+ \\ B(\cos\alpha\sin\gamma + \sin\alpha\sin\beta\cos\gamma)+ \\ \Gamma(\sin\alpha\sin\gamma - \cos\alpha\sin\beta\cos\gamma) \end{matrix} & 1 \end{pmatrix}$$

Firstly, the derivatives of the local rotations with respect to global translations are just null because the local axis orientations do not change because of a global translation. Furthermore, one can easily see that $\mathbf{R}_{\delta\mathbf{a}}$ does not contain any dependence with $\mathbf{T}_M$ (i.e. neither T_x, T_y nor T_z appear in $\mathbf{R}_{\delta\mathbf{a}}$), therefore its derivatives must be null:

$$\frac{\partial r}{\partial T} = 0$$

The remaining part is the derivatives of the local rotations with respect to the global ones, $\partial r/\partial R$. Then, the partial derivatives with respect to each global rotation are obtained by making the other global rotations null (i.e. considering independently each global rotation) and after that identifying each element with its derivative. For example:

$$(A, B = \Gamma = 0) \;\rightarrow\; \mathbf{R}_{\delta\mathbf{a}}^A = \begin{pmatrix} 1 & -A\sin\beta & -A\cos\beta\sin\gamma \\ A\sin\beta & 1 & -A\cos\beta\cos\gamma \\ A\cos\beta\sin\gamma & A\cos\beta\cos\gamma & 1 \end{pmatrix}$$

And now, identifying $\mathbf{R}_{\delta\mathbf{a}}^A$ with $\mathbf{R}'_{\delta\mathbf{a}}$ for small rotations (like rotation of expression C.4), one has:

$$\mathbf{R}'_{\delta\mathbf{A}} = \begin{pmatrix} 1 & -\gamma & \beta \\ \gamma & 1 & -\alpha \\ -\beta & \alpha & 1 \end{pmatrix}$$

one can write how the the local axis rotate if there is a global rotation with respect the global A axis:

$$\frac{\partial \alpha}{\partial A} = \cos\beta\cos\gamma \;\; ; \;\; \frac{\partial \beta}{\partial A} = -\cos\beta\sin\gamma \;\text{ and }\; \frac{\partial \gamma}{\partial A} = \sin\beta$$

The similar technique must be follow for the other two angles to finally obtain the complete derivative matrix:

$$\frac{\partial r}{\partial R} = \begin{pmatrix} \cos\beta\cos\gamma & \cos\alpha\sin\gamma + \sin\alpha\sin\beta\cos\gamma & \sin\alpha\sin\gamma - \cos\alpha\sin\beta\cos\gamma \\ -\cos\beta\sin\gamma & \cos\alpha\cos\gamma - \sin\alpha\sin\beta\sin\gamma & \sin\alpha\cos\gamma + \cos\alpha\sin\beta\sin\gamma \\ \sin\beta & -\sin\alpha\cos\beta & \cos\alpha\cos\beta \end{pmatrix}$$

which is just the inverse of the rotation part, $\mathbf{R}_M$, of the $\mathbf{H}_M$ transform. Reached this point, the four blocks of the jacobian-like matrix have been computed and can be put together as:

$$\frac{\partial \mathbf{a}}{\partial \mathbf{A}} = \begin{pmatrix} \mathbf{R}_M^{-1} & (\mathbf{T}_M \times \hat{a}) \cdot \hat{b} \\ 0 & \mathbf{R}_M^{-1} \end{pmatrix}$$

D

Datasets for the top quark mass studies

The top quark mass measurement study presented in this thesis has been done using MC data based on the official TopView ntuples generated within *Athena* framework (release 12.14.0.3) for the CSC challenge. The different requested signal and physics backgrounds are stored in different datasets. The dataset names have a common naming convention: prefix+suffix [134]. They have a common prefix which identify the TopView version and some important information (like bugfixes, etc...) and a custom suffix which identify basically the dataset number and give the sample description (generator type, etc...). This common prefix is:

```
user.top.TopViewCSC121403_StacoTauRec_30um.trig1_misal1_mc12.
```

This prefix tells that it has been produced with TopView within the CSC exercise and using *Athena* framework release 12.14.0.3 as has been said before. Moreover, it has the "StacoTauRec" label which means that the *STACO*[1] and *TAUREC*[2] algorithms are used for muon and τ reconstruction respectively. The label "30um" is related with a LAr bug which affected the e/γ energy scale. Finally, the label "misal1" means the geometry explained in section 8.2.5.

MC generators used to simulate the signal and the background samples were: PYTHIA, HERWIG/JIMMY, AcerMC, ALPGEN and MC@NLO. Parton-level MC generators are either PYTHIA [6] or HERWIG/JIMMY [151] [152] for hadronisation (HERWIG hadronisation was complemented by an underlying event simulation from the JIMMY program [153]) and underlying event modelling. Data from the Tevatron and other experiments was used to tune the

[1] STACO is a muon reconstruction algorithm that performs the tracking within the Muon System (see section 2.3.3 in chapter 2) and uses an algorithm (called Muonboy) which extrapolates the tracks to the ID. This extrapolation accounts for MCS and energy loss in calorimeters considering the crossed material.

[2] TAUREC is a calorimetry based algorithm for the τ hadronic decay reconstruction. This is a difficult task since it is quite difficult to distinguish leptonic modes from primary e and μ. It starts from clusters reconstructed in the calorimeters (see section 2.3.2 in chapter 2) and builds the identification variables based on information from the tracker and the calorimeter.

underlying event model parameters [154] used by these generators. The AcerMC generator is dedicated for generation of the SM background processes in pp collisions at the LHC and it is used together with HERWIG. Then, ALPGEN generator [155] is mostly used for the production of EW bosons in association with jet. Finally, the MC@NLO event generator [137] is one of the few MC tools which incorporates full NLO QCD corrections to a selected set of processes in a consistent way.

D.1 Requested signal

The suffix of dataset name which contains the requested "signal" is:

```
005200.T1_McAtNlo_Jimmyv12000604
```

This dataset has 146 files with 3750 events per file, i.e. 547500 events and it contains simulated $t\bar{t}$ events at NLO in the perturbative SM theory (it was produced with the MC@NLO generator), where either both W bosons decay leptonically or one of them decays hadronically, i.e. it contains the requested "signal", the dileptonic background and part of the fully hadronic background (that is, when the τ's decay hadronically). Moreover, it includes ISR and FSR (gluon radiation) and a generated fixed top mass (M_t^{gen}) equal to 175 GeV/c^2 (with no decay width, i.e. $\Gamma_t = 0$).

Finally, in order to study the stability of the method several LO datasets (AcerMC generator) with different generated top masses were used. In particular, these datasets had the following masses: M_t^{gen} = 160 GeV/c^2, 165 GeV/c^2, 170 GeV/c^2, 180 GeV/c^2, 185 GeV/c^2 and 190 GeV/c^2. The suffix names are:

```
005573.AcerMCttbar160v12000601.001
005574.AcerMCttbar165v12000601.001
005575.AcerMCttbar170v12000601.001
005577.AcerMCttbar180v12000601.001
005578.AcerMCttbar185v12000601.001
005579.AcerMCttbar190v12000601.001
```

D.2 Physics backgrounds

The suffixes of the dataset names for the physics backgrounds which have been considered in the present analysis are the following:

- Dilepton channel (the dataset is the same as the "signal" but the background events where selected using the truth information) (MC@NLO generator):

  ```
  005200.T1_McAtNlo_Jimmyv12000604
  ```

- Fully hadronic channel (one of the dataset is the same as the "signal" but the background events where selected using the truth information) (MC@NLO generator):

  ```
  005200.T1_McAtNlo_Jimmyv12000604
  005204.TTbar_FullHad_McAtNlo_Jimmyv12000601.001
  ```

- Single top production (AcerMC generator):

```
005501.AcerMC_schanv12000604.001
005502.AcerMC_tchanv12000604.001
005500.AcerMC_Wtv12000604.001
```

- W + jets production (ALPGEN generator + HERWIG/JIMMY):

```
008245.AlpgenJimmyWmunuNp3_pt20_filt3jetv12000605.001
008246.AlpgenJimmyWmunuNp4_pt20_filt3jetv12000601.001
008247.AlpgenJimmyWmunuNp5_pt20_filt3jetv12000605.001
008248.AlpgenJimmyWtaunuNp2_pt20_filt3jetv12000605.001
008249.AlpgenJimmyWtaunuNp3_pt20_filt3jetv12000605.001
008250.AlpgenJimmyWtaunuNp4_pt20_filt3jetv12000605.001
```

- W+ $b\bar{b}$ and W + $c\bar{c}$ (ALPGEN generator + HERWIG/JIMMY):

```
006280.AlpgenJimmyWbbNp0v12000605.001
006281.AlpgenJimmyWbbNp1v12000605.001
006282.AlpgenJimmyWbbNp2v12000605.001
006283.AlpgenJimmyWbbNp3v12000605.001
006284.AlpgenJimmyWccNp0v12000605.001
006285.AlpgenJimmyWccNp1v12000605.001
006286.AlpgenJimmyWccNp2v12000605.001
006287.AlpgenJimmyWccNp3v12000605.001
```

E

Energy calibration and uncertainties using MC for jets and leptons

This appendix will show the energy calibration for jets as well as the energy reconstruction resolutions for leptons and for jets using MC information in both cases.

E.1 Jet energy calibration using MC

The procedure to calibrate jets using MC information is simple considering the relation $E^{truth}_{parton}/E^{reco}_{jet}$ for light jets and for b-jets (differentiating b-jets with and without muon decays), separately. Thus, for given bins of the reconstructed jet energy (E^{reco}_{jet}) and η, a gaussian-like distribution is obtained from this quotient. Then, these distributions can be fitted to a gaussian and the mean value of the gaussian peak is selected as the correction factor α_{jet}, assuming therefore:

$$E^{truth}_{parton} = \alpha_E E^{reco}_{jet}$$

where α_E is slightly higher than 1 because the reconstructed jets have always lower energy than their original partons ($E^{truth}_{parton} > E^{reco}_{jet}$) due to the reconstruction performance. Figures E.1 and E.2 show the maps with the jet energy correction factors (α_E) as function of the reconstructed energy and η for light jets and b-jets without muon decays, respectively. Since there is too low statistics to build a map, the calibration factors for b-jet with muon decays are given just for two fixed cases, $\alpha_E = 1.6$ for $E^{reco}_{jet} < 100$ GeV and $\alpha_E = 1.4$ for $E^{reco}_{jet} \geq 100$ GeV, being $\alpha_E = 1.6$ and $\alpha_E = 1.4$, respectively.

Taking a look to figures E.1 and E.2, one can see how generally the correction factors α_E decrease with the energy and increase with η.

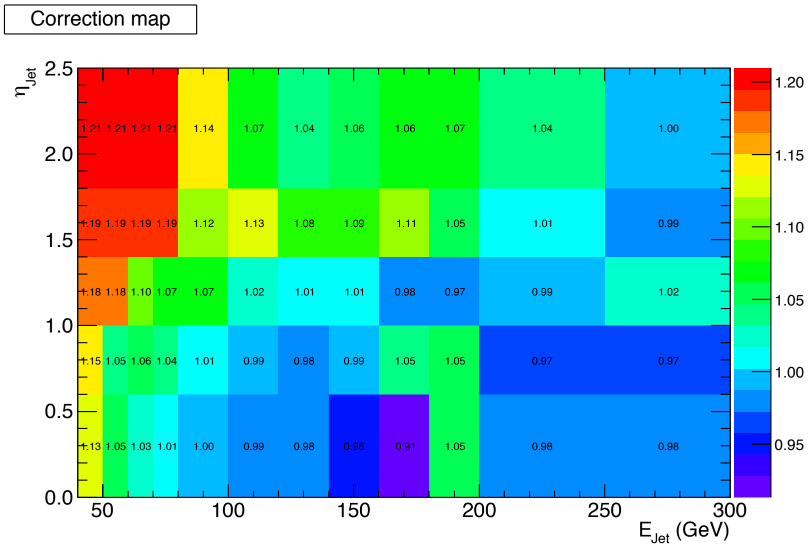

Figure E.1: *Map for light jets with the correction factors (α_{jet}) as function of the energy and η of the reconstructed jet.*

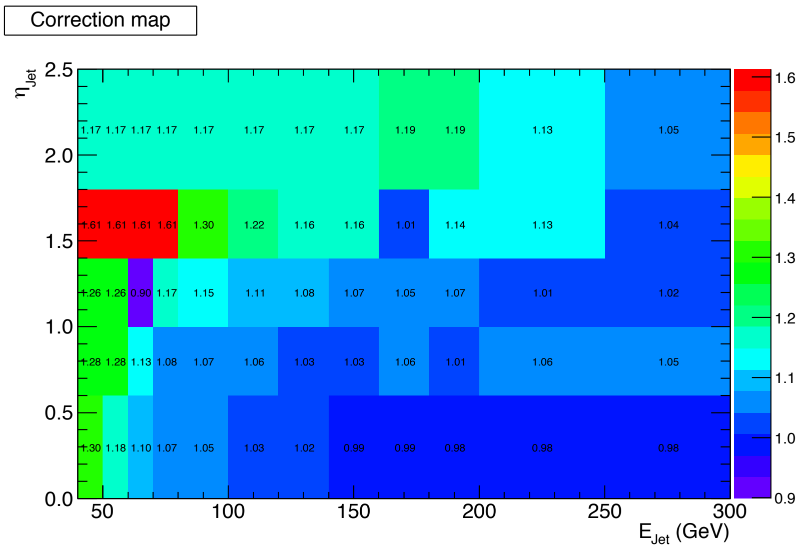

Figure E.2: *Map for b-jets without decaying muons with the correction factors (α_{jet}) as function of the energy and η of the reconstructed jet.*

E.2 Computing the energy uncertainties using MC

E.2.1 Energy uncertainties for leptons

Figures 8.15 and 8.20 showed the energy resolution dependence with E^{reco} and η for electrons and muons respectively. Specially, one can see how the resolution behaves with E^{reco} for each case. Then, to compute the energy uncertainties (σ_{E_ℓ}, being $\ell = e, \mu$), the procedure is almost the same as in the previous section but now using the distribution $E_\ell^{reco} - E_\ell^{MC}$. The main difference is that one extracts the width instead of the mean. Moreover, instead of building a discrete map, an energy parametrization is done in order to improve the computations. Thus, $\sigma(E_\ell^{reco} - E_\ell)^{reco}$ is plotted as a function of E_ℓ^{reco} for five η regions (η regions: $0.6 \leq |\eta| < 1.0$, $1.0 \leq |\eta| < 1.4$, $1.4 \leq |\eta| < 1.8$, $1.4 \leq |\eta| < 1.8$, $1.8 \leq |\eta| < 2.5$) and then the results are fitted. As already said on section 8.3:

- For electrons the fit function is: $\sigma_{E_e} = a\sqrt{E_e} + bE_e$
- While for muons is $\sigma_{E_\mu} = aE_\mu^2 + bE_\mu$

being a and b free real parameters.

Figures E.3 (a) and (b) give two examples for two different η regions which illustrates the uncertainty dependence with the energy, together with their fits.

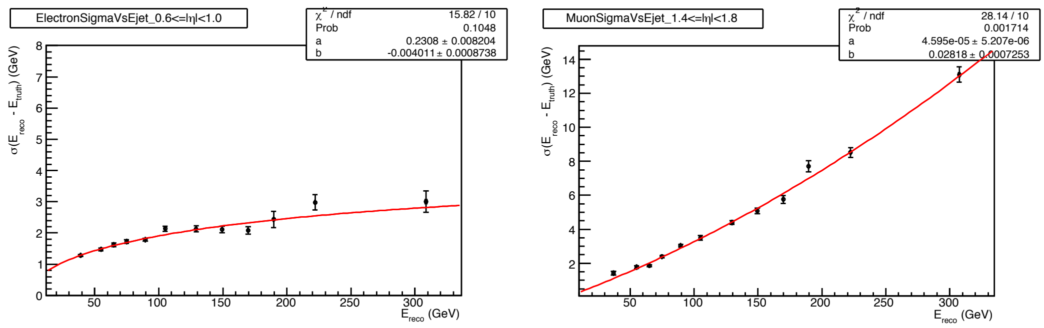

(a) $0.6 \leq |\eta| < 1.0$ (b) $1.4 \leq |\eta| < 1.8$

Figure E.3: *Two examples to illustrate the energy uncertainty computations for electrons (a) and for muons (b). Data is fitted to different functions for each case according with the discussion on section 8.3.*

To summarize, one can say that the energy uncertainty for electrons is on average O(1-10 GeV) for all η regions while for muons is slightly higher, O(1-20 GeV).

E.2.2 Energy uncertainties for jets

The same procedure is used to compute the jet energy uncertainties (using the same five η regions). The fit function was the same as for electrons (see section 8.3 for explanations).

Figures E.4 (a) and (b) contain two examples for the same η region for light jets and b-jets without muon decays, respectively. For b-jets with muon decays, two energy regions were computed due to the low statistics of this kind of b-jets.

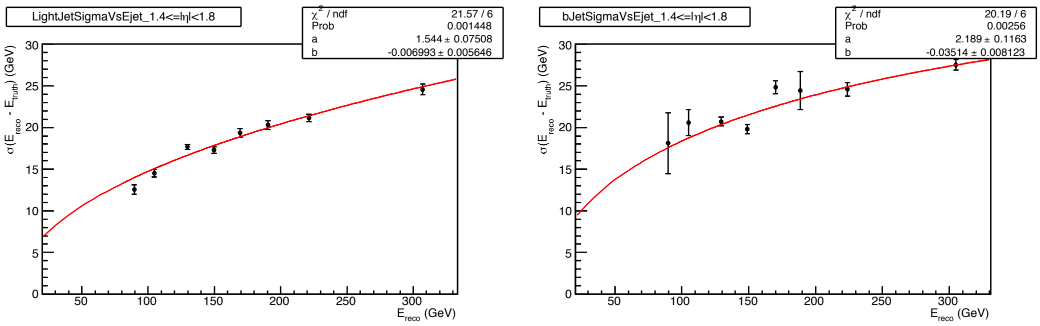

(a) $1.4 \leq |\eta| < 1.8$

(b) $1.4 \leq |\eta| < 1.8$

Figure E.4: *Two examples to illustrate the energy uncertainty computations for light jets (a) and b-jets without muon decays (b). Data is fitted to* $\sigma_{E_{jet}} = a\sqrt{E_{jet}} + bE_{jet}$*, being a and b two free parameters.*

To finalize, is worth to say that the energy uncertainty for light jets and for b-jets without muon decays is on average $\mathcal{O}$(5-30 GeV), while for b-jets with muon decays is 12.4 for $E < 100$ GeV and 33.9 for $E > 100$ GeV.

List of Acronyms

ACML: AMD Core Math Library

ALICE: A Large Ion Collider Experiment

ATLAS: A Toroidal LHC Apparatus

BS: Beam Spot

BR: Branching Ratio

CAF: CERN Analysis Facility

CDF: Collider Detector at Fermilab

CERN: *Conseil Européen pour la Reserche Nucléaire*

CIEMAT: Centro de Investigaciones Energéticas, Medioambientales y Tecnológicas

CKM: Cabibbo-Kobayashi-Maskawa

CL: Confidence Level

CMM: Coordinate Measurement Machine

CMS: Compact Muon Solenoid

CNGS: CERN Neutrinos to Gran Sasso

CSC: Computing System Commissioning

DAQ: Data AcQuisition

DDM: Distributed Data Management

DOCA: Distance-Of-Closest-Approach

DoF: Degree of Freedom

ECAL: Electromagnetic Calorimeter

EDM: Event Data Model

EF: Event Filter

EW: ElectroWeak theory

FCNC: Flavour Changing Neutral Current

FDR: Full Dress Rehearsal

FE: Front-End

FNAL: Fermilab

FSI: Frequency Scanning Interferometry

FWHM: Full-Width Half-Maximum

GR: General Relativity

GUT: Grand Unified Theory

HCAL: Hadronic Calorimeter

HEP: High Energy Physics

HLT: High Level Trigger

HV: High-Voltage

ID: Inner Detector

IFAE: Instituto de Física de Altas Energías

IFCA: Instituto de Física de Cantábria

IFIC: Instituto de Física Corpuscular

ISOLDE: Isotope Separation OnLine DEvice

IOV: Interval Of Validity service

IP: Impact Parameter

ISR: Initial State Radiation

JES: Jet Enery Scale

KF: Kinematic Fit

LCG: LHC Computing Grid

LEP: Large Electron Positron collider

LHC: Large Hadron Collider, an accelerator at CERN

LHCb: the Large Hadron Collider beauty experiment

LHCf: Large Hadron Collider forward

LINAC: LINear ACcelerators

LM: Lagrange Multiplier

LO: Leading Order

LVL1: Level-1 trigger

LVL2: level-2 trigger

MBTS: Minimum Bias Trigger Scintillator

MC: Monte Carlo

MCC: Module-Control Chip

MCS: Multiple Coulomb Scattering

MDT: Monitored Drift Tubes

MPI: Message Passing Interface standards

MSSM: Minimal Supersymmetric Standard Model

NLL: Next to Leading Logarithm

NLO: Next to Leading Order

OSG: Open Science Grid

PEB: Partial Event Building algorithms

PIC: Port d'Informació Científica

PRD: PrepRawData

PS: Proton Synchrotron

PSB: Proton Synchrotron Booster

QCD: Quantum ChromoDynamics theory

QED: Quantum ElectroDynamics theory

RAL: Rutherford Appleton Laboratory

RDOs: Raw Data Objects

ROBs: ReadOut Drivers

RoI: Region of Interest

RPC: Resistive Plate Chamber

SC: SynchroCyclotron

SCT: SemiConductor Tracker

SFO: SubFarm Output

SLAC: Stanford Linear Accelerator Center

SLC: Stanford Linear Collider

SM: Standard Model

SP: SpacePoints

SPS: Super Proton Synchrotron

SSB: Spontaneous Symmetry Breaking

SUSY: SUperSYmmetry

SVN: SubVersioN

S/N: Signal/Noise

TDR: Technical Design Report

TES: Transient Event Store

TGC: Thin Gap Chamber

TOF: Time Of Flight

ToT: Time-over-Threshold

TOTEM: Total Cross Section, Elastic Scattering and Diffraction Dissociation

TRT: Transition Radiation Tracker

UAM: Universidad Autónoma de Madrid

UB: Universitat de Barcelona

USC: Universidad de Santiago de Compostela

Bibliography

[1] D. Perkins. *Introduction to High Energy Physics, Cambridge University Press, 4th edition*. 2000.

[2] E. D. Bloom *et al*. High-energy inelastic $e-p$ scattering at 6^o and 10^o. *Phys. Rev. Lett.*, 23(16):930–934, Oct 1969.

[3] F. Abe *et al*. Observation of top quark production in $p\bar{p}$ collisions with the collider detector at fermilab. *Phys. Rev. Lett.*, 74(14):2626–2631, Apr 1995.

[4] P. M. Watkins. Discovery of the w and z bosons. *Contemp. Phys.*, 27:291–324, 1986.

[5] C. Amsler *et al*. (Particle Data Group). The Review of Particle Physics. 2008. Physics Letters B667, 1.

[6] PYTHIA website. http://home.thep.lu.se/~torbjorn/Pythia.html.

[7] G. Aad *et al*. [The ATLAS Collaboration]. Expected Performance of the ATLAS Experiment - Detector, Trigger and Physics. 2009.

[8] J. M. Campbell *et al*. Hard interactions of quarks and gluons: a primer for LHC physics. 2007. Rep. Prog. Physics, Volume 70, page 89-193.

[9] Combination of CDF and D0 Results on the Mass of the Top Quark. *arXiv:hep-ex/0903.2503*, 2009.

[10] Lep/tev ew wg plots for summer 2009. http://lepewwg.web.cern.ch/LEPEWWG/plots/summer2009.

[11] A. Djouadi, J. Kalinowski, and M. Spira. Hdecay: a program for higgs boson decays in the standard model and its supersymmetric extension. *Computer Physics Communications*, 108:56, 1998.

[12] H. Georgi and S. Glashow. Unity of All Elementary-Particle Forces. 1974. Physical Review Letters, 32 438.

[13] Tevatron New Phenomena, Higgs working group, for the CDF collaboration, and DZero collaboration. Combined CDF and DZero Upper Limits on Standard Model Higgs-Boson Production with up to 4.2 fb-1 of Data. *arXiv:0903.4001 [hep-ex]*, 2009.

[14] H. T. Haber *et al*. The search for supersymmetry: probing physics beyond the standard model. 1985. Physics Reports 117, page 75.

[15] N. Brett at al. Black Hole Production at the LHC: the Discovery Reach of the ATLAS Experiment. *ATL-PHYS-INT-2007*, 2008.

[16] CERN website. http://www.cern.ch.

[17] L. Evans and P. Bryant (editors). LHC Machine. 2008. JINST 3 S08001.

[18] The ATLAS Collaboration, G. Aad *et al*. The ATLAS Experiment at the CERN Large Hadron Collider. 2008. JINST 3 S08003.

[19] The CMS Collaboration, S. Chatrchyan *et al*. The CMS experiment at the CERN Large Hadron Collider. 2008. JINST 3 S08004.

[20] The LHCb Collaboration, A. Augusto Alves Jr *et al*. The LHCb Detector at the Large Hadron Collider. 2008. JINST 3 S08005.

[21] The ALICE Collaboration, K. Aamodt *et al*. The ALICE experiment at the CERN Large Hadron Collider. 2008. JINST 3 S08002.

[22] The TOTEM Collaboration, G. Anelli *et al*. The TOTEM Experiment at the CERN Large Hadron Collider. 2008. JINST 3 S08007.

[23] The LHCf Collaboration, O. Adriani *et al*. The LHCf detector at the CERN Large Hadron Collider. 2008. JINST 3 S08006.

[24] LHC Computing Grid project website. http://lcg.web.cern.ch.

[25] NorduGrid project website. http://www.nordugrid.org.

[26] The ATLAS Collaboration. ATLAS Technical Proposal for a General-Purpose pp Experiment at the Large Hadron Collider at CERN. 1994. CERN-LHCC-94-43.

[27] The ATLAS Collaboration. ATLAS Inner Detector: Technical Design Report, volume 1. 1997. CERN-LHCC-97-016.

[28] The ATLAS Collaboration. ATLAS Magnet System: Technical Design Report. 1997. CERN-LHCC-97-018.

[29] The ATLAS Collaboration. ATLAS Liquid Argon Calorimeter: Technical Design Report. 1996. CERN-LHCC-96-041.

[30] The ATLAS Collaboration. ATLAS Tile Calorimeter: Technical Design Repor. 1996. CERN-LHCC-96-042.

[31] The ATLAS Collaboration. ATLAS Muon Spectrometer: Technical Design Report. 1997. CERN-LHCC-97-022.

[32] The ATLAS Collaboration. ATLAS Level-1 Trigger: Technical Design Report. 1998. CERN-LHCC-98-014.

[33] The ATLAS Collaboration. P. Jenni *et al*. *ATLAS high-level trigger, data-acquisition and controls : Technical Design Report*. 2003. CERN-LHCC-2003-022.

[34] S. Snow and A. Weidberg. The effect of inner detector misalignments on track reconstruction. Technical report, 1997. ATL-INDET-97-160.

[35] S. Haywood. Offline Alignment And Calibration of the Inner Detector. 1999. ATL-INDET-2000-005.

[36] S. Correard *et al*. b-tagging with dc1 data. Technical Report ATL-COM-PHYS-2003-049, 2003.

[37] E. Bouhova-Thacker *et al*. Studies into the impact of inner detector misalignments on physics. Technical Report ATL-PHYS-PUB-2009-080. ATL-COM-PHYS-2009-281, 2009.

[38] E. Bouhova-Thacker *et al*. Impact of inner detector and muon spectrometer misalignments on physics. Technical report, 2009. ATL-COM-GEN-2009-022.

[39] ATLAS Collaboration. Misalignment and b-tagging. Technical report, 2009. ATL-PHYS-PUB-2009-020.

[40] S. González-Sevilla. *ATLAS Inner detector performance and alignment studies*. PhD thesis, Universitat de València, 2008.

[41] The ATLAS Collaboration. Pixel Detector Technical Design Report. 1998. CERN/LHCC 98-13.

[42] A. Abdesselam *et al*. Engineering for the ATLAS SemiConductor Tracker (SCT) end-cap. *JINST*, 3:P05002, 2008.

[43] Project specification: Abcd3t asic. Technical Report Version: V1.2, 2000.

[44] A. Ahmad *et al*. The Silicon microstrip sensors of the ATLAS semiconductor tracker. *Nucl. Instrum. Meth.*, A578:98–118, 2007.

[45] The ATLAS Collaboration. ATLAS Detector and Physics Technical Design Report. 1999. CERN/LHCC/99-14. CERN/LHCC/99-15.

[46] InDetGeometryFrames twiki. 2009. https://twiki.cern.ch/twiki/bin/view/Atlas/InDetGeometryFrames.

[47] S. Haywood. Local Coordinate Frames for Alignment of Silicon Detectors. 2004. ATL-COM-INDET-2004-001.

[48] R. Hawkings. Coordinate Frames for Offine Reconstruction. 2006. ATL-COM-SOFT-2006-019.

[49] B. Nicquevert. Co-ordinate axis systems. Technical Report ATL-GE-QA-2041, CERN, Geneva, Apr 1998.

[50] A. Bocci and W. Hulsbergen. TRT Alignment For SR1 Cosmics and Beyond. *ATL-INDET-PUB-2007-009. ATL-COM-INDET-2007-011, CERN-ATL-COM-INDET-2007-01*, 2007.

[51] P. Åkesson *et al*. Atlas tracking event data model. Technical Report ATL-SOFT-PUB-2006-004. ATL-COM-SOFT-2006-005. CERN-ATL-COM-SOFT-2006-005, CERN, Geneva, Jul 2006.

[52] T. Cornelissen *et al*. Updates of the atlas tracking event data model (release 13). Technical Report ATL-SOFT-PUB-2007-003. ATL-COM-SOFT-2007-008, CERN, Geneva, Jun 2007.

[53] A. Ahmad *et al*. Alignment of the pixel and sct modules for the 2004 atlas combined test beam. *J. Instrum.*, 3(arXiv:0805.3984):P09004. 22 p, May 2008.

[54] R. Härtel. *Iterative local Chi2 alignment approach for the ATLAS SCT detector*. PhD thesis, Master's thesis MPI Munich MPP-2005-174, 2005.

[55] T. Golling. Alignment of the Silicon Tracking Detector using Survey Constraints. Technical Report ATL-INDET-PUB-2006-001. ATL-COM-INDET-2006-002 CERN-ATL-INDET-PUB-2006-001, CERN, Geneva, Mar 2006.

[56] V. Kostyukhin A. Andreazza and R. J. Madaras. Survey of the atlas pixel detector components. Technical Report ATL-INDET-PUB-2008-012. ATL-COM-INDET-2008-006, CERN, Geneva, Mar 2008.

[57] A. Catinaccio. Inner detector survey and positioning inside atlas. Technical Report ATL-I-ER-0013, CERN, Geneva, Jun 2008.

[58] The ATLAS Collaboration, D. Adams *et al*. The ATLAS Computing Model. 2005. CERN-LHCC-2004-037/G-085.

[59] B. Pinto. Alignment data stream for the atlas inner detector. Technical Report To be published in the CHEP09 proceedings, 2009.

[60] The ATLAS Collaboration. Athena. The ATLAS Common Framework. Developer Guide. 2004.

[61] The LHCb Collaboration. LHCb software architecture group. GAUDI-Architecture design document. CERN-LHCb-98-064.

[62] Z. Broklova *et al*. SCT End-Cap Module Description In Athena Framework. 2005. CERN-ATL-INDET-INT-2005-001; ATL-COM-INDET-2005-006.

[63] O. E. Brandt and P. Bruckman de Renstrom. Hit Quality Selection for Track-Based Alignment with the InDetAlignHitQualSelTool in M8+. 2009. ATL-COM-INDET-2009-015.

[64] F. Heinemann. *Robust Track Based Alignment of the ATLAS Silicon Detectors and Assessing Parton Distribution Uncertainties in Drell-Yan Processes*. PhD thesis, University of Oxford, 2007.

[65] O. Brandt *et al*. Extension of the track-based robust alignment algorithm for the atlas silicon tracker. Technical Report ATL-COM-INDET-2009-041, 2009.

[66] J. Alison *et al*. Alignment of the inner detector using misaligned csc data. Technical Report ATL-COM-INDET-2008-014, CERN, Geneva, Sep 2009.

[67] J. Alison *et al*. Inner detector alignment within the atlas full dress rehearsal. Technical Report ATL-COM-INDET-2009-033, CERN, Geneva, Jul 2009.

[68] E. Abat *et al*. Combined performance tests before installation of the atlas semiconductor and transition radiation tracking detectors. *J. Instrum.*, 3:P08003. 67 p, 2008.

[69] The ATLAS Collaboration. Alignment of the atlas inner detector using cosmic tracks. Technical Report To be published, 2009.

[70] T. Göttfert. *Iterative local Chi2 alignment algorithm for the ATLAS Pixel detector*. PhD thesis, Master's thesis University Würzburg and MPI Munich MPP-2006-118, 2006.

[71] P. Brückman de Renström, A. Hicheur, S. Haywood. Globalχ^2 approach to the Alignment of the ATLAS Silicon Tracking Detectors. *ATL-INDET-2005-002*, 2005.

[72] S. M. Gibson. The ATLAS SCT Alignment System and a Comparative Study of Misalignment at CDF and ATLAS. 2004. PhD. Thesis.

[73] F. James. *Statistical Methods in Experimental Physics*, volume 2nd Edition. 2006.

[74] V. Blobel. Millepede: Linear Least Squares Fits with Large Number of Parameters. *Nucl. Instrum. Meth. A 566*, 2006.

[75] M. Karagöz Ünel and P. Brückman de Renström. Parallel computing studies for the alignment of the ATLAS Silicon Tracker. *Proceedings of the Statistical problems in Particle Physics, Astrophysics and Cosmology conference (CHEP06), Mumbai (India)*, 2006.

[76] G. Z. Molière. *Theorie der Streuung schneller geladener Teilchen. I. Einzelstreuung am abgeschirmten Coulomb-Field*, volume Z. Naturforsch 2a, 133 - 145. 1947.

[77] G. Z. Molière. *Theorie der Streuung schneller geladener Teilchen. II. Mehrfach- und Vielfachstreuung*, volume Z. Naturforsch 3a 78 - 97. 1948.

[78] T. Cornelissen. *Track fitting in the ATLAS Experiment*. PhD thesis, Nationaal Instituut voor Kernfysica en Hoge-Energiefysica (NIKHEF), 2006.

[79] S. Martí and M. J. Costa. Track fitting and alignment (in ATLAS). *Taller de Altas Energías (TAE)*, September 2009. http://www.hep.uniovi.es/TAE2009/presentations/100909-2-ATLAS-SMarti.pdf.

[80] B. M. Irons. A frontal solution scheme for finite element analysis. 1970. Int. J. Numer. Methods Eng. 2, 5–32.

[81] C. C. Paige and M. A. Saunders. Solution of sparse indefinite systems of linear equations. 1975. SIAM J. Numerical Analysis 12, 617-629.

[82] CLHEP - A Class Library for High Energy Physics (Reference Guide). http://wwwasd.web.cern.ch/wwwasd/lhc++/clhep/manual/RefGuide/index.html.

[83] BLAS (Basic Linear Algebra Subprograms). http://www.netlib.org/blas.

[84] LAPACK - Linear Algebra PACKage. http://www.netlib.org/lapack.

[85] ScaLAPACK - Scalable Linear Algebra PACKage. http://www.netlib.org/scalapack.

[86] SiGlobalChi2AlgebraUtils package documentation. https://twiki.cern.ch/twiki/bin/view/Atlas/SiGlobalChi2AlgebraUtils.

[87] S. González-Sevilla and J. Sanchez. ALINEATOR - Meeting Silicio (IFIC). 2007. Private communication.

[88] Myrinet. Open Specifications and Documentation. *Myricom, Inc*, 2009. http://www.myri.com/open-specs/.

[89] InfiniBand Architecture Specification. *InfiniBand Trade Association*, 2009. http://www.infinibandta.org.

[90] The Message Passing Interface (MPI) standard. http://www.mcs.anl.gov/research/projects/mpi/.

[91] Alineator twiki. https://twiki.ific.uv.es/twiki/bin/view/Atlas/Alineator.

[92] I. S. Duff and J. K. Reid. MA27 - A set of Fortran subroutines for solving sparse symmetric sets of linear equations. 1982. Tech. AERE R10533, HMSO, London.

[93] I. S. Duff and S. Iain. Ma57 - a code for the solution of sparse symmetric definite and indefinite systems. *ACM Trans. Math. Softw.*, 2004.

[94] PARDISO Solver Project. http://www.pardiso-project.org.

[95] ARPACK Software. http://www.caam.rice.edu/software/ARPACK.

[96] V. Blobel. Alignement algorithms. *1st LHC Detector Alignment Workshop proceedings*, 2007.

[97] B. D. Cooper J. Alison and T. Goettfert. Production of residual systematically misaligned geometries for the atlas inner detector. Technical Report ATL-INDET-INT-2009-003. ATL-COM-INDET-2009-003, CERN, Geneva, Oct 2009. Approval requested a second time to resolve issues in CDS.

[98] A. Ahmad, D.Froidevaux, S.González-Sevilla, G.Gorfine and H.Sandaker. Inner Detector as-built detector description validation for CSC. *ATL-INDET-INT-2007-002*, 2007.

[99] W. Seligman, M. Shapiro, I. Hinchliffe, M. Zdrazil. Cosmic Generator. https://svnweb.cern.ch/trac/atlasoff/browser/Generators/CosmicGenerator/trunk.

[100] W. Ashmanskas *et al*. Performance of the CDF online silicon vertex tracker. *IEEE Trans. Nucl. Sci.*, 49:1177–1184, 2002.

[101] C. Escobar. Why do we need cosmics? *Inner Detector Alignment meeting*, October 2007. http://indico.cern.ch/conferenceDisplay.py?confId=22676.

[102] J. Alison *et al*. Inner detector alignment and performance monitoring. Technical Report ATL-INDET-INT-2009-006. ATL-COM-INDET-2009-027, CERN, Geneva, Jun 2009.

[103] O. C. Allkofer *et al*. Electromagnetic Interactions of High-Energy Cosmic-Ray Muons. Phys. Rev. D 4, 638 (1971).

[104] C. Escobar. Global Alignmnent using SR1 cosmics. *Inner Detector Alignment meeting*, December 2006. http://indico.cern.ch/conferenceDisplay.py?confId=9338.

[105] R. Achenbach *et al*. Analysis of the initial performance of the atlas level-1 calorimeter trigger. (ATL-DAQ-PROC-2008-005. ATL-COM-DAQ-2008-010):5 p, Sep 2008. this note was endorsed by the TDAQ project leader.

[106] The ATLAS Collaboration. The ATLAS Inner Detector commissioning and calibration. *arXiv:1004.5293v1 [physics.ins-det]*, 2010.

[107] R. Crupi. Muon reconstruction and selection at the last trigger level of the atlas experiment. Technical Report ATL-DAQ-PROC-2009-041. ATL-COM-DAQ-2009-106, CERN, Geneva, Dec 2009.

[108] S. Ask J. Lane and J. Masik. Track reconstruction in the atlas high level trigger using cosmic ray muons. Technical Report ATL-DAQ-PROC-2009-038. ATL-COM-DAQ-2009-136, CERN, Geneva, Nov 2009.

[109] M. J. Costa T. Cornelissen and M. Moreno Llacer. Atlas combined muon performance with cosmic rays data. Technical Report ATL-COM-PHYS-2009-632, CERN, Geneva, Dec 2009.

[110] S. Agostinelli *et al*. Geant4: A simulation toolkit. Nucl. Instrum. Meth. A506 (2003) 250303.

[111] K. Assamagan *et al*. The atlas monte carlo project. Technical Report ATL-COM-SOFT-2008-024, CERN, Dec 2008.

[112] A. Dar. Atm. Neutrinos, Astrophysical Neutrons and Proton-Decay experiments. *Physics Review Letters 51 (1983) 227*.

[113] J. Schieck. ATLAS Inner Detector Alignment with Cosmics. *3rd LHC Detector Alignment Workshop*, June 2009. http://indico.cern.ch/conferenceOtherViews.py?view=standard&confId=50502.

[114] Approved Combined Inner Detector Plots. 2009. https://twiki.cern.ch/twiki/bin/view/Atlas/ApprovedPlotsID.

[115] R. Moles *et al*. Cosmic09 alignment. *Inner Detector Alignment EVO meeting*, December 2009. http://indicobeta.cern.ch/conferenceDisplay.py?confId=75804.

[116] Public Run Statistics and Luminosity Plots for Collision Data. 2009. https://twiki.cern.ch/twiki/bin/view/Atlas/RunStatsPublicResults.

[117] T. Golling *et al*. Alignment Monitoring with first data. *Inner Detector Alignment EVO meeting*, December 2009. http://indicobeta.cern.ch/conferenceDisplay.py?confId=75805.

[118] Public Inner Detector Plots for Collision Data. 2009. https://twiki.cern.ch/twiki/bin/view/Atlas/InnerDetPublicResults.

[119] F. Abe *et al*. Observation of top quark production in $\bar{p}p$ collisions. *Phys. Rev. Lett.*, 74:2626–2631, 1995.

[120] S. Abachi *et al*. Observation of the top quark. *Phys. Rev. Lett.*, 74:2632–2637, 1995.

[121] The DONUT Collaboration. Observation of Tau Neutrino Interactions. *Phys.Lett.B504:218-224,2001*.

[122] A. Sirlin. Radiative corrections in the $su(2)_L \times u(1)$ theory: A simple renormalization framework. *Phys. Rev. D 22, 971981*, Aug 1980.

[123] *et al*. D0 Collaboration. V. Abazov. Combination of ttbar cross section measurements and constraints on the mass of the top quark and its decays into charged higgs bosons. *arXiv:0903.5525v2 [hep-ex]*, 2009.

[124] L. Randall and R. Sundrum. An Alternative to Compactification. *Phys.Rev.Lett.83:4690-4693*. *arXiv:hep-th/9906064v1*, 1999.

[125] M. Cacciari, S. Frixione, G. Ridolfi, M. Mangano and P. Nason. 2008.

[126] N. Kidonakis and R. Vogt. *arXiv:0805:3844*, 2008.

[127] S. Moch and P. Uwer. *arXiv:0807.2794*, 2008.

[128] I. Antoniadis *et al*. New Dimensions at a Millimeter to a Fermi and Superstrings at a TeV. *Phys.Lett.B436:257-263*. *arXiv:hep-ph/9804398v1*, 1998.

[129] N. Kidonakis. Higher-order corrections to top-antitop pair and single top quark production. *arXiv:0909.0037v1 [hep-ph]*, 2009.

[130] TopPhysicsTwiki twiki (2008 Production section). 2009. https://twiki.ific.uv.es/twiki/bin/view/Atlas/TopPhysics#2008_Production_Release_14_2_x_1.

[131] AlignmentForDayZero twiki. 2009. https://twiki.cern.ch/twiki/bin/view/Atlas/AlignmentForDayZero.

[132] Search for the standard model higgs boson at lep. Technical Report DELPHI-2001-113-CONF-536. CERN-DELPHI-2001-113-CONF-536. L3-Note-2699. OPAL-Physics-Note-PN-479. LHWG-Note-2001-03. CERN-ALEPH-CONF-2001-046. CERN-ALEPH-2001-066. CERN-EP-2001-055, CERN, Geneva, Jul 2001.

[133] I. Borjanovic *et al*. Investigation of top mass measurements with the ATLAS detector at LHC. *Eur. Phys. J.*, C39S2:63–90, 2005.

[134] TopView Ntuple Availability twiki. 2008. https://twiki.cern.ch/twiki/bin/viewauth/AtlasProtected/TopNtupleAvailability.

[135] Top level tags in the ATLAS Geometry Database twiki. 2009. https://twiki.cern.ch/twiki/bin/view/Atlas/AtlasGeomDBTags.

[136] Cool Production Tags twiki. 2009. https://twiki.cern.ch/twiki/bin/view/Atlas/CoolProdTags.

[137] S. Frixione and B. R. Webber. Matching NLO QCD computations and parton shower simulations. 2002. JHEP06(2002)029.

[138] S. Frixione *et al*. Single-top hadroproduction in association with a W boson. 2008. JHEP07(2002)029.

[139] S. Hassani *et al*. A muon identification and combined reconstruction procedure for the atlas detector at the lhc using (muonboy, staco, mutag) reconstruction packages. *NIM A572*, pages 77–79, 2007.

[140] J. Abdallah *et al*. Atlas Missing ET overall performance. 2008. CSC note to be published as ATLAS internal note.

[141] V. Kostioukhine. VKalVrt - package for vertex reconstruction in ATLAS. *Geneva: CERN, 25 Aug 2003.- 18 p*.

[142] A. I. Etienvre, A. Marzin, J. P. Meyer and J. Schwindling. Top quark mass measurement in the lepton plus jets channel with a kinematic fit on the full final state. *ATL-PHYS-INT-2008-021. ATL-COM-PHYS-2008-049*, 2008.

[143] Top Physics at IFIC twiki (2008 Production section). https://twiki.ific.uv.es/twiki/bin/view/Atlas/TopPhysics#2008_Production_Release_14_2_x_1.

[144] ROOT Website. http://root.cern.ch.

[145] A. Shibata. Topview - atlas top physics analysis package. Technical Report ATL-SOFT-PUB-2007-002. ATL-COM-SOFT-2007-006. CERN-ATL-COM-SOFT-2007-006, CERN, Geneva, May 2007.

[146] I. Borjanovic *et al*. Investigation of top mass measurements with the ATLAS detector at LHC. *Eur.Phys.J. C39S2 (2005) 63-90*.

[147] W. M. Yao *et al*. (Particle Data Group). The Review of Particle Physics. 2006. Journal of Physics G33.

[148] C. Peterson *et al*. Scaling violations in inclusive e+e- annihilation spectra. 1983. Phys. Rev. D 27, 105111.

[149] T. Cornelissen. CTBTracking: track reconstruction for the testbeam and cosmics. *ATL-INDET-INT-2006-001. ATL-COM-INDET-2006-003*, 2006.

[150] P. Brückman de Renström and S. Haywood. Least Squares approach to the alignment of the generic high precision tracking system. *Proceedings of the Computing in High Energy and Nuclear Physics conference (PHYSTAT05), Oxford (UK)*, 2005.

[151] G. Corcella *et al*. HERWIG 6.5. 2001. JHEP0101(2001)010.

[152] J. M. Butterworth *et al*. Multiparton Interactions in Photoproduction at HERA. *Z.Phys.C72:637-646*, 1996.

[153] JIMMY Generator. http://projects.hepforge.org/jimmy.

[154] C. Buttar A. Moraes and I. Dawson. Prediction for minimum bias and the underlying event at LHC energies. *Eur. Phys. J.*, C50:435–466, 2007.

[155] M. L. Mangano *et al*. ALPGEN, a generator for hard multiparton processes in hadronic collisions. 2003. JHEP07(2003)001.

The Large Hadron Collider (LHC) era started with its first proton-proton collisions produced in November 2009 at the CERN laboratory. In the coming decade, the high energy physics program will be dominated by the LHC and its experiments. Discoveries such as the Higgs or supersymmetric particles are some of the dreams that hopefully the LHC will bring us. This thesis is framed within the ATLAS experiment, which is one of the four large detectors located at the LHC.

The work presented in this thesis is divided in two parts. The first part is dedicated to the alignment of the ATLAS silicon tracking detector using the Globalχ^2 algorithm, which is the actual baseline algorithm. It covers performance studies with Monte Carlo samples with a realistic detector description, with real cosmic rays as well as with LHC collisions at 900 GeV. The main achievement was the production of a set of alignment constants for the real ATLAS detector. Those constants were obtained from the alignment of real cosmic ray data, and they were used to successfully reconstruct the first ever LHC collisions. The second part is devoted to perform preliminary studies of the top quark mass measurement based on Monte Carlo samples at 14 TeV, and considering 1 fb^{-1} of integrated luminosity. In particular, the semileptonic decay channel of the $t\bar{t}$ pair is used to perform a kinematic fit based on the Globalχ^2 formalism. Actually, the main goal of this part is the introduction this method, though the achieved performance is evaluated, discussing its advantages, limitations and, of course, results.

VNIVERSITAT DE VALÈNCIA